Light-induced dynamics in photoactive metal complexes with secondary chromophores

Dissertation

- kumulative Dissertation -

zur Erlangung des akademischen Grades doctor rerum naturalium

(Dr. rer. nat)

FRIEDRICH-SCHILLER-UNIVERSITÄT JENA

vorgelegt dem Rat der Chemisch-Geowissenschatlichen Fakultät der
Friedrich-Schiller-Universität Jena

von Diplom-Chemiker Joachim Kübel
geboren am 15. April 1988 in Gießen

Gutachter:

1. Prof. Dr. Benjamin Dietzek, Institut für Physikalische Chemie, Friedrich-Schiller-Universität Jena

2. Prof. Dr. Antonín Vlček, School of Biological and Chemical Sciences, Queen Mary University of London, United Kingdom

3. apl. Prof. Dr. Michael Schmitt, Institut für Physikalische Chemie, Friedrich-Schiller-Universität Jena

Tag der öffentlichen Verteidigung: 25. Oktober 2017

Contents

Contents

Publication authorship declaration

Erklärung zu Eigenanteilen an Publikationen und Zweitpublikationsrechten bei einer kumulativen Dissertation

Für alle in dieser kumulativen Dissertation verwendeten Manuskripte liegen die notwendigen Genehmigungen der Verlage („Reprint permissions") für die Zweitpublikation vor.

Die Co-Autoren der in dieser kumulativen Dissertation verwendeten Manuskripte sind sowohl über die Nutzung, als auch über die auf den folgenden Seiten angegebenen Eigenanteile der weiteren Doktoranden/Doktorandinnen als Koautoren an den Publikationen informiert und Zweitpublikationsrechten bei einer kumulativen Dissertation informiert und stimmen dem zu (es wird empfohlen, diese grundsätzliche Zustimmung bereits mit Einreichung der Veröffentlichung einzuholen bzw. die Gewichtung der Anteile parallel zur Einreichung zu klären).

Joachim Kübel   25.06.2017   Jena   . . . .

Ich bin mit der Abfassung der Dissertation als publikationsbasiert, d.h. kumulativ, einverstanden und bestätige die oben und auf den folgenden Seiten gegebenen Angaben. Eine entsprechend begründete Befürwortung mit Angabe des wissenschaftlichen Anteils des Doktoranden/der Doktorandin an den verwendeten Publikationen werde ich parallel an den Rat der Fakultät der Chemisch-Geowissenschaftlichen Fakultät richten.

Prof. Dr. Benjamin Dietzek   25.06.2017   Jena   . . . .

P1   Photoredox-active Dyads Based on a Ru(II) Photosensitizer Equipped with Electron Donor or Acceptor Polymer Chains: A Spectroscopic Study of Light-Induced Processes toward Efficient Charge Separation

Joachim Kübel*, Robert Schroot*, Maria Wächtler, Ulrich S. Schubert, Benjamin Dietzek and Michael Jäger

* both authors contributed equally

The Journal of Physical Chemistry C, **2015**, 119 (9), pp 4742–4751

DOI: 10.1021/acs.jpcc.5b00866

Authors	JK	RS	MW	USS	BD	MJ
Synthesis		✓				
Characterization	✓	✓			✓	
Time-resolved spectroscopy	✓					
Data analysis and processing	✓					
Data interpretation	✓		✓		✓	✓
Concept development		✓			✓	✓
Preparation of the manuscript	✓	✓				✓
Correction of the manuscript	✓	✓	✓	✓	✓	✓
Supervision of JK			✓		✓	
Proposed publication equivalents	**1.0**					

P2   New Ruthenium Bis(terpyridine) Methanofullerene and Pyrrolidino-fullerene Complexes: Synthesis and Electrochemical and Photophysical Properties

Kevin Barthelmes*, Joachim Kübel*, Andreas Winter, Maria Wächtler, Christian Friebe, Benjamin Dietzek and Ulrich S. Schubert

* both authors contributed equally

Inorganic Chemistry, **2015**, 54 (7), pp 3159–3171

DOI: 10.1021/ic502431x

This publication is part of the cumulative thesis of Kevin Barthelmes. There are no limitations for its further use in this thesis due to the complementary contributions as authors from different disciplines.

Authors	KB	JK	AW	MW	CF	BD	USS
Synthesis	✓						
Characterization	✓	✓		✓	✓		
Time-resolved spectroscopy		✓		✓			
Concept development	✓	✓	✓	✓		✓	
Preparation of the manuscript	✓	✓					
Correction of the manuscript		✓	✓	✓	✓	✓	✓
Supervision of JK				✓		✓	
Proposed publication equivalents	**1.0**						

P3 Structure–Property Relationships in an Iridium(III) Bis(Terpyridine) Complex with Extended Conjugated Side Chains

Joachim Kübel, Andreas Winter, Ulrich S. Schubert and Benjamin Dietzek

Authors	JK	AW	USS	BD
Synthesis		✓		
Characterization	✓	✓		
Time-resolved spectroscopy	✓			
Concept development	✓	✓	✓	✓
Preparation of the manuscript	✓			
Correction of the manuscript		✓	✓	✓
Supervision of JK				✓
Proposed publication equivalents	**1.0**			

P4 Energy transfer and formation of long-lived ^{3}MLCT states in multi-metallic complexes coordinating extended highly conjugated bis-terpyridyl ligands

Maria Wächtler, Joachim Kübel, Kevin Barthelmes, Andreas Winter, Alexander Schmiedel, Torbjörn Pascher, Christoph Lambert, Ulrich S. Schubert and Benjamin Dietzek.

Authors	MW	JK	KB	AW	AS	TP	CL	USS	BD
Synthesis			✓						
Characterization	✓	✓	✓						
Time-resolved spectroscopy	✓	✓			✓	✓			
Data analysis and processing	✓	✓							
Data interpretation	✓	✓							✓
Concept development	✓	✓	✓	✓				✓	✓
Preparation of the manuscript	✓								
Correction of the manuscript	✓	✓	✓	✓	✓	✓	✓	✓	✓
Supervision of JK	✓								✓
Proposed publication equivalents	**0.75**								

P5   Excitation-power modulates energy-transfer dynamics in a supramolecular RuII-FeII-RuII triad

Joachim Kübel, Maria Wächtler and Benjamin Dietzek.

Ursprüngliche Version:

Aktuelle Version:

Authors	JK	MW	BD
Time-resolved spectroscopy	✓		
Data analysis and processing	✓		
Data interpretation	✓	✓	✓
Concept development	✓	✓	✓
Preparation of the manuscript	✓		
Correction of the manuscript		✓	✓
Supervision of JK		✓	✓
Proposed publication equivalents	**1.0**		

P6 Efficient Energy Transfer and Metal Coupling in Cyanide-Bridged Heterodinuclear Complexes Based on (Bipyridine)(terpyridine)ruthenium(II) and (Phenylpyridine)iridium(III) Complexes

Kevin Barthelmes, Michael Jäger, Joachim Kübel, Christian Friebe, Andreas Winter, Maria Wächtler, Benjamin Dietzek and Ulrich S. Schubert

This publication is part of the cumulative thesis of Kevin Barthelmes. There are no limitations for its further use in this thesis due to the complementary contributions as authors from different disciplines.

Authors	KB	MJ	JK	CF	AW	MW	BD	USS
Synthesis	✓							
Characterization	✓		✓	✓				
Time-resolved spectroscopy			✓					
Data analysis and processing			✓					
Data interpretation	✓		✓			✓	✓	
Computational study		✓						
Concept development	✓							
Preparation of the manuscript	✓	✓	✓					
Correction of the manuscript		✓	✓	✓	✓	✓	✓	✓
Supervision of JK						✓	✓	
Proposed publication equivalents			**0.5**					

List of abbreviations and symbols

Spectroscopic methods and terms

EPR	electron paramagnetic resonance
OD	optical density
SEC	spectroelectrochemistry
SC	streak camera
TA	transient absorption
TCSPC	time-correlated single photon counting
Ti:Sa	titanium doped sapphire (Al_2O_3)
UV	ultraviolet
VIS	visible

Chemical terms

ACN	acetonitrile
bpy	2,2'-bipyridine
*t*Bu	*tert*-butyl
DCM	dichloromethane
DMF	*N,N*-dimethylformamide
DMPU	*N,N*-dimethylpyrrolidine-urimid
dtbbpy	4,4'-di-*tert*-butyl-2,2'-bipyridine
Me	methyl
Mes	mesityl (2,4,6-trimethylbenzyl)
NDI	naphthalene-diimide

Ph	phenyl
phen	1',10'-phenanthroline
ppy	2-phenylpyridine
TEA	triethylamine
THF	tetrahydrofuran
TOL	toluene
tpy	2,2':6',2"-terpyridine
ttpy	4'-tolyl-2,2':6',2"-terpyridine

Photophysics

CT	charge-transfer
MLCT	metal-to-ligand charge-transfer
LC	ligand-centered
ILCT	intramolecular/intraligand charge-transfer

List of Figures

1 Introduction

$$6\,CO_2 + 6\,H_2O + \text{sunlight} \longrightarrow C_6H_{12}O_6 + 6\,O_2$$

This very placative reaction equation is widely known as the summarizing description of photosynthesis.[1–3] The importance of this process can not be overestimated. Biologists and spectroscopists have been concerned with studying the structure and the function of the constituents forming the photosynthetic apparatuses for decades.[4,5] Due to the complexity of the natural systems, the precise determination of the structure of the sophisticated pigment arrays within the light-harvesting proteins of plants[6,7] and photosynthetic bacteria[8] has been a prerequisite for a molecular understanding of the data obtained from spectroscopic studies.

The refinement of the structures of the photosynthetic proteins is ongoing, and just recently structures of both the supercomplex between photosystem I (PSI) and light-harvesting complex I (LHCI, based on X-ray crystallography, $2.6\,\text{Å}$[9]) as well as the supercomplex between PSII and LHCII (based on cryo-electron microscopy, $3.2\,\text{Å}$[10]) could be determined.

The PSII membrane protein (Fig. 1.1) is dimeric and each monomer consists of several protein subunits which contain numerous chromophores (e.g. chlorophylls, carotenoids).[10–13] The sophisticated arrangement could only be studied through combined efforts of biochemists (by obtaining protein sequences and crystal structures) and spectroscopists (by applying cutting-edge methods such as broadband multidimensional spectroscopy). A common scheme in photosynthetic light-harvesting units is that the chromophores and with that their transition dipole moments are purposefully arranged relative to each other, which is crucial for controlling the transport of excitation energy between the individual molecules.[14,15] Much attention received the discovery of the distinctive energy transfer pathways between the seven chromophore molecules in the FENNA-MATTHEWS-OLSON-complex[16] (a light-harvesting protein found in photosynthetic bacteria) using multidimensional spectroscopy in the visible spectral region.[17] Long-lived beating patterns were tentatively attributed to electronic coherence,[18] suggesting that energy transfer in biological systems may be promoted

1

(a)

membrane

(b)

special pair

(c)

LHCII trimer

Mn$_4$CaO$_5$ cluster
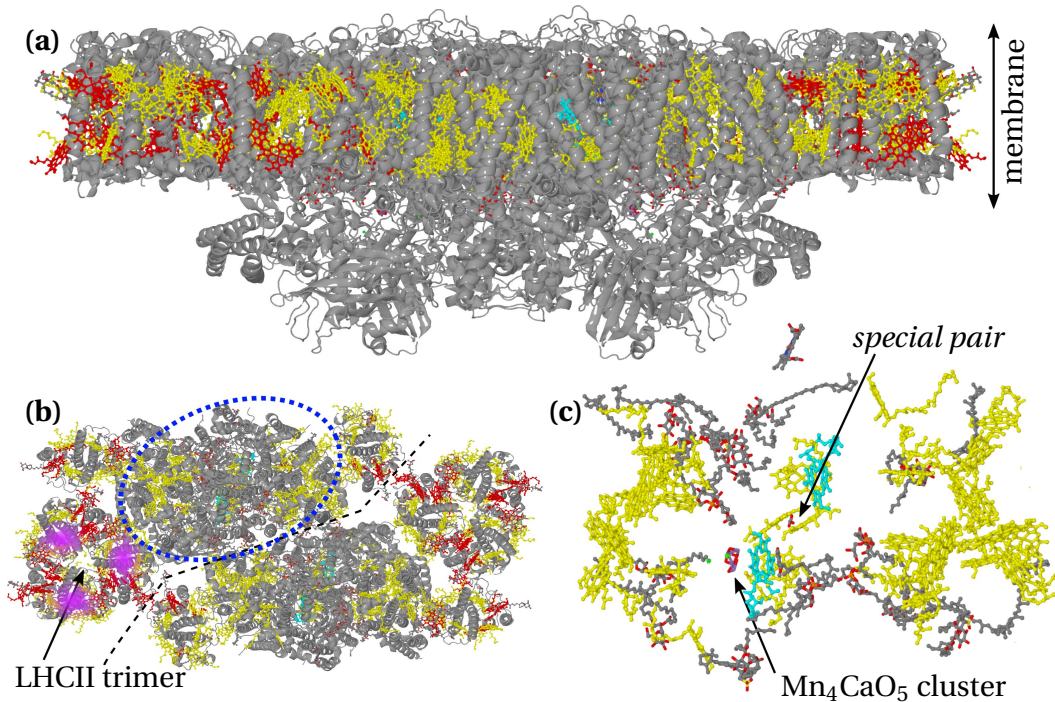
Figure 1.1: Structure of the supercomplex between plant photosystem II and light-harvesting complex II from spinach.[10] The chlorophyll a and b molecules are colored red and yellow, respectively. The pheophytin molecules are colored cyan. Panel (a): Front-view of the membrane showing the entire homo-dimer of the supercomplex. Panel (b): Top-view of the supercomplex showing the dimeric nature of the entity (the two units are divided approximately along the dashed line). The blue dashed ellipse marks the PSII core complex. Panel (c): Top-view of the PSII core complex (the protein backbone is omitted for clarity) showing the sophisticated arrangement of the reaction center. The figures were created using Jmol and the protein structure 3JCU from the Protein Data Bank (`http://www.rcsb.org`).

via quantum effects. This interpretation is however still heavily debated,[19] and alternative explanations for such oscillations have been suggested.[19–21] The antenna complex (LH2) of purple bacteria is much smaller as compared to the green plant LHC2, and quite well understood.[22]

Nevertheless, even excluding the possibility of quantum effects in natural light-harvesting, the energy transfer pathways and properties of the electron transfer chain in the light-harvesting antennas[23,24] and the reaction centers are quite complex and not understood in all detail. The lack of understanding is particularly pronounced with respect to the structural dynamics associated with the energy- and electron transfer processes. Direct probing of structural changes in photoactive proteins has recently become possible using the unique capabilities of X-ray free electron lasers.[25–27] However, such instrumentation is still rare, and corresponding experiments are vastly expensive and sophisticated.

An important, yet somewhat disillusioning conclusion that has to be drawn from the studies on natural photosynthesis is that the complexity of the natural photosynthetic apparatus is by far too sophisticated in order for it to be reproduced and adapted.[1,2,28,29] A main reason for that is that chromophores are embedded in a protein environment, thereby enforcing e.g. specific conformations. Furthermore, amino acids in the vicinity of the chromophores can markedly influence the electrostatic potential or even undergo specific interactions with the chromophores; through both mechanisms the chromophores may have quite different properties as compared to the isolated molecules in solution, which is certainly the case for almost any protein with a photoactive molecule as the primary light-responsive unit.[30–32] While the interactions between a protein environment and the embedded chromophores are often highly sophisticated, there are examples for which the specific interactions are quite well understood, e.g. for LH2 from purple bacteria:[33] Bacteriochlorophyll units undergo excitonic coupling,[33,34] which shifts their absorption spectra considerably to the red.[22,24,35]

While the natural systems are too complex to be artificially recreated, some structural aspects may be generalized and certain working principles and mechanisms may be adapted in artificial photosynthesis.[3,28,36]

The field of artificial photosynthesis has grown significantly in the past two decades and has been a hot topic in recent years as can be judged from the very high number of reviews available.[1,2,29,37–41] The overarching goal in artificial photosynthesis is the construction of functional artificial systems, which are capable of splitting water into

hydrogen and oxygen using sunlight. [38,41–44]

The fundamental fact that motivates efforts in this field is the relatively low energy necessary to drive the desired chemical reaction: 1.23 V is the reversible potential for water splitting. [45] In a microscopic picture, only 1.23 eV are needed to be inserted into chemical bonds; [46] this energy corresponds to a photon with a wavelength of ca. 1000 nm. This is just a bit more than half the energy contained in a photon in the visible portion of the electromagnetic spectrum (a green photon at 530 nm corresponds to an energy of 2.34 eV). However, things are apparently not as simple as they might seem. This is partially because of energy dissipation into vibrational modes and into the surrounding solvent by collisions between the excited chromophore and solvent molecules. While such intrinsic relaxation mechanisms are hardly avoidable, molecular design can be optimized in order to limit energy loss on early time-scales and guide the excited-state relaxation into *productive* channels as desired, e.g. by **efficient** and **directed** energy transfer processes and (essentially) **unidirectional** charge transfer. These principles are traceable in natural photosynthesis and essential to its success. [2,5,47]

There are two main directions or applications within artificial photosynthesis: On the one hand, in dye-sensitized solar cells light energy from sunlight is converted into electrical energy. [48–51] This is accomplished by linking a photosensitizer (PS, which can be a photoactive metal complex, an organic dye or a perovskite structure [52,53]) to the surface of a semiconductor. After initial excitation of the PS, depending on its redox abilities and the properties of the surface, charge carriers will be injected into the semiconductor surface: The excited state of the PS is quenched by electron transfer from the surface (e.g. nickel oxide, corresponding to a hole injection into the surface) or from the excited state to the semiconductor surface (e.g. for titanium dioxide). The charge on the PS is transferred to a redox mediator (e.g. I_2/I_3^-), leaving the PS in its initial state. The charged redox mediator transports the charge to the counter-electrode; the resulting electric potential can be tapped, or, in terms of research, fed into electronics for diagnostics.

On the other hand, excitation energy that is temporally available in the excited state of a photoactive compound may be exploited in supramolecular photocatalysis. [54–57] This approach aims at the conversion of light energy into chemical energy; most frequently the targeted molecules are hydrogen and oxygen from water splitting and carbon monoxide as reduction product from carbon dioxide. [57–62] The general layout consists of a primary light absorbing unit (the PS), which is brought in close vicinity to a catalytic unit (e.g. a metal complex or a nanoparticle). Following charge transfer between the excited
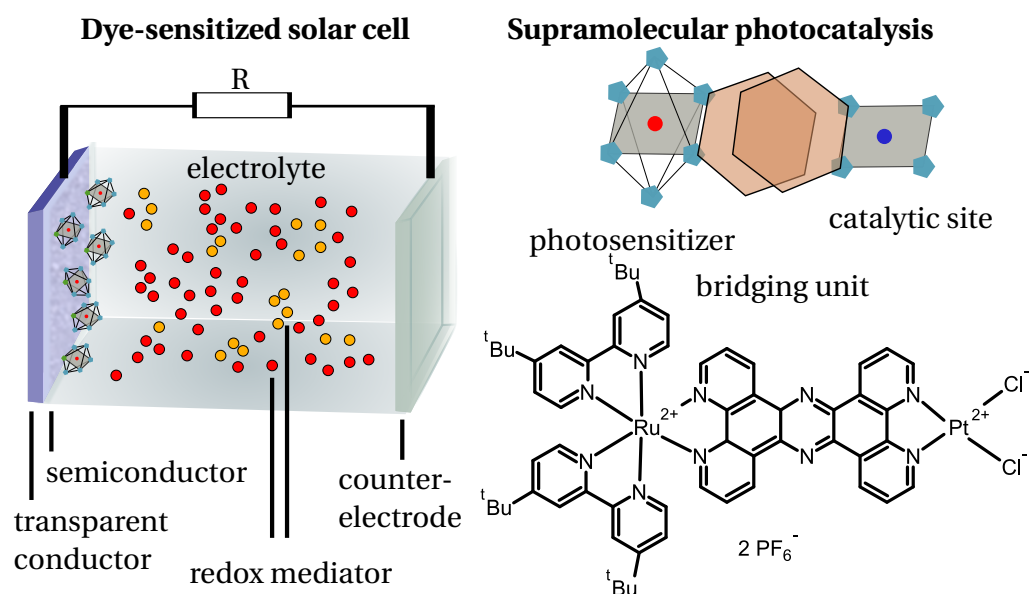
Figure 1.2: Illustrations showing the general layout of a dye-sensitized solar cell and a supramolecular photocatalyst. The chemical structure of a prototypical photocatalyst for hydrogen generation is given as reference. [58,62]

PS and the catalytic unit a chemical reaction is ought to occur due to the modulated redox potential of the catalytic unit.

Photoactive transition metal complexes play a fundamental role in the field of artificial photosynthesis. Most attention has been drawn to Ruthenium complexes, and Ruthenium-polypyridine complexes in particular. [63] In these complexes Ruthenium in the oxidation state +2 is coordinated in an octahedral environment by several pyridine-containing ligands (it may be noted that ligands with annulated pyridin rings, e.g. 1,10-phenanthrolin, also count as polypyridine ligands; a slightly more generalizing term which can be referred to is polyimine ligands). In such complexes there exist metal-to-ligand charge transfer (MLCT) states, in which an electron has been transferred from the metal d-orbitals onto one of the ligands. The electronic resonances of the respective transitions are typically in the visible spectral region with considerable oscillator strengths. [64,65] Their intrinsic properties render such metal complexes excellent model systems for fundamental studies on light-triggered processes in molecular systems. Apart from Ruthenium, also its homologues in the periodic table, Iron and Osmium, and to some extent their neighbors (Cobalt, Rhodium, Iridium) form complexes with similar ligand structures. Variation of the metal ion has strong impact on the photophysical properties of the respective metal complex.

A metal complex in its lowest excited MLCT state may be useful by itself, e.g. its

emission in organic light-emitting diodes [66] or ion sensing, [67] or, given its excited state lifetime is long enough to allow for reactive collisions with other molecules in solution, for chemical reactions: When a sacrificial electron donor (e.g. triethylamine or ascorbate) is added to the solution, which is an easily oxidizable compound that can reduce the oxidized metal complex, the basic requirements for photocatalysis are met: Driven by (sun-)light, a cheap electron donor is consumed in order to perform a desired chemical transformation based on a (one electron) reduction. This rather simple approach has proven to be useful in organic syntheses in the laboratory scale, [68] but is not suitable in the industrial scale due to a number of factors (e.g. the high cost of the rare transition metal catalyst and the difficult purification while retrieving the catalyst).

With respect to dye-sensitized solar cells or supramolecular photocatalysts, it is favorable to remove the charge from the ligand quickly and guide electron transfer on a *productive* pathway. By attaching suitable functional units to the ligand, the electron can be efficiently transferred away from the ligand to allow fast injection into a semiconductor surface or to create a long-lived charge-separated state.

This thesis contains detailed photophysical studies on mono- and multimetallic metal complexes with additional functional chromophores. The purpose of the presented studies is to analyze the photophysics in terms of excited-state processes and deactivation pathways with the goal to improve the general understanding of the relevant mechanisms and establish structure-property relationships. The presented studies are expected to provide relevant information and guidance regarding fundamental properties of metal complex chromophore dyads. The results may help to develop novel design concepts for photoactive materials.

The purpose of this thesis is to **investigate photophysical properties** of substituted photoactive transition metal complexes, to **characterize the electronic interplay** of the complexes with additional functional units and chromophores on the ligands and to **detail structural and electronic dynamics** upon photo-excitation of the metal complex or the adjacent chromophore.

1.1 Investigated chemical structures and their properties

Schematic representations of the metal complex-chromophore systems relevant to this thesis are sketched in Fig. 1.3. The systems discussed can be assigned to general architectures with specific coupling schemes. A central role with respect to the coupling play the structural and electronic properties of the bridging unit between the metal complex and the chromophore. The following types of structures are considered:

- The bridging unit contains one or several sp^3 hybridized carbon atoms. Such a bridge breaks the conjugation and inhibits electronic delocalization. Therefore in such structures essentially no electronic interactions in the ground state are observed. Systems of this type (**1**) discussed here are Ru(II) polypyridine complexes connected to an electron acceptor, such as naphthalene-diimide (NDI, Section 1.2.1) or C$_{60}$ fullerene (Section 2.1).

- The specific type of compounds regarded in the intermediate coupling regime are metal complexes based on 4'-phenyl substituted 2,2':6',2"-terpyridine (tpy) ligands with conjugated chromophores attached to the phenyl ring; in such complexes electronic delocalization of the ^{3}MLCT states is typically limited to the tpy-adjacent phenyl ring. [69–71] Nevertheless, there is moderate electronic interaction in the ground state between metal complex and chromophore, e.g. by formation of charge transfer states - in Ru(II), Fe(II), Os(II) or Ir(III) complexes with extended conjugated ligands (**2**, **3**, **4** and **5**, Sections 2.2 and 3.1).

- A cyanide ligand bridging two metal complexes causes close spatial proximity, and promotes electronic interaction of the metal centers. There is moderately strong interaction in the ground state, e.g. in the hetero-bimetallic cyanide-bridged Ir(III)-Ru(II) structures (**5**, Section 3.2).

- Very strong interaction in the ground state causes two chromophoric units to essentially become one - observed here in a phenanthroline-extended Cu(II) porphyrine with a binding site for a Ru(II) polypyridine complex (**6**, Section 3.3).

   If the electronic communication between complex fragment and secondary chromophore in the electronic ground state is rather weak, the electronic states can be regarded as spatially well separated. This is convenient for the creation of arrays including
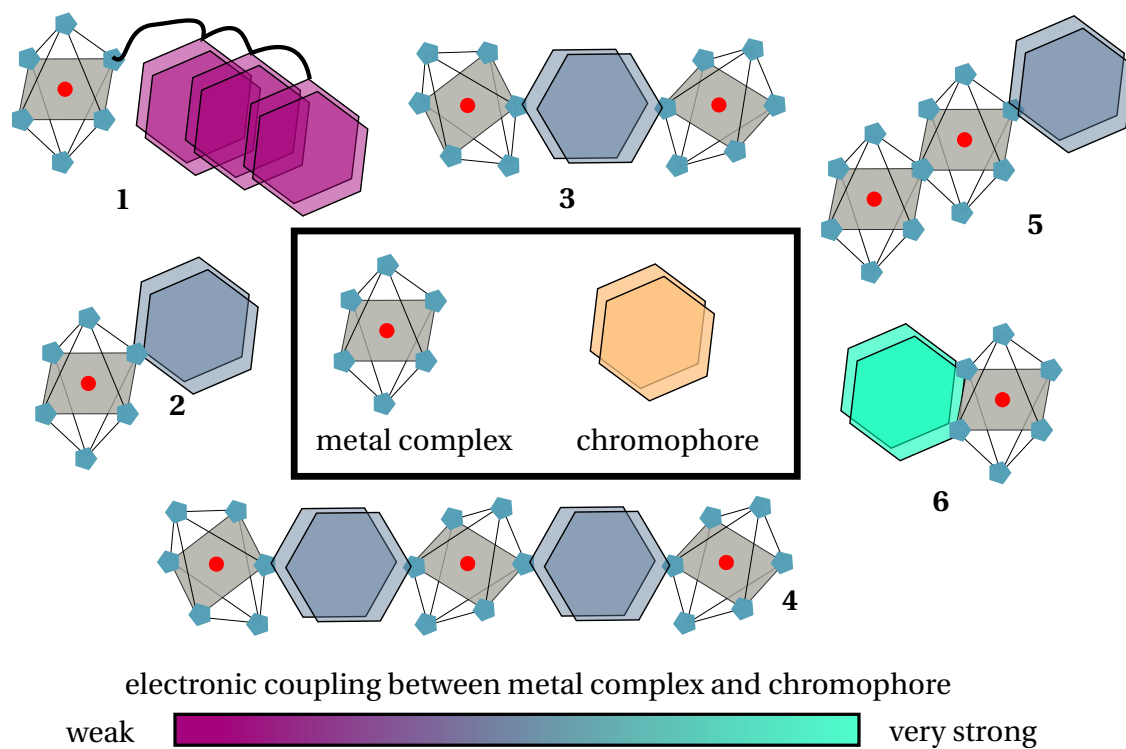
Figure 1.3: Schematic representation of different electronic coupling schemes in compounds relevant to this thesis.

multiple units, as properties of the individual units are mostly preserved upon coupling them. However, one exception from this behavior is presented in Section 3.3, where a phenanthroline-fused-tetra-mesityl porphyrin serves as ligand in a Ruthenium(II)-polypyridine complex. [72,73]

The photophysical properties of the molecular dyads and triads depend on the properties of the individual components, i.e. the isolated metal complexes and chromophores. Some constituents of the functional systems discussed in this thesis have already been subjects of earlier studies; novel aspects of the present systems will be pointed out and data is evaluated with respect to the data reported earlier.

The scientific approaches and experimental techniques applied in this thesis will be introduced in Section 1.2. In this context, selected data from publication **P1** is discussed to point out the scope and capabilities of the techniques and methods. The molecular structures involved are a Ru(II)-polyimine complex with donor- or acceptor-chromophores bound on a polymeric backbone and a heteroleptic cyclometallated Iridium(III)-complex.

The major part of this thesis deals with compounds based on 4'-substituted 2,2':6',2''-terpyridine (in short tpy). The general design of these compounds is derived from phenylene-vinylene-structures, [74–76] with tpy units as metal binding sites. A noteworthy structural feature of such systems is the linear arrangement of the substituents in 4' positions. This has important implications on the functionality of these arrays, e.g. by avoiding close interaction between the chromophores attached on opposite sides of the metal complex. [64] The linear structure of polymeric arrays based on 4'-connected tpy units has been demonstrated. [77–80] By complementing the well-defined architecture with a well-defined energetic landscape, hierarchic structures based on coordination oligomers may be created. This requires the combination of suitable functional chromophores and metal complex fragments. Here, the photophysical properties of building blocks for such arrays are discussed. The compounds are constructed with reappearing structural features as schematically shown in Fig. 1.4. The photophysical properties of compounds following this general architecture have been subject of earlier studies in the Dietzek group: ligands [81,82], mono- [71,83–85], and homo-bimetallic complexes [85]. For this thesis, additional functional units are included such as fullerene C_{60} as electron acceptor (Section 2.1), the variety of metal ions is increased by considering Iridium(III) as central ion in the tpy complexes (Section 2.2) and the scope of photophysical processes and complexity is increased by inspecting hetero-multimetallic complexes (Sections 3.1
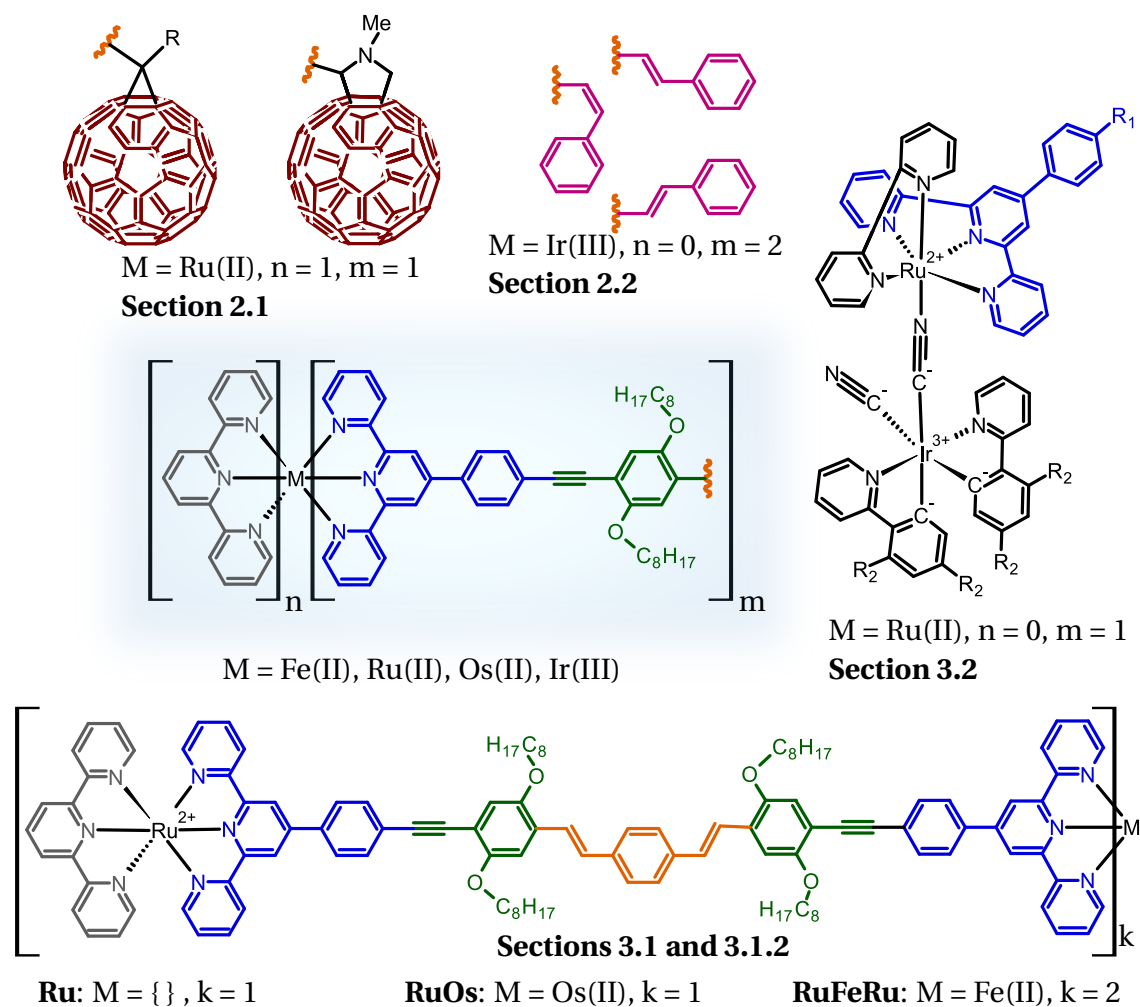
Figure 1.4: Overview of the compounds investigated in this thesis with potential to be used as building blocks for hierarchic coordination oligomers based on 4'-substituted 2,2':6',2"-terpyridine. The corporate structural features are highlighted.

and 3.2). Of these, a trinuclear complex with two Ru-units and an Iron-tpy unit is subjected to high excitation fluence; under such conditions the photo-induced dynamics occurring as a result of multiple excited-states in the same molecule can be probed (Section 3.1.2). The compounds based on the tpy architecture were synthesized and characterized by Kevin Barthelmes and Dr. Andreas Winter in the group of Prof. Ulrich S. Schubert (Laboratory of Organic and Macromolecular Chemistry, Friedrich Schiller University Jena).

In Section 3.3 the photophysics of the strongly coupled neocuproine-derived complex **CuRu** are discussed in light of the weak photocatalytic activity of this complex to reduce CO_2 to CO.

The thesis concludes by summarizing the most relevant results and provides an outlook to possible follow-up studies.

1.2 Methods and scientific approaches - the case of Ru-pNDI

Parts of this chapter have been published in this article: **P1** - J. Kübel, R. Schroot, M. Wächtler, U. S. Schubert, B. Dietzek, M. Jäger *J. Phys. Chem. C* **2015**, *119*, 4742-4751.

In this chapter the relevant photophysical background and processes are discussed. Subsequently the methods and experimental techniques employed to address the photophysical parameters will be introduced.

The **Ru-pNDI** system is used as a reference compound to illustrate the general methodological approaches. The relevant chemical structures are shown in Fig. 1.5. The metal complex (Ru(dqp)$_2$) is formed by a Ru^{2+} ion and two tridentate 2,6-di(quinolin-8-yl)pyridine (dqp) ligands. This type of ligand allows for the creation of linear arrays with respect to ligands in 4-position of the central pyridine ring as mentioned for tpy-based structures. However, **Ru-pNDI** is not a single conjugated compound, but individual chromophores are attached to a polymer chain. This way, the properties of the individual chromophores remain unaltered, but the chromophores can, if they are in close distance, participate in energy or charge transport. [86–88]

Two different chromophores placed in the side chain of a polymer are considered: A triarylamine as potential electron donor in **Ru-pTARA**, and a napthalene-diimide derivative as electron acceptor in **Ru-pNDI**.

2 PF$_6^-$ dpq = 2,6-di(quinolin-8-yl)pyridine

Rudqp: R=H

Rudqp-OH: R=OH

Ru-pNDI: R=O-pNDI

Ru-pTARA: R=O-pTARA

photosensitizer

$[Ru(dqp)(dqp-R)]^{2+}$

electron donor

electron acceptor
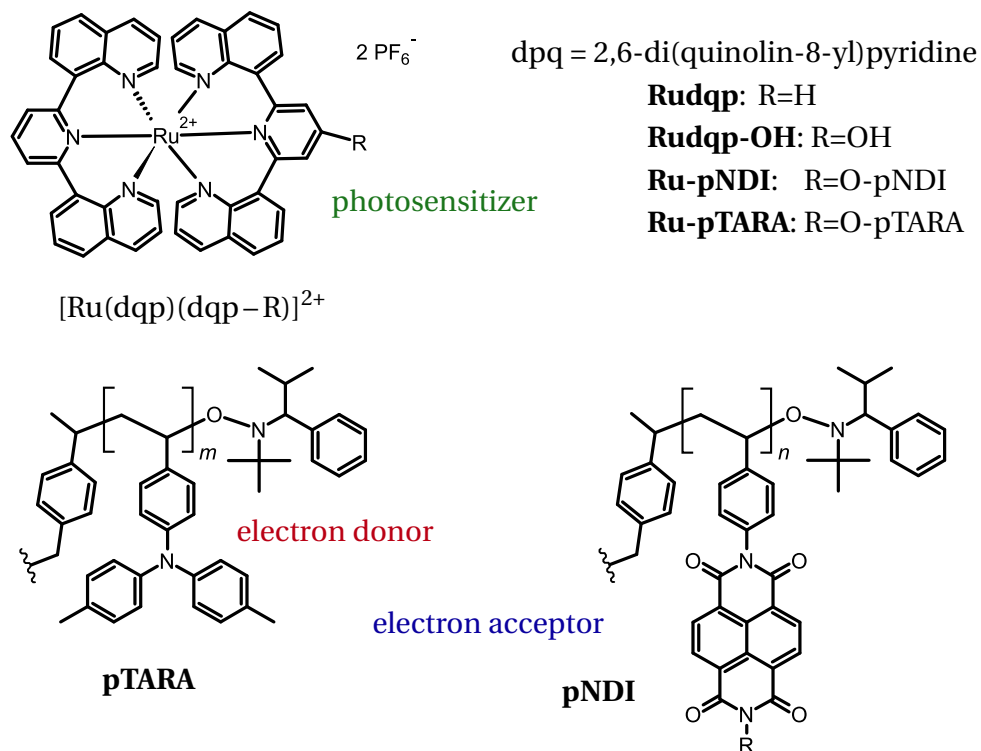
pTARA

pNDI

Figure 1.5: Chemical structures of the studied metal complex-polymer architectures created by Robert Schroot and Dr. Michael Jäger in the group of Prof. Ulrich S. Schubert (Laboratory of Organic and Macromolecular Chemistry, Friedrich Schiller University Jena). The number of chromophore units (m,n) is ca. 15 for **Ru-pTARA**. [89]

An overview over some of the photophysical processes occurring in the different functional chromophoric systems investigated in this thesis is shown in Fig. 1.6: The exemplary JABLONSKI diagram provides information on the excited state landscape of **Ru-pNDI** (structure given in Fig. 1.5).

The dominant, ligand-centered singlet transition ($^{NDI}S_1$) is identical for **Ru-pNDI** and **pNDI** (the pure acceptor polymer). Apart from a somewhat lower absorption between 250 to 350 nm, **pNDI** lacks the low-energy band centered at ca. 500 nm. The absorption spectrum of **Ru-pNDI** in the visible spectral region is dominated by the optically allowed singlet metal-to-ligand charge transfer (^{1}MLCT) transition. This transition is unique to the central Ru(II)-complex fragment. Noteworthy, the absorption spectrum of **Ru-pNDI** is identical to the sum of the absorption spectra of the components, **Rudqp-OH** and **pNDI**.[90] This suggests that electronic communication between both weakly coupled fragments is absent in the electronic ground state.

The **Ru-pNDI** system was designed to absorb visible light via the ^{1}MLCT-transition, which is the only electronic transition with considerable oscillator strength beyond 400 nm.

Excitation of the ^{1}MLCT band in the pristine metal complex **Rudqp-OH** leads to ^{3}MLCT-phosphorescence in absence of the **pNDI** acceptor polymer. This is explained by fast and frequently quantitative intersystem crossing (ISC) from the ^{1}MLCT state into the ^{3}MLCT state, as commonly observed in Ru(II)-polypyridine complexes.[91]

The ^{3}MLCT-emission is not observed for the coupled complex-chromophore system **Ru-pNDI**.[90] Such emission quenching can be caused by excitation energy transfer or reductive (oxidative) quenching corresponding to electron (hole) transfer. The spectroscopic tools that allow accessing the relevant electronic states in the visible spectral region and fast enough to monitor the relevant photophysical processes are (femtosecond-) transient absorption (TA) spectroscopy and time-resolved emission spectroscopy (TRE). The two methods are complementary: TA is sensitive to all electronic states, which possess spectral signatures in the probed spectral interval. Since the absorption cross section per molecule is very small, absorption spectroscopy in general is not considered a very sensitive method and produces signals that are ensemble averages. Contrary, common detectors used in emission spectroscopy, and TRE in particular, possess very high sensitivity down to the single photon level. Also, a single detected photon emitted from a sample already contains information, while information in absorption spectroscopy is only accessible through the detection of at least two photons. Due to the intrinsic contrast mechanism, emission spectroscopy

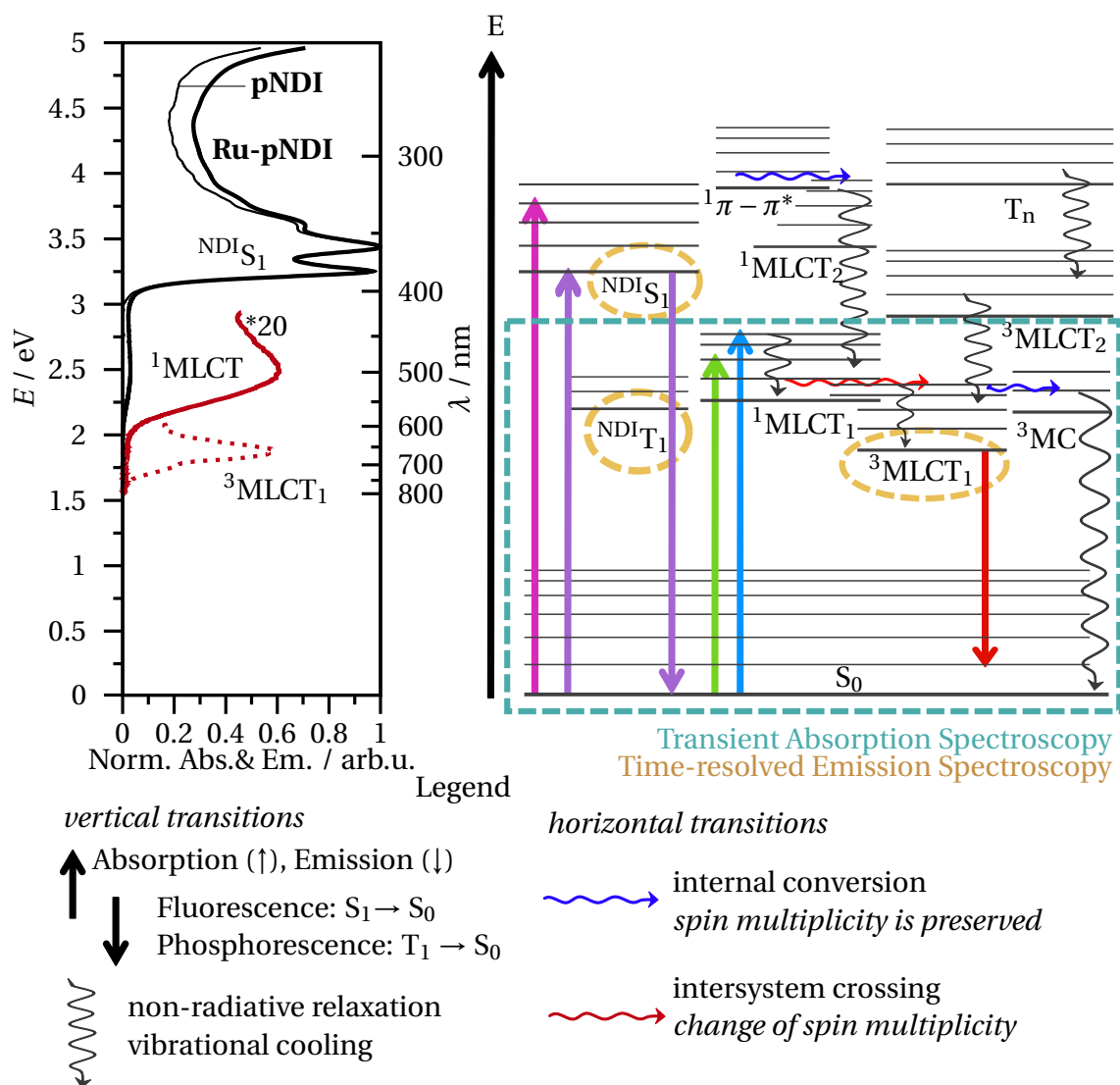**Figure 1.6:** UV/Vis absorption spectra (solvent: air-equilibrated Dichloromethane (DCM)) of
Ru-pNDI (thick black line) and **pNDI** (thin black line). The ^{1}MLCT band is scaled by
a factor of 20 (red line). The ^{3}MLCT-phosphorescence (dashed red line) shown is
that of **Rudqp-OH**. The bands in the spectra are lined up with the relevant electronic
states states in the JABLONSKI diagram.

is sensitive only to electronic states which decay radiatively (so-called bright states, as opposed to dark states, which do not decay radiatively). For the **Ru-pNDI** system, radiative relaxation is observed mainly for the ligand-centered $^{NDI}S_1$ and the lowest lying ^{3}MLCT state. These states are therefore accessible in emission spectroscopy. In order to clarify the mechanism of emission quenching, both TA and TRE experiments have been performed. The respective methods will be shortly introduced, followed by a discussion of the acquired data and its information content.

1.2.1 Introduction to transient absorption spectroscopy

The molecular processes that determine the fate of an excited-state in most molecules occur on timescales from hundreds of femtoseconds to few nanoseconds. [92–94] Probably the most common method to monitor the photophysical processes on such time scales is transient absorption spectroscopy: By applying a sequence of two pulses with tunable inter-pulse time delay, snapshots of the evolution in the excited-state following an initial excitation can be recorded. The method relies on the *pump-probe*-scheme: The first pulse (*pump*) initiates a photo-induced response of the sample and the second pulse (*probe*) interrogates the state of the excited sample after a chosen time delay. Typically, the *pump* is intense*, spectrally narrow and is tuned to be resonant to a selected electronic transition in the sample. On the other hand, the *probe* is rather weak (it should not serve as a second pump) and spectrally very broad in order to cover a large spectral range.

The transient absorption setups applied in this thesis are based on amplified titanium doped sapphire (Ti:Sa) lasers. The typical output of such laser (fourier-transform limited pulses centered around 800 nm, pulse durations ≤100 fs, pulse energies ≥1 mJ, repetition rate 1 kHz) is split as needed. The most intense portion is sent to an optical parametric amplifier (OPA), which is used to generate the tunable pump pulses with essentially arbitrary wavelengths throughout the visible spectrum (the UV region is accessible by subsequent frequency doubling). Broadband probe pulses are generated by focusing a strongly attenuated portion of the fundamental in a sapphire plate, which results in a super-continuum which allows covering a spectral window of ca. 460 to 710 nm. The relative polarization of pump and probe is set to 54.7° (magic angle) using a Berek compensator in the pump beam path in order to remove pseudo-kinetics due to rotational diffusion of the chromophores. Pump and probe beams are focused and

---

*Usually a few percent of the molecules in the focal spot should be excited. By increasing the pump power, the excitation probability is increased, which has been exploited in Section 3.1.2

overlapped at the sample position, where the chromophore in a chosen solvent is kept inside a 1 mm quartz cuvette. The probe beam is recollimated behind the sample and is sent, vertically offset from a reference portion of the probe beam, to the entrance slit of a spectrograph with a double stripe diode array at the exit. The diode array is read out at the repetition rate of the laser. A chopper in the pump beam path blocks every second pump pulse, such that two consecutive probe pulses hit the sample in a pumped (I_p) and un-pumped (I_0) state, respectively. The delay Δt between pump and probe is scanned using an optical delay line in the pump beam path. The transient optical density (OD) of the sample is calculated for all wavelengths and time points via[95]:

$$\Delta OD(\Delta t) = -\log_{10}\left(\frac{I_0}{I_p} \cdot \frac{I_p^{\mathrm{ref}}}{I_0^{\mathrm{ref}}}\right). \tag{1.1}$$

The possible signal contributions to ΔOD are explained below.

The differential optical density is - just as steady-state absorption data - interpretable based on the LAMBERT-BEER law in the presence of multiple species:

$$OD = \log_{10}\frac{I_0}{I} = d \cdot \sum_i (\varepsilon_i(\lambda) \cdot c_i(\Delta t)), \tag{1.2}$$

where ε is the absorption coefficient,[96] c the concentration and d the sample thickness. In TA, one has to consider the optical density as a function of delay time, and the typical (*bi-linear*) assumption is that the concentration is the only time-dependent parameter.[94] A TA dataset is a two-dimensional matrix depending on delay time and wavelength, which can be inspected in vertical or horizontal traces, corresponding to transient kinetics and absorption spectra, respectively. For a quantitative description of time-resolved datasets usually global analysis methods are applied. These are based on Eq. (1.2), i.e. the dataset is reconstructed from a number of discrete species each with a characteristic spectrum and kinetic profile (concentration as a function of delay time). More details on such procedures are provided in the appendix.

TA experiments depend on numerous parameters, and specific variation of e.g. pump wavelength or solvent allows to study the influence of these parameters on the observed signal. By changing the solvent, the influence of polarity and viscosity on the light-triggered processes can be studied.[97] Variation of the pump wavelength is particularly useful to unravel the photo-induced dynamics in the multimetallic arrays which are discussed in Chapter 3. The isolated excitation of an electronic transition of interest is most convenient, but possible mainly in structures in which - with respect to Fig. 1.3 -

metal complex and the additional chromophore are only weakly coupled (and ideally the absorption bands of the constituents are not overlapping in the spectral region of interest). In such cases, the isolated excitation of either chromophore is still possible in the coupled system. However, in the case of overlapping absorption bands and strong coupling, the simultaneous excitation of several transition might not be avoidable and will make data analysis more difficult.

Parameter variations such as excitation wavelength and solvent can be helpful to decipher complicated excited state dynamics. Another approach is the generation of possible transient species in separate experiments and determine their characteristic absorption features. In this regard, spectroelectrochemistry (SEC) has proven extremely useful to guide the interpretation of TA data from the UV to the mid-IR. [98,99] This is particularly interesting for charged species or radicals forming in time-resolved experiments e.g. as a result of photo-induced charge transfer. SEC experiments relevant to this thesis have not been performed by the author, but are contained in selected manuscripts.

Transient absorption experiments on the donor-polymer metal complex dyad **Ru-pTARA** and the acceptor-polymer system **Ru-pNDI** were performed in order to detail the mechanism of ^{3}MLCT-emission quenching observed for **Ru-pNDI**. The dyad **Ru-pTARA** serves as a reference for the pristine metal complex **Rudqp-OH** since no electronic interaction between the excited metal complex and the chromophores in the **pTARA** chain occurs under the given conditions.

In Fig. 1.7a TA spectra recorded upon excitation at 480 nm at selected delay times are shown for **Ru-pTARA**. The TA spectrum at the earliest timepoint has negative amplitude below ca. 570 nm and positive amplitude at longer wavelengths. The negative signal contribution can be attributed to ground state bleach (GSB): The portion of molecules which is excited by the pump does not show the ground state absorption features. Therefore, the ground state absorption of these molecules appears as negative feature (plotted as gray dashed line) corresponding to a reduced optical density with respect to the unpumped state of the sample. The negative appearance of ground state features is caused by the negative sign in Eq. (1.1). In turn, positive amplitude in TA spectra is induced absorption due to absorption bands from the populated excited state into higher excited states (excited-state absorption, ESA). Additional signal contributions are stimulated emission (negative amplitude) and absorption of a photoproduct (positive amplitude). These latter two contributions are less relevant to this work: Stimulated emission can occur from singlet states only, and the transition metal complexes treated

in this thesis typically undergo intersystem crossing on the sub-200 fs time-scale. Photo-product formation would imply that decomposition occurs, which is for the compounds studied here typically negligible judged from UV/Vis absorption spectra recorded before and after the measurements. At an inter-pulse time delay of 0 ps (*time zero*), i.e. when there is temporal overlap of the pump and probe pulses, additional signal contributions from the *coherent artifact* are observed as a result of the two short pulses interacting in a polarizable medium. [92,100,101] Such signals can be the major signal contribution at early delay times, such that data analysis is usually carried out omitting an interval (typically a few hundred femtoseconds for pulse lengths ≤100 fs) around *time zero.*

The spectral signatures observed in the transient absorption spectra for **Ru-pTARA** are consistent with the typical signatures of a ^{3}MLCT state in Ru(II)-polypyridine and related complexes. The TA spectra remain essentially unaltered within the delay time range probed, indicating that no significant dynamics occur. Since all the features of the initial spectrum are preserved, most molecules seem to rest in the same electronic state, the ^{3}MLCT. With respect to the molecular structure it is emphasized that the **pTARA** chain does not impact the photo-induced dynamics after excitation of the ^{1}MLCT(Ru) band. This reflects the choice of the specific chromophores as **pTARA** can reduce the oxidized metal complex, but not the neutral one. [90]

The TA spectra measured for **Ru-pNDI** change with increasing delay time resembling photo-induced dynamics. At early delay times (1 and 5 ps) the same features as for **Ru-pTARA** are observed with GSB and ESA below and above 570 nm, respectively, indicative of the ^{3}MLCT state. At longer delay times distinctive changes occur: The GSB decreases, while at 610 nm an additional ESA feature is formed. Both features can be related to spectroelectrochemical data for **pNDI**: Upon reduction of **pNDI** several absorption bands throughout the visible spectral region are formed. [90] While the absorption maximum of reduced **pNDI** is located at ca. 470 nm and masked by pump scatter (the region below 500 nm was excluded from data analysis), its red edge can be associated with the reduced GSB. The sharp peak at 610 nm is well visible in the TA spectra and is a clear indication of reduced **pNDI** being formed. The formation of the 610 nm band can be followed more clearly by inspecting kinetic traces, see Fig. 1.7c: While for **Ru-pTARA** both the 610 nm and the 650 nm traces are similar with the exception of an offset, there is an additional rise in the 610 nm trace for **Ru-pNDI** which is not observed at 650 nm.

The presented TA data indicates photo-induced electron transfer is occurring after excitation of the ^{1}MLCT-band in **Ru-pNDI** due to observation of signatures attributable to the reduced **pNDI**-chain. Therefore, the emission depletion observed in steady-state
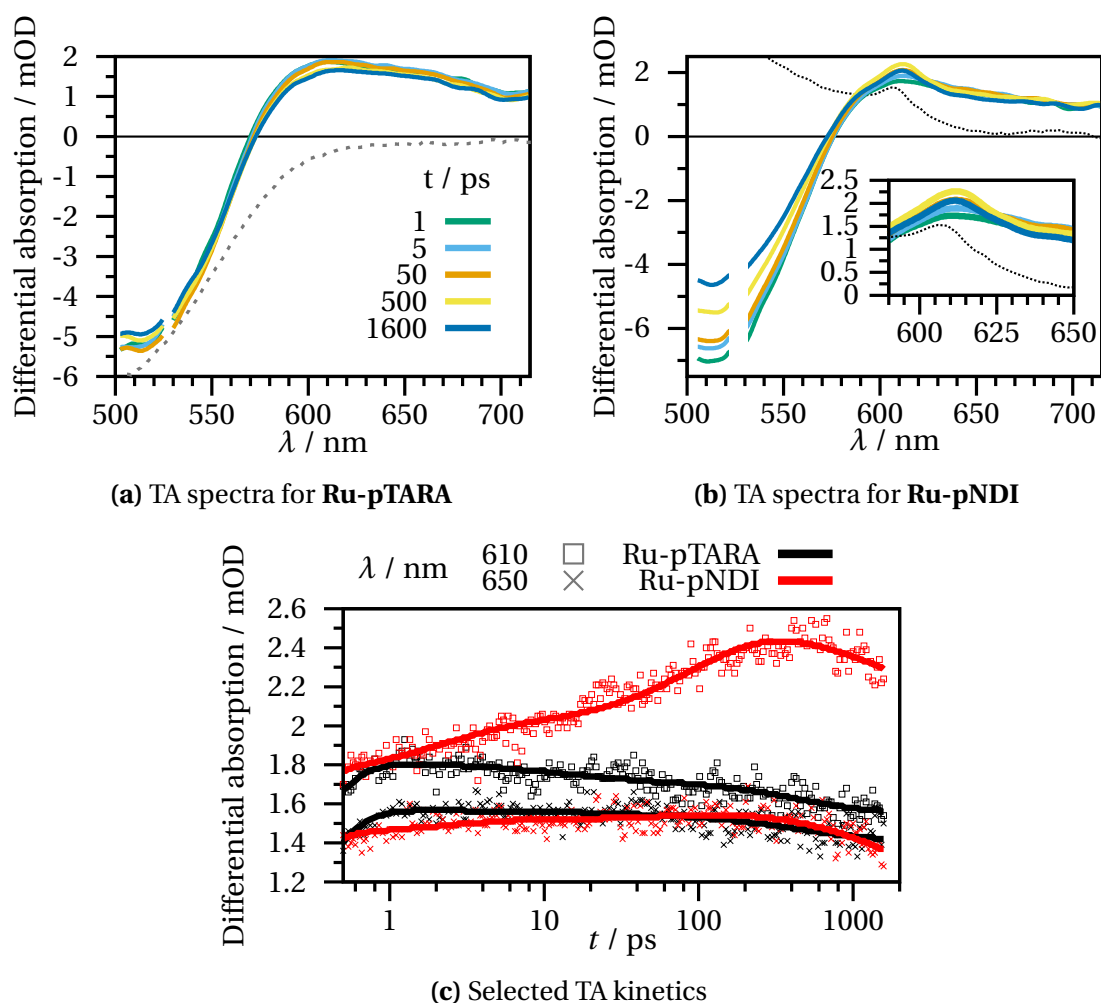
(a) TA spectra for **Ru-pTARA**

(b) TA spectra for **Ru-pNDI**

(c) Selected TA kinetics

Figure 1.7: Transient absorption spectra (excitation wavelength 480 nm, solvent dichloromethane) at selected delay times for **(a) Ru-pTARA** and **(b) Ru-pNDI**. The dotted black line in **(b)** is the (arbitrarily shifted and scaled) spectrum of reduced **pNDI** obtained from SEC. [90] The data for **Ru-pTARA** is essentially equivalent to that of **Rudqp-OH** and the respective data can therefore serve as a reference for the ^{3}MLCT(Ru) dynamics in absence of an interacting chromophore. Panel **(c)** contains kinetic traces at 610 and 650 nm showing the formation of an additional signal at 610 nm attributed to the formation of the **pNDI** anion.

experiments is likely attributable to photo-induced electron transfer as primary quenching mechanism. This observation is complemented by results from TRE experiments, which is discussed in the following.

1.2.2 Time-resolved emission spectroscopy

Depending on the multiplicity change during the radiative transition, the commonly observed types of emission are fluorescence (spontaneous emission) in which the (electronic) multiplicity is preserved, and phosphorescence, which is the emission from the lowest excited triplet state to the singlet ground state. Both fluorescence (as stimulated emission) and phosphorescence can contribute to transient absorption signals with a negative sign, but the dedicated setups described here are much more sensitive as compared to the TA setups and allow for lifetime determination based on data with a much higher dynamic range.

Fluorescence and phosphorescence are often characterized by commonly observed values for e.g. emission lifetime (fluorescence: nanoseconds, phosphorescence: microseconds to milliseconds) and quantum yield (fluorescence: 1 to 100 %, phosphorescence $\leq 1 \times 10^{-3}$ %).[102] In the field of transition metal photophysics, these borders that may exist for pure organic molecules are less clear: The fluorescence quantum yield may be orders of magnitude lower than the phosphorescence quantum yield.[103] On the other hand, phosphorescence lifetimes of less than 1 ns may occur.[104]

Emission spectroscopy can be used only to probe emissive states. Nevertheless, since detectors with a sensitivity down to the single photon level readily exist, emission spectroscopy is an invaluable tool to decipher excited state photophysics by complementing e.g. (time-resolved) absorption spectroscopy.

Two different TRE spectroscopic techniques have been applied in the course of this thesis: Time-correlated single photon counting (TCSPC) using an avalanche photodiode and a streak camera (SC). While TCSPC with an avalanche photodiode produces spectrally integrated data, a streak camera is a device that is capable of recording emission data which is resolved both spectrally and temporally. Nevertheless, placing suitable color filter combinations in the emission beam path is a means of selecting a spectral interval of interest for TCSPC.

While a streak camera system suffers from light loss due the gratings in the spectrograph, a TCSPC module allows for measurements with higher sensitivity and dynamic range. Both measurement devices have specific characteristics, such that either technique may be ideal for specific issues.

In the setup employed in our labs a Ti:Sa oscillator serves as the pulsed laser source for both techniques. The fundamental (tunable between ca. 700 to 1000 nm) is sent through an acousto-optic modulator to reduce the repetition rate for the respective application and sample: The pulse-to-pulse interval at the original repetition rate of ca. 80 MHz is 12.5 ns. Since it is favorable to monitor complete decays after an excitation pulse, it may be necessary to reduce the repetition rate down to 80 kHz (12.5 μs) if emission decay times on the order of μs are of interest. The second or third harmonic of the fundamental wavelength is employed as excitation light that is absorbed by the sample, which consequently emits photons. The emitted light is collected in 90° with respect to the beam path of the excitation light. The light is sent to the entrance slit of a spectrograph in the case of the streak camera, or is weakly focused on the active area of the avalanche photodiode. The intensity of the excitation light is chosen such that the count-rate is ca. 1 to 3 % of the repetition rate. The sample is typically kept in a 1 cm fluorescence cuvette, which optionally may be placed in a cryostat to record emission data at temperatures between room temperature and 77 K.

The streak camera is attached to the exit of the spectrograph and transforms the time axis into a local, vertical axis with the help of a cathode ray tube. This is done by first converting the incoming photons (spectrally resolved in x-direction) into electrons using a photo cathode, which are subsequently accelerated. In the ray tube, two sweep electrodes are used to cause a vertical deflection of the electrons in y-direction. The sweep electrode voltage is controlled electronically employing the trigger signal of the laser. The spectrum-time (x-y)-resolved emission is detected as an image using an image detector (in older models a video camera is used to visually record the image on a phosphor screen, while modern streak cameras employ CCD cameras).

Time-correlated single photon counting (TCSPC)

TRE data obtained via TCSPC data recorded for **Ru-pNDI**, **pNDI** and a binary mixture of **pNDI** and **Rudqp-OH**, denoted **Ru+pNDI**, are shown in Fig. 1.8. Several observations can be made and insightful conclusions drawn:

- The emission decay is strongly non-linear for all three compounds, which reflects the polymeric character of the compounds. Non-linear decays are often observed for polymeric or biological samples. [102]

- The emission intensity for **Ru-pNDI** drops much faster than for **Ru+pNDI**. This indicates that the quenching (by electron transfer) is unique in the covalently
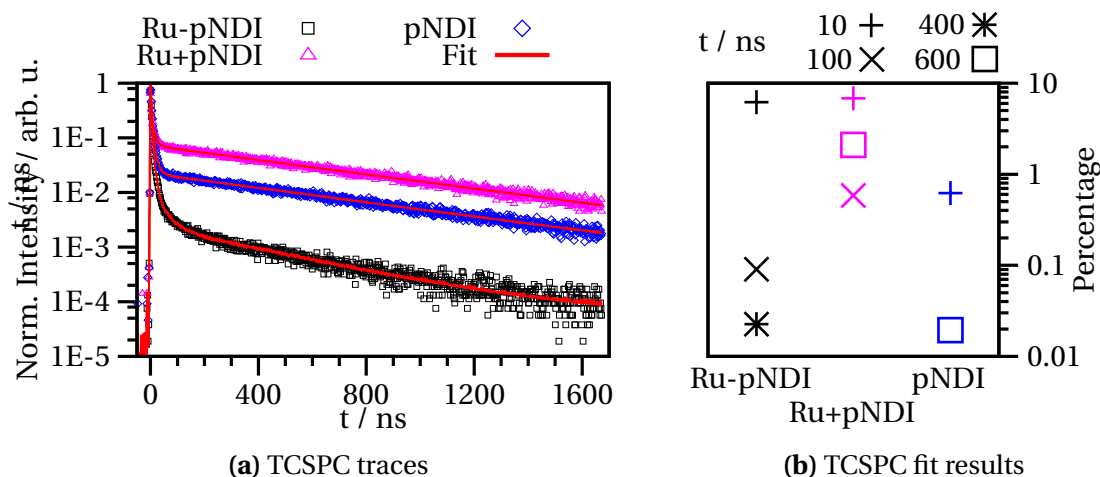
(a) TCSPC traces

(b) TCSPC fit results

Figure 1.8: Emission data (λ_{ex} = 500 nm, solvent DCM) of **Ru-pNDI** and the reference samples **pNDI** and **Ru+pNDI**, a binary mixture of **Rudqp-OH** and **pNDI**: **(a)** Normalized TCSPC traces and **(b)** results from a multiexponetial fit in terms of the amplitudes (logarithmic scale) corresponding to the respective time constants (for all three samples a fast component with a time constant of ≤2 ns and an amplitude of more than 90 % was omitted for clarity). For **Ru-pNDI** the slowest decay (400 ns) is different to that for **Ru+pNDI** and **pNDI**, indicating that the corresponding emission occurs from a different electronic state.

bound donor-acceptor system **Ru-pNDI**.

- The low emission intensity in **Ru-pNDI** is indicative of a strongly reduced emission quantum yield as compared to **Ru+pNDI**.

- A quantification of the emission decay curves in terms of multi-exponential fits reveals different origin of the emission components in the different samples. For example the decay component with a lifetime ≥ 600 ns corresponds to ^{3}MLCT-emission for **Ru+pNDI**, whereas in **pNDI** there is no metal complex, such that emission is attributed to excimer emission based on interactions between the chromophores of the **pNDI** chain. [90]

The high dynamic range accessible in TCSPC experiments allows the detection of species with low abundance or quantum yield. For **Ru-pNDI** the TCSPC results confirm and complement the experimental observations from steady-state and TA experiments.

For compounds with very long lifetimes (the maximum observation window in the TCSPC setup is 2 µs) and if the simultaneous detection of emission spectra and lifetimes is required, streak camera measurements are inevitable.

Photon counting with a streak camera

The capabilities of time-resolved streak camera measurements will be discussed at the example of cyclometalated Iridium complexes from a joint study with the group of Prof. Sven Rau (University of Ulm).[105] Cyclometalated Iridium(III) complexes such as $Ir(ppy)_3$ (ppy = 2-phenylpyridine) are employed e.g. as triplet emitters in organic light emitting diodes.[106–108] The remarkable properties of this class of compounds include excellent tunability of the emission color[106,109,110] and very high emission quantum yields, exceeding 90 percent (e.g. for $Ir(ppy)_3$).[108,111]

Here, an Ir(III) complex carrying a multifunctional bibenzimidazole next to two ppy ligands is investigated. The structures of the relevant complexes are shown in Fig. 1.9a. The bibenzimidazole ligand ($BBIH_2$) is multidentate and can be deprotonated.[105,112] For the respective Ru(II) complex $[Ru(bipy)_2(BBIH_2)]^{2+}$ a pH-dependent off-switch for the ^{3}MLCT-phosphorescence was observed. The quenching could be attributed to a dark triplet state located on the deprotonated BBI ligand. In contrast to the analogous Ru-complex, emission from $[Ir(ppy)_2(BBIH_2)]^{2+}$ (in short **IrBBIH**) persists upon deprotonation, and even the fully deprotonated species $[Ir(ppy)_2(BBIH)]^-$ (in short **IrBBINa**) shows strong emission. In steady-state emission experiments somewhat different emission spectra of the protonated and the deprotonated species were observed. Using the streak camera, the different emission contributions can be characterized: Raw streak camera data for **IrBBIH** and **IrBBINa** are shown in Figs. 1.9b and 1.9c. The data was recorded in different time windows in order to fully cover the emission decay. Already from visual inspection of the two-dimensional streak camera images the different emission characteristics of the protonated and deprotonated complex are deducible. Detailed information is accessible by inspecting vertical or horizontal traces of selected intervals corresponding to kinetic profiles and transient emission spectra, respectively as shown in Figs. 1.9d and 1.9e. The emission spectrum of **IrBBINa** has its maximum at 485 nm (Fig. 1.9d) and the decay is almost complete after 150 ns (Fig. 1.9d). In contrast, the emission maximum for **IrBBIH** is at 520 nm with shoulders at 485 and 560 nm in the first 150 ns. Notably, at later times the emission spectrum of **IrBBIH** lacks the shoulder at 485 nm. The kinetics traces for two spectral intervals shown for **IrBBIH** are clearly different: The blue edge of the emission decays faster than the red edge. Furthermore, the kinetics in the blue edge are very similar for the protonated and the deprotonated species. A quantitative analysis reveals two discrete emission lifetimes of 44 and 329 ns for the protonated and one lifetime (ca. 50 ns) for the deprotonated complex. Due to the similarity of the spectrum determined for the 44 ns emission component in the

protonated with the emission spectrum of the deprotonated species, the origin of this emission is likely connected to the ppy ligand. Thus, the dominant emission component for the protonated complex with a lifetime of 329 ns and an emission maximum at 520 nm is assigned to the BBI ligand. This emission is quenched upon deprotonation, while the ppy-localized emission is not influenced by deprotonation. This is attributed to the specific properties of Iridium(III) complexes with respect to strong spin-orbit coupling and its interplay with structural aspects. Simultaneous emission from two different states in a small metal complex is a rather peculiar behavior, but has been reported for a number of mono-nuclear complexes based on Iridium(III) [113] or Platinum(II) [114] and for a specific dinuclear Ru(II) complex. [115,116]

$[Ir(ppy)_2(tmBBIH_2)]^+$ $[Ir(ppy)_2(tmBBI)]^-$

(a) Molecular structure of the protonated and unprotonated Iridium(III)-bibenzimidazole complex. The colored ligands mark the localization of the determined bright, i.e. emissive, states.

(b) $[Ir(ppy)_2(tmBBIH_2)]^+$ in $CHCl_3$

(c) $[Ir(ppy)_2(tmBBI)]^-$ in $CHCl_3$

(d) Spectra (horizontal profiles)
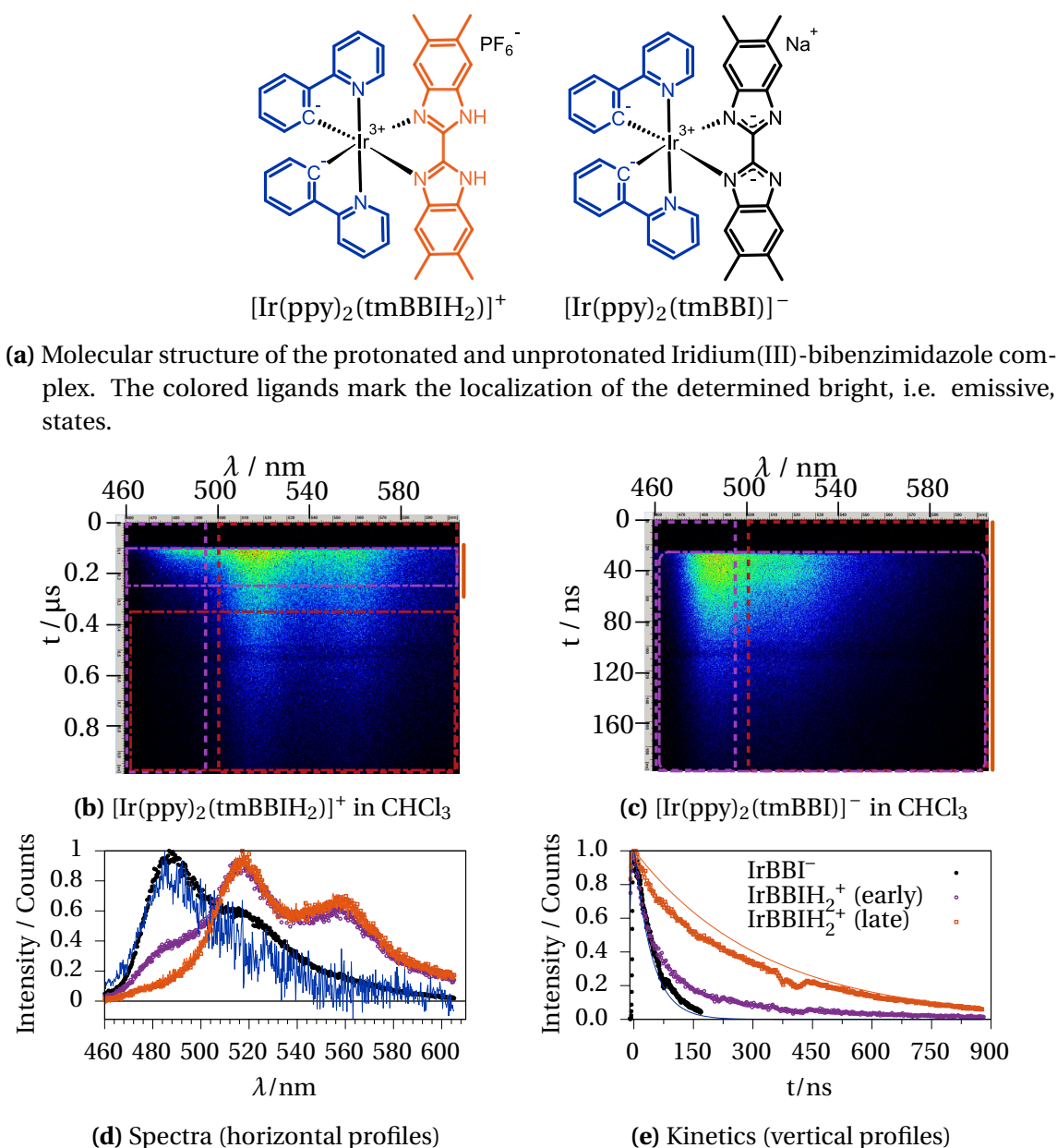

(e) Kinetics (vertical profiles)

Figure 1.9: Panel **a**: Molecular structures of the relevant IrBBI species. Panels **b**, **c**: Two-dimensional Streak camera images recorded for $[Ir(ppy)_2(tmBBIH_2)]^+$ (1 µs window) and $[Ir(ppy)_2(tmBBI)]^-$ (200 ns window). The green star marks an instrument artifact, where the detector has lower sensitivity. Panels **d**, **e**: Selected horizontal and vertical profiles (raw experimental data as symbols) from the data in panels b, c. The legend for panel **d** is the same as the one contained in panel **e** (for the spectra *early* refers to the blue portion of the spectrum from 460 to 495 nm, while *late* refers to the red part of the spectrum from 500 to 605 nm; in the kinetic data *early* and *late* refer to the first 150 ns and the last 650 ns, respectively). The pure kinetic profiles (in **e**) and emission spectra (**d**) from a global fit are shown as solid lines (corresponding colors the ligands, blue: ppy, orange: BBI). Note: The orange line in d) lies exactly on top of the orange symbols. The vertical orange bar on the right of the 2D plots marks an interval of 200 ns.

This chapter has introduced the subject and the molecular systems under investigation. Examples of the **Rudpq**-derived systems as well as an Ir(ppy)$_2$-derivative are discussed with emphasis on the scientific and experimental methodologies. The next chapter contains studies on mono-metallic tpy complexes where chromophores are covalently bound in 4'-position of the central tpy ring yielding highly conjugated multi-chromophore systems.

2 Metal complex-chromophore dyads

In this chapter mono-metallic complexes based on Ru(II) and Ir(III) are discussed. In Section 2.1 the localization of the ^{3}MLCT states in presence of a chromophore in 4'-position of the tpy unit is described for a Ru(II) tpy complex fragment. This is followed by a discussion of the interactions of the relevant electronic states with respect to the energy transfer dynamics between the metal complex and a fullerene acceptor unit.

Structural dynamics in 4'-substituted tpy complexes and their interplay with the electronic properties are discussed in Section 2.2. The subject is a homoleptic Ir(III)-complex with highly conjugated ligands, that shows distinctive differences to the analogous complexes with Fe(II), Ru(II) or Os(II) central ions.

2.1 Ruthenium(II)-terpyridine-fullerene dyads

Parts of this chapter have been published in this article: **P2** - K. Barthelmes, J. Kübel, M. Wächtler, C. Friebe, A. Winter, B. Dietzek, U. S. Schubert, *Inorg. Chem.* **2015**, *54*, 3159-3171.

The fundamental understanding of the photo-physical properties of Ru(II) tpy C_{60} dyads is a prerequisite for the proper and successful design of larger chromophoric arrays with multiple functional units, i.e. combinations of metal complex fragments with bridging chromophores and acceptor moieties. Fullerenes are prototypical electron acceptors[117] and have been shown to produce long-lived charge-separated states in molecular systems.[118] In the systems at hand, a Ru(II)-tpy fragment serves as donor unit, while the fullerene is the energy sink. The bridge between complex and fullerene can have different roles: On the one hand, it can alter the properties of the metal complex fragment by allowing for an additional delocalization of the ^{3}MLCT state by enabling mixing with orbitals located on the bridge chromophore.[119] On the other hand, charge-transfer or locally excited (triplet) states can participate themselves in an energy- or electron-transfer process across the bridging units.[120,121]
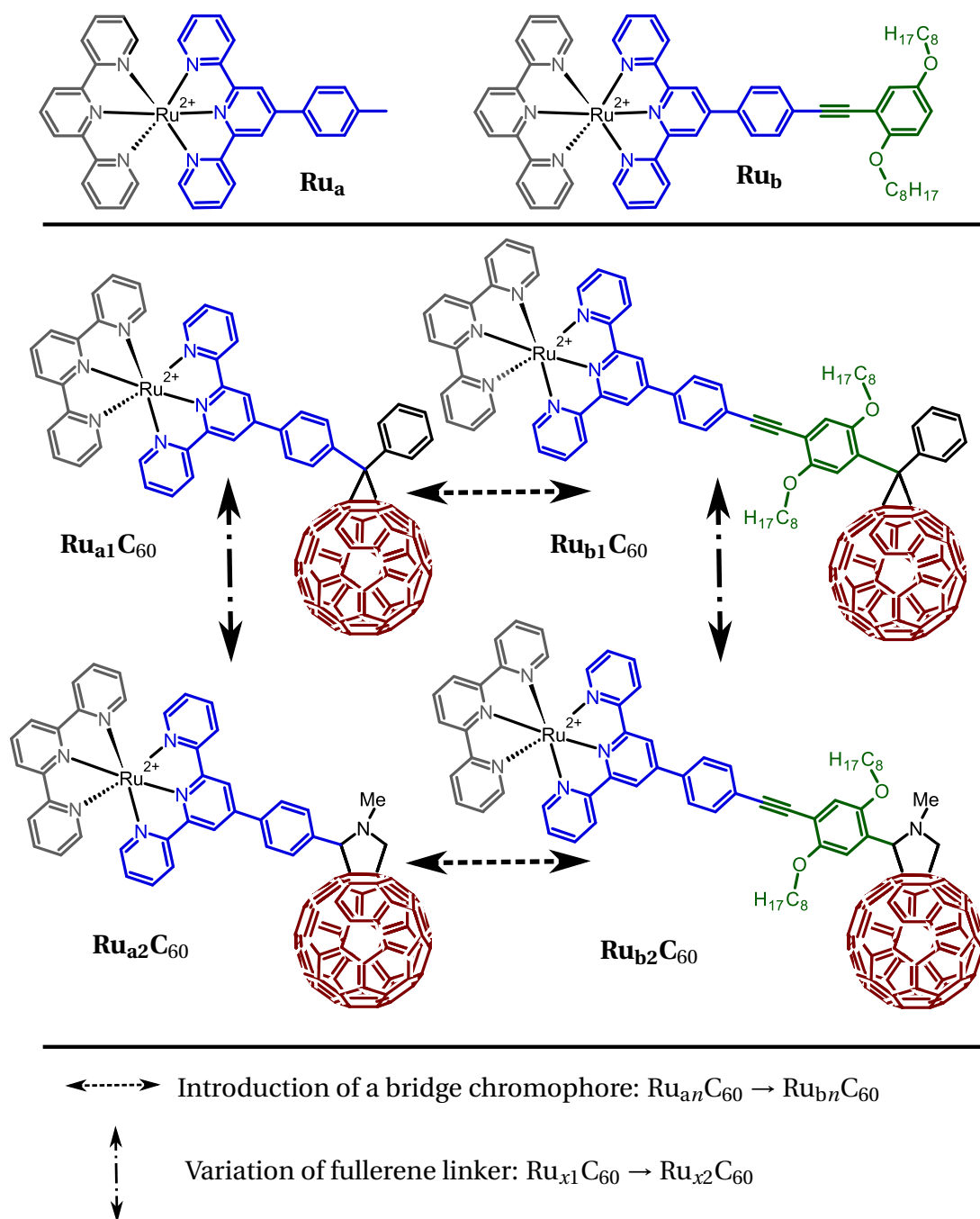
Figure 2.1: Molecular structures relevant to this chapter: The Ru(II)-tpy complex fragments (**Ru**) are attached to the fullerene unit (**C₆₀**) by either of two possible linker types (**1** for a cyclopropyl-unit, **2** for a *N*-Methyl-pyrrolidine unit) in absence (**Ru_a**) or presence (**Ru_b**) of a bridging unit/chromophore. The colored parts of the respective molecules correspond to the re-occurring units introduced in Fig. 1.4 in Section 1.1.
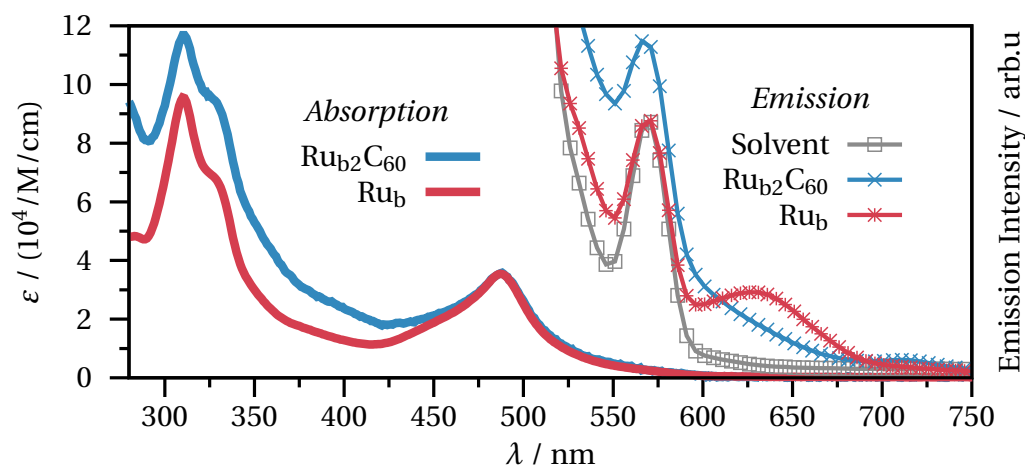
Figure 2.2: Absorption (solid lines) and emission spectra (lines with symbols, excited at 488 nm) of the dyad **Ru$_{b2}$C$_{60}$** and the reference complex without the fullerene unit, **Ru$_b$** (solvent: CH$_2$Cl$_2$).

The absorption spectrum of **Ru$_{b2}$**C$_{60}$ as well as that of the corresponding fullerene-free model complex **Ru$_b$** in CH$_2$Cl$_2$ solution are plotted in Fig. 2.2. The metal complex **Ru$_b$** shows intense absorption features in the UV with the most prominent band at 310 nm, which is due to $\pi - \pi^*$ transitions in the terpyridine units.[122] The very prominent feature in the visible spectral range is due to metal-to-ligand-charge-transfer (^{1}MLCT) excitations with the absorption maximum at 488 nm.[65] The absorption spectrum of the metal complex fullerene dyad **Ru$_{b2}$**C$_{60}$ does not clearly contain additional absorption features as compared to that of Ru$_b$, yet there is an offset which can be attributed to the presence of the C$_{60}$.[119] It is therefore deducible that there is negligible electronic communication between metal complex and fullerene acceptor in the ground state.

Ru$_b$ exhibits very weak emission between 600 to 700 nm, peaking at 630 nm, which can be attributed to weak phosphorescence stemming from the ^{3}MLCT state. The lifetime in air-equilibrated acetonitrile (ACN) solution was determined to 2.3 ns,[119] which is short in terms of what generally is expected for phosphorescence, but is almost an order of magnitude longer than the excited state lifetime of the parent complex [Ru(tpy)$_2$]$^{2+}$ (ca. 250 ps).[123] Such prolongation of the excited-state lifetime has been attributed to an extension and stabilization of the chromophoric system due to the delocalization of the ^{3}MLCT state[71] and furthermore equilibration between close-lying triplets[124]. This was observed earlier for binuclear 4'-substituted tpy complexes following the similar architecture as the ones regarded in this chapter.[70] Such lifetime-

enhancement is particularly pronounced for Ru(II) tpy complexes, where, without 4'
substituents, the low energy barrier between the ^{3}MLCT and a metal-centered triplet
state (^{3}MC) causes efficient deactivation of the ^{3}MLCT via dd-states of the metal. The
phosphorescence quantum yield is very low giving rise to an emission band, which
is actually weaker than the Raman bands of the solvent under the same conditions.
The dyad **Ru$_{b2}$C$_{60}$** shows an emission spectrum that is clearly different from that of
Ru$_b$. While there is no ^{3}MLCT phosphorescence, there seems to be at least one other
species contributing to the emission spectrum observed in the dyad: The weak peak
at 710 nm can be assigned to C$_{60}$ fluorescence. Since the emission spectra for both the
metal complex as well as the dyad were recorded under the same conditions exciting the
^{1}MLCT transition, the absence of ^{3}MLCT phosphorescence in the dyad hints towards
a quenching process in the excited state, which depopulates the ^{3}MLCT state. This
behavior is investigated in more detail in TA experiments with a pump wavelength of
520 nm, i.e. exciting the red flank of the ^{1}MLCT band.

Selected results from TA experiments are summarized in Fig. 2.3. The discussion here
focuses on the photophysical processes relevant to the excited state processes leading
to a deactivation of the ^{3}MLCT state. The initially formed ^{3}MLCT state has an ESA
maximum at ca. 630 nm. The TA spectra measured for **Ru$_b$** are in good agreement with
the typical signatures of Ru(II)-polypyridine complexes: The negative signal below ca.
540 nm is due to ground state bleach (GSB) of the ^{1}MLCT band, and positive signal above
540 nm is due to excited-state absorption that is indicative of the respective ^{3}MLCT
state. These signatures are comparable to those observed for the **Rudqp/Rudqp-OH**
complex (Section 1.2). However, the tpy ligand and its π-system are smaller than it is
the case for the dqp ligand, which also causes the ^{1}MLCT band and with that the GSB
signature to be spectrally more narrow in the tpy case. [104]

The influence of the bridge chromophore in the **Ru$_b$** complex is deducible by com-
parison of the ESA signatures determined for **Ru$_b$** with that of **Ru$_a$**. [119] The red-shift
of the ESA maximum in presence of the additional dimethoxyphenyl chromophore is
attributed to the larger π-system and the delocalization of the ^{3}MLCT state. [125,126]

A process with a time-constant of 238 ps leads to a decrease of GSB and a weak
decrease of ESA with a broad maximum between 590 and 610 nm. This process is
attributed to equilibration between the initially populated ^{3}MLCT$_1$ and a second state
with more $\pi - \pi^*$-character, [119] denoted ^{3}MLCT$_2$. A process with a time-constant of
$\geq$1.5 ns leads to an overall signal decay; since the longest decay time accessible in the
experimental setup (1.8 ns) was not sufficient to cover the complete decay, the lifetime
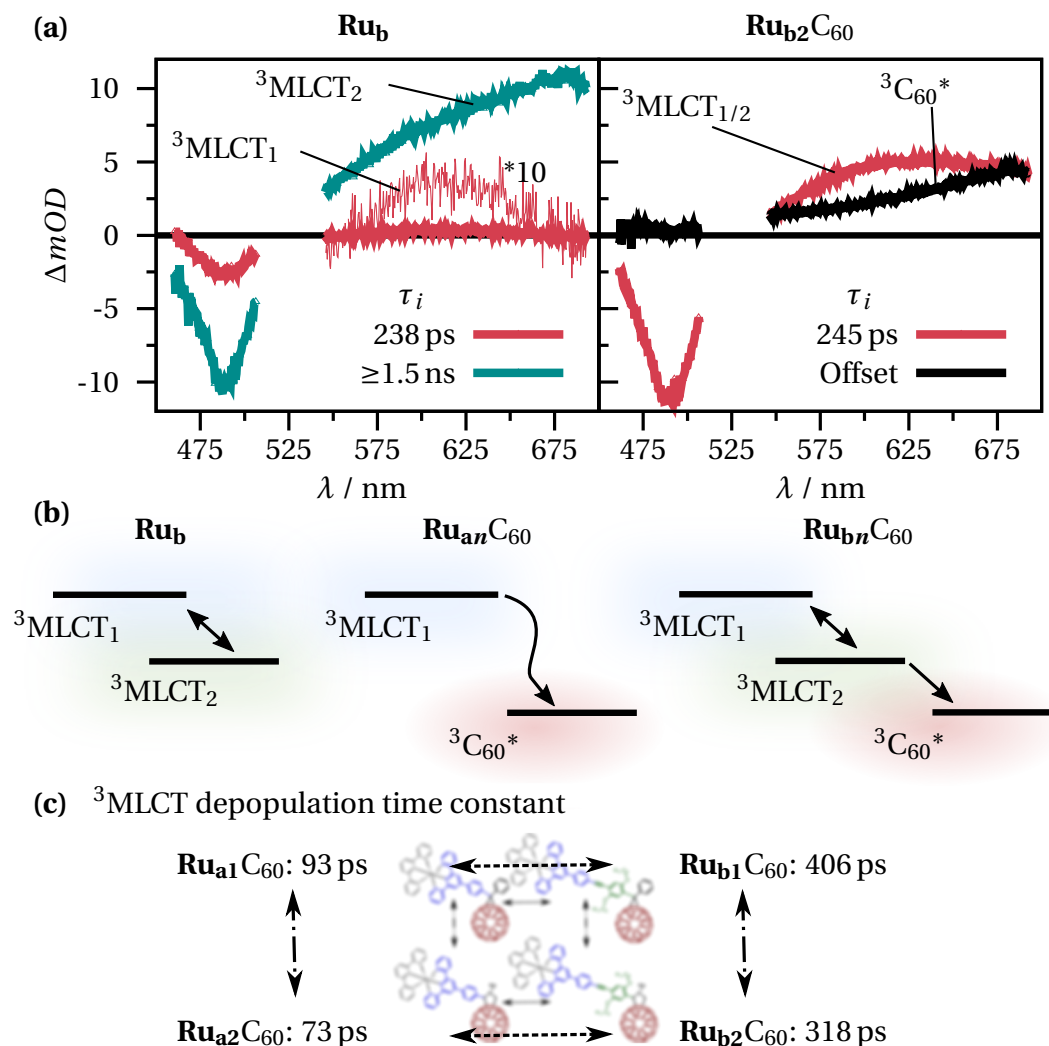
(a)

(b)

(c) ^{3}MLCT depopulation time constant

Ru$_{a1}$C$_{60}$: 93 ps   **Ru$_{b1}$**C$_{60}$: 406 ps

Ru$_{a2}$C$_{60}$: 73 ps   **Ru$_{b2}$**C$_{60}$: 318 ps

Figure 2.3: Selected results from TA spectroscopy are shown in terms of decay-associated spectra for **Ru$_b$** and **Ru$_{b2}$C$_{60}$** in **(a)**. Two kinetic components with time-constants in the sub-ps and few-ps time range were excluded for clarity. For **Ru$_b$** a complete decay of the ^{3}MLCT state is observed ($\tau \geq 1.5$ ns). For **Ru$_{b2}$C$_{60}$** the formation of the long-lived ^{3}C$_{60}$* state ($\tau \geq 0.8\,\mu$s in presence of O$_2$, determined in separate experiments) is observed. Panel **(b)** Relaxation scheme in **Ru$_b$** and in presence of C$_{60}$ depending on the bridge chromophore. The photo-induced dynamics in the four dyads introduced in Fig. 2.1 can be rationalized: For all four compounds the ^{3}MLCT is depleted and the ^{3}C$_{60}$* is formed. The actual rate depends on the presence of the bridge chromophore as well as the type of linker, see panel **(c)**.

determined in the TA experiments is not precise. Therefore, the lifetime determined via TA is consistent with the lifetime determined from the emission decay (2.3 ns in ACN[119]).

The early photo-induced dynamics of the dyad $\mathbf{Ru_{b2}C}_{60}$ are similar to those observed for $\mathbf{Ru_b}$, i.e. the initial relaxation and excited-state localization of a 4'-substituted Ru(II)-2,2'-6,6''-terpyridine complex is observed.[119] However, the behavior at later delay times is very different for the dyad: A process with a time-constant of 245 ps, i.e. a similar time dependence as the equilibration in $\mathbf{Ru_b}$, leads to a decay of all signatures that correspond to either ^{3}MLCT state. A long-lived state is formed, which was identified as the fullerene triplet state, ^{3}C$_{60}$*. This leads to the conclusion that in presence of the C$_{60}$ unit intramolecular energy transfer occurs from the Ru-tpy unit towards the fullerene. The mechanism is most likely a Dexter-type transfer in which the extended π-system of the metal complex is in close spatial distance to the fullerene π-system. Furthermore, the participation of bridge-localized triplet state has been reported for related systems. This has been called a *hopping*-type energy transfer, which can proceed over multiple repetitive units.[126]

Notably, there is no indication of initial charge transfer as judged from a comparison of TA data measured in DCM or ACN.[119] The altered solvent parameters (primarily the increase of polarity in terms of the relative permittivity when changing DCM to ACN) lead are minor variations in time constants that may be attributable to a weak solvent dependence of the relative energetic positions of the ^{3}MLCT states.[119]

The formation of ^{3}C$_{60}$* is observed for all four dyads investigated, i.e. irrespective of the presence of the bridge chromophore and irrespective of the type of fullerene linker. Nevertheless, the dynamics of ^{3}MLCT depopulation depend on the specific compound and are influenced by both the presence of bridge chromophore and linker type. The relevant mechanisms are summarized in Fig. 2.3b. In presence of the bridge, and via the pyrrolidine linker, i.e. in $\mathbf{Ru_{a2}C}_{60}$, the energy transfer time constant is 318 ps (in ACN, 245 ps in DCM). In absence of the bridge chromophore, i.e. in $\mathbf{Ru_{a2}C}_{60}$, the ^{3}MLCT is depopulated much faster ($\tau = 73$ ps). Replacing the linker slows down ^{3}C$_{60}$* formation to 93 and 406 ps for $\mathbf{Ru_{a1}C}_{60}$ and $\mathbf{Ru_{b1}C}_{60}$, respectively. The bridge chromophore has clearly a large influence on the energy transfer process to the ^{3}C$_{60}$* state. Variation of the linker has a minor impact on the energy transfer rate with the rate being somewhat faster with the pyrrolidine linker. While reports found that cyclopropane linkers allow for better electronic communication as compared to the pyrrolidine linkers,[127] the data presented here suggests the opposite. This contradiction may be resolved by realizing

that in absence of the additional phenyl substituent at the cyclopropane linker, there may indeed be an increased sp^2 character via the cyclopropane linker.[127] However, in the presented compounds the phenyl substituent at the cyclopropane linker enforces sp^3 character, thus reducing electronic communication as compared to the pyrrolidine linker.

The close electronic interaction between the metal complex and the bridge chromophore has large impact on the properties of the entire compound. Furthermore, the analysis of the energy transfer dynamics between the metal complex and the fullerene unit suggests a decisive role of the bridge chromophore.

An aspect that was excluded in this section is the role of structural dynamics. These occur on the few- to tens of ps timescale for the compounds discussed in this chapter and their spectral signatures are rather subtle.[119] However, a planarization between the central ring of the tpy unit and the phenyl ring attached in 4'-position is an essential step in the initial relaxation of the ^{3}MLCT state. In the next section, an Ir(III) tpy derivative is discussed, in which structural dynamics play a central role in the excited-state landscape.

2.2 Photophysical properties of an Ir(III) complex with extended conjugated side chains

Parts of this chapter have been published in this article: **P3** - J. Kübel, A. Winter, U. S. Schubert, B. Dietzek, *J. Phys. Chem. A* **2014**, *118*, 12137-12148.

Ir(III) tpy complexes have been shown to have far superior photophysical properties as compared to their Ru(II) analogues: While the excited state lifetime of [Ru(tpy)$_2$]$^{2+}$ is below 1 ns even in oxygen-free solution,[123] that of [Ir(tpy)$_2$]$^{3+}$ is in the microsecond time range with a phosphorescence quantum yield of a few percent.[128] The different properties are related to the intrinsic electronic properties of the Ir(III)-tpy unit. In contrast to most derivatives of [Ru(tpy)$_2$]$^{2+}$ and [Os(tpy)$_2$]$^{2+}$, the lowest excited state of 4'-substituted Ir(III) tpy complexes is not a ^{3}MLCT state, but either a ligand-localized (^{3}LC) or an intraligand (intramolecular) charge-transfer state (^{3}ILCT).[129] The energetically high-lying MLCT states in Ir(III) tpy complexes are a result of the high oxidation potential of the metal ion. As a consequence, Ir(III) tpy fragments are excellent electron mediators in supramolecular arrays as *rogue* triplet states* are absent. An example for

---

**rogue states are e.g. the energetically low ^{3}MLCT states in Ru(II) or Os(II) tpy complexes, which can serve
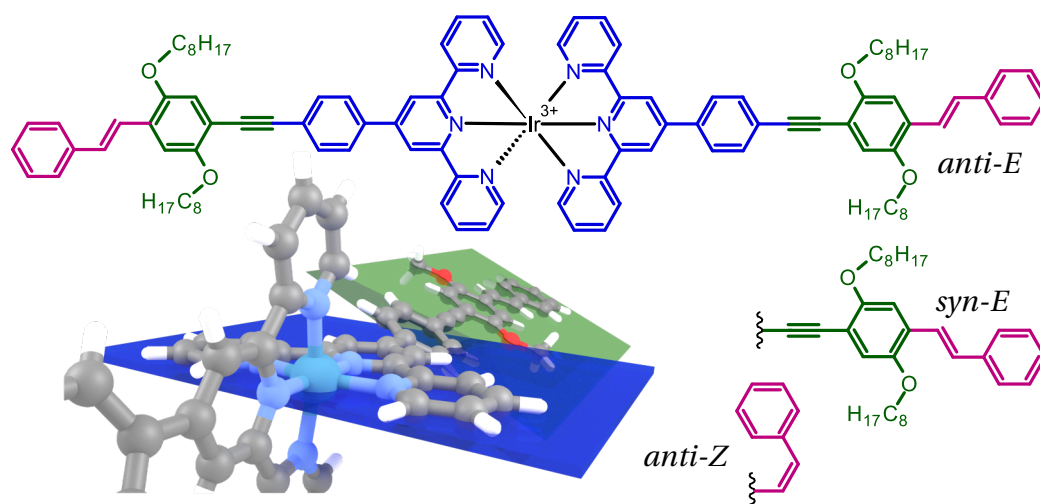
Figure 2.4: Molecular structure of the homoleptic complex **Ir**. The three-dimensional representation of the metal complex is augmented with colored planes emphasizing the non-planarity of the tpy unit and the phenyl unit attached in 4'-position of the central pyridine ring. A planarization after photoexcitation is a common process for many related tpy derivatives. The possible orientations of the styrene fragment and configurations of the double bond give rise to different isomers of **Ir**.

a successful implementation of an Ir(III) tpy unit is an Ir(III)-coupled donor-acceptor system with a room-temperature lifetime of 120 μs. [131]

In the context of building blocks for hierarchic coordination oligomers, in this chapter a homoleptic Ir(III) complex, **Ir**, is studied (Fig. 2.4). The photophysical properties of the analogous complexes with Fe(II), Ru(II) and Os(II) central ions were reported earlier. [84] Here, the particular effects of the Ir(III) central ion in the complex and its interaction with the ligand structure are detailed. A remarkable property of the respective Ru(II) and Os(II) complexes is a dual emission: Both ligand-originating fluorescence as well as metal complex based phosphorescence is observed. [83–85] Interestingly, the emission properties of **Ir** are very different from its analogues: No phosphorescence is observed at room temperature, but fluorescence, the spectrum of which depends on the excitation wavelength. Both these observations are addressed in this chapter. For the discussion it is important to identify potentially flexible parts in the molecular structure of **Ir** (Fig. 2.4), which can impact the electronic properties:

- Commonly observed in 4'-phenyl-terpyridine ligands and complexes is non-planarity in the ground state: The attached phenyl ring is twisted out of the plane

as sink for excitation energy. [130]

of the tpy ligand.[82] As a result of photoexcitation in such compounds, planarization can occur, serving as gating for electronic communication between the metal complex and the adjacent chromophore. Such process can open additional relaxation pathways as reported for numerous tpy derived metal complexes.[84,120]

- The terminal styrene unit with the dialkoxy-phenyl unit can be regarded as a dialkoxy-stilbene unit. Therefore, the photophysical properties of **Ir** should be evaluated with respect to the properties of the stilbene chromophore, which shows rich photophysics by itself, including Z/E-isomerization.[132,133]

A first glance on the interplay between structure and electronics is provided by the UV/Vis absorption spectrum of **Ir** (Fig. 2.5). The spectrum is dominated by transitions in the UV, yet there is a band centered at ca. 450 nm. Notably, neither the free ligand nor [Ir(ttpy)$_2$]$^{3+}$ (ttpy is 4'-tolyl-2,2':6',2"-terpyridine) show any absorption at wavelengths longer than 450 nm.[134] Therefore, the low-energy shoulder in **Ir** is due to electronic interactions between the metal complex fragment and the ligand chromophore. Based on the solvent dependence of this band†, it is assigned as an ^{1}ILCT transition. By comparing UV/Vis absorption spectra of **Ir** in different solvents an impact of both solvent polarity and viscosity on the ^{1}ILCT band is found.[134] This is a clear indication that the actual molecular structure impacts the electronic properties of **Ir**.

Emission (i.e. fluorescence) of **Ir** is observed only at excitation wavelengths ≤450 nm, i.e. fluorescence spectroscopy can not provide information with respect to the ^{1}ILCT transition. This is in line with the absence of the ^{1}ILCT band in fluorescence excitation spectra recorded for emission wavelengths ≥450 nm.[134] In fact, the red edge of the fluorescence excitation spectra corresponds approximately to the red edge of the absorption spectrum of the free ligand. Furthermore, the shape of the emission band of **Ir** is similar to that of the free ligand when excited at the same wavelength. These observations suggest that the part of the potential energy landscape of the ligand relevant fluorescence is not significantly altered upon binding the Ir(III) ion via the tpy unit (similar conclusions can be drawn from quantum chemical calculations[134]). Nevertheless, there are distinctive variations of the fluorescence band shape for **Ir** when the excitation wavelength is varied (Fig. 2.5). The maximum of the emission spectra shifts from ≥440 nm to ca. 460 nm (i.e. by more than 1000 cm^{-1}). Since the general appearance of the spectra does not change much, i.e. the spectral position of shoulders in the emission spectra are

---

†negative solvatochromism, shifting an absorption band bathochromically when the solvent polarity is reduced [135]
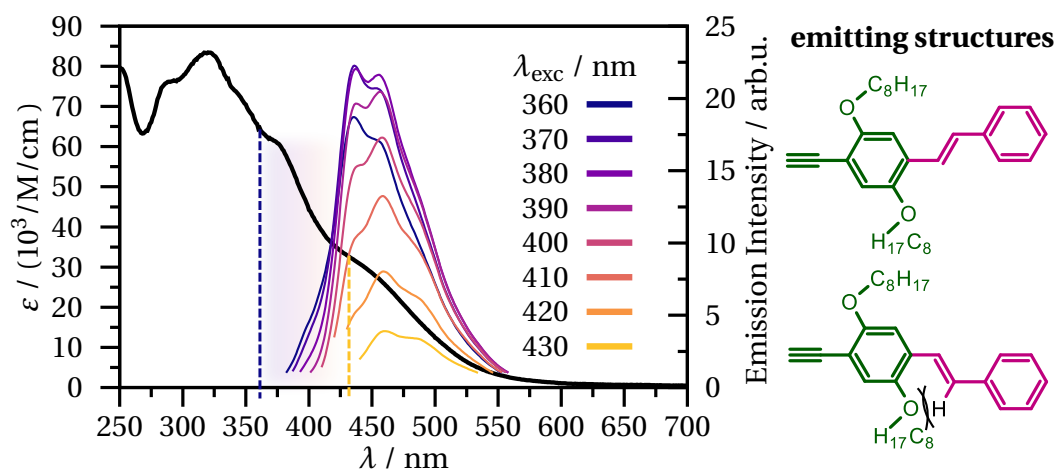
Figure 2.5: UV/Vis absorption spectrum (in tetrahydrofuran, left scale) of **Ir** and emission spectra (in toluene, right scale) at different excitation wavelengths. The range of excitation wavelengths is marked with vertical dashed lines for the lowest and highest excitation wavelength considered. The origin of the excitation-wavelength dependent shift of the emission spectra is attributed to structural heterogeneities in solution, e.g. the *anti* and *syn* configuration of the terminal stilbene unit. Notably, the low-energy absorption band overlaps entirely with the shown emission spectra and is attributed to a dark ^{1}ILCT transition.

largely consistent and do not shift when the excitation wavelength is varied, it is likely the same electronic state that is responsible for the different emission spectra.

Such situation may be related to the possible rotamers within the dialkoxy-stilbene subunit: As depicted in Figs. 2.4 and 2.5, two possible orientations of the styrene unit with respect to the dialkoxy-stilbene chromophore are possible giving rise to the *anti*- and *syn*-rotamers. These *rotamers* are closely related regarding their electronic structure, but not energetically equivalent due to the repulsion between of the hydrogen atoms at the double bond and the alkoxygroup (as marked in Fig. 2.5). Interconversion between the rotamers in the excited-state is unlikely to occur due to the high energetic barrier that needs to be crossed for a bond twist; i.e. a ground state molecule with *anti*- or *syn*-structure will most likely preserve the rotational configuration in the excited-state.[‡]

The photo-induced dynamics in **Ir** following excitation of the ^{1}ILCT transition were probed via TA spectroscopy (Fig. 2.6). As expected in light of the steady-state emission data, no signal contributions attributable to fluorescence are observed irrespective of the solvent and the delay time. Based on the low fluorescence quantum yield determined for

---

[‡]The described effect is comparable to red-edge excitation shifts frequently observed e.g. in polymers with structural inhomogeneities [102]

Ir of 2 % in comparison to 74 % for the free ligand, [83] fast intersystem crossing from the singlet into the triplet manifold is expected within the first 200 fs after photoexcitation due to the presence of the heavy Ir(III) ion causing strong spin-orbit couplings. In order to detail the electronic and structural dynamics, TA data is recorded in different solvent: polar and fluid ACN, semi-polar and fluid THF as well as polar and viscous DMPU. As apparent in both transient spectra and kinetics (Fig. 2.6 a and b, respectively) there is a significant impact of the solvent on the photo-induced dynamics:

- The signal amplitude is largest in ACN, followed by THF and DMPU. Therefore, this trend rather follows the viscosity trend than that of solvent polarity.

- The time at which the maximum signal amplitude is reached decreases in the order ACN, THF and DMPU, i.e. following the solvent viscosity.

- For THF and DMPU there is a pronounced dynamic blue shift of the ESA maximum from ca. 650 nm to 550 nm. In the case of ACN there is a dominant maximum at ca. 560 nm for all delay times.

These observations can be interpreted as follows (for a quantitative analysis see[134]):

1. The fast signal rise in ACN hints to the formation of a charge-transfer state, which is formed efficiently only in the fluid and polar environment of ACN. Already within the first picosecond the signal amplitude begins to decrease. Notably, this decay occurs within a few-ps timescale, i.e. a typical time window for solvent relaxation and vibrational cooling. The signal decay is accompanied by a weak blue shift, which could be due to a planarization (see above and Fig. 2.4) as reported for the free ligand[82] and the **Ir**-analogue complexes of Ru(II) and Os(II).[84] Planarization is known to enhance electronic coupling between the tpy unit and the adjacent chromophore (especially in Ru(II)-tpy complexes planarization leads to an increased delocalization and stabilization of the ^{3}MLCT state). If, as in **Ir**, the initially excited state is an intraligand charge-transfer state, enhanced electronic coupling could in fact promote charge recombination and thereby cause quenching of the charge transfer state.

2. In THF the signal rise is much slower than in ACN, and so is the signal decay. It should be noted that planarization alone is not expected to cause a significant blue shift as the one observed for the ESA maximum, which shifts by more than 2000 cm^{-1}.[134] Some of the features in the transient absorption spectra between

0.25 and 7.5 ps are reminiscent of the transient absorption features of Z- and E-stilbene with maxima at 634 and 582 nm, [136] respectively. Therefore, the photo-induced dynamics of **Ir** could involve Z/E-isomerization at the terminal styrene unit, which involves major structural rearrangement and the rate for this process will be heavily affected by solvent viscosity. Due to the strong conjugation in **Ir**, the isomerization process could be part of a structural reorganization associated with the formation of a charge-transfer state and occur much faster than in an isolated stilbene molecule. [136]

3. The transient spectra at long delay times are very similar in all solvents, suggesting that the final state is non-polar, e.g. a delocalized $^3\pi - \pi^*$ state. This is also explains the absence of phosphorescence from the Ir-tpy unit, because a ligand centered-decay is observed.

Ir is a fascinating example of a metal-complex in which electronic and structural dynamics are strongly interlacing. The Ir(III) ion seems to contribute primarily with its positive charge by increasing the electron withdrawing character of the tpy unit. The results here support the usefulness of Ir(III)-tpy fragments as electron relay units in multi-chromophoric and multi-metallic arrays. [137]
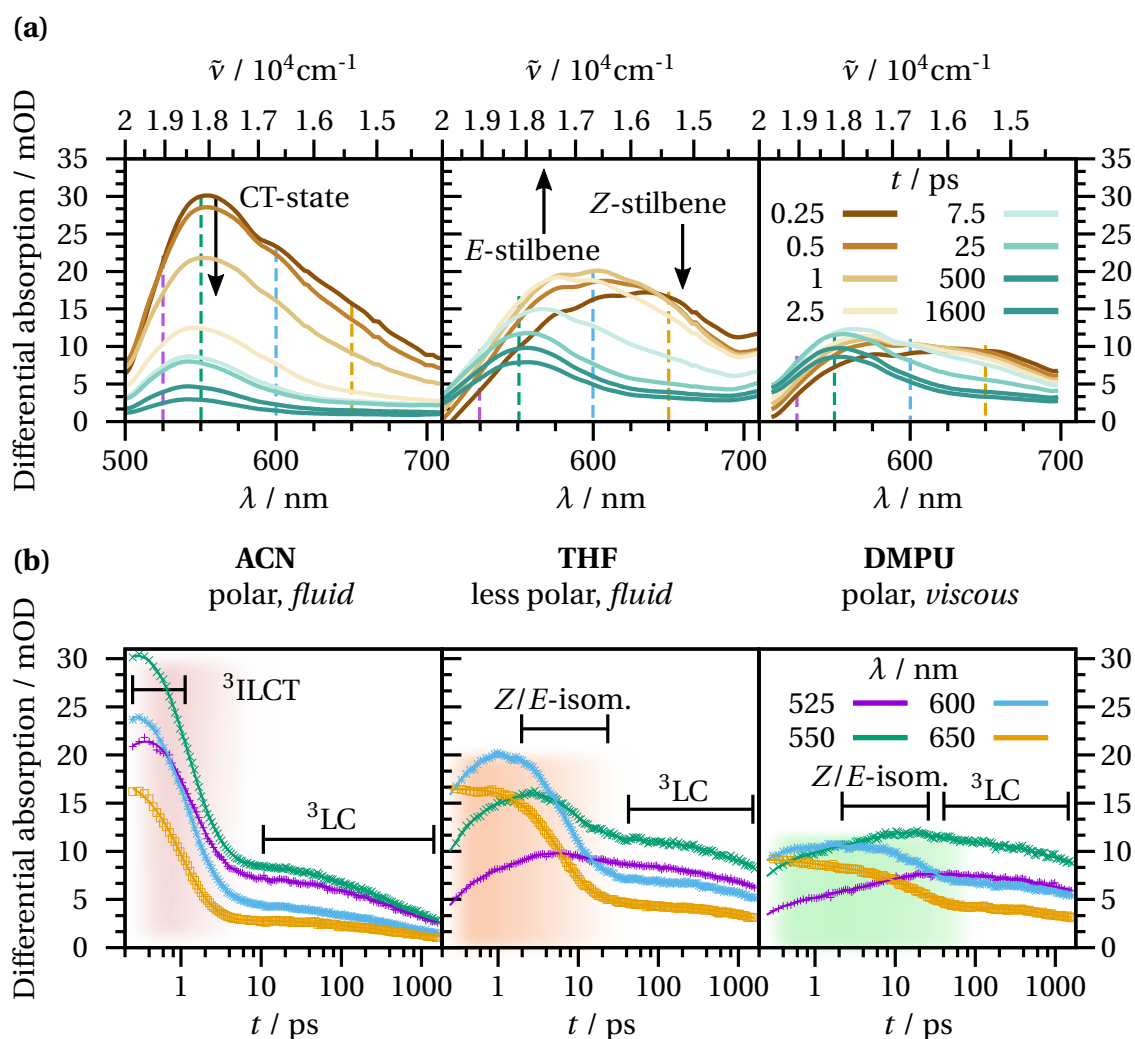
(a)

(b)

Figure 2.6: TA data (excitation at 480 nm) for **Ir**: **(a)** Spectra at selected delay times and **(b)** kinetic traces at selected wavelengths in three different solvents. A strong solvent dependence is apparent in both spectra and kinetics, suggesting significant impact of both solvent polarity as well as viscosity on the photo-induced dynamics. The signatures of relevant states and processes are labeled accordingly. The colored shades in the background of the kinetic traces mark the respective intervals in which the major structural rearrangements occur.

3 Multimetallic complexes

The scope and functionality of hetero-multimetallic complexes exceeds that of mono-metallic complexes since the interaction between the different metal complex fragments can strongly impact the properties of the individual metal complexes. The characterization of monometallic tpy complexes of Fe(II), Ru(II), Os(II) metal ions with extended ligand chromophores has been reported previously, [84] or is described for Ir(III) in the previous chapter. The photo-induced dynamics in homo-bimetallic complexes have been studied earlier, [70] but due to the symmetry of their potential energy landscapes such systems are primarily useful as excitation energy reservoirs. In this chapter, the symmetry of the potential energy landscape is altered and hetero-bi- and trimetallic complexes are investigated. The detailed characterization of the photo-induced dynamics in these compounds is crucial in order to resolve the excitation energy pathways that occur between different metal complex fragments bound to the same ligand. Therefore, the results presented here are a prerequisite for the proper design of increasingly complex systems with multiple metal complex fragments.

3.1 Multimetallic quasi-linear tpy-based structures

Parts of this chapter have been published in these articles: **P4** - M. Wächtler, J. Kübel, K. Barthelmes, A. Winter, A. Schmiedel, T. Pascher, C. Lambert, U. S. Schubert, B. Dietzek, *Phys. Chem. Chem. Phys.* **2016**, *18*, 2350-2360. **P5** - J. Kübel, M. Wächtler, B. Dietzek, *ChemPhysChem* **2017**, *submitted*.

Hetero-bi- and trimetallic complexes with Ruthenium(II), Iron(II) and Osmium(II) will be the topic of this chapter. After discussing the basic photophysical properties of the multinuclear species the focus of the discussion will be results from an in-depth study of the photo-induced dynamics involving pump-wavelength and intensity dependent TA experiments and advanced fitting procedures for the complicated kinetics. The chemical structures relevant to this section are shown in Fig. 3.1. Complexes of a bis-terpyridine ligand with a styrylstilbene chromophore as the ligand backbone are

studied: The heterodinuclear **RuOs** and the trinuclear **RuFeRu** are compared to the mononuclear **Ru** as a reference.

Ground state absorption spectra of the complexes are displayed in Fig. 3.1. The absorption spectra of all four compounds are dominated by a broad and intense band centered at 425 nm, which is due to $\pi - \pi^*$ transitions in the ligand backbone. While this intense band is the lowest-wavelength absorption band for the metal-free ligand, in the complexes there are additional bands which can be assigned to ^{1}MLCT-transitions (and direct $S_0 \rightarrow {}^3$MLCT(Os) transitions for the Os(II)-containing complex). It may be noted that the absorption coefficient of the 425 nm band is reduced by a factor of 2 upon metal-binding. Consequently, for the trinuclear complex with two ligand units, the absorption coefficient is again roughly that of the free ligand. The hypochromic effect upon metal-binding may be attributed to a significant electronic interaction between the ligand and the respective metal ion. Apart from the occurrence of the ^{1}MLCT absorption bands, the induction of intraligand-charge-transfer bands was discussed for related ligand structures.[84] Such weak bands that do not correspond to the lowest-energy transition are not dominant in the absorption spectra, but they might contribute to the broad absorption between the main transitions at 425 and 488 nm.[84]

The emission of the compounds in this chapter is not a suitable probe for possible intramolecular energy-transfer events. This is because:

- The metal-free ligand is a strong emitter (fluorescence quantum yield in the order of 90 %).[81] Upon metal-binding, the fluorescence is significantly quenched due to a significantly increased rate for ISC in the presence of heavy-metal ions. Residual fluorescence may hamper the unambiguous detection of weak phosphorescence due to spectral overlap of the different emissions.

- The mononuclear complex **Ru** does not show detectable ^{3}MLCT emission, in contrast to the corresponding homodinuclear Ru(II) complex of the same ligand.[70] Therefore, absence of Ru(II)-based ^{3}MLCT emission in **RuOs** and **RuFeRu** does not have to be an indication of intramolecular quenching such as energy or electron transfer.

- Fe(II)-polypyridine complexes are typically non-luminescent due to short-lived ^{1}MLCT and ^{3}MLCT states (lifetimes as short as 50 fs for $[Fe(bpy)_3]^{2+}$ have been reported[138]).

- $[Os(tpy)_2]^{2+}$ is a stronger emitter as compared to the Ru(II)-analogue. However, since the ^{1}MLCT transitions of Ru(II)- and Os(II)-tpy fragments are degenerate,
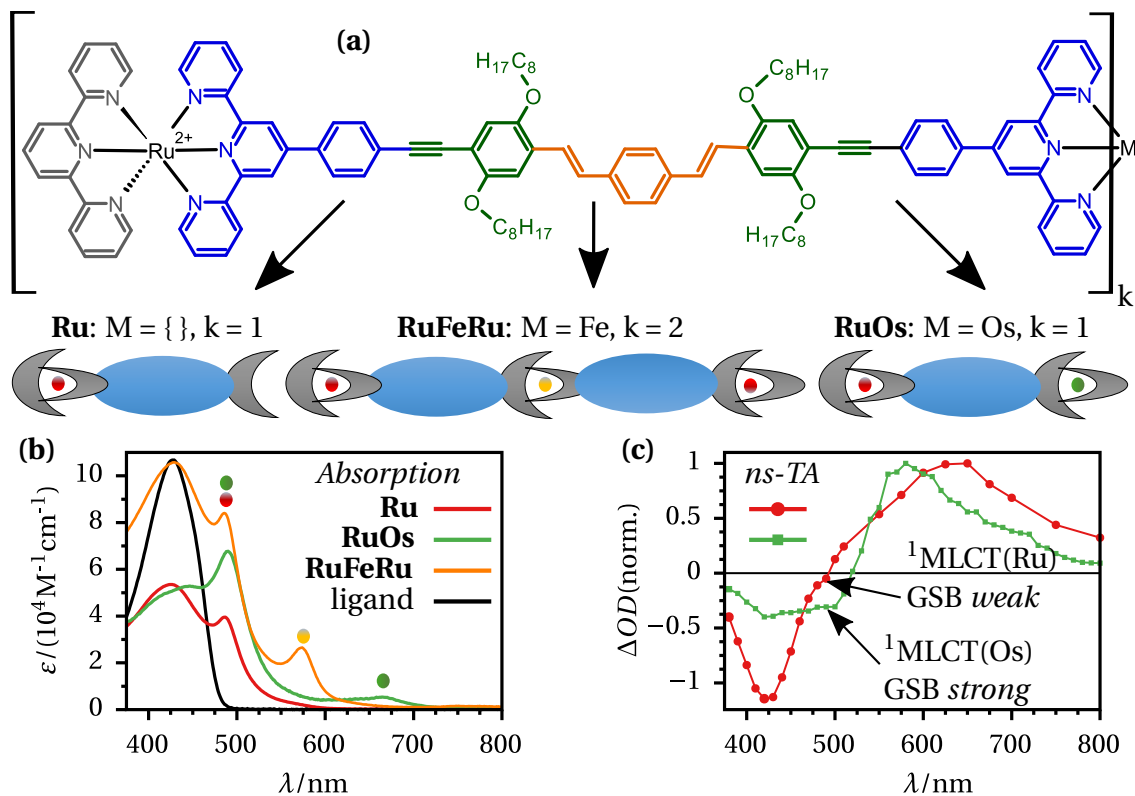
Figure 3.1: **(a)** Chemical structures of **Ru**, **RuOs** and **RuFeRu** with schematic representations (colored spheres are the metal ions; Ru: red, Fe: yellow, Os: green) that will be referred to in the text. UV/Vis absorption spectra of the three complexes as well as that of the ligand are shown in **(b)**. The characteristic absorption features due to MLCT transitions for the three metals are marked with the colored spheres. Panel **(c)** contains nanosecond transient absorption spectra for **Ru** and **RuOs**; notably, both GSB and ESA regions are different for both compounds. While the ^{1}MLCT(Ru) GSB bleach is weak for **Ru** and the GSB of the ligand-centered transition at 425 nm is much more dominant, in **RuOs** the GSB of the degenerate ^{1}MLCT(Ru/Os) band is much stronger as compared to the GSB of the ligand-centered transition. The different spectra are indicative of different long-lived states in both compounds: A ligand-centered state in **Ru** and a ^{3}MLCT(Os) state in **RuOs**.

i.e. are excited at the same wavelengths, it is not possible to excite the ^{1}MLCT(Ru) transition without exciting the ^{1}MLCT(Os) at the same time.

With respect to the complexes considered in this chapter, only **RuOs** shows measurable phosphorescence. The emission decay time was determined in air-equilibrated solution using TCSPC (ca. 100 ns, [139]). This number agrees with the excited-state lifetime (84 ns) determined in ns-TA experiments ($\lambda_{\text{exc}} = 530$ nm). [139] The long-lived excited-state absorption spectrum of **RuOs** is characterized by GSB signatures of the ground state absorption bands attributed to the ligand-centered transition at ca. 425 nm and the ^{1}MLCT-band at ca. 488 nm. The ratio of the GSB amplitudes is different from the ratio of the extinction coefficients. This is, taken together with the observation of Os-based phosphorescence only, an indication, that the long-lived excited-state of **RuOs** is dominated by Os-centered ^{3}MLCT contributions (i.e. the Ru-fragment is already in the ground state).

The long-lived state of **Ru** is different from that of **RuOs**, despite the fact that there are both GSB and ESA contained in the spectrum: A closer look reveals that the ^{1}MLCT(Ru)-GSB is absent and the ESA band is shifted bathochromically in **Ru** as compared to **RuOs**. Analogous experiments performed on **RuFeRu** produced a quasi-identical spectrum as that determined for **Ru** with the same lifetime (129 ns for **RuFeRu** and 132 ns for **Ru**). [139] Considering the absence of phosphoresence in **Ru** and **RuFeRu** the long-lived state may primarily be a ^{3}LC state or at least a ^{3}MLCT with significant $\pi - \pi^*$-character, which causes a low radiative rate as compared to a pure ^{3}MLCT state. [108,140]

Therefore, as dark states are contributing to the excited-state landscape of these compounds, femto- to nanosecond TA spectroscopy is the method of choice to probe the photo-induced dynamics that lead to the population of the long-lived excited states.

In order to (as far as possible) selectively excite and populate either metal complex fragment in the multi-metallic complexes, pump wavelengths of 520 nm (hardly specific, as the ^{1}MLCT(Os) and ^{1}MLCT(Ru) are degenerate, and the ^{1}MLCT(Fe) contributes as well), 580 nm (specific for the ^{1}MLCT(Fe)) or 660 nm (specific for Os) were employed. With these pump wavelengths, it is possible to extract information about the photo-induced dynamics for each of the metal complex fragments.

A complication arises in **RuFeRu** due to the fact that, since there are two Ru-tpy fragments in the compound, both ^{1}MLCT(Ru) transitions may be excited at the same time (i.e. corresponding to the formation of **Ru*FeRu***). Additionally, since both the ^{1}MLCT(Ru) and the ^{1}MLCT(Fe) contribute to the absorption at 520 to 530 nm, at this pump-wavelength also a mixed-doubly excited species **Ru*Fe*Ru** may be formed. The
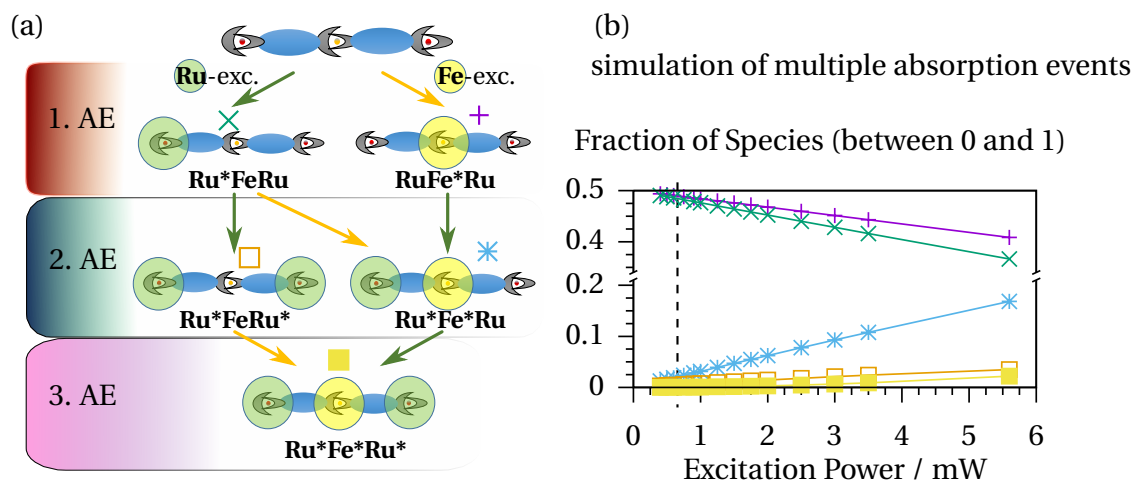
Figure 3.2: (a) Possible pathways for multiple absorption events (AE) to form singly-, doubly-
or triply excited species. **(b)** An approximate simulation of the multiple absorption
evens under typical experimental conditions suggests that at elevated pump powers -
apart from the singly excited species - primarily the mixed doubly-excited **Ru*Fe*Ru**
is formed (the legend is given in terms of the symbols next to the schematic repre-
sentations in **(a)**). The vertical dashed line marks the end of the linear excitation
regime. All measurements discussed in Section 3.1.1 are performed with pump
powers corresponding to the linear regime.

possible pathways for multiple excitation are visualized in Fig. 3.2. Based on a crude
approximation (neglecting ESA and GSB contributions), multiple excitation based on
the remaining ground state absorption was simulated[*], suggesting that under typical
measurement conditions ($P_{pump} \leq 0.6$ mW) only the singly-excited species are formed.
Furthermore, upon an increase in pump power, the only multiply excited species that is
formed with considerable probability is the mixed doubly excited **Ru*Fe*Ru**.

In the next section, the photophysical properties of exclusively singly-excited species
are discussed. Thereafter the variation of the photo-induced dynamics of **RuFeRu** upon
elevated pump powers is described.

3.1.1 Light-induced processes in the singly excited-complexes

In order to disentangle the complex photo-induced dynamics of the multinuclear com-
plexes, a number of measurements were recorded using an experimental setup with

---

[*]sample OD of 0.18 in a 1 mm cuvette, beam diameter at sample position 480 μm

technical capabilities beyond the one described in Section 1.2.1.[†]

In the absence of a second metal ion, the Ru(II)-complex with the extended ligand structure **Ru** behaves initially as a typical Ru(II)-polypyridine complex: Upon photo-excitation of the ^{1}MLCT transition, instantaneous bleach of the ^{1}MLCT band is observed. Above 520 nm ESA increases on a few ps-timescale. Subsequently a further increase of ESA occurs, accompanied by a signal decrease of the ^{1}MLCT GSB around 488 nm, and an increase of the GSB signature peaking at 425 nm. After that only minor intensity variations occur, while the spectral signatures are not affected. The spectrum at long-delay times corresponds to the one determined in ns-TA experiments (Fig. 3.1), i.e. a primarily delocalized state of $\pi - \pi$*-nature. The loss of GSB in the ^{1}MLCT region at the same time as an increase of GSB of the ligand-centered absorption band suggests a deactivation of the ^{3}MLCT(Ru) towards a ^{3}LC. Interestingly, the time-scale of this process coincides with the time-scale of planarization observed in related complexes. This may allow the conclusion, that a stabilization of the ^{3}MLCT due to the additional delocalization on the planarized chromophore in fact opens also an efficient pathway for deactivation via a ligand-centered decay.

In **RuOs** a different long-lived state was identified (Fig. 3.1), consistent with a ^{3}MLCT(Os) state. The corresponding femto- to picosecond TA data is not shown here, but described in short (for the plots see figures 6 and 7 in **P5**, [139]): After excitation of the degenerate ^{1}MLCT-transition instantaneous GSB of the ^{1}MLCT band and a flat excited-state absorption in the red part of the spectrum at wavelength larger 510 nm is observed. Within the experimentally accessible time range of 2 ns only minor amplitude variations occur. The same spectral features and very similar kinetics are observed when directly populating the ^{3}MLCT(Os) using a pump wavelength of 660 nm. The invariance of the data with respect to the excitation wavelengths suggests that only a Os-centered decay is observed, which means that there is ultrafast deactivation of initially excited ^{1}MLCT(Ru) states, which populates ^{1}MLCT(Os) states on the sub-200 fs time scale. Such ultrafast singlet-singlet energy transfer from Ru(II) towards Os(II) in complexes with polypyridine ligands has been described in literature. [141]

The photo-induced dynamics of the trinuclear complex **RuFeRu** are much more complex than that for **Ru** or **RuOs**. The transient absorption data recorded after directly populating the ^{1}MLCT(Fe) transition (pump wavelength of ca. 575 nm, Fig. 3.3b) will be discussed first, as due to the electronic structure of **RuFeRu** under the chosen condi-

---

[†]The measurements with an extended probe window of 350 to 850 nm and a maximum pump-probe delay of ca. 8 ns were performed in Prof. Lambert's laser lab (Universität Würzburg) by Dr. Maria Wächtler.

tions no participation of the higher-lying Ru(II)-based states is observed. Within the time-resolution of the experiment a strong GSB of the ^{1}MLCT(Fe) absorption band between 500 to 600 nm is observed. Weak ESA is found at wavelength above 600 nm. Characteristic spectral features are furthermore observed below 500 nm: ESA is observed between 450 and 480 nm (peaking at 460 nm) and GSB between 380 and 450 nm. On the sub-100 ps timescale the ESA above 600 nm and most of the GSB below 450 nm is lost. After that an overall signal decrease is observed without changes of the spectral features. The data is consistent with dynamics that are entirely centered on the Fe-tpy unit: After excitation of the ^{1}MLCT(Fe), ultrafast intersystem crossing leads to population of the ^{3}MLCT(Fe). Within the triplet manifold vibrational relaxation and solvation are followed by planarization. The GSB at around in 425 nm is rather weak, suggesting only weak participation of the ligand chromophore. As commonly observed in Fe(II) polypyridine complexes, the ^{3}MLCT state is deactivated via a second intersystem crossing populating a high-spin Quintet state. This state decays with a lifetime of 4.2 ns to the ground state.

The TA data is qualitatively and quantitatively different when primarily the ^{1}MLCT(Ru) transition (at 520 nm) is excited in **RuFeRu**: While the transient spectra are dominated by **Ru**-like features on the early ps-timescale, at later delay times the Fe-tpy based signatures dominate the signal evolution. However, there is a difference when comparing the spectra at late delay times recorded after either excitation at 520 or 575 nm: While the ESA features above 600 nm are completely lost in the data recorded upon excitation at 580 nm, ESA is found on the ns-timescale in the data recorded upon 520 nm excitation. More insight is provided by a quantitative analysis, which is summarized in the following.

For the data recorded after selective excitation of just one metal complex fragment (520 nm for **Ru**, 660 nm for **RuOs**, 580 nm for **RuFeRu**) the data is treated well by applying a kinetic model of consecutive first-order reactions. Species spectra produced using such fit routine (figure 5 in **P5**, [139]) are consistent with the model assumptions and, where applicable, with literature. [139] Interestingly, the photo-induced dynamics after excitation at 520 nm in the bi-nuclear complex **RuOs** seem to be well described using a consecutive model as well. This is plausible in light of the ultrafast energy transfer as described above.

The TA data measured for **RuFeRu** after excitation at 520 nm is not properly described using the simple consecutive relaxation model. The main reason for this is that initial excitation at 520 nm does not exclusively populate the ^{1}MLCT(Ru), but also the
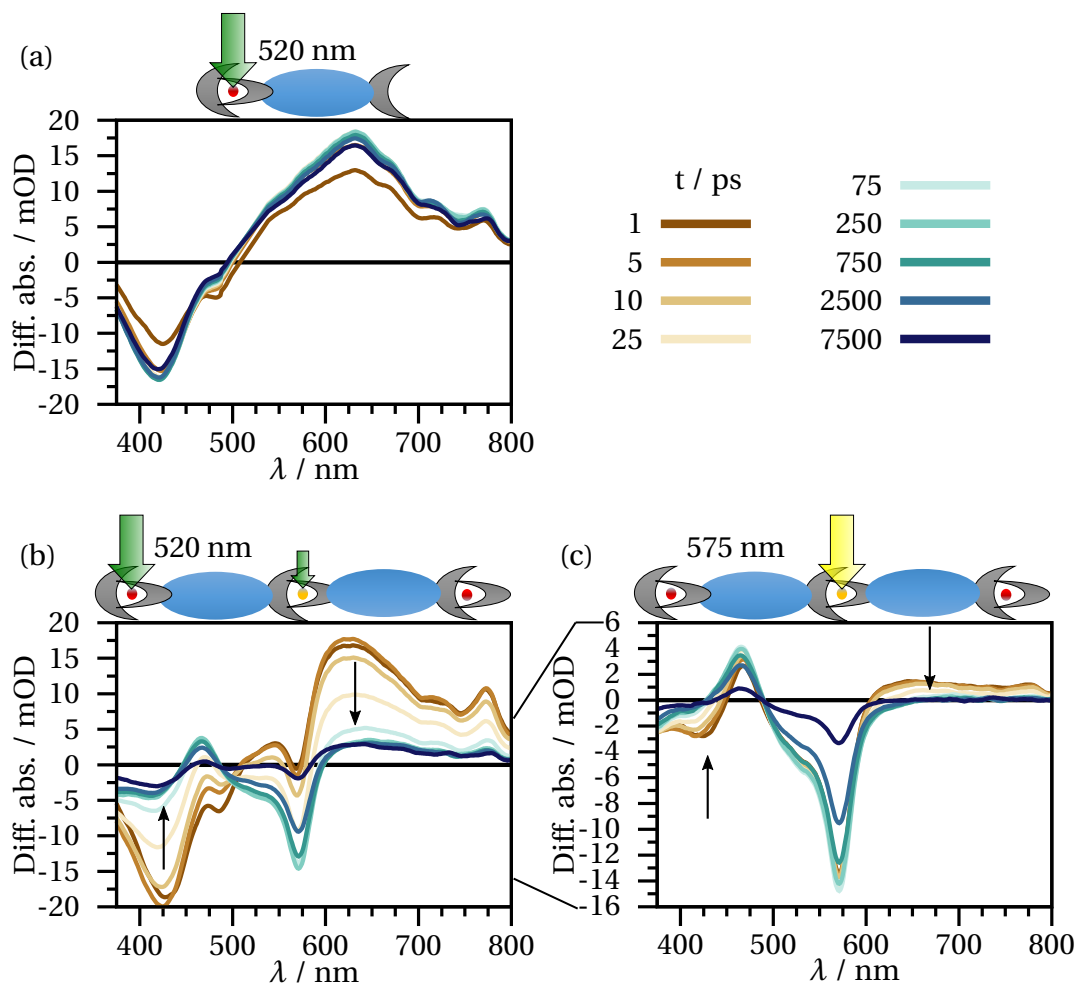
Figure 3.3: TA data for **Ru (a)** and **RuFeRu** at two different excitation wavelengths: **(b)** 520 nm and **(c)** 575 nm. The black lines between panels **(b)** and **(c)** illustrate the relation between the y scales in both plots.
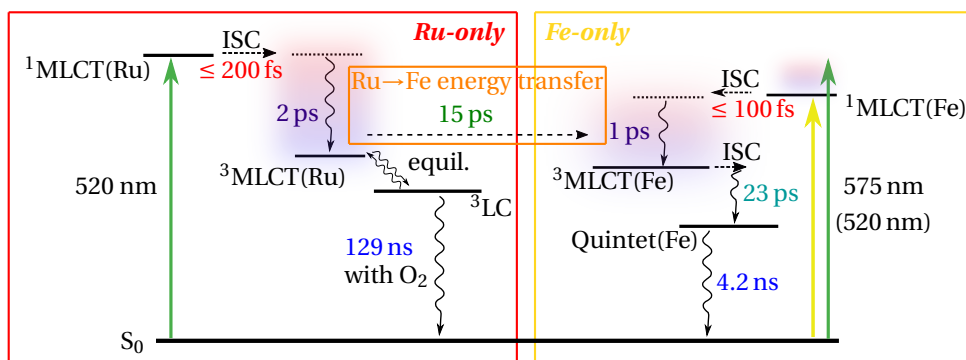
Figure 3.4: JABLONSKI diagram for **RuFeRu** showing the relaxation pathways after excitation at 520 nm and 575 nm, respectively. The red box marks the part of the decay channels accessible after excitation of the ^{1}MLCT(Ru) in absence of the iron center. The yellow box shows the relaxation scheme after sole excitation of the ^{1}MLCT(Fe). The energy-transfer component (orange box) is the important component that needs to be included in the kinetic scheme to describe Ru→Fe excitation energy transfer.

^{1}MLCT(Fe)-a situation calling for a parallel fit model.

A suitable kinetic scheme (see Fig. 3.4) was developed and implemented in a numerical fit routine. As part of the overall decay scheme, the individual relaxation pathways for pure Ru- and Fe-excitation, respectively, are shown as well (in colored boxes). The developed model produces species spectra that are clearly attributable to either metal complex fragment, suggesting that the kinetic scheme is valid. [139]

The kinetic scheme contains a single decay channel for the relaxed ^{3}MLCT(Ru): A process with a time-constant of 15 ps is assigned to energy transfer from the Ru- to the Fe-tpy unit. Remarkably, this time-constant coincides approximately with the time-constant assigned to planarization in **Ru**. It may be concluded that the energy transfer occurs via the ligand chromophore: The planarization allows for a delocalization of the ^{3}MLCT(Ru) state, but opens up a pathway for efficient population transfer to ligand centered states as in **Ru**. However, due to the presence of the Fe(II)-tpy unit, an additional decay channel is opened towards the ^{3}MLCT(Fe) and ultimately the Quintet(Fe) state. Interestingly, the decay via the Fe-tpy states is not quantitative, i.e. a certain portion of the initially excited ^{1}MLCT(Ru) states resides in the ^{3}LC state, not decaying via the Quintet(Fe) state.

It may be pointed out that the lifetime of the ^{3}MLCT(Fe) state is remarkably long (23 ps) in comparison to other Fe(II)-polypyridine complexes, [138] and may be attributed to the stabilization of the ^{3}MLCT(Fe) by delocalization and electronic interactions with the extended ligand chromophore.

In this section the Ru(II)-tpy unit has been identified as possible donor fragment in building blocks for hierarchic coordination oligomers. In presence of an Os(II)-tpy unit, ultrafast singlet-singlet energy transfer occurs quantitatively, while with an Fe(II)-tpy unit, there is energy-transfer on the tens of picosecond time-scale. Despite the fact that the data discussed so far has included excitation of different transitions at the same wavelengths, there has been no double excitation of the same molecule. Apart from the *accidental* use of high-powers in spectroscopic studies (that led e.g. to the discovery of singlet-singlet annihilation in natural light harvesting units[4,142]), increasing the pump power in a well defined molecular system under strictly controlled experimental conditions allows to study intrinsic molecular mechanisms. As shown in Fig. 3.2 for **RuFeRu**, gradual increases in pump powers have impact on the composition of the ensemble of excited molecules including an increasing portion of the mixed-doubly excited **Ru*Fe*Ru**. The next section discusses the alteration of photo-induced dynamics in **RuFeRu** at elevated pump powers[‡].

## 3.1.2 Multiple excitation processes in RuFeRu

The electronic structure of **RuFeRu** with its weakly coupled metal complex fragments renders this compound a suitable candidate to study the impact of increasing excitation powers on the photoinduced dynamics. The possible pathways for the formation of multiply excited species of **RuFeRu** are shown in Fig. 3.2(a). Within the accessible parameter space, the only doubly-excited species forming considerably is **Ru*Fe*Ru**, in which both the ^{1}MLCT(Ru) and the ^{1}MLCT(Fe) have been excited.

A total of 14 complete TA measurements at defined excitation powers were acquired in order to be able to resolve the photoinduced dynamics and their power-dependent variations gradually. Datasets at four selected powers are presented in Fig. 3.5a; the data is normalized to the respective excitation power. With such normalization, the amplitudes in the spectra should be identical in case of a linear relationship between excitation power and sample response, i.e. absolute signal amplitude. There are deviations of the spectra at different pump powers, e.g. with respect to the GSB signatures: While the GSB amplitude in the spectral interval of the ^{1}MLCT(Ru) band is hardly dependent on the pump power, the amplitude in the region of ^{1}MLCT(Fe) GSB reduces considerably in the data recorded at elevated pump powers.

[‡]The well distinguishable spectral features of either metal complex fragment in **RuFeRu** are helpful in disentangling complicated photo-induced dynamics, such that **RuFeRu** is much more suited for such investigation than **RuOs**.
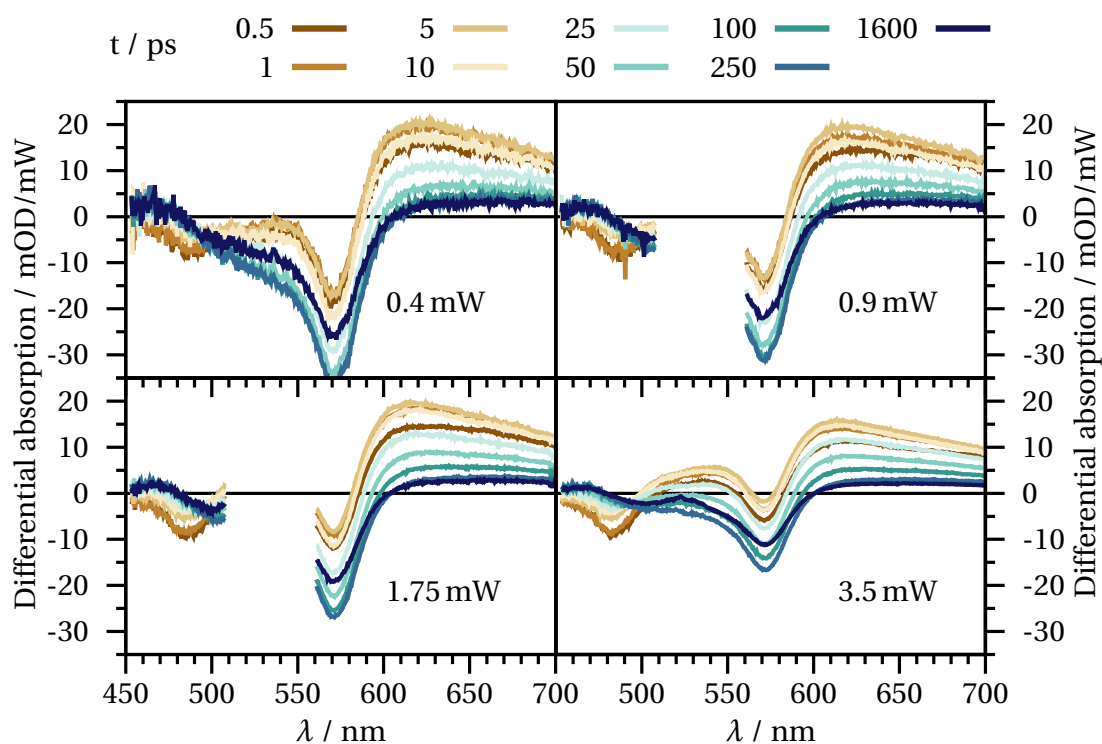
(a) Pump-power normalized datasets at four selected excitation powers.
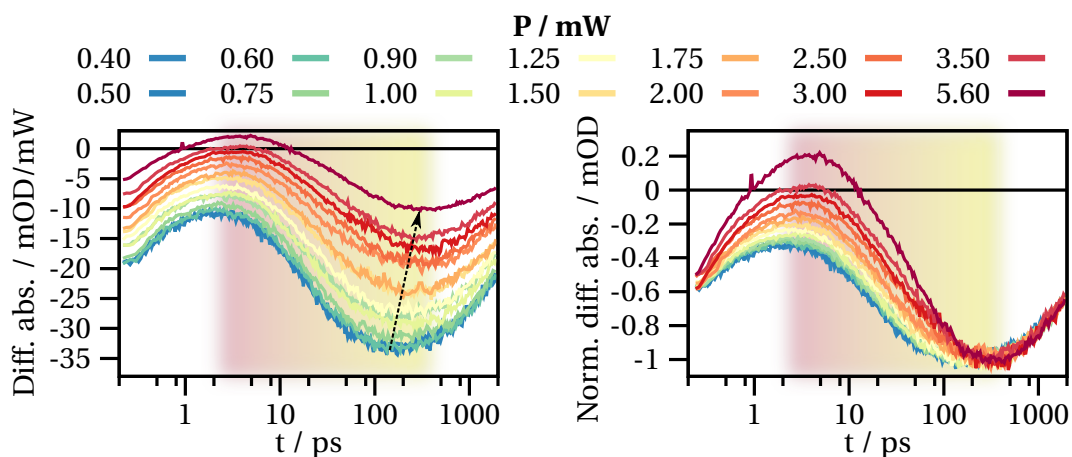
(b) 577 nm kinetics norm. by P

(c) 577 nm kinetics norm. at min.

Figure 3.5: TA data for **RuFeRu** recorded at elevated excitation powers. A normalization by the respective excitation power emphasizes the relative changes in the TA data. Transient spectra covering the accessible delay range are shown for four excitation powers (a). Kinetic traces at 577 nm are shown normalized to the excitation power (b) and the respective minima (c). The color of the kinetic traces color codes the excitation power from blue (low power) to red (high power). The colored area behind the kinetics marks the temporal interval in which energy-transfer occurs at low excitation power.

Kinetic traces at 577 nm contain signatures of both the [3]MLCT(Ru) manifold and Fe-tpy centered states. An inspection of the kinetics at this wavelengths in dependence of the pump power reveals for two different normalizations:

Normalization by the pump power : Fig. 3.5b - the time, after which the minimum is reached, increases with increasing pump power.

Normalization at the minimum : Fig. 3.5c - the overall decay via the Quintet(Fe) state does not seem to be influenced by the pump power.

The kinetics at 577 nm prominently represent the interconversion from Ru- towards Fe-centered states, i.e. the energy transfer introduced in the previous section. Therefore a delay in these kinetics, where the time at which the minimum is reached is shifted to later delay times, indicates a slowed-down energy transfer at elevated pump powers. This observation can be correlated with the enhanced probability to create the mixed-doubly excited **Ru*Fe*Ru** (see Fig. 3.2, Page 45) based on the experimental parameters. Based on that, it may be concluded, that energy-transfer can not occur, if both the [1]MLCT(Ru) and the [1]MLCT(Fe) are populated at the same time, and therefore the [3]MLCT(Ru) population can not decay via energy-transfer to the [3]MLCT(Fe) as long as the acceptor unit is populated, i.e. occupied. This blockage results in an increased lifetime of the [3]MLCT(Ru) state. While no indication of additional decay channels such as triplet-triplet annihilation is found in the data described here, it may be deducible that a prolonged lifetime of an energetically high-lying excited state could lead to unwanted side reactions.

A photophysical model is suggested to account for the kinetic hindrance in dependence of the acceptor state occupation o:

$$ffac = \frac{1}{\exp\left((o - o_{\text{full}})/w\right) + 1}$$

The functional dependence is similar to that of the FERMI distribution function and has two parameters, which determine threshold (o_{full}) and slope (w) of the kinetic hindrance. For the suggested model (Fig. 3.6) k_3(low-P) is considered constant in the *low-P* scheme, and is modulated by the acceptor state occupation in the *high-P* scheme via *ffac* ($k_3' = k_3 * ffac$). The steps taken for data simulation based on the proposed model are visualized in Fig. 3.6.

The observation of a blockage in the excited state that slows down energy transfer is striking and has possible general implications for the design of artificial light-harvesting
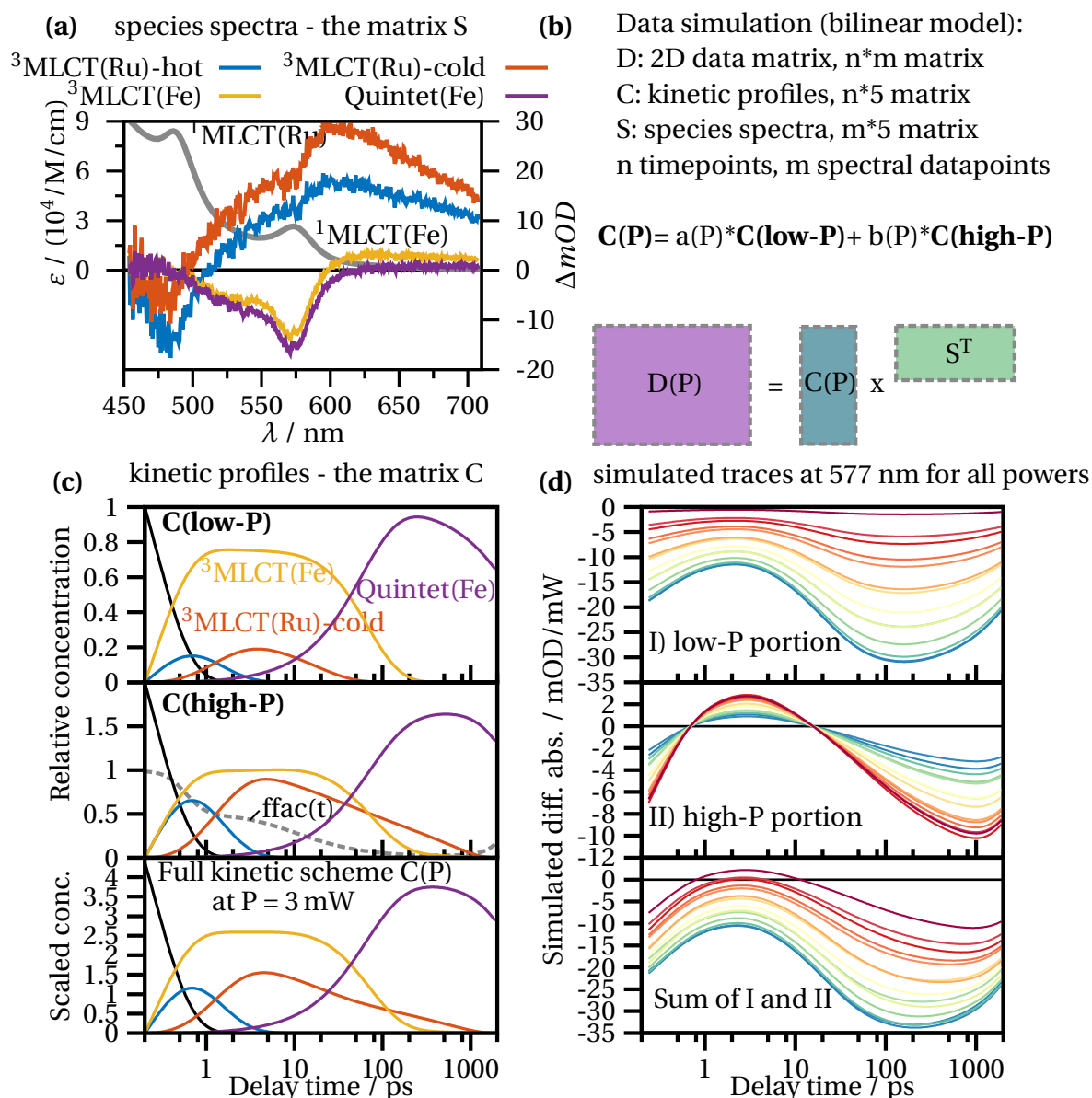
(a) species spectra - the matrix S

^{3}MLCT(Ru)-hot —— ^{3}MLCT(Ru)-cold ——
^{3}MLCT(Fe) —— Quintet(Fe) ——

(b) Data simulation (bilinear model):
D: 2D data matrix, n*m matrix
C: kinetic profiles, n*5 matrix
S: species spectra, m*5 matrix
n timepoints, m spectral datapoints

$$C(P) = a(P)*C(low\text{-}P) + b(P)*C(high\text{-}P)$$

$$D(P) = C(P) \times S^T$$

(c) kinetic profiles - the matrix C

(d) simulated traces at 577 nm for all powers

Figure 3.6: Details on the photophysical model for the light-induced dynamics in **RuFeRu** at elevated excitation powers. The species spectra **(a)** are obtained from applying the kinetic model on the TA data in the linear regime. These are combined with the concentration profiles as given in **(b)**. Two different kinetic schemes are regarded, called *low-P* and *high-P*. The *low-P* kinetics are entirely based on the time constants (Fig. 3.4) determined in the linear regime, while the *high-P* kinetics contain an acceptor-state dependent modulation of the energy transfer rate: *ffac* ∗ k_3. The contribution of each model is scaled by a fitted factor for each pump power (a and b, respectively), such that a weighted sum of both gives the overall concentration profile matrix C(P) at each pump power. In panel **(c)** the concentration profiles for the *low-P* and the *high-P* model are shown; it is pointed out that *ffac* is calculated at each time point (gray dashed line in **(c)**). The individual signal contributions of the two kinetic schemes are shown for the 577 nm kinetics as well as their sum, which can be qualitatively and to some extent quantitatively compared to the experimentally determined kinetics (Fig. 3.5).

systems: Many chemical system designs for potential use in artificial photosynthesis involve multiple light-absorbing units, which are ought to provide excitation energy for a single catalytic site. [42,143–146] Multiple donor units forming excitons in spatial proximity are prone to undergo annihilation processes, [147,148] which reduce the number of excitons available for the desired process such as catalysis.

3.2 Cyanide-bridged Ir(III)-Ru(II)-complexes

Parts of this chapter have been published in this article: **P6** - K. Barthelmes, M. Jäger, J. Kübel , C. Friebe, A. Winter, M. Wächtler, B. Dietzek, and U. S. Schubert, *Inorg. Chem.* **2016**, *55*, 5152-5167.

Hetero-bimetallic complexes with a cyanide bridging ligand were reported for e.g. Ru(II) and Cr(III) ions. [149] In such systems, excitation of the ^{1}MLCT(Ru) band results in Cr(III)-localized emission from a dd-state, [150] thus suggesting efficient intramolecular energy transfer between the metal complex fragments. In this section, an [Ir(ppy)$_2$(CN)]$^-$ complex fragment is combined with a [Ru(bpy)(tpy)(CN)]$^+$ complex (Fig. 3.7a). Substituents in 4'-position of the tpy unit (the derived tpy ligands are abbreviated **S** and **L**, respectively) are varied. A terminal aldehyde group allows for possible derivatization of the compounds. Furthermore, influence of fluorination at the ppy ligands within the Ir(III) complex fragment is investigated.

A three-dimensional structure of the cyanide-bridged complex **IrFRuS** in shown in Fig. 3.7b: The complex fragments can rotate around the connecting cyanide bridge, which has minor impact on the electronic properties of the dyads. [151,152]

The complexes show strong metal-metal interactions as intervalence charge transfer bands are observed in the near infrared. [152]

UV/Vis absorption spectra (Fig. 3.8) show that the ^{1}MLCT(Ru) bands of the coupled Ir(III)-Ru(II) complexes are blue-shifted with respect to the Ru(II) model complexes. The impact of fluorination is well resolved for both ligand structures (**S**, **L**) by a slightly stronger blue-shift of the ^{1}MLCT(Ru) bands. No clear evidence of a populated ^{3}MLCT(Ir) state is visible in the transient spectra; reasons for that can a low population as well as the low absorption coefficients of the Ir(III)-centered transitions. At a delay time of 10 ps, i.e. after initial relaxation, the GSB signatures are mostly consistent to the spectral positions of the ground-state absorption bands, suggesting that a state with dominant ^{3}MLCT(Ru) character is populated in all cases. Nevertheless, the ESA signatures are

(a) Chemical structures **(b)** 3D model of **IrFRuS**
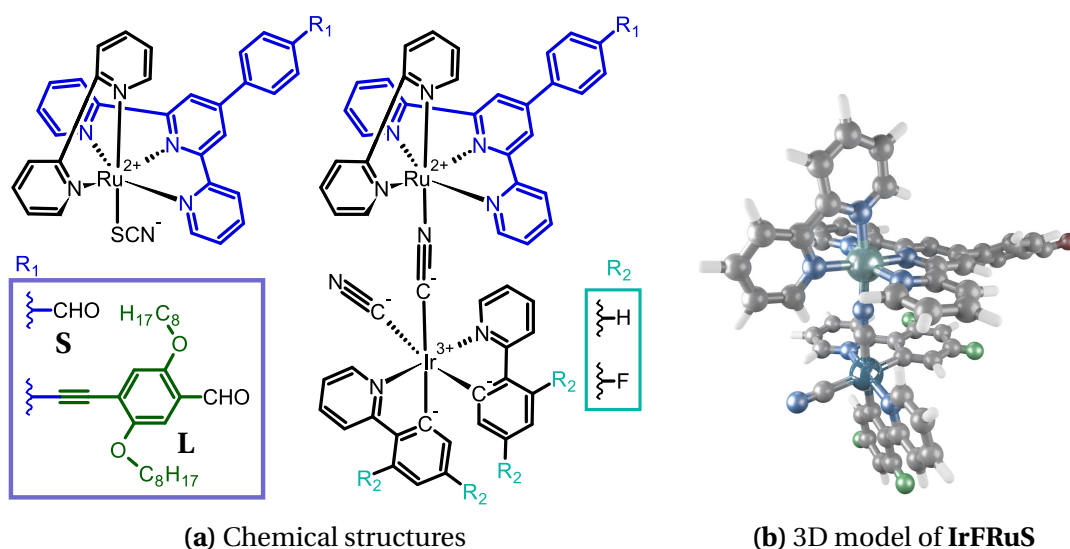
Figure 3.7: Chemical structures of cyanide-bridged Ir(III)-Ru(II) complexes. The relevant compounds (see a) have either 4'-substituted tpy ligand (e.g. **IrRuS** or **IrRuL**) at the Ru(II) ion and the ppy ligands coordinating the Ir(III) are unsubstituted or fluorinated (e.g. **IrRuS** and **IrFRuS**). The mononuclear Ru(II) reference compounds (**SCNRuS** and **SCNRuL** have a thiocyanate ligand instead of the bridging cyanide ligand. An exemplary 3D model is shown for **IrRuS** (b).

somewhat different for the Ru(II) model complexes than those for the binuclear complexes. Therefore, the ESA signatures are sensitive probes for electronic coupling, and suggest a certain degree of mixing between the Ir(III) and Ru(II) orbitals via the cyanide bridge.

The complex electronic interplay between both metal ions and the their ligand spheres can be further inferred from the emission lifetimes given in Table 3.1:

- The ^{3}MLCT(Ru) emission maxima are blueshifted upon changing the S to the L ligand, and by fluorination of the ppy ligands.

- The ^{3}MLCT(Ru) emission lifetime is longer for the S ligand as for the L ligand in both the SCN$^-$-containing reference compounds as well as the binuclear complexes, with the exception of the fluorinated compounds, in which the lifetimes are roughly the same.

- The ^{3}MLCT(Ir) emission lifetime is identical in the non-fluorinated binuclear complexes with either ligand S or L, but is significantly altered in the fluorinated analogues. An even more significant lifetime change is observed upon solvent variation from ACN to DCM, pointing towards very sensitive electronic effects.
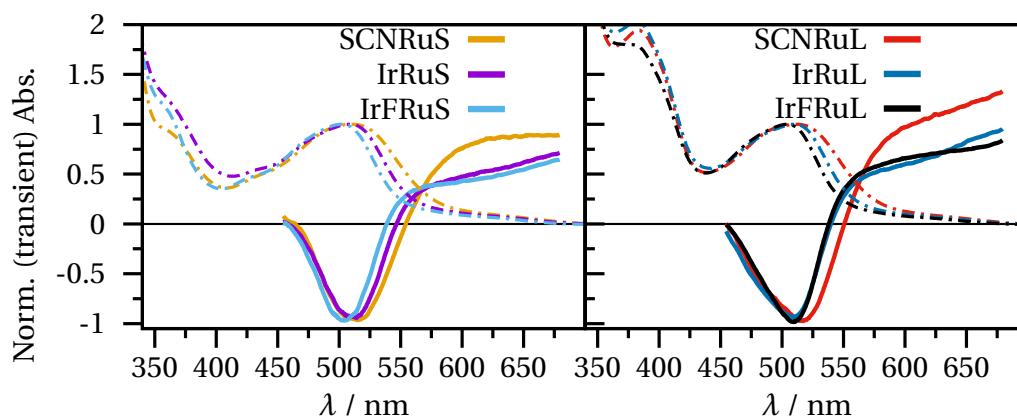
Figure 3.8: Absorption spectra (dashed-dotted lines) and mean transient absorption spectra (solid lines) after 100 ps of cyanide-bridges Ir(III)-Ru(II) complexes and Ru(II) model complexes.

- The ^{3}MLCT(Ir) emission lifetimes in the Ir(III) reference compounds are clearly different from those in the binuclear complexes.

The presented data shows the complicated electronic interplay between two closely coupled metal complexes. For a more profound analysis of the excited-state composition and processes, more powerful spectroscopic methods, such as TA with probing in the deep-UV have to be applied. [153]

Compound	Solvent	^{3}MLCT(Ru) λ_{max} / nm	τ / ns	^{3}MLCT(Ir) τ / ns
SCNRuS	ACN	718	50	-
SCNRuL	ACN	711	32	-
IrRuS	ACN	700	71	39
IrRuL	ACN	694	45	39
IrFRuS	ACN	691	53	60
IrFRuL	ACN	684	55	33
	DCM	685	45	343
IrCN	ACN	-	-	90
	DCM	-	-	93
IrFCN	ACN	-	-	183
	DCM	-	-	163

Table 3.1: Emission lifetimes in aerated solution determined from streakcamera measurements. **IrCN** and **IrFCN** are the respective Ir(III) model complexes based, i.e. $[Ir(ppy)_2CN_2]^-$ and its fluorinated analogue.

3.3 A strongly coupled dyad combining a Ru(II) polypyridine complex and a Cu(II)-porphyrin

Porphyrins are ubiquitous motives in nature.[154] The versatility of porphyrinoids (i.e. porphyrins and derivatives thereof) is reflected by the large variety of tasks these molecules fulfill in natural systems: Chlorophyll A is a Mg(II) porphyrin and arguably the most important light harvesting molecule on our planet.[155] The metal-free pheophytins are essential constituents of the electron transfer chain in PSII.[156] The active site of several proteins contains a porphyrin: Oxygen transport in the human body is controlled by Myoglobin, in which O_2 reversibly binds to an Fe(II)-porphyrin (heme). The class of heme proteins includes numerous proteins with manifold essential functions in living organisms.[157]

Porphyrins are also widely used photosensitizers and active units in model systems for fundamental studies on energy and electron transfer.[158–163]

The potential of porphyrins in the field of artificial photosynthesis is therefore manifold.[164] Paramagnetic porphyrins have been shown to be efficient electrocatalysts for the reduction of CO_2 to CO,[41,165] Also electrochemical water oxidation[166], oxygen reduction[167] and proton reduction[168,169] were demonstrated.

However, little is known with respect to the potential of porphyrins in photocatalysis. Examples include e.g. antimony porphyrins.[170] Here examined is a dyad consisting of

a Cu(II)-porphyrin with an extended chromophoric system including a phenanthrolin unit and a Ru(II)-polypyridine complex (structures given in Fig. 3.9) The syntheses and catalytic experiments were performed by Corinna Matlachowski and Dr. Matthias Schwalbe (Humboldt-Universität zu Berlin).

The compounds **Cu** and **CuRu**[72] show very low catalytic activity for the reduction of CO_2 to CO,[73] indicating that the catalytically active species is formed rather inefficiently. Furthermore, catalytic activity is found exclusively when UV light between 305 and 375 nm is used;[73] a similar observation was made in a related study.[171] Notably, under identical conditions no catalytic activity is found for the analogue free-base porphyrin even in presence of the Ru(II)-complex fragment.[73]

The discussion in this section addresses two specific aspects: Firstly, within the general scientific scope of this thesis: What can be deduced with respect to the electronic communication between the metal complex and the porphyrin? This question is addressed using steady-state and TA spectroscopy with different pump wavelengths. In this context it may be noted that the porphyrin, a metal complex itself, can be regarded as a part of an extended chromophore of a ligand in a Ru(II)-polypyridine complex. Secondly, based on TA experiments mimicking the catalytic conditions, possible molecular mechanisms that may explain the low catalytic activity are discussed.

Porphyrin UV/Vis absorption spectra are characterized by two dominant contributions: B (or Soret) and Q bands denoting the transitions from the ground state (here the sing-doublet state $^2S_0$) to the $^2S_2$ and $^2S_1$, respectively.[172] These assignments are based on a four-orbital model proposed by GOUTERMAN.[173] Upon symmetry reduction, e.g. due to the extension of the π system by attaching the pyrazine-phenanthroline unit, the B and Q bands split in orthogonal contributions resulting in B_x/B_y and Q_x/Q_y transitions, respectively.[174,175] The absorption spectra for **Cu** and **CuRu** (Fig. 3.9 a and b, measured in toluene, TOL) are consistent with the symmetry reduction and its impact on the absorption spectra.[174,175] There is a remarkable red-shift of the dominant absorption bands in the visible spectral region in **CuRu** as compared to **Cu**. This red-shift explicitly demonstrates the close electronic interaction between the π-system of the porphyrin and the Ru(II)-coordinated phenanthroline unit: The B_y and B_x bands are shifted from 408 to 421 nm (757 cm^{-1}) and 443 to 466 nm (1114 cm^{-1}), respectively upon coordination of the Ru(II) complex fragment.[72] Furthermore, an additional absorption band at 496 nm is found for **CuRu**, which is not present for **Cu**. This band is likely to originate at least in part from a ^{1}MLCT(Ru) transition. For comparison, the ^{1}MLCT(Ru) in [Ru(tbbpy)$_2$(phen)]$_2$$^+$ (phen = 1',10'-phenanthroline) is found between 400 and 500 nm
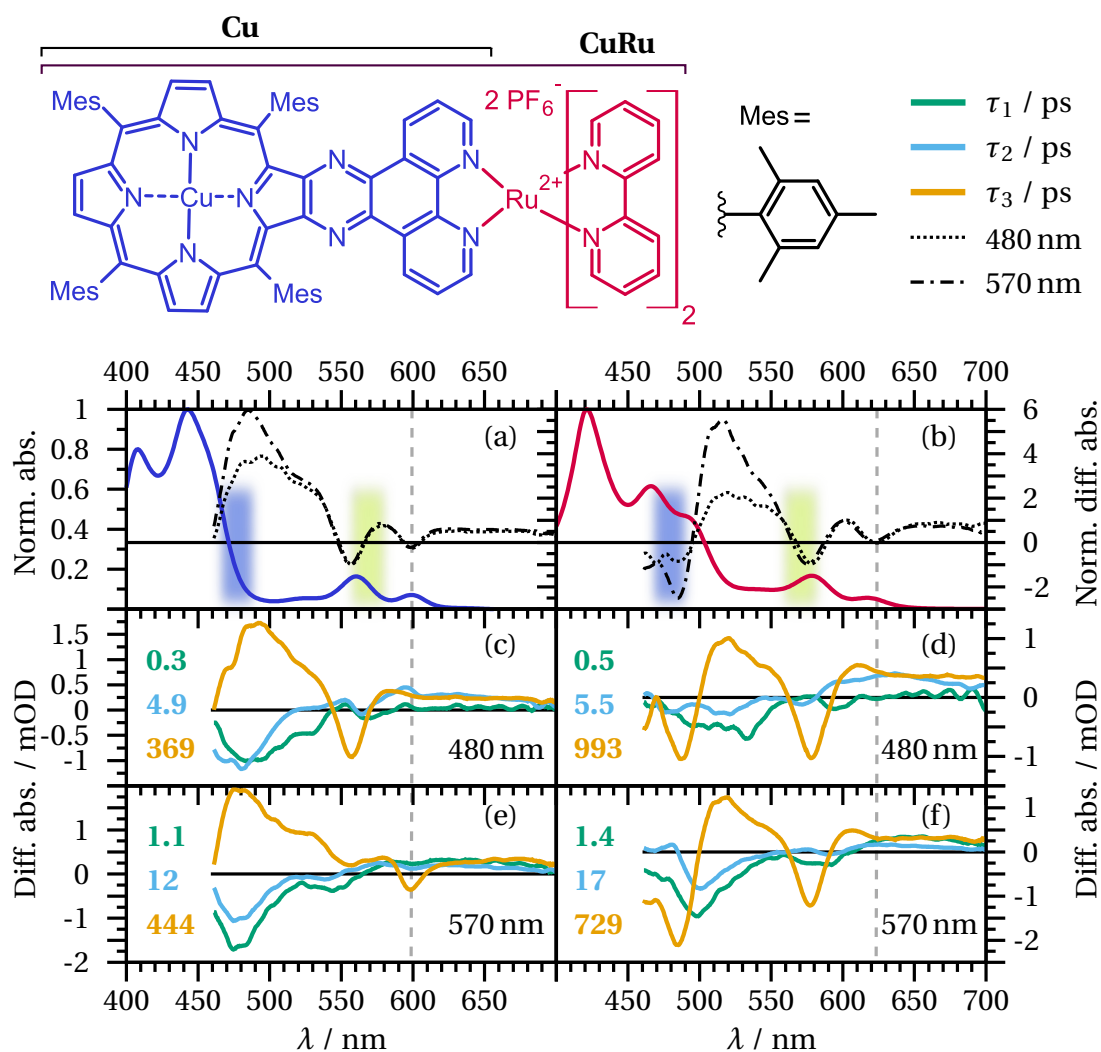
Figure 3.9: Molecular structure of the phenanthrolin-extended Copper(II)-tetra mesityl por-
phyrin (**Cu**) and the respective dyad (**CuRu**) with a [Ru(dtbbpy)$_2$]$^{2+}$ (mesityl is 2,4,6-
trimethylbenzyl, dtbbpy is 4,4'-di-*tert*-butyl-2,2'-bipyridine) complex fragment.[72]
The UV/Vis absorption spectra in TOL are given as solid lines for **Cu** (blue, panel
a) and **CuRu** (red, panel b). TA data is provided in terms of DAS from global fits for
data acquired using pump wavelengths of 480 and 570 nm (pump wavelengths are
marked appropriately colored as shades in the absorption spectra) for **Cu** (panel c,e)
and **CuRu** (panels d, f). The individual components are characterized by spectra and
time-constants and colored consistently. A long-lived component that does not de-
cay on the timescale of our experiment (ca. 2 ns) was found for both 480 and 570 nm
excitation in both compounds; the corresponding spectra are contained in panels a
and b for **Cu** and **CuRu**, respectively (dotted line: 480 nm pump data, dash-dotted
line: 570 nm pump data). The gray dashed lines mark the center of the lower Q band
in each column of plots.

and a red-shift of this band upon an extension of the π system is deducible, just as observed for **CuRu**.

Photo-induced dynamics in Cu(II) porphyrins have been intensively investigated for decades. [176–180] The electronic structure of Cu(II) porphyrins includes an unpaired electron at the copper ion, such that the overall spin system is a combination of the unpaired electron and the π system. [181] A general relaxation scheme [176] upon Q band excitation involves excitation from the doublet ground state ($^2S_0$) into an excited sing-doublet ($^2S_1$) state followed by fast (sub 1 ps) ISC into the trip-doublet ($^2T_1$) state, possibly mediated via a CT state. [182] The trip-doublet state is expected to be in thermal equilibrium with a trip-quartet ($^4T_1$) state (corresponding to a spin flip of the unpaired electron) as both states are separated in energy by ca. 300 to 400 cm^{-1}. [183] Early reports on the relevance of CT and dd states close in energy to the $^2T_1$ and $^4T_1$ states [176,184,185] were contradicted by more recent electron paramagnetic resonance (EPR) experiments. [180,186–188] While earlier studies report on the manifestation of $^2T_1 \rightleftharpoons {}^4T_1$ equilibration on the sub-ns timescale, [176] this was contradicted later by showing that the time constant of this process coincides with the rotational diffusion time in two reference compounds. [179] Therefore, the contribution of this process can be eliminated by setting the polarization between pump and probe beams to 54.7° (magic-angle). [179]

The now widely accepted view is that symmetry reductions, e.g. JAHN-TELLER distortions [189] play a major role in the photophysics of porphyrines. [190,191] Non-planar distortions can promote vibronic coupling leading e.g. to fast excited-state decay. [178,183] An illustrative example for such behavior is the longer emission lifetime of Cu(II)-tetra-mesityl-porphyrin (CuTMP, 101 ns [192]) in contrast to that Cu(II)-tetra-phenyl-porphyrin (CuTPP, 29 ns [183]): There are essentially no changes in the electronics of the porphyrin π system in these compounds, but in CuTMP there are additional steric constraints due to the methyl groups of the mesityl units. [192]

The photoinduced dynamics of **Cu** and **CuRu** have been probed using pump wavelengths of 480 and 570 nm, i.e. exciting the red-edge of the B band region or the most intense Q-band. The extension and stabilization of the porphyrinic π system in presence of the Ru(II) complex fragment is apparent also in the excited state, as can be deduced from an inspection of the transient spectrum of the long-lived excited state which is formed within 2 ns (dotted and dash-dotted lines in Fig. 3.9 a and b): The GSB signatures are consistent with the spectral positions in the ground-state absorption spectra (blue and red spectra for **Cu** and **CuRu**, respectively, in Fig. 3.9 a/b). Also the ESA signatures are red-shifted in **CuRu** as compared to **Cu**, suggesting that the nature

of the excited-state is preserved upon binding of the Ru-fragment.[177] However, the shape of the spectra of the long-lived states depend on the excitation wavelengths in both **Cu** and **CuRu**: In the respective spectra determined for **Cu**, which are normalized at the GSB maximum in the Q-band region, the ESA signature between 460 and 540 nm is somewhat weaker upon 480 nm as compared to 570 nm excitation. For **CuRu**, there is a discrepancy in the same spectral range including both GSB at (460 to 500 nm) and ESA (500 to 560 nm).§ Such behavior has been also observed for closed-shell porphyrins with (formally) D_{4h} symmetry (MgTPP, CdTPP).[193] Additionally, **Cu** and **CuRu** are open-shell systems and contain a porphyrin with reduced symmetry; both aspects likely give rise to much more complex light-induced dynamics as compared to structurally and electronically simpler analogs. With an extended π system, the participation of orbitals in the Soret-bands apart from the four Gouterman orbitals is likely,[194] leading to somewhat different ESA signatures. Additionally, non-linear absorption properties were found upon Soret-band excitation for several paramagnetic porphyrins at rather low excitation power thresholds,[195,196] with some examples showing saturable absorption.[197] Such effects may contribute to the excited state composition causing varied ESA signals.

Therefore, the different long-lived spectra for B- vs. Q-band excitation in both **Cu** and **CuRu** are at least in part attributed to the presence of the pyrazine/phenanthroline unit, i.e. upon 480 nm excitation the excited state composition is somewhat different to that created upon 570 nm excitation even in **Cu**, where there is no contribution from the ^{1}MLCT(Ru).

Three processes and a non-decaying component are needed for a quantitative description of the photo-induced dynamics in both **Cu** (DAS in Fig. 3.9 c/e for 480 and 570 nm excitation, respectively) and **CuRu** (DAS Fig. 3.9 d/f for 480 and 570 nm excitation, respectively). Data recorded following excitation of **Cu** using 480 nm produces time constants of 0.3, 4.9 and 369 ps in a multiexponential global fit. The first process (green DAS, 0.3 ps) leads to an increase of ESA between 460 and 540 nm and a weak positive feature at 555 nm in the Q band region can be associated with the build-up of GSB. The second process (light blue DAS, 4.9 ps) causes build-up of ESA peaking at 480 nm and the DAS further contains signatures that can be related to the build-up of GSB of the Q-bands and the reduction of the flat ESA in the red-part of the spectrum. The slowest process (orange DAS, 369 ps) contains spectral signatures mostly similar to

---

§If data were normalized to the ESA maximum, the spectra recorded upon 480 nm excitation would have a positive offset spanning over the Q-band region between ca. 550 and 700 nm.

that of the long-lived state (dotted line in Fig. 3.9a), with the exception of the red part of the spectrum, which does not contain any contribution of the lower Q-band. The observations related to the DAS and corresponding time-constants for **Cu** and **CuRu** may be rationalized based on a mutual comparison as follows:

1. The time-constants of the involved processes are faster upon B- than for Q-band excitation. The exception is the τ_3 process in **CuRu**, which was determined to 993 ps for B- vs. 729 ps for Q-band excitation. A possible explanation could be the contribution of the ^{1}MLCT(Ru) band to the absorption at 480 nm.

2. The two faster components have rather similar spectra and primarily contribute to the build-up of ESA for **Cu** and GSB/ESA for **CuRu** in the spectral region between 460 and 550 nm. The spectrum of the 5.5 ps-process (light blue DAS in Fig. 3.9d) for **CuRu** at 480 nm excitation might contain contributions from a decaying MLCT state based on a reduction of GSB below 500 nm and ESA between 600 and 700 nm. However, these signatures overlap with spectral features that are porphyrin-specific and also detected in **Cu**.

3. The τ_3 DAS are similar, but not quite identical to the respective long-lived spectra.[¶]

The TA data are consistent with an inclusion of the Ru(II) complex fragment in the porphyrinic π-system. Notably, no emission from the ^{3}MLCT(Ru) is observed, suggesting that **CuRu** behaves as a single chromophore, whose photophysical properties are dominated by porphyrin contributions; both ground and excited state absorption features in **CuRu** are considerably red-shifted as compared to that of **Cu** due to the participation of orbitals from the Ru(II) complex fragment in the π system of the porphyrin.[‖]

The second part of the discussion concerns experiments performed under similar conditions as the catalytic experiments, [73] i.e. solvent *N,N*-dimethylformamide (DMF), triethylamine (TEA) as sacrificial electron donor and an excitation wavelength of 345 nm. For reference, the respective experiments are performed in four different solvents: TOL (non-polar, non-coordinating), ACN (polar, coordinating), DMF (polar, weakly coordinating) and DMF/TEA (polar, coordinating). UV/Vis absorption spectra of **CuRu** in these solvents are shown in Fig. 3.10a. It is deducible that the solvent influences the electronic situation in **CuRu**. There is an apparent blue-shift of all bands in the

---

[¶] The time range coincides with that of the $^2T_1 \rightleftharpoons {}^4T_1$ equilibration, [176] which had later been contradicted. [179] The measurements presented here were performed using the magic angle configuration, such that the origin of this component may be attributable to such equilibration after all.

[‖] Rapid deactivation of ^{3}MLCT(Ru) states towards a porphyrin in spatial proximity was reported. [198]

(a) UV/Vis absorption spectra
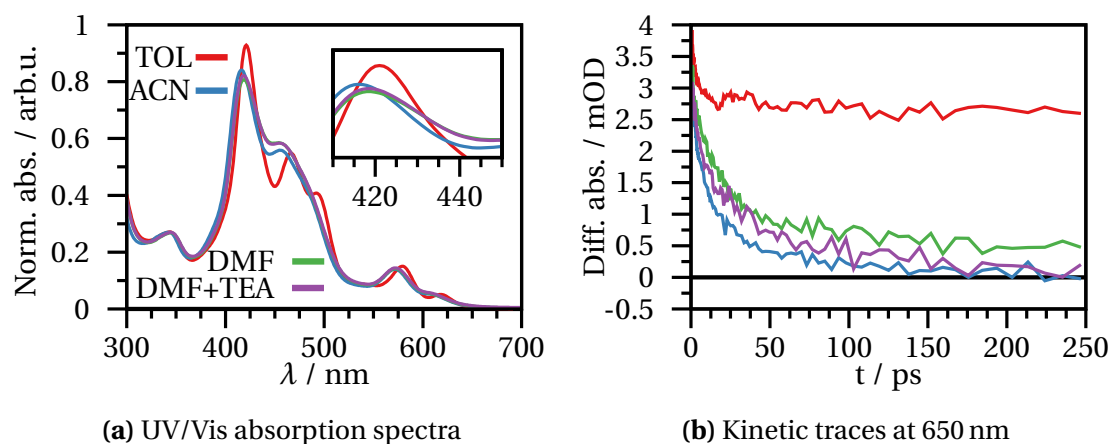
(b) Kinetic traces at 650 nm

Figure 3.10: UV/Vis absorption spectra of **CuRu** in selected solvents (panel a) and identical optical density at 345 nm. The solvent markedly influences all absorption bands and the photoinduced dynamics upon 345 nm excitation: Kinetic traces at 650 nm (panel b) show the formation of a plateau within 250 ps in TOL and in DMF, while a decay to the ground-state is observed on the same time scale in ACN and DMF/TEA (the solvent of the catalytic experiments [73]).

visible spectral region upon an increase in solvent polarity, i.e. in ACN, DMF and DMF/TEA as compared to TOL. The shift is most pronounced for the B-bands and the ^{1}MLCT(Ru) band in particular. Latter absorption band is hardly distinguishable from the main B_x band in the three polar solvents. Such blue-shift upon an increase of solvent polarity is indicative of negative solvatochromism, i.e. light-induced charge-transfer that opposes the direction of the dipole moment in the ground state (as observed for **Ir**, see Section 2.2). [135] In light of the molecular structure, such solvent dependence can be interpreted as another indication for a contribution of charge-transfer from the Ru(II) ion towards the porphyrin π-system, i.e. from a ^{1}MLCT(Ru) as described above. The band at ca. 345 nm is hardly influenced by a change in solvent polarity, suggesting it corresponds to a locally excited state. The band is not visible in **Cu** [72] and may therefore be associated with the extended phenanthroline unit.

The solvent has strong impact on the photoinduced dynamics as visualized with the kinetic traces at 650 nm (Fig. 3.10b). Due to experimental reasons the photo-induced dynamics were monitored up to maximum pump-probe delay time of 250 ps. Interestingly, in the coordinating solvents ACN and DMF/TEA there is a complete signal decay on this time scale. On the other hand, a plateau at low positive amplitude is formed in DMF after ca. 100 ps, while in TOL there is a plateau reached after ca. 25 ps at 75 % of the initial signal intensity.

Based on a quantitative description of the TA data the following points may be raised:

1. The data recorded in TOL is largely consistent with that described above for visible excitation (Fig. 3.9, Page 59); there are two processes in the ps time regime with similar time constants: 1.0 and 15 ps for 345 nm data and 1.4 and 17 ps for Q-band excitation. Also, for both excitation wavelengths the spectral amplitudes of the two processes are rather low and they contribute both in similar spectral intervals. A third process similar to the one observed after Q-band excitation (729 ps) is not contained in the 345 nm data due to the limited delay range of 250 ps.

2. In the polar solvents ACN, DMF and DMF/TEA there is a blue-shift of the GSB of the dominant Q-band on the few- to tens of ps time scale.

3. The final, decaying spectrum in the coordinating solvents is fairly similar to that detected in TOL apart from a blue-shift, which is also present in the ground state absorption spectra.

4. The spectrum of the final, non-decaying state in DMF has very low amplitude, but the features visible rather correspond to that of a ^{3}MLCT(Ru) than to a porphyrin centered ^{4}T$_1$ state.

With respect to the catalytic experiments it may be realized that an excited state lifetime of 100 ps as found for **CuRu** in DMF/TEA is very short: Any diffusion controlled reaction between a molecule in solution and the excited catalyst will be very inefficient due to the low probability of a reactive collision. This might be a reason for the low catalytic activity of **CuRu** in the CO_2 reduction experiments.[73] For related compounds, which combine the phenanthroline extended Cu(II) porphyrin introduced here with a Rhenium(I) tricarbonyl unit, no correlation between the catalytic activity and the photophysical properties were found.[199] However, it has to be noted that the catalytic activity in **CuRu** depends on the porphyrin central metal,[73] while in the compounds with an Re complex fragment the latter is the catalytic site.[199]

Efficient quenching of the excited states in Cu(II) porphyrins in coordinating solvents is known and attributed to axial coordination of a Lewis base (here ACN and TEA, and to some extent DMF) to the Cu(II) ion.[200–202] The TA data recorded under catalytically relevant conditions is consistent with such quenching by an axial ligand.**

**Due to solubility reasons, the selection of solvents suitable for the photocatalytic experiments is limited.[73]
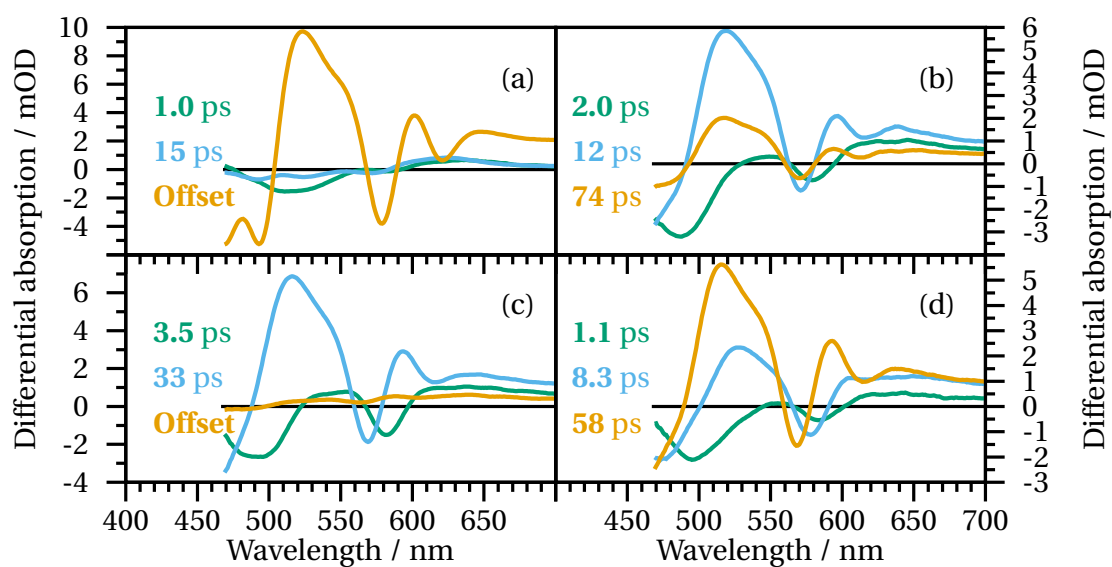
Figure 3.11: Decay-associated spectra from global fits of TA experiments (excitation at 345 nm) on **CuRu** in different solvents: (a) TOL, (b) ACN, (c) DMF and (d) DMF/TEA. A complete decay is observed in the coordinating solvents ACN and DMF/TEA, while long-lived excited states are formed in TOL (probably the $^4T_1$) and DMF (probably a ^{3}MLCT(Ru)). The data was recorded up to a maximum time delay of 250 ps.

4 Summary

In order to improve our access to the essentially unlimited and free supply with energy from space that is sunlight, scientists have studied natural photosynthesis for decades and many essential aspects concerning structure and function of the molecular structures that constitute the natural light harvesting systems are known to date. Long range and directed electron transfer steps are essential to the efficiency of natural photosynthesis, but rely on well-balanced kinetic and energetic parameters in a protein environment- which developed over the course of more than two billion years.[203] Unfortunately, the recreation of these natural systems is and probably will remain out of reach of human abilities. The scientific community is concerned with numerous complementary approaches which aim in many different paths on the same goal: Creating artificial systems, which allow for the efficient conversion of sunlight into more useable forms of energy. The field of artificial photosynthesis comprises two main directions, which aim either on the direct conversion of sunlight into electrical energy using dye-sensitized solar cells or on the conversion of sunlight into chemical energy e.g. by producing molecular hydrogen in (supramolecular or nanoparticle based) photocatalysis. For both main directions, photoactive transition metal complexes have favorable properties with respect to the conversion of sunlight into chemical energy: Many of these complexes possess absorption bands in the visible spectral region, which originate from metal-to-ligand charge transfer (MLCT) transitions. Following light absorption, an electron is promoted from the metal to the ligand. Depending on the specific properties of the metal complex, such MLCT states can possess lifetimes in the microsecond time range; a time span of microseconds may be sufficient for chemical reactions to occur, e.g. an electron transfer from the ligand to a reactant in solution. However, a negative charge on the ligand sphere can also resemble the first step in a number of electron transfer events when brought in spatial and energetic proximity to suitable acceptor units.

Transition metal complexes are usually stable and convenient to synthesize, which allows for the systematic investigation of their photophysics in dependence of well-

controlled structural and electronic parameters. The potential gain from such studies will be an improved understanding of the fate of excited states in transition metal complexes: By characterizing electronic and structural dynamics after photo-excitation energy loss pathways can be identified, and molecular properties that support the desired deactivation channels may be specified. An efficient molecular design is a prerequisite in order for larger artificial light harvesting arrays with multiple subunits to fulfill the desired functions as determined by the interplay of structure and function in molecular systems in general.

In this thesis spectroscopic properties and light-induced dynamics in selected mono- and multi-metallic compounds are discussed. The experimental techniques applied for the work are steady-state and time-resolved spectroscopic methods, in particular transient absorption spectroscopy in the femto- to picosecond time regime. Analysis of experimental data is performed with numerical fitting routines and customized kinetic schemes if necessary.

The relevant compounds combine photo-active transition metal complexes based on Ru(II), Fe(II), Os(II) or Ir(III) central ions with additional organic or metal-organic chromophores. The treated compounds are classified in six different coupling schemes based on the electronic coupling strength between metal complex and chromophore Fig. 1.3 (page 8). The coupling schemes impact electronic interaction and delocalization of the electronic state belonging to the individual chromophoric units; the coupling strength depends on the molecular and electronic structure of the bridging unit: Saturated (i.e. involving sp^3-hybridized carbon atoms) and possibly flexible bridge units (type **1** in Fig. 1.3, e.g. aliphatic chains) break conjugation between the π systems of the metal complex and that of the additional chromophore, while fully conjugated systems (type **2-5**) allow for enhanced electronic delocalization in the coupled compounds, which exceeds the delocalization that is possible in the individual chromophores. The compounds of type **2-5** resemble potential building blocks for hierarchic terpyridine-based coordination oligomers. Such architecture allows to study energy- and electron-transfer processes in energetically and structurally well-ordered compounds of increasing complexity. The building blocks under investigation in this thesis are mono- and multi-metallic tpy complexes with conjugated chromophores as the ligand backbone. This thesis also treats a compound in which the bridge unit is a fused aromatic ring (type **6**), which causes the individual chromophores to merge essentially into one chromophoric unit.

With respect to type **1** structures, **Ru-pNDI** is discussed in Section 1.2. The com-

pound comprises a $[Ru(dqp)_2]^{2+}$ metal complex fragment and naphthalene-diimide chromophores as electron acceptors attached to a polymer backbone (**pNDI**); metal complex and chromophore chain are linked via an aliphatic chain, which breaks conjugation. The structural flexibility of the connecting piece between both units allows for effective quenching of the excited Ru(II) complex, i.e. its ^{3}MLCT state, as demonstrated in steady-state and time-resolved emission experiments. Using transient absorption experiments the formation of the characteristic absorption features of the NDI anion in the visible spectral region could be resolved, indicating an electron transfer from the initially excited Ru-unit to the **pNDI** chain on the few to tens of ps time scale. The TA dynamics further suggest an additional decay channel for the ^{3}MLCT state besides electron transfer, such as triplet-triplet energy transfer towards the chromophores in the **pNDI** chain. In the **Ru-pTARA** system, which has an architecture similar to that of **Ru-pNDI**, but is equipped with electron donating triarylamine chromophores instead of the NDI units, there is no indication of photo-induced electron transfer, consistent with the reduction and oxidation potentials of the constituents.[90]

The dual emission in the cyclometallated Ir(III) complex $[Ir(ppy)_2(IrBBIH_2)]^+$ is attributed to independently decaying excited states localized on the ppy (emission from a ^{3}MLCT state) or the BBI ligand (emission from a state with presumably mixed ^{3}MLCT/$^3\pi$-π^* character).

In Section 2.1 four different dyads consisting of a Ru(II)-tpy complex and a fullerene (C_{60}) acceptor unit connected by two different linkers and in presence or absence of an additional bridge chromophore are investigated. Transient absorption data suggests Dexter-type energy transfer populating the $^3C_{60}^*$ state, its dynamics depend on the presence of the bridge chromophore and the type of linker (Fig. 2.3, page 31). While the presence of the bridge chromophore increases the time constant for energy transfer by a factor ≥ 4, variation of the fullerene linker from a pyrrolidine to a cyclopropyl unit increases the time constant by ca. 30 %.

The role of an Ir(III) metal ion in the tpy units regarded here is discussed in Section 2.2. Data from steady-state and time-resolved absorption and emission experiments points towards a complex interplay between electronic and molecular structure in the given compound. Fluorescence spectra which depend on the excitation wavelength are attributed to different rotamers of the terminal stilbene unit, which do not interconvert in the excited state. The light-induced dynamics are strongly solvent dependent (Fig. 2.6, page 39) and involve a structurally gated population of an intraligand charge transfer state, which is most important in ACN, while in the less polar THF and the polar but

viscous DMPU spectroscopic signatures of a Z/E isomerization are more dominant. The Ir(III) metal ion has considerable electrostatic influence on the entire compound, but due to high-lying ^{3}MLCT(Ir) states the optically accessible excited states have primarily contributions from the ligand chromophore.

Energy transfer dynamics in the bimetallic complex **RuOs** and the trimetallic complex **RuFeRu** are the main subject in Section 3.1. In **RuOs** ultrafast singlet-singlet energy transfer from the Ru(II) fragment to the Os(II) tpy unit is observed within 200 fs producing an emissive ^{3}MLCT(Os) state. More complex processes are observed in **RuFeRu**, where the photo-induced dynamics are quite different in dependence of the excitation wavelength (Fig. 3.4, page 49): If only the ^{1}MLCT(Fe) is excited, relaxation is entirely located on the Fe(II) tpy fragment via the Quintet(Fe) state. On the other hand, initial excitation of the ^{1}MLCT(Ru) leads to non-quantitative energy-transfer in the triplet manifold, populating states associated with the Fe(II) tpy unit on the ps time scale, and the Fe-centered excited-state decay is observed; a fraction of the initially excited molecules resides on a ligand-centered state, which is not populated when exciting the ^{1}MLCT(Fe). Simultaneous excitation of the ^{1}MLCT(Ru) and the ^{1}MLCT(Fe) (Section 3.1.2) leads to a blockage of the triplet energy transfer between both units, which is attributed to a kinetic hindrance due to the occupation of the acceptor states. A kinetic model (related to a FERMI distribution function) to account for such situation is suggested. Whether and how similar effects are relevant in a more generalized context remains subject to discussion; multi-chromophoric arrays are a common architecture in both natural photosynthesis and artificial light harvesting, making it likely that similar situations may arise in such systems, where multiple excited donor units are ought to transfer excitation energy to a limited number of acceptor units.

Examples of cyanide-bridged hetero-bimetallic Ir(III)-Ru(II) complexes and their excited-state landscapes are described in Section 3.2. Emission from the Ir(III) fragment is very weak in the bimetallic complexes, while the dominant emission in these complexes can be assigned to ^{3}MLCT(Ru) phosphorescence. The photoinduced dynamics upon excitation in the UV are dominated by features associated with the Ru(II) fragment on the ps time scale, indicative of fast depopulation of Ir(III)-centered states. Nevertheless, subtle variations of the Ru(II) spectral signatures resemble the close metal-metal interaction which give rise to a certain degree of Ir(III) contributions mixing into the ^{3}MLCT(Ru) manifold.

The photophysics of the weak CO_2 reduction catalysts **Cu** and **CuRu** are detailed in Section 3.3. A phenanthroline unit fused via a pyrazine ring to the porphyrine core

extends the porphyrinic π system in both compounds and allows for a strong electronic coupling between the porphyrin unit and the additional ligand binding site. In **CuRu** additionally the Ru(II) bpy complex fragment contributes to the central π system, as indicated by considerable red-shifts of the visible absorption bands. Fast quenching of the excited states in coordinating solvents, and under conditions similar to that of catalytic experiments, may be an explanation for the low catalytic activity of both **Cu** and **CuRu**.

In this thesis the photophysics in a number of different chemical structures based on photoactive transition metal complexes are investigated and electronic and structural dynamics are highlighted. The presented results extend our understanding of transition metal photophysics in interplay with additional chromophores and are the basis for future research on multi-chromophoric arrays of increasing complexity.

5 Zusammenfassung

Die Sonne ist die stärkste Energiequelle in unserem Universum und versorgt die Erde mit letztlich unbegrenzten Mengen von Energie in Form von Sonnenlicht; die natürliche Photosynthese ist nicht weniger als die Grundlage für das Leben auf der Erde und von unschätzbarer Bedeutung in der Erdgeschichte und für die globale Zukunft. Wissenschaftler sind seit Jahrzenten damit befasst, die Struktur und Funktion der natürlichen Lichtsammeleinheiten und der Proteinstrukturen, in die Erstgenannte eingebettet sind, zu untersuchen, um die relevanten Mechanismen der Photosynthese zu verstehen. Von maßgeblicher Bedeutung für die Effizienz der beteiligten Prozesse sind energetisch und örtlich gerichtete Energie- und Elekronentransferprozesse über - in molekularen Dimensionen - erhebliche Distanzen. Hier stoßen wir auf die faszinierenden Proteinstrukturen, die sich innerhalb von mehr als zwei Milliarden Jahren entwickelt haben, [203] und die das Rückgrat für die ausgeklügelten Anordnungen der invidiuellen Chromophoreinheiten und Redoxeinheiten untereinander bilden, welche so entscheidend für den Erfolg der photosynthetischen Apparate auf der Erde sind.

Aus heutiger Sicht und aufgrund der heute nur bedingt verfügbaren Fähigkeiten, komplexe Strukturen ähnlich den natürlichen (Photosynthese-)Proteinen zu erschaffen, ist es nicht absehbar, ob und wie entsprechende natürliche Systeme tatsächlich eines Tages im chemischen Labor (und sei es unter Beteiligung von Syntheserobotern) nachgebaut werden können. Realistisch ist hingegen das Vorhaben, dem Vorbild der Natur zu folgen und Prinzipien aus der natürlichen Photosynthese zu adaptieren, um artifizielle Systeme zu erschaffen, deren Funktionalität zumindest in Teilaspekten der Funktionalität natürlicher Systeme nachempfunden ist. Im Rahmen der Bemühungen um *artifizielle Photosynthese* sind Forschergruppen weltweit damit befasst, (supra-)molekulare oder halbleiterbasierte Strukturen zu erschaffen, mit denen Energie aus Sonnenlicht in vorhaltbare Energieformen umgewandelt werden kann. Üblich ist dabei die Unterscheidung von farbstoffsensibilisierten Solarzellen und (supramolekularer) Photokatalyse; während erstere Anwedung auf die direkte Umwandlung von Lichtenergie in elektrischen Strom abzielt, wird in der Photokatalyse die Umwandlung von Lichtenergie in

chemische Energie, beispielsweise in Form von molekularem Wasserstoff oder Kohlen-
monoxid (durch die Reduktion von Kohlendioxid), angestrebt. Für beide genannten
Verfahren haben photoaktive Übergangsmetallkomplexe große Bedeutung erlangt; dies
ist auf die intrinsische Eigenschaft vieler dieser Verbindungen zurückzuführen, dass
die elektronischen Resonanzen lichtinduzierter Ladungstransferübergänge, bei der ein
Elektron vom Metallion auf die Ligandensphäre übertragen wird, im sichtbaren Spektral-
bereich liegen. Von der Ligandensphäre kann das Elektron auf räumlich angrenzende
funktionelle Gruppen übertragen werden; Metall-zu-Ligand Ladungstransferübergänge
(engl. *metal-to-ligand charge transfer*, MLCT) können folglich dazu genutzt werden, in
Gegenwart entsprechender Akzeptorstrukturen Elektronentransferkaskaden auszulö-
sen.

In diesem Zusammenhang relevante Übergangsmetallkomplexe sind stabil und syn-
thetisch gut zugänglich, sodass systematische photophysikalische Untersuchungen in
Abhängigkeit wohldefinierter struktureller und elektronischer Parameter durchgeführt
werden können. Solche Studien sollen dazu dienen, unser Verständnis in Bezug auf die
Schicksale angeregter Zustände in Übergangsmetallkomplexen zu erweitern: Durch die
Charakterisierung der elekronischen und strukturellen Dynamiken nach Lichtanregung
können mögliche Verlustpfade bei Relaxation der angeregten Zustände identifiziert und
Indizien darauf gewonnen werden, welche molekularen Eigenschaften einen positiven
Einfluss auf die Bevorzugung gewünschter Relaxationspfade haben. Aufgrund der en-
gen Verbindung zwischen Struktur und Eigenschaften in molekularen Systemen ist der
Aufbau komplexer artifizieller Lichtsammeleinheiten nur möglich, wenn die einzelnen
Bestandteile sowie deren mögliche strukturelle und elektronische Wechselwirkungen
bekannt sind und aufeinander abgestimmt werden können.

In der vorliegenden Arbeit werden spektroskopische Eigenschaften von und die licht-
induzierten Dynamiken in ausgewählten ein- und mehrkernigen Metallkomplexen auf
Basis stationärer und zeitaufgelöster absorptions- und emissionsspektroskopischer
Methoden, inbesondere der transienten Absorptionsspektroskopie (TA) auf der Femto-
bis Pikosekunden Zeitskala, diskutiert. Die Analyse der experimentellen Daten erfolgt
mittels numerischer Anpassung und ggf. unter Nutzung spezieller, selbstentwickelter
kinetischer Modelle.

Die untersuchten Verbindungen sind Konstrukte aus photoaktiven Übergangsme-
tallkomplexen mit den Zentralionen Ru(II), Fe(II), Os(II) oder Ir(III) und zusätzlichen
organischen oder metallorganischen Chromophoren; die Verbindungen können an-
hand der Stärke der elektronischen Kopplung zwischen dem Metallkomplex und dem
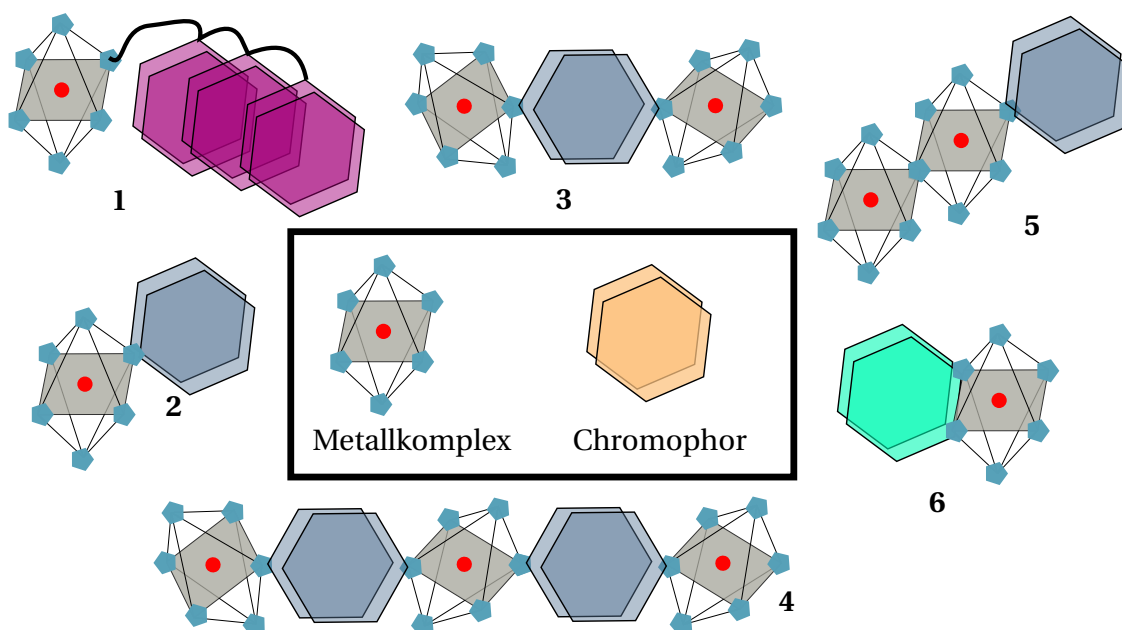
elektronische Kopplung zwischen dem Metallkomplex und dem zusätzlichen Chromophor

schwach   sehr stark

Abbildung 5.1: Schematische Darstellung der verschiedenen Klassen von Strukturen mit unterschiedlichen elektronischen Kopplungsstärken der in dieser Arbeit diskutierten Verbindungen.

zusätzlichen Chromophor entsprechend der schematischen Darstellungen in Abb. 5.1 klassifiziert werden.

Die jeweilige Kopplungsstärke betrifft die elektronischen Wechselwirkungen zwischen den Fragmenten sowie den Grad der Delokalisation der elektronischen Zustände beider Fragmente. Die Stärke der elektronischen Kopplung hängt maßgeblich von der elektronischen und räumlichen Struktur des verbrückenden Molekülteils ab: Während gesättigte (d.h. sp^3 hybridisierte Kohlenstoffatome enthaltende) und möglicherweise flexible Brückeneinheiten (Klasse **1** in Abb. 5.1, z.B. Aliphaten) die elektronische Konjugation zwischen den π-Elektronensystemen von Metallkomplex und Chromophor unterbrechen, ist es in vollständig konjugierten Systemen (Klassen **2-5**) möglich, dass die Delokalisation der elektronischen Zustände im jeweiligen Gesamtkonstrukt größer ist als in den nicht-gekoppelten Fragmenten. Die im Rahmen dieser Arbeit untersuchten Konstrukte der Klassen **2-5** stellen mögliche Bausteine für terpyridin(tpy)-basierte hierarchisch organisierte Koordinationsoligomere dar. Eine derartige molekulare Architektur eignet sich, um daran grundlegende photophysikalische Untersuchungen in Hinblick auf Energie- und Elektronentransferprozesse in strukturell und elektronisch wohl

definierten Systemen, deren Komplexität graduell erhöht werden kann, durchzuführen. Die konkreten molekularen Strukturen sind ein- und mehrkernige Terpyridinkomplexe, wobei das Rückgrat der Liganden aus einem konjugierten Chromophor besteht. Im Rahmen dieser Arbeit wird außerdem ein stark gekoppeltes System untersucht (Klasse **6**), in dem die aromatischen π-Elektronensysteme der Fragmente durch einen annelierten aromatischen Heterocyclen verbrückt werden.

Die zur Klasse **1** gehörende Verbindung **Ru-pNDI** (Abschnitt 1.2) besteht aus einem $[Ru(dcp)_2]^{2+}$-abgeleiteten Metallkomplex (dcp ist 2,6-Di(chinolin-8-yl)pyridin) sowie Napthalindiimid-Einheiten als Elektronenakzeptoren, die über ein Polymerrückgrat miteinander verbunden sind; das Polymerfragment wird als **pNDI** bezeichnet. Da der Metallkomplex und die organischen Chromophore über eine aliphatische Kette miteinander verbunden sind, ist die Konjugation der π-Elektronensysteme unterbrochen. Nichtsdestotrotz erlaubt die räumliche Flexibilität der aliphatischen Brückeneinheit eine Löschung des angeregten ^{3}MLCT(Ru) Zustands durch die Wechselwirkung mit den Chromophoren in der **pNDI** Kette, was anhand von stationären und zeitaufgelösten Emissionsexperimenten gezeigt werden kann. Mit Hilfe von transienten Absorptionsexperimenten wurde die Ausbildung der spektralen Signatur eines Naphtalindiimid-Anions im sichtbaren Spektralbereich nachgewiesen. Daraus lässt sich folgern, dass ein Elektronentransfer vom angeregten Rutheniumkomplex zu den Chromophoreinheiten in der **pNDI** Kette erfolgt. Darüber hinaus suggerieren die Messdaten die Existenz eines weiteren Zerfallskanals für den ^{3}MLCT(Ru) Zustand, welcher beispielsweise Triplett-Triplett-Energietransfer zuzuordnen sein könnte. Das Referenzsystem **Ru-pTARA**, das analog zu **Ru-pNDI** aufgebaut ist, jedoch Triarylamin-Chromophore als Elektronendonoren anstelle der Napthalindiimid-Einheiten enthält, zeigt unter gleichen Bedingungen keine lichtinduzierte Dynamik, die mit einem Elektronentransfer zwischen den Chromophoren und dem Metallkomplex in Verbindung gebracht werden kann.

Die duale Emission des cyclometallierten Ir(III) Komplexes $[Ir(ppy)_2(IrBBIH_2)]^+$ wird mit zwei unabhängig voneinander relaxierenden angeregten Zuständen erklärt, die auf dem ppy (Emission aus einem ^{3}MLCT Zustand) bzw. dem BBI Liganden (Emission aus einem Zustand, der vermutlich gemischten ^{3}MLCT/$^3\pi$-π^* Charakter besitzt) lokalisiert sind.

In Abschnitt 2.1 werden vier Konstrukte bestehend aus einem Ru(II)-tpy Komplex und einem Fulleren (C_{60}) als Akzeptoreinheit beschrieben, wobei die Fullerenverknüpfung auf zwei unterschiedliche Arten erfolgt, und für beide Verknüpfungen zudem der Einfluss der An-/Abwesenheit eines Brückenchromophors untersucht wird. Anhand von

Daten aus transienten Absorptionsexperimenten konnte ein Dexter-Energietransfer vom ^{3}MLCT(Ru) Zustand zum ^{3}C$_{60}$* des Fullerens beobachtet werden, wobei die Dynamik sowohl von der Anwesenheit des Brückenchromophors als auch von der Art der Verknüpfung abhängt: Die Anwesenheit des Brückenchromophors führt zu einer Vervierfachung der Zeitkonstante für den Energietransfer, und im Hinblick auf die Variation der Verknüpfung führt der Austausch des Pyrrolidinrings mit einem Cyclopropylring zu einer Vergrößerung der Zeitkonstante um 30 %.

Die Rolle eines Ir(III) Zentralions in Wechselwirkung mit einem Liganden der typischen tpy Architektur, die in dieser Arbeit Verwendung findet, ist in 2.2 ausgeführt. Spekroskopische Daten aus stationären sowie zeitaufgelösten Absorptions- und Emissionsexperimenten deuten auf ein komplexes Wechselspiel zwischen elektronischer und räumlicher Struktur in der untersuchten Verbindung **Ir** hin. Fluoreszenz, deren Spektrum von der Anregungswellenlänge abhängt, wird auf Rotamere im Zusammenhang mit der terminalen Styreneinheit zurückgeführt, welche sich im angeregten Zustand nicht in einander umwandeln. Die licht-induzierte Dynamik ist stark lösungsmittelabhängig , und beinhaltet die Bevölkerung eines Intraligand-Ladungstransferzustands, welche von Änderungen in der Molekülstruktur begleitet wird. Der Ladungstransferzustand ist in Acetonitril von großer Bedeutung, während im weniger polaren Tetrahydrofuran und im polaren, aber viskosen Dimethylpropylenharnstoff die spektralen Signaturen einer Z/E Isomerisierung größere Beiträge zur beobachteten Dynamik leisten. Der Einfluss des Ir(III) Zentralions hat erheblichen elektrostatischen Einfluss auf das gesamte Molekül, allerdings dominiert aufgrund der energetisch hochliegenden ^{3}MLCT(Ir) Zustände die Dynamik des Ligandchromophors die photoinduzierte Dynamik in **Ir**.

Energietransferdynamiken in einem zweikernigen (**RuOs**) und in einem dreikernigen Komplex (**RuFeRu**) sind das Thema von Abschnitt 3.1. In **RuOs** erfolgt ultraschneller Singulett-Singulett Energietransfer (≤200 fs) von der Ru(II)- zur Os(II)-tpy-Einheit, der zur Besetzung des emittierenden ^{3}MLCT(Os) führt. Kompliziertere Prozesse werden für **RuFeRu** beobachtet, wobei die licht-induzierten Dynamiken für verschiedene Anregungswellenlängen sehr unterschiedlich sind: Infolge einer Anregung des ^{1}MLCT(Fe) Übergangs wird eine Relaxationsdynamik beobachtet, die allein in der Fe(II)-tpy Sphäre stattfindet, und über einen Quintettzustand zurück in den Grundzustand führt. Wird hingegen der ^{1}MLCT(Ru) angeregt, erfolgt ein unvollständiger Energietransfer zwischen Triplettzuständen (^{3}MLCT(Ru) → ^{3}MLCT(Fe)), bei dem der ^{3}MLCT(Fe) auf der Pikosekunden-Zeitskala besetzt wird. Die nachgelagerte Relaxation erfolgt ebenfalls

über den Quintettzustand. Ein Bruchteil der initial in den ^{1}MLCT(Ru) überführten Moleküle relaxiert jedoch nicht durch Energietransfer in den ^{3}MLCT(Fe), sondern verbleibt auf einem ligandzentrierten Zustand, der nicht besetzt wird, wenn initial lediglich der ^{1}MLCT(Fe) angeregt wird.

Bei gleichzeitiger Anregung des ^{1}MLCT(Ru) und des ^{1}MLCT(Fe) wird eine kinetische Blockade des Energietransfers zwischen den Triplettzuständen beobachtet, welche auf die initiale Besetzung der Akzeptorzustände zurückgeführt wird. Ein kinetisches Modell, das an den funktionalen Zusammenhang einer FERMI-Verteilung angelehnt ist, kann genutzt werden, um die Abhängigkeit der Energietransferrate vom Besetzungsgrad des Akzeptorzustands zu beschreiben. Molekulare Strukturen mit mehreren Einheiten für die Lichtabsorption, die Anregungsenergie für wenige Akzeptoren, wie z.B. katalytische Zentren, zur Verfügung stellen, sind gängig und prädestiniert dafür, von ähnlichen Effekten betroffen zu sein. Daher stellt sich die Frage, ob und in welcher Weise derartige kinetische Effekte in Bezug auf natürliche sowie andere artifizielle Energietransfersysteme relevant sind.

Beispiele für cyanidverbrückte Ir(III)-Ru(II)-Komplexe und die Natur ihrer angeregten Zustände werden in Abschnitt 3.2 beschrieben. Die Ir(III)-basierte Emission in den zweikernigen Komplexen ist sehr schwach, aber wird parallel zur Phosphoreszenz aus den ^{3}MLCT(Ru) Zuständen beobachtet. Die licht-induzierte Dynamik in den Komplexen nach Anregung im UV wird dominiert von Beiträgen, die ^{3}MLCT(Ru)-Zuständen zuzuordnen sind, was darauf hinweist, dass energetisch höher liegende, Ir-zentrierte Zustände zugunsten der energetisch niedriger liegenden Ru-zentrierten Zustände desaktiviert werden. Fluorsubstituenten in der Ir(III)-Sphäre verursachen eine Blauverschiebung der ^{1}MLCT(Ru)-Banden im sichtbaren Spektralbereich; dies suggeriert eine Beteiligung Ir(III)-zentrierter Orbitale an den ^{3}MLCT(Ru) Zuständen, die durch die räumliche Nähe und die durch den verbrückenden Cyanidliganden geförderte elektronische Kommunikation der Metallzentren hervorgerufen wird.

Photophysikalische Eigenschaften der potentiellen Photokatalysatoren **Cu** und **CuRu** für die lichtgetriebene Reduktion von CO_2 werden in 3.3 erläutert. In **Cu** ist das π-System eines Cu(II)-Porphyrins durch Annelierung mit einem Phenanthrolinliganden verbunden; durch diese Art der Verknüpfung ist eine sehr starke elektronische Delokalisation der Porphyrinzustände bis auf die Phenanthrolinsphäre möglich. Die starke Kopplung wird inbesondere für **CuRu** deutlich, in dem ein Ru(II)-bis-Bipyridin Komplexfragment an den Phenanthrolinliganden koordiniert ist: Die Rotverschiebung der Q- und B-Banden ist ein klares Indiz für die vergrößerte Delokalisation in **CuRu**

im Vergleich mit **Cu**. Als mögliche Ursache für die niedrige katalytische Aktivität der Verbindungen wird die schnelle Löschung der angeregten Zustände auf einer Zeitskala ≤250 ps in koordinierenden Lösungsmitteln herangezogen.

Die vorliegende Arbeit behandelt die Photophysik verschiedener auf photoaktiven Übergangsmetallkomplexen basierenden Verbindungen. Dabei werden elektronische und strukturelle Aspekte in den licht-induzierten Dynamiken herausgestellt. Die dargelegten Ergebnisse tragen zu einem verbesserten Verständnis der Photophysik photoaktiver Übergangsmetallkomplexe und der Wechselwirkungen dieser mit zusätzlichen Chromophoren bei. Diese Arbeit liefert damit grundlegende Erkenntnisse für die künftige Forschung im Bereich komplexer Multichromophorsysteme.

Bibliography

[1] Gust, D., Moore, T. A. & Moore, A. L. Solar Fuels via Artificial Photosynthesis. Accounts of Chemical Research **42**, 1890–1898 (2009).

[2] McConnell, I., Li, G. & Brudvig, G. W. Energy Conversion in Natural and Artificial Photosynthesis. Chemistry & Biology **17**, 434–447 (2010).

[3] Blankenship, R. E. et al. Comparing Photosynthetic and Photovoltaic Efficiencies and Recognizing the Potential for Improvement. Science **332**, 805–809 (2011).

[4] Vos, M. et al. Singlet-singlet annihilation at low temperatures in the antenna of purple bacteria. Biochimica et Biophysica Acta (BBA) - Bioenergetics **850**, 501–512 (1986).

[5] van Grondelle, R., Dekker, J. P., Gillbro, T. & Sundström, V. Energy transfer and trapping in photosynthesis. Biochimica et Biophysica Acta (BBA) - Bioenergetics **1187**, 1–65 (1994).

[6] Liu, Z. et al. Crystal structure of spinach major light-harvesting complex at 2.72 AA resolution. Nature **428**, 287–292 (2004).

[7] Amunts, A., Drory, O. & Nelson, N. The structure of a plant photosystem I supercomplex at 3.4 Å resolution. Nature **447**, 58–63 (2007).

[8] Li, Y.-F., Zhou, W., Blankenship, R. E. & Allen, J. P. Crystal structure of the bacteriochlorophyll a protein from Chlorobium tepidum1. Journal of Molecular Biology **271**, 456 – 471 (1997).

[9] Mazor, Y., Borovikova, A., Caspy, I. & Nelson, N. Structure of the plant photosystem I supercomplex at 2.6 Å resolution. Nature Plants **3**, 17014 (2017).

[10] Wei, X. et al. Structure of spinach photosystem II-LHCII supercomplex at 3.2 Å resolution. Nature **534**, 69–74 (2016).

[11] Schatz, G. H., Brock, H. & Holzwarth, A. R. Kinetic and Energetic Model for the Primary Processes in Photosystem II. Biophysical Journal **54**, 397–405 (1988).

[12] Dau, H. Molecular mechanisms and quantitative models of variable photosystem ii fluorescence. Photochemistry and Photobiology **60**, 1–23 (1994).

[13] Ahn, T. K. et al. Architecture of a Charge-Transfer State Regulating Light Harvesting in a Plant Antenna Protein. Science **320**, 794–797 (2008).

[14] Akimoto, S. & Mimuro, M. Application of Time-Resolved Polarization Fluorescence Spectroscopy in the Femtosecond Range to Photosynthetic Systems. Photochemistry and Photobiology **83**, 163–170 (2007).

[15] Ginsberg, N. S. et al. Solving structure in the CP29 light harvesting complex with polarization-phased 2D electronic spectroscopy. Proceedings of the National Academy of Sciences **108**, 3848–3853 (2011).

[16] Fenna, R. E. & Matthews, B. W. Chlorophyll arrangement in a bacteriochlorophyll protein from Chlorobium limicola. Nature **258**, 573–577 (1975).

[17] Brixner, T. et al. Two-dimensional spectroscopy of electronic couplings in photosynthesis. Nature **434**, 625–628 (2005).

[18] Engel, G. S. et al. Evidence for wavelike energy transfer through quantum coherence in photosynthetic systems. Nature **446**, 782–786 (2007).

[19] Pullerits, T., Zigmantas, D. & Sundström, V. Beatings in electronic 2D spectroscopy suggest another role of vibrations in photosynthetic light harvesting. Proceedings of the National Academy of Sciences **110**, 1148–1149 (2013).

[20] Fassioli, F., Dinshaw, R., Arpin, P. C. & Scholes, G. D. Photosynthetic light harvesting: excitons and coherence. Journal of The Royal Society Interface **11** (2013).

[21] Tiwari, V., Peters, W. K. & Jonas, D. M. Electronic resonance with anticorrelated pigment vibrations drives photosynthetic energy transfer outside the adiabatic framework. Proceedings of the National Academy of Sciences **110**, 1203–1208 (2013).

[22] Kühlbrandt, W. Structure and function of bacterial light-harvesting complexes. Structure **3**, 521 – 525 (1995).

[23] van Grondelle, R. & Novoderezhkin, V. I. Energy transfer in photosynthesis: experimental insights and quantitative models. Physical Chemistry Chemical Physics **8**, 793–807 (2006).

[24] Mirkovic, T. et al. Light Absorption and Energy Transfer in the Antenna Complexes of Photosynthetic Organisms. Chemical Reviews **117**, 249–293 (2017).

[25] Neutze, R. Opportunities and challenges for time-resolved studies of protein structural dynamics at X-ray free-electron lasers. Philosophical Transactions of the Royal Society of London B: Biological Sciences **369** (2014).

[26] Levantino, M., Yorke, B. A., Monteiro, D. C., Cammarata, M. & Pearson, A. R. Using synchrotrons and XFELs for time-resolved X-ray crystallography and solution scattering experiments on biomolecules. Current Opinion in Structural Biology **35**, 41 – 48 (2015).

[27] Martin-Garcia, J. M., Conrad, C. E., Coe, J., Roy-Chowdhury, S. & Fromme, P. Serial femtosecond crystallography: A revolution in structural biology. Archives of Biochemistry and Biophysics **602**, 32 – 47 (2016).

[28] Gust, D., Moore, T. A. & Moore, A. L. Mimicking Photosynthetic Solar Energy Transduction. Accounts of Chemical Research **34**, 40–48 (2001).

[29] Berardi, S. et al. Molecular artificial photosynthesis. Chemical Society Reviews **43**, 7501–7519 (2014).

[30] Voityuk, A. A., Kummer, A. D., Michel-Beyerle, M.-E. & Rösch, N. Absorption spectra of the GFP chromophore in solution: comparison of theoretical and experimental results. Chemical Physics **269**, 83 – 91 (2001).

[31] Polli, D. et al. Conical intersection dynamics of the primary photoisomerization event in vision. Nature **467**, 440–443 (2010).

[32] Hanf, R. et al. Protein-Induced Excited-State Dynamics of Protochlorophyllide. The Journal of Physical Chemistry A **115**, 7873–7881 (2011).

[33] Eisfeld, A. & Briggs, J. The J- and H-bands of organic dye aggregates. Chemical Physics **324**, 376 – 384 (2006).

[34] Liuolia, V., Valkunas, L. & van Grondelle, R. Excitons in Chains of Dimers. The Journal of Physical Chemistry B **101**, 7343–7349 (1997).

[35] Sundström, V., Pullerits, T. & van Grondelle, R. Photosynthetic Light-Harvesting: Reconciling Dynamics and Structure of Purple Bacterial LH2 Reveals Function of Photosynthetic Unit. The Journal of Physical Chemistry B **103**, 2327–2346 (1999).

[36] Scholes, G. D., Fleming, G. R., Olaya-Castro, A. & van Grondelle, R. Lessons from nature about solar light harvesting. Nature Chemistry **3**, 763–774 (2011).

[37] Ziessel, R. & Harriman, A. Artificial light-harvesting antennae: electronic energy transfer by way of molecular funnels. Chemical Communications **47**, 611–31 (2011).

[38] Tachibana, Y., Vayssieres, L. & Durrant, J. R. Artificial photosynthesis for solar water-splitting. Nature Photonics **6**, 511–518 (2012).

[39] Wen, F. & Li, C. Hybrid Artificial Photosynthetic Systems Comprising Semiconductors as Light Harvesters and Biomimetic Complexes as Molecular Cocatalysts. Accounts of Chemical Research **46**, 2355–2364 (2013).

[40] Kärkäs, M. D., Verho, O., Johnston, E. V. & Åkermark, B. Artificial Photosynthesis: Molecular Systems for Catalytic Water Oxidation. Chemical Reviews **114**, 11863–12001 (2014).

[41] Kim, D., Sakimoto, K. K., Hong, D. & Yang, P. Artificial Photosynthesis for Sustainable Fuel and Chemical Production. Angewandte Chemie International Edition **54**, 3259–3266 (2015).

[42] Puntoriero, F. et al. Photoinduced water oxidation using dendrimeric Ru(II) complexes as photo-sensitizers. Coordination Chemistry Reviews **255**, 2594 – 2601 (2011).

83

[43] Kang, D. et al. Electrochemical Synthesis of Photoelectrodes and Catalysts for Use in Solar Water Splitting. Chemical Reviews **115**, 12839–12887 (2015).

[44] Wang, W.-H., Himeda, Y., Muckerman, J. T., Manbeck, G. F. & Fujita, E. CO2 Hydrogenation to Formate and Methanol as an Alternative to Photo- and Electrochemical CO2 Reduction. Chemical Reviews **115**, 12936–12973 (2015).

[45] Nocera, D. G. The Artificial Leaf. Accounts of Chemical Research **45**, 767–776 (2012).

[46] Lewis, N. S. & Nocera, D. G. Powering the planet: Chemical challenges in solar energy utilization. Proceedings of the National Academy of Sciences **103**, 15729–15735 (2006).

[47] Ferreira, K. N., Iverson, T. M., Maghlaoui, K., Barber, J. & Iwata, S. Architecture of the Photosynthetic Oxygen-Evolving Center. Science **303**, 1831–1838 (2004).

[48] O'Regan, B. & Gratzel, M. A low-cost, high-efficiency solar cell based on dye-sensitized colloidal TiO2 films. Nature **353**, 737–740 (1991).

[49] Grätzel, M. Photoelectrochemical cells. Nature **414**, 338–344 (2001).

[50] Brabec, C. J., Sariciftci, N. S. & Hummelen, J. C. Plastic Solar Cells. Advanced Functional Materials **11**, 15–26 (2001).

[51] Vougioukalakis, G. C., Philippopoulos, A. I., Stergiopoulos, T. & Falaras, P. Contributions to the development of ruthenium-based sensitizers for dye-sensitized solar cells. Coordination Chemistry Reviews **255**, 2602 – 2621 (2011).

[52] Green, M. A., Ho-Baillie, A. & Snaith, H. J. The emergence of perovskite solar cells. Nature Photonics **8**, 506–514 (2014).

[53] Saparov, B. & Mitzi, D. B. Organic–Inorganic Perovskites: Structural Versatility for Functional Materials Design. Chemical Reviews **116**, 4558–4596 (2016).

[54] Pellegrin, Y. & Odobel, F. Molecular devices featuring sequential photoinduced charge separations for the storage of multiple redox equivalents. Coordination Chemistry Reviews **255**, 2578 – 2593 (2011).

[55] Schulz, M., Karnahl, M., Schwalbe, M. & Vos, J. G. The role of the bridging ligand in photocatalytic supramolecular assemblies for the reduction of protons and carbon dioxide. Coordination Chemistry Reviews **256**, 1682 – 1705 (2012).

[56] Vallavoju, N. & Sivaguru, J. Supramolecular photocatalysis: combining confinement and non-covalent interactions to control light initiated reactions. Chemical Society Reviews **43**, 4084–4101 (2014).

[57] White, J. L. et al. Light-Driven Heterogeneous Reduction of Carbon Dioxide: Photocatalysts and Photoelectrodes. Chemical Reviews **115**, 12888–12935 (2015).

[58] Rau, S. *et al.* A Supramolecular Photocatalyst for the Production of Hydrogen and the Selective Hydrogenation of Tolane. Angewandte Chemie International Edition **45**, 6215–6218 (2006).

[59] Takeda, H. & Ishitani, O. Development of efficient photocatalytic systems for CO2 reduction using mononuclear and multinuclear metal complexes based on mechanistic studies. Coordination Chemistry Reviews **254**, 346 – 354 (2010).

[60] Windle, C. D. & Perutz, R. N. Advances in molecular photocatalytic and electrocatalytic CO2 reduction. Coordination Chemistry Reviews **256**, 2562 – 2570 (2012).

[61] Blakemore, J. D., Crabtree, R. H. & Brudvig, G. W. Molecular Catalysts for Water Oxidation. Chemical Reviews **115**, 12974–13005 (2015).

[62] Pfeffer, M. G. *et al.* Palladium versus platinum: the metal in the catalytic center of a molecular photocatalyst determines the mechanism of the hydrogen production with visible light. Angewandte Chemie International Edition **54**, 5044–8 (2015).

[63] Balzani, V. & Juris, A. Photochemistry and photophysics of Ru(II) polypyridine complexes in the Bologna group. From early studies to recent developments. Coordination Chemistry Reviews **211**, 97 – 115 (2001).

[64] Sauvage, J. P. *et al.* Ruthenium(II) and Osmium(II) Bis(terpyridine) Complexes in Covalently-Linked Multicomponent Systems: Synthesis, Electrochemical Behavior, Absorption Spectra, and Photochemical and Photophysical Properties. Chemical Reviews **94**, 993–1019 (1994).

[65] Campagna, S., Puntoriero, F., Nastasi, F., Bergamini, G. & Balzani, V. Photochemistry and Photophysics of Coordination Compounds: Ruthenium, vol. 280 of Topics in Current Chemistry, 117–214 (Springer Berlin Heidelberg, Berlin, Heidelberg, 2007).

[66] Müllen, K. & Scherf, U. Organic Light-Emitting Devices: Synthesis, properties, and applications (Wiley-VCH, Weinheim, 2006).

[67] Carraway, E. R., Demas, J. N., DeGraff, B. A. & Bacon, J. R. Photophysics and photochemistry of oxygen sensors based on luminescent transition-metal complexes. Analytical Chemistry **63**, 337–342 (1991).

[68] Prier, C. K., Rankic, D. A. & MacMillan, D. W. C. Visible Light Photoredox Catalysis with Transition Metal Complexes: Applications in Organic Synthesis. Chemical Reviews **113**, 5322–5363 (2013).

[69] Presselt, M. *et al.* A Concept to Tailor Electron Delocalization: Applying QTAIM Analysis to Phenyl-Terpyridine Compounds. The Journal of Physical Chemistry A **114**, 13163–13174 (2010).

[70] Siebert, R. *et al.* Direct Observation of Temperature-Dependent Excited-State Equilibrium in Dinuclear Ruthenium Terpyridine Complexes Bearing Electron-Poor Bridging Ligands. The Journal of Physical Chemistry C **115**, 12677–12688 (2011).

[71] Siebert, R. et al. Ruthenium(II)-bis(4'-(4-ethynylphenyl)-2,2':6',2''-terpyridine) — A versatile synthon in supramolecular chemistry. Synthesis and characterization. Central European Journal of Chemistry **9**, 990–999 (2011).

[72] Matlachowski, C. & Schwalbe, M. Synthesis and characterization of mono- and dinuclear phenanthroline-extended tetramesitylporphyrin complexes as well as UV-Vis and EPR studies on their one-electron reduced species. Dalton Transactions **42**, 3490–3503 (2013).

[73] Matlachowski, C. & Schwalbe, M. Photochemical CO2-reduction catalyzed by mono- and dinuclear phenanthroline-extended tetramesityl porphyrin complexes. Dalton Transactions **44**, 6480–6489 (2015).

[74] Marks, R. N., Halls, J. J. M., Bradley, D. D. C., Friend, R. H. & Holmes, A. B. The photovoltaic response in poly(p-phenylene vinylene) thin-film devices. Journal of Physics: Condensed Matter **6**, 1379 (1994).

[75] Günes, S., Neugebauer, H. & Sariciftci, N. S. Conjugated Polymer-Based Organic Solar Cells. Chemical Reviews **107**, 1324–1338 (2007).

[76] Brabec, C. J., Scherf, U. & Dyakonov, V. Organic Photovoltaics: Materials, Device Physics, and Manufacturing Technologies, 2nd Edition (2014), second edition edn.

[77] Kelch, S. & Rehahn, M. Synthesis and Properties in Solution of Rodlike, 2,2':6',2''-Terpyridine-Based Ruthenium(II) Coordination Polymers. Macromolecules **32**, 5818–5828 (1999).

[78] Schubert, U. S. et al. 2,2':6',2''-Terpyridine Metal Complexes as Building Blocks for Extended Functional Metallo-Supramolecular Assemblies and Polymers. Synthetic Metals **121**, 1249–1252 (2001).

[79] Dobrawa, R. & Würthner, F. Photoluminescent Supramolecular Polymers: Metal-Ion Directed Polymerization of Terpyridine-Functionalized Perylene Bisimide Dyes. Chemical Communications 1878–1879 (2002).

[80] Constable, E. C. 2,2':6',2''-Terpyridines: From Chemical Obscurity to Common Supramolecular Motifs. Chemical Society Reviews **36**, 246–253 (2007).

[81] Siebert, R. et al. Spectroscopic Investigation of the Ultrafast Photoinduced Dynamics in π-Conjugated Terpyridines. ChemPhysChem **10**, 910–919 (2009).

[82] Siebert, R., Winter, A., Schubert, U. S., Dietzek, B. & Popp, J. Excited-State Planarization as Free Barrierless Motion in a π-Conjugated Terpyridine. The Journal of Physical Chemistry C **114**, 6841–6848 (2010).

[83] Siebert, R., Winter, A., Dietzek, B., Schubert, U. S. & Popp, J. Dual Emission from Highly Conjugated 2,2':6':2''-Terpyridine Complexes-A Potential Route to White Emitters. Macromolecular Rapid Communications **31**, 883–888 (2010).

[84] Siebert, R., Winter, A., Schubert, U. S., Dietzek, B. & Popp, J. The Molecular Mechanism of Dual Emission in Terpyridine Transition Metal Complexes—Ultrafast Investigations of Photoinduced Dynamics. Physical Chemistry Chemical Physics **13**, 1606–1617 (2011).

[85] Siebert, R. et al. Light-Induced Dynamics in Conjugated Bis(terpyridine) Ligands - A Case Study Toward Photoactive Coordination Polymers. Macromolecular Rapid Communications **33**, 481–497 (2012).

[86] Puodziukynaite, E., Wang, L., Schanze, K. S., Papanikolas, J. M. & Reynolds, J. R. Poly(fluorene-co-thiophene)-based ionic transition-metal complex polymers for solar energy harvesting and storage applications. Polymer Chemistry **5**, 2363–2369 (2014).

[87] Borg, L. z. et al. Light-induced charge separation in a donor-chromophore-acceptor nanocomposite poly[TPA-Ru(tpy)2]@ZnO. J. Mater. Chem. C **1**, 1223–1230 (2013).

[88] Dixon, D. W., Thornton, N. B., Steullet, V. & Netzel, T. Effect of DNA Scaffolding on Intramolecular Electron Transfer Quenching of a Photoexcited Ruthenium(II) Polypyridine Naphthalene Diimide. Inorganic Chemistry **38**, 5526–5534 (1999).

[89] Schroot, R. et al. Nitroxide-Mediated Polymerization of Styrenic Triarylamines and Chain-End Functionalization with a Ruthenium Complex: Toward Tailored Photoredox-Active Architectures. Macromolecules **46**, 2039–2048 (2013).

[90] Kübel, J. et al. Photoredox–Active Dyads Based on a Ru(II) Photosensitizer Equipped with Electron Donor or Acceptor Polymer Chains: A Spectroscopic Study of Light-Induced Processes Towards Efficient Charge Separation. The Journal of Physical Chemistry C **119**, 4742–4751 (2015).

[91] Damrauer, N. H. et al. Femtosecond Dynamics of Excited-State Evolution in [Ru(bpy)3]2+. Science **275**, 54–57 (1997).

[92] Kovalenko, S. A., Dobryakov, A. L., Ruthmann, J. & Ernsting, N. P. Femtosecond spectroscopy of condensed phases with chirped supercontinuum probing. Physical Review A **59**, 2369–2384 (1999).

[93] Berera, R., van Grondelle, R. & Kennis, J. T. M. Ultrafast transient absorption spectroscopy: principles and application to photosynthetic systems. Photosynthesis Research **101**, 105–118 (2009).

[94] Ruckebusch, C., Sliwa, M., Pernot, P., de Juan, A. & Tauler, R. Comprehensive data analysis of femtosecond transient absorption spectra: A review. Journal of Photochemistry and Photobiology C: Photochemistry Reviews **13**, 1–27 (2012).

[95] Blanchet, L. et al. Chemometrics description of measurement error structure: study of an ultrafast absorption spectroscopy experiment. Analytica Chimica Acta **642**, 19–26 (2009).

[96] Braslavskyz, S. E. Glossary of terms used in photochemistry, 3rd edition (IUPAC Recommendations 2006). Pure and Applied Chemistry **79**, 293–465 (2007).

[97] Horng, M. L., Gardecki, J. A., Papazyan, A. & Maroncelli, M. Subpicosecond Measurements of Polar Solvation Dynamics: Coumarin 153 Revisited. The Journal of Physical Chemistry **99**, 17311–17337 (1995).

[98] Kaim, W. & Fiedler, J. Spectroelectrochemistry: the best of two worlds. Chemical Society Reviews **38**, 3373–3382 (2009).

[99] Zedler, L. et al. Resonance-Raman spectro-electrochemistry of intermediates in molecular artificial photosynthesis of bimetallic complexes. Chemical Communications **50**, 5227–5229 (2014).

[100] Dobryakov, A. L., Kovalenko, S. A. & Ernsting, N. P. Electronic and vibrational coherence effects in broadband transient absorption spectroscopy with chirped supercontinuum probing. The Journal of Chemical Physics **119**, 988–1002 (2003).

[101] Dietzek, B., Pascher, T., Sundström, V. & Yartsev, A. Appearance of coherent artifact signals in femtosecond transient absorption spectroscopy in dependence on detector design. Laser Physics Letters **4**, 38–43 (2007).

[102] Lakowicz, J. R. Principles of Fluorescence Spectroscopy (Springer, New York, N.Y, 2006), 3 edn.

[103] Chergui, M. Ultrafast Photophysics of Transition Metal Complexes. Accounts of Chemical Research **48**, 801–808 (2015).

[104] Hammarström, L. & Johansson, O. Expanded bite angles in tridentate ligands. Improving the photophysical properties in bistridentate RuII polypyridine complexes. Coordination Chemistry Reviews **254**, 2546 – 2559 (2010).

[105] Rommel, S. A. et al. Protonation-Dependent Luminescence of an Iridium(III) Bibenzimidazole Chromophore. European Journal of Inorganic Chemistry **2015**, 3730–3739 (2015).

[106] Tsuboyama, A. et al. Homoleptic Cyclometalated Iridium Complexes with Highly Efficient Red Phosphorescence and Application to Organic Light-Emitting Diode. Journal of the American Chemical Society **125**, 12971–12979 (2003).

[107] Wong, W.-Y. & Ho, C.-L. Heavy metal organometallic electrophosphors derived from multi-component chromophores. Coordination Chemistry Reviews **253**, 1709 – 1758 (2009).

[108] Yersin, H., Rausch, A. F., Czerwieniec, R., Hofbeck, T. & Fischer, T. The triplet state of organo-transition metal compounds. Triplet harvesting and singlet harvesting for efficient {OLEDs}. Coordination Chemistry Reviews **255**, 2622 – 2652 (2011).

[109] Beeby, A., Bettington, S., Samuel, I. D. W. & Wang, Z. Tuning the emission of cyclometalated iridium complexes by simple ligand modification. Journal of Materials Chemistry **13**, 80–83 (2003).

[110] Tamayo, A. B. et al. Synthesis and Characterization of Facial and Meridional Tris-cyclometalated Iridium(III) Complexes. Journal of the American Chemical Society **125**, 7377–7387 (2003).

[111] Lamansky, S. et al. Highly Phosphorescent Bis-Cyclometalated Iridium Complexes: Synthesis, Photophysical Characterization, and Use in Organic Light Emitting Diodes. Journal of the American Chemical Society **123**, 4304–4312 (2001).

[112] Rau, S. et al. A Bibenzimidazole-Containing Ruthenium(II) Complex Acting as a Cation-Driven Molecular Switch. Inorganic Chemistry **39**, 1621–1624 (2000).

[113] Ladouceur, S. et al. A rare case of dual emission in a neutral heteroleptic iridium(iii) complex. Dalton Transactions **42**, 8838–8847 (2013).

[114] Geist, F., Jackel, A. & Winter, R. F. Ligand Based Dual Fluorescence and Phosphorescence Emission from BODIPY Platinum Complexes and Its Application to Ratiometric Singlet Oxygen Detection. Inorganic Chemistry **54**, 10946–10957 (2015).

[115] Glazer, E. C., Magde, D. & Tor, Y. Dual Emission from a Family of Conjugated Dinuclear RuII Complexes. Journal of the American Chemical Society **127**, 4190–4192 (2005).

[116] Magde, D., Jr., M. D. M. & Glazer, E. C. So-called "dual emission" for 3MLCT luminescence in ruthenium complex ions: What is really happening? Coordination Chemistry Reviews **306, Part 2**, 447 – 467 (2016).

[117] Arbogast, J. W. et al. Photophysical properties of sixty atom carbon molecule (C60). The Journal of Physical Chemistry **95**, 11–12 (1991).

[118] Wróbel, D. & Graja, A. Photoinduced electron transfer processes in fullerene–organic chromophore systems. Coordination Chemistry Reviews **255**, 2555 – 2577 (2011).

[119] Barthelmes, K. et al. New Ruthenium Bis(terpyridine) Methanofullerene and Pyrrolidinofullerene Complexes: Synthesis and Electrochemical and Photophysical Properties. Inorganic Chemistry **54**, 3159–3171 (2015).

[120] Laine, P., Campagna, S. & Loiseau, F. Conformationally Gated Photoinduced Processes Within Photosensitizer–Acceptor Dyads Based on Ruthenium(II) and Osmium(II) Polypyridyl Complexes With an Appended Pyridinium Group. Coordination Chemistry Reviews **252**, 2552–2571 (2008).

[121] Maity, D., Bhaumik, C., Mondal, D. & Baitalik, S. Photoinduced intramolecular energy transfer and anion sensing studies of isomeric RuIIOsII complexes derived from an asymmetric phenanthroline-terpyridine bridge. Dalton Transactions **43**, 1829–45 (2014).

[122] Schubert, U. S., Winter, A. & Newkome, G. R. Terpyridine-Based Materials: For Catalytic, Optoelectronic and Life Science Applications (Wiley-VCH, Weinheim, 2011).

[123] Hewitt, J. T., Vallett, P. J. & Damrauer, N. H. Dynamics of the 3MLCT in Ru(II) Terpyridyl Complexes Probed by Ultrafast Spectroscopy: Evidence of Excited-State Equilibration and Interligand Electron Transfer. The Journal of Physical Chemistry A **116**, 11536–11547 (2012).

[124] McClenaghan, N. D., Leydet, Y., Maubert, B., Indelli, M. T. & Campagna, S. Excited-State Equilibration: A Process Leading to Long-Lived Metal-to-Ligand Charge Transfer Luminescence in Supramolecular Systems. Coordination Chemistry Reviews **249**, 1336–1350 (2005).

[125] Amouyal, E., Bahout, M. & Calzaferri, G. Excited states of M(II,d6)-4'-phenylterpyridine complexes: electron localization. The Journal of Physical Chemistry **95**, 7641–7649 (1991).

[126] Chaignon, F. et al. Distance-independent photoinduced energy transfer over 1.1 to 2.3 nm in ruthenium trisbipyridine-fullerene assemblies. New Journal of Chemistry **29**, 1272–1284 (2005).

[127] La Rosa, A. et al. Does a Cyclopropane Ring Enhance the Electronic Communication in Dumbbell-Type C60 Dimers? The Journal of Organic Chemistry **79**, 4871–4877 (2014).

[128] Collin, J.-P. et al. Synthesis and Photophysical Properties of Iridium(III) Bisterpyridine and Its Homologues: a Family of Complexes with a Long-Lived Excited State. Journal of the American Chemical Society **121**, 5009–5016 (1999).

[129] Flamigni, L. et al. Luminescent Iridium(III)-Terpyridine Complexes - Interplay of Ligand Centred and Charge Transfer States. European Journal of Inorganic Chemistry **2005**, 1312–1318 (2005).

[130] Baranoff, E., Collin, J.-P., Flamigni, L. & Sauvage, J.-P. From Ruthenium(II) to Iridium(III): 15 Years of Triads Based on Bis-Terpyridine Complexes. Chemical Society Reviews **33**, 147–155 (2004).

[131] Flamigni, L., Baranoff, E., Collin, J.-P. & Sauvage, J.-P. A Triad Based on an Iridium(III) Bisterpyridine Complex Leading to a Charge-Separated State with a 120-μs Lifetime at Room Temperature. Chemistry - A European Journal **12**, 6592–6606 (2006).

[132] Lewis, G. N., Magel, T. T. & Lipkin, D. The Absorption and Re-emission of Light by cis- and trans-Stilbenes and the Efficiency of their Photochemical Isomerization. Journal of the American Chemical Society **62**, 2973–2980 (1940).

[133] Waldeck, D. H. Photoisomerization Dynamics of Stilbenes. Chemical Reviews **91**, 415–436 (1991).

[134] Kübel, J., Winter, A., Schubert, U. S. & Dietzek, B. Structure–Property Relationships in an Iridium(III) Bis(Terpyridine) Complex with Extended Conjugated Side chains. The Journal of Physical Chemistry A **118**, 12137–12148 (2014).

[135] Reichardt, C. Solvatochromic Dyes as Solvent Polarity Indicators. Chemical Reviews **94**, 2319–2358 (1994).

[136] Quick, M. et al. Photoisomerization Dynamics of Stiff-Stilbene in Solution. The Journal of Physical Chemistry B **118**, 1389–1402 (2014).

[137] Flamigni, L., Collin, J.-P. & Sauvage, J.-P. Iridium Terpyridine Complexes as Functional Assembling Units in Arrays for the Conversion of Light Energy. Accounts of Chemical Research **41**, 857–871 (2008).

[138] Gawelda, W. et al. Ultrafast Nonadiabatic Dynamics of [FeII(bpy)3]2+ in Solution. Journal of the American Chemical Society **129**, 8199–8206 (2007).

[139] Wächtler, M. et al. Energy transfer and formation of long-lived 3MLCT states in multimetallic complexes coordinating extendet highly conjugated bis-terpyridyl ligands. Physical Chemistry Chemical Physics **18**, 2350–2360 (2016).

[140] Chou, P.-T., Chi, Y., Chung, M.-W. & Lin, C.-C. Harvesting luminescence via harnessing the photophysical properties of transition metal complexes. Coordination Chemistry Reviews **255**, 2653 – 2665 (2011).

[141] Andersson, J. et al. New paradigm of transition metal polypyridine complex photochemistry. Faraday Discussions **127**, 295–305 (2004).

[142] Barzda, V. et al. Singlet–Singlet Annihilation Kinetics in Aggregates and Trimers of LHCII. Biophysical Journal **80**, 2409–2421 (2001).

[143] Puntoriero, F., Nastasi, F., Cavazzini, M., Quici, S. & Campagna, S. Coupling synthetic antenna and electron donor species: A tetranuclear mixed-metal Os(II)–Ru(II) dendrimer containing six phenothiazine donor subunits at the periphery. Coordination Chemistry Reviews **251**, 536–545 (2007).

[144] Morseth, Z. A. et al. Ultrafast Dynamics in Multifunctional Ru(II)-Loaded Polymers for Solar Energy Conversion. Accounts of Chemical Research **48**, 818–827 (2015).

[145] Ashford, D. L. et al. Molecular Chromophore–Catalyst Assemblies for Solar Fuel Applications. Chemical Reviews **115**, 13006–13049 (2015).

[146] Yuan, Y.-J., Yu, Z.-T., Chen, D.-Q. & Zou, Z.-G. Metal-complex chromophores for solar hydrogen generation. Chemical Society Reviews **46**, 603–631 (2017).

[147] Kellogg, R. E. Radiationless Intermolecular Energy Transfer. IV. Triplet—Triplet Annihilation. The Journal of Chemical Physics **41**, 3046–3047 (1964).

[148] Yu, S. et al. Intramolecular triplet-triplet energy transfer enhanced triplet-triplet annihilation upconversion with a short-lived triplet state platinum(ii) terpyridyl acetylide photosensitizer. RSC Advances **5**, 70640–70648 (2015).

[149] Cadranel, A., Albores, P., Yamazaki, S., Kleiman, V. D. & Baraldo, L. M. Efficient energy transfer via the cyanide bridge in dinuclear complexes containing Ru(II) polypyridine moieties. Dalton Transactions **41**, 5343–50 (2012).

[150] Cadranel, A. et al. Emissive cyanide-bridged bimetallic compounds as building blocks for polymeric antennae. Dalton Transactions **42**, 16723–16732 (2013).

[151] Tsai, C.-N. et al. Characterization of Low Energy Charge Transfer Transitions in (terpyridine)(bipyridine)Ruthenium(II) Complexes and their Cyanide-Bridged Bi- and Tri-Metallic Analogues. Inorganic Chemistry **50**, 11965–11977 (2011).

[152] Barthelmes, K. et al. Efficient Energy Transfer and Metal Coupling in Cyanide-Bridged Heterodinu-clear Complexes Based on (Bipyridine)(terpyridine)ruthenium(II) and (Phenylpyridine)iridium(III) Complexes. Inorganic Chemistry **55**, 5152–5167 (2016).

[153] Cannizzo, A. Ultrafast UV spectroscopy: from a local to a global view of dynamical processes in macromolecules. Physical Chemistry Chemical Physics **14**, 11205–11223 (2012).

[154] Lemberg, R. Porphyrins in Nature, 299–349 (Springer Vienna, Vienna, 1954).

[155] Lichtenthaler, H. K. [34] Chlorophylls and carotenoids: Pigments of photosynthetic biomembranes. Methods in Enzymology **148**, 350 – 382 (1987).

[156] Holzwarth, A. R. et al. Kinetics and mechanism of electron transfer in intact photosystem II and in the isolated reaction center: Pheophytin is the primary electron acceptor. Proceedings of the National Academy of Sciences **103**, 6895–6900 (2006).

[157] Poulos, T. L. Heme Enzyme Structure and Function. Chemical Reviews **114**, 3919–3962 (2014).

[158] Kuciauskas, D. et al. Energy and photoinduced electron transfer in porphyrin-fullerene dyads. Journal of Physical Chemistry **100**, 15926–15932 (1996).

[159] Guldi, D. M. Fullerene-porphyrin architectures; photosynthetic antenna and reaction center models. Chem. Soc. Rev. **31**, 22–36 (2002).

[160] Ha, J.-H. et al. Excitonic Coupling Strength and Coherence Length in the Singlet and Triplet Excited States of meso–meso Directly Linked Zn(II)porphyrin Arrays. ChemPhysChem **5**, 57–67 (2004).

[161] Maiuri, M. et al. Ultrafast Energy Transfer and Excited State Coupling in an Artificial Photosynthetic Antenna. The Journal of Physical Chemistry B **117**, 14183–14190 (2013).

[162] Rozzi, C. A. et al. Quantum coherence controls the charge separation in a prototypical artificial light-harvesting system. Nature Communications **4**, 1602 (2013).

[163] Pelado, B. et al. Role of the Bridge in Photoinduced Electron Transfer in Porphyrin–Fullerene Dyads. Chemistry – A European Journal **21**, 5814–5825 (2015).

[164] Auwarter, W., Ecija, D., Klappenberger, F. & Barth, J. V. Porphyrins at interfaces. Nature Chemistry **7**, 105–120 (2015).

[165] Lin, S. et al. Covalent organic frameworks comprising cobalt porphyrins for catalytic CO2 reduction in water. Science **349**, 1208–1213 (2015).

[166] Han, Y., Wu, Y., Lai, W. & Cao, R. Electrocatalytic Water Oxidation by a Water-Soluble Nickel Porphyrin Complex at Neutral pH with Low Overpotential. Inorganic Chemistry **54**, 5604–5613 (2015).

[167] Wu, Z.-S. et al. High-Performance Electrocatalysts for Oxygen Reduction Derived from Cobalt Porphyrin-Based Conjugated Mesoporous Polymers. Advanced Materials **26**, 1450–1455 (2014).

[168] Sirbu, D., Turta, C., Gibson, E. A. & Benniston, A. C. The ferrocene effect: enhanced electrocatalytic hydrogen production using meso-tetraferrocenyl porphyrin palladium(ii) and copper(ii) complexes. Dalton Transactions **44**, 14646–14655 (2015).

[169] Cui, S., Qian, M., Liu, X., Sun, Z. & Du, P. A Copper Porphyrin-Based Conjugated Mesoporous Polymer-Derived Bifunctional Electrocatalyst for Hydrogen and Oxygen Evolution. ChemSusChem **9**, 2365–2373 (2016).

[170] Ertl, M., Wöß, E. & Knör, G. Antimony porphyrins as red-light powered photocatalysts for solar fuel production from halide solutions in the presence of air. Photochemistry & Photobiological Sciences **14**, 1826–1830 (2015).

[171] Bonin, J., Chaussemier, M., Robert, M. & Routier, M. Homogeneous Photocatalytic Reduction of CO2 to CO Using Iron(0) Porphyrin Catalysts: Mechanism and Intrinsic Limitations. ChemCatChem **6**, 3200–3207 (2014).

[172] Gouterman, M. Spectra of porphyrins. Journal of Molecular Spectroscopy **6**, 138 – 163 (1961).

[173] Gouterman, M., Wagnière, G. H. & Snyder, L. C. Spectra of porphyrins. Journal of Molecular Spectroscopy **11**, 108 – 127 (1963).

[174] Vannelli, T. A. & Karpishin, T. B. Neocuproine-Extended Porphyrin Coordination Complexes. Inorganic Chemistry **38**, 2246–2247 (1999).

[175] Vannelli, T. A. & Karpishin, T. B. Neocuproine-Extended Porphyrin Coordination Complexes. 2. Spectroscopic Properties of the Metalloporphyrin Derivatives and Investigations into the HOMO Ordering. Inorganic Chemistry **39**, 340–347 (2000).

[176] Kim, D., Holten, D. & Gouterman, M. Evidence from picosecond transient absorption and kinetic studies of charge-transfer states in copper(II) porphyrins. Journal of the American Chemical Society **106**, 2793–2798 (1984).

[177] Rodriguez, J., Kirmaier, C. & Holten, D. Optical properties of metalloporphyrin excited states. Journal of the American Chemical Society **111**, 6500–6506 (1989).

[178] McMillin, D. R. & McNett, K. M. Photoprocesses of Copper Complexes That Bind to DNA. Chemical Reviews **98**, 1201–1220 (1998).

[179] Sazanovich, I. V., Ganzha, V. A., Dzhagarov, B. M. & Chirvony, V. S. Dichroism of the triplet–triplet transient absorption of copper(II) porphyrins in liquid solution. New interpretation of the sub-nanosecond relaxation component. Chemical Physics Letters **382**, 57 – 64 (2003).

[180] Iyudin, V. S., Kandrashkin, Y. E., Voronkova, V. K., Tyurin, V. S. & Kirichenko, E. N. Time-Resolved EPR Spectra of Photoexcited Copper Porphyrin. Applied Magnetic Resonance **40**, 75–89 (2011).

[181] Ake, R. L. & Gouterman, M. Porphyrins XIV. Theory for the luminescent state in VO, Co, Cu complexes. Theoretica chimica acta **15**, 20–42 (1969).

[182] Ha-Thi, M.-H., Shafizadeh, N., Poisson, L. & Soep, B. An Efficient Indirect Mechanism for the Ultrafast Intersystem Crossing in Copper Porphyrins. The Journal of Physical Chemistry A **117**, 8111–8118 (2013).

[183] Asano, M., Kaizu, Y. & Kobayashi, H. The lowest excited states of copper porphyrins. The Journal of Chemical Physics **89**, 6567–6576 (1988).

[184] Yan, X. & Holten, D. Effects of temperature and solvent on excited-state deactivation of copper(II) octaethyl- and tetraphenylporphyrin: relaxation via a ring-to-metal charge-transfer excited state. The Journal of Physical Chemistry **92**, 5982–5986 (1988).

[185] Jeoung, S. C., Takeuchi, S., Tahara, T. & Kim, D. Ultrafast decay dynamics of photoexcited Cu(II)(TMpy-P4) in water solvent. Chemical Physics Letters **309**, 369 – 376 (1999).

[186] Cunningham, K. L. et al. EPR Spectra, Luminescence Data, and Radiationless Decay Processes of Copper(II) Porphyrins. Inorganic Chemistry **36**, 608–613 (1997).

[187] Kandrashkin, Y. & van der Est, A. Light-induced electron spin polarization in rigidly linked, strongly coupled triplet–doublet spin pairs. Chemical Physics Letters **379**, 574 – 580 (2003).

[188] Rozenshtein, V. et al. Light-induced electron spin polarization in the ground state of water-soluble copper porphyrins. Israel Journal of Chemistry **43**, 373–381 (2003).

[189] Jahn, H. A. & Teller, E. Stability of Polyatomic Molecules in Degenerate Electronic States. I. Orbital Degeneracy. Proceedings of the Royal Society of London. Series A, Mathematical and Physical Sciences **161**, 220–235 (1937).

[190] Walters, V. A., De Paula, J. C., Babcock, G. T. & Leroi, G. E. Resonance Raman spectrum of the lowest triplet state of zinc(II) tetraphenylporphyrin. Journal of the American Chemical Society **111**, 8300–8302 (1989).

[191] De Paula, J. C., Walters, V. A., Nutaitis, C., Lind, J. & Hall, K. Transient resonance Raman spectrum of meso-tetraphenylporphine: an analysis of chemical factors that influence the dynamics of the excited triplet states of metalloporphyrins. The Journal of Physical Chemistry **96**, 10591–10594 (1992).

[192] Asano-Someda, M. & Kaizu, Y. Red-shifted emission spectra of several meso-substituted copper porphyrins in fluid solution. Journal of Photochemistry and Photobiology A: Chemistry **87**, 23 – 29 (1995).

[193] Liang, Y. et al. Ultrafast Dynamics of meso-Tetraphenylmetalloporphyrins: The Role of Dark States. ChemPlusChem **78**, 1244–1251 (2013).

[194] Baerends, E., Ricciardi, G., Rosa, A. & van Gisbergen, S. A DFT/TDDFT interpretation of the ground and excited states of porphyrin and porphyrazine complexes. Coordination Chemistry Reviews **230**, 5 – 27 (2002).

[195] Velate, S., Liu, X. & Steer, R. P. Does the radiationless relaxation of Soret-excited metalloporphyrins follow the energy gap law? Chemical Physics Letters **427**, 295 – 299 (2006).

[196] Lukaszewicz, A. et al. Photophysical processes in electronic states of zinc tetraphenyl porphyrin accessed on one- and two-photon excitation in the soret region. Chemical Physics **331**, 359 – 372 (2007).

[197] Barbosa Neto, N. M. et al. Nonlinear Absorption Dynamics in Tetrapyridyl Metalloporphyrins. The Journal of Physical Chemistry B **109**, 17340–17345 (2005).

[198] Petersson, J., Henderson, J., Brown, A., Hammarström, L. & Kubiak, C. P. Time-Resolved Electron Transfer in Porphyrin-Coordinated Ruthenium Dimers: From Mixed-Valence Dynamics to Hot Electron Transfer. The Journal of Physical Chemistry C **119**, 4479–4487 (2015).

[199] Matlachowski, C., Braun, B., Tschierlei, S. & Schwalbe, M. Photochemical CO2 Reduction Catalyzed by Phenanthroline Extended Tetramesityl Porphyrin Complexes Linked with a Rhenium(I) Tricarbonyl Unit. Inorganic Chemistry **54**, 10351–10360 (2015).

[200] Liu, F. et al. Luminescence Quenching of Copper(II) Porphyrins with Lewis Bases. Inorganic Chemistry **34**, 2015–2018 (1995).

[201] Jeoung, S. C., Kim, D., Cho, D. W., Yoon, M. & Ahn, K.-H. Transient Raman Spectroscopic Investigations on RuIITPP(L)2 (L = Pyridine and Piperidine) and RuIITPP(CO)(py) in Various Solvents: Alternation of Excited Charge Transfer Depending on Axial Ligation. The Journal of Physical Chemistry **100**, 8867–8874 (1996).

[202] Szintay, G. & Horváth, A. Five-coordinate complex formation and luminescence quenching study of copper(II) porphyrins. Inorganica Chimica Acta **324**, 278 – 285 (2001).

[203] Blankenship, R. E. Early Evolution of Photosynthesis. Plant Physiology **154**, 434–438 (2010).

Appendix

Data structure and analysis

Time-resolved absorption and emission spectroscopy are particularly useful when covering a broad spectral window at a time. This is often achieved by using probe pulses with high spectral bandwidth (e.g. a supercontinuum) and an array detector for time-resolved absorption and e.g. using a streak camera for time-resolved emission spectroscopy. Resulting datasets will therefore contain (time-resolved) spectra for numerous delay times. For a given measurement with spectra that consist of y datapoints, which have been measured for x time points, the complete dataset can be viewed as x*y matrix (*D*). In such matrix the rows correspond to the spectra at a specific delay time, while the columns are individual kinetic traces at a specific wavelength.

The most common approach to analyze such two-dimensional datasets is based on the so-called bi-linear assumption, [94] treating kinetics and spectra independent of each other: It is assumed that the dataset can be described as the sum of n independent components with characteristic spectra and kinetic profiles. Mathematically, this corresponds to the matrix D being composed of a $x * n$ matrix C containing the kinetic profiles and a $y * n$ matrix S with the individual spectra (so-called evolution-associated spectra, EAS), i.e.

$$D = C \cdot S^T. \tag{1}$$

The number of components n needed for a proper description of the dataset has to be sufficient to cover all important temporal and spectral features, but too many components may worsen the physical interpretabilty of the individual components.

A rank analysis based on singular value decomposition (SVD) is an unbiased way to obtain a general idea of the composition of the dataset and obtain a lower border for n. The SVD of the $x * y$ matrix (*D*) yields a $x * x$ matrix (*L*) with the left singular vectors, a $x * y$ diagonal matrix (*M*) and a $y * y$ matrix (*R*) with the right singular vectors:

$$D = L \cdot M \cdot R^T \tag{2}$$

Every matrix possesses singular values, but their physical interpretability is not necessarily provided. This can be easily understood considering the two-dimensional dataset *D* depending on time and wavelengths: SVD will produce left singular vectors ("'temporal concentration profiles"') and right singular vectors ("'individual spectra"'). While for the spectra both positive and negative features may be expected (a transient absorption data set consists of difference spectra), negative values in the temporal profiles would correspond to negative concentrations and these are physically not interpretable. Such negative concentrations may occur e.g. when spectral shifts are present in the dataset. This is generally a challenge when performing data analysis based on the bi-linear assumption: Since one component has one kinetic profile and one characteristic spectrum, spectral shifts are only describable considering the two spectra of interconverting components. In such case, the first component resembles the start-spectrum before the shift, while the second spectrum defines the end point of the shift and the spectra in between the time points are linear combinations of start- end endspectra.

The common approach to avoid ambiguity due to negative concentrations is the definition of a kinetic model. A starting point is generally a sum of exponential functions, such that the (differential) absorption for any given wavelength (A_i) becomes

$$A_i(t) = \sum_{j=1}^{n} A_{i,j} \cdot \exp\left(-t \cdot k_j\right) \tag{3}$$

Typically, the parameters (i.e. the coefficients $A_{i,j}$ and the rates k_j) are typically determined in a two-step routine: the rates are optimized globally for all wavelengths at the same time, while the coefficients are optimized for every wavelength individually.

Eq. (3) requires the individual lifetimes τ_j to be sufficiently different from each other (i.e. $k_1 \ll k_2$). Then, this model corresponds to a sequential reaction scheme, in which the decay of one component leads to the rise of the next component:

Consider an initially excited state *B*, which converts to a state *C*, which then decay back to the ground state:

$$\text{B} \xrightarrow{k_1} \text{C} \xrightarrow{k_2} \text{GS}$$
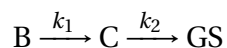
The corresponding set of differential equations is:

$$\frac{dc_B(t)}{dt} = -k_1 \cdot c_B(t)$$

$$\frac{dc_C(t)}{dt} = +k_1 \cdot c_B(t) - k_2 \cdot c_C(t) \tag{4}$$

$$\frac{dc_{GS}(t)}{dt} = +k_2 \cdot c_C(t)$$

If $k_1 \ll k_2$, then the integration of Eq. (4) to obtain expressions for time-dependent concentrations can be carried out for each state individually, and by multiplying the expression for the time-dependent concentrations with an amplitude coefficient (A_i) the expression in Eq. (3) can be obtained.

In cases with more complex kinetic schemes, particularly when parallel reactions are involved, the analytic solutions of the differential equations become either untraceable or integration is even impossible. For such cases the kinetic scheme has to be solved numerically.

Acknowledgement

I have to (and truly want to) thank **Prof. Dr. Benjamin Dietzek** for having me as Ph.D. student in his group. Benjamin, your ongoing readiness for data and paper discussions has been a key ingredient for our achievements and for that I am very grateful. Thank you for your trust in my abilities and handing over responsibilities in lab related matters and beyond early on, from which I have learned and profited considerably.

Many thanks to **Prof. Dr. Antonín Vlček** and **apl. Prof. Dr. Michael Schmitt** as the second and third referee for this thesis.

I thank **Dr. Maria Wächtler** for very productive teamwork and support, countless on- and off-topic discussions and the many positive experiences* we made and shared in the labs.

Thanks a lot to **Dr. Denis Akimov** for his support in setup maintenance, alignment and indispensable practical advice. In this context I also need to thank **Dr. Torbjörn Pascher**, for approaching and fixing *peculiar* and obvious issues with detector electronics, and many scientific discussions during your visits.

I thank the colleagues from the organic chemistry in Jena for our fruitful collaborations, especially **Prof. Dr. Ulrich S. Schubert**, **Dr. Andreas Winter**, **Dr. Michael Jäger** and the ones in lab: **Kevin Barthelmes** and **Robert Schroot**. Furthermore, I thank all other colleagues and collaborators I got to work with in the many side projects including the groups of **Dr. Matthias Schwalbe** (HU Berlin), **Prof. Dr. Sven Rau** (Uni Ulm), **Prof. Dr. Stefan Spange** (TU Chemnitz) and **Prof. Dr. Rainer Beckert** (FSU).

I thank **Prof. Dr. Christoph Lambert** (Uni Würzburg) for making his setup available for the additional measurements on **RuFeRu** (and thank you, Maria, for performing them!). This data set really caught me.

I thank **Prof. Dr. Andrea Cannizzo**, **Dr. Ariana Rondi** and **Michela Gazzetto** for welcoming me in Bern for my STSM; I learned a lot from working with your experimental setup and heavily enjoyed our scientific and technical discussions. Also, thanks to COST Action CM1202 for financially supporting the trip.

I thank the very reliable technical and administrative staff at the IPHT, especially **Thomas Büttner** and his workshop crew. Thanks to **Benita Göbel** for extraordinary helpfulness with respect to my bibliographic needs.

I thank **Dr. Eckhard Birckner** for stimulating discussions concerning the possible origin of wavelength-dependent fluorescence.

---

*and, if I remember correctly, possibly a few challenging technical situations... :)

I thank **Dr. Stephan Kupfer** for both scientific and non-scientific discussions, especially after hours, and for proofreading parts of this thesis.

I thank all my long- and short-term office mates and colleagues for a pleasant work atmosphere in- and outside the labs.

A special thanks to the members and part-time members of our regularly irregular Monday night events: **Frank**, **Martin**, **Matthias**, **Daniel**, **Roman**[†]; sharing ideas over good food and drinks is how the real deals are made!

Thanks to all Ultimate players in Jena for years of practices, joint workouts and motivating, successful and some more educational tournament trips.

Finally, I am deeply indebted to my family. With only one son remaining in Jena, maintaining the household had become very different, but **Annedore Kübel** managed to find friendly and charismatic tenants, who kept the welcoming spirit of our home. Ich danke **Prof. Dr. Sabine Wienker-Piepho** und **PD Dr. Ulrich Müller** für die unterhaltsamen und faszinierenden Geschichten in den abendlichen Gesprächen. Ich danke Euch, **Annette** und **Axel Weidauer**, dass ihr mich so herzlich in den Kreis der Familie aufgenommen habt und ich danke Euch für **Cindy**. Liebe Cindy, du hast mir, so sehe ich das heute, fast schon zu viel Rücksicht und Empathie entgegengebracht, nicht zuletzt für viel länger als geplant dauernde Laboraufenthalte und Nachtschichten, aber mir trotzdem stets klar gemacht, das Wesentliche nicht aus den Augen zu verlieren: Dich.

[†]and Marcus, who managed to join us at least once before he moved to Würzburg

P1 - Photoredox-active Dyads Based on a Ru(II) Photosensitizer Equipped with Electron Donor or Acceptor Polymer Chains: A Spectroscopic Study of Light-Induced Processes toward Efficient Charge Separation

Photoredox-active Dyads Based on a Ru(II) Photosensitizer Equipped with Electron Donor or Acceptor Polymer Chains: A Spectroscopic Study of Light-Induced Processes toward Efficient Charge Separation

Joachim Kübel,[⊥,Δ,#] Robert Schroot,[†,#] Maria Wächtler,[⊥,Δ] Ulrich S. Schubert,[†,‡] Benjamin Dietzek,*[⊥,Δ,‡] and Michael Jäger*[†,‡]

[†]Laboratory of Organic and Macromolecular Chemistry (IOMC), Friedrich Schiller University Jena, Humboldtstraße 10, 07743 Jena, Germany

[‡]Jena Center for Soft Matter (JCSM), Friedrich Schiller University Jena, Philosophenweg 7, 07743 Jena, Germany

[⊥]Institute of Physical Chemistry (IPC) and Abbe Center of Photonics, Friedrich Schiller University Jena, Helmholtzweg 4, 07743 Jena, Germany

[Δ]Leibniz Institute of Photonic Technology (IPHT), Albert-Einstein-Straße 9, 07745 Jena, Germany

Ⓢ *Supporting Information*

ABSTRACT: A photosensitizer−multielectron-acceptor dyad ($P-A_n$) was synthesized via controlled nitroxide-mediated polymerization of styrenic naphthalene diimide (NDI) and subsequent functionalization with a $[Ru(dqp)_2]^{2+}$ photosensitizer (dqp is 2,6-di(quinolin-8-yl)pyridine) at the chain terminus. The optical and electrochemical analysis showed the preserved properties of the individual subunits, corroborated by the analysis of the related multielectron donor assembly (D_n-P) based on triarylamine (TARA). A detailed photophysical study of both dyads is presented to elucidate the primary light-induced energy- and electron-transfer events. While the D_n-P dyad displays the unchanged ^{3}MLCT-based (MLCT is metal-to-ligand charge transfer) emission of the pristine photosensitizer, the $P-A_n$ system revealed efficient emission quenching and the occurrence of the NDI radical anion signature. The time-resolved emission data revealed a nonmonoexponential decay attributed to the conformational freedom by the flexible linkage, while the transient absorption data confirmed the rapid formation of the reduced acceptor.
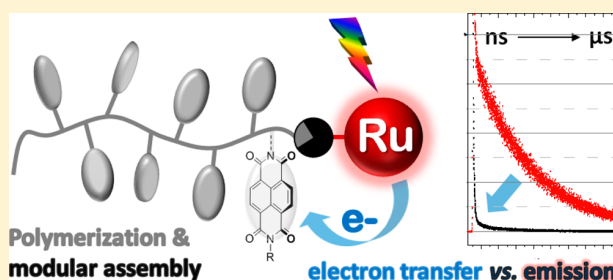
INTRODUCTION

The efficient conversion of sun light into storable energy forms constitutes a long-standing well-recognized scientific and technological challenge, that is closely connected to environmental and social aspects.[1] In general, the necessary elementary steps require photon absorption, primary charge separation, and subsequent translocation of the redox equivalents. On a molecular level, photo- and redox-active units with adjustable optical and redox-chemical properties can be assembled and, thereby, control the energy- and electron-transfer kinetics. A multitude of sophisticated dyads and triads based on Ruthenium−polypyridyl complexes as the photoactive core were designed and studied in great depth, and give rise to excellent quantum yields of charge separation.[2−6]

The ruthenium-based photosensitizer combines several advantageous photochemical properties, such as strong absorption in the visible light region, suitable redox-properties in the ground and excited state, (photo)chemical stability, and sufficiently long excited state lifetimes.[7−9] The enormous variability of the ligand framework allows the tuning of the desired optical and redox-chemical properties for a specific task,

for example, to tailor the rates of subsequent photochemical processes through the localization of excited states,[10] or to accumulate charges upon protonation/re-excitation.[11] In addition, the versatile synthetic modification of the ligand's periphery enables the preparation of sophisticated photoredox-active assemblies,[12] which is particularly attractive to control sequential accumulative charge transfer employing multiple redox-active units.[13] The electron-/energy-transfer kinetics can be tailored by the nature of the link ("bridge") and is conveniently controlled by the driving force, the reorganizational energy, and electronic communication via π-conjugation along intervening units (e.g., p-phenylenes).[14−16] However, such well-tuned architectures often rely on linear convergent syntheses, which leads to long multistep routes with increasingly challenging purification protocols. Alternatively, the decoration of polymer scaffolds provides a valuable approach to host multiple photo- and/or redox-active units,

as exemplified by Meyer's and Fréchet's pioneering work on light harvesting using $[Ru(bpy)_3]^{2+}$ (bpy is 2,2′-bipyridine) sensitizers:[2,17,18] Efficient resonant energy transfer was demonstrated from coumarin dyes to ruthenium centers,[17,18] while very efficient energy migration among the ruthenium centers was reported due to their long phosphorescence lifetime.[19,20] The harvested excitation energy can be subsequently utilized to drive electron transfer, as demonstrated upon incorporation of a donor−photosensitizer−acceptor (D−P−A) (Scheme 1a).[21] However, the generated charges

Scheme 1. Selected Examples of Photoredox-Active Polymer Architectures Designed for Energy Harvesting (Structures a and b) and Charge Transport (Structures c and d)[a]
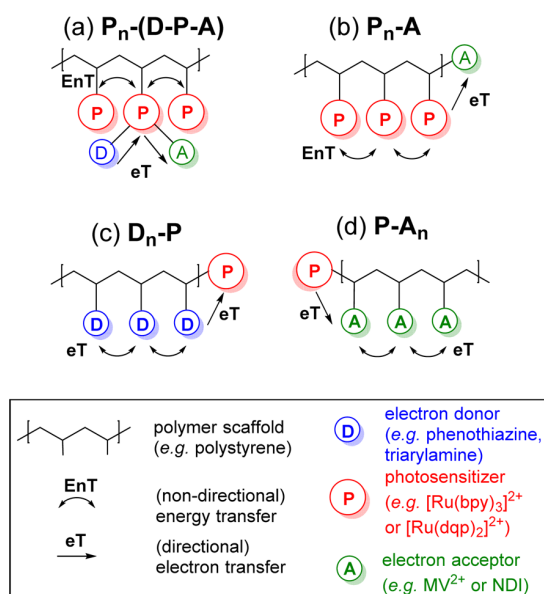
[a]Based on (a) a local triad (D−P−A, ref 2), (b) a terminal acceptor unit (A, ref 24), (c) by attachment of multiple donor sites (D$_n$, ref 25), or (d) of acceptor sites (A$_n$, this work). Arrows indicate nondirectional (double-ended) and directional (single-ended) pathways for energy transfer (EnT) and electron transfer (eT).

are trapped locally and ultimately undergo recombination, since no further donor nor acceptor units are present to provide a
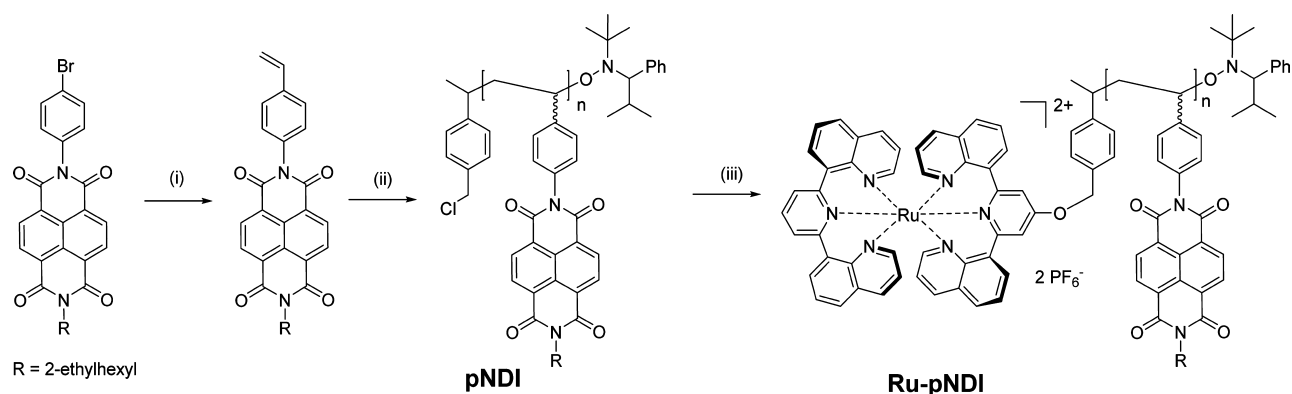
percolating pathway. In principle, such a pathway can be ensured through a (redox-active) polymer-backbone, for example, in a Ru-decorated poly(fluorene-thiophene),[22] or by attaching a redox-active block to transport and store multiple charges.[23] The desired hierarchical control of the polymer architecture becomes possible by modern polymerization techniques, as exemplified by equipping the antenna polymers with an electron-accepting methyl viologen (Scheme 1b),[24] or by an poly(triarylamine) block.[23,25] Zentel et al. used the latter materials to coat semiconductor nanoparticles for electron injection,[23] which leads to the formation of a positively charged polymer corona after excitation. Such approaches constitute a promising strategy to exploit the injected charges by subsequent catalytic processes.[26] In essence, modern controlled radical polymerization techniques enable an access to well-defined block copolymer architectures (Scheme 1c,d) by means of the high end-group fidelity for terminal functionalization, controlled molar masses, and low dispersity, and a wide range of tolerated functional monomers with tailored redox properties. Noteworthy, the facile design and synthesis of such polymer-based photoredox-active architectures causes some important functional implications. The unsaturated polymer backbone leads to less efficient electronic communication, while the conformational freedom results in multiple pathways with different transfer rates. For example, a molecular dyad of $[Ru(bpy)_3]^{2+}$ tethered with naphthalene diimide (NDI) via a flexible alkyl chain showed multiexponential excited state decay up to tens of nanoseconds.[27] Hence, two important design criteria are (a) a sufficiently long excited state lifetime to ensure highest quantum efficiencies of charge separation, and (b) the linear alignment of the donor and acceptor units at the photosensitizer to maximize their mutual distance, in order to minimize charge recombination caused by spatial proximity.[28]

The family of functionalized $[Ru(dqp)_2]^{2+}$-complexes (dqp is 2,6-di(qinolin-8-yl)pyridine) fulfill both the photophysical and structural criteria of such photosensitizers,[29] that is, micro-second excited state lifetimes, broad absorption in the visible light region, and enhanced photostability compared to $[Ru(bpy)_3]^{2+}$.[30] The versatility of this particular sensitizer for photoinduced charge separation has been demonstrated for a molecular D−P−A triad approaching unit quantum efficiency, while the related dyads showed rapid recombination.[31] Recently, we reported the modular synthesis of a side-chain decorated multielectron-donor−polymer (D$_n$) via nitroxide-
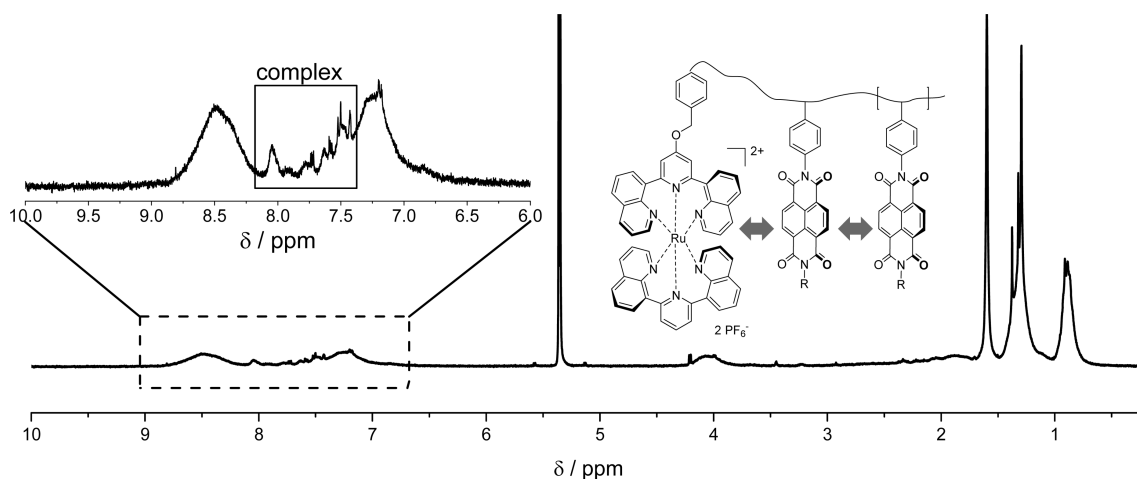
Scheme 2. Synthetic Route to Ru-pNDI[a]

R = 2-ethylhexyl   **pNDI**   **Ru-pNDI**

[a](i) Vinyl siloxane, Pd(dba)$_2$, phosphine ligand, THF, 60 °C. (ii) NMP. (iii) [Ru(dqp)(dqpOH)][PF$_6$]$_2$, K$_2$CO$_3$, DMF, 60 °C.

Figure 1. ^{1}H NMR spectrum (400 MHz, CD$_2$Cl$_2$) Ru-pNDI with chemical structure. Arrows indicate π–π-interactions, leading to broad NDI proton signals and complex Ru proton signals (see inset of aromatic NMR region).

mediated polymerization (NMP), and the subsequent functionalization of the poly(triarylamine) with a photosensitizer at specifically one chain terminus (D$_n$–Ru, Scheme 1c).[25] Numerous related dyad and triad systems have been reported that employ triarylamine and/or naphthalene diimide as the redox-active motifs.[32–34] Hence, the synthetic methodology was extended to naphthalene diimide (NDI) to yield an acceptor analogue (Ru–A$_n$, Scheme 1d), which should be capable to undergo light-induced electron transfer from the excited Ru complex. The optical and (spectro)electrochemical properties are presented, and discussed with respect to the individual components. The initial energy- and electron-transfer processes are explored for both dyads (Ru–A$_n$ and D$_n$–Ru) by time-resolved emission and absorption spectroscopy. The results suggest that covalently organized polymer-based systems provide a valuable platform for subsequent charge separation, which may exploit the favorable redox-chemical/charge-transporting properties of triarylamine[35] and naphthalene diimides,[36–39] and assemblies thereof, respectively.

■ RESULTS AND DISCUSSION

The design principles of the polymer-based photoredox-active assemblies are outlined in the introduction. In this section, the synthesis and molecular characterization is presented, followed by the optical and (spectro)electrochemical analysis. Finally, the light-induced processes are explored by time-resolved measurements.

Synthesis and Molecular Characterization. The desired styrenic monomer was readily obtained by vinylation of the bromophenyl naphthalene diimide derivative[40] applying our protocol for the Pd-catalyzed Hiyama coupling using abundant vinyl siloxanes,[41] without further optimization of the reaction conditions. The asymmetric monomer was isolated in fair yield (28%) after column chromatography. The molecular characterization by mass spectrometry (MS), nuclear magnetic resonance (NMR) spectroscopy, and elemental analysis confirmed the identity and purity of the monomer. Subsequently the nitroxide-mediated polymerization (NMP) protocol was adopted from literature using a chlorobenzyl-functionalized initiator.[25] The ^{1}H NMR spectrum of **pNDI** displays broadened signals and a significant high-field shift of the naphthalene protons ($\Delta\delta = -0.3$ ppm) with respect to the

monomer, attributed to π–π interactions among the NDI subunits (*vide infra*). A similar shift is reported for a poly(norbornene)-based system[42] and upon aggregation in solution.[43] However, it is difficult to quantify the exact extent of stacking from the proton chemical shifts, as the polymer backbone restricts the conformational freedom of the NDI units and may not allow for the same "ideal" coplanar arrangement as in solution. The UV-SEC trace shows a monomodal distribution with a minor high-molar mass shoulder, attributed to some radical–radical chain coupling products. The MALDI spectrum displays a weak distribution with the characteristic mass difference of the repeating unit (see Supporting Information); however, no isotope-resolved peaks were obtained varying the matrix, laser intensity, or salt additive. This finding is in line with the strong competing absorption of the incident laser light by the analyte, difficult desorption, and/or concomitant thermal decomposition of the nitroxide. A detailed investigation of the polymerization kinetics and characterization is beyond the scope of this work and will be reported in due course.

Next, the Ru complex was attached via nucleophilic substitution at the chloromethyl group of the former initiator fragment. Noteworthy, extended reaction times were required as monitored by UV/vis–SEC analysis, as often observed for polymer-analogous reactions (see Supporting Information). The product was readily purified by simple column chromatography, facilitated by the significant polarity differences between **Ru-pNDI** and both the less polar **pNDI** and the more polar Ru complex. The ^{1}H NMR spectra of the polymer-based dyad **Ru-pNDI** is dominated by the NDI units (Figure 1). While the aromatic and aliphatic protons remain unchanged upon functionalization, the disappearance of the chloro-methylene protons was noticed. In addition, the complex' protons were found in the typical region (see inset Figure 1); however, the low signal intensity and the overlap with the NDI signals prevent a more detailed analysis. Nevertheless, parts of the ligand's spin systems were detectable in 2D correlation spectra, that is, the COSY and HSQC cross peaks (see Supporting Information). A similar effect has been reported for the molecular [Ru^{II}(bpy)$_3$]-NDI dyad connected by a flexible alkyl linker, which was attributed to the different local magnetic environment due to intramolecular stacking between NDI units
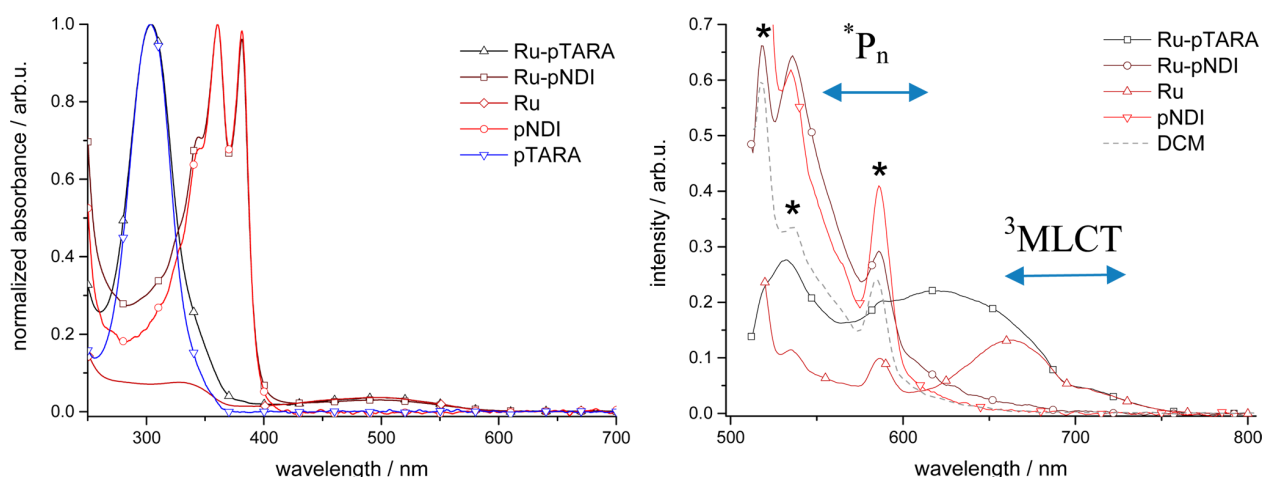
Figure 2. Normalized absorption spectra (left) and emission spectra (500 nm, corrected for matched absorptivity) including solvent spectrum with Raman bands (marked with an asterisk (∗)), assignment of the (weak) emission origin by labeled arrows (right): *P_n denotes localization on polymer chain. Note that the emission spectra of Ru and Ru-pTARA were recorded using slightly different settings.

and the ligand framework.[43] In line with the difficulties to obtain MS data of the nonfunctionalized polymer, all attempts to obtain meaningful MALDI-ToF or ESI-ToF data were unsuccessful. However, the connectivity of the Ru complex and the NDI-polymer is supported by the SEC- and NMR data, and corroborated by the detailed photophysical characterization (*vide infra*).

Absorption and Emission Properties. The photophysical properties of the photo- and/or redox-active compounds were investigated by steady state absorption and emission spectroscopy in aerated dichloromethane solution (Figure 2 and Supporting Information), and are compiled in Table 1 with the

Table 1. Optical and Photophysical Properties

compound	absorption (nm) ($\varepsilon/10^3$ M^{-1} cm^{-1})	emission (nm) (E/eV)	lifetime (ns)
$[Ru(dqp)_2]^{2+}$	490 (14.0)[d]	652 (1.90)[d]	3000[d]
Ru	500 (n.d.)	662 (1.87), 710[b]	>639[a]
pNDI	360 (19.2), 381 (18.5)[c]	<450[e]	8.1; 635[f]
Ru-pTARA	500 (n.d.)	620, 710[b]	3.8; 655[f]
Ru-pNDI	500 (n.d)	607, 710[b]	4.6; 44.5; 387[f]

[a]From monoexponential fit. [b]Characteristic shoulder of $[Ru(dqp)_2]^{2+}$ complexes. [c]Molar extinction coefficients calculated per repeating unit neglecting the chain ends. [d]Ar-purged EtOH−MeOH (v/v 4:1) solution. [e]Indication of a weak emission at 610 nm. [f]The fits also include a very fast decay between 0.3 and 0.5 ns.

time-resolved data (*vide infra*). The absorption spectrum of the nonfunctionalized **pNDI** closely resembles the corresponding monomer, that is, two intense $\pi-\pi^*$-transitions at 360 and 381 nm, respectively. This result parallels the retained optical signatures observed in a related norbornene-based polymer.[42] Surprisingly, no indication of $\pi-\pi$-stacking nor aggregation was found—judged from the absence of a noticeable peak shift or shoulder, which is reported upon polarity-induced aggregation of NDI molecules in solution.[44] As mentioned earlier, the polymer backbone may prevent the formation of the ideal coplanar NDI pairs, as the mutual distance of the poly(styrene) C3-bridge does not allow for the typical plane-to-plane distance of about 3.5 Å.[45] The reference complex **Ru** shows the typical ^{1}MLCT band in the visible light region around 500 nm, and

ligand-centered transition in the UV region below 400 nm. The absorption spectra of the dyads **Ru-pTARA** (TARA is triarylamine) and **Ru-pNDI** match the ones of their individual constituents without any noticeable additional features.

The emission characteristics were determined by excitation in the ^{1}MLCT region at 500 nm (Figure 2). The reference complex **Ru** displays a broad emission band centered at 662 nm with a bathochromic shoulder above 700 nm. In comparison to typical values reported in acetonitrile solution,[30] a noticeable blue-shift (by 30−40 nm, corresponding to 0.1 eV) is observed in the dichloromethane solution. This effect was also observed for the parental complex $[Ru(dqp)_2]^{2+}$ and is tentatively attributed to the lower solvent polarity and thereby weakened stabilization of the ^{3}MLCT state—similar to the typical blue-shift observed for the complex in frozen glass due to restricted solvent reorientation.[30] The **Ru-pTARA** displays similar ^{3}MLCT emission characteristics, without detectable quenching with respect to an *iso*-absorbing solution of the reference complex (Figure 2 right). However, an additional broad and structure-less emission feature appears at wavelengths below 650 nm. In the case of the acceptor dyad **Ru-pNDI**, a similar but much weaker emission band was found, which extends up to the almost completely quenched ^{3}MLCT wavelength region. At higher concentration and more sensitive detector settings, this emission feature is clearly reproduced, that is, it does not originate from the solvent dichloromethane or impurities therein (Supporting Information). Noteworthy, the pristine polymers (**pTARA** or **pNDI**) show no detectable absorption in this wavelength region, and no dual emission is observed for the reference complex **Ru**. A tentative explanation ascribes this additional emission feature of the Ruthenium-containing dyads to the population of (triplet) states located on the redox-active chain,[46] likely caused by the interaction with the neighboring Ru fragment (*vide infra*).

Although polymer-based triplet excited states are generally not directly accessible after photon absorption at room temperature due to the spin-forbidden intersystem crossing, they are experimentally observed by low-temperature phosphorescence for naphthalene diimide (600 to 650 nm)[47] or triphenylamine (420 to 500 nm).[48] In the case of $\pi-\pi$ interaction of two chromophores, that is, the formation of H−

or *J*−aggregates, their emission characteristics also change considerably, both with respect to intensity, energy, and quantum yield. For example, the aggregation of naphthalene diimides leads to strongly enhanced and red-shifted emission (450 to 600 nm) even at room temperature.[44] In this regards, polystyrene films were also reported to display low-temperature phosphorescence in a similar spectral range (400 to 600 nm).[49]

Higher-Lying Emissive States. The emission behavior prompted us to systematically elucidate its origin by means of the excitation profiles of the [3]MLCT-based and the polymer-assigned band (Supporting Information). The excitation spectrum (at 700 nm detection wavelength) of the binary mixture[50] matches the typical [1]MLCT absorption envelope of **Ru** (Figure 3), confirming the origin of the emission from the
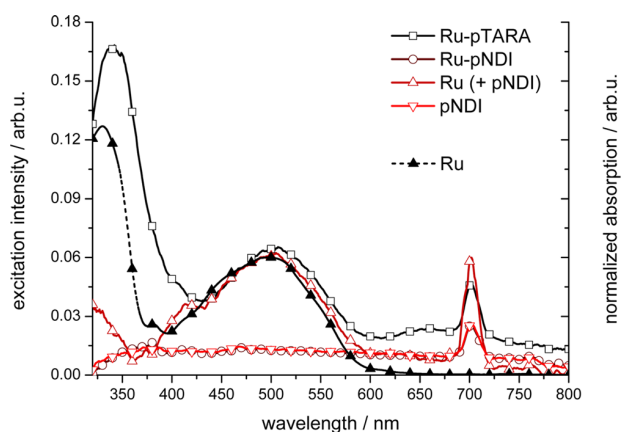
Figure 3. Excitation spectra in dichloromethane recorded at 700 nm (lines with open symbols, left axis) and absorption spectrum of Ru (arbitrarily scaled, dashed lines with solid symbols, right axis) showing similar [1]MLCT envelopes between 400 and 600 nm.

thermally equilibrated [3]MLCT state as reported for a series of $[Ru(dqp)_2]^{2+}$-based complexes.[30] Likewise, the covalent dyad **Ru-pTARA** displays a similar excitation profile in the [1]MLCT spectral region. At shorter wavelength (<400 nm), an additional contribution is observed and attributed to the TARA unit, since the excitation profile (a) clearly exceeds the absorptivity of the mere ruthenium fragment and (b) the rise coincides with the TARA absorption (Supporting Information). Although a contribution from the low-energy tail of the very intense fluorescence cannot be strictly ruled out, sensitization of the ruthenium center may also play a role: First, the covalent attachment of the TARA units along the polymer backbone assures their close proximity, allowing for exchange processes to occur among TARA units and/or directed to the ruthenium fragment (Dexter mechanism).[51] Second, most of the TARA

units (approximately 15 in **Ru-pTARA**[25]) are within the typical operation range of the Förster mechanism (approximately 20 Å).[51] Note that also the required spectral overlap of the TARA fluorescence and Ru absorption is fulfilled (Supporting Information). In case of the **Ru-pNDI**, the absence of [3]MLCT emission prevents us to draw any similar conclusion about the sensitization, but the emission quenching is a strong indication of energy transfer or electron transfer between the ruthenium center and the adjacent acceptor chain.

The interpretation of the second emission feature that is tentatively assigned to the polymer by means of the corresponding excitation spectra (<600 nm) turned out to be less straightforward (Supporting Information). In all studied cases, the spectral signature of NDI or TARA is unambiguously identified in the excitation spectra, accompanied by an additional contribution (bathochromic shoulder) upon comparison to the corresponding absorption spectra. In the case of pristine **pNDI**, the red-edge excitation shoulder is weak and structure-less, which can be explained by a very small fraction of electronically interacting NDI units. In relation to the ^{1}H NMR data, the effect of π−π stacking seems inferior with respect to aggregation in solution.[44] For **Ru-pNDI**, a slightly more pronounced excitation shoulder is found, whereas **Ru-pTARA** revealed an intense band around 375 nm. A further investigation of the dual emission behavior is beyond the scope of this study, despite its potential for sensitization of the [3]MLCT state, which nevertheless should govern the charge separation (*vide infra*).

Redox-States by (spectro)-Electrochemical Analysis. The redox potentials of all relevant electro-active species are presented in Table 2. The cyclic voltammogram of **pNDI** shows two quasi-reversible reductions. The first reduction wave displays an unusual peak shape with a large peak split (167 mV) centered around −1.03 V, as commonly observed for polymers with multiple proximal redox-active centers (see Supporting Information). The formal $E_{1/2}$ potential is anodically shifted by approximately 100 mV with respect to the reported values of NDI derivatives,[52] which is attributed to the plausible charge-transfer stabilization of a reduced NDI unit by its neighbors. The driving forces for oxidative and reductive quenching of the excited photosensitizer, respectively, were estimated using the Rehm−Weller equation omitting the Coulombic work term.[53] In line with the emission quenching data, electron transfer from *Ru^{II} to **pNDI** is thermodynamically allowed (−0.25 eV), whereas the reductive quenching pathway by **pTARA** is energetically uphill (+0.20 eV). Hence, the photo-oxidized Ru^{III} formed after initial electron-transfer to NDI can be re-reduced by **pTARA** (−0.26 eV) to regenerate the photoactive Ru^{II} chromophore.

The oxidation of $[Ru(dqp)_2]^{2+}$ leads to a bleach of the [1]MLCT region around 500 nm (Figure 4), accompanied by

Table 2. Electrochemical Data of Redox-Active Species and Estimated Driving Forces for Electron Transfer

compound	E_{red}/V	E_{red}/V	E_{ox}/V	E_{ox}/V	ΔG/eV	ΔG/eV	ΔG/eV
compound	$dqp^{0/\bullet-}$	$NDI^{0/\bullet-}$	$TARA^{0/\bullet+}$	$Ru^{III/II}$	vs $Ru^{III/II}$	vs $Ru^{*II/IIe}$	vs $Ru^{II/I}$
$[Ru(dqp)_2]^{2+a,b}$	−1.73			+0.63	0		0
pTARA^{a,c}			+0.35		−0.28	+0.18^f	
Ru-pTARA^{a,c}	−1.73		+0.37^d	+0.63^d	−0.26	+0.20^f	
pNDI^b		−1.03^d				−0.25^g	−0.70

^{a}From ref 25. ^{b}In DMF. ^{c}In dichloromethane. ^{d}From DPV data. $^e E_{0-0}$ = 1.90 eV (λ_{em} = 652 nm). ^{f}By reductive quenching of Ru: $E^{exc,ox} = E^{ground,red} + E_{0-0}$. ^{g}By oxidative quenching of Ru: $E^{exc,red} = E^{ground,ox} - E_{0-0}$.
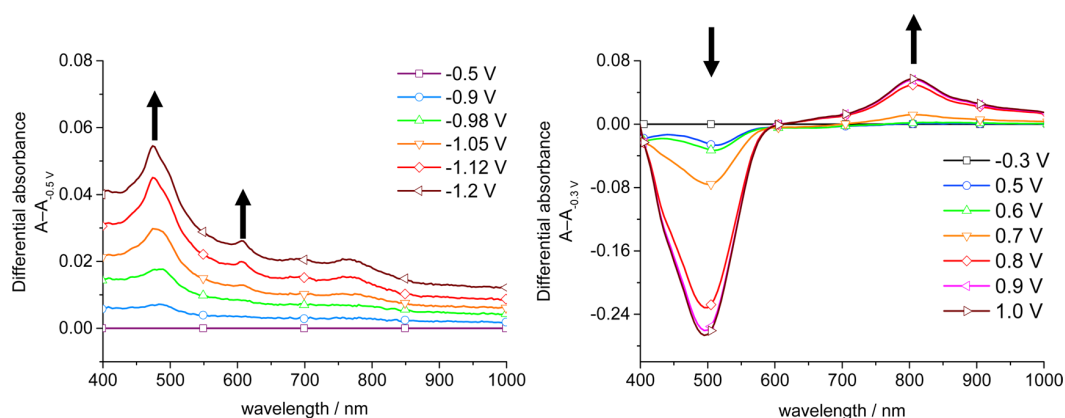
Figure 4. Differential absorption spectra in dichloromethane containing 0.1 M Bu$_4$NPF$_6$ of pNDI upon reduction (left) and oxidation of [Ru(dqp)$_2$]$^{2+}$ (right). Potentials are given vs Fc$^{+/0}$, arrows indicate the increase(decrease) of characteristic bands.
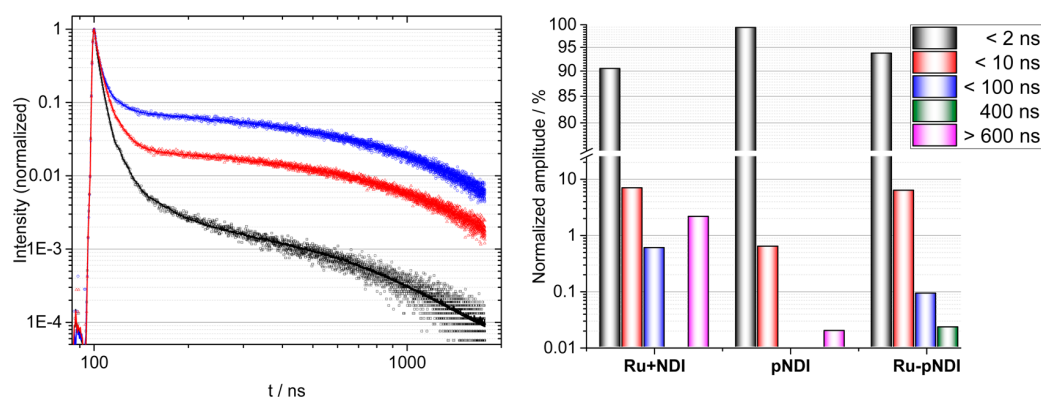

Figure 5. Time-correlated single photon counting data recorded after excitation at 500 nm with 525 and 540 nm long-pass filters: Left: Measured decay curves (symbols, normalized by division of the whole curve by the respective count maximum) and respective fit curves (lines) of pNDI (red), the binary mixture Ru+pNDI (blue), and the covalent dyad Ru-pNDI (black). It should be noted that not all curves were measured to yield an equal number of counts in the maximum such that no information regarding the quantum yields can be extracted from the area under the curves. Right: Respective fit parameters obtained from applying a fit routine for consecutive first-order-reactions including convolution with the instrument response function. Note the scale break from 25 to 75%.

broad absorptions at higher wavelength (>600 nm).[30] The spectro-electrochemical data of **pNDI** show broad absorption bands around 475 and 610 nm upon reduction, in good agreement with reported values of related NDI derivatives.[52] Despite this excellent qualitative agreement, the spectral changes indicate an incomplete reduction of the NDI units in the applied voltage range: The onset of reduction occurs at about −0.9 V, and only a fraction of the NDI is reduced at −1.2 V judged from the remaining $\pi-\pi^*$ transitions and the rise of the NDI$^-$ absorptions. This observation corroborates the previous assignment of interacting NDI$^-$ units, based on the broad CV wave and the large formal peak split. More importantly, the individual spectral signatures of NDI$^-$ and Ru^{III} will assist the analysis of the time-resolved transient absorption measurements (*vide infra*).

Time-Resolved Studies. The emission lifetimes of NDI-containing samples, that is, **Ru-pNDI**, **pNDI**, and the binary mixture of **Ru** and **pNDI**, were determined by time-correlated single-photon counting (TCSPC) in aerated dichloromethane solution after excitation at 500 nm (Figure 5). All curves strongly deviate from a monoexponential decay which shows that either multiple deactivation pathways exist or that more than one species emits. This result is reasonable in view of the flexible linkage, which allows for multiple conformations and/or

stacking (*vide supra*). For example, a related molecular dyad based on [Ru(bpy)$_3$]$^{2+}$, connected by a flexible bridge, was reported to follow three-exponential decay kinetics with lifetimes of 0.34 ns (88%), 1.99 ns (11%), and 12.6 ns (1%), respectively.[27] A similar time-window was observed for rigidified bridges in Ruthenium-acceptor assemblies with lifetimes ranging from 0.2 ns to 7.9 ns.[54]

The emission decay curve of the covalent dyad **Ru-pNDI** differs from that of the binary mixture (**BM**) of **Ru** with **pNDI** (Figure 5): The emission intensity of **Ru-pNDI** drops to less than 1% of the maximum intensity within 50 ns after excitation, while the emission of **BM** is still at ca. 10% of the initial intensity. This finding is attributed to quenching occurring in the covalent dyad, which is not occurring in the **BM**. It also implies that diffusional quenching of excited **Ru** by **pNDI** in the binary mixture is ineffective. Therefore, the longest lifetime component (>600 ns) determined for the **BM** should in principle be the lifetime of the ^{3}MLCT emission of the **Ru** unit. However, this value is shortened by a factor of 5 compared to typical lifetimes of [Ru(dqp)$_2$]$^{2+}$-based complexes,[29,30] which is attributed to the different solvent and the presence of oxygen as a triplet quencher. The quenching in **Ru-pNDI** is in agreement with the steady state emission data. The longest lifetime
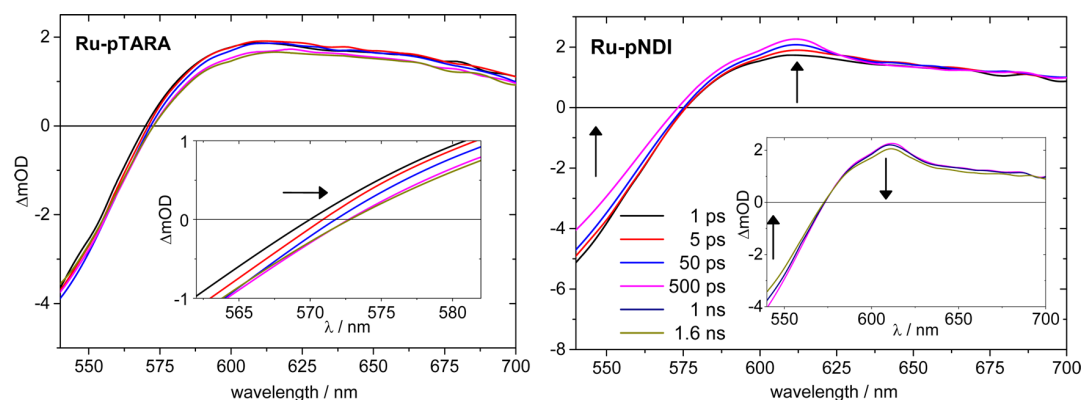
Figure 6. Transient absorption spectra at selected delay times for Ru-pTARA (left) and Ru-pNDI (right): 1 ps (black), 5 ps (red), 50 ps (blue), 500 ps (pink), 1 ns (dark blue, shown only for Ru-pNDI), 1.6 ns (beige). The insets contain a zoom in on the zero-crossing region in the left panel and the evolution of the transient absorption spectra at delay times after 500 ps in the right panel, respectively. All shown spectra were smoothed using a 10-point FFT filter to remove a systematic noise pattern (see SI).

(400 ns) for this compound is still in the same order of magnitude as the lifetime of the unquenched Ru complex.

However, the decay-curve approaches the background (prezero) signal level only for **Ru-pNDI**, which provides a qualitative measure of the minimal emission quantum yield. The long-lived contributions may originate from residual nonattached sensitizer in the sample, or from nonfunctionalized polymer (*vide infra*). For comparison, no emission occurring on the 100 ns time-scale was reported for the molecular dyad system,[27] and the contribution of this emitting species to the total steady state emission data is unclear due to the unknown extinction coefficient and quantum yield. Hence, the pristine **pNDI** was studied to elucidate any potential interaction due to the proximity of NDI units within the polymer. A long emission lifetime (>600 ns) was observed, which is in the same order as the Ru-based ^{3}MLCT emission despite the absence of this sensitizer. Such a long lifetime is indicative for phosphorescence, but would require intersystem crossing for triplet formation. For example, bis-*N*-alkylated NDI exhibits phosphorescence at 77 K in frozen ethanol glass containing 10% methyl iodide, characterized by a narrow emission band at 610 nm (2.03 eV) and a lifetime of 62 μs.[47] A detailed study of mono-*N*-arylated NDI chromophores at room temperature showed the presence of a broad emission band in the same spectral region as **pNDI** (500 to 650 nm, see Supporting Information), which was attributed to partial charge transfer involving the phenyl ring and fast intersystem crossing (30 ps).[55] The lifetime of the formed triplet state was reported to be 450 ns, in good agreement with the value determined for **pNDI**. Such triplet formation was originally achieved using concentrated solutions and 350 nm excitation,[55] whereas the polymer-connected NDIs enable the excimer formation also at lower bulk concentration, and may further lead to a sensitization at 500 nm due to *H*- and *J*-aggregates.[44] Despite the low extent of stacking of two NDI on the basis of the optical and ^{1}H NMR data of **pNDI**, the very sensitive TCSPC technique is capable of detecting any emissive specimen, which corroborates all previous assignments based on absorption and excitation data (*vide supra*). Hence, the weak excimer absorption is expected to be only of inferior importance in the presence of the dominating ruthenium-based ^{1}MLCT band.

Transient Absorption. The early photoinduced events (<2 ns) occurring after excitation at 500 nm were studied for the dyads **Ru-pTARA** and **Ru-pNDI**. Transient absorption data for a probe range between 500 and 700 nm was recorded and is presented in terms of transient absorption spectra at selected delay times (Figure 6). First, for both compounds the instantaneous bleach of the ^{1}MLCT band and excited state absorption is observed below 570 nm and above 570 nm, respectively. In the case of **Ru-pTARA**, the spectral characteristics are retained on the time-scale of our experiment. A weak red-shift is observed during the first 500 ps (see inset). The spectral features correspond very well with those reported for nonfunctionalized [Ru(dqp)$_2$]$^{2+}$,[30] indicating that the methoxy-substituent and the nearby **pTARA**-chain has a negligible electronic influence on the photosensitizer. In contrast, **Ru-pNDI** shows the development of an additional band at 610 nm on the picosecond time scale. This band coincides with the position of the reduced NDI[52] upon electrochemical reduction of **pNDI** (*vide supra*). The rise of this peak is associated with the decrease of the bleach signature around 550 nm, caused by ground state recovery and/or a buildup of excited state absorption, which suggests electron transfer from the excited chromophore to the NDI acceptor. It should be pointed out, that absorption features of NDI triplet states are typically found at shorter wavelengths,[47] and we thus emphasize the explicit indication of electron transfer. At delay times >500 ps a weak signal decay is observed over the entire spectral range shown (see inset).

For a quantitative interpretation a global fit routine was applied to the transient absorption data (see the experimental section in the Supporting Information for details). The results of the kinetic analysis for **Ru-pNDI** are shown in terms of decay-associated spectra (DAS) in Figure 7 (for the respective DAS for **Ru-pTARA** see Supporting Information). The multiexponential fit includes an offset to model a nondecaying component. The lifetimes (inverse time constants) of the other involved processes are 2.1 ps (blue DAS), 99 ps (pink DAS), and 1.9 ns (green DAS). Both picosecond processes are characterized by rather similar DAS with negative values over the entire spectral range investigated. The faster process can be assigned to solvent relaxation in accordance with literature reports.[56,57] The 99 ps process describes the buildup of positive signal including the feature at 610 nm, which is the indication of the NDI radical anion being formed (*vide supra*). Therefore, this process can be related to electron-transfer between the
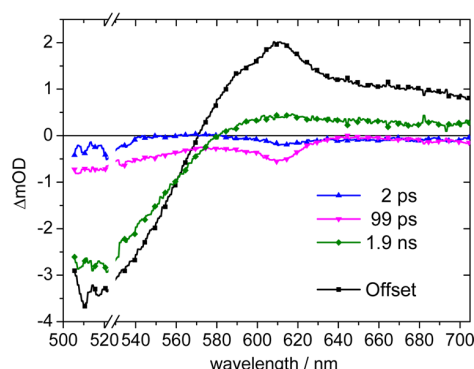
Figure 7. Decay-associated spectra of Ru-pNDI (DAS) obtained from a global multiexponential fit applied on the transient absorption data with corresponding lifetimes (inverse time constants) of 2 ps (blue curve), 99 ps (pink curve), 1.9 ns (green curve). The black curve corresponds to a constant offset, that is, to a process with a lifetime significantly exceeding 2 ns. A fast process with a lifetime of 0.1 ps was also included in the fit but is excluded from this figure (see Supporting Information). The spectral interval from 522 to 530 nm was removed from the data set because of a measurement artifact.

complex unit and the NDI-acceptor polymer chain. The process on the early nanosecond time scale (1.9 ns, green DAS) reduces negative signal contributions below 570 nm and positive contributions at longer wavelength. Actually, the DAS of the 1.9 ns component contains the characteristic absorption features of the ^{3}MLCT state. A tentative interpretation assigns this process to a secondary deactivation channel of the ^{3}MLCT state which could be triplet−triplet energy transfer to a pNDI-centered state. Also, pNDI itself may contribute to the photoinduced dynamics, and a process with a lifetime of 700 ps and similar spectral characteristics (with an inversed sign) was identified for a related NDI derivative.[55] The transient absorption spectrum at late delay times (black curve in Figure 7) should in principle be composed of the spectra of electrochemically generated reduced pNDI and oxidized Ru(III), as well as the ground-state bleach signature of the ^{1}MLCT band. However, attempts to quantitatively reproduce the spectrum from the individual components failed due to the limited spectral window accessible in our transient absorption setup. Also we cannot exclude the possibility that additional species contribute to the transient absorption data. Such species could originate from the pNDI chain, which would be plausible with regard to the excitation spectra and TCSPC data. Finally, no significant recombination is detected up to 2 ns as no decay of the 610 nm band is observed. The charge recombination seems to be significantly slowed down in comparison to molecular dyad systems,[54] which usually display fast back electron transfer. Although the current transient absorption setup prevents a further analysis at longer time scales, the TCSPC-emission decay and the steady state emission intensity clearly suggest that light-induced electron transfer within the designed covalent dyad Ru-pNDI is effective.

CONCLUSION

A new redox-active poly(styrene)-based naphthalene diimide was synthesized via nitroxide-mediated polymerization and characterized by NMR, MS, and SEC analyses. These analyses revealed the shielding effect of the stacked π-systems, while the virtually preserved optical and (spectro)electrochemical properties (in comparison to NDI derivatives) suggest only a low

extent of stacking. The polymer was connected via its chain terminus to a long-lived phosphorescent ruthenium photo-sensitizer, in order to readily prepare a hierarchical controlled congener of molecular dyads based on $[Ru(bpy)_3]^{2+}$. The driving forces for charge separation were estimated from the redox-properties of the individual components; that is, Ru-pNDI may undergo oxidative quenching, while the related donor-functionalized dyad (Ru-pTARA) would undergo secondary electron transfer after photooxidation of the Ru center. The second part details the spectroscopic analyses of the dyads, complemented by the respective nonfunctionalized polymers, and a binary mixture of the sensitizer with pNDI. In agreement with the redox-properties, Ru-pTARA shows the typical phosphorescence of the photosensitizer around 660 nm, while Ru-pNDI is significantly quenched. In addition, broad emission bands were observed in both cases, which originate from the redox-active polymer as confirmed by the excitation spectra. The time-correlated single photon counting analysis of Ru-pTARA shows a monoexponential decay after 50 ns, but in the case of Ru-pNDI a clear nonmonoexponential decay. Noteworthy, pNDI itself shows a similar phosphorescence lifetime in agreement with literature reports, which explains the discrepancy between the efficient quenching of Ru-pNDI observed in the steady state data vs the significant contribution (amplitude) of long-lived components in the TCSPC data. Transient absorption spectroscopy data confirmed the forward electron transfer to generate the NDI anion-radical, without noticeable decay up to ca. 2 ns. The apparent recovery in the ^{1}MLCT region is tentatively assigned to the decay of pNDI-based state(s) in satisfying agreement to a literature report. In summary, the polymer-based Ru-pNDI shows efficient ^{3}MLCT emission quenching by electron transfer, irrespective of the unsaturated and flexible linkage by the polymer scaffold. In combination with the synthetic versatility of the presented modular approach, hierarchically defined functional macro-molecules can be designed and readily prepared. The potential of such architectures to translocate the generated charge along the polymer chains is currently under investigation.

ASSOCIATED CONTENT

Supporting Information

Additional experimental, photophysical and electrochemical data, as well as NMR and MS spectra. This material is available free of charge via the Internet at http://pubs.acs.org.

AUTHOR INFORMATION

Corresponding Authors
*E-mail: benjamin.dietzek@uni-jena.de.
*E-mail: michael.jager.iomc@uni-jena.de.
Author Contributions
#J.K. and R.S. contributed equally to this work.
Notes
The authors declare no competing financial interest.

ACKNOWLEDGMENTS

sample preparation and steady-state measurements, and Sarah Crotty for MALDI-ToF measurements.

■ REFERENCES

(1) Lewis, N. S.; Nocera, D. G. Powering the Planet: Chemical Challenges in Solar Energy Utilization. *Proc. Natl. Acad. Sci. U.S.A.* **2006**, *103*, 15729−15735.

(2) Alstrum-Acevedo, J. H.; Brennaman, M. K.; Meyer, T. J. Chemical Approaches to Artificial Photosynthesis. 2. *Inorg. Chem.* **2005**, *44*, 6802−6827.

(3) Berardi, S.; Drouet, S.; Francas, L.; Gimbert-Surinach, C.; Guttentag, M.; Richmond, C.; Stoll, T.; Llobet, A. Molecular Artificial Photosynthesis. *Chem. Soc. Rev.* **2014**, 7501−7519.

(4) Faunce, T.; Styring, S.; Wasielewski, M. R.; Brudvig, G. W.; Rutherford, A. W.; Messinger, J.; Lee, A. F.; Hill, C. L.; de Groot, H.; Fontecave, M.; et al. Artificial Photosynthesis as a Frontier Technology for Energy Sustainability *Energ. Environ. Sci.* **2013**, *6*, 1074−1076.

(5) Gust, D.; Moore, T. A.; Moore, A. L. Realizing Artificial Photosynthesis. *Faraday Discuss.* **2012**, *155*, 9−26.

(6) Sun, L. C.; Hammarström, L.; Akermark, B.; Styring, S. Towards Artificial Photosynthesis: Ruthenium−Manganese Chemistry for Energy Production. *Chem. Soc. Rev.* **2001**, *30*, 36−49.

(7) Meyer, T. J. Photochemistry of Metal Coordination-Complexes—Metal to Ligand Charge-Transfer Excited-States. *Pure Appl. Chem.* **1986**, *58*, 1193−1206.

(8) Juris, A.; Balzani, V.; Barigelletti, F.; Campagna, S.; Belser, P.; von Zelewsky, A. Ru(II) Polypyridine Complexes—Photophysics, Photochemistry, Electrochemistry, and Chemi-luminescence. *Coord. Chem. Rev.* **1988**, *84*, 85−277.

(9) Thompson, D. W.; Ito, A.; Meyer, T. J. Ru(bpy)$_3^{2+*}$ and Other Remarkable Metal-to-Ligand Charge Transfer (MLCT) Excited States. *Pure Appl. Chem.* **2013**, *85*, 1257−1305.

(10) Tschierlei, S.; Karnahl, M.; Presselt, M.; Dietzek, B.; Guthmuller, J.; Gonzalez, L.; Schmitt, M.; Rau, S.; Popp, J. Photochemical Fate: The First Step Determines Efficiency of H$_2$ Formation with a Supramolecular Photocatalyst. *Angew. Chem., Int. Ed.* **2010**, *49*, 3981−3984.

(11) Zedler, L.; Kupfer, S.; de Moraes, I. R.; Waechtler, M.; Beckert, R.; Schmitt, M.; Popp, J.; Rau, S.; Dietzek, B. Trapped in Imidazole: How to Accumulate Multiple Photoelectrons on a Black-Absorbing Ruthenium Complex. *Chem.—Eur. J.* **2014**, *20*, 3793−3799.

(12) Huynh, M. H. V.; Dattelbaum, D. M.; Meyer, T. J. Exited State Electron and Energy Transfer in Molecular Assemblies. *Coord. Chem. Rev.* **2005**, *249*, 457−483.

(13) Pellegrin, Y.; Odobel, F. Molecular Devices Featuring Sequential Photoinduced Charge Separations for the Storage of Multiple Redox Equivalents. *Coord. Chem. Rev.* **2011**, *255*, 2578−2593.

(14) Wenger, O. S. How Donor−Bridge−Acceptor Energetics Influence Electron Tunneling Dynamics and Their Distance Dependences. *Acc. Chem. Res.* **2010**, *44*, 25−35.

(15) Albinsson, B.; Mårtensson, J. Long-Range Electron and Excitation Energy Transfer in Donor−Bridge−Acceptor Systems. *J. Photochem. Photobiol., C: Photochem. Rev.* **2008**, *9*, 138−155.

(16) Natali, M.; Campagna, S.; Scandola, F. Photoinduced Electron Transfer Across Molecular Bridges: Electron- and Hole-Transfer Superexchange Pathways. *Chem. Soc. Rev.* **2014**, 4005−4018.

(17) Schultze, X.; Serin, J.; Adronov, A.; Frechet, J. M. J. Light Harvesting and Energy Transfer in a Ruthenium−Coumarin-2 Copolymer. *Chem. Commun.* **2001**, 1160−1161.

(18) Serin, J.; Schultze, X.; Adronov, A.; Frechet, J. M. J. Synthesis and Study of the Absorption and Luminescence Properties of Polymers Containing Ru(BpyMe$_2$)$_3^{2+}$ Chromophores and Coumarin Laser Dyes. *Macromolecules* **2002**, *35*, 5396−5404.

(19) Fleming, C. N.; Maxwell, K. A.; DeSimone, J. M.; Meyer, T. J.; Papanikolas, J. M. Ultrafast Excited-State Energy Migration Dynamics in an Efficient Light-Harvesting Antenna Polymer Based on Ru(II) and Os(II) Polypyridyl Complexes. *J. Am. Chem. Soc.* **2001**, *123*, 10336−10347.

(20) Sun, Y.; Chen, Z.; Puodziukynaite, E.; Jenkins, D. M.; Reynolds, J. R.; Schanze, K. S. Light Harvesting Arrays of Polypyridine Ruthenium(II) Chromophores Prepared by Reversible Addition−Fragmentation Chain Transfer Polymerization. *Macromolecules* **2012**, *45*, 2632−2642.

(21) Sykora, M.; Maxwell, K. A.; DeSimone, J. M.; Meyer, T. J. Mimicking the Antenna-Electron Transfer Properties of Photosynthesis. *Proc. Natl. Acad. Sci. U.S.A.* **2000**, *97*, 7687−7691.

(22) Puodziukynaite, E.; Wang, L.; Schanze, K. S.; Papanikolas, J. M.; Reynolds, J. R. Poly(fluorene-co-thiophene)-Based Ionic Transition-Metal Complex Polymers for Solar Energy Harvesting and Storage Applications. *Polym. Chem.* **2014**, *5*, 2363−2369.

(23) zur Borg, L.; Domanski, A. L.; Breivogel, A.; Burger, M.; Berger, R.; Heinze, K.; Zentel, R. Light-induced Charge Separation in a Donor-Chromophore-Acceptor Nanocomposite Poly TPA-Ru(tpy)$_2$ @ZnO. *J. Mater. Chem. C* **2013**, *1*, 1223−1230.

(24) Fang, Z.; Ito, A.; Keinan, S.; Chen, Z.; Watson, Z.; Rochette, J.; Kanai, Y.; Taylor, D.; Schanze, K. S.; Meyer, T. J. Atom Transfer Radical Polymerization Preparation and Photophysical Properties of Polypyridylruthenium Derivatized Polystyrenes. *Inorg. Chem.* **2013**, *52*, 8511−8520.

(25) Schroot, R.; Friebe, C.; Altuntas, E.; Crotty, S.; Jäger, M.; Schubert, U. S. Nitroxide-Mediated Polymerization of Styrenic Triarylamines and Chain-End Functionalization with a Ruthenium Complex: Toward Tailored Photoredox-Active Architectures. *Macromolecules* **2013**, *46*, 2039−2048.

(26) Reisner, E.; Powell, D. J.; Cavazza, C.; Fontecilla-Camps, J. C.; Armstrong, F. A. Visible Light-Driven H$_2$ Production by Hydrogenases Attached to Dye-Sensitized TiO$_2$ Nanoparticles. *J. Am. Chem. Soc.* **2009**, *131*, 18457−18466.

(27) Dixon, D. W.; Thornton, N. B.; Steullet, V.; Netzel, T. Effect of DNA Scaffolding on Intramolecular Electron Transfer Quenching of a Photoexcited Ruthenium(II) Polypyridine Naphthalene Diimide. *Inorg. Chem.* **1999**, *38*, 5526−5534.

(28) Sauvage, J.-P.; Collin, J.-P.; Chambron, J. C.; Guillerez, S.; Coudret, C.; Balzani, V.; Barigelletti, F.; Decola, L.; Flamigni, L. Ruthenium(II) and Osmium(II) Bis(Terpyridine) Complexes in Covalently-Linked Multicomponent Systems—Synthesis, Electrochemical-Behavior, Absoprtion-Spectra, and Photochemical and Photophysical Properties. *Chem. Rev.* **1994**, *94*, 993−1019.

(29) Jäger, M.; Kumar, R. J.; Görls, H.; Bergquist, J.; Johansson, O. Facile Synthesis of Bistridentate RuII Complexes Based on 2,6-Di(quinolin-8-yl)pyridyl Ligands: Sensitizers with Microsecond ³MLCT Excited State Lifetimes. *Inorg. Chem.* **2009**, *48*, 3228−3238.

(30) Abrahamsson, M.; Jäger, M.; Kumar, R. J.; Österman, T.; Persson, P.; Becker, H.-C.; Johansson, O.; Hammarström, L. Bistridentate Ruthenium(II)polypyridyl-Type Complexes with Microsecond ³MLCT State Lifetimes: Sensitizers for Rod-like Molecular Arrays. *J. Am. Chem. Soc.* **2008**, *130*, 15533−15542.

(31) Kumar, R. J.; Karlsson, S.; Streich, D.; Jensen, A. R.; Jäger, M.; Becker, H.-C.; Bergquist, J.; Johansson, O.; Hammarström, L. Vectorial Electron Transfer in Donor-Photosensitizer-Acceptor Triads Based on Novel Bis-tridentate Ruthenium Polypyridyl Complexes. *Chem.—Eur. J.* **2010**, *16*, 2830−2842.

(32) Hankache, J.; Wenger, O. S. Microsecond Charge Recombination in a Linear Triarylamine-Ru(bpy)$_3^{2+}$-Anthraquinone Triad. *Chem. Commun.* **2011**, *47*, 10145−10147.

(33) Kaiser, C.; Schmiedel, A.; Holzapfel, M.; Lambert, C. Long-Lived Singlet and Triplet Charge Separated States in Small Cyclophane-Bridged Triarylamine−Naphthalene Diimide Dyads. *J. Phys. Chem. C* **2012**, *116*, 15265−15280.

(34) Klein, J. H.; Sunderland, T. L.; Kaufmann, C.; Holzapfel, M.; Schmiedel, A.; Lambert, C. Stepwise versus Pseudo-Concerted Two-Electron-Transfer in a Triarylamine-Iridium Dipyrrin-Naphthalene Diimide Triad. *Phys. Chem. Chem. Phys.* **2013**, *15*, 16024−16030.

(35) Thelakkat, M. Star-Shaped, Dendrimeric and Polymeric Triarylamines as Photoconductors and Hole Transport Materials for Electro-optical Applications. *Macromol. Mater. Eng.* **2002**, *287*, 442−461.

(36) Katz, H. E.; Lovinger, A. J.; Johnson, J.; Kloc, C.; Siegrist, T.; Li, W.; Lin, Y. Y.; Dodabalapur, A. A Soluble and Air-Stable Organic Semiconductor with High Electron Mobility. *Nature* **2000**, *404*, 478−481.

(37) Zhan, X. W.; Facchetti, A.; Barlow, S.; Marks, T. J.; Ratner, M. A.; Wasielewski, M. R.; Marder, S. R. Rylene and Related Diimides for Organic Electronics. *Adv. Mater.* **2011**, *23*, 268−284.

(38) Bhosale, S. V.; Jani, C. H.; Langford, S. J. Chemistry of Naphthalene Diimides. *Chem. Soc. Rev.* **2008**, *37*, 331−342.

(39) Thalacker, C.; Roeger, C.; Wuerthner, F. Synthesis and Optical and Redox Properties of Core-Substituted Naphthalene Diimide Dyes. *J. Org. Chem.* **2006**, *71*, 8098−8105.

(40) Kondratenko, M.; Moiseev, A. G.; Perepichka, D. F. New Stable Donor-Acceptor Dyads for Molecular Electronics. *J. Mater. Chem.* **2011**, *21*, 1470−1478.

(41) Jäger, M.; Görls, H.; Günther, W.; Schubert, U. S. Pd-Catalyzed Ring Assembly by Vinylation and Intramolecular Heck Coupling: A Versatile Strategy towards Functionalized Azadibenzocyclooctynes. *Chem.—Eur. J.* **2013**, *19*, 2150−2157.

(42) Kumar, N. S. S.; Gujrati, M. D.; Wilson, J. N. Evidence of Preferential π-Stacking: A Study of Intermolecular and Intramolecular Charge Transfer Complexes. *Chem. Commun.* **2010**, *46*, 5464−5466.

(43) Steullet, V.; Dixon, W. D. Self-Stacking of Naphthalene Bis(dicarboximide)s Probed by NMR. *J. Chem. Soc., Perk. Trans. 2* **1999**, 1547−1558.

(44) Kumar, M.; George, S. J. Spectroscopic Probing of the Dynamic Self-Assembly of an Amphiphilic Naphthalene Diimide Exhibiting Reversible Vapochromism. *Chem.—Eur. J.* **2011**, *17*, 11102−11106.

(45) Janiak, C. A Critical Account on π-π Stacking in Metal Complexes with Aromatic Nitrogen-Containing Ligands. *J. Chem. Soc., Dalton Trans.* **2000**, 3885−3896.

(46) Köhler, A.; Bässler, H. Triplet States in Organic Semiconductors. *Mater. Sci. Eng.: Rep.* **2009**, *66*, 71−109.

(47) Rogers, J. E.; Kelly, L. A. Nucleic Acid Oxidation Mediated by Naphthalene and Benzophenone Imide and Diimide Derivatives: Consequences for DNA Redox Chemistry. *J. Am. Chem. Soc.* **1999**, *121*, 3854−3861.

(48) Kasha, M.; Rawls, H. R.; Ahraf El-Bayoumi, M. The Exciton Model in Molecular Spectroscopy. *Pure Appl. Chem.* **1965**, *11*, 371−392.

(49) George, G. A. The Phosphorescence Spectrum and Photo-degradation of Polystyrene Films. *J. Appl. Polym. Sci.* **1974**, *18*, 419−426.

(50) Note that the spectra of Ru were extracted from the binary mixture with pNDI, and only show the contribution of nonquenched Ru

(51) Lakowicz, J. R. *Principles of Fluorescence Spectroscopy*, 3rd ed.; Springer Verlag: Berlin, 2006.

(52) Gosztola, D.; Niemczyk, M. P.; Svec, W.; Lukas, A. S.; Wasielewski, M. R. Excited Doublet States of Electrochemically Generated Aromatic Imide and Diimide Radical Anions. *J. Phys. Chem. A* **2000**, *104*, 6545−6551.

(53) Rehm, D.; Weller, A. Kinetics of Fluorescence Quenching by Electron and H-Atom Transfer. *Isr. J. Chem.* **1970**, *8*, 259−271.

(54) Johansson, O.; Borgström, M.; Lomoth, R.; Palmblad, M.; Bergquist, J.; Hammarström, L.; Sun, L.; Åkermark, B. Electron Donor−Acceptor Dyads Based on Ruthenium(II) Bipyridine and Terpyridine Complexes Bound to Naphthalenediimide. *Inorg. Chem.* **2003**, *42*, 2908−2918.

(55) Ganesan, P.; Baggerman, J.; Zhang, H.; Sudhölter, E. J. R.; Zuilhof, H. Femtosecond Time-Resolved Photophysics of 1,4,5,8-Naphthalene Diimides. *J. Phys. Chem. A* **2007**, *111*, 6151−6156.

(56) Horng, M. L.; Gardecki, J. A.; Papazyan, A.; Maroncelli, M. Subpicosecond Measurements of Polar Solvation Dynamics: Coumarin 153 Revisited. *J. Phys. Chem.* **1995**, *99*, 17311−17337.

(57) Bhasikuttan, A. C.; Suzuki, M.; Nakashima, S.; Okada, T. Ultrafast Fluorescence Detection in Tris(2,2′-bipyridine)ruthenium-(II) Complex in Solution: Relaxation Dynamics Involving Higher Excited States. *J. Am. Chem. Soc.* **2002**, *124*, 8398−8405.

Supporting Information

Photoredox–active Dyads Based on a Ru(II) Photosensitizer Equipped With Electron Donor or Acceptor Polymer Chains: A Spectroscopic Study of Light-induced Processes Towards Efficient Charge Separation

Joachim Kübel,[⊥,Δ,#] Robert Schroot,[†,#] Maria Wächtler, [⊥,Δ] Ulrich S. Schubert,[†,‡] Benjamin Dietzek,*[,⊥,Δ,‡] and Michael Jäger*[,†,‡,]

# J. K. and R. S. contributed equally to this work

Table of Contents

1. Experimental Methods

Materials

All reagents were purchased from Sigma-Aldrich, Alfa Aesar, Apollo Scientific, Acros Organics, TCI chemicals or ABCR and used without further purification unless otherwise noted. Dry pyridine and dry *N-N*-dimethylformamide were commercially available. All solvents were degased before use. Toluene was dried using a PureSolv-EN Solvent Purification System (Innovative Technology). Dichloromethane for use in polymerizations was dried by refluxing over phosphorus pentoxide. 2-(4-Bromophenyl)-7-(2-ethylhexyl)benzo[lmn][3,8]phenanthroline-1,3,6,8(2H,7H)-tetraone[1] precursor and [Ru(dqp)(dqp-OH)](PF$_6$)$_2$[2] were synthesized as reported.

_N_-(2-Ethyl-hexyl)-_N'_-(vinylphenyl)-naphthalene-1,4,5,8-dicarboxydiimide (NDI)
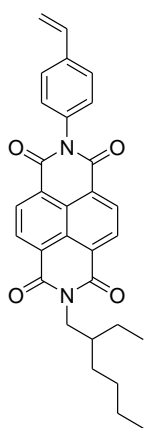
A flask was charged with 2-(4-bromophenyl)-7-(2-ethylhexyl)benzo[lmn][3,8]phenanthroline-1,3,6,8(2H,7H)-tetraone (1.4 g, 2.62 mmol), bis(dibenzylideneacetone)palladium(0) (0.075 g, 0.131 mmol), biphenyl-2-yldi-*tert*-butylphosphine (0.078 g, 0.262 mmol), tetrabutyl-ammonium fluoride trihydrate (0.828 g, 2.62 mmol) and THF (Volume: 20 mL). The reaction vessel was flushed with protective gas (nitrogen), and 2,4,6,8-tetramethyl-2,4,6,8-tetravinyl-1,3,5,7,2,4,6,8-tetraoxatetrasilocane (0.452 g, 1.312 mmol) was added dropwise. The reaction mixture was heated to 60 °C for 18 hours under at inert atmosphere (N$_2$). Excess of solvent was removed under reduced pressure, and the solids titurated with diethyl ether (200 mL) and water (100 mL). The organic layer was filtered to remove insoluble parts, dried over anhydrous sodium sulfate and adsorbed on Silica. The crude product was purified by flash chromatography (Silica gel, SNAP 100 g, eluting with a gradient of hexane/dichloromethane (80/20 to 0/100). The fractions were analyzed by thin layer chromatography, and the combined pure fractions yielded a first crop (0.354 g, 28%). ^{1}H NMR (250 MHz, CDCl$_3$): δ 8.81 (s, 4H, NaphH), 7.61 (d, *J* = 8.5 Hz, 2H, ArH), 7.29 (d, *J* = 8.5, 2H, ArH), 6.81 (dd, *J* = 17.5, 11 Hz, 1H, C**H**=CH$_2$), 5.84 (d, *J* = 17.5 Hz, 1H, CH=C**H**$_2$-trans), 5.37 (d, *J* = 11 Hz, 1H, CH=C**H**$_2$-cis), 4.32–4.02 (m, 2H, CH$_2$), 2.07–1.84 (m, 1H, CH), 1.49–1.21 (m, 8H, 4×CH$_2$), 1.02–0.82 (m, 6H, 2×CH$_3$). ^{13}C NMR (63 MHz, CDCl$_3$): δ 163.2, 163.0, 138.6, 136.0, 133.8, 131.4, 131.1, 128.6, 127.3, 127.1, 127.0, 126.9, 126.7, 115.5, 44.7, 38.0, 30.7, 28.6, 24.1, 23.0, 14.1, 10.6. Elem. anal. calcd. for C$_{30}$H$_{28}$N$_2$O$_4$: C, 74.98%; H, 5.87%; N, 5.83%; found: C, 75.10%; H, 5.75%; N, 5.69%. MS (ESI-TOF) m/z: 481.280 ([M+H]$^+$).

pNDI. A glass tube equipped with a septum and an external overhead flushing with nitrogen gas was used for the polymerizations. The reaction vessel was charged with **NDI** (0.500 g, 1.040 mmol), *N-tert*-butyl-*O*-[1-[4-(chloromethyl)phenyl]ethyl]-*N*-(2-methyl-1-phenylpropyl)hydroxylamine (0.019 g, 0.051 mmol) and dimethylformamide (3 mL). After heating to 120 °C for 40 hours, the reaction mixture was diluted with dichloromethane and precipitated in cold methanol. Unreacted monomer was removed by preparative size exclusion chromatography (Bio-Beads SX3, dichloromethane). The polymer was obtained as a pale yellow powder after precipitation in methanol. Yield: 0.186 g. Analytical size-exclusion chromatography (chloroform/*iso*-propanol/triethylamine 94/2/4, polystyrene calibration): M$_n$ = 9,040 g/mol, PDI = 1.37. ^{1}H NMR (400 MHz, CD$_2$Cl$_2$): δ 8.47 (broad, 4H), 7.22 (broad, 4H), 4.55 (broad, 0.12H),

4.07 (broad, 2H), 2.37 (broad, 1H), 1.86 (broad, 2H), 1.28 (broad, 8H), 0.86 (broad, 6H). See below for NMR and MALDI-MS spectra.

Ru-pNDI. A flask was charged with **pNDI** (0.050 g, 0.007 mmol), [Ru(dqp)(dqpOH)][PF$_6$]$_2$ (0.009 g, 0.008 mmol) and potassium carbonate (0.001 g, 0.008 mmol). The reaction vessel was purged for 15 minutes. N,N-Dimethylformamide (2.0 mL) was added and the reaction mixture was placed in a pre-heated oil bath at 60 °C. After 96 hours, the solution was precipitated in water. The red precipitate was re-dissolved in dichloromethane and washed with water. Further purification by column chromatography (aluminium oxide, dichloromethane/methanol 18/1) yielded the product as a red solid. Yield: 0.021 g. ^{1}H NMR (400 MHz, CD$_2$Cl$_2$) δ 9.01–6.30 (broad), 4.45–3.55 (broad), 2.46–0.29 (broad). See supporting for NMR, MS and 3D-SEC spectra.

Instrumentation

NMR spectra were recorded on a 250 or 400 MHz NMR spectrometer (Bruker AVANCE or Fourier 300) in deuterated solvents at 298 K. Chemical shifts are reported in parts per million (ppm, δ scale) relative to the residual solvent signal.[3]

MALDI-TOF MS spectra were measured on an Ultraflex III TOF/TOF (Bruker Daltonics GmbH) equipped with a Nd:YAG laser and a collision cell. The spectra were recorded in the positive reflector or linear mode using dithranol or DHB as matrix.

ESI-Q-TOF MS measurements were executed on a micrOTOF (Bruker Daltonics GmbH) mass spectrometer, which was equipped with an automatic syringe pump for sample injection. The pump was supplied from KD Scientific. It was operated in the positive ion mode. The standard electrospray ion (ESI) source was used to generate ions. Mixtures of dichloromethane and acetonitrile were used as solvent. The ESI-Q-TOF-MS instrument was calibrated in the m/z range 50 to 3,000 using an internal calibration standard (Tunemix solution) which was supplied from Agilent.

Elemental analyses were performed on a λ EuroVector EuroEA3000 elemental analyzer. Differential scanning calorimetry was performed on a DSC 204 F1 Phoenix by Netsch in a nitrogen atmosphere. IR measurements were carried out on a fourier transform infrared spectrometer IRAffinity-1 (Shimadzu).

Electrochemical measurements were carried out on a Metrohm Autolab PGSTAT30 potentiostat with a standard three-electrode configuration using a glassy-carbon-disk working electrode, a platinum-rod auxiliary electrode and an Ag/AgCl reference electrode. Scan rates were varied from 50 to 5,000 mV/s. The experiments were carried out in dimethylformamide containing tetra-n-butylammonium hexafluorophosphate (0.1 M). Ferrocene was added as internal standard at the end of each experiment. UV-Vis absorption measurements were accomplished on a Perkin Elmer Lambda 750 spectrometer. Emission spectra were recorded on a Jasco FP-6500 spectrofluorometer. The reaction progress was monitored by thin-layer chromatography using precoated aluminum sheets (silica gel 60 F254, Merck). Flash column chromatography was carried out on a Biotage Isolera One System using Biotage SNAP Cartridges KP-Sil. Preparative size exclusion chromatography was either performed by using Bio-Beads (SX1, dichloromethane).

Analytical size exclusion chromatography was performed on two different systems:
1. Shimadzu system (controller: SCL-10A VP, degasser: DGU-14A, pump: LC-10AD VP, auto sampler: SIL-10AD VP, oven: Techlab, UV detector: SPD-10AD VP, RI detector: RID-10, eluent: chloroform/iso-propanol/triethylamine [94:2:4], flow rate: 1 mL/min, temperature: 40 °C, column: PSS SDV pre/lin S column)

2. Waters system (degasser: DG-980-50, pump: HPLC 1515, oven: Column Heater 1500, UV-Vis-detector: PDA detector 2996, RI-detector: RID 2414, eluent: DMAc + 0.08% NH_4PF_6, flow rate: 1 mL/min, temperature: 50 °C, column: Waters pre/Phenomenex Phenogel 103 Å/105 Å, separation range: 1,000 to 1,000,000 g/mol)

Photophysical instrumentation

Emission lifetimes are obtained by time-correlated single-photon counting. Here, a Titan:Sapphire laser (Tsunami, Newport Spectra-Physics GmbH) is used as the light source. The repetition rate is reduced to 400 kHz by a pulse selector (Model 3980, Newport Spectra-Physics GmbH). Afterwards the fundamental beam of the Ti-Sapphire oscillator is frequency doubled in a second harmonic generator (Newport Spectra-Physics GmbH) to create the 500-nm pump beam. The emission is detected by a Becker & Hickl PMC-100-4 photon-counting module. The instrument response function is recorded from scattered light from a cuvette containing pure water or a Ludox solution. Data fitting was accomplished in Scilab[4] using a home-written algorithm. Samples are prepared to yield an optical density of 0.1 at 500 nm in 1 cm cuvettes.

Steady-state absorption spectra are recorded on a Jasco V-670 spectrophotometer. The fluorescence spectra are measured using a Jasco FP-6200 spectrofluorimeter.

The time-resolved transient absorption measurements were performed on two different setups. Each setup is based on an amplified Ti:sapphire oscillator (800 nm, 1 kHz). One of them produces pulses of 35 fs at 3.5 mJ (Legend-Elite, Coherent Inc.) and the other one 100 fs at 950 µJ (Libra, Coherent Inc.). Appropriate beamsplitters split the pulses to attenuate the intensity to pump, in case of the former setup, a collinear optical-parametric amplifier (TOPAS-C, LightConversion Ltd.; output of 480 nm) with 1.35 W or, for latter setup, a non-collinear optical-parametric amplifier (TOPASwhite, Lightconverison Ltd.; output of 520 nm) with 0.5 W. For both setups white light is used as the probe, which is generated by focusing a minor fraction of the amplifier output into a sapphire plate. The white light is split by means of a beam splitter to obtain the probe and reference beams. The pump pulses are delayed in time with respect to the probe pulses by means of an optical delay line, and their polarization was rotated by 54.7° (magic angle) with respect to the probe beam by using a Berek compensator. The probe beam is focused and recollimated using 50 cm (20 cm) spherical mirrors, while the focus of the pump beam is behind the sample in order to obtain a homogenously excited sample volume. The pump pulse is blocked after the sample, while the probe pulse is sent to a double-stripe diode-array detection system (Pascher Instruments AB) together with the reference pulse. The diode array is read out with the repetition rate of the laser and the ΔA signal is calculated for individual pairs of laser pulses corresponding to pump-on and pump-off conditions. The energy of the pump pulse is attenuated to 0.5 µJ (0.4 µJ), while typical probe intensities fall into the range of a few hundred nanojoules. Steady-state absorption spectra are frequently recorded to ensure sample integrity. Prior to data analysis, the experimental differential absorption data is chirp corrected and afterward fitted with a global fitting routine.
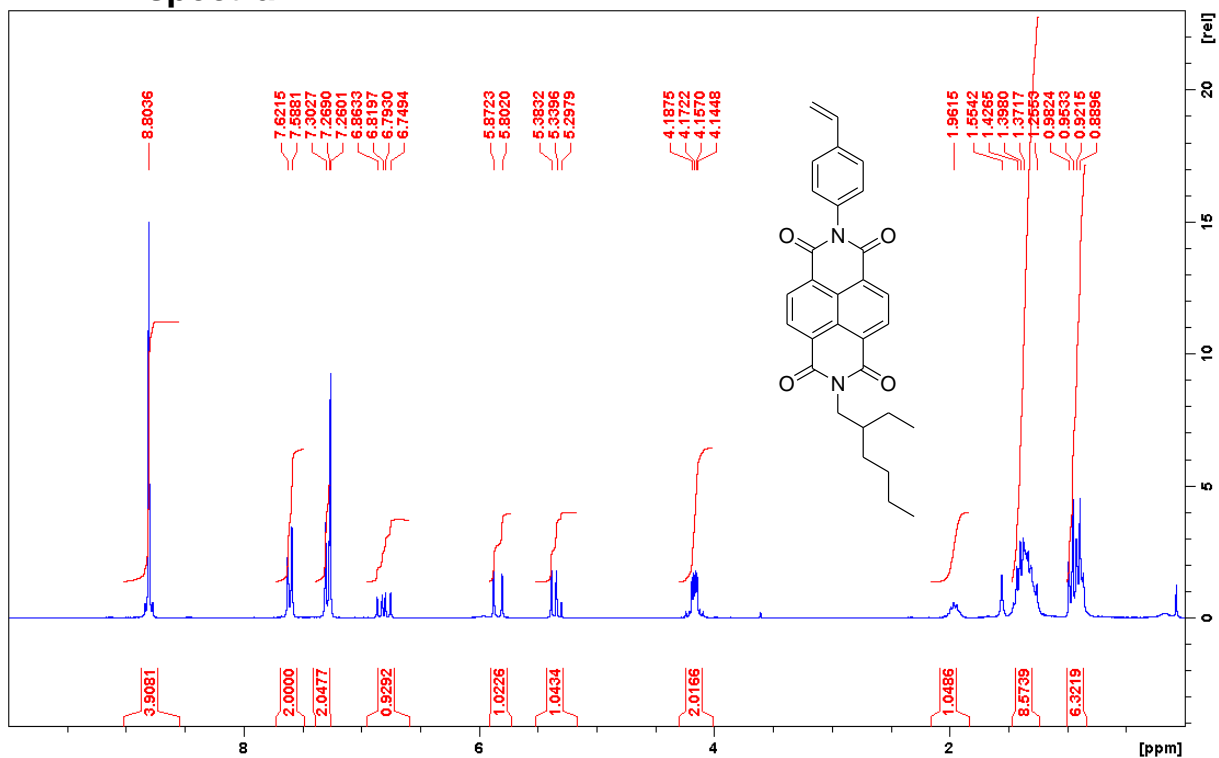
2. NMR spectra

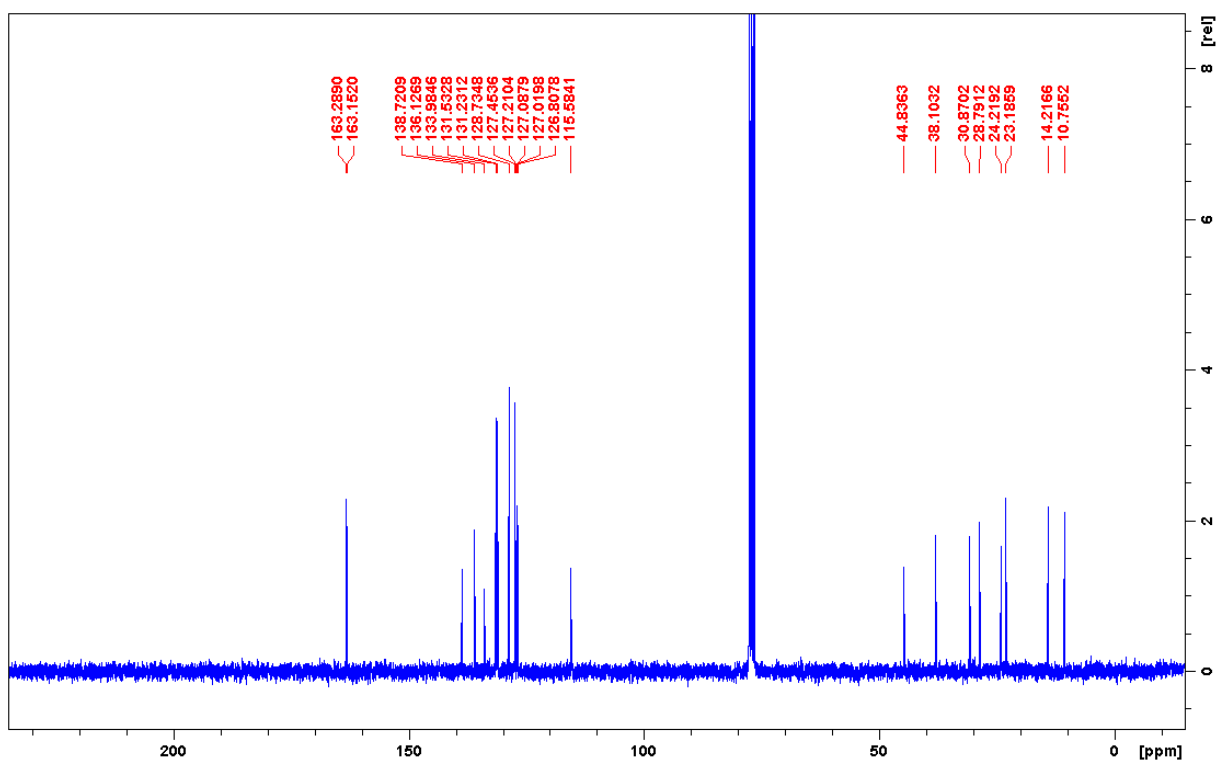Figure 1. ^{1}H NMR (CDCl$_3$, 300 MHz) of NDI-vinyl.

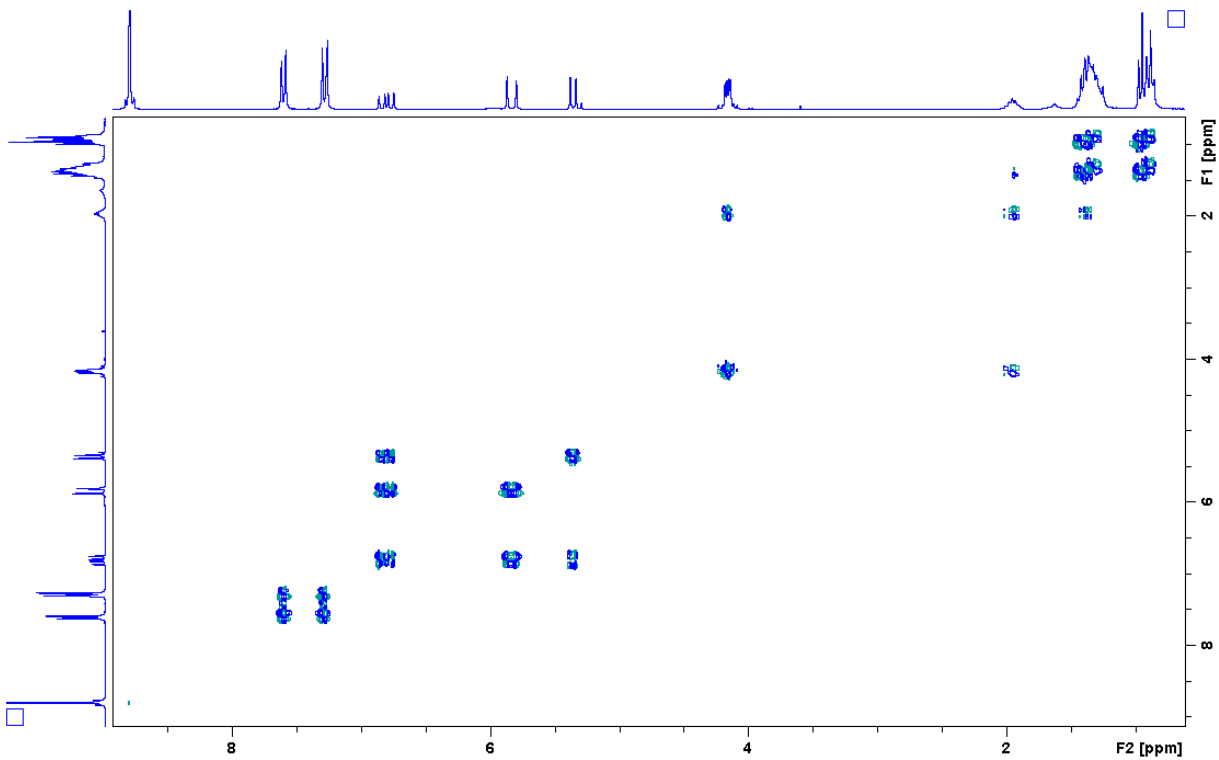Figure 2. ^{13}C NMR (CDCl$_3$, 75 MHz) of NDI-vinyl.
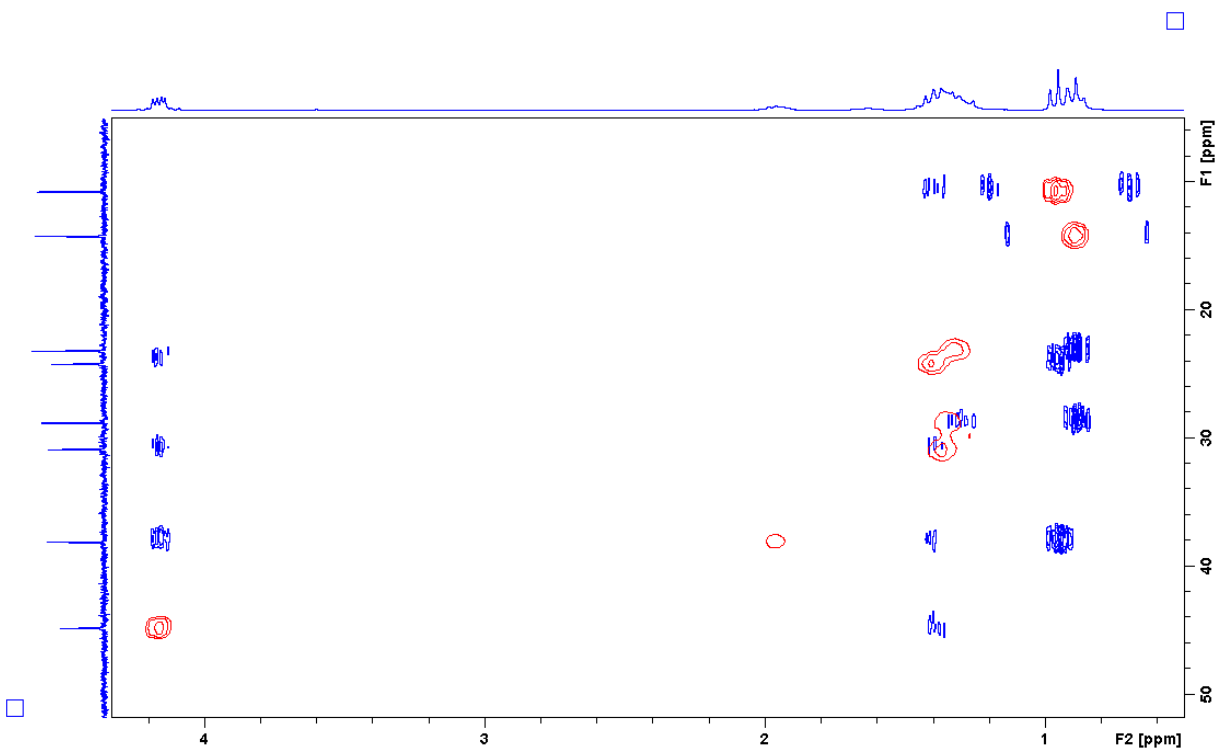
Figure 3. COSY (CDCl$_3$) of NDI-vinyl.

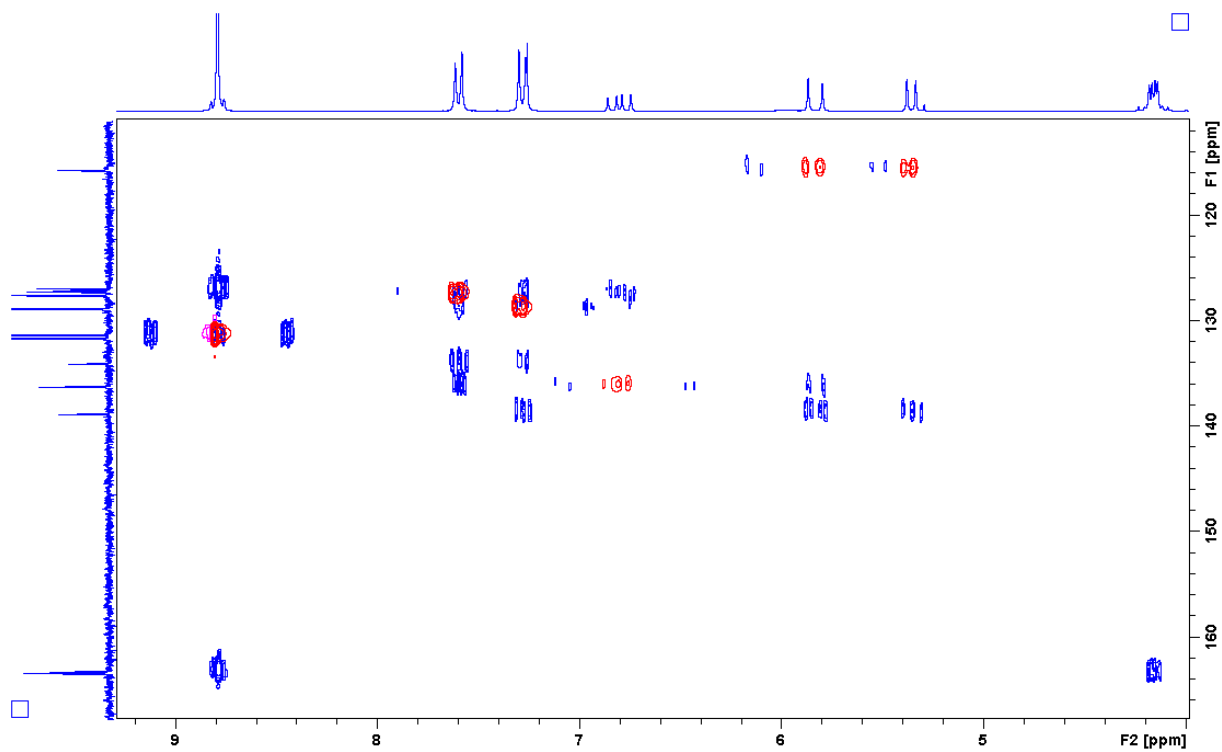Figure 4. Aliphatic region of HSQC (red) and HMBC (blue) (CDCl$_3$) of NDI-vinyl.

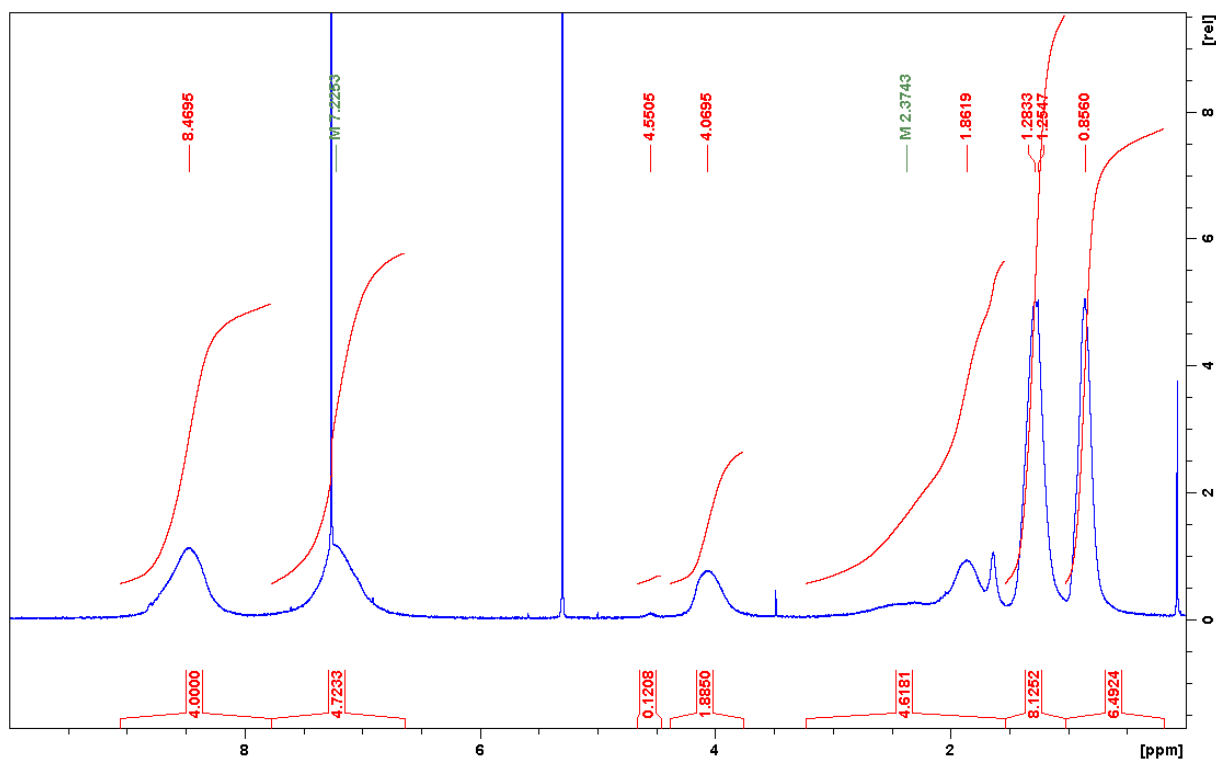Figure 5. Aromatic region of HSQC (red) and HMBC (blue) (CDCl$_3$) of NDI-vinyl.

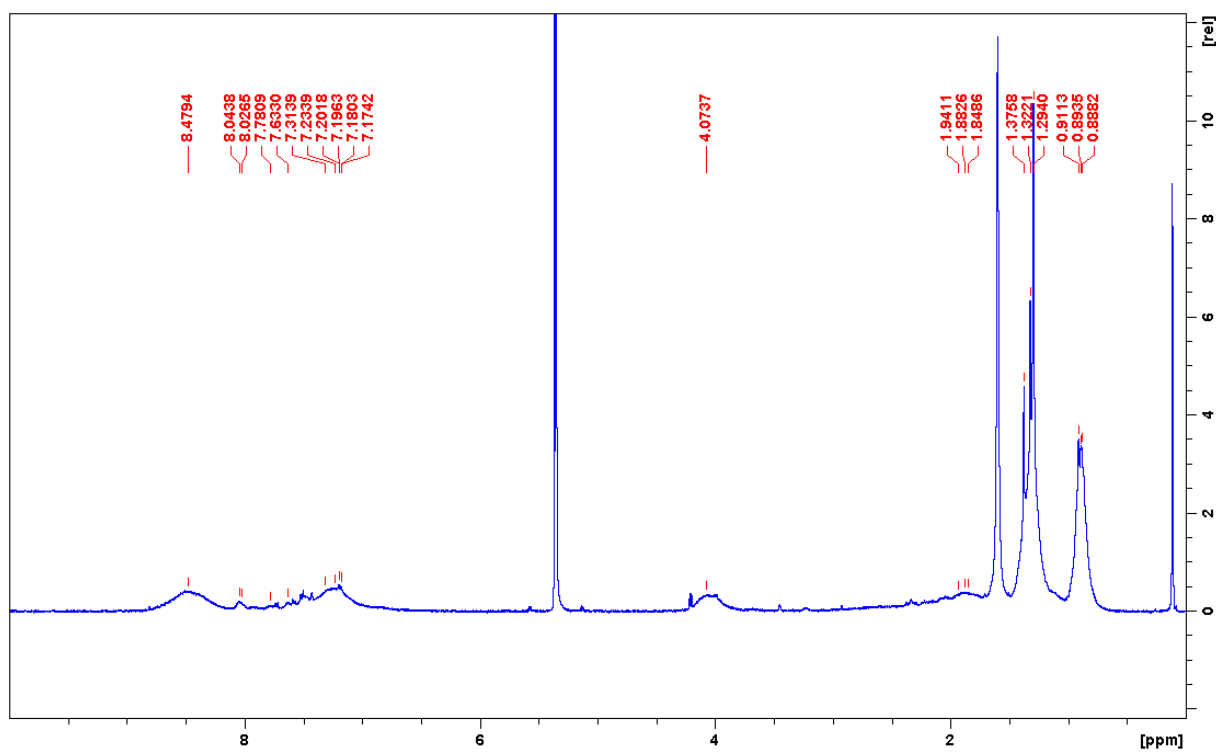
Figure 6. ^{1}H NMR (CDCl$_3$, 300 MHz) of pNDI.
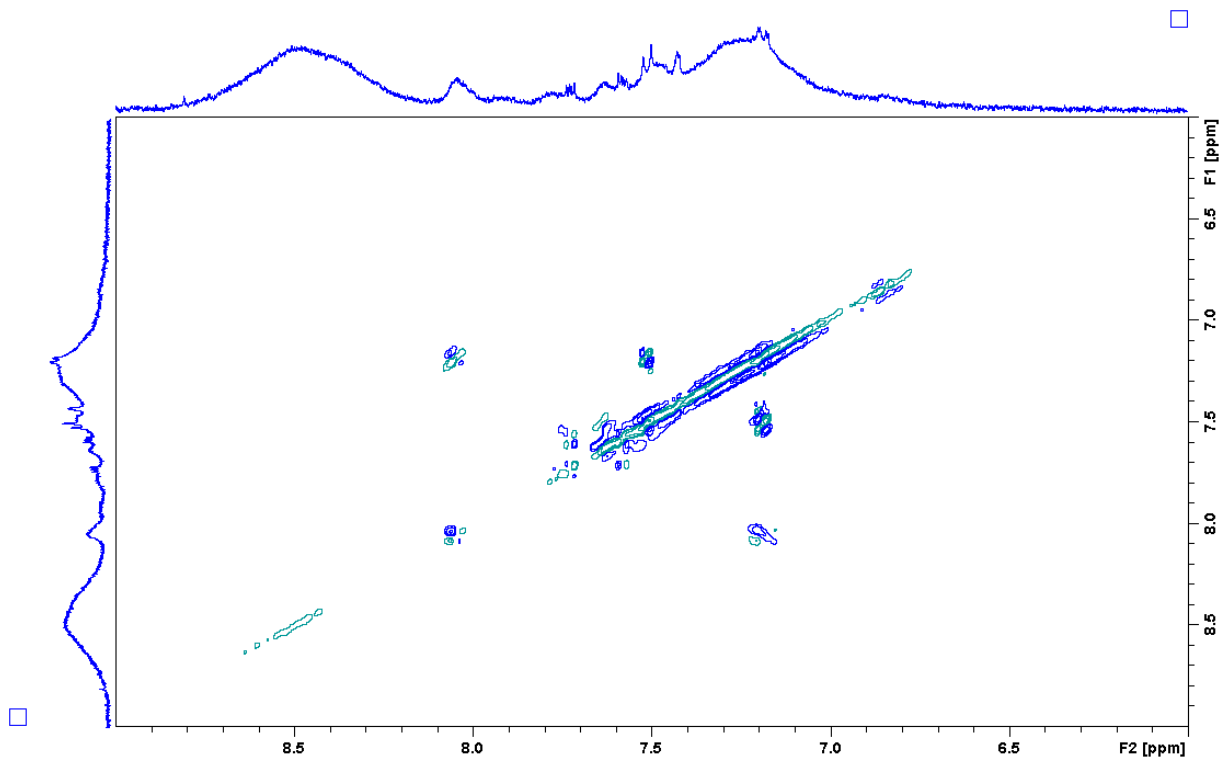
Figure 7. ^{1}H NMR (CD$_2$Cl$_2$, 400 MHz) of Ru-pNDI.

Figure 8. Aromatic region of COSY (CD$_2$Cl$_2$) of Ru-pNDI.
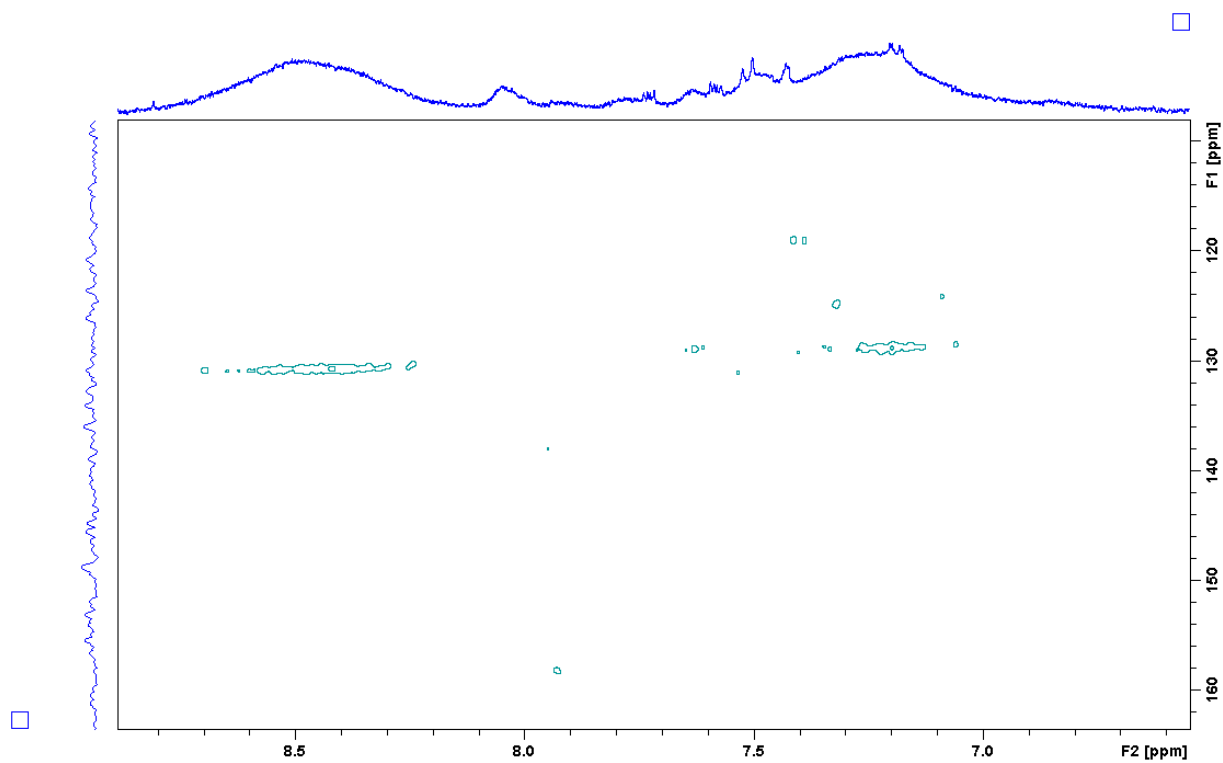
Figure 9. Aromatic region of HSQC (CD$_2$Cl$_2$) of Ru-pNDI.

3. MALDI-ToF spectrum
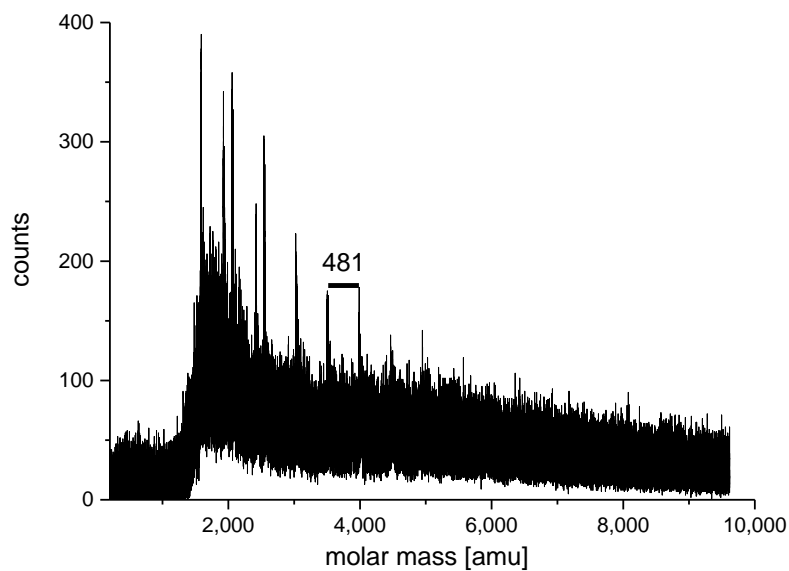
Figure 10. MALDI spectrum of pNDI (repeating unit 481 amu).

4. Size-exclusion chromatogramm
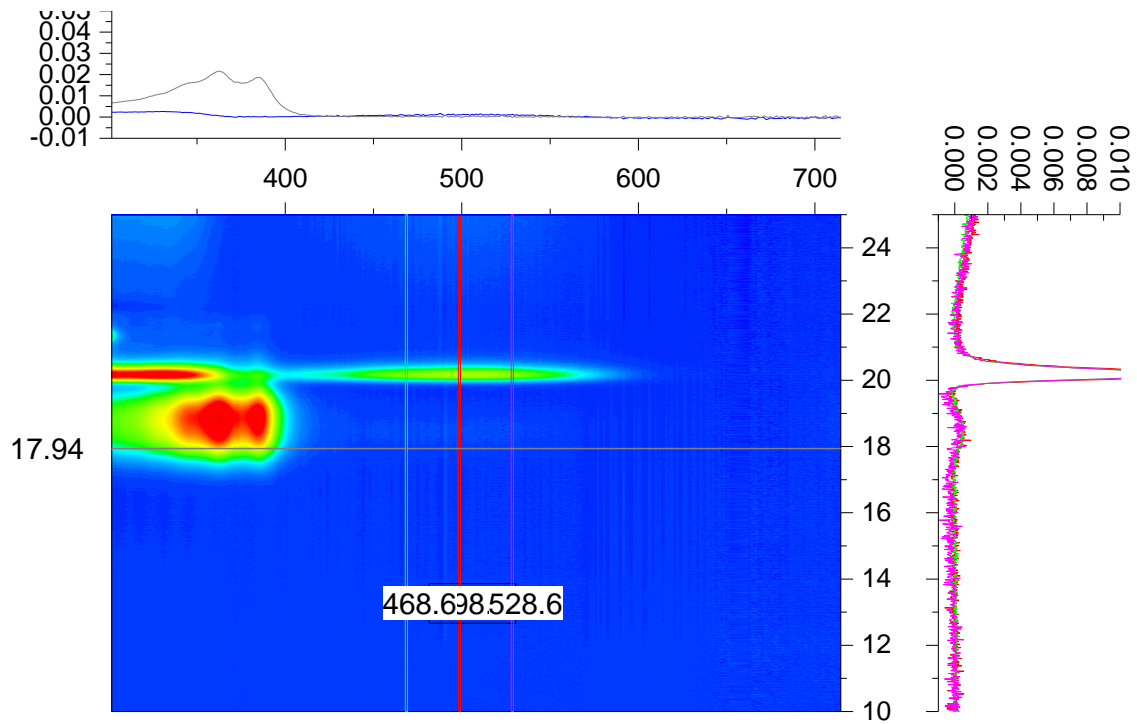
Figure 11. 3D UV-SEC plot of Ru-pNDI showing the attachement of Ru to pNDI at 18 and 19 min (right vertical projection, 468 to 528 nm detection).

5. Absorption spectra
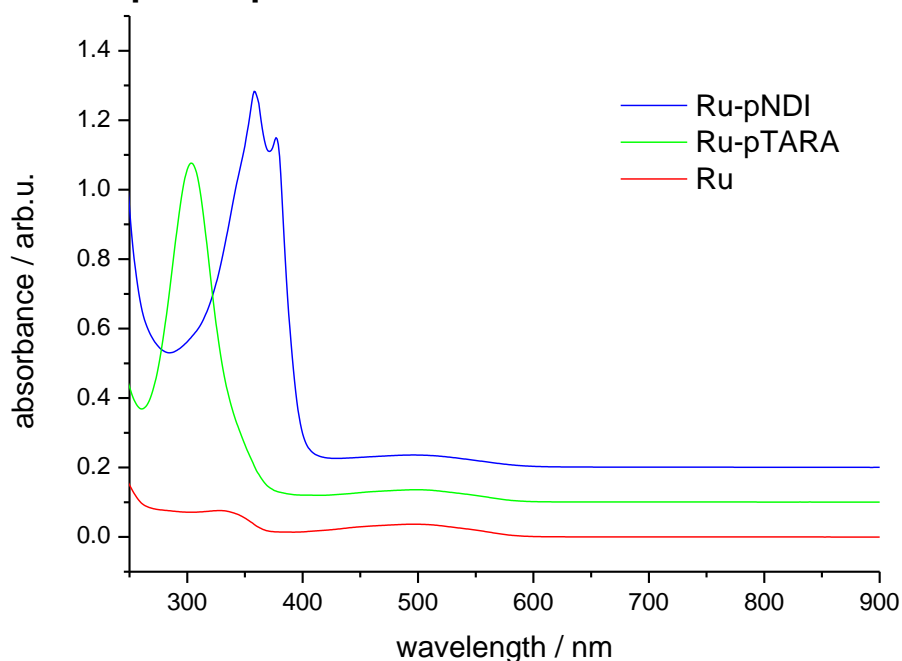
Figure 12. Absorption spectra (CH$_2$Cl$_2$) of studied compounds: Ru-pNDI (blue, top), Ru-pTARA (green, middle, off-set) and Ru (red, bottom). The spectra of Ru-pNDI (+0.2) and Ru-pTARA (+0.1) are shifted for clearity.
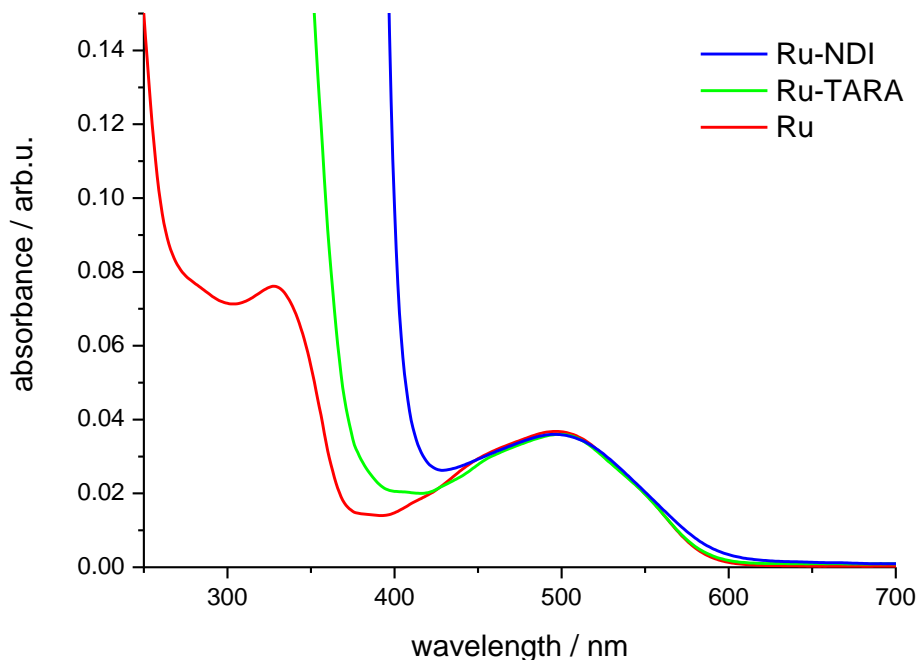

Figure 13. Expansion of absorption spectra (CH$_2$Cl$_2$) of studied compounds: Ru-pNDI (blue, top), Ru-pTARA (green, middle, off-set) and Ru (red, bottom). The spectra of Ru-pNDI (+0.2) and Ru-pTARA (+0.1) are shifted for clearity.
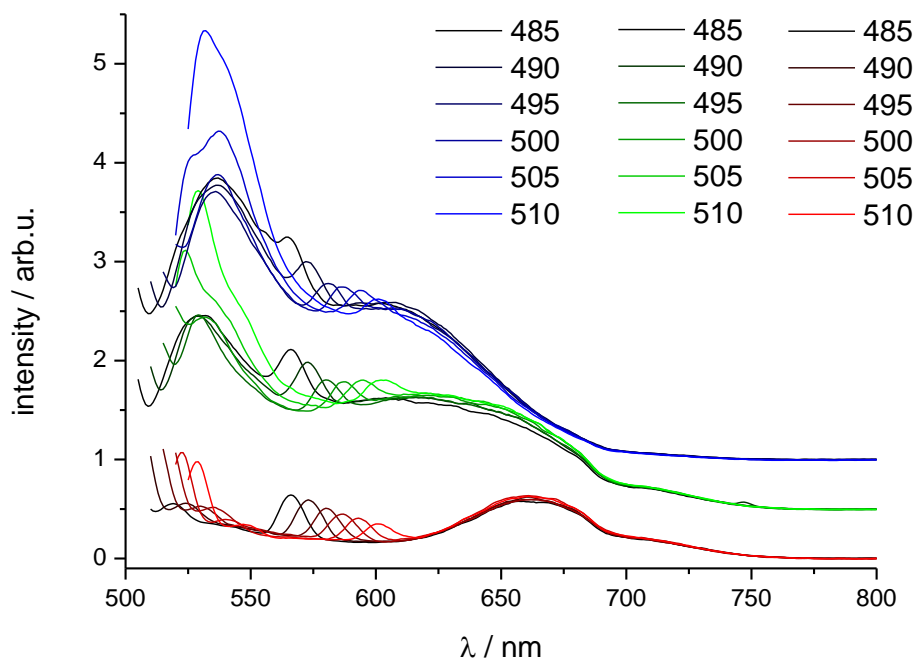
6. Emission spectra

Figure 14. Emission spectra of Ru-pNDI (blue, top), Ru-pTARA (green, middle, off-set) and Ru (red, bottom) of iso-absorbing solutions in CH_2Cl_2 (0.036 at 500 nm) with various excitation wavelengths (see legend). The spectra are vertically shifted for clearity: Ru-pNDI (+1.0) and Ru-pTARA (+0.5).
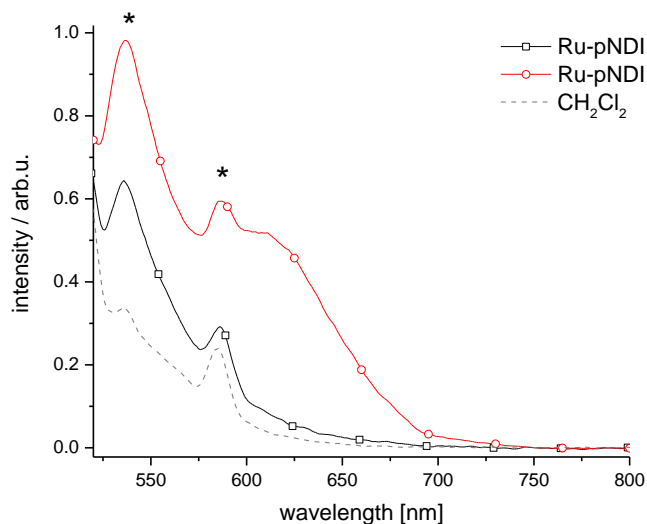

Figure 15. Emission of Ru-pNDI samples with increased concentration and detector settings: dilute sample (optical density at 500 nm 0.017, black curve) and concentrated sample (optical density at 500 nm 0.035, red) with opened slits. The Raman signals of pure dichloromethane are shown for comparison (grey dotted line). Raman peaks of solvent marked by *.
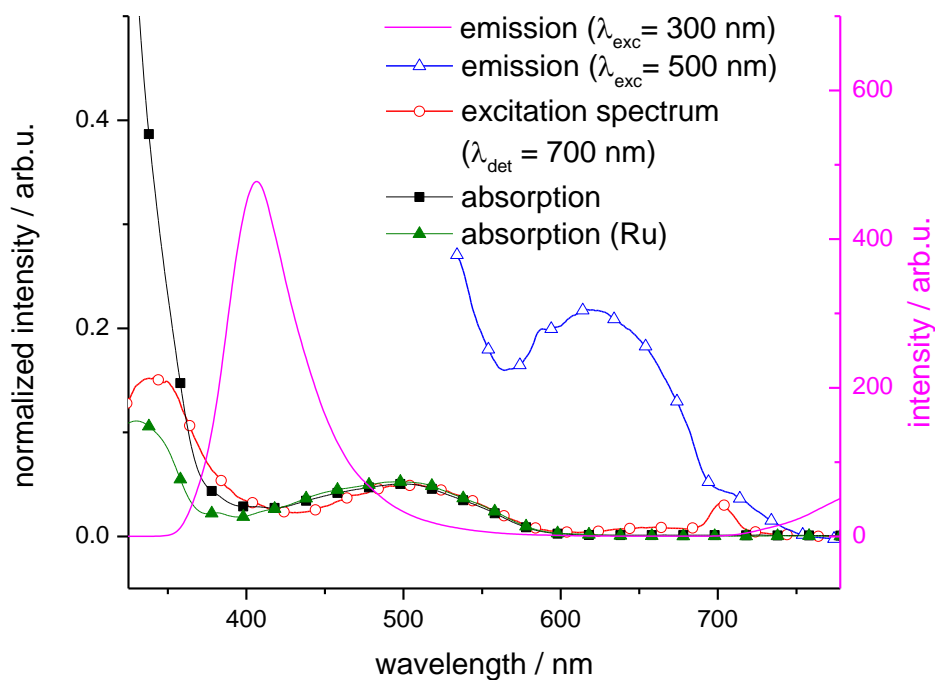
7. Excitation spectra

Figure 16. Spectra of Ru-pTARA (CH_2Cl_2): Absorption spectrum (black, filled squares) showing the ^{1}MLCT band (400-600 nm) and strong ^{1}pTARA band (<380 nm), excitation spectrum (red lines, open circles) recorded at 700 nm detection (^{3}MLCT band), emission spectra (blue lines) upon excitation of ^{1}MLCT band (at 500 nm, open triangles) or pTARA band (at 300 nm, open circles).
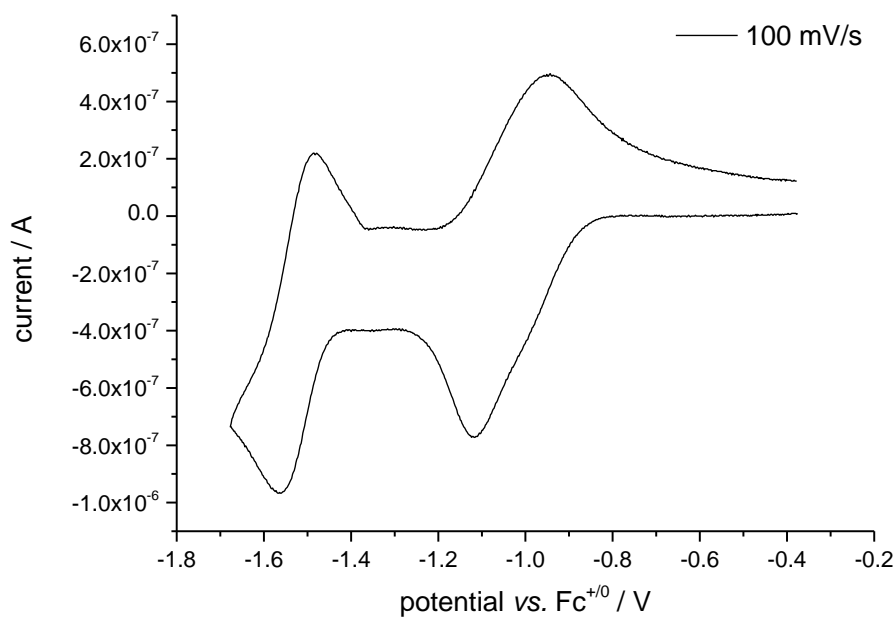
8. Electrochemical data

Figure 17. Cyclovoltammogramm of pNDI in CH_2Cl_2 vs. Ferrocene (0.1M TBAPF$_6$).
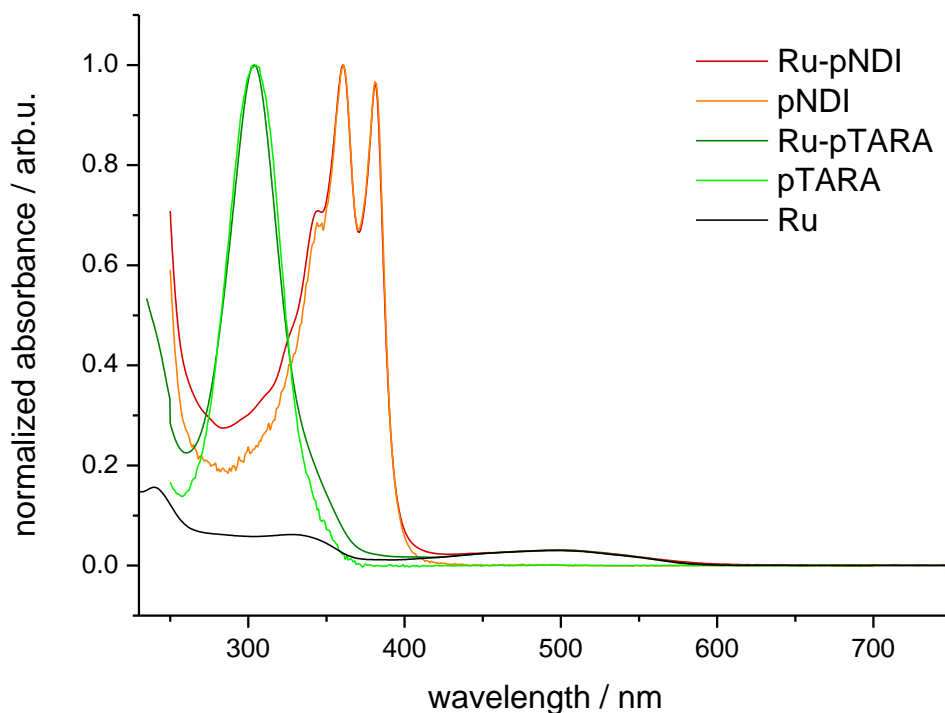
9. Time-resolved data

Figure 18. Normalized absorption spectra (CH$_2$Cl$_2$) of Ru-pNDI (dark red) vs pNDI (orange), and Ru-pTARA (dark green) *vs.* TARA (light green), including reference complex Ru (black) for comparison.
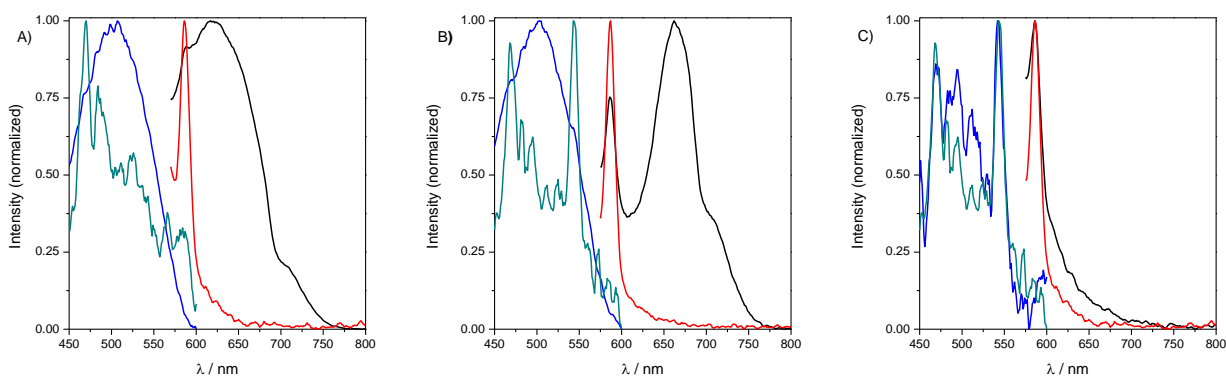

Figure 19. Normalized steady-state fluorescence (CH$_2$Cl$_2$) for λ_{exc} = 500 nm (black) and fluorescence excitation spectra for λ_{em} = 700 nm (blue) obtained for isoabsorbing solutions of Ru-TARA (left panel), the binary mixture RuOH+NDI (middle panel) and Ru-NDI (right panel). The red (emission) and cyan (excitation) curve show the respective data obtained for the pure solvent (dichloromethane) due to Raman-scattering and instrumental artifacts.
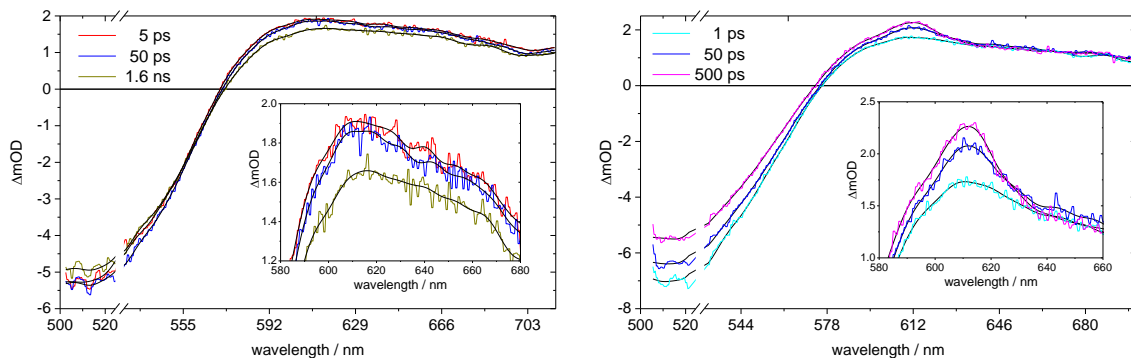
Figure 20. Raw transient absorption spectra (CH$_2$Cl$_2$) at selected delay times for Ru-pTARA (left) and Ru-pNDI (right): 1 ps (cyan), 5 ps (red), 50 ps (blue), 500 ps (pink), 1.6 ns (beige) with respective smoothed curves (black), obtained by applying a 10 point FFT filter.
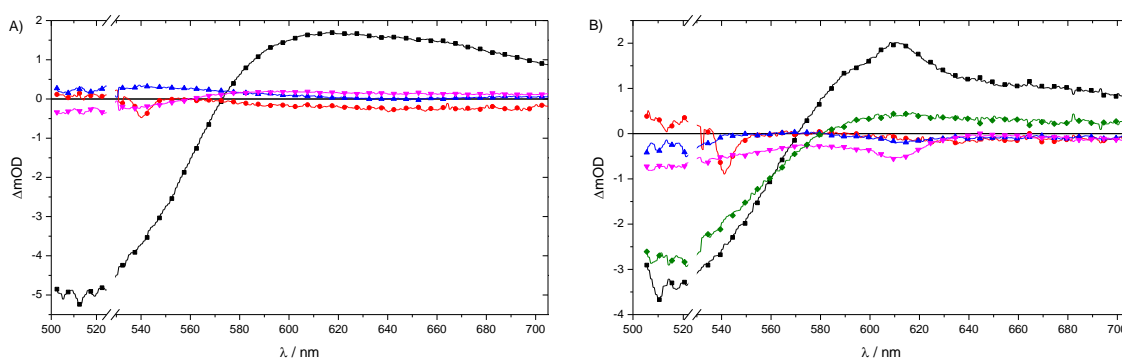
Figure 21. Decay-associated spectra (CH$_2$Cl$_2$) of Ru-pTARA (panel A) Ru-pNDI (panel B) from a global multiexponential fit applied on the transient absorption data. The corresponding lifetimes (inverse time constants) are: Panel A: 0.2 ps (red curve), 12 ps (blue curve), 460 ps (pink curve); Panel B: 0.1 ps (red curve), 2 ps (blue curve), 99 ps (pink curve), 1870 ps (green curve). The black curve corresponds to a constant offset, i.e. to a process with a lifetime significantly exceeding 2 ns. The spectral interval from 522 to 530 nm was removed from the data set because of a measurement artifact.

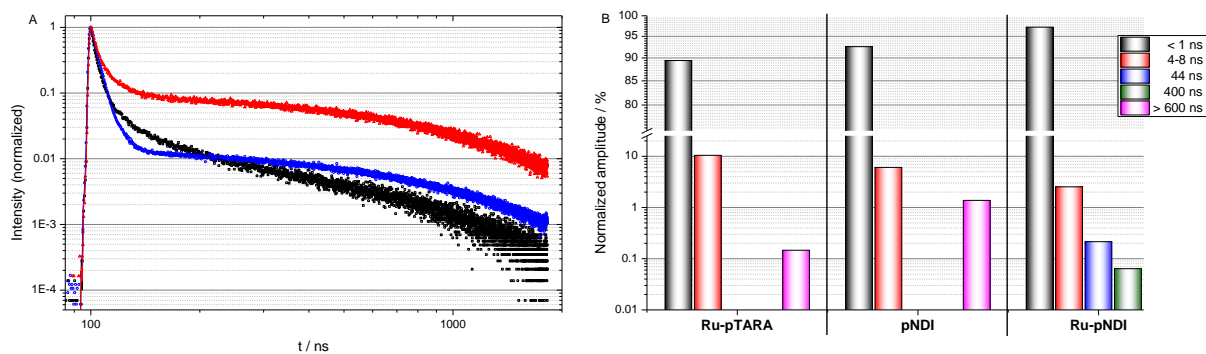Figure 22. Time-correlated single photon counting data (CH_2Cl_2) recorded after excitation at 500 nm with a 525 nm long-pass filter: Panel A contains measured decay curves (symbols, normalized by division of the whole curve by the respective count maximum) and respective fit curves (lines) of pNDI (red), the binary mixture Ru-pTARA (blue) and the covalent dyad Ru-pNDI (black). Note, that not all curves were measured to yield an equal number of counts in the maximum such that no information regarding the quantum yields can be extracted from the area under the curves. Panel B shows the respective fit parameters obtained from applying a fit routine for consecutive first-order-reactions including convolution with the instrument response function. The fit gave evolution associated amplitudes. These were subtracted from each other to yield decay associated amplitudes, which were renormalized and are presented here. The scale is cut from 25 to 75 %.

References

(1) Kondratenko, M.; Moiseev, A. G.; Perepichka, D. F. New Stable Donor-Acceptor Dyads for Molecular Electronics *J. Mater. Chem.* **2011**, *21*, 1470-1478.

(2) Schroot, R.; Friebe, C.; Altuntas, E.; Crotty, S.; Jäger, M.; Schubert, U. S. Nitroxide-Mediated Polymerization of Styrenic Triarylamines and Chain-End Functionalization with a Ruthenium Complex: Toward Tailored Photoredox-Active Architectures *Macromolecules* **2013**, *46*, 2039-2048.

(3) Gottlieb, H. E.; Kotlyar, V.; Nudelman, A. NMR Chemical Shifts of Common Laboratory Solvents as Trace Impurities *J. Org. Chem.* **1997**, *62*, 7512-7515.

(4) Scilab Enterprises (2012). Scilab: Free and Open Source software for numerical computation (OS, Version 5.XX) [Software]. Available from: http://www.scilab.org

P2 - New Ruthenium Bis(terpyridine) Methanofullerene and Pyrrolidinofullerene Complexes: Synthesis and Electrochemical and Photophysical Properties

New Ruthenium Bis(terpyridine) Methanofullerene and Pyrrolidinofullerene Complexes: Synthesis and Electrochemical and Photophysical Properties

Kevin Barthelmes,[†,‡,⊥] Joachim Kübel,[§,‖,⊥] Andreas Winter,[†,‡] Maria Wächtler,[§,‖] Christian Friebe,[†,‡] Benjamin Dietzek,*[,‡,§,‖] and Ulrich S. Schubert*[,†,‡]

[†]Laboratory of Organic and Macromolecular Chemistry (IOMC), Friedrich Schiller University Jena, Humboldtstraße 10, 07743 Jena, Germany

[‡]Jena Center for Soft Matter (JCSM), Friedrich Schiller University Jena, Philosophenweg 7, 07743 Jena, Germany

[§]Institute of Physical Chemistry (IPC) and Abbe Center of Photonics, Friedrich Schiller University Jena, Helmholtzweg 4, 07743 Jena, Germany

[‖]Leibniz Institute of Photonic Technology e.V. (IPHT), Albert-Einstein-Straße 9, 07745 Jena, Germany

Ⓢ *Supporting Information*

ABSTRACT: A series of terpyridine (tpy) methanofullerene and pyrrolidinofullerene dyads linked via *p*-phenylene or *p*-phenyleneethynylenephenylene (PEP) units is presented. The coordination to ruthenium(II) yields donor−bridge−acceptor assemblies with different lengths. Cyclic voltammetry and UV−vis and luminescence spectroscopy are applied to study the electronic interactions between the active moieties. It is shown that, upon light excitation of the ruthenium(II)-based [1]MLCT transition, the formed [3]MLCT state is readily quenched in the presence of C_{60}. The photoinduced dynamics have been studied by transient absorption spectroscopy, which reveals fast depopulation of the [3]MLCT (73−406 ps). As a consequence, energy transfer occurs, populating a long-lived triplet state, which could be assigned to the $^3C_{60}^*$ state.
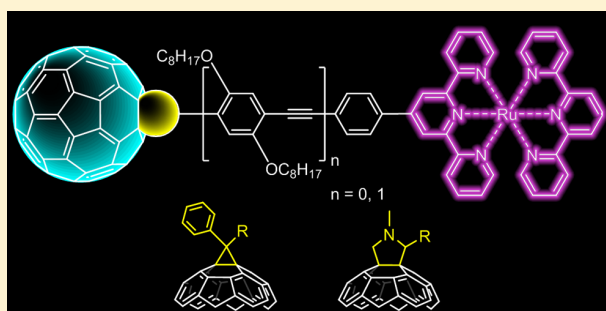
■ INTRODUCTION

The development of artificial devices that mimic light-triggered reactions in natural photosynthetic systems, which are based on the fundamental processes of energy and/or electron transfer, has become an attractive field in modern science and technology.[1−10] A general challenge in the molecular design of donor−bridge−acceptor systems is the generation of long-lived charge-separated (CS) states.[8,11,12] Fullerenes, in particular C_{60}, have high electron affinities, which make them favorable systems regarding their electron-accepting ability. Photoinduced electron transfer and energy transfer in (macro)-molecular assemblies containing donors, such as ferrocene,[13,14] porphyrin,[15] tetrathiafulvalene,[16,17] and others,[18,19] which are covalently linked to fullerene, were extensively studied; their electrochemical and photophysical properties are of particular interest.[20,21] Ruthenium(II) polypyridyl complexes as donors are promising materials due to their intense light absorption in the visible range and extended excited-state lifetimes.[22−24] Previous studies on Ru(II)−polypyridine−C_{60} assemblies showed that both electron and energy transfer is possible in such systems: the intermediate CS state may undergo charge recombination to the final lower lying triplet excited $^3C_{60}^*$ state.[25−30] Furthermore, the linker plays a crucial role in the

electronic communication between the donor and acceptor parts. Several wirelike bridging units have been studied in recent years, including π-conjugated oligomers consisting of phenyleneethynylenes,[16,26] phenylenevinylenes,[31] and fluorene units[13,17] and nonconjugated oligomers consisting of glycol,[32,33] cyclohexane,[28] and peptide units.[34]

In this work, we report the investigation of new donor−acceptor systems, in which Ru(II) bis(terpyridine) complexes are connected to C_{60}. The series contains short phenyl-bridged as well as longer octyloxy-substituted phenyleneethynylenephenylene-bridged systems (Figure 1). These were chosen for their rigidity and π conjugation with low attenuation factors β,[35] which provide pathways for an efficient charge transport. Photophysical studies of these bridging units, especially in ruthenium(II) bis(terpyridine) complexes, have been thoroughly described by us previously.[36−39] This latter concept was further extended for the functionalization on C_{60} by cyclo-addition reactions of 1,3-dipolar reagents with one [6,6]-double bond to form pyrrolidine or cyclopropane monoadducts. Martín and co-workers could show that cyclopropane adducts
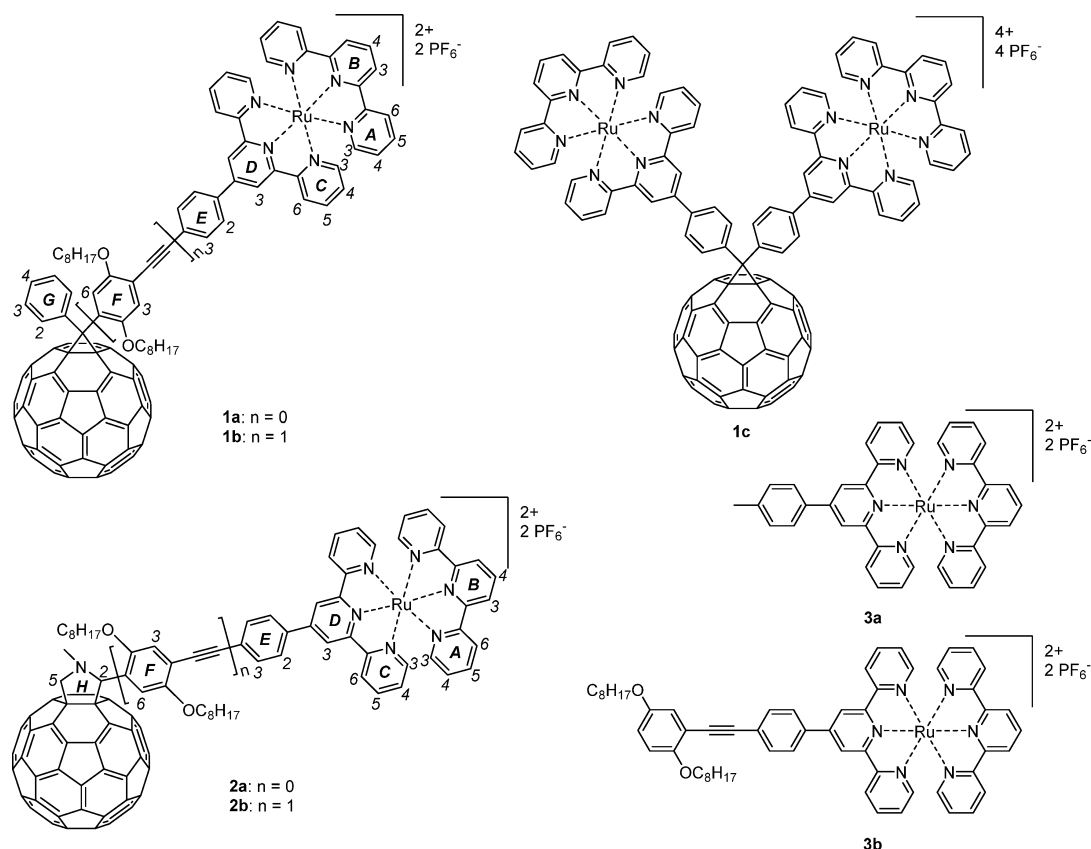
Figure 1. Schematic representations of the Ru(II)−bis(terpyridine)−C$_{60}$ assemblies **1** and **2** as well as reference compounds **3** studied in this work, along with a numbering scheme for the complexes and precursors.

Scheme 1. Schematic Representation of the Synthetic Route^{a}
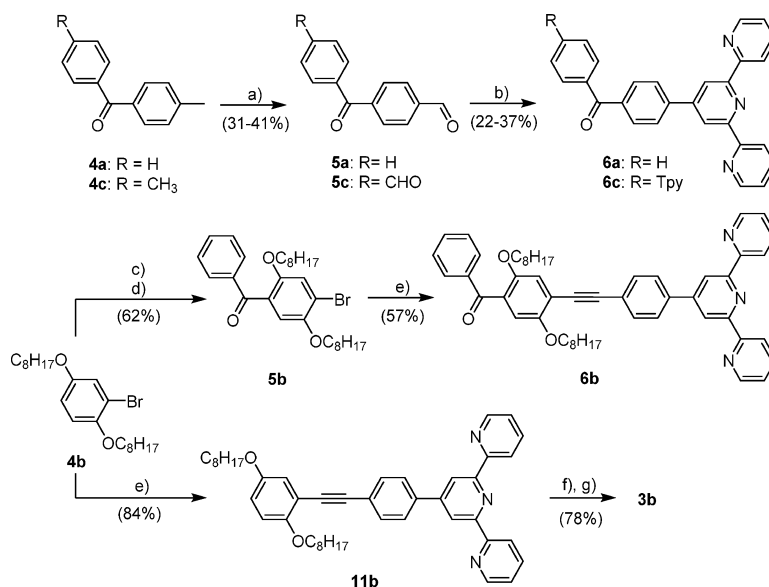
^{a}Legend: (a) CrO$_3$, H$_2$SO$_4$, acetic anhydride, room temperature, 16 h; (b) (i) 2-acetylpyridine, NaOH, grinding, room temperature, 30 min, (ii) ammonia (aqueous), EtOH, room temperature, 48 h; (c) benzoyl chloride, AlCl$_3$, dichloromethane, room temperature, 16 h; (d) 1-bromooctane, KOH, DMSO, room temperature, 22 h; (e) 4′-(4-ethynylphenyl)-2,2′:6′,2″-terpyridine, [Pd(PPh$_3$)$_4$], CuI, NEt$_3$, THF, 60 °C, 48−72 h; (f) [Ru(tpy)Cl$_3$], AgBF$_4$, acetone, 70 °C, 2 h; (g) (i) DMF, 160 °C, 3 h, (ii) excess NH$_4$PF$_6$.

generally enhance the electronic communication between fluorene and C$_{60}$ in comparison to pyrrolidine rings.^{40} In

addition to the mononuclear complexes **1a,b** and **2a,b**, we report the symmetrical dinuclear complex **1c**, bearing two

Scheme 2. Schematic Representation of the Synthetic Route toward the Studied Ru(II) Complexes 1a−c and 2a,b[a]
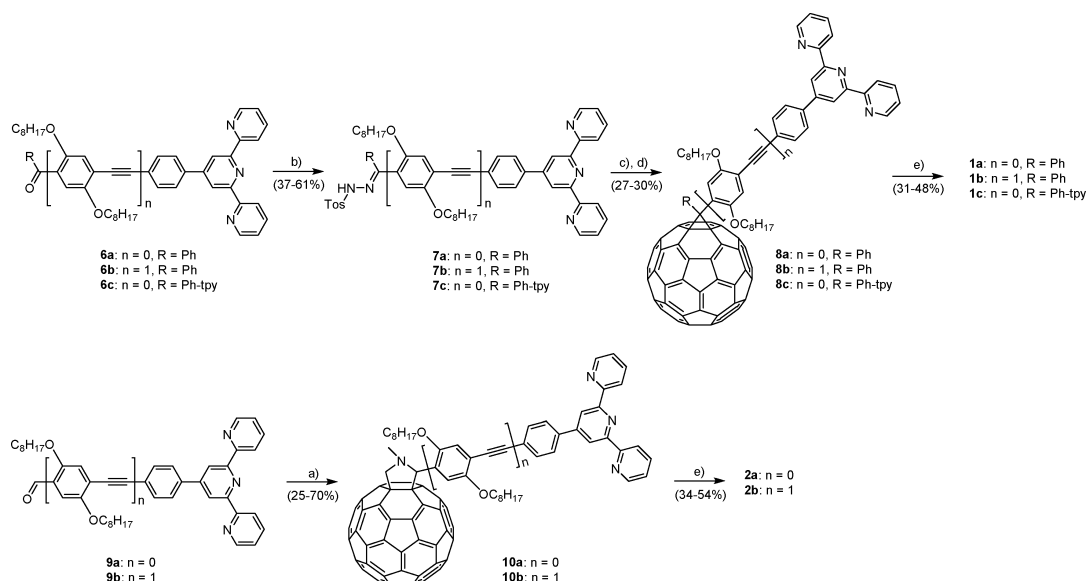
[a]Legend: (a) C_{60}, N-methylglycine, toluene, 120 °C, 24 h; (b) tosylhydrazine, tosylic acid, THF, 80 °C, 2−5 days; (c) NaOCH$_3$, pyridine, room temperature, 20 min; (d) C_{60}, o-dichlorobenzene, 180 °C, 24 h; (e) [Ru(tpy)(MeCN)$_3$](PF$_6$)$_2$, DMF, 140 °C, microwave, 30 min.

Table 1. Electrochemical Data Obtained by Cyclic Voltammetry[a]

	$E_{1/2,ox}$(Ru and/or irr P)/V	$E_{1/2,red}$(C_{60},1)/V	$E_{1/2,red}$(C_{60},2)/V	$E_{1/2,red}$(tpy,1)/V	$E_{1/2,red}$(C_{60},3 and/or tpy,2)/V
C_{60}[b]		−1.00	−1.39		−1.86
8a		−1.11	−1.49		−1.98
8b		−1.14	−1.52		−2.02
8c		−1.11	−1.48		−1.98
10a	+0.99[c]	−1.15	−1.51		−2.03
10b	+0.92[c]	−1.13	−1.53		e
1a	+0.91	−1.09	−1.45	−1.68	e
1b	+0.89	−1.12	−1.49	−1.65	e
1c	+0.92	−1.08	−1.46	−1.66	e
2a	+0.90[d]	−1.11	−1.50	−1.65	e
2b	+0.90[d]	−1.14	−1.50	−1.63	e
3a	+0.91			−1.63	−1.95
3b	+0.89			−1.59	−1.95

[a]Conditions: potentials referenced to Fc$^+$/Fc; scan rate 200 mV s^{-1}; glassy-carbon-disk working electrode; AgCl/Ag reference electrode; Pt-rod counter electrode; 0.1 M Bu$_4$NPF$_6$ in dichloromethane. [b]Taken from ref 68. [c]Irreversible process. The peak potential is shown. [d]Two processes. [e]Not detectable.

bis(terpyridine) ruthenium(II) centers and one C_{60} unit. The major aim of these studies is to figure out the influence of the length of the linker as well as the way the linker is connected to the C_{60} on the electrochemical and photophysical properties of the new compounds.

■ RESULTS AND DISCUSSION

Synthesis. The synthetic routes are depicted in Schemes 1 and 2. The benzophenone building blocks with rigid phenyl units as spacers were synthesized in a two-step reaction. Starting from para-substituted methylbenzophenones **4a,c**, the oxidation with chromium(VI) oxide yielded the desired mono- and bis-formylated[41] compounds **5a,c**, respectively. The terpyridine fragments **6a** and **6c** were prepared according to a modified Kröhnke-type procedure reported previously.[42] By grinding the starting material **5a** or **5c**, 2-acetylpyridine, and NaOH, the diketone intermediate can be prepared under these

solvent-free conditions in 30 min. When the bridge length was increased, octyloxy chains were introduced to improve the solubility. For this purpose, the starting material **4b** was synthesized according to literature procedures.[43] Compound **5b** was prepared by Friedel−Crafts acylation with benzoyl chloride (during the reaction, one octyl group was cleaved off and reintroduced by alkylation). A Sonogashira cross-coupling reaction with 4′-(4-ethynylphenyl)-2,2′:6′,2″-terpyridine was applied to prepare **6b**.[44] The reference ligand **11b** was synthesized in good yield by an analogous route. The respective methanofullerenes **8a,b** as well as the symmetrical bis-(terpyridine)−C_{60} compound **8c** were obtained in a three-step reaction. First, the terpyridine-functionalized benzophe-nones **6a−c** were reacted with tosylhydrazine and catalytic amounts of tosylic acid to yield the desired tosyl hydrazone derivatives **7a−c**. Elimination of the tosyl group with sodium methoxide by a mechanism analogous to the Bamford−Stevens

reaction yielded in situ the 1,3-dipolar diazo compounds, which reacted with C_{60} to form pyrazolinofullerene derivates as intermediates.[45,46] Further thermal treatment eliminated molecular nitrogen, and the desired methanofullerenes were obtained in low to moderate yields. Recently, we reported the synthesis of the aldehyde-functionalized 2,2′:6′,2″-terpyridines **9a,b** used in this study.[47,48] Pyrrolidinofullerenes **10a,b** were synthesized by the 1,3-dipolar cycloaddition of azomethine ylides, derived from **9a,b**, respectively, and *N*-methylglycine to C_{60} in an optimized 1:10:4 ratio.[49] The compounds were obtained in low to good yields, respectively, mainly due to the enhanced solubility of **9b**. All fullerene ligands were purified by column chromatography using neutral alumina and *n*-hexane/toluene mixtures to remove and recover the unreacted C_{60}. [Ru(tpy)(MeCN)$_3$](PF$_6$)$_2$ was used as a precursor to obtain the corresponding heteroleptic ruthenium(II) complexes **1a−c** and **2a,b** in moderate yields. The reaction was performed under microwave irradiation for 30 min at 140 °C in DMF. Since column chromatography using silica with potassium nitrate was not applicable for these C_{60}-containing complexes, the dark red complexes were purified by treatment of a concentrated acetonitrile solution with diethyl ether vapor to force slow precipitation. So far, we have not been able to obtain single crystals suitable for X-ray structure analysis. The reference ligands 4′-(4-methylphenyl)-2,2′:6′,2″-terpyridine (ttpy) and **11b** were coordinated to ruthenium by standard complexation procedures in ethanol[50,51] or DMF.[52] All complexes exhibited a good solubility in polar solvents, such as acetonitrile, and have been characterized by NMR spectroscopy, mass spectrometry, and elemental analysis.

Electrochemical Properties. The redox behavior of the complexes **1a−c** and **2a,b**, the ligands **8a−c** and **10a,b**, and the references **3a,b** was studied by cyclic voltammetry. The data are summarized in Table 1, and representative spectra are depicted in Figure 2. The electrochemical measurements were
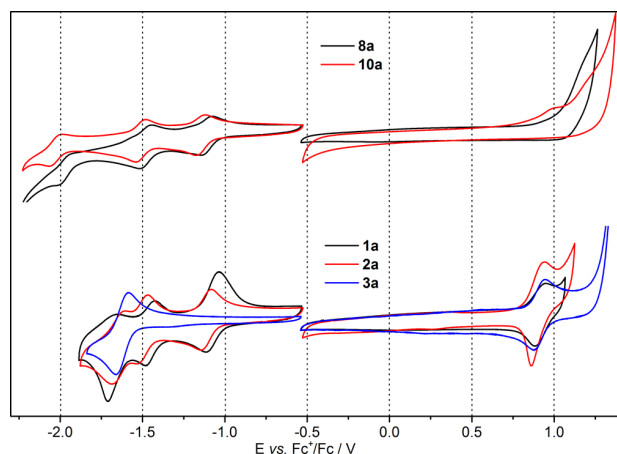

Figure 2. Cyclic voltammograms of phenyl-bridged methano- and pyrrolidinofullerene ligands and complexes in dichloromethane (with 0.1 M Bu$_4$NPF$_6$).

performed in dichloromethane at room temperature with Bu$_4$NPF$_6$ as the conducting salt. For complexes **1a−c** and **2a,b**, the first oxidation wave at ca. 0.9 V arises from the reversible Ru(III)/Ru(II) redox couple. In addition, for the ligands **10a,b**, a second, irreversible oxidation, which is overlaid by the ruthenium oxidation in **2a,b**, was observed. This process is

attributed to the electrochemical retrocycloaddition of the pyrrolidinofullerene fragment.[53] There is no significant difference for the Ru(III)/Ru(II) redox potentials within the series (and also in comparison to the reference complexes **3a,b**), indicating the negligible influence of the ligand sphere on the energy of the highest occupied molecular orbital. Within the accessible potential window, all fullerene-containing compounds of the series feature three reversible C_{60}-based reduction waves of similar redox potentials at around −1.1, −1.5, and −2.0 V. The half-wave potentials are shifted cathodically in comparison to pristine C_{60}. This can be attributed to the attached pyrrolidine and cyclopropane units, causing a disruption of π conjugation and a decreased electron affinity of C_{60}.[54] As reported elsewhere,[40] the values for the C_{60} reductions are slightly cathodically shifted (around 20 mV) on comparison of pyrrolidine to cyclopropane rings attached to C_{60}. Accordingly, electron delocalization is more efficient in the methanofullerene compounds. Another trend that holds true—at least for the first C_{60}-based reduction—is the cathodic shift on changing to larger bridge lengths. The third reduction wave at around −1.65 V of **1a−c** and **2a,b** is attributed to the first reduction of the terpyridine unit. The assignment is proven by comparison of the dinuclear complex **1c** to the parent mononuclear ruthenium complex **1a**. Apparently, the dinuclear complex shows similar values for the half-wave potentials but increased currents for the ruthenium- and terpyridine-related redox couples, while the C_{60}-based peak currents stay nearly constant (see Figure S3 in the Supporting Information). The second reduction of the terpyridine unit is in the same range as the third C_{60}-based reduction. According to the model complexes **3a,b**, the redox potential of the second terpyridine reduction is at ca. −1.95 V (see Figure S2 in the Supporting Information). In the methanofullerene ruthenium(II) complexes **1a−c** there is another irreversible process around −1.98 V (see Figure S4 in the Supporting Information). As is known from the literature, this process has to be assigned to the electrochemical retrocycloaddition of Bingel adducts.[55] However, this process can only be observed for the investigated complexes and is absent for the ligands **8a−c**.

Photophysical Properties. The UV−vis absorption data are summarized in Table 2. A comparison of the UV−vis absorption spectra of C_{60}, **2b**, and **3b**, as shown in Figure 3, reveals that the spectrum of **2b** can be regarded as a superposition of the spectra of C_{60} and **3b**. In agreement

Table 2. UV−Vis Absorption Data[a]

	λ_{abs}/nm ($\varepsilon/10^3$ M^{-1} cm^{-1})[b]
C_{60}	405 (2.7), 329 (50.9), 258 (189.6)
8a	430 (2.6), 327 (46.0), 259 (150.0)
8b	430 (4.0), 328 (78.2), 259 (157.5)
8c	430 (3.1), 323 (61.4), 276 (sh, 172.9), 259 (195.5)
10a	430 (6.2), 317 (sh, 45.0), 271 (sh, 107.0), 256 (123.8)
10b	430 (10.3), 311 (87.4), 269 (sh, 126.5) 255 (149.0)
1a	484 (25.1), 327 (sh, 78.1), 310 (97.7), 270 (112.6)
1b	487 (31.6), 327 (sh, 83.9), 311 (107.2), 273 (105.4)
1c	484 (47.0), 326 (sh, 131.5), 310 (174.5), 273 (159.7)
2a	485 (22.8), 327 (sh, 59.3), 309 (83.7), 273 (85.8)
2b	488 (35.8), 327 (sh, 95.0), 311 (116.8), 270 (113.9)
3a	484 (23.4), 327 (sh, 43.4), 309 (77.5), 274 (49.3)
3b	487 (35.4), 326 (69.2), 310 (95.6), 274 (52.3)

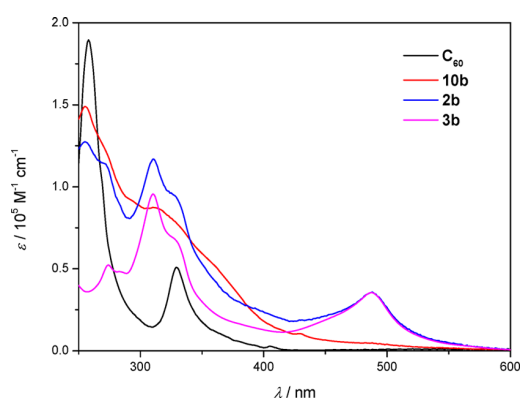[a]Measured in dichloromethane at 20 °C. [b]sh = shoulder.

Figure 3. UV−vis absorption spectra of the long bridged pyrrolidinofullerene ligand and complexes measured in dichloromethane.

with the electrochemical measurements, there is no evidence for an electronic interaction between the Ru(II) center and the fullerene unit in the ground state. The spectral properties are similar throughout the series: while intense absorption bands between 250 and 350 nm are based on $\pi-\pi^*$ transitions within the fullerene, phenyl, and terpyridine groups, absorption bands in the region around 485 nm are related to Ru(II)-based metal-to-ligand charge-transfer (MLCT) transitions.[56] With an increased bridge length in compounds **1b** and **2b**, the additional phenylene and ethynylene groups cause a slight bathochromic shift of the $\pi-\pi^*$ transitions. An analogous behavior is observed for the MLCT transition (shift of around 3 nm), in concert with increases in the molar extinction coefficients. The fullerene ligands **8a−c** and **10a,b** possess a sharp absorption band at around 430 nm, which is bathochromically shifted in comparison to pristine C_{60} (405 nm). This transition is characteristic of closed-[6,6] fullerene monoadducts.[57,58] In the complexes, this transition is only weakly defined, because it is overlaid by the tail of the strong MLCT transition. The emission properties of **8a−c** and **10a,b** were studied in dichloromethane and compared to the reference systems ttpy and **11b**. Upon excitation of the $\pi-\pi^*$ transition (λ_{ex} = 315 or 325 nm), there is a strong quenching of the spacer- and terpyridine-based fluorescence by a factor of ca. 200 when the C_{60} unit is attached (for details, see the

Supporting Information). Additionally, the fullerene-based fluorescence at ca. 700 nm is only weakly pronounced.[13] The initially weak Ru(II)-based emission at room temperature of the reference complexes (**3a**, λ_{max} = 627 nm; **3b**, λ_{max} = 645 nm) is almost fully quenched in complexes **1a−c** and **2a,b** (Figure 4). The quenching indicates an electronic interaction between the ^{3}MLCT state and the fullerene unit, as detailed below.

Photoinduced Dynamics. *Formation of the Long-Lived Excited State.* The photoinduced dynamics occurring after excitation of the ^{1}MLCT transition (λ_{exc} = 520 nm) were investigated using transient absorption (TA) spectroscopy in order to clarify the quenching mechanism. To provide consistency with the steady-state data, we will focus on the TA experiments performed in dichloromethane. Figure 5 contains transient absorption data for **2b** and for the C_{60}-free complex **3b**, as reference. The transient absorption spectra recorded for **3b** (Figure 5A) match those of typical Ru^{II} polypyridine complexes featuring ground-state bleach (GSB) in the region of the ^{1}MLCT absorption band and excited-state absorption (ESA) above 550 nm. The electronic delocalization of the ^{3}MLCT state over the extended ligand is apparent: the ESA maximum of **3a**, where ^{3}MLCT delocalization is limited to the ttpy ligand, is at ca. 560 nm in acetonitrile (see the Supporting Information). However, for **3b** the ESA maximum is located at ca. 690 nm, clearly indicating the presence of an extended π system.[59] This was also noted for related methoxyphenyl-substituted [Ru(bpy)$_3$]$^{2+}$ derivatives.[26] The kinetic traces (Figure 5B) illustrate that the signal decay is not completely resolved, at least within the time scale of the experiment. However, this decay likely corresponds to the decay of the ^{3}MLCT (see below).

The quantitative interpretation of the TA data is based on global multiexponential fits corresponding to a kinetic scheme involving consecutive first-order reactions (details are given in the Experimental Section). In the case of **3b**, four kinetic components are used to fit the data. The decay-associated spectra (DAS) and the corresponding characteristic time constants are given in Figure 6. The DAS (τ_4 = 1.6 ns) features a much higher amplitude than the other DAS: i.e., it plays a dominant role in the photoinduced dynamics of **3b**. The DAS (τ_4) reflects the shape of the TA spectra recorded at long delay times, indicating that τ_4 describes the decay of the
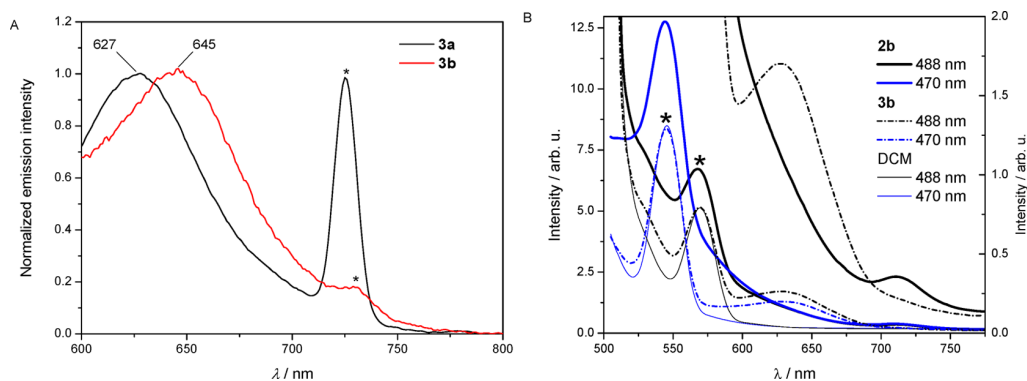
Figure 4. (A) Normalized emission spectra (λ_{ex} = 483 or 488 nm) of the reference complexes **3a,b** measured in dichloromethane at room temperature. Asterisks mark the scattered excitation light. (B) Emission spectra of isoabsorbing solutions at 487 nm of **3b** and **2b** in dichloromethane together with the signal obtained from the pure solvent. The right scale shows a magnification of the spectral region containing ^{3}MLCT phosphorescence and C_{60} fluorescence (solvent and spectra recorded at 470 nm are omitted for clarity).

Figure 5. Transient absorption spectra (A, C) at selected delay times between 0.2 and 1.8 ns (from red to black) and selected kinetic traces (B, D) with corresponding fit curves: 488 nm (black squares), 560 nm (red circles), 620 nm (blue triangles), and 690 nm (cyan stars) for **3b** (A, B) and **2b** (C, D).
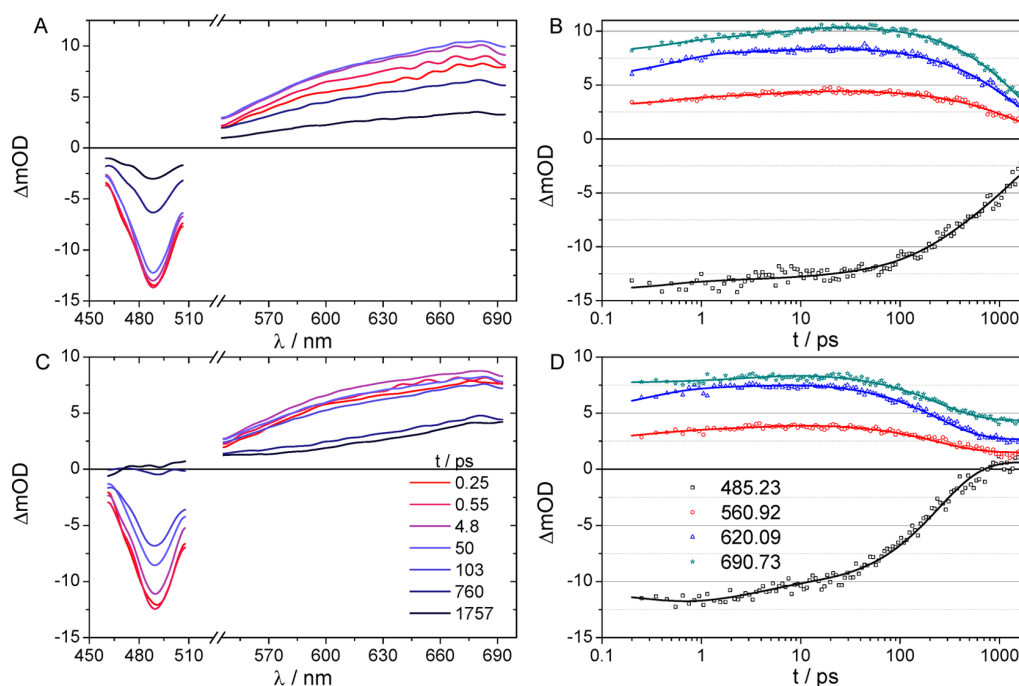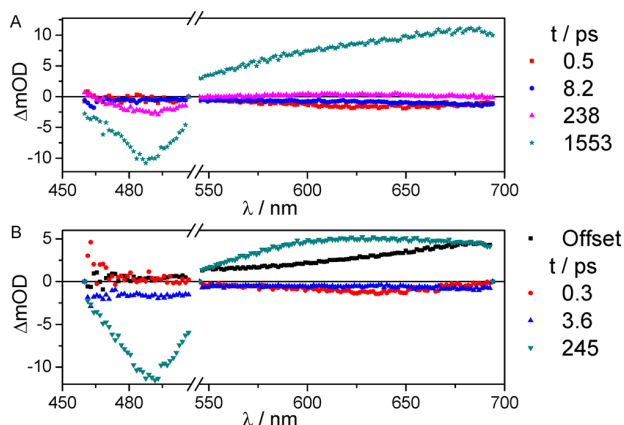

Figure 6. Global fit results in terms of decay-associated spectra for **3b** (A) and **2b** (B). The characteristic time constants are given in the legends.

[3]MLCT and, thus, the overall decay to the ground state. This is also supported by the emission decay time of **3b** (2.3 ns in acetonitrile), determined by time-correlated single-photon counting (see the Supporting Information). This value can be compared to the 1.6 ns decay time determined in the TA experiments, as in the latter decay time there is a relatively large uncertainty due to the limited delay time range (1.8 ns) accessible in our experimental setup.

The fastest component ($\tau_1 = 0.5$ ps) is assigned to solvent relaxation and vibrational energy dissipation[60,61] and causes an increase of the ESA between 550 and 700 nm. Generally, the picosecond components ($\tau_2 = 8.2$ ps, $\tau_3 = 238$ ps) can be attributed to the presence of the organic chromophore attached at the 4′-position of the tpy unit:[62] Here, the process associated with τ_2 is assigned to photoinduced planarization of the

extended terpyridine ligand: i.e., excited-state torsional motion around the pyridine–phenyl bond.[63] Planarization causes an increase in the ESA in the visible part of the spectrum due to an enhanced π conjugation of the ligand. DFT calculations on **3b** suggest a strong mixing of [3]MLCT states with ligand-centered orbitals (see the Supporting Information) leading to delocalized states with different amounts of [3]MLCT and [3]LC character. Therefore, τ_3 (238 ps) has to be assigned to an equilibration between close-lying, mixed triplet states.[39,64]

Dyad **2b** shows transient absorption features similar to those observed for **3b** at early delay times (see Figure 5A,B). Both the spectra and the kinetic traces are similar up to 30 ps. Later, in **2b** a more pronounced decay is observed, which is not complete: i.e., the kinetic traces reach a plateau after ca. 1 ns. The transient absorption spectra at delay times >1.5 ns are positive over the entire spectral range probed in our experiment, including a rise toward 700 nm. Thus, the nanosecond dynamics of **2b** are clearly different from those of **3b**, leading to the formation of a long-lived species unique for the dyad. The global fit routine produces three kinetic components and an offset corresponding to the spectrum of the long-lived species formed. The nature of this species will be discussed in conjunction with results of nanosecond transient absorption experiments. The sub-picosecond component ($\tau_1 = 0.3$ ps) is similar to the fastest process observed for **3b** and can be rationalized equivalently. The picosecond processes, i.e. the processes associated with τ_2 and τ_3, are accelerated in **2b** in comparison to those in **3b**. In detail, a process with $\tau_2 = 3.6$ ps shows spectral characteristics similar to those of the equilibration process (τ_3) observed in **3b**. The time constant $\tau_3 = 245$ ps of **2b** is identical with the value of τ_3 of **3b** (238 ps), but the corresponding DAS (τ_3) in the case of **2b** is basically identical with the DAS (τ_4) of **3b** describing the overall decay, as discussed above. Therefore, the depopulation of the [3]MLCT
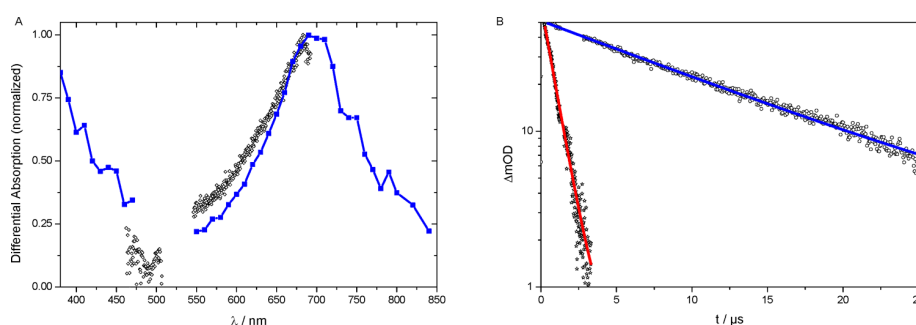
Figure 7. Nanosecond transient absorption data of **2b** in dichloromethane: (A) absorption spectra of the long-lived species constructed from integrated intervals of nanosecond transient absorption kinetics (blue solid squares) with the offset component from the femtosecond TA data (black hollow symbols) for comparison; (B) decay of the positive absorption at λ = 700 nm after photoexcitation of **2b** at 520 nm in aerated (solid stars) and deaerated (hollow spheres) solutions with respective fit curves for τ = 800 ns (red curve) and τ = 13 μs (blue curve).

(or rather a mixed ^{3}MLCT/$\pi-\pi^*$) state occurs very quickly for **2b** with the same time constant that was assigned to excited-state equilibration in **3b**. Given the fact that the long-lived state in **2b** is due to the fullerene unit, the process that deactivates the ^{3}MLCT is the same process that populates the long-lived state (see below).

Nature of the Long-Lived Excited State. Nanosecond transient absorption experiments on **2b** (Figure 7) were conducted to detail the nature of the long-lived state: kinetic traces for the nano- to microsecond decay were recorded for selected wavelengths. From these curves, nanosecond transient absorption spectra were constructed. A broad absorption peak is found with a maximum at ca. 700 nm and steep flanks on both the high- and low-energy sides. A shoulder is observed at ca. 800 nm, and there are hints toward a rise at wavelengths shorter than 450 nm. The offset component determined from the femtosecond transient absorption data is in good agreement with the nanosecond transient absorption spectrum. Furthermore, the nanosecond spectrum coincides with the known absorption features of the ^{3}C$_{60}^*$ state,[31] in particular the maximum at around 700 nm and the long-wavelength shoulder. Additional support for the assignment of the long-lived state as ^{3}C$_{60}^*$ is based on oxygen-quenching experiments: Triplet states of organic molecules are prone to undergo quenching reactions with triplet oxygen, strongly reducing the excited-state lifetime.[65] From a comparison of kinetic traces of the ESA decay at 700 nm recorded in the presence and absence of oxygen (Figure 7B), it is taken that the lifetime significantly increases in the absence of oxygen, indicative of a triplet state. The lifetimes of 800 ns and 13 μs with and without oxygen, respectively, are consistent with literature reports on ^{3}C$_{60}^*$.[31]

Three possible quenching mechanisms leading to the ^{3}C$_{60}^*$ state were discussed in the literature,[26] of which resonant triplet–triplet energy transfer (Förster-type) is unlikely to happen due to the weak acceptor absorption. Other possibilities are charge separation, i.e. a transport of the negative charge located on the ligand toward the fullerene after ^{1}MLCT excitation followed by a fast recombination, and Dexter-type energy transfer. The former would, however, yield a reduced C$_{60}$ species, which would absorb in the NIR region at around 1100 nm.[31]

Solvent-polarity-dependent TA spectroscopy was performed to yield additional insight into the photoinduced processes and validate the absence of a photoinduced charge-transfer reaction. Therefore, additional TA measurements on **2b** and **3b** were performed in acetonitrile: despite the higher polarity of

acetonitrile in comparison to dichloromethane, the data reveal almost identical spectral and temporal characteristics (see the Supporting Information). In particular, no significantly different time constants were found, ruling out the possibility that charge separation is contributing to the photophysics of **2b**. Similar observations are made for **2a**, i.e. the short-bridged analogue, as well as the methano-fullerene dyads **1a,b**, as the photoinduced dynamics probed in transient absorption experiments are rather similar for all of these compounds (see the Supporting Information). This holds true also for the dinuclear complex **1c**.

Nevertheless, the quenching kinetics are not identical for the compounds at hand. In fact, the rate constant for energy transfer measured in acetonitrile (corresponding to the process causing the ^{3}MLCT absorption characteristics to vanish) depends on both the linker type and the size of the bridge between terpyridine and fullerene moieties (see Figure 8). The
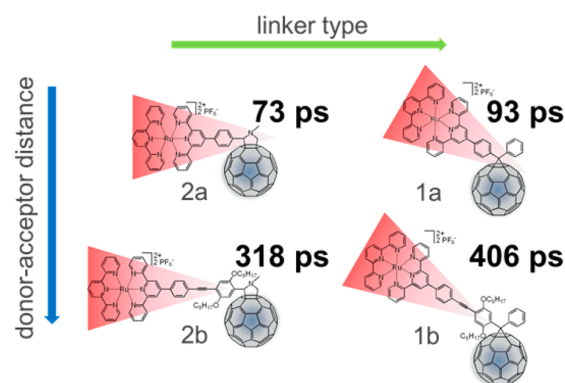
Figure 8. Schematic representation of the distance and linker dependence of the energy transfer (^{3}MLCT depopulation) rate.

fastest ^{3}MLCT deactivation (73 ps) is observed for the short-bridged pyrrolidinofullerene dyad **2a**. In **1a** the energy transfer is somewhat slower (93 ps), possibly due to the different angle of the complex fragment with respect to the fullerene surface. The larger bridge, increasing the donor–acceptor distance in the assemblies **1b** and **2b**, causes a significant prolongation of the energy transfer time.

The fact that **3b** and **2b** possess strongly delocalized ^{3}MLCT states involving orbitals of the organic chomophore indicates that orbital overlap with the fullerene unit might favor rapid Dexter-type energy transfer in the Ru(II)–C$_{60}$ dyads. As soon as the extended ligand is planarized and electronic communi-

cation between the metal center and the orbitals of the organic chromophore is enhanced, there is close spatial proximity with orbitals of the fullerene acceptor and an efficient deactivation pathway of the ^{3}MLCT is accessible.

CONCLUSION

A series of mono- and dinuclear ruthenium(II) bis(terpyridine) methanofullerene and pyrrolidinofullerene assemblies connected with phenylene and phenyleneethynylenphenylene units was synthesized. The key step of the synthetic route was the cycloaddition reaction of the terpyridine building blocks onto the fullerene unit. The complexes were compared to related reference compounds with regard to their electrochemical and photophysical properties. The methanofullerene compounds feature better electronic communication between the active units in comparison to pyrrolidinofullerenes, indicated by a small anodic shift of the C_{60}-based redox potentials. The ground-state absorption spectra are mainly a superposition of the individual moieties' characteristics, indicating weak interaction between the redox-active subunits in the ground state. However, steady-state emission spectroscopy revealed a strong interaction in the excited state: namely, by quenching of the ligand-based fluorescence and Ru(II)-based phosphorescence. Photoexcitation of the Ru(II)-based ^{1}MLCT transition results in a fast population of the lowest-lying triplet C_{60} state. A distance and linker dependence of the energy transfer rate was found. We believe that the photophysical and electrochemical properties of the presented complexes have a high potential in formation of light-induced charge-separated states for artificial photosynthetic devices, in particular when the assemblies are extended from dyads to triads by incorporation of lateral organic or organometallic donor entities. This is the topic of ongoing research.

EXPERIMENTAL SECTION

General Remarks. 2-Bromo-1,4-bis(octyloxy)benzene (**4b**),[43] 4'-(4-ethynylphenyl)-2,2':6',2''-terpyridine,[47] 2,5-bis(octyloxy)-4-(4-[2,2':6',2'']terpyridin-4'-ylphenylethynyl)benzaldehyde (**9b**),[47,48] bis-(4,4'-formyl)benzophenone (**5c**),[41] 4'-(4-formylphenyl)-2,2':6',2''-terpyridine (**9a**),[47] 4'-(4-methylphenyl)-2,2':6',2''-terpyridine (ttpy),[66] [Ru(tpy)Cl$_3$],[67] and [Ru(tpy)(MeCN)$_3$](PF$_6$)$_2$[50] were synthesized according to literature procedures. Dry toluene, THF, and dichloromethane were obtained from a Pure-Solv MD-4-EN solvent purification system (Innovative Technologies Inc.). Triethylamine was dried over KOH and distilled. All other chemicals were purchased from commercial suppliers and used as received. All reactions were performed in oven-dried flasks and were monitored by thin-layer chromatography (TLC) (silica gel on aluminum sheets with fluorescent dye F254, Merck KGaA). Microwave reactions were carried out using a Biotage Initiator Microwave synthesizer. NMR spectra were recorded on a Bruker AVANCE 250 MHz, AVANCE 300 MHz, or AVANCE 400 MHz instrument in deuterated solvents (Euriso-Top) at 25 °C. ^{1}H and ^{13}C resonances were assigned using appropriate 2D correlation spectra. Chemical shifts are reported in ppm using the solvent as internal standard. Matrix-assisted laser desorption ionization time of flight (MALDI-TOF) mass spectra were obtained using an Ultraflex III TOF/TOF mass spectrometer in reflector mode. High-resolution electrospray ionization time of flight mass spectrometry (ESI-Q-TOF MS) was performed on an ESI-(Q)-TOF-MS microTOF II (Bruker Daltonics) mass spectrometer. Melting points (mp) were determined on a Stuart SMP-3 apparatus. UV–vis absorption spectra were recorded on a PerkinElmer Lambda 750 UV/vis spectrophotometer and emission spectra on Jasco FP6500 and FP-6200 instruments, respectively. Measurements were carried out using 10^{-6} M solutions of the respective solvents (spectroscopy grade) in 1 cm quartz cuvettes at room temperature. However, some emission

spectra were recorded using higher absorbances (ca. 0.2 in the maximum of the ^{1}MLCT band). Cyclic voltammetry measurements were performed on a Metrohm Autolab PGSTAT30 potentiostat with a standard three-electrode configuration using a glassy-carbon-disk working electrode, a platinum-rod auxiliary electrode, and a AgCl/Ag reference electrode; a scan rate of 200 mV s^{-1} was applied. The experiments were carried out in deaerated solvents (spectroscopy grade) containing 0.1 M Bu$_4$NPF$_6$ salt. At the end of each measurement, ferrocene was added as an internal standard.

Time-Resolved Spectroscopy. The femtosecond transient absorption measurements (λ_{exc} 520 nm) were performed on two different setups. Each setup is based on an amplified Ti:sapphire oscillator (800 nm, 1 kHz). One setup produces pulses of 35 fs at 3.5 mJ (Legend-Elite, Coherent Inc., used for measurements in acetonitrile) and the other setup 100 fs at 950 μJ (Libra, Coherent Inc., used for measurements in dichloromethane). Appropriate beam splitters split the pulses to attenuate the intensity to pump: in case of the former setup, a collinear optical-parametric amplifier (TOPAS-C, LightConversion Ltd.) with 1.35 W or, for the latter setup, a noncollinear optical-parametric amplifier (TOPASwhite, Lightconverison Ltd.) with 0.5 W. The pump pulses delayed in time with respect to the probe pulses by means of an optical delay line, and their polarization was rotated by 54.7° (magic angle) with respect to the probe beam by using a Berek compensator. For both setups white light was used as the probe, which was generated by focusing a minor fraction of the amplifier output into a sapphire plate. The probe beam is focused and recollimated using 50 cm (20 cm) spherical mirrors, while the focus of the pump beam is behind the sample in order to obtain a homogeneously excited sample volume. The pump pulse is blocked after the sample, while the probe pulse is sent to a double-stripe diode-array detection system (Pascher Instruments AB) together with the reference pulse. The pump pulse energy was typically adjusted to 1 μJ while the integrated probe intensity was a few hundred nanojoules. The sample solution (OD typically ca. 0.2 at the excitation wavelength) was kept in a 1 mm quartz cuvette. Prior to data analysis, the experimental differential absorption data was chirp corrected and afterward fitted globally.

The excited-state lifetimes were determined using a nanosecond transient absorption setup. Nanosecond pump pulses at 520 nm were delivered by a Continuum Surelite OPO Plus pumped by a Continuum Surelite Nd:YAG laser (pulse duration 5 ns; pulse to pulse repetition rate 10 Hz). A 75 W xenon arc lamp provided the probe light. Spherical concave mirrors were used to focus the probe light into the sample and to refocus the light on the entrance slit of a monochromator (Acton, Princeton Instruments). The probe light was detected by a Hamamatsu R928 photomultiplier tube mounted on a five-stage base at the monochromator exit slit, and the signal was processed by a commercially available detection system (Pascher Instruments AB). Some measurements were performed in oxygen-free solutions produced by performing several freeze−pump−thaw cycles. All measurements were performed in 1 cm fluorescence cuvettes, allowing a 90° angle between pump and probe beam.

4-Formylbenzophenone (5a). The oxidation of the terminal methyl group was performed according to a related literature procedure.[41] Concentrated sulfuric acid (6 mL, 113 mmol) was added dropwise to a stirred solution of 4-methylbenzophenone (**4a**; 3 g, 15.29 mmol) in acetic anhydride (30 mL) at 0 °C. To this was added a solution of chromium(VI) oxide (4.13 g, 41.3 mmol) in acetic anhydride (20 mL) dropwise at such a rate that the temperature did not exceed 10 °C. After all the chromium(VI) oxide was added, stirring was continued for a further 16 h at room temperature. Subsequently, the reaction mixture was added to an ice−water mixture (150 mL) and the solid was collected by filtration. Further material was extracted from the solution with diethyl ether (2 × 50 mL); the ethereal extracts were dried, and the solvent was evaporated. The combined solid products were washed with 2% aqueous sodium carbonate solution (1 × 50 mL) and then heated at reflux in ethanol/water/concentrated sulfuric acid (53 mL, 10/10/1) for 30 min. The solution was cooled to room temperature, the product was extracted with ethyl acetate (4 × 50 mL), the combined organic extracts were

washed with saturated aqueous sodium hydrogen carbonate solution (2 × 50 mL) and dried with Na$_2$SO$_4$, and the solvent was evaporated to yield the crude product. Further purification was achieved by flash chromatography (silica, *n*-hexane/dichloromethane 1/3) to give a yellow solid (1 g, 4.76 mmol, 31%). Mp: 67−68 °C. ^{1}H NMR (300 MHz, CDCl$_3$, ppm): δ 10.13 (s, 1H, −C*H*O), 8.00 (d, ^3J = 8.4 Hz, 2H, *H*^{E3}), 7.92 (d, ^3J = 8.2 Hz, 2H, *H*^{E2}), 7.86−7.77 (m, 2H, *H*^{G2}), 7.63 (t, ^3J = 7.4 Hz, 1H, *H*^{G4}), 7.51 (t, ^3J = 7.5 Hz, 2H, *H*^{G3}). ^{13}C NMR (75 MHz, CDCl$_3$, ppm): δ 195.94, 191.75, 142.70, 138.61, 136.88, 133.26, 130.45, 130.24, 129.62, 128.67. Anal. Calcd for C$_{14}$H$_{10}$O$_2$: C, 79.98; H, 4.79. Found: C, 80.11; H, 4.87.

General Procedure for Kröhnke-Type Terpyridine Synthesis. 2-Acetylpyridine (2.2 equiv per aldehyde group), aldehyde derivate **5** (1 equiv), and sodium hydroxide (2.2 equiv per aldehyde group) were ground in a mortar until a bright yellow powder was formed (10−20 min). The solid was transferred to a flask, ethanol (10 mL) and 25% aqueous ammonia solution (5 mL) were added, and the suspension was stirred at room temperature for 48 h. The gray precipitate that formed was filtered and washed with water (15 mL) and ethanol (5 mL). The crude product was recrystallized in THF.

4′′′-[2,2′:6′,2′′]Terpyridin-4′-ylbenzophenone (6a). According to the general procedure for Kröhnke-type terpyridine synthesis, 2-acetylpyridine (0.38 g, 3.14 mmol), 4-formylbenzophenone (**5a**; 0.3 g, 1.427 mmol), and sodium hydroxide (0.126 g, 3.14 mmol) were reacted to yield a beige solid (217 mg, 0.525 mmol, 37%). Mp: 122 °C. ^{1}H NMR (300 MHz, CDCl$_3$, ppm): δ 8.78 (s, 2H, *H*^{D3}), 8.73 (d, ^3J = 4.7 Hz, 2H, *H*^{C6}), 8.68 (d, ^3J = 8.0 Hz, 2H, *H*^{C3}), 8.01 (d, ^3J = 8.4 Hz, 2H, *H*^{E3}), 7.94 (d, ^3J = 8.3 Hz, 2H, *H*^{E2}), 7.92−7.81 (m, 4H, *H*^{C4}, *H*^{G2}), 7.62 (t, ^3J = 7.4 Hz, 1H, *H*^{G4}), 7.52 (t, ^3J = 7.4 Hz, 2H, *H*^{G3}), 7.36 (ddd, ^3J = 7.3 Hz, ^3J = 4.8 Hz, ^4J = 0.9 Hz, 2H, *H*^{C5}). ^{13}C NMR (75 MHz, CDCl$_3$, ppm): δ 196.35, 156.27, 156.09, 149.28, 149.25, 142.58, 137.90, 137.66, 137.07, 132.71, 130.83, 130.20, 128.51, 127.41, 124.12, 121.52, 119.12. MS (MALDI-TOF, dithranol, *m/z*): 414.17, C$_{28}$H$_{20}$N$_3$O ([M + H]$^+$) requires 414.16. Anal. Calcd for C$_{28}$H$_{19}$N$_3$O·H$_2$O: C, 77.94; H, 4.91; N, 9.74. Found: C, 77.68; H, 4.81; N, 9.56. UV−vis (CH$_2$Cl$_2$): λ$_{max}$/nm (ε/L mol$^{−1}$ cm$^{−1}$) 284 (57700).

Bis(4′′′,4′′′′′-[2,2′:6′,2′′]terpyridin-4′-yl)benzophenone (6c). According to the general procedure for Kröhnke-type terpyridine synthesis, 2-acetylpyridine (0.671 g, 5.54 mmol), bis(4,4′-formyl)-benzophenone (**5c**; 0.3 g, 1.26 mmol), and sodium hydroxide (0.222 g, 5.54 mmol) were reacted to yield a beige solid (180 mg, 0.279 mmol, 22%). Mp: >250 °C dec. ^{1}H NMR (300 MHz, CDCl$_3$, ppm): δ 8.80 (s, 4H, *H*^{D3}), 8.74 (d, ^3J = 4.1 Hz, 4H, *H*^{C6}), 8.69 (d, ^3J = 7.9 Hz, 4H, *H*^{C3}), 8.05 (d, ^3J = 8.3 Hz, 4H, *H*^{E3}), 7.99 (d, ^3J = 8.3 Hz, 4H, *H*^{E2}), 7.89 (td, ^3J = 7.8 Hz, ^4J = 1.3 Hz, 4H, *H*^{C4}), 7.37 (dd, ^3J = 6.6 Hz, ^3J = 5.2 Hz, 4H, *H*^{C5}). ^{13}C NMR (75 MHz, CDCl$_3$, ppm): δ 195.84, 156.33, 156.14, 149.34, 149.26, 142.79, 137.84, 137.07, 130.87, 127.54, 124.13, 121.54, 119.17. MS (MALDI-TOF, dithranol, *m/z*): 645.21, C$_{43}$H$_{29}$N$_6$O ([M + H]$^+$) requires 645.24. Anal. Calcd for C$_{43}$H$_{28}$N$_6$O × 2 H$_2$O: C, 75.87; H, 4.74; N, 12.35. Found: C, 75.63; H, 4.87. N, 12.33. UV−vis (CH$_2$Cl$_2$): λ$_{max}$/nm (ε/L mol$^{−1}$ cm$^{−1}$) 285 (68300).

4-Bromo-2,5-bis(octyloxy)benzophenone (5b). A solution of 2-bromo-1,4-bis(octyloxy)benzene (**4b**; 400 mg, 0.968 mmol) and benzoyl chloride (204 mg, 1.451 mmol) in dichloromethane (5 mL) was stirred at 0 °C under nitrogen, while a mixture of aluminum(III) trichloride (194 mg, 1.451 mmol) was slowly added. The solution was stirred overnight at room temperature before being poured onto iced 2 M HCl solution (50 mL). The dichloromethane layer was separated, and the aqueous phase was extracted with dichloromethane (3 × 30 mL). The combined organic layers were dried over Na$_2$SO$_4$, and the organic solvents were removed under reduced pressure. The solid residue was dissolved in dichloromethane (100 mL) and washed successively with 2 M sodium hydroxide solution (3 × 30 mL) and brine (50 mL) before the solution was dried and evaporated. The residue was purified by column chromatography (silica, *n*-hexane/dichloromethane 2/1) to yield a yellow viscous liquid (277 mg, 0.683 mmol, 71%). ^{1}H NMR indicated the formation of 4-bromo-5-hydroxy-2-octyloxybenzophenone by the loss of one octyloxy group during the reaction. The group was reintroduced according to the literature

procedure. Therefore, KOH powder (190 mg, 3.38 mmol) was stirred in dried DMSO (6 mL) and the solution was deaerated. 4-Bromo-5-hydroxy-2-octyloxybenzophenone (274 mg, 0.676 mmol) in DMSO (1.5 mL) and 1-bromooctane (259 µL, 1.487 mmol) in DMSO (1.5 mL) were added. The mixture was stirred for 22 h at room temperature. The resulting solid was filtered off and dissolved in toluene (50 mL). The toluene solution was extracted with water (3 × 20 mL) and dried with Na$_2$SO$_4$, and the organic solvent was removed under reduced pressure. The residue was purified by column chromatography (silica, *n*-hexane/dichloromethane 1/1) to yield a low-melting white solid (312 mg, 0.603 mmol, 89%, 62% overall yield). Mp: 40 °C. ^{1}H NMR (300 MHz, CD$_2$Cl$_2$, ppm): δ 7.80−7.72 (m, 2H, *H*^{G2}), 7.60−7.52 (m, 1H, *H*^{G4}), 7.48−7.40 (m, 2H, *H*^{G3}), 7.22 (s, 1H, *H*^{F3}), 7.02 (s, 1H, *H*^{F6}), 4.00 (t, ^3J = 6.5 Hz, 2H, α-OC*H*$_2$), 3.80 (t, ^3J = 6.3 Hz, 2H, α-OC*H*$_2$), 1.89−1.75 (m, 2H, β-C*H*$_2$), 1.58−1.44 (m, 2H, β-C*H*$_2$), 1.44−1.05 (m, 20H, γ-η-C*H*$_2$), 1.04−0.84 (m, 6H, C*H*$_3$). ^{13}C NMR (75 MHz, CD$_2$Cl$_2$, ppm): δ 196.02, 151.70, 150.45, 138.83, 133.37, 129.92, 129.29, 128.79, 118.60, 115.96, 114.91, 70.71, 69.94, 32.45, 32.38, 29.91, 29.87, 29.81, 29.76, 29.69, 29.50, 26.59, 26.19, 23.30, 23.27, 14.52, 14.51. HRMS (ESI-TOF, *m/z*): 517.2300, C$_{29}$H$_{42}$BrO$_3$ ([M + H]$^+$) requires 517.2312.

General Procedure for Sonogashira Cross-Coupling Reactions. Copper(I) iodide (0.1−0.15 equiv) and [Pd(PPh$_3$)$_4$] (0.1−0.15 equiv) were added to a deaerated solution of an aromatic bromine (1 equiv) in a mixture of THF (10 mL) and triethylamine (5 mL). With vigorous stirring, 4′-(4-ethynylphenyl)-2,2′:6′,2′′-terpyridine (1.2 equiv) in THF (2 mL) was added. Subsequently, the reaction mixture was heated to 60 °C for 48−72 h. After the mixture was cooled to room temperature, the precipitated ammonia salt was filtered off and washed intensely with THF, and the solvent was removed under reduced pressure. Dichloromethane was added, and the solution was washed with saturated aqueous ammonium chloride/EDTA (1/1) solution and dried with Na$_2$SO$_4$. Further purification was achieved by column chromatography (neutral alumina, dichloromethane/*n*-hexane).

2,5-Bis(octyloxy)-4-(4-[2,2′:6′,2′′]terpyridin-4′-ylphenylethynyl)-benzophenone (6b). According to the general procedure for Sonogashira cross-coupling reactions, copper(I) iodide (16.6 mg, 0.087 mmol), [Pd(PPh$_3$)$_4$] (100 mg, 0.087 mmol), 4-bromo-2,5-bis(octyloxy)benzophenone (**5b**; 300 mg, 0.580 mmol), and 4′-(4-ethynylphenyl)-2,2′:6′,2′′-terpyridine (232 mg, 0.696 mmol) were reacted for 72 h. Further purification was achieved by column chromatography (neutral alumina, dichloromethane/*n*-hexane 2/1) to yield an off-white solid (252 mg, 0.327 mmol, 57%). Mp: 110−112 °C. ^{1}H NMR (300 MHz, CDCl$_3$, ppm): δ 8.76 (s, 2H, *H*^{D3}), 8.74 (d, ^3J = 4.7 Hz, 2H, *H*^{C6}), 8.68 (d, ^3J = 7.9 Hz, 2H, *H*^{C3}), 7.93 (d, ^3J = 8.5 Hz, 2H, *H*^{E2}), 7.89 (td, ^3J = 7.7 Hz, ^4J = 1.7 Hz, 2H, *H*^{C4}), 7.82−7.77 (m, 2H, *H*^{G2}), 7.70 (d, ^3J = 8.4 Hz, 2H, *H*^{E3}), 7.55 (t, ^3J = 7.3 Hz, 1H, *H*^{G4}), 7.43 (t, ^3J = 7.5 Hz, 2H, *H*^{G3}), 7.36 (ddd, ^3J = 7.4 Hz, ^3J = 4.8 Hz, ^4J = 1.0 Hz, 2H, *H*^{C5}), 7.11 (s, 1H, *H*^{F3}), 7.01 (s, 1H, *H*^{F6}), 4.06 (t, ^3J = 6.4 Hz, 2H, OC*H*$_2$−), 3.84 (t, ^3J = 6.3 Hz, 2H, α-OC*H*$_2$), 1.93−1.80 (m, 2H, β-C*H*$_2$), 1.63−1.49 (m, 2H, β-C*H*$_2$), 1.46−0.93 (m, 20H, γ-η-C*H*$_2$), 0.93−0.81 (m, 6H, C*H*$_3$). ^{13}C NMR (75 MHz, CDCl$_3$, ppm): δ 196.32, 156.26, 156.19, 154.17, 150.81, 149.51, 149.27, 138.46, 138.41, 137.06, 132.90, 132.33, 130.00, 129.63, 128.29, 127.41, 124.23, 124.05, 121.52, 118.80, 117.27, 116.26, 113.99, 94.91, 87.21, 69.86, 69.27, 31.96, 31.88, 29.51, 29.48, 29.46, 29.29, 29.20, 29.07, 26.22, 25.75, 22.82, 22.77, 14.23, 14.23. HRMS (ESI-TOF, *m/z*): 792.4076, C$_{52}$H$_{55}$N$_3$O$_3$Na ([M + Na]$^+$) requires 792.4136. Anal. Calcd for C$_{52}$H$_{55}$N$_3$O$_3$: C, 81.11; H, 7.20; N, 5.46. Found: C, 81.01; H, 7.30; N, 5.47. UV−vis (CH$_2$Cl$_2$): λ$_{max}$/nm (ε/L mol$^{−1}$ cm$^{−1}$) 360 (31500), 303 (58000).

4′-(4-((2,5-Bis(octyloxy)phenyl)ethynyl)phenyl)-2,2′:6′,2′′-terpyridine (11b). According to the general procedure for Sonogashira cross-coupling reactions, copper(I) iodide (9.5 mg, 0.050 mmol), [Pd-(PPh$_3$)$_4$] (0.058 g, 0.050 mmol), 2-bromo-1,4-bis(octyloxy)benzene (**4b**; 207 mg, 0.5 mmol), and 4′-(4-ethynylphenyl)-2,2′:6′,2′′-terpyridine (200 mg, 0.600 mmol) were reacted for 48 h. Further purification was achieved by column chromatography (neutral alumina, dichloromethane/*n*-hexane 1/2, then 1/1) to yield a white

solid (280 mg, 0.420 mmol, 84%). Mp: 65−67 °C. ^{1}H NMR (300 MHz, CDCl$_3$, ppm): δ 8.76 (s, 2H, H^{D3}), 8.73 (d, ^3J = 4.4 Hz, 2H, H^{C6}), 8.67 (d, ^3J = 8.0 Hz, 2H, H^{C3}), 7.95−7.83 (m, 4H, H^{E2}, H^{C4}), 7.67 (d, ^3J = 8.3 Hz, 2H, H^{E3}), 7.35 (ddd, ^3J = 7.5 Hz, ^3J = 4.8 Hz, ^4J = 1.2 Hz, 2H, H^{C5}), 7.06 (d, ^4J = 1.8 Hz, 1H, H^{F6}), 6.92−6.77 (m, 2H, H^{F4}, H^{F3}), 4.03 (t, ^3J = 6.4 Hz, 2H, α-OCH$_2$), 3.93 (t, ^3J = 6.5 Hz, 2H, α-OCH$_2$), 1.93−1.70 (m, 4H, β-CH$_2$), 1.63−1.20 (m, 20H, γ-η-CH$_2$), 0.98−0.78 (m, 6H, CH$_3$). ^{13}C NMR (75 MHz, CDCl$_3$, ppm): δ 156.3, 156.1, 154.4, 153.0, 149.6, 149.3, 138.0, 137.0, 132.2, 127.3, 124.7, 124.0, 121.5, 118.8, 118.5, 117.0, 114.3, 113.6, 93.1, 87.8, 70.0, 68.9, 32.99, 31.97, 29.6, 29.6, 29.5, 29.5, 29.4, 26.3, 26.2, 22.83, 22.81, 14.3. MS (MALDI-TOF, dithranol, m/z): 666.42, C$_{45}$H$_{52}$N$_3$O$_2$ ([M + H]$^+$) requires 666.41. Anal. Calcd for C$_{45}$H$_{51}$N$_3$O$_2$: C, 81.17; H, 7.72; N, 6.31. Found: C, 81.15; H, 8.07; N, 6.47. UV−vis (CH$_2$Cl$_2$): λ$_{max}$/nm (ε/L mol^{-1} cm^{-1}) 338 (27400), 292 (44300) nm.

General Procedure for Hydrazone Condensation Synthesis. A two-neck flask was loaded with benzophenone derivate **6** (1 equiv), p-toluenesulfonyl hydrazide (2 equiv), tosylic acid monohydrate (0.05 equiv), and THF or toluene and the mixture heated to reflux for 48 h under nitrogen. After the mixture was cooled to room temperature, the solvent was evaporated and the residue further purified by column chromatography (neutral alumina, chloroform/ethyl acetate 95/5). When applicable, deviations from this general protocol are given below.

[2,2′:6′,2″]Terpyridin-4′-ylbenzophenone p-Tosyl Hydrazone (7a). According to the general procedure for hydrazone condensation synthesis, 4‴-[2,2′:6′,2″]terpyridin-4′-yl-benzophenone (**6a**; 131 mg, 0.317 mmol), p-toluenesulfonyl hydrazide (118 mg, 0.634 mmol), and tosylic acid monohydrate (3 mg, 0.016 mmol) in toluene (10 mL) were reacted to yield a white solid (68 mg, 0.117 mmol, 37%). ^{1}H NMR suggests a mixture of cis- and trans-hydrazone isomers, which was used directly for the synthesis of **8a**. Mp: >240 °C dec. ^{1}H NMR (300 MHz, CDCl$_3$, ppm): δ 8.79−8.59 (m, 6H, H^{D3}, H^{C6}, H^{C3}), 7.98 (d, ^3J = 8.3 Hz, 1H, H^{E2}), 7.90 (d, ^3J = 8.2 Hz, 2H, Ar^{tosyl}-H), 7.92−7.75 (m, 4H, H^{C4}, H^{G2}), 7.59−7.46 (m, 4H, H^{E2}, H^{G3}, H^{G4}), 7.39−7.30 (m, 5H, NH, H^{C5}, Ar^{tosyl}-H), 7.29−7.24 (m, 1H, H^{E3}), 7.20−7.13 (m, 1H, H^{E3}), 2.43 (two singlets, 3H, Ar^{tosyl}-CH$_3$). ^{13}C NMR (75 MHz, CDCl$_3$, ppm): 156.27, 156.13, 156.07, 156.03, 153.92, 153.77, 149.41, 149.27, 149.20, 149.06, 144.42, 144.30, 140.54, 139.85, 137.14, 137.05, 136.48, 135.69, 135.59, 131.79, 131.06, 130.36, 130.09, 129.94, 129.85, 129.83, 129.17, 128.73, 128.46, 128.42, 128.26, 128.11, 128.09, 127.76, 127.24, 124.12, 124.02, 121.50, 119.01, 118.83, 21.77, 21.76. HRMS (ESI-TOF, m/z): 582.1903, C$_{35}$H$_{28}$N$_5$O$_2$S ([M + H]$^+$) requires 582.1958. Anal. Calcd for C$_{35}$H$_{27}$N$_5$O$_2$S·H$_2$O: C, 70.10; H, 4.87; N, 11.68; S, 5.35. Found: C, 69.93; H, 4.71; N, 11.32; S, 5.16.

2,5-Bis(octyloxy)-4-(4-[2,2′:6′,2″]terpyridin-4′-yl-phenylethynyl)-benzophenone p-Tosyl Hydrazone (7b). According to the general procedure for hydrazone condensation synthesis, 2,5-bis(octyloxy)-4-(4-[2,2′:6′,2″]terpyridin-4′-ylphenylethynyl)benzophenone (**6b**; 100 mg, 0.130 mmol), p-toluenesulfonyl hydrazide (48 mg, 0.260 mmol), and tosylic acid monohydrate (1.2 mg, 6.5 μmol) were reacted in THF (10 mL) for 11 days. The reaction was monitored by MALDI-TOF MS. After 6 days, additional p-toluenesulfonyl hydrazide (1 equiv) and tosylic acid monohydrate (0.1 equiv) were added. After purification by column chromatography (neutral alumina, chloroform) and recrystallization (n-hexane), a white solid (74 mg, 0.079 mmol, 61%) was obtained. ^{1}H NMR suggests a mixture of cis- and trans-hydrazone isomers, which was used directly for the synthesis of **8b**. Mp: 83 °C. ^{1}H NMR (300 MHz, CDCl$_3$, ppm): δ 8.81−8.65 (m, 6H, H^{D3}, H^{C6}, H^{C3}), 8.01−7.84 (m, 6H, Ar^{tosyl}-H, H^{E2}, H^{C4}), 7.77 (s, 1H, NH), 7.70 (d, ^3J = 8.4 Hz, 2H, H^{E3}), 7.57−7.47 (m, 2H, H^{G2}), 7.42−7.27 (m, 7H, H^{C5}, H^{G3}, H^{G4}, Ar^{tosyl}-H), 7.16 (s, 1H, H^{F3}), 6.51 (s, 1H, H^{F6}), 3.91 (t, ^3J = 6.4 Hz, 2H, α-OCH$_2$), 3.79 (t, ^3J = 6.3 Hz, 2H, α-OCH$_2$), 2.41 (s, 3H, Ar^{tosyl}-CH$_3$), 1.75−1.46 (m, 4H, β-CH$_2$), 1.46−0.93 (m, 20H, γ-η-CH$_2$), 0.95−0.78 (m, 6H, CH$_3$); ^{13}C NMR (75 MHz, CDCl$_3$, ppm): δ 156.26, 156.22, 154.69, 151.75, 149.48, 149.42, 149.28, 143.92, 138.56, 137.04, 136.66, 136.04, 132.35, 129.77, 129.68, 129.62, 129.18, 128.34, 128.32, 128.13, 127.53, 127.43, 127.37, 124.05, 121.64, 121.52, 118.79, 118.20, 115.91, 113.78, 94.86, 86.70, 69.85, 69.82, 32.00, 31.94, 31.84, 29.49, 29.44, 29.40, 29.26, 29.20, 28.93, 26.18,

25.65, 22.81, 22.76, 21.72, 14.23, 14.22. MS (MALDI-TOF, dithranol, m/z): 938.43, C$_{59}$H$_{64}$N$_5$O$_4$S ([M + H]$^+$) requires 938.47.

Bis(4‴,4‴′′-[2,2′:6′,2″]terpyridin-4′-yl)benzophenone p-Tosyl Hydrazone (7c). According to the general procedure for hydrazone condensation synthesis, bis(4‴,4‴′′-[2,2′:6′,2″]terpyridin-4′-yl)-benzophenone (**6c**; 120 mg, 0.186 mmol), p-toluenesulfonyl hydrazide (69 mg, 0.372 mmol), and tosylic acid monohydrate (2 mg, 0.011 mmol) were reacted in toluene (10 mL) to yield a white solid (60 mg, 0.074 mmol, 40%). Mp >240 °C dec. ^{1}H NMR (300 MHz, CDCl$_3$, ppm): δ 8.79−8.61 (m, 12H, H^{D3}, H^{C6}, H^{C3}), 8.26−8.14 (m, 1H, NH), 8.02−7.94 (m, 4H, H^{E2}), 7.93−7.81 (m, 4H, H^{C4}), 7.77 (d, ^3J = 8.5 Hz, 2H, Ar^{tosyl}-H), 7.59 (d, ^3J = 8.4 Hz, 2H, Ar^{tosyl}-H), 7.44−7.28 (m, 8H, H^{E3}, H^{C5}), 2.45 (s, 3H, Ar^{tosyl}-CH$_3$). ^{13}C NMR (75 MHz, CDCl$_3$, ppm): δ 156.29, 156.13, 156.07, 153.32, 149.39, 149.30, 149.23, 149.08, 144.53, 140.68, 139.92, 137.07, 135.68, 131.60, 129.95, 129.28, 128.76, 128.35, 128.21, 127.30, 124.12, 124.03, 121.54, 121.50, 119.09, 118.87, 29.83; MS (MALDI-TOF, dithranol, m/z): 813.29, C$_{50}$H$_{37}$N$_8$O$_2$S ([M + H]$^+$) requires 813.28.

General Procedure for Methanofullerene Synthesis. To a solution of the p-tosyl hydrazone derivate **7** (1 equiv) in anhydrous pyridine (3 mL) was added sodium methoxide (1.1 equiv) under a nitrogen atmosphere. After the mixture was stirred at room temperature for 15 min, a nitrogen-purged solution of C$_{60}$ (3−4 equiv) in o-dichlorobenzene (15 mL) was added at once and the mixture was heated to 180 °C for 24 h. After it was cooled to room temperature, the reaction mixture was purified by column chromatography (neutral alumina, toluene/n-hexane 1/1) and precipitation in methanol.

1-Phenyl-1-(4-[2,2′:6′,2″]terpyridin-4′-ylphenyl)methanofullerene (8a). According to the general procedure for methanofullerene synthesis, [2,2′:6′,2″]terpyridin-4′-yl-benzophenone p-tosyl hydrazone (**7a**; 60 mg, 0.103 mmol), sodium methoxide (6 mg, 0.111 mmol), and C$_{60}$ (276 mg, 0.383 mmol) were reacted to yield a brown solid (32 mg, 0.029 mmol, 28%). Mp: >360 °C. ^{1}H NMR (300 MHz, CDCl$_3$, ppm): δ 8.79 (s, 2H, H^{D3}), 8.73 (d, ^3J = 4.8 Hz, 2H, H^{C6}), 8.69 (d, ^3J = 7.9 Hz, 2H, H^{C3}), 8.27 (d, ^3J = 8.3 Hz, 2H, H^{E2}), 8.22−8.15 (m, 2H, H^{G2}), 8.02 (d, ^3J = 8.3 Hz, 2H, H^{E3}), 7.90 (td, ^3J = 7.8 Hz, ^4J = 1.8 Hz, 2H, H^{C4}), 7.53 (t, ^3J = 7.5 Hz, 2H, H^{G3}), 7.46−7.33 (m, 3H, H^{G4}, H^{C5}). MS (MALDI-TOF, negative mode, terthiophene, m/z): 1117.14, C$_{88}$H$_{19}$N$_3$ ([M + e]$^-$) requires 1117.16. Anal. Calcd for C$_{88}$H$_{19}$N$_3$·2.5H$_2$O·3(hexane): C, 89.55; H, 4.68; N, 2.96. Found: C, 89.57; H, 4.51; N, 3.01.

1-Phenyl-1-(2,5-Bis(octyloxy)-4-(4-[2,2′:6′,2″]terpyridin-4′-ylphenylethynyl))methanofullerene (8b). According to the general procedure for methanofullerene synthesis, 2,5-bis(octyloxy)-4-(4-[2,2′:6′,2″]terpyridin-4′-ylphenylethynyl)benzophenone p-tosyl hydrazone (**7b**; 57 mg, 0.061 mmol), sodium methoxide (4 mg, 0.074 mmol), and C$_{60}$ (175 mg, 0.243 mmol) were reacted to yield a dark brown solid (24 mg, 0.016 mmol, 27%). Mp: 148 °C. ^{1}H NMR (300 MHz, CDCl$_3$, ppm): δ 8.76 (s, 2H, H^{D3}), 8.74 (d, ^3J = 4.8 Hz, 2H, H^{C6}), 8.68 (d, ^3J = 7.9 Hz, 2H, H^{C3}), 8.24 (d, ^3J = 7.1 Hz, 2H, H^{G2}), 7.96−7.82 (m, 4H, H^{E2}, H^{C4}), 7.68 (d, ^3J = 8.2 Hz, 2H, H^{E3}), 7.64 (s, 1H, H^{F6}), 7.50 (t, ^3J = 7.3 Hz, 2H, H^{G3}), 7.46−7.38 (m, 1H, H^{G4}), 7.36 (dd, ^3J = 6.8 Hz, ^3J = 5.4 Hz, 2H, H^{C5}), 7.18 (s, 1H, H^{F3}), 4.27−3.98 (m, 4H, α-OCH$_2$), 2.13−1.99 (m, 2H, β-CH$_2$), 1.93−1.78 (m, 2H, β-CH$_2$), 1.75−1.10 (m, 20H, γ-η-CH$_2$), 0.97−0.79 (m, 6H, CH$_3$). MS (MALDI-TOF, negative mode, terthiophene, m/z): 1473.38, C$_{112}$H$_{55}$N$_3$O$_2$ ([M + e]$^-$) requires 1473.43. Anal. Calcd for C$_{112}$H$_{55}$N$_3$O$_2$·8H$_2$O: C, 83.10; H, 4.42%; N, 2.60. Found: C, 83.34; H, 4.47; N, 2.49.

1,1-Bis(4-[2,2′:6′,2″]terpyridin-4′-ylphenyl)methanofullerene (8c). According to the general procedure for methanofullerene synthesis, bis(4‴,4‴′′-[2,2′:6′,2″]terpyridin-4′-yl)benzophenone p-tosyl hydrazone (**7c**; 60 mg, 0.074 mmol), sodium methoxide (4 mg, 0.074 mmol), and C$_{60}$ (227 mg, 0.315 mmol) were reacted to yield a brown solid (30 mg, 0.022 mmol, 30%). Mp: >360 °C. ^{1}H NMR (300 MHz, CDCl$_3$, ppm): δ 8.79 (s, 4H, H^{D3}), 8.73 (d, ^3J = 4.0 Hz, 4H, H^{C6}), 8.68 (d, ^3J = 8.0 Hz, 4H, H^{C3}), 8.31 (d, ^3J = 8.2 Hz, 4H, H^{E2}), 8.04 (d, ^3J = 8.2 Hz, 4H, H^{E3}), 7.88 (td, ^3J = 7.7 Hz, ^4J = 1.7 Hz, 4H, H^{C4}), 7.35 (ddd, ^3J = 7.4 Hz, ^3J = 4.8 Hz, ^4J = 0.9 Hz, 4H, H^{C5}). MS (MALDI-

TOF, negative mode, terthiophene, m/z): 1348.23, $C_{103}H_{28}N_6$ ([M + e]⁻) requires 1348.24. Anal. Calcd for $C_{103}H_{28}N_6\cdot 4H_2O\cdot 5$(hexane): C, 86.24; H, 5.77; N, 4.54. Found: C, 86.11; H, 5.48; N, 4.44.

N-Methyl-2-(4-[2,2':6',2″]terpyridin-4'-ylphenyl)-pyrrolidinofullerene (10a). A mixture of (4-formylphenyl)-2,2':6',2″-terpyridine (**9a**; 33 mg, 0.098 mmol), N-methylglycine (87 mg, 0.978 mmol), and C_{60} (282 mg, 0.391 mmol) in deaerated, anhydrous toluene (200 mL) was stirred at 120 °C for 24 h under a nitrogen atmosphere. After the mixture was cooled to room temperature, the solvent was evaporated. The crude product was purified by column chromatography (neutral alumina, toluene then chloroform), and slow vapor diffusion of diethyl ether into a concentrated solution yielded a brown solid (26.5 mg, 0.024 mmol, 25%). Mp: >360 °C. ^{1}H NMR (300 MHz, CDCl₃, ppm): δ 8.74 (s, 2H, H^{D3}), 8.72 (d, ^3J = 4.8 Hz, 2H, H^{C6}), 8.67 (d, ^3J = 7.9 Hz, 2H, H^{C3}), 8.00−7.93 (m, 4H, H^{E2}, H^{E3}), 7.87 (td, ^3J = 7.8 Hz, ^4J = 1.7 Hz, 2H, H^{C4}), 7.35 (ddd, ^3J = 7.5 Hz, ^3J = 4.8 Hz, ^4J = 1.1 Hz, 2H, H^{C5}), 5.02 (d, ^2J = 9.2 Hz, 1H, H^{H5}), 5.02 (s, 1H, H^{H2}), 4.30 (d, ^2J = 9.5 Hz, 1H, H^{H5}), 2.85 (s, 3H, NCH₃). MS (MALDI-TOF, negative mode, terthiophene, m/z): 1083.26, $C_{84}H_{19}N_4$ ([M − H]⁻) requires 1083.16. Anal. Calcd for $C_{84}H_{20}N_4\cdot 6H_2O$: C, 84.56; H, 2.70; N, 4.70. Found: C, 84.26; H, 2.44; N, 5.40.

N-Methyl-2-(2,5-Bis(octyloxy)-4-(4-[2,2':6',2″]terpyridin-4'-ylphenylethynyl))pyrrolidinofullerene (10b). A mixture of 2,5-bis-(octyloxy)-4-(4-[2,2':6',2″]-terpyridin-4'-ylphenylethynyl)-benzaldehyde (**9b**; 69 mg, 0.1 mmol), N-methylglycine (89 mg, 1.0 mmol), and C_{60} (144 mg, 0.2 mmol) in deaerated, anhydrous toluene (200 mL) was stirred at 120 °C for 24 h under a nitrogen atmosphere. After the mixture was cooled to room temperature, the solvent was evaporated. The crude product was purified by column chromatography (neutral alumina, n-hexane/toluene 3/1 then toluene) to yield a dark brown-black solid (101 mg, 0.07 mmol, 70%). Mp: 155 °C. ^{1}H NMR (400 MHz, CD₂Cl₂, ppm): δ 8.77 (s, 2H, H^{D3}), 8.71 (d, ^3J = 4.7 Hz, 2H, H^{C6}), 8.68 (d, ^3J = 7.9 Hz, 2H, H^{C3}), 7.93−7.86 (m, 4H, H^{E2}, H^{C4}), 7.67 (d, ^3J = 8.5 Hz, 2H, H^{E3}), 7.65 (s, 1H, H^{F5}), 7.37 (ddd, ^3J = 7.4 Hz, ^3J = 4.8 Hz, ^4J = 1.1 Hz, 2H, H^{C5}), 7.09 (s, 1H, H^{F2}), 5.58 (s, 1H, H^{H2}), 4.97 (d, ^2J = 9.4 Hz, 1H, H^{H5}), 4.33 (d, ^2J = 9.5 Hz, 1H, H^{H5}), 4.20 (dt, ^2J = 9.5 Hz, ^3J = 6.6 Hz, 1H, α-OCH₂), 4.10 (dt, ^2J = 9.6 Hz, ^3J = 6.4 Hz, 1H, α-OCH₂), 4.03 (dt, ^2J = 13.1 Hz, ^3J = 6.5 Hz, 1H, α-OCH₂), 3.74 (dt, ^2J = 8.6 Hz, ^3J = 6.5 Hz, 1H, α-OCH₂), 2.83 (s, 3H, NCH₃), 1.87−1.76 (m, 2H, β-CH₂), 1.73−1.49 (m, 6H, β-CH₂, γ-CH₂), 1.48−1.17 (m, 16H, δ-η-CH₂), 0.96−0.73 (m, 6H, CH₃). ^{13}C NMR (100 MHz, CD₂Cl₂, ppm): δ 157.34, 156.51, 156.39, 155.57, 154.70, 154.68, 154.36, 152.03, 149.59, 149.58, 147.66, 147.22, 147.15, 146.62, 146.60, 146.56, 146.47, 146.43, 146.41, 146.32, 146.31, 146.14, 145.99, 145.90, 145.66, 145.64, 145.60, 145.58, 145.54, 145.48, 144.97, 144.92, 144.85, 144.72, 143.40, 143.36, 143.03, 142.99, 142.91, 142.74, 142.70, 142.62, 142.57, 142.50, 142.49, 142.47, 142.34, 142.19, 142.10, 142.08, 140.50, 140.45, 139.97, 139.91, 137.24, 136.83, 136.76, 136.54, 135.09, 132.45, 128.24, 127.65, 124.72, 124.34, 121.50, 118.88, 116.49, 115.24, 113.12, 93.52, 88.23, 77.05, 76.00, 70.33, 70.17, 69.77, 69.21, 40.24, 32.35, 32.32, 30.11, 29.93, 29.90, 29.82, 29.74, 29.73, 29.67, 26.55, 26.48, 23.19, 23.14, 21.55, 14.40, 14.35. MS (MALDI-TOF, negative mode, terthiophene, m/z): 1440.42, $C_{108}H_{56}N_4O_2$ ([M + e]⁻) requires 1440.44. Anal. Calcd for $C_{108}H_{56}N_4O_2\cdot 0.5$(hexane): C, 89.79; H, 4.28; N, 3.77. Found: C, 89.78; H, 4.43; N, 3.83.

General Procedure for the Synthesis of Heteroleptic Ruthenium Bis(terpyridine) Complexes. A microwave vial was charged with $[Ru(tpy)(MeCN)_3](PF_6)_2$ (1 equiv per terpyridine group), terpyridine derivative (1 equiv), and DMF (3 mL). The vial was capped, purged with nitrogen for 20 min, and heated through microwave irradiation at 140 °C for 30 min. Subsequently, the solution was cooled to room temperature and the product was precipitated by addition of an aqueous ammonium hexafluorophosphate solution. The solid was collected by filtration, washed thoroughly with water and diethyl ether, and dissolved in acetonitrile. The solution was concentrated and treated with diethyl ether vapor to slowly precipitate the complex. When applicable, deviations from this general protocol are given below.

[Ru(tpy)(8a)](PF₆)₂ (1a). According to the general procedure for heteroleptic ruthenium bis(terpyridine) complexes, $[Ru(tpy)-(MeCN)_3](PF_6)_2$ (6.4 mg, 8.5 μmol) and **8a** (9.4 mg, 8.4 μmol) were reacted to yield a dark red solid (6 mg, 3.4 μmol, 41%). ^{1}H NMR (400 MHz, CD₃CN, ppm): δ 9.02 (s, 2H, H^{D3}), 8.75 (d, ^3J = 8.2 Hz, 2H, H^{B3}), 8.69−8.57 (m, 4H, H^{E2}, H^{C3}), 8.48 (d, ^3J = 8.1 Hz, 2H, H^{A3}), 8.41 (t, ^3J = 8.1 Hz, 1H, H^{B4}), 8.35 (d, ^3J = 7.2 Hz, 4H, H^{G2}, H^{E3}), 8.00−7.80 (m, 4H, H^{C4}, H^{A4}), 7.61−7.48 (m, 2H, H^{G3}), 7.49−7.39 (m, 1H, H^{G4}), 7.38−7.30 (m, 4H, H^{A6}, H^{C6}), 7.21−7.01 (m, 4H, H^{C5}, H^{A5}). ^{13}C NMR (100 MHz, CD₃CN, ppm): δ 159.05, 159.00, 156.47, 156.28, 153.58, 153.22, 149.57, 149.52, 148.25, 146.94, 146.80, 146.20, 145.72, 145.70, 145.61, 145.36, 145.27, 144.83, 143.96, 143.89, 143.17, 143.08, 142.46, 141.83, 139.77, 139.10, 139.01, 138.84, 138.69, 137.71, 136.89, 133.19, 132.11, 130.11, 129.73, 129.38, 128.52, 128.47, 125.49, 124.76, 122.70, 80.14, 58.87. HRMS (ESI-TOF, m/z): 726.0829, $C_{103}H_{30}N_6Ru$ ([M − $2PF_6$]²⁺) requires 726.0785.

[Ru(tpy)(8b)](PF₆)₂ (1b). According to the general procedure for heteroleptic ruthenium bis(terpyridine) complexes, $[Ru(tpy)-(MeCN)_3](PF_6)_2$ (6.4 mg, 8.5 μmol) and **8b** (9 mg, 6.1 μmol) were reacted to yield a dark red solid (4 mg, 1.9 μmol, 31%). ^{1}H NMR (300 MHz, CD₃CN, ppm): δ 8.96 (s, 2H, H^{D3}), 8.75 (d, ^3J = 8.2 Hz, 2H, H^{B3}), 8.59 (d, ^3J = 7.3 Hz, 2H, 2H, H^{C3}), 8.49 (d, ^3J = 8.3 Hz, 2H, H^{A3}), 8.41 (t, ^3J = 8.1 Hz, 1H, H^{B4}), 8.35 (d, ^3J = 5.8 Hz, 2H, H^{G2}), 8.21 (d, ^3J = 7.5 Hz, 2H, H^{E2}), 7.99−7.78 (m, 7H, H^{E3}, H^{F6}, H^{C4}, H^{A4}), 7.56−7.39 (m, 3H, H^{G3}, H^{G4}), 7.39 (d, ^3J = 5.2 Hz, 2H, H^{A6}), 7.34 (d, ^3J = 5.3 Hz, 2H, H^{C6}), 7.25 (s, 1H, H^{F3}), 7.21−7.07 (m, 4H, H^{C5}, H^{A5}), 4.29−4.10 (m, 3H, α-OCH₂), 4.08−3.92 (m, 1H, α-OCH₂), 1.85−1.59 (m, 4H, β-CH₂), 1.55−1.02 (m, 20H, γ-η-CH₂), 0.91−0.67 (m, 6H, CH₃). HRMS (ESI-TOF, m/z): 904.2109, $C_{127}H_{66}N_6O_2Ru$ ([M − $2PF_6$]²⁺) requires 904.2143.

[Ru₂(tpy)₂(8c)](PF₆)₄ (1c). According to the general procedure for heteroleptic ruthenium bis(terpyridine) complexes, $[Ru(tpy)-(MeCN)_3](PF_6)_2$ (9.7 mg, 13 μmol) and **8c** (8.7 mg, 6.5 μmol) were reacted to yield a dark red solid (8 mg, 3.1 μmol, 48%). ^{1}H NMR (300 MHz, CD₃CN, ppm): δ 9.08 (s, 4H, H^{D3}), 8.80 (d, ^3J = 8.1 Hz, 4H, H^{E2}), 8.75 (d, ^3J = 8.2 Hz, 4H, H^{B3}), 8.67 (d, ^3J = 7.9 Hz, 4H, H^{C3}), 8.54−8.37 (m, 10H, H^{A3}, H^{E3}, H^{B4}), 8.00−7.86 (m, 8H, H^{C4}, H^{A4}), 7.42 (d, ^3J = 5.2 Hz, 4H, H^{A6}), 7.36 (d, ^3J = 5.2 Hz, 4H, H^{C6}), 7.23−7.10 (m, 8H, H^{C5}, H^{A5}). ^{13}C NMR (63 MHz, CD₃CN, ppm): δ 159.07, 156.56, 156.33, 153.58, 153.32, 149.39, 148.32, 146.92, 146.27, 146.24, 145.74, 145.68, 145.46, 144.86, 144.05, 143.98, 143.15, 143.07, 141.96, 141.91, 139.13, 139.06, 138.81, 138.09, 136.89, 133.46, 129.54, 128.54, 128.49, 125.58, 125.47, 124.76, 122.76, 79.99, 58.28. HRMS (ESI-TOF, m/z): 504.5643, $C_{133}H_{50}N_{12}Ru_2$ ([M − $4PF_6$]⁴⁺) requires 504.5599.

[Ru(tpy)(10a)](PF₆)₂ (2a). According to the general procedure for heteroleptic ruthenium bis(terpyridine) complexes, $[Ru(tpy)-(MeCN)_3](PF_6)_2$ (8.9 mg, 12 μmol) and **10a** (13 mg, 12 μmol) were reacted to yield a dark red solid (7 mg, 4.1 μmol, 34%). ^{1}H NMR (300 MHz, CD₃CN, ppm): δ 9.00 (s, 2H, H^{D3}), 8.74 (d, ^3J = 8.2 Hz, 2H, H^{B3}), 8.62 (d, ^3J = 7.8 Hz, 2H, H^{C3}), 8.48 (d, ^3J = 8.1 Hz, 2H, H^{A3}), 8.40 (t, ^3J = 8.5 Hz, 1H, H^{B4}), 8.34−8.19 (m, 4H, H^{E2}, H^{E3}), 7.98−7.86 (m, 4H, H^{C4}, H^{A4}), 7.40 (d, ^3J = 5.5 Hz, 2H, H^{A6}), 7.32 (d, ^3J = 5.1 Hz, 2H, H^{C6}), 7.21−7.08 (m, 4H, H^{C5}, H^{A5}), 5.29 (s, 1H, H^{H2}), 5.14 (d, ^2J = 9.5 Hz, 1H, H^{H5}), 4.44 (d, ^2J = 9.7 Hz, 1H, H^{H5}), 2.91 (s, 3H, NCH₃). HRMS (ESI-TOF, m/z): 709.5853, $C_{99}H_{31}N_7Ru$ ([M − $2PF_6$]²⁺) requires 709.5839.

[Ru(tpy)(10b)](PF₆)₂ (2b). According to the general procedure for heteroleptic ruthenium bis(terpyridine) complexes, $[Ru(tpy)-(MeCN)_3](PF_6)_2$ (15.6 mg, 21 μmol) and **10b** (30 mg, 21 μmol) were reacted to yield a dark red solid (23 mg, 11 μmol, 54%). ^{1}H NMR (400 MHz, CD₂Cl₂, ppm): δ 8.83 (s, 2H, H^{D3}), 8.69 (d, ^3J = 8.1 Hz, 2H, H^{B3}), 8.51 (d, ^3J = 7.8 Hz, 2H, H^{C3}), 8.48−8.36 (m, 3H, H^{B4}, H^{A3}), 8.12 (d, ^3J = 8.0 Hz, 2H, H^{E2}), 7.99−7.87 (m, 4H, H^{C4}, H^{A4}), 7.86 (d, ^3J = 7.9 Hz, 2H, H^{E3}), 7.69 (s, 1H, H^{F5}), 7.39 (d, ^3J = 5.4 Hz, 2H, H^{A6}), 7.32 (d, ^3J = 5.7 Hz, 2H, H^{C6}), 7.26−7.17 (m, 4H, H^{C5}, H^{A5}), 7.14 (s, 1H, H^{F2}), 5.61 (s, 1H, H^{H2}), 5.01 (d, ^2J = 9.6 Hz, 1H, H^{H5}), 4.37 (d, ^2J = 9.4 Hz, 1H, H^{H5}), 4.28−4.18 (m, 1H, α-OCH₂), 4.18−4.09 (m, 1H, α-OCH₂), 4.10−4.00 (m, 1H, α-OCH₂), 3.82−3.71 (m, 1H, α-OCH₂), 2.86 (s, 3H, NCH₃), 1.90−1.78 (m, 2H, β-CH₂), 1.73−1.12 (m, 22H, β-CH₂, γ-η-CH₂), 0.94−0.75 (m, 6H, CH₃). ^{13}C NMR (100 MHz, DMSO-d_6, ppm): δ 157.91, 157.74,

157.04, 155.14, 155.00, 154.72, 154.25, 153.91, 153.54, 152.13, 152.07, 151.16, 146.80, 146.69, 146.62, 146.35, 145.74, 145.68, 145.65, 145.63, 145.57, 145.42, 145.25, 145.08, 144.99, 144.79, 144.71, 144.55, 144.49, 144.13, 143.98, 143.92, 143.85, 142.54, 142.16, 142.07, 141.89, 141.84, 141.75, 141.63, 141.49, 141.32, 141.21, 141.11, 139.65, 139.55, 139.43, 138.87, 138.77, 138.14, 138.04, 137.92, 135.85, 135.78, 135.56, 134.34, 133.52, 131.95, 129.63, 129.59, 127.92, 127.79, 127.70, 127.63, 124.88, 124.85, 124.84, 124.58, 124.56, 124.54, 124.02, 120.93, 120.91, 116.41, 114.44, 114.43, 114.40, 112.16, 109.46, 93.04, 88.81, 76.32, 75.05, 69.10, 69.06, 68.47, 40.43, 31.36, 31.30, 29.03, 28.95, 28.80, 28.73, 28.39, 25.49, 25.45, 22.25, 22.13, 14.05, 14.01. HRMS (ESI-TOF, m/z): 887.7307, $C_{123}H_{67}N_7O_2Ru$ ([M − 2PF$_6$]$^{2+}$) requires 887.7212.

[Ru(tpy)(ttpy)](PF$_6$)$_2$ (3a). According to the general procedure for heteroleptic ruthenium bis(terpyridine) complexes, [Ru(tpy)-(MeCN)$_3$](PF$_6$)$_2$ (58.5 mg, 0.078 mmol) and ttpy (25.3 mg, 0.078 mmol) were reacted in ethanol (5 mL) at 130 °C. Subsequently, the solvent was evaporated and the resulting residue was purified by column chromatography (silica, MeCN/H$_2$O/saturated aqueous KNO$_3$ solution 40/4/1). Concentration of the product fraction in vacuo and precipitation by addition of an aqueous ammonium hexafluorophosphate solution yielded a red solid (56 mg, 0.059 mmol, 76%). ^{1}H NMR (300 MHz, CD$_3$CN, ppm): δ 8.99 (s, 2H, H^{D3}), 8.76 (d, ^3J = 8.1 Hz, 2H, H^{B3}), 8.64 (d, ^3J = 8.1 Hz, 2H, H^{C3}), 8.50 (d, ^3J = 8.1 Hz, 2H, H^{A3}), 8.41 (t, ^3J = 8.1 Hz, 1H, H^{B4}), 8.11 (d, ^3J = 8.1 Hz, 2H, H^{E2}), 8.00−7.87 (m, 4H, H^{C4}, H^{A4}), 7.58 (d, ^3J = 7.9 Hz, 2H, H^{E3}), 7.43 (d, ^3J = 5.5 Hz, 2H, H^{A6}), 7.35 (d, ^3J = 5.4 Hz, 2H, H^{C6}), 7.22−7.11 (m, 4H, H^{C5}, H^{A5}), 2.54 (s, 3H, Ph−CH$_3$). ^{13}C NMR (75 MHz, CD$_3$CN, ppm): δ 159.20, 159.08, 156.41, 156.38, 153.54, 153.36, 149.42, 142.07, 139.05, 139.01, 136.71, 134.91, 131.30, 128.67, 128.46, 128.42, 125.48, 125.40, 124.70, 122.37, 21.43. Anal. Calcd for $C_{37}H_{28}F_{12}N_6P_2Ru$: C, 46.89; H, 2.98; N, 8.87. Found: C, 46.53; H, 3.02; N, 8.76.

[Ru(tpy)(11b)](PF$_6$)$_2$ (3b). A mixture of [Ru(tpy)]Cl$_3$ (4.4 mg, 10 μmol) and silver(I) tetrafluoroborate (5.8 mg, 30 μmol) in deaerated acetone (3 mL) was heated to 70 °C for 2 h. After cooling and filtration, DMF (2 mL) was added to the filtrate and the acetone was removed in vacuo. The resulting blue solution of [Ru(tpy)(acetone)$_3$]-(BF$_4$)$_3$ was added to a solution of 4′-(4-((2,5-Bis(octyloxy)phenyl)-ethynyl)phenyl)-2,2′:6′,2″-terpyridine (11b; 20 mg, 14 μmol) in DMF (3 mL), and the mixture was heated to 160 °C for 3 h. Subsequently, the reaction mixture was cooled to room temperature and a solid was precipitated by addition of an aqueous ammonium hexafluorophosphate solution. After filtration, the solid was further purified by column chromatography (silica, MeCN/H$_2$O/saturated aqueous KNO$_3$ solution 40/4/1). Concentration of the product fraction in vacuo and precipitation by addition of an aqueous ammonium hexafluorophosphate solution yielded a red solid (10 mg, 7.8 μmol, 78%). ^{1}H NMR (300 MHz, CD$_3$CN, ppm): δ 9.01 (s, 2H, H^{D3}), 8.76 (d, ^3J = 8.2 Hz, 2H, H^{B3}), 8.65 (d, ^3J = 8.0 Hz, 2H, H^{C3}), 8.50 (d, ^3J = 8.0 Hz, 2H, H^{A3}), 8.42 (t, ^3J = 8.1 Hz, 1H, H^{B4}), 8.25 (d, ^3J = 8.5 Hz, 2H, H^{E2}), 8.00−7.84 (m, 6H, H^{C4}, H^{A4}, H^{E3}), 7.42 (d, ^3J = 4.9 Hz, 2H, H^{A6}), 7.36 (d, ^3J = 4.9 Hz, 2H, H^{C6}), 7.22−7.13 (m, 4H, H^{C5}, H^{A5}), 7.09 (d, ^4J = 2.4 Hz, 1H, H^{F6}), 7.02−6.90 (m, 2H, H^{F4}, H^{F3}), 4.08 (t, ^3J = 6.3 Hz, 2H, α-OCH$_2$), 3.97 (t, ^3J = 6.5 Hz, 2H, α-OCH$_2$), 1.91−1.68 (m, 4H, β-CH$_2$), 1.67−1.21 (m, 20H, γ-η-CH$_2$), 1.01−0.80 (m, 6H, CH$_3$). ^{13}C NMR (75 MHz, CD$_3$CN, ppm): δ 159.09, 159.05, 156.6, 156.3, 155.2, 153.9, 153.6, 153.4, 148.2, 139.12, 139.07, 137.4, 136.9, 133.4, 129.0, 128.5, 128.5, 126.5, 125.6, 125.4, 124.7, 122.4, 119.5, 118.1, 115.3, 113.7, 93.2, 89.7, 70.4, 69.6, 32.61, 32.59, 30.2, 30.14, 30.11, 30.07, 30.04, 30.02, 26.9, 26.7, 23.5, 23.4, 14.5, 14.4. HRMS (ESI-TOF, m/z): 500.1984, $C_{60}H_{62}N_6O_2Ru$ ([M − 2PF$_6$]$^{2+}$) requires 500.1992.

■ ASSOCIATED CONTENT

ⓢ Supporting Information

Figures S1−S62, giving cyclic voltammograms, absorption and emission spectra, time-resolved data, DFT calculations, NMR data, and MS spectra. This material is available free of charge via the Internet at http://pubs.acs.org.

■ AUTHOR INFORMATION

Corresponding Authors
*E-mail for B.D.: benjamin.dietzek@ipht-jena.de.
*E-mail for U.S.S.: ulrich.schubert@uni-jena.de.

Author Contributions
$^{\perp}$The manuscript was written through contributions of all authors. All authors have given approval to the final version of the manuscript. These authors contributed equally.

Notes
The authors declare no competing financial interest.

■ REFERENCES

(1) Artero, V.; Chavarot-Kerlidou, M.; Fontecave, M. *Angew. Chem., Int. Ed.* 2011, 50, 7238.
(2) Andreiadis, E. S.; Chavarot-Kerlidou, M.; Fontecave, M.; Artero, V. *Photochem. Photobiol.* 2011, 87, 946.
(3) Artero, V.; Fontecave, M. *Coord. Chem. Rev.* 2005, 249, 1518.
(4) Natali, M.; Campagna, S.; Scandola, F. *Chem. Soc. Rev.* 2014, 43, 4005.
(5) Sartorel, A.; Bonchio, M.; Campagna, S.; Scandola, F. *Chem. Soc. Rev.* 2013, 42, 2262.
(6) Carraro, M.; Sartorel, A.; Toma, F. M.; Puntoriero, F.; Scandola, F.; Campagna, S.; Prato, M.; Bonchio, M. *Top. Curr. Chem.* 2011, 303, 121.
(7) Barber, J.; Tran, P. D. *J. R. Soc. Interface* 2013, 10.
(8) Gust, D.; Moore, T. A.; Moore, A. L. *Acc. Chem. Res.* 2001, 34, 40.
(9) Berardi, S.; Drouet, S.; Francàs, L.; Gimbert-Suriñach, C.; Guttentag, M.; Richmond, C.; Stoll, T.; Llobet, A. *Chem. Soc. Rev.* 2014, 43, 7501.
(10) Sun, L.; Gao, Y.; Yu, Z.; Ding, X.; Duan, L. *Faraday Discuss.* 2014, DOI: 10.1039/c4fd00127c.
(11) Fukuzumi, S.; Ohkubo, K.; Suenobu, T. *Acc. Chem. Res.* 2014, 47, 1455.
(12) Wenger, O. S. *Chem. Soc. Rev.* 2011, 40, 3538.
(13) Schubert, C.; Wielopolski, M.; Mewes, L. H.; de Miguel Rojas, G.; van der Pol, C.; Moss, K. C.; Bryce, M. R.; Moser, J. E.; Clark, T.; Guldi, D. M. *Chem. Eur. J.* 2013, 19, 7575.
(14) Guldi, D. M.; Maggini, M.; Scorrano, G.; Prato, M. *J. Am. Chem. Soc.* 1997, 119, 974.
(15) Guldi, D. M. *Chem. Soc. Rev.* 2002, 31, 22.
(16) Wielopolski, M.; Atienza, C.; Clark, T.; Guldi, D. M.; Martín, N. *Chem. Eur. J.* 2008, 14, 6379.
(17) Wielopolski, M.; Santos, J.; Illescas, B. M.; Ortiz, A.; Insuasty, B.; Bauer, T.; Clark, T.; Guldi, D. M.; Martín, N. *Energy Environ. Sci.* 2011, 4, 765.
(18) Ventura, B.; Barbieri, A.; Zanelli, A.; Barigelletti, F.; Seneclauze, J. B.; Diring, S.; Ziessel, R. *Inorg. Chem.* 2009, 48, 6409.
(19) Liu, Y. F.; Zhao, J. Z. *Chem. Commun.* 2012, 48, 3751.
(20) Martín, N.; Sánchez, L.; Illescas, B.; Pérez, I. *Chem. Rev.* 1998, 98, 2527.
(21) Armaroli, N. *Photochem. Photobiol. Sci.* 2003, 2, 73.
(22) Medlycott, E. A.; Hanan, G. S. *Chem. Soc. Rev.* 2005, 34, 133.
(23) Medlycott, E. A.; Hanan, G. S. *Coord. Chem. Rev.* 2006, 250, 1763.
(24) *Photochemistry and Photophysics of Coordination Compounds I*; Balzani, V., Campagna, S., Eds.; Springer: Berlin/Heidelberg, 2007.

(25) Armaroli, N.; Accorsi, G.; Felder, D.; Nierengarten, J. F. *Chem. Eur. J.* **2002**, *8*, 2314.

(26) Chaignon, F.; Torroba, J.; Blart, E.; Borgström, M.; Hammarström, L.; Odobel, F. *New J. Chem.* **2005**, *29*, 1272.

(27) Zhou, Z. G.; Sarova, G. H.; Zhang, S.; Ou, Z. P.; Tat, F. T.; Kadish, K. M.; Echegoyen, L.; Guldi, D. M.; Schuster, D. I.; Wilson, S. R. *Chem. Eur. J.* **2006**, *12*, 4241.

(28) Maggini, M.; Guldi, D. M.; Mondini, S.; Scorrano, G.; Paolucci, F.; Ceroni, P.; Roffia, S. *Chem. Eur. J.* **1998**, *4*, 1992.

(29) Allen, B. D.; Benniston, A. C.; Harriman, A.; Mallon, L. J.; Pariani, C. *Phys. Chem. Chem. Phys.* **2006**, *8*, 4112.

(30) Karlsson, S.; Modin, J.; Becker, H. C.; Hammarström, L.; Grennberg, H. *Inorg. Chem.* **2008**, *47*, 7286.

(31) Armaroli, N.; Barigelletti, F.; Ceroni, P.; Eckert, J. F.; Nicoud, J. F.; Nierengarten, J. F. *Chem. Commun.* **2000**, 599.

(32) Sariciftci, N. S.; Wudl, F.; Heeger, A. J.; Maggini, M.; Scorrano, G.; Prato, M.; Bourassa, J.; Ford, P. C. *Chem. Phys. Lett.* **1995**, *247*, 510.

(33) Armspach, D.; Constable, E. C.; Diederich, F.; Housecroft, C. E.; Nierengarten, J. F. *Chem.—Eur. J.* **1998**, *4*, 723.

(34) Polese, A.; Mondini, S.; Bianco, A.; Toniolo, C.; Scorrano, G.; Guldi, D. M.; Maggini, M. *J. Am. Chem. Soc.* **1999**, *121*, 3446.

(35) Albinsson, B.; Mårtensson, J. *J. Photochem. Photobiol., C* **2008**, *9*, 138.

(36) Siebert, R.; Winter, A.; Dietzek, B.; Schubert, U. S.; Popp, J. *Macromol. Rapid Commun.* **2010**, *31*, 883.

(37) Siebert, R.; Winter, A.; Schubert, U. S.; Dietzek, B.; Popp, J. *J. Phys. Chem. C* **2010**, *114*, 6841.

(38) Siebert, R.; Hunger, C.; Guthmuller, J.; Schlutter, F.; Winter, A.; Schubert, U. S.; González, L.; Dietzek, B.; Popp, J. *J. Phys. Chem. C* **2011**, *115*, 12677.

(39) Siebert, R.; Winter, A.; Schubert, U. S.; Dietzek, B.; Popp, J. *Phys. Chem. Chem. Phys.* **2011**, *13*, 1606.

(40) La Rosa, A.; Gillemot, K.; Leary, E.; Evangeli, C.; González, M. T.; Filippone, S.; Rubio-Bollinger, G.; Agraït, N.; Lambert, C. J.; Martín, N. *J. Org. Chem.* **2014**, *79*, 4871.

(41) Denholm, A. A.; George, M. H.; Hailes, H. C.; Tiffin, P. J.; Widdowson, D. A. *J. Chem. Soc., Perkin Trans. 1* **1995**, 541.

(42) Cave, G. W. V.; Raston, C. L. *J. Chem. Soc., Perkin Trans. 1* **2001**, 3258.

(43) Egbe, D. A. M.; Carbonnier, B.; Ding, L. M.; Mühlbacher, D.; Birckner, E.; Pakula, T.; Karasz, F. E.; Grummt, U. W. *Macromolecules* **2004**, *37*, 7451.

(44) Schlütter, F.; Wild, A.; Winter, A.; Hager, M. D.; Baumgärtel, A.; Friebe, C.; Schubert, U. S. *Macromolecules* **2010**, *43*, 2759.

(45) Hirsch, A. *Synthesis* **1995**, 895.

(46) Yamada, M.; Akasaka, T.; Nagase, S. *Chem. Rev.* **2013**, *113*, 7209.

(47) Winter, A.; Egbe, D. A. M.; Schubert, U. S. *Org. Lett.* **2007**, *9*, 2345.

(48) Winter, A.; Friebe, C.; Hager, M. D.; Schubert, U. S. *Eur. J. Org. Chem.* **2009**, 801.

(49) Maggini, M.; Donò, A.; Scorrano, G.; Prato, M. *J. Chem. Soc., Chem. Commun.* **1995**, 845.

(50) Schulze, B.; Escudero, D.; Friebe, C.; Siebert, R.; Görls, H.; Sinn, S.; Thomas, M.; Mai, S.; Popp, J.; Dietzek, B.; González, L.; Schubert, U. S. *Chem. - Eur. J.* **2012**, *18*, 4010.

(51) Sinn, S.; Schulze, B.; Friebe, C.; Brown, D. G.; Jäger, M.; Kübel, J.; Dietzek, B.; Berlinguette, C. P.; Schubert, U. S. *Inorg. Chem.* **2014**, *53*, 1637.

(52) Barigelletti, F.; Flamigni, L.; Balzani, V.; Collin, J. P.; Sauvage, J. P.; Sour, A.; Constable, E. C.; Cargill Thompson, A. M. W. *J. Am. Chem. Soc.* **1994**, *116*, 7692.

(53) Lukoyanova, O.; Cardona, C. M.; Altable, M.; Filippone, S.; Martín Domenech, Á.; Martín, N.; Echegoyen, L. *Angew. Chem., Int. Ed.* **2006**, *45*, 7430.

(54) Hirsch, A.; Brettreich, M. *Fullerenes*; Wiley-VCH: Weinheim, Germany, 2005.

(55) Herranz, M. Á.; Diederich, F.; Echegoyen, L. *Eur. J. Org. Chem.* **2004**, 2299.

(56) Schubert, U. S.; Winter, A.; Newkome, G. R. *Terpyridine-based Materials*; Wiley-VCH: Weinheim, Germany, 2011.

(57) Thomas, K. G.; Biju, V.; Guldi, D. M.; Kamat, P. V.; George, M. V. *J. Phys. Chem. B* **1999**, *103*, 8864.

(58) Bensasson, R. V.; Bienvenüe, E.; Fabre, C.; Janot, J. M.; Land, E. J.; Leach, S.; Leboulaire, V.; Rassat, A.; Roux, S.; Seta, P. *Chem. Eur. J.* **1998**, *4*, 270.

(59) Amouyal, E.; Mouallem-Bahout, M.; Calzaferri, G. *J. Phys. Chem.* **1991**, *95*, 7641.

(60) Horng, M. L.; Gardecki, J. A.; Papazyan, A.; Maroncelli, M. *J. Phys. Chem.* **1995**, *99*, 17311.

(61) Bhasikuttan, A. C.; Suzuki, M.; Nakashima, S.; Okada, T. *J. Am. Chem. Soc.* **2002**, *124*, 8398.

(62) Maestri, M.; Armaroli, N.; Balzani, V.; Constable, E. C.; Cargill Thompson, A. M. W. *Inorg. Chem.* **1995**, *34*, 2759.

(63) Lainé, P. P.; Campagna, S.; Loiseau, F. *Coord. Chem. Rev.* **2008**, *252*, 2552.

(64) McClenaghan, N. D.; Leydet, Y.; Maubert, B.; Indelli, M. T.; Campagna, S. *Coord. Chem. Rev.* **2005**, *249*, 1336.

(65) Grewer, C.; Brauer, H.-D. *J. Phys. Chem.* **1994**, *98*, 4230.

(66) Winter, A.; van den Berg, A. M. J.; Hoogenboom, R.; Kickelbick, G.; Schubert, U. S. *Synthesis* **2006**, 2873.

(67) Sullivan, B. P.; Calvert, J. M.; Meyer, T. J. *Inorg. Chem.* **1980**, *19*, 1404.

(68) Igartúa-Nieves, E.; Ocasio-Delgado, Y.; Torres-Castillo, M. D. L. A.; Rivera-Betancourt, O.; Rivera-Pagán, J. A.; Rodriguez, D.; López, G. E.; Cortés-Figueroa, J. E. *Dalton Trans.* **2007**, 1293.

Supporting Information for:

New Ruthenium Bisterpyridine Methanofullerene and Pyrrolidinofullerene Complexes: Synthesis, Electrochemical and Photophysical Properties

Kevin Barthelmes,[†,§] Joachim Kübel,[‡,Γ] Andreas Winter,[†,§] Maria Wächtler,[‡,Γ] Christian Friebe,[†,§]
Benjamin Dietzek,[§,‡,Γ] Ulrich S. Schubert*[,†,§]

[†] Laboratory of Organic and Macromolecular Chemistry (IOMC), Friedrich Schiller University Jena, Humboldtstr. 10, 07743 Jena, Germany

[§] Jena Center for Soft Matter (JCSM), Friedrich Schiller University Jena, Philosophenweg 7, 07743 Jena, Germany

[‡] Institute of Physical Chemistry (IPC) and Abbe Center of Photonics, Friedrich Schiller University Jena, Helmholtzweg 4, 07743 Jena, Germany

[Γ] Leibniz Institute of Photonic Technology e.V. (IPHT), Albert-Einstein-Str. 9, 07745 Jena, Germany

E-mail: ulrich.schubert@uni-jena.de

Table of Contents:

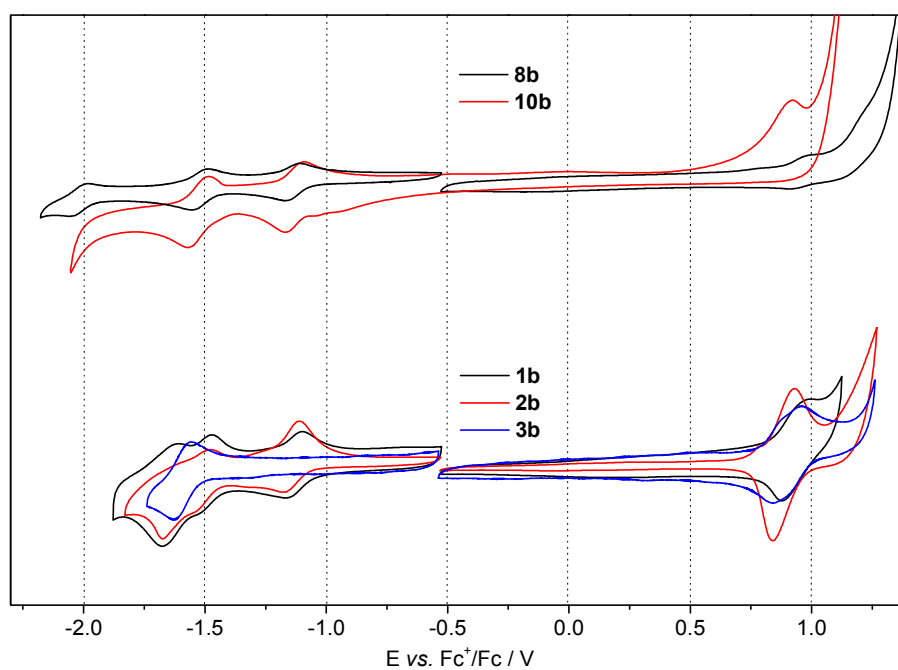# 1. Electrochemical data

Figure S1. CV spectra of PEP bridged methano- and pyrrolidinofullerene ligands **8b**, **10b** and complexes **1b**, **2b** as well as reference **3b** measured in dichloromethane (0.1 M NBu_4PF_6, scan rate = 0.2 Vs^{-1})
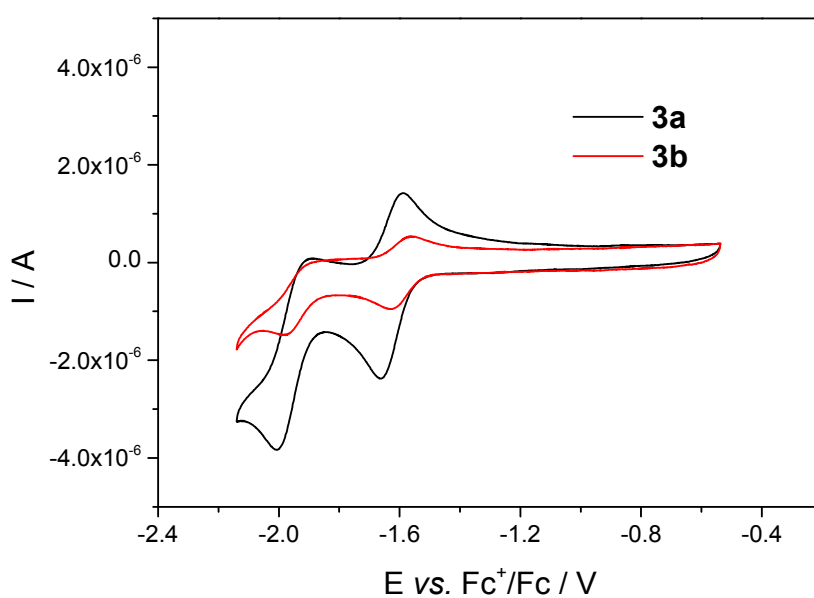

Figure S2. CV spectra (cathodic region) of the model complexes **3a** and **3b** measured in dichloromethane (0.1 M NBu_4PF_6, scan rate = 0.2 Vs^{-1}). The spectra show the two reversible terpyridine reduction waves.
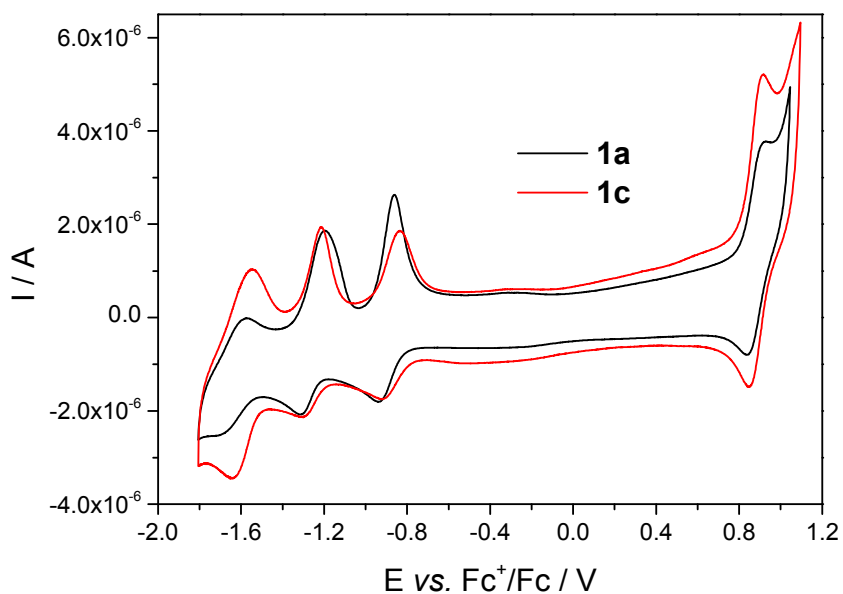
Figure S3. CV spectra comparison of the mono- and dinuclear ruthenium(II) complex **1a** and **1c** measured in dichloromethane (0.1 M NBu$_4$PF$_6$, scan rate = 0.2 Vs^{-1}).
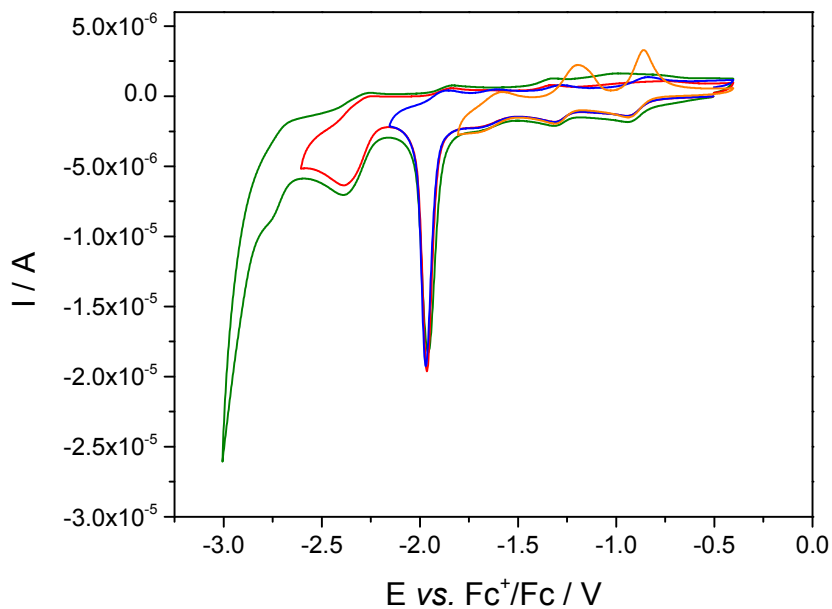

Figure S4. CV spectra of **1a** with varied potential range measured in dichloromethane (0.1 M NBu$_4$PF$_6$, scan rate = 0.2 Vs^{-1}). The irreversible process at ca. −1.98 V is assigned as retro-cycloaddition reaction.

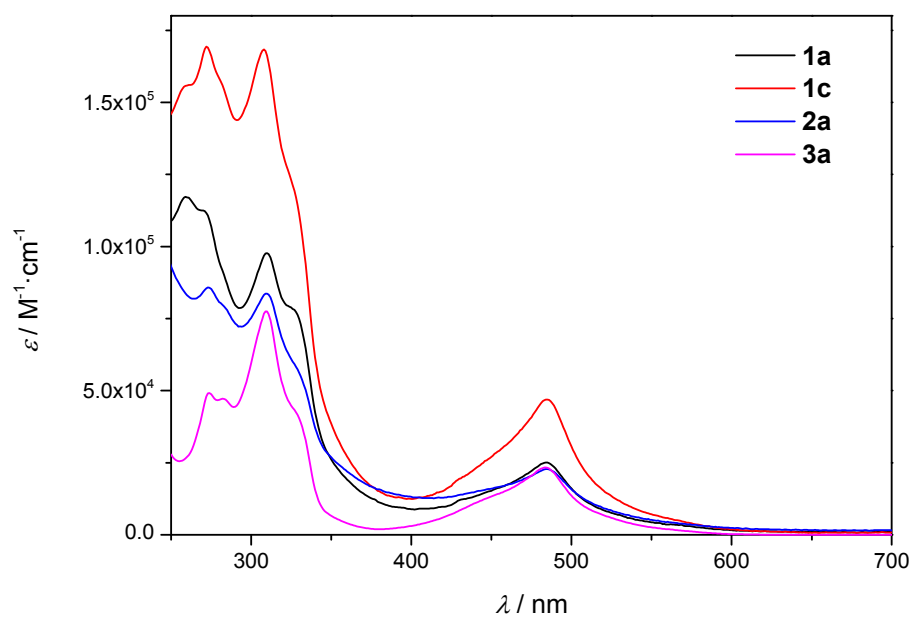## 2. Absorption and emission spectra

Figure S5. Absorption spectra of the short-bridged ruthenium(II) complexes **1a**, **1c**, **2a** and **3a** measured in dichloromethane.
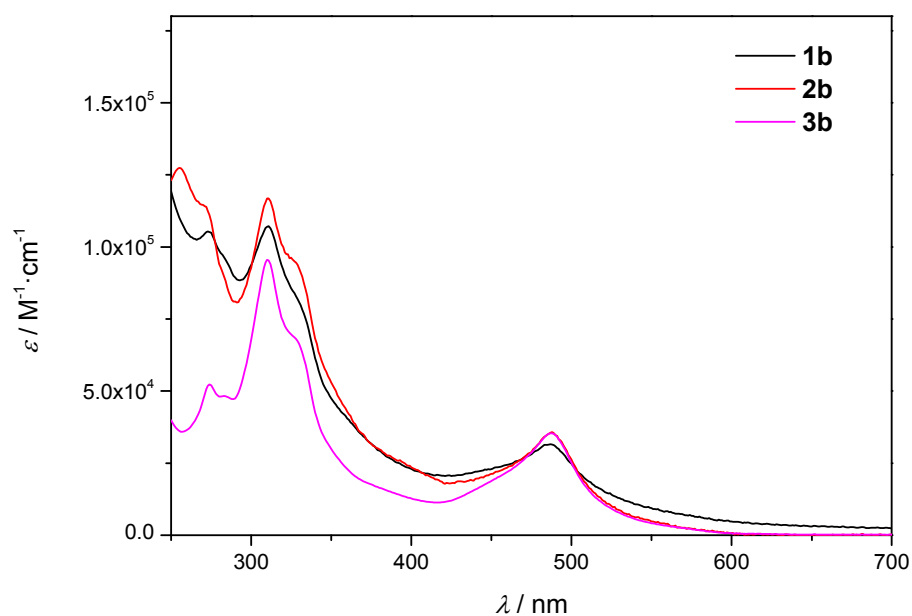

Figure S6. Absorption spectra of the long-bridged ruthenium(II) complexes **1b**, **2b**, and **3b** measured in dichloromethane.

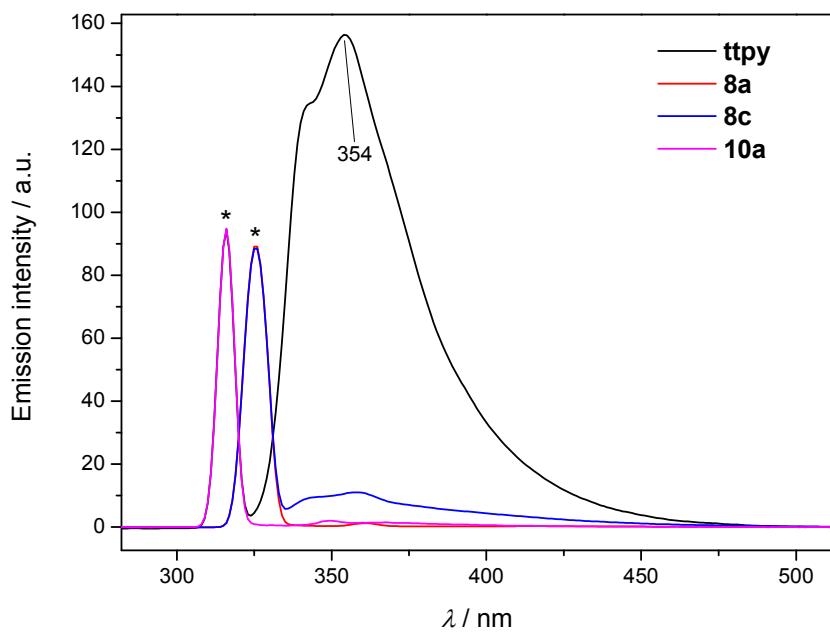**Figure S7.** Emission spectra (λ_{exc} = 315 or 325 nm) of the short ligands measured in dichloromethane at room temperature. Asterisks marks instrumental excitation wavelength or artefacts.

Figure S8. Emission spectra (λ_{ex} = 315 or 325 nm) of the long ligands measured in dichloromethane at room temperature. Asterisks marks instrumental excitation wavelength or artefacts.
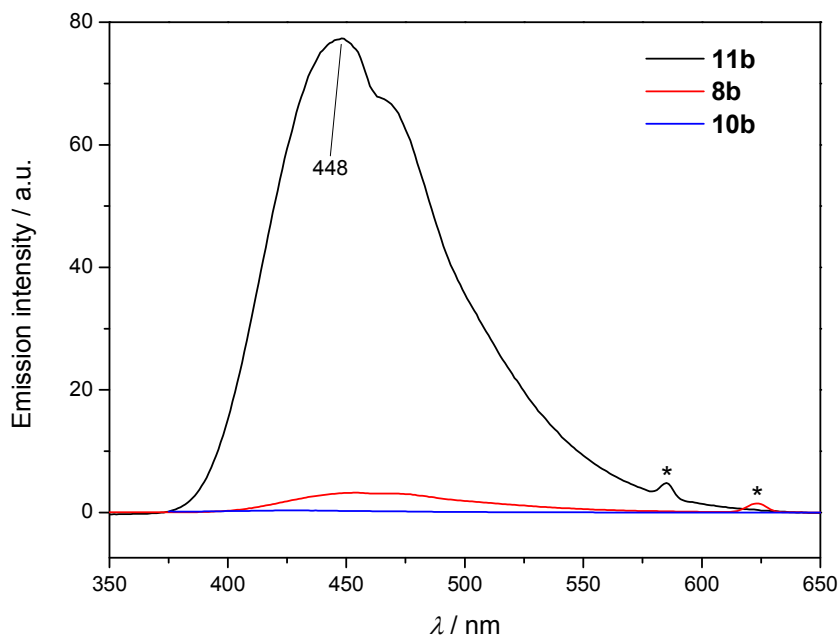
3. Time-resolved data
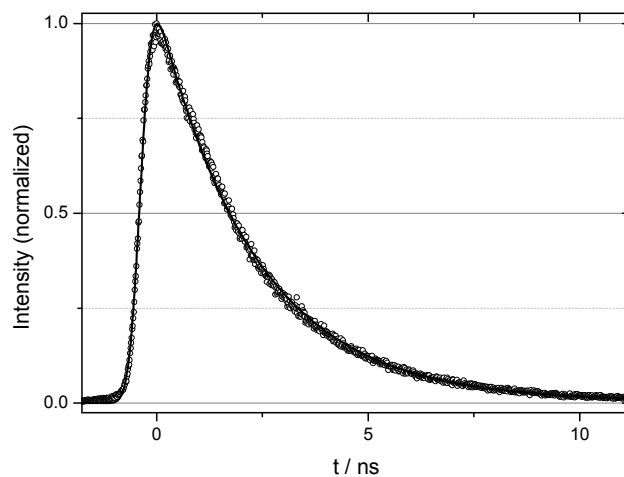
Figure S9. Emission decay curve (hollow symbols) of **3b** in acetonitrile obtained via time-correlated-single-photon-counting (λ_{exc} = 435 nm) recorded with a 520 nm LP filter. The solid line represents a monoexponential fit curve (2.3 ns) including a convolution with a Gaussian as instrumental response function.
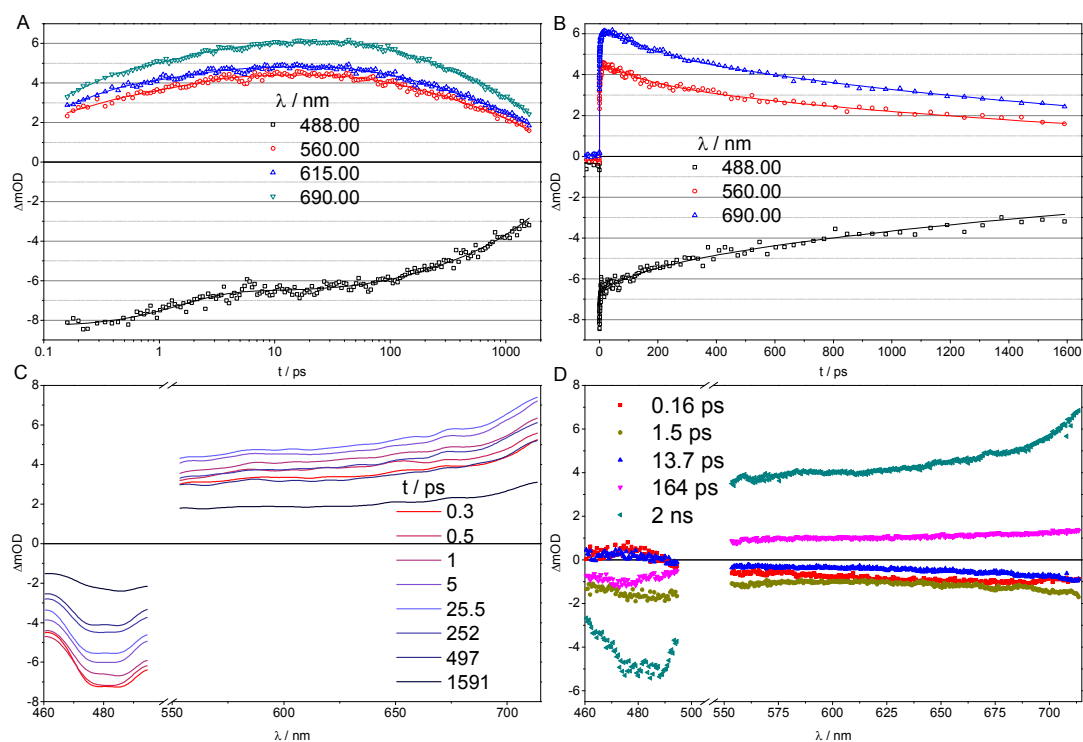
Figure S10. Transient absorption data of **3b** in acetonitrile (λ_{exc} = 520 nm): Kinetics with respective fit curves in logarithmic scale (panel A), linear scale (B), smoothed transient absorption spectra at selected delay times (C) and global fit results (D).
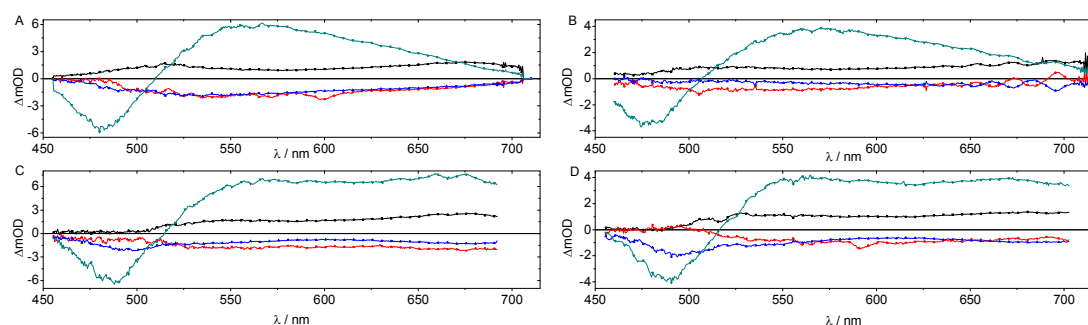
Figure S11. Global fit results (decay associated spectra, DAS) from transient absorption experiments on **2a** (panel A), **1a** (B), **2b** (C) and **1b** (D) performed in acetonitrile (λ_{exc} = 520 nm). The curve colors correspond to the respective time constants (see **Table S1**): red (τ_1), blue (τ_2), cyan (τ_3) and black (offset).

|	2a	1a	2b	1b
τ_1 / ps	0.2	0.8	0.4	0.2
τ_2 / ps	3.2	4.7	3.1	1.9
τ_3 / ps	73	93	318	406

Table S1. Global fit results (time constants) from transient absorption experiments on **1a**, **1b**, **2a** and **2b** performed in acetonitrile (λ_{exc} = 520 nm).
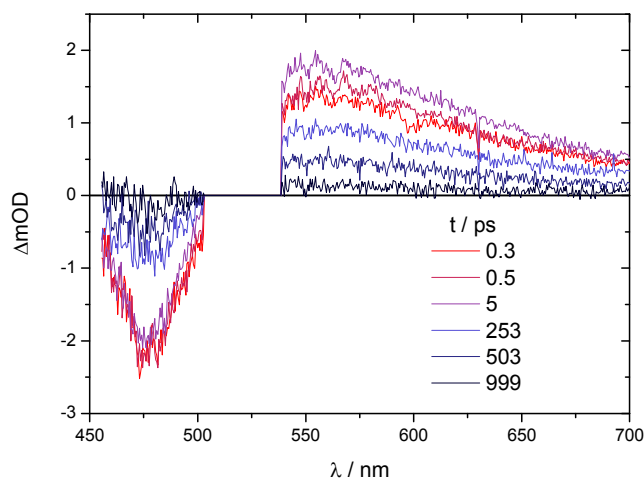

Figure S12. Raw transient absorption spectra (λ_{exc} = 520 nm) of **3a** ([Ru(tpy)(ttpy)]$^{2+}$, ttpy = 4'-tolyl-2,2':6',2''-terpyridine) at selected delay times, recorded in acetonitrile.
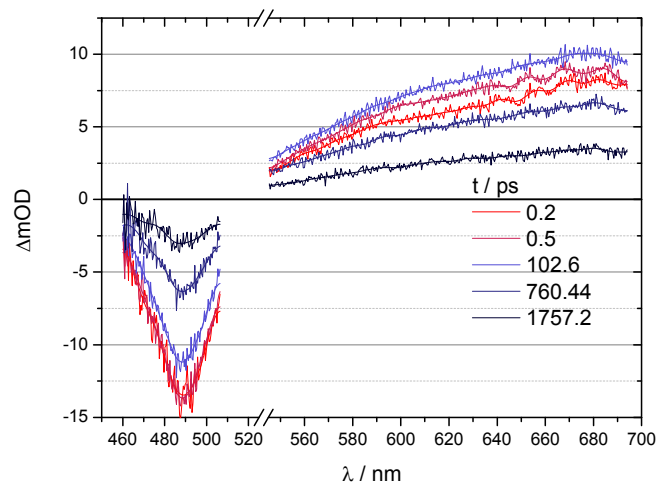
Figure S13. Raw and smoothed (10-point FFT filter) transient absorption spectra (λ_{exc} = 520 nm) of **3b** in dichloromethane at selected delay times.

Determination of the number of fit components

Generally speaking the number of fit components should be as small as possible. The reasons for that are manifold: Additional components may induce ambiguities, which can be quite obvious in some cases, e.g. when the DAS of two components are mirror-images. An important aspect to consider is the signal-to-noise ratio of the measurement as in many scenarios the detection of processes with weak spectral impact is tough and often an improved signal-to-noise ratio may allow the detection of additional components. The pure mathematical description of the experimental data will be improved by adding fit parameters, but without additional information from complementary experiments or theory the physical meaning of these additional fit components may be unclear.

For this study we chose to fit the transient absorption data generally with three kinetic components and an offset, which sufficiently describes the experimental data (see the discussion in the paper) and allows us to provide a more scholarly presentation. However, we noted that an additional fit component improves the fits particularly for **1b** and **2b** (and also **1c**, see below). Figure S14 exemplarily contains selected kinetic traces with fit curves in logarithmic and linear scale for **1b** fitted with three (panels A,C) and four exponentials (panels B,D), respectively. The fit with three exponentials causes some error particularly for the last 8-10 data points, while with four exponentials there is no systematic deviation of the fit curve with respect to the measured data points. In the particular case where the late data points are not correctly described, it should be noted that the long delay times are especially sensitive towards slight alignment errors, i.e. a non-parallel delay-line adjustment may cause a beam-drift at the sample position causing the kinetics at longer delay-times to be erroneous. While care had been taken performing the measurements, a misalignment cannot be ruled out. On the other hand, there could be a physical meaning of the additional component: The 406 ps-component from the three-exponential fit breaks into two components when four exponentials are used. While there is no change for the fastest processes, the other two time constants are 86 and 579 ps with similar DAS, yet different intensities. It is noted that the average of the two new component's time constants (332.5 ps) deviates from the original value of 407 ps suggesting that the

fit actually is improved by the additional component. Physical aspects that could influence the ^{3}MLCT deactivation could be structural inhomogeneities, e.g. caused by an interaction of the long alkoxy chains and the fullerene units as two different conformers are possible. It is out of the scope of this paper to detail any kind of specific interaction.
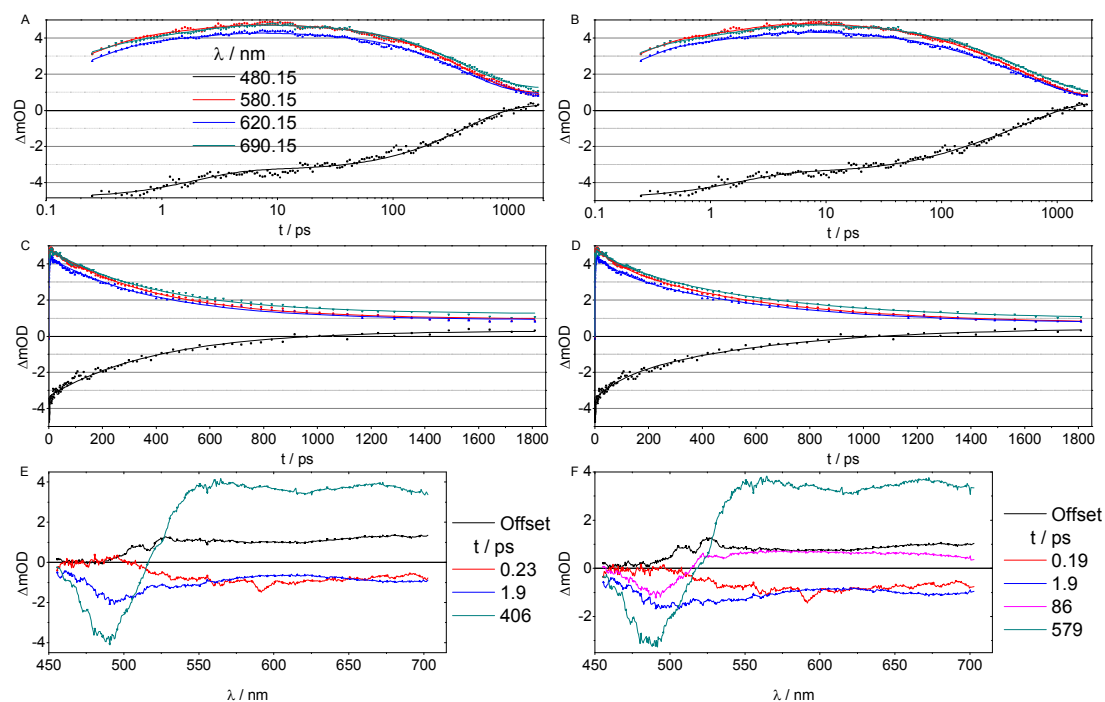

Figure S14. Transient absorption data of **1b**: Kinetic traces at selected wavelengths (see legend in panel A) in logarithmic and linear scale for **1b** fitted with three (panels A,C) and four exponentials (panels B,D), respectively. Panels E and F contain the respective DAS of the fits with three and four exponentials, respectively.

Transient absorption data for the dinuclear complex 1c

The dinuclear complex **1c** carries two Ru^{II}-terpyridine units and may be doubly excited (i.e. both metal centers), which can result in quenching effects, e.g. due to triplet-triplet-annihilation (see for example *Chem. Commun.* **2011**, *47*, 3820-3821). Typically, the two-fold excitation of one molecule only occurs at very high photon fluxes, but can lead to strongly altered photoinduced dynamics. We carried out TA experiments on **1c** (Figure S15) with a (typical) pump power of 0.5 mW (i.e. 1 µJ pulse energy) and also with higher pump power of 2 mW (4 µJ).

The transient absorption kinetics of **1c** are very similar to those of **1a**, its mono-ruthenium-analogue, at both pump powers. A three-exponential fit produces almost identical time-constants and DAS at both pump conditions and the fit data is similar to that of **1a**: Even the time-constants of the slowest process (105 and 102 ps, respectively) nicely compare with the 93 ps determined for **1a**. While the three-exponential fits in principle sufficiently describe the data, adding the fourth fit component improves the fit markedly for the measurement recorded at high pump power. This is shown exemplarily in panel F for $\lambda_{probe} = 580$ nm. It can be noted that the fourth fit component causes only a very slight

improvement for the data recorded at lower pump power. The time-constants of processes that cause a signal reduction of the ^{3}MLCT absorption signature produced by the four-exponential fit are smaller at high pump energy. A reason for that could be triplet-triplet annihilation that becomes a more prominent decay pathway when the photon flux is increased, but further investigations at this point are out of the scope of this study.
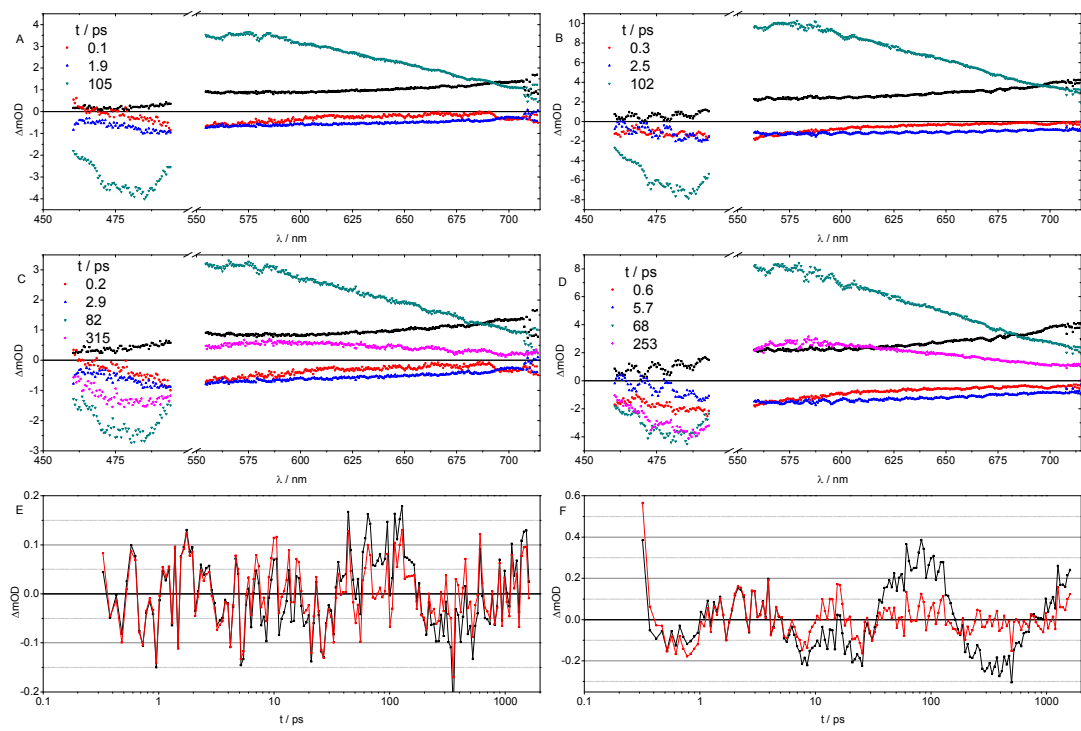
Figure S15. Transient absorption data (λ_{exc} = 520 nm) of **1c** recorded with low (0.5 mW, panels A,C,E) and high pump power (2 mW, panels B,D,F): DAS from three- (panels A,B) and four-exponential fits (C,D) are shown and the residuals (E,F for low and high pump power, respectively) at λ_{probe} = 580 nm for both three- (black curve) and four-exponential (red curve) fits. The black symbols in panels A-D resemble the offset, i.e. the absorption spectrum of the long-lived $^3C_{60}$* species.

4. DFT calculations

The S_0 molecular structure of **3b** was optimized using DFT applying B3LYP/6-31G(d,p) (the ECP MWB28 was used for the ruthenium atom) in the Gaussian 09 program. Solvent effects (dichloromethane) were included with the IEFPCM formalism. A frequency calculation was performed to ensure that the structure corresponds to a local minimum on the PES. Vertical excitation energies from the S_0 to the lowest-excited triplet states were calculated applying TD-B3LYP and the same basis set. Selected Kohn-Sham orbitals were plotted at an isosurface value of 0.025.

state	E / eV	λ / nm	transition			$2*c^2$ / %	character
T_1	1.98	627					
			190	→	192	26	MLCT
			191	→	192	53	MLCT, π- π*
T_2	2.23	556					
			188	→	193	77	MLCT', LLCT
T_3	2.29	541					
			187	→	192	27	π- π*, ILCT
			188	→	193	16	MLCT', LLCT
			190	→	192	27	MLCT
			191	→	192	13	MLCT, π- π*
T_4	2.34	529					
			187	→	193	15	LLCT
			190	→	193	22	MLCT'
			191	→	193	61	MLCT'
T_5	2.36	525					
			189	→	192	88	MLCT
T_6	2.37	523					
			189	→	193	91	MLCT

187 (HOMO-4)

188 (HOMO-3)

189 (HOMO-2)

190 (HOMO-1)

191 (HOMO)

192 (LUMO)

193 (LUMO+1)
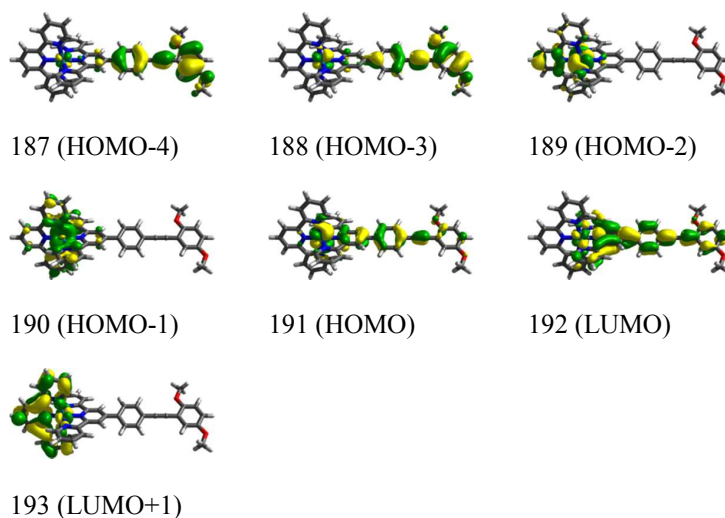
5. NMR spectra
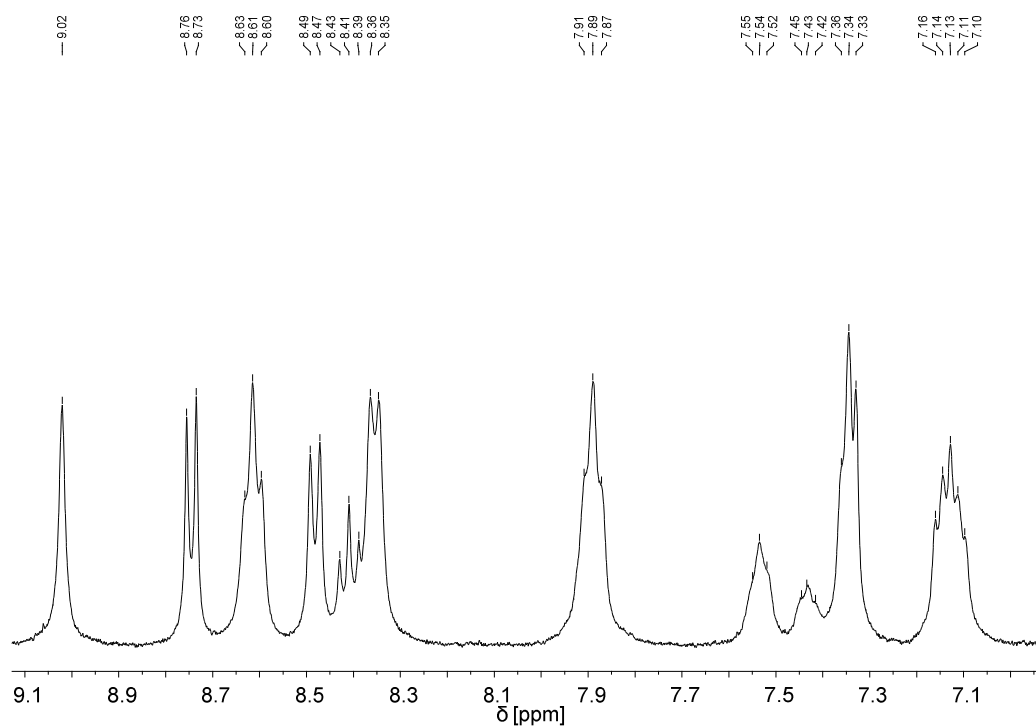
Figure S16. ^{1}H NMR (400 MHz, CD$_3$CN) of **1a**.
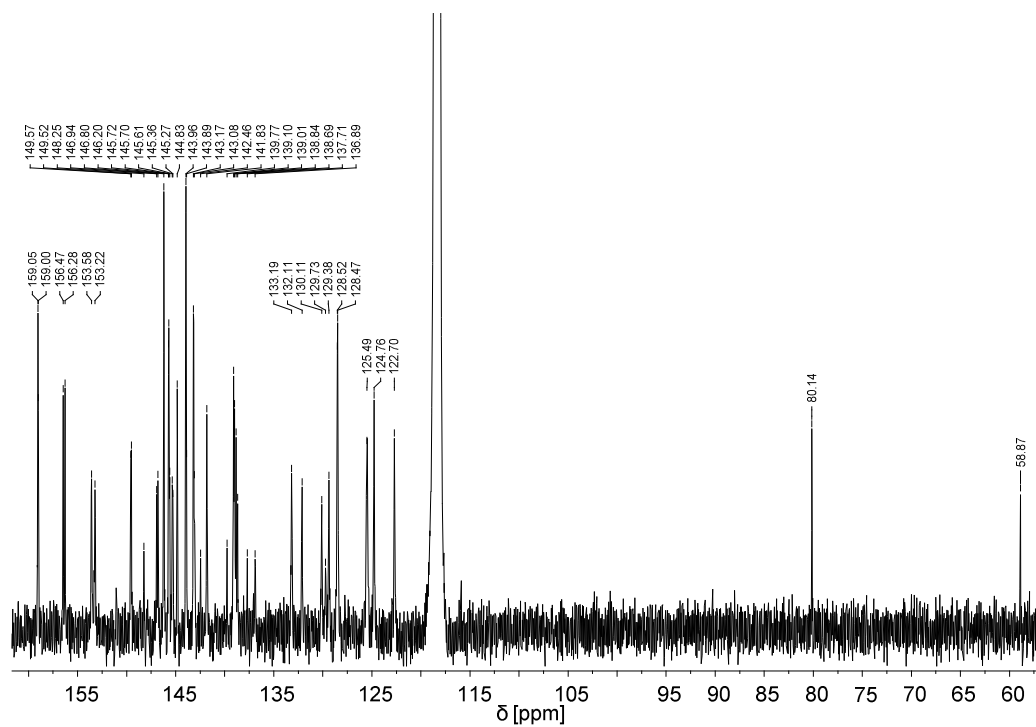
Figure S17. ^{13}C NMR (100 MHz, CD$_3$CN) of **1a**.
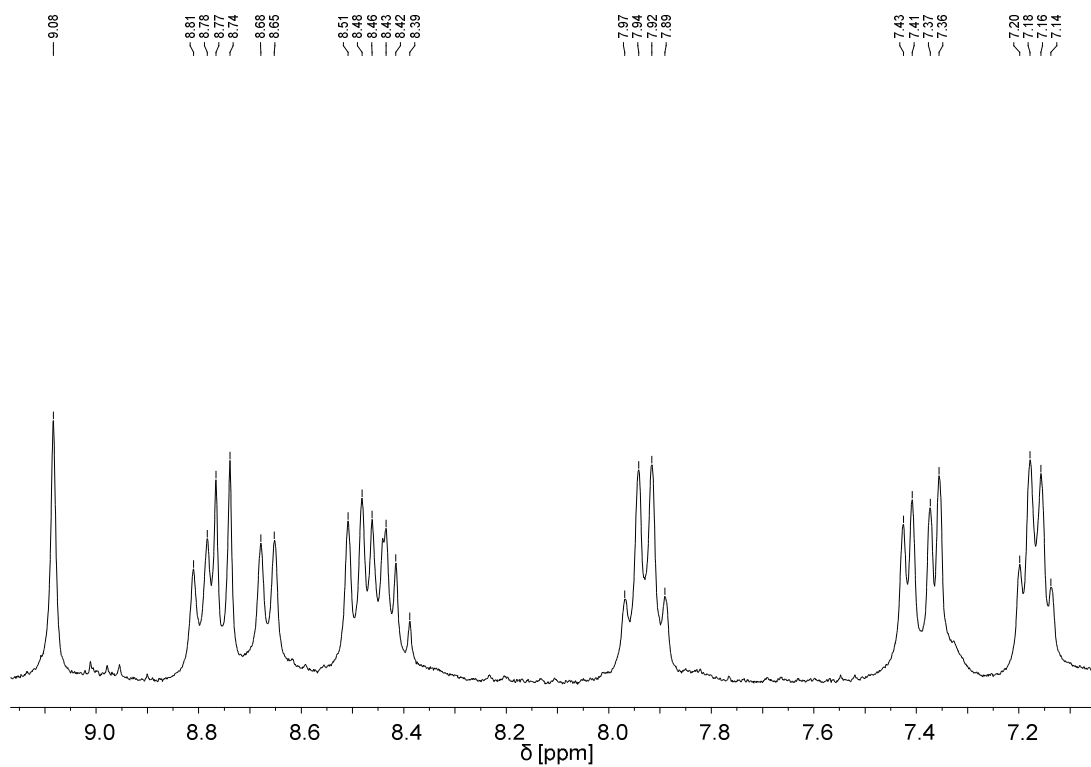
Figure S18. ^{1}H NMR (300 MHz, CD$_3$CN) of **1c**.
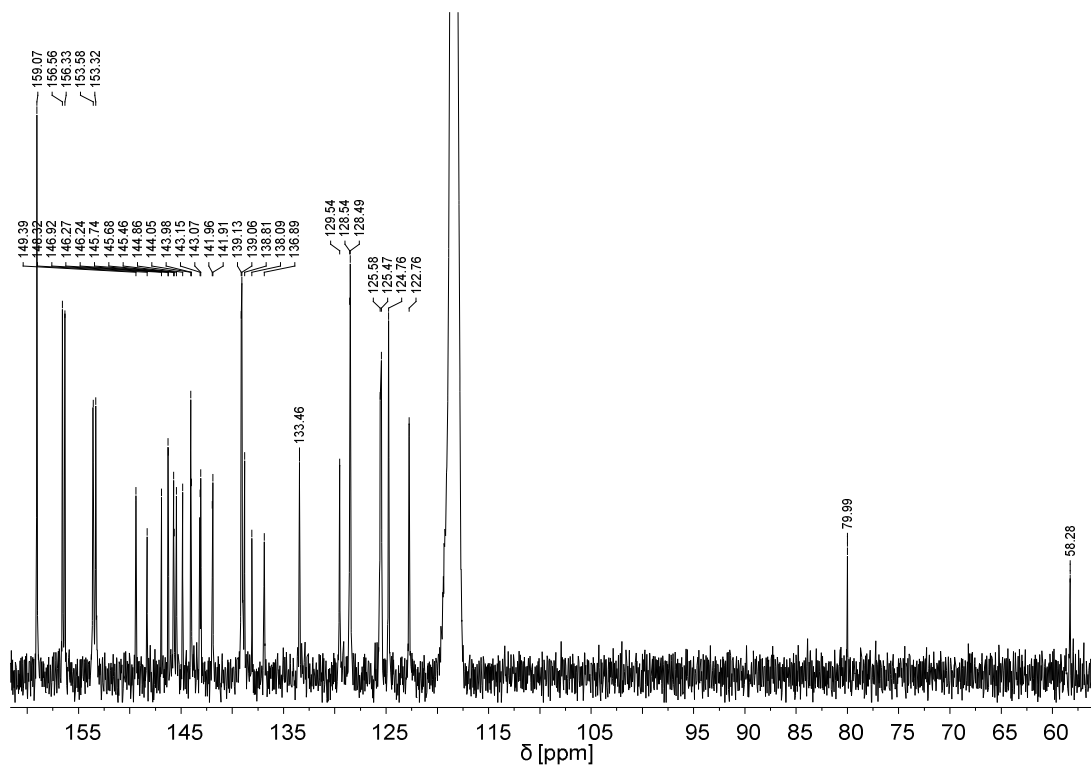
Figure S19. ^{13}C NMR (63 MHz, CD$_3$CN) of **1c**.
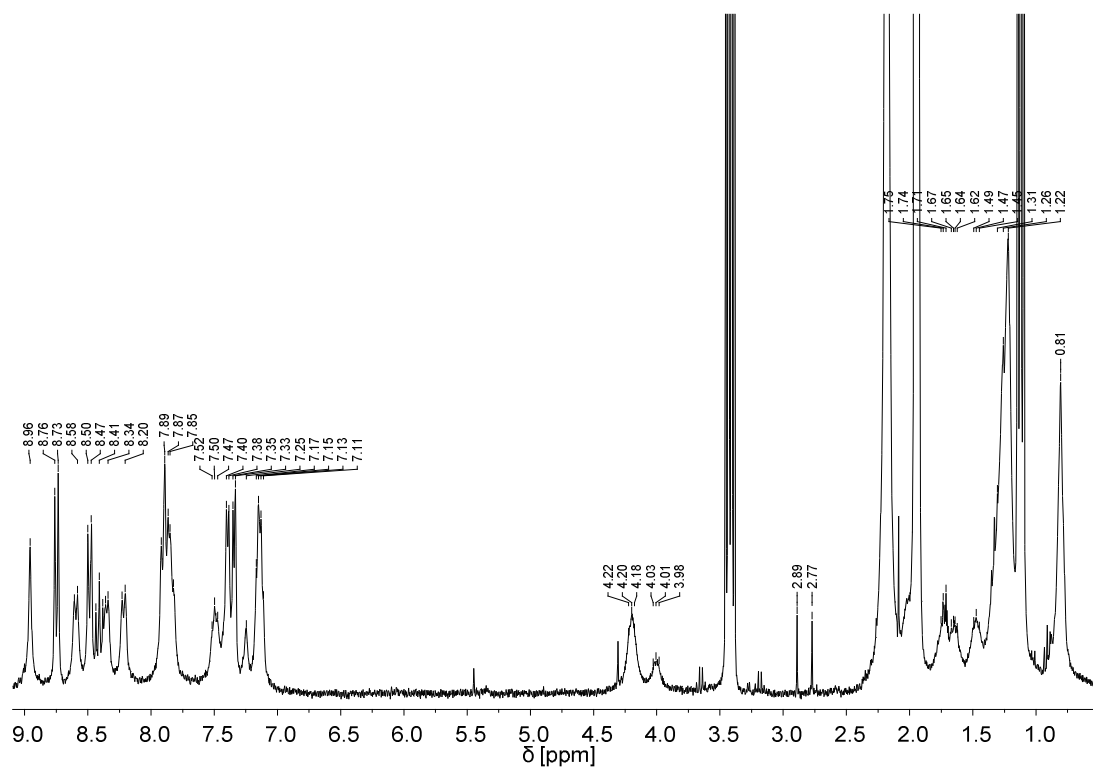
Figure S20. ^{1}H NMR (300 MHz, CD$_3$CN) of **1b**.
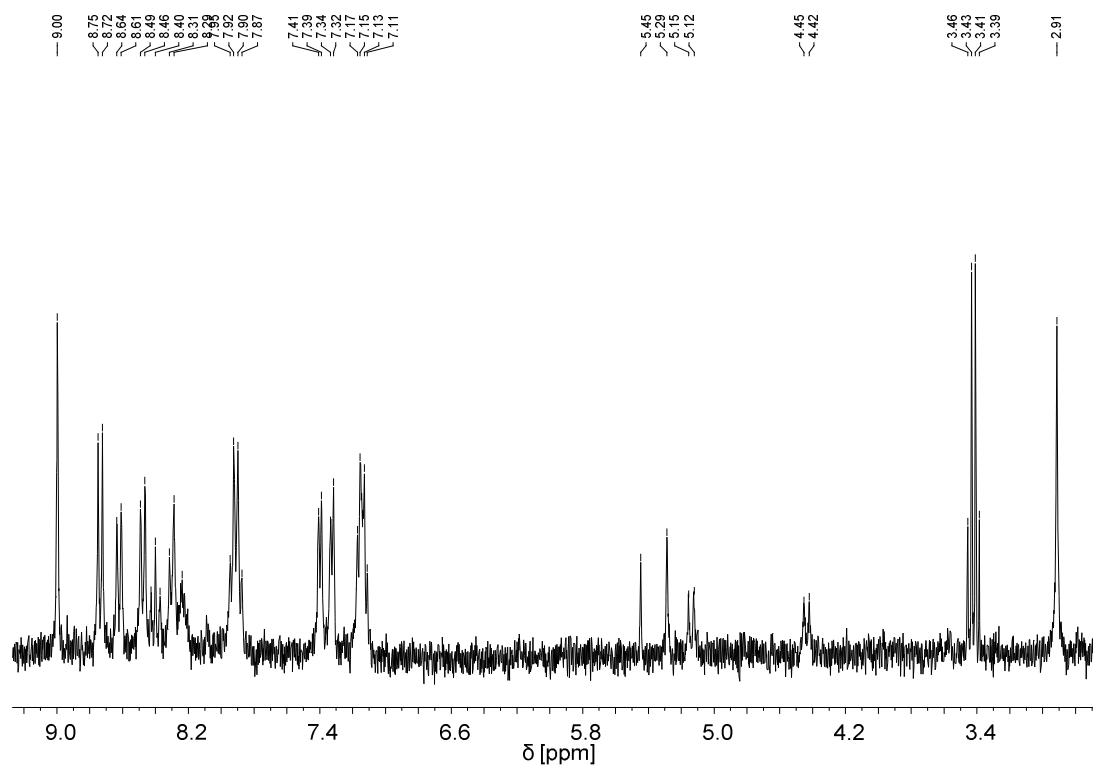
Figure S21. ^{1}H NMR (300 MHz, CD$_3$CN) of **2a**.

S15
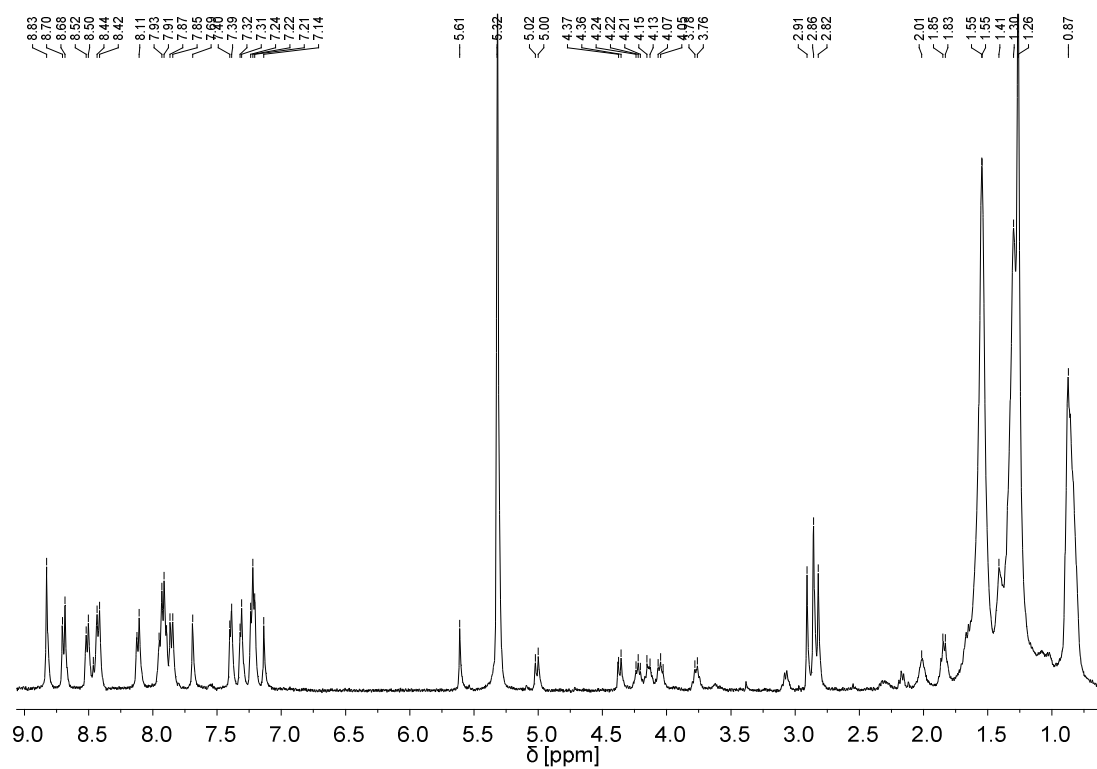
Figure S22. ^{1}H NMR (400 MHz, CD$_2$Cl$_2$) of **2b**.
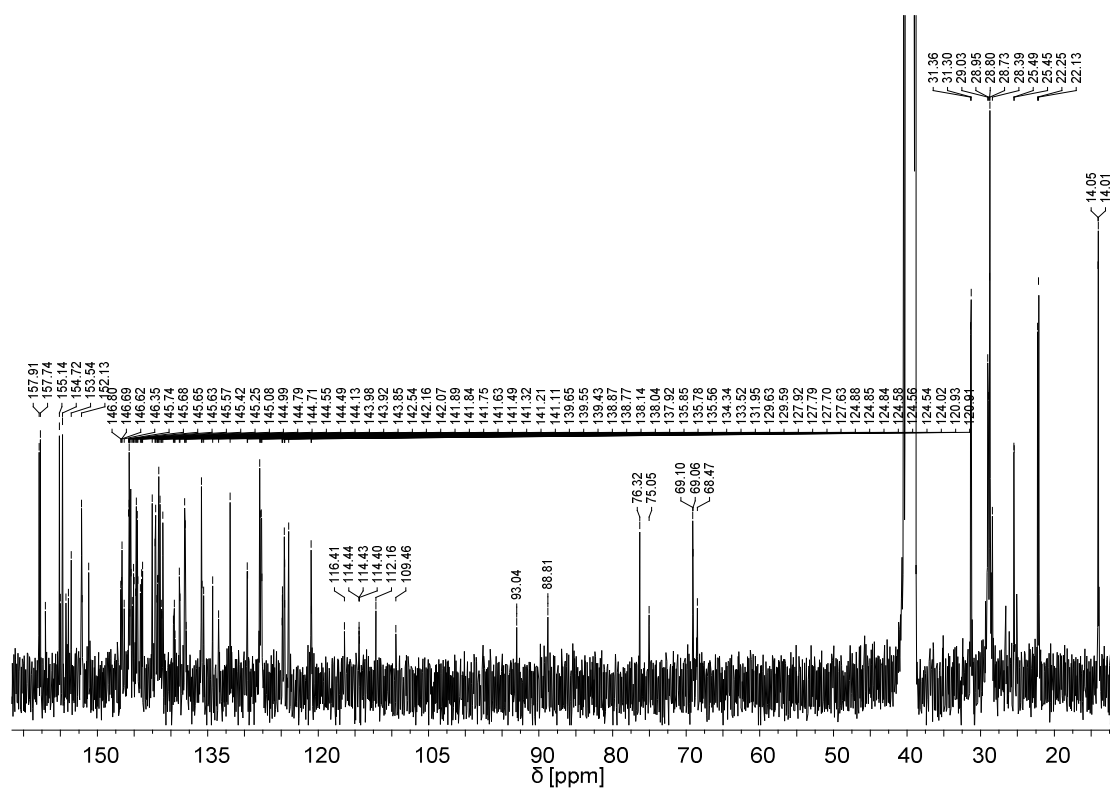
Figure S23. ^{13}C NMR (100 MHz, DMSO-d$_6$) of **2b**.
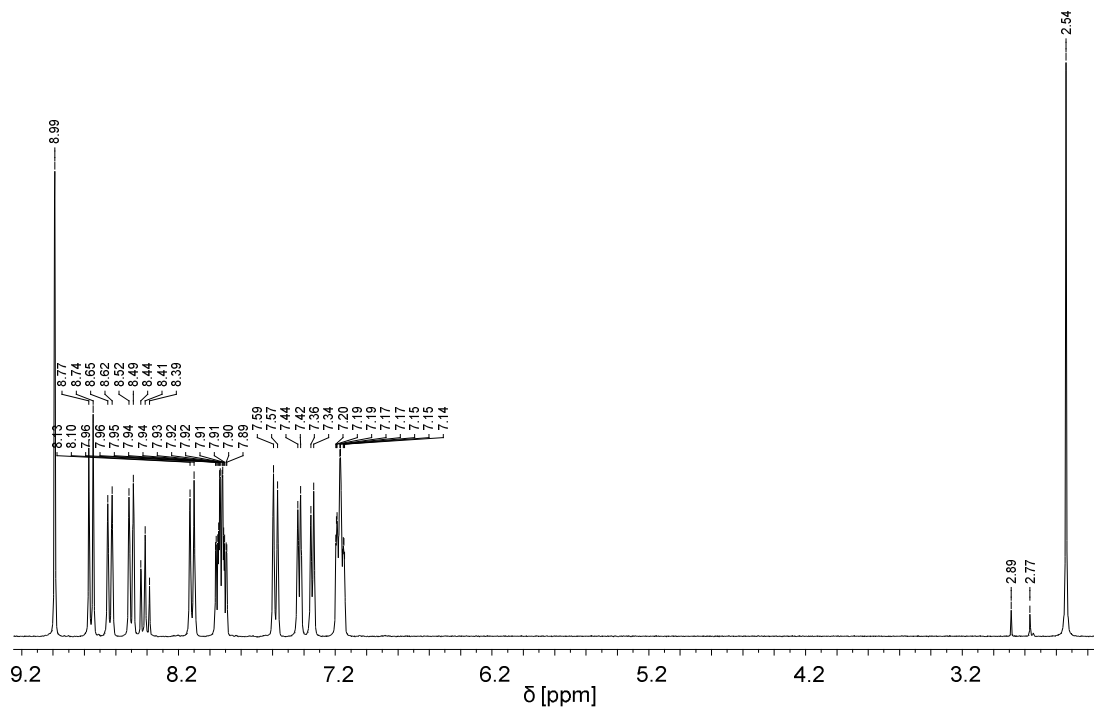
Figure S24. ^{1}H NMR (300 MHz, CD$_3$CN) of **3a**.
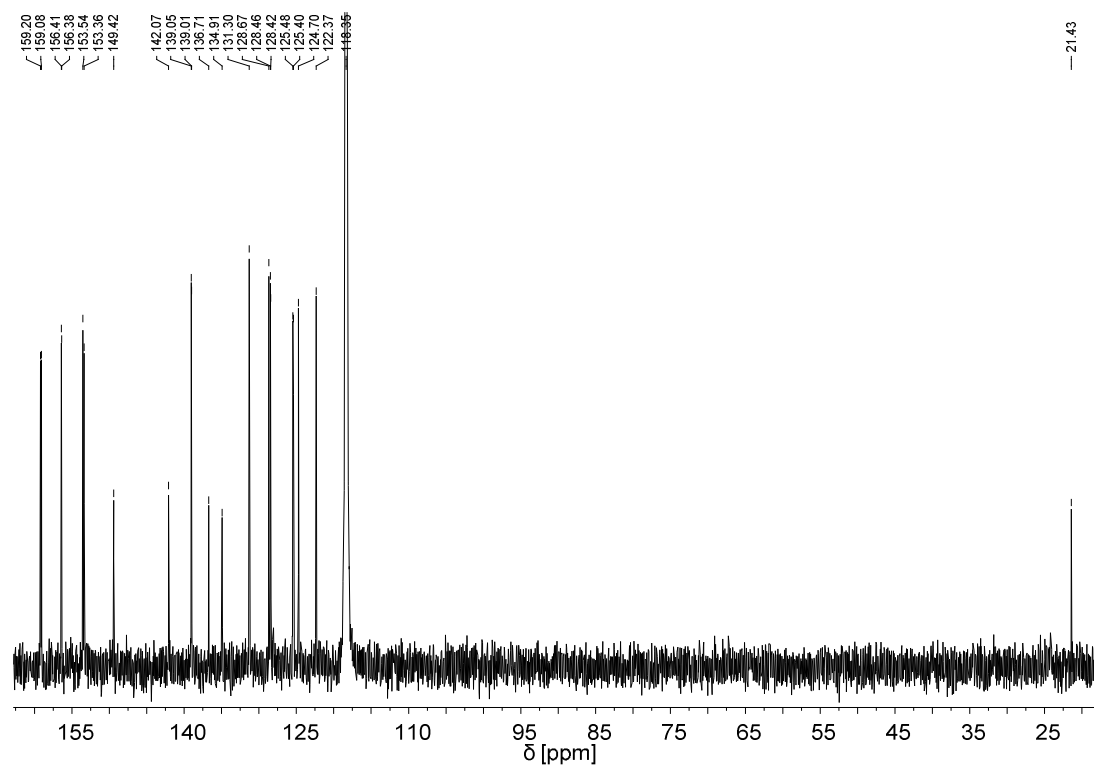
Figure S25. ^{13}C NMR (75 MHz, CD$_3$CN) of **3a**.

S17
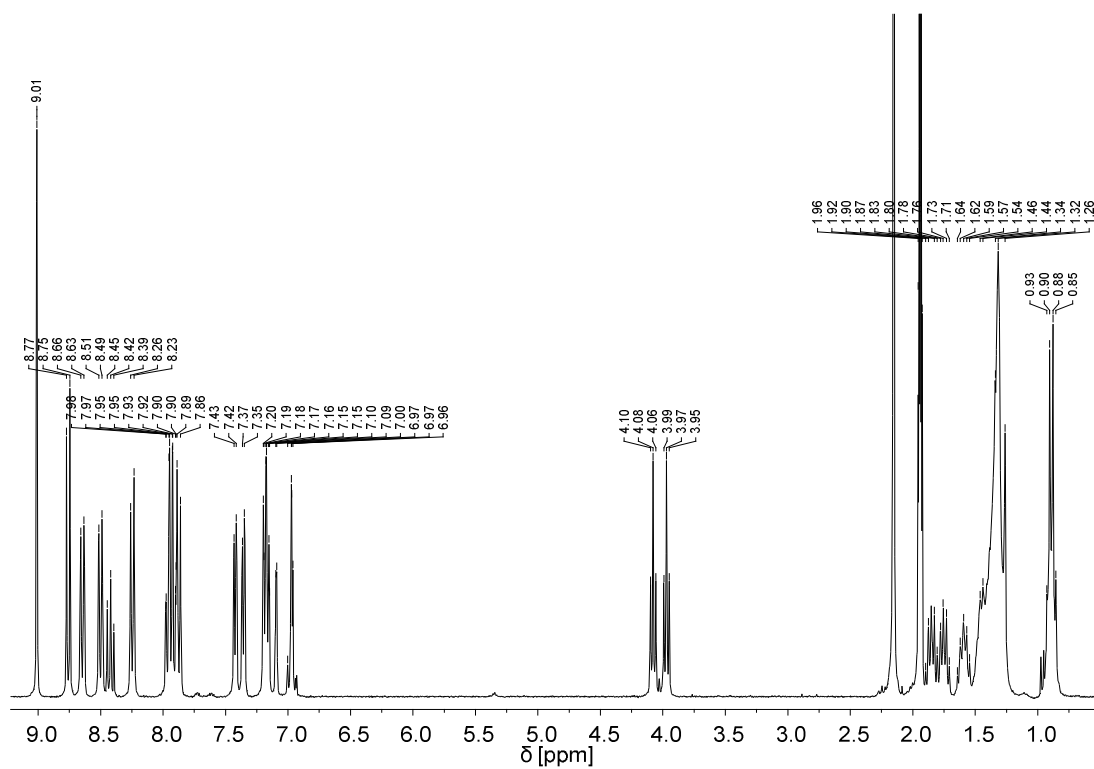
Figure S26. ^{1}H NMR (300 MHz, CD$_3$CN) of **3b**.
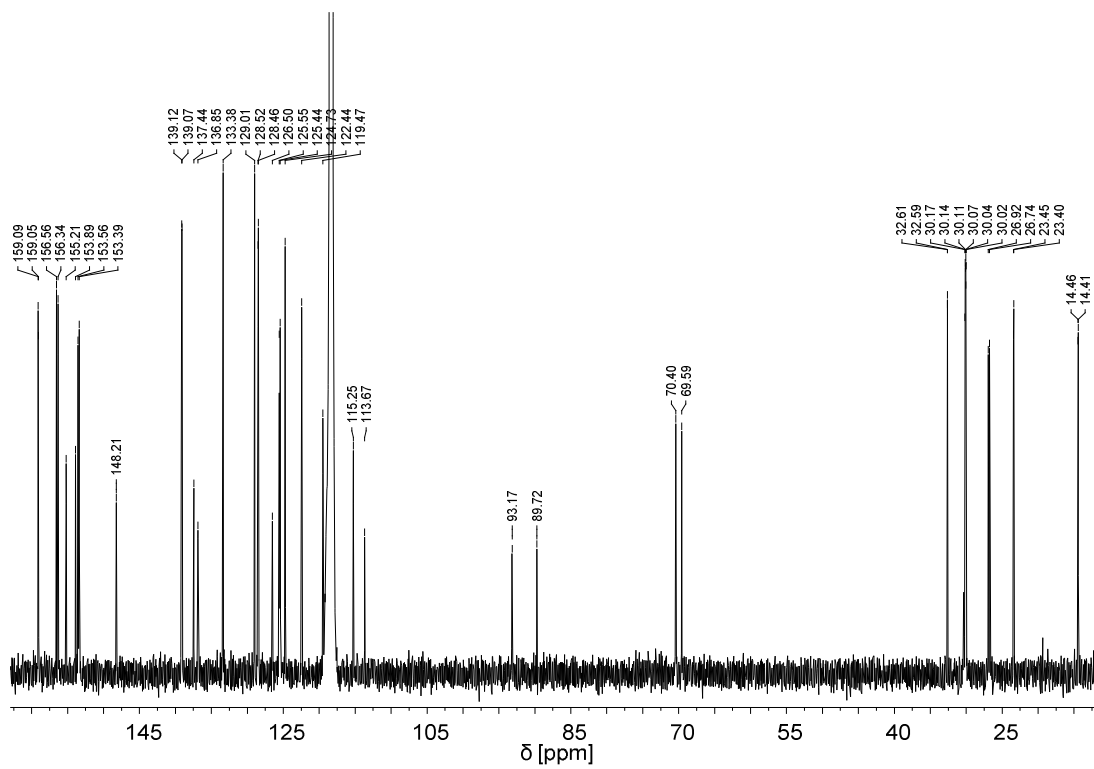
Figure S27. ^{13}C NMR (75 MHz, CD$_3$CN) of **3b**.

S18
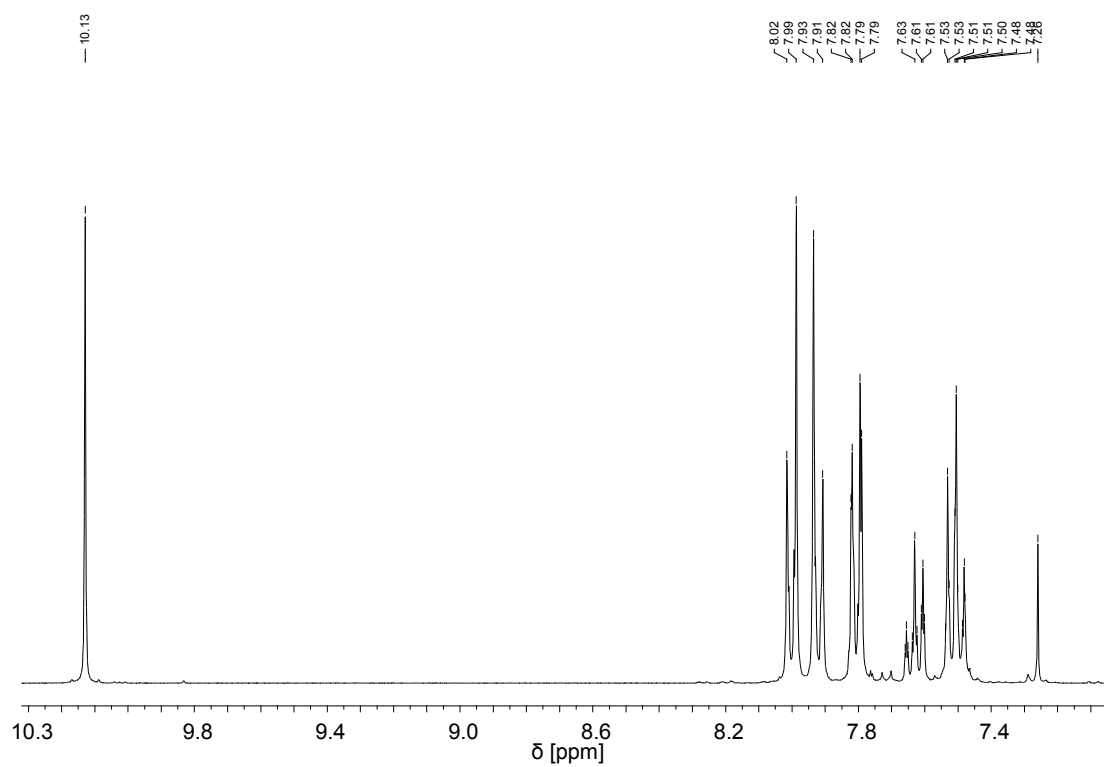
Figure S28. ^{1}H NMR (300 MHz, CDCl$_3$) of **5a**.
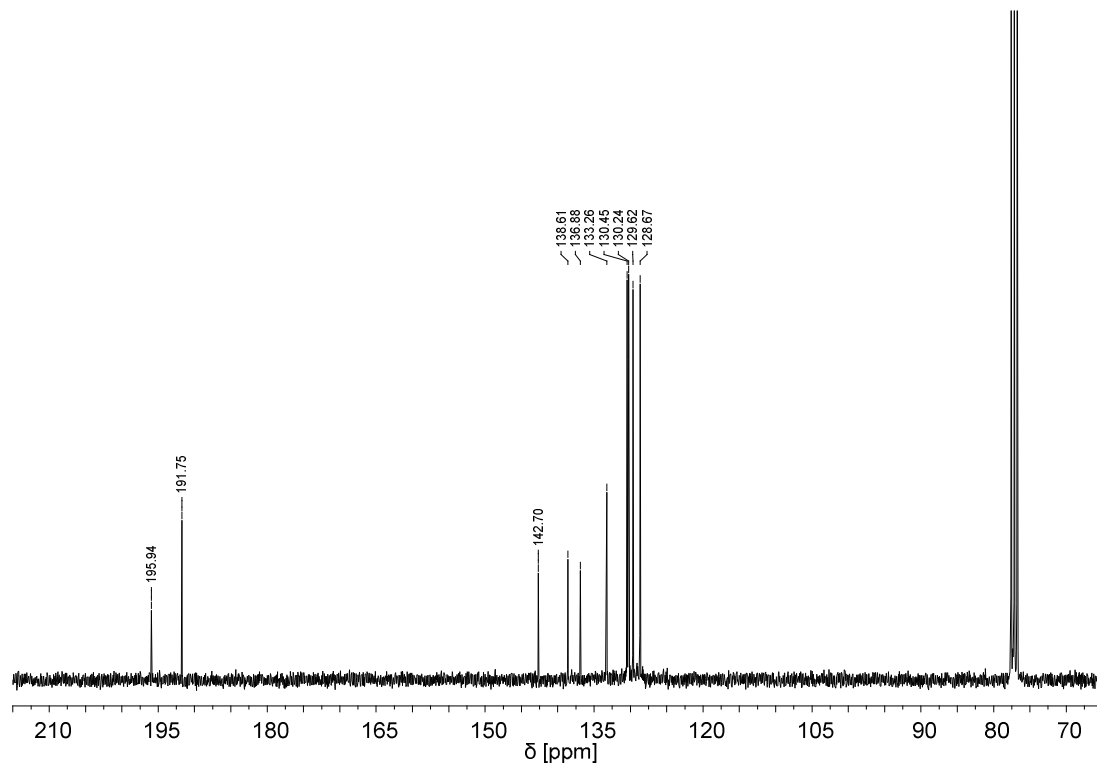
Figure S29. ^{13}C NMR (75 MHz, CDCl$_3$) of **5a**.
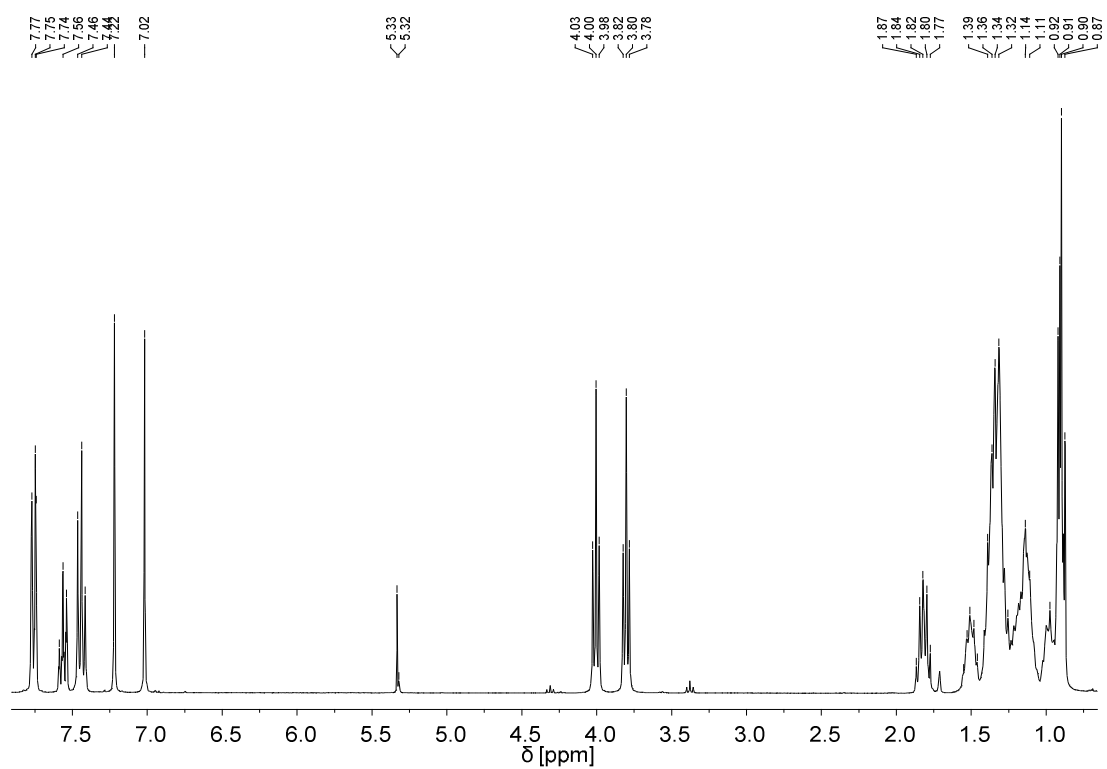
Figure S30. ^{1}H NMR (300 MHz, CD$_2$Cl$_2$) of **5b**.
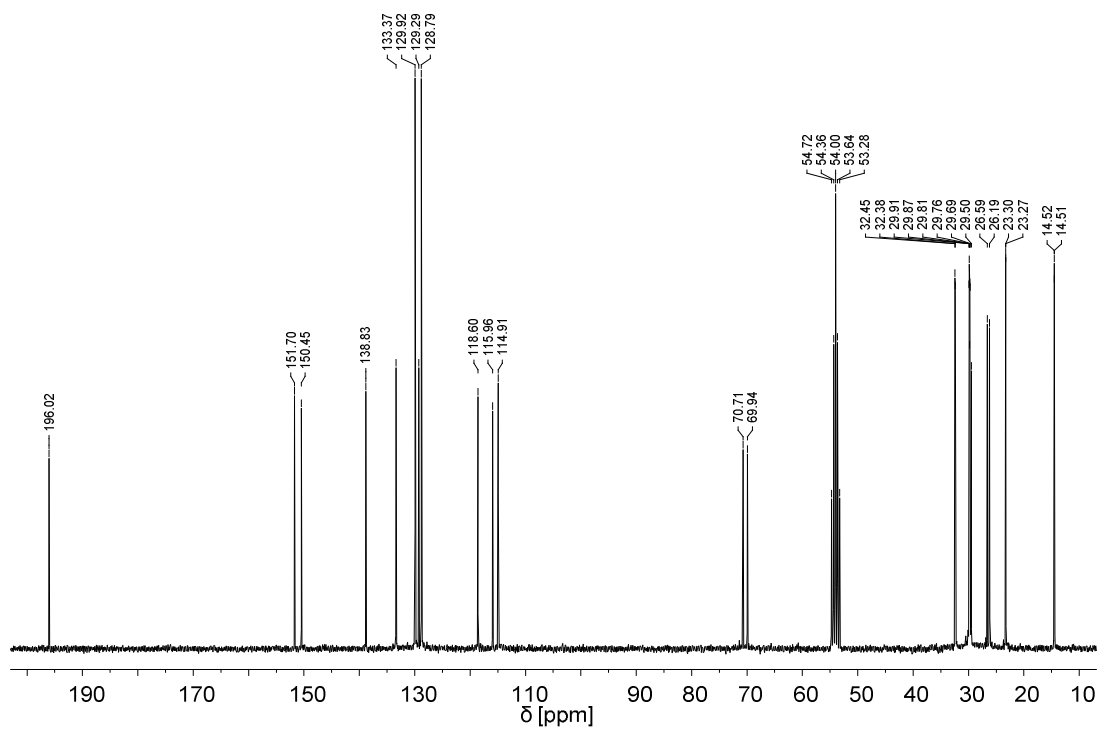
Figure S31. ^{13}C NMR (75 MHz, CD$_2$Cl$_2$) of **5b**.

S20
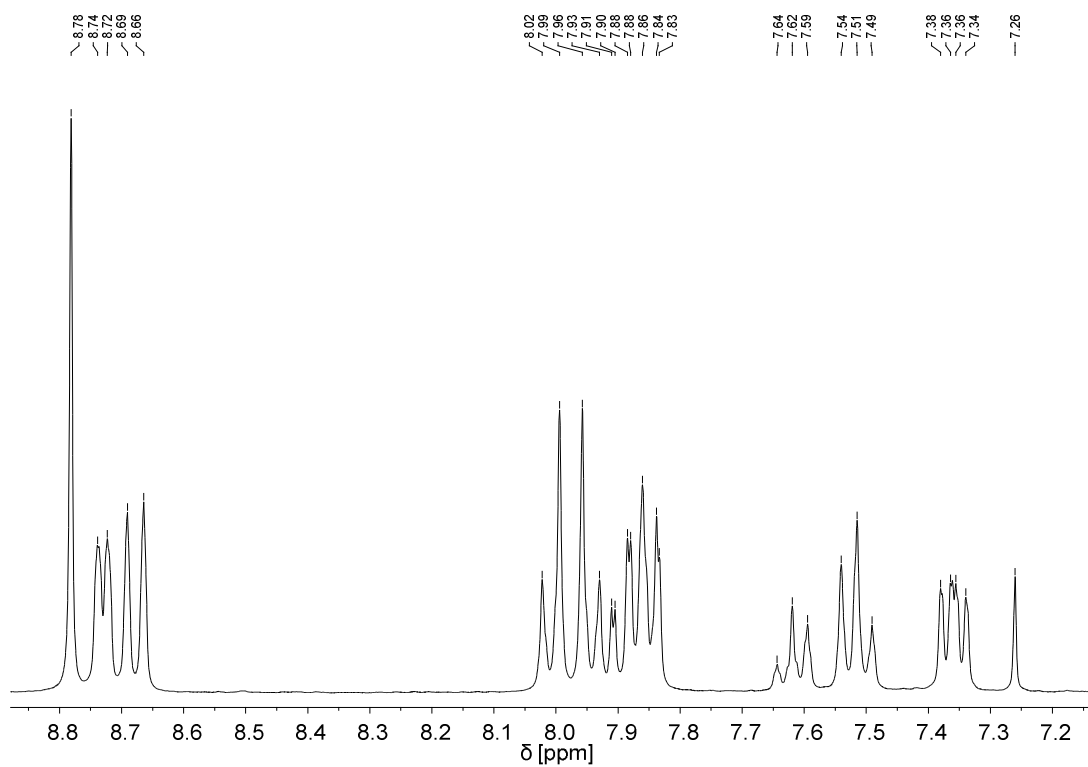
Figure S32. ^{1}H NMR (300 MHz, CDCl$_3$) of **6a**.
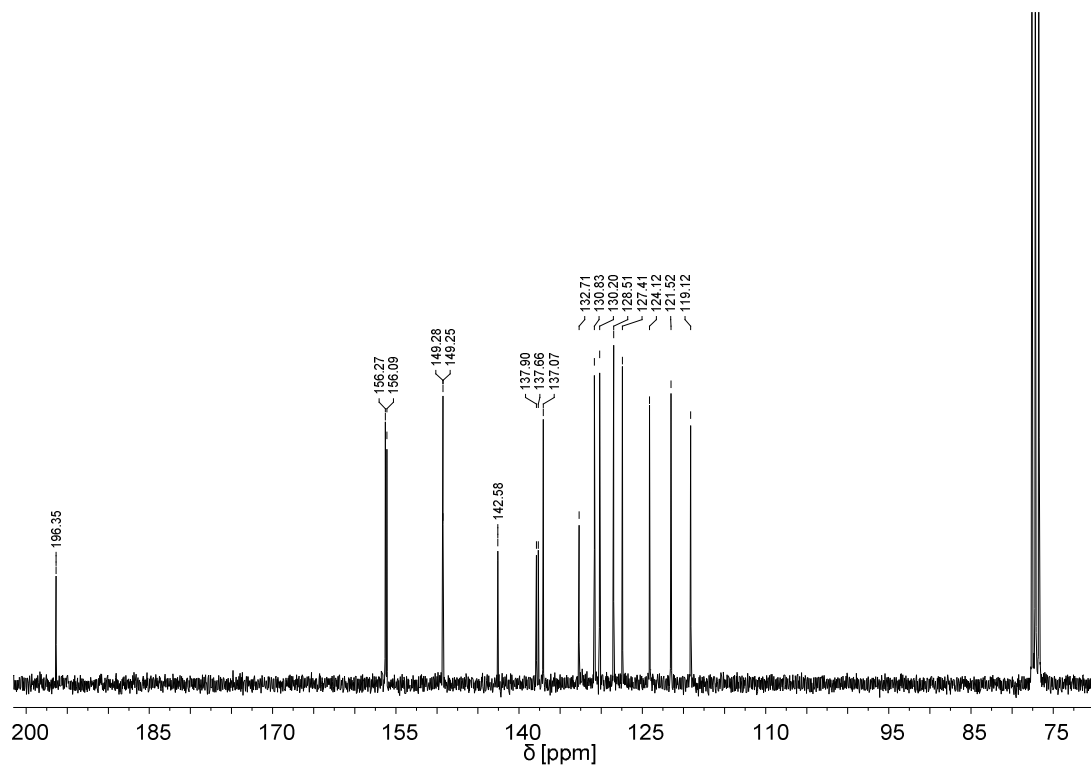
Figure S33. ^{13}C NMR (75 MHz, CDCl$_3$) of **6a**.
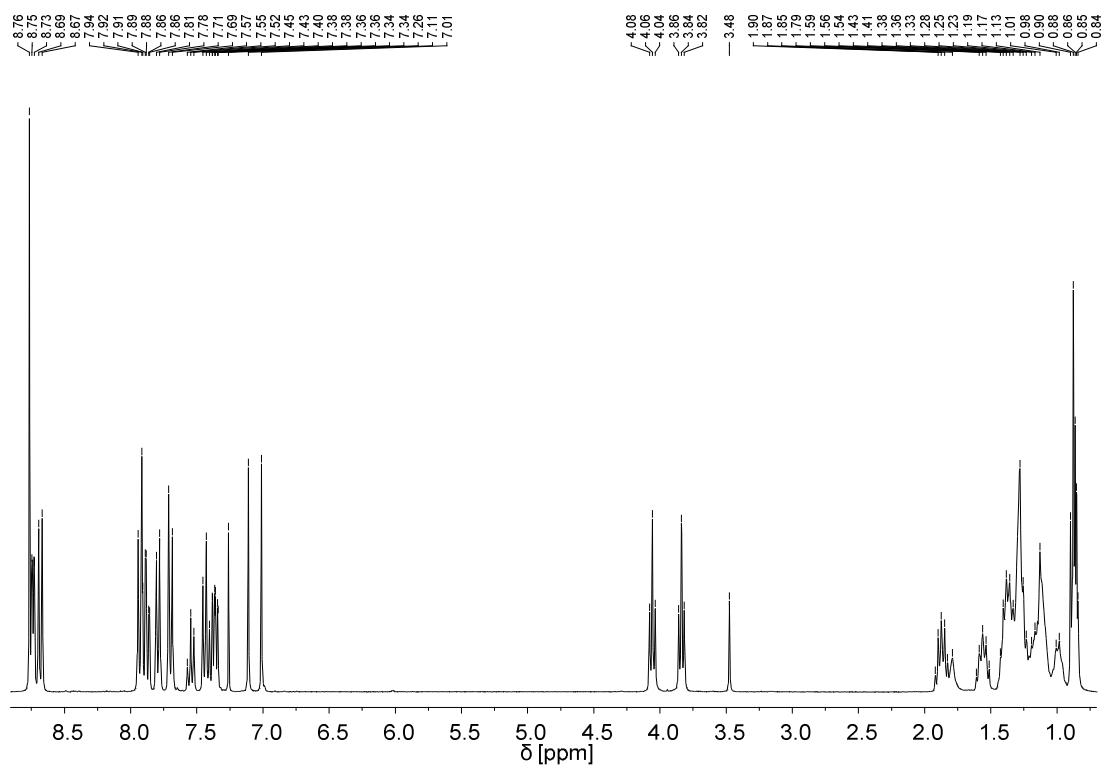
Figure S34. ^{1}H NMR (300 MHz, CDCl$_3$) of **6b**.
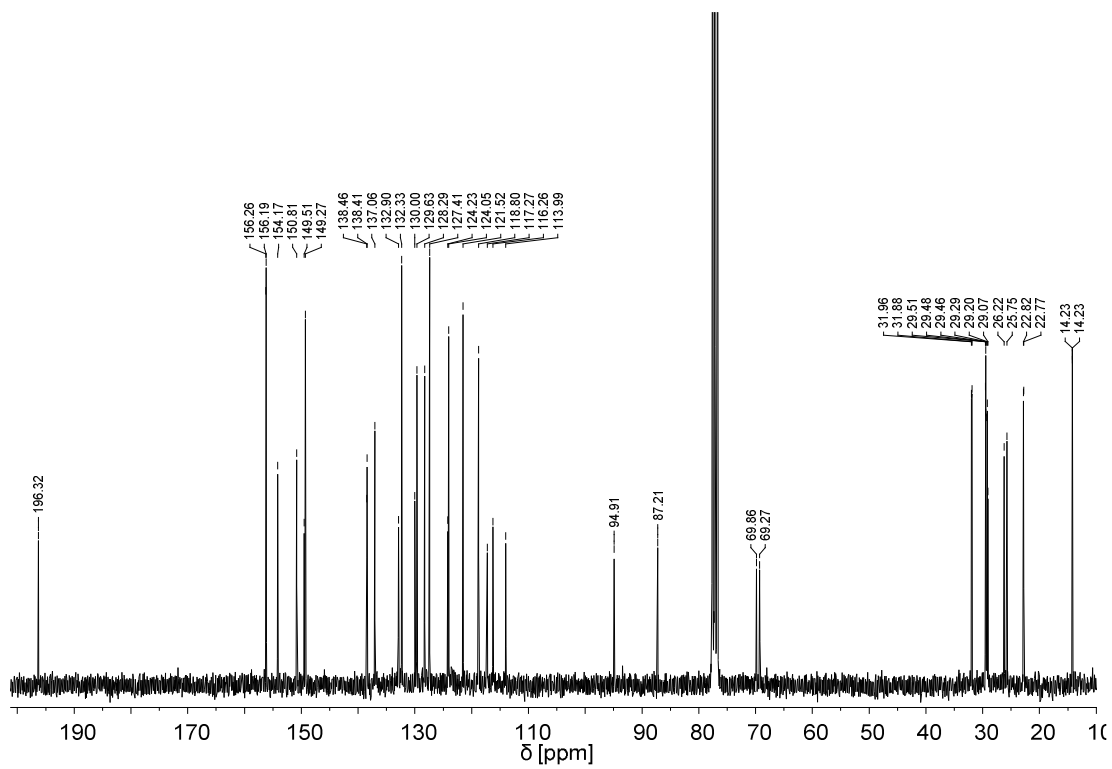
Figure S35. ^{13}C NMR (75 MHz, CDCl$_3$) of **6b**.

S22
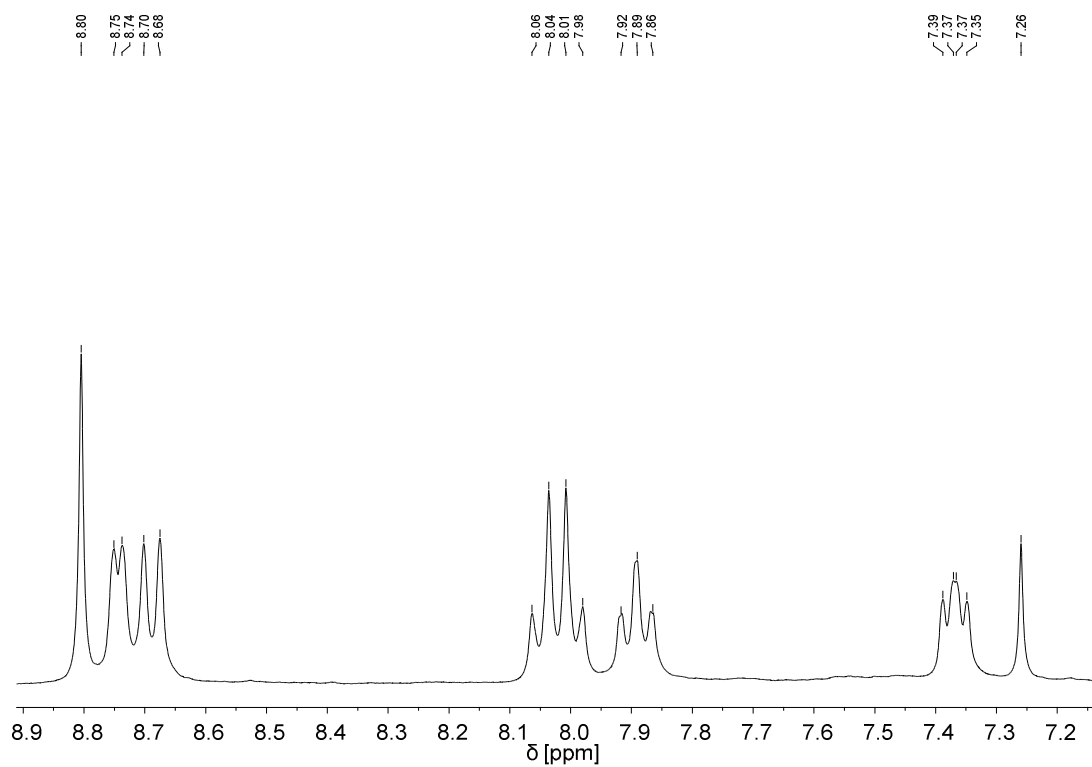
Figure S36. ^{1}H NMR (300 MHz, CDCl$_3$) of **6c**.
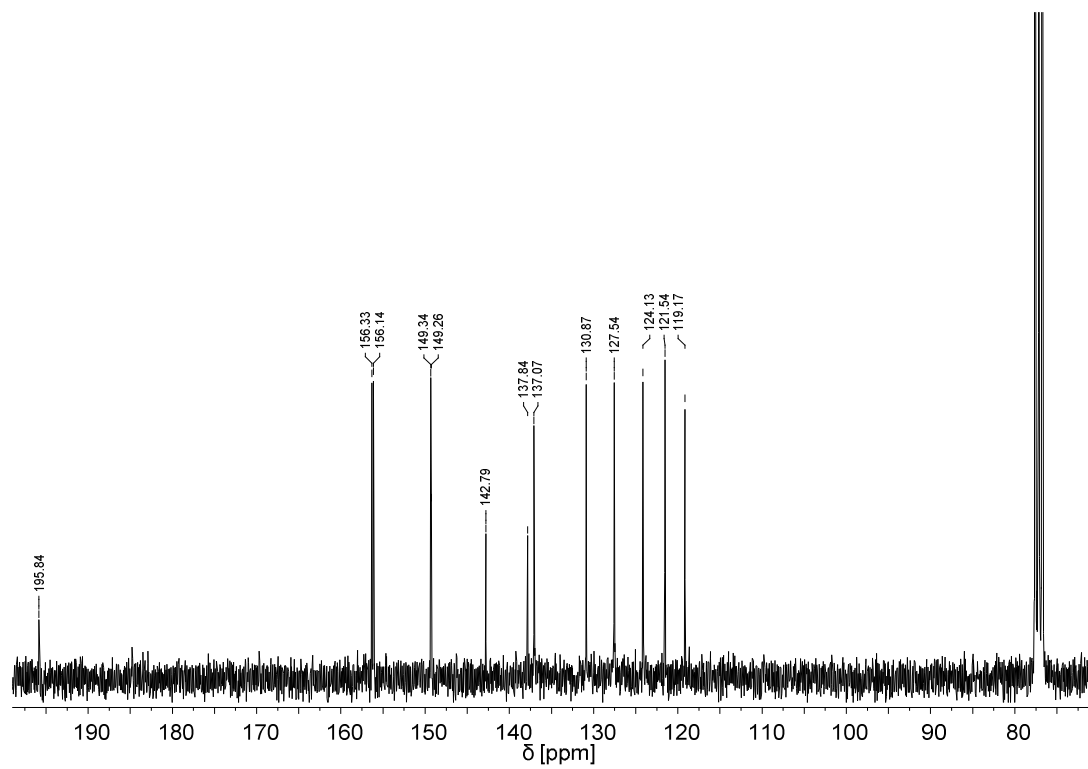
Figure S37. ^{13}C NMR (75 MHz, CDCl$_3$) of **6c**.

S23
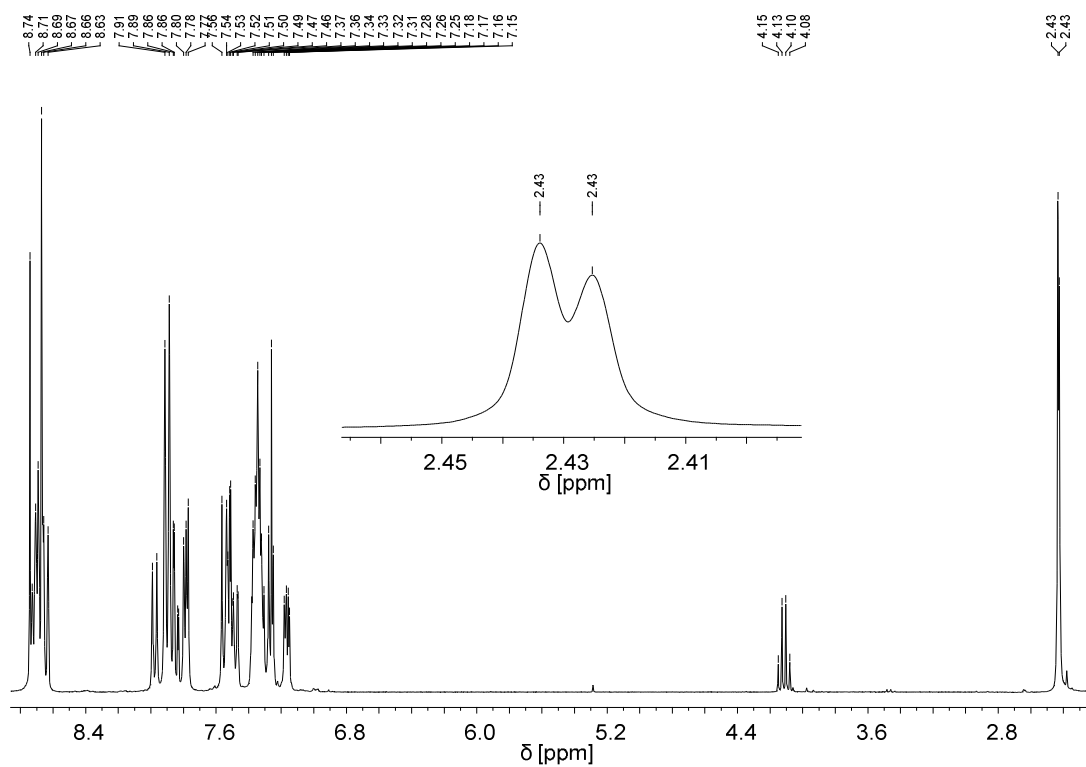
Figure S38. ^{1}H NMR (300 MHz, CDCl$_3$) of **7a.**
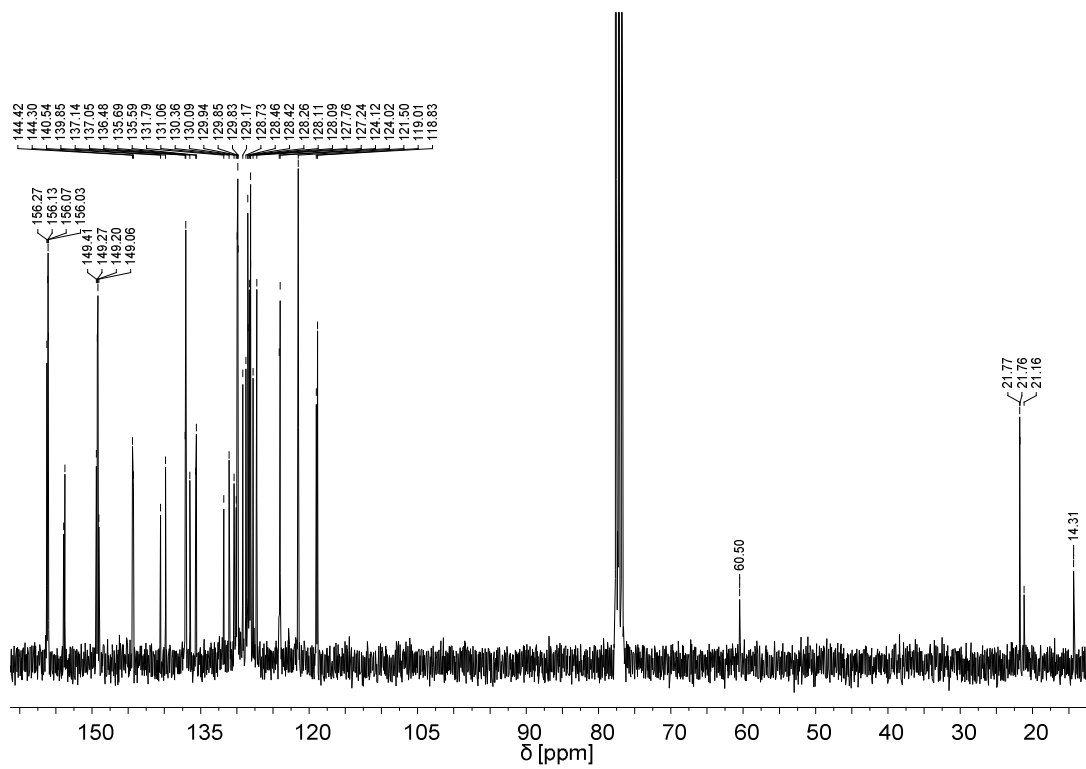
Figure S39. ^{13}C NMR (75 MHz, CDCl$_3$) of **7a**.
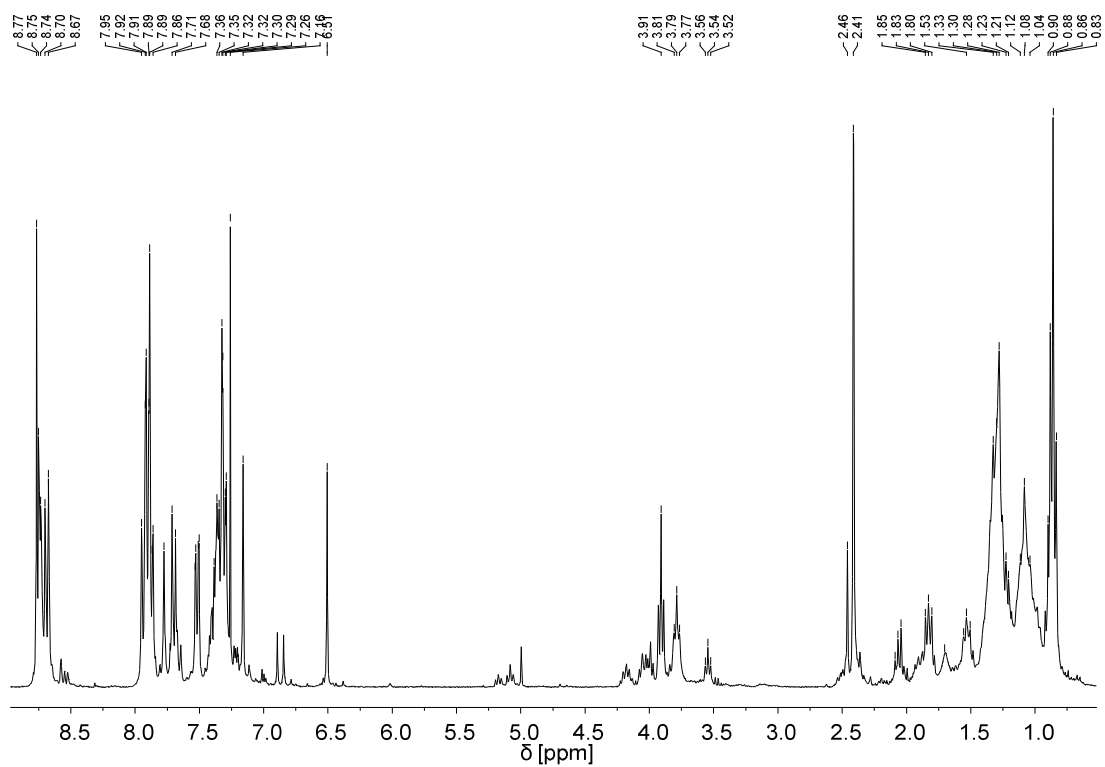
Figure S40. ^{1}H NMR (300 MHz, CDCl$_3$) of **7b**.
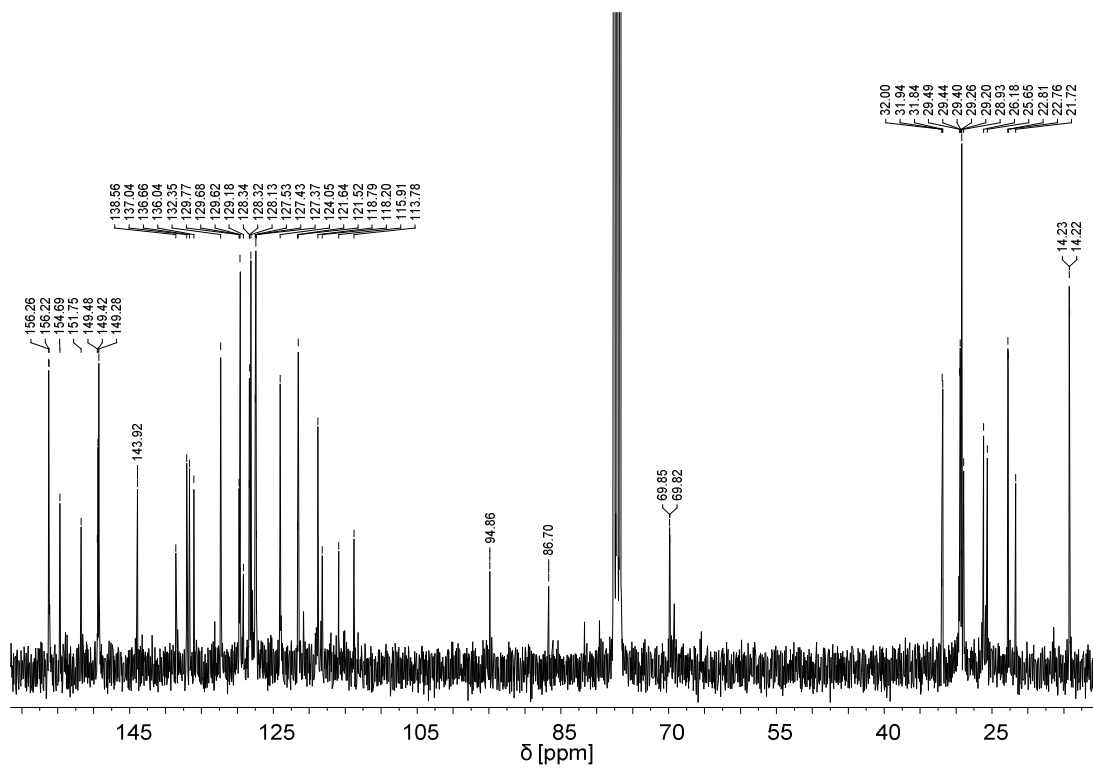
Figure S41. ^{13}C NMR (75 MHz, CDCl$_3$) of **7b**.

S25
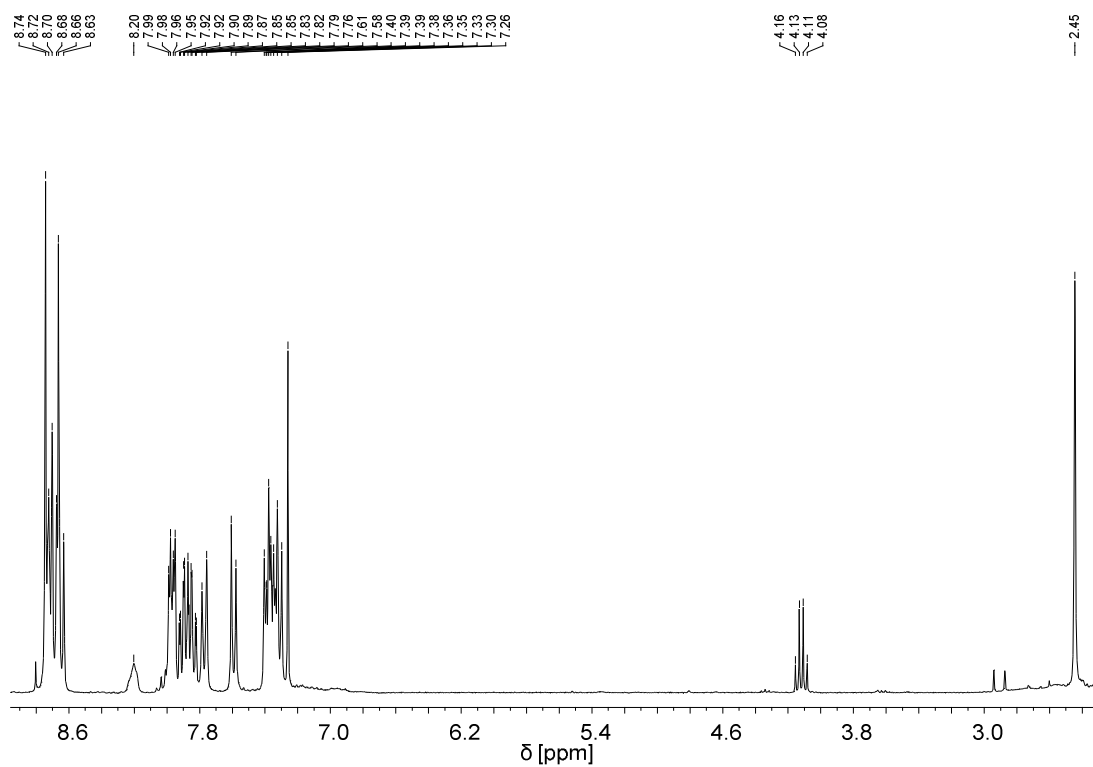
Figure S42. ^{1}H NMR (300 MHz, CDCl$_3$) of **7c**.
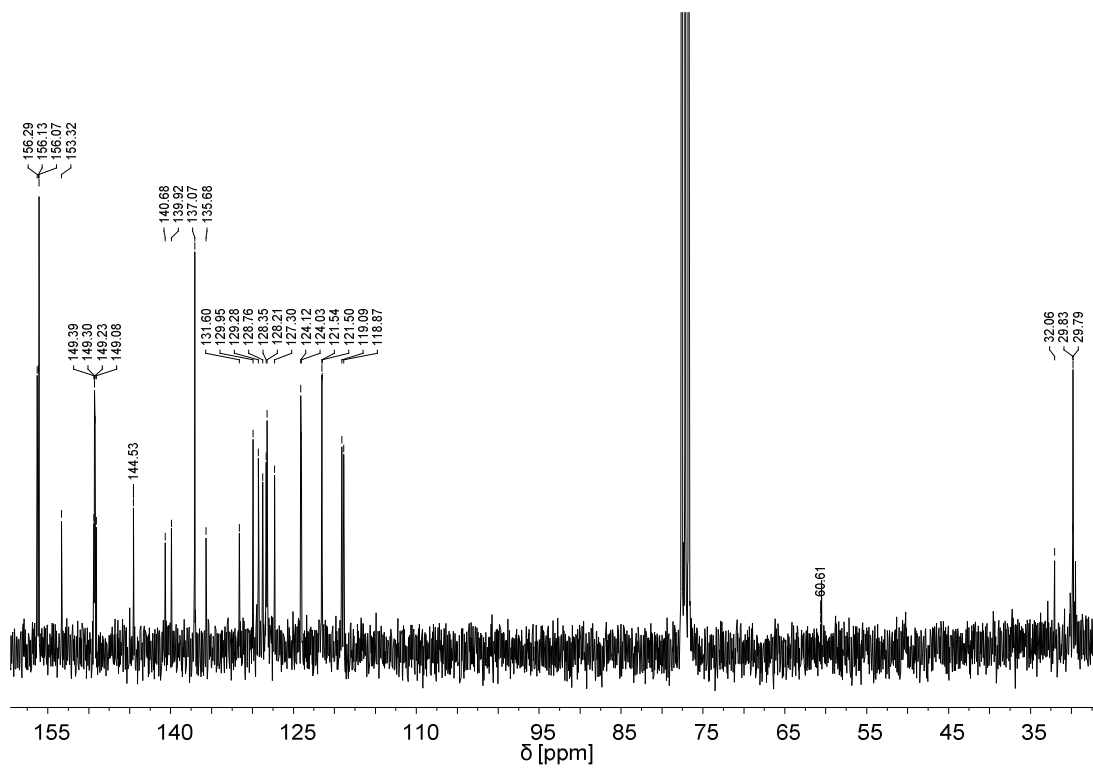
Figure S43. ^{13}C NMR (75 MHz, CDCl$_3$) of **7c**.
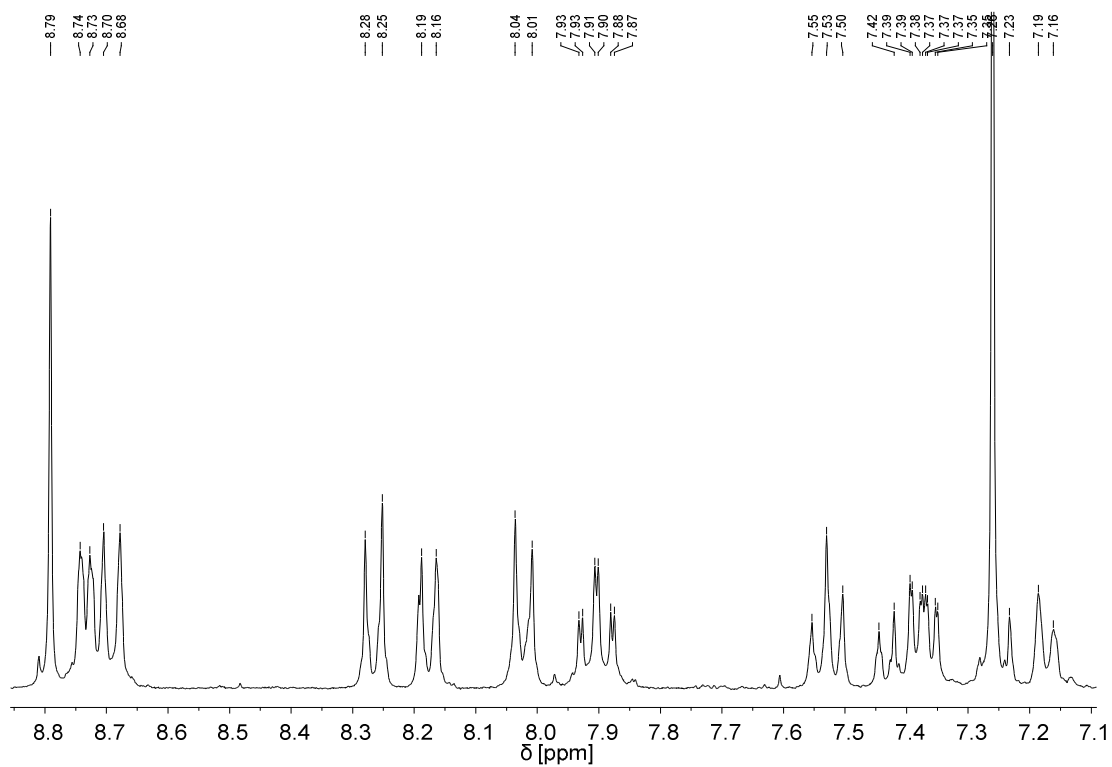
Figure S44. ^{1}H NMR (300 MHz, CDCl$_3$) of **8a**.
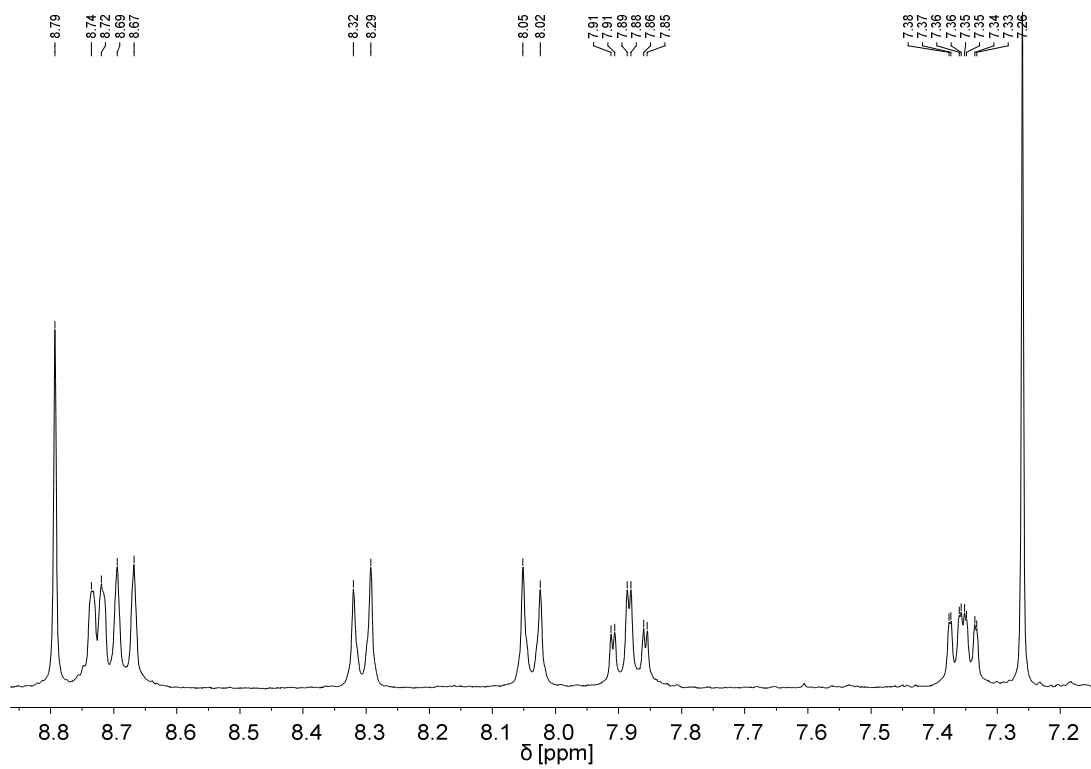
Figure S45. ^{1}H NMR (300 MHz, CDCl$_3$) of **8c**.

S27
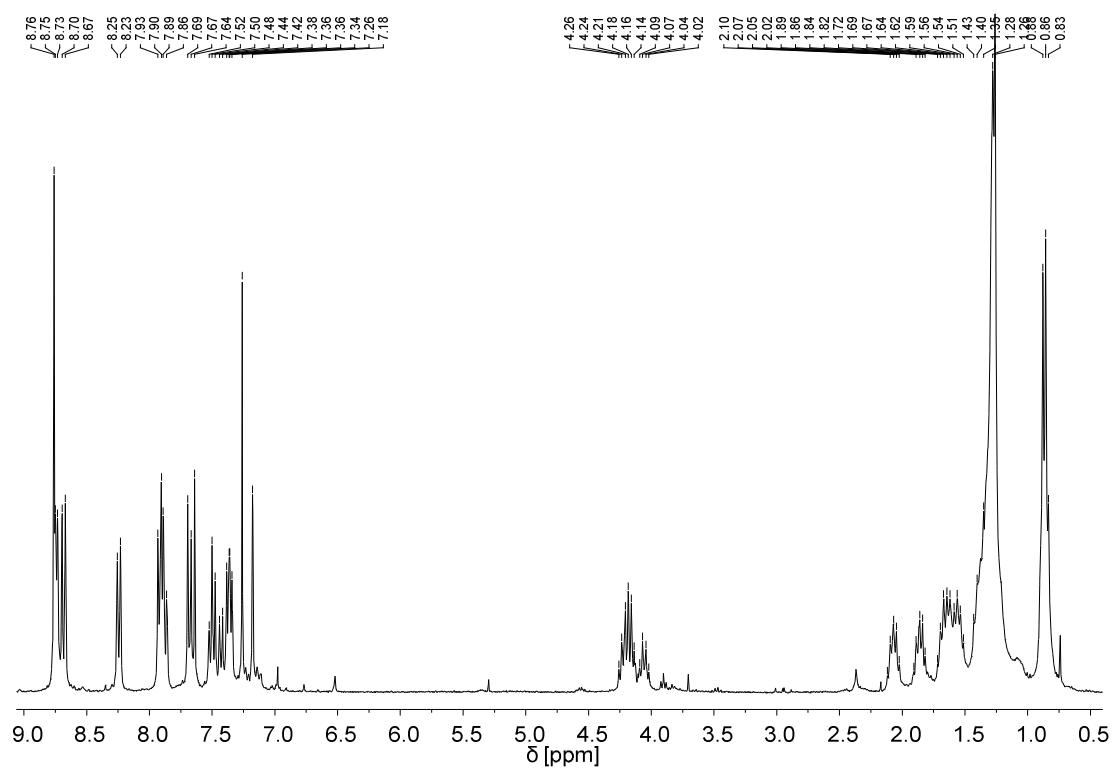
Figure S46. ^{1}H NMR (300 MHz, CDCl$_3$) of **8b**.
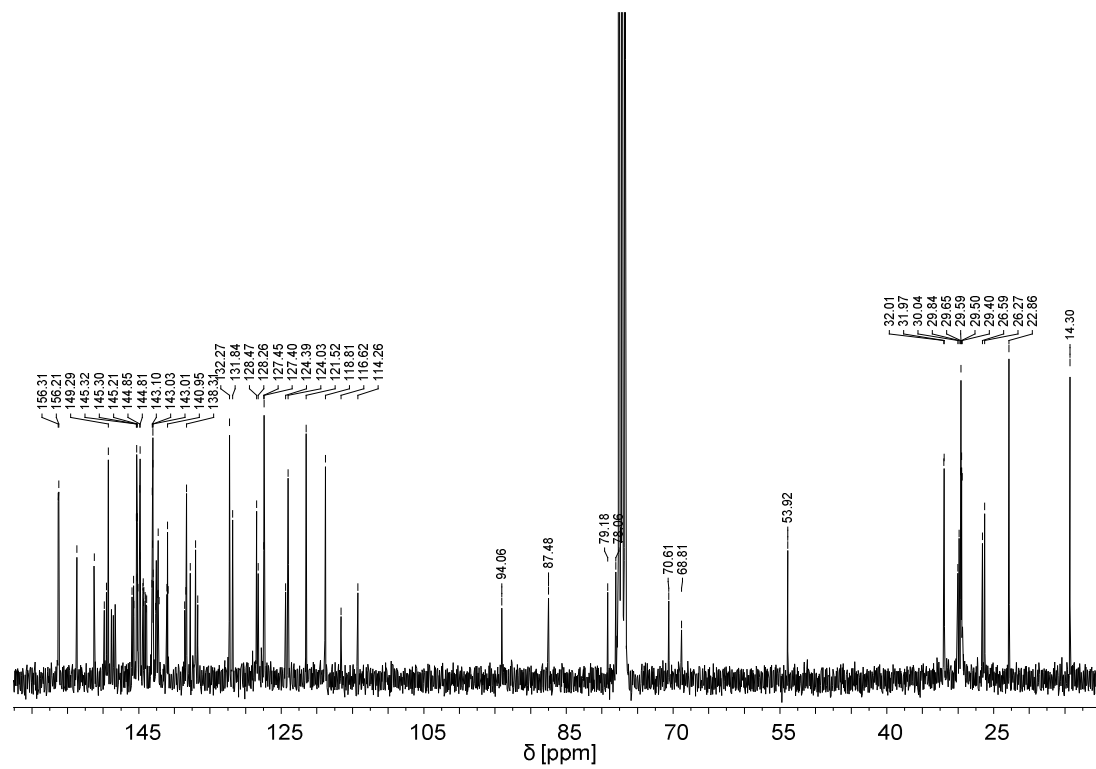
Figure S47. ^{13}C NMR (75 MHz, CDCl$_3$) of **8b**.
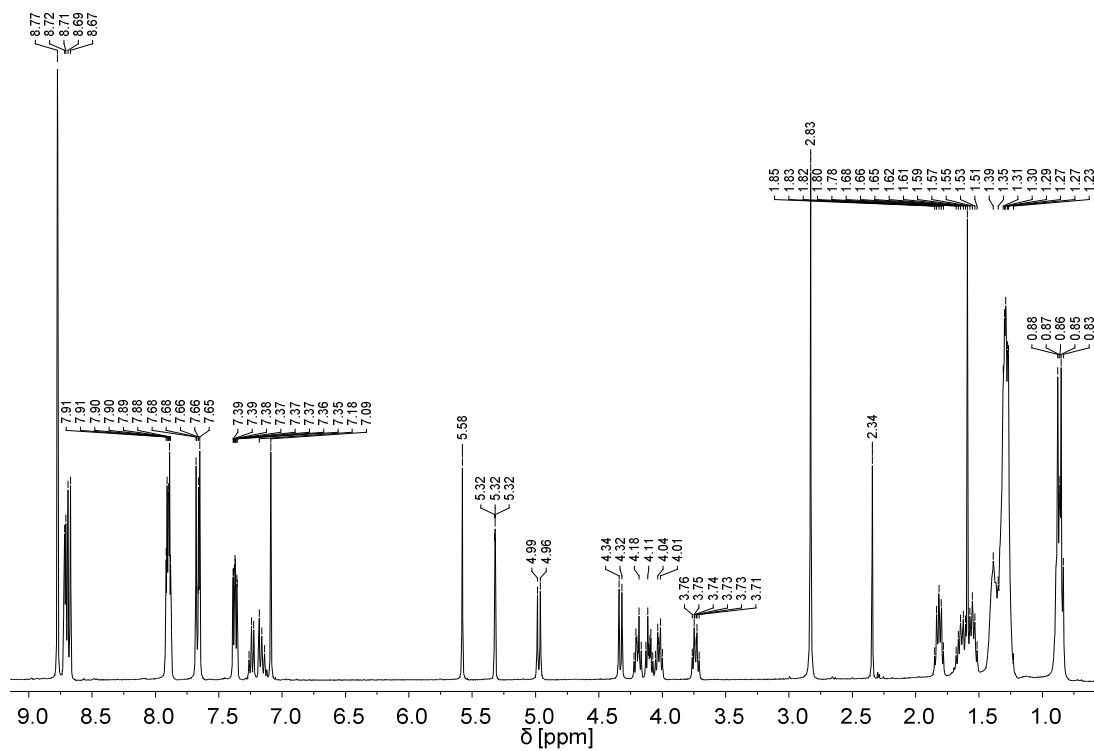
Figure S48. ^{1}H NMR (400 MHz, CD$_2$Cl$_2$) of **10b**.
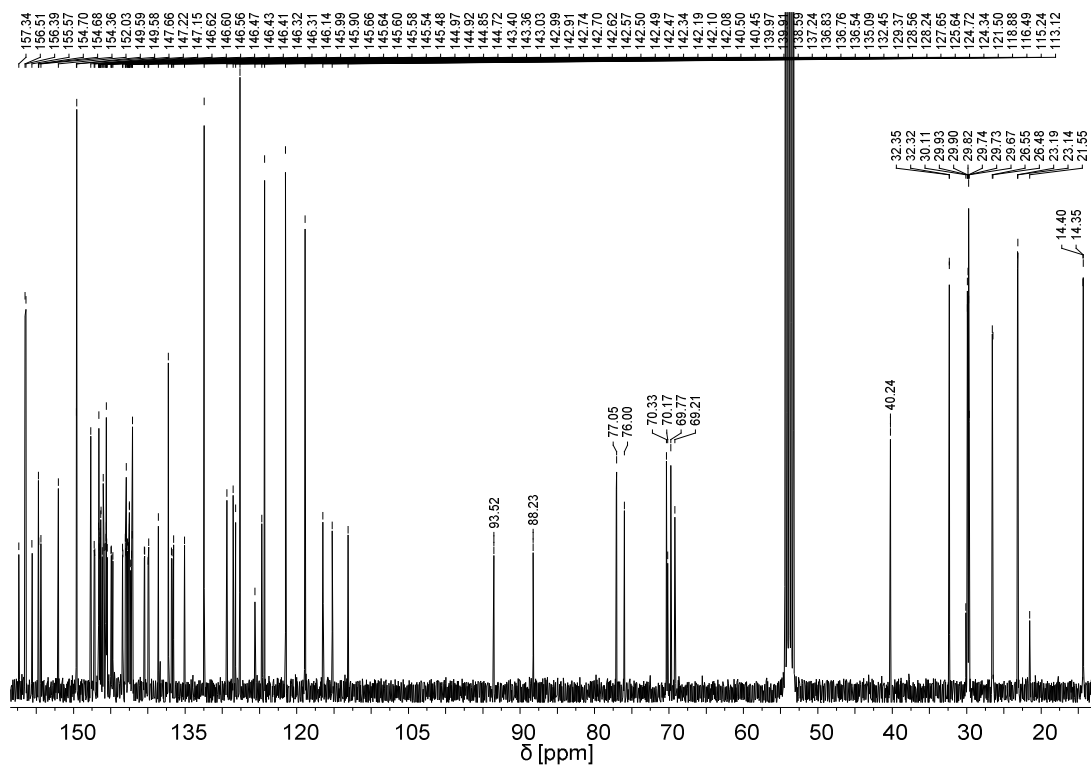
Figure S49. ^{13}C NMR (100 MHz, CD$_2$Cl$_2$) of **10b**.

S29
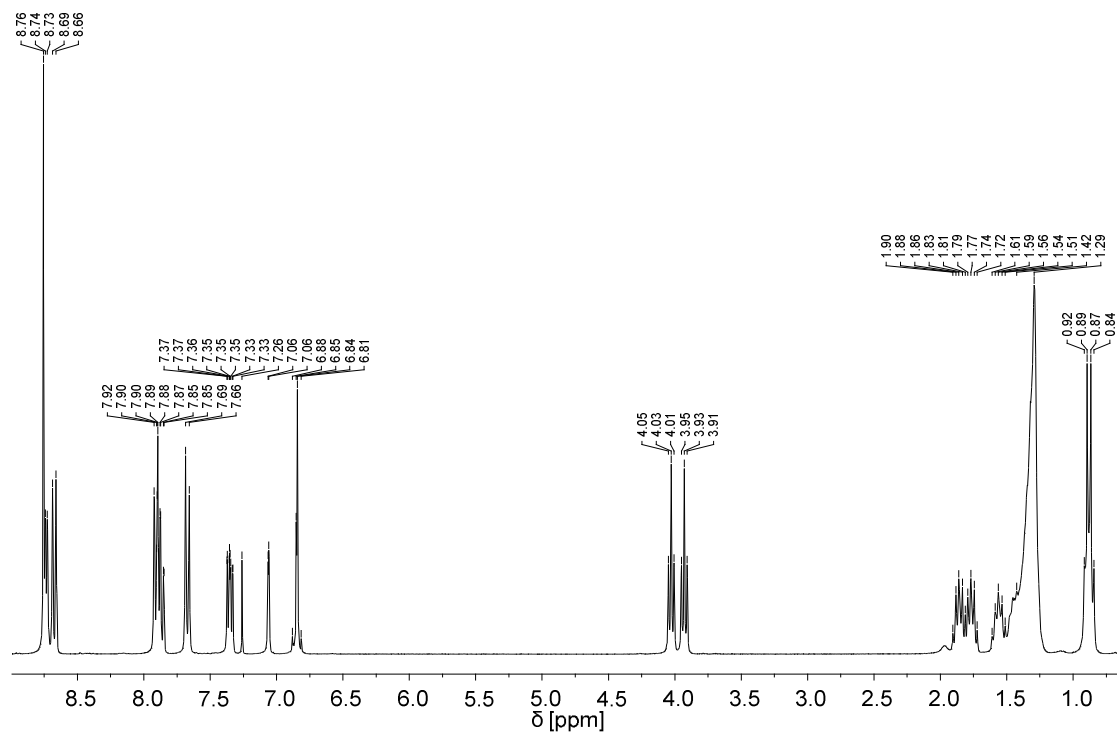
Figure S50. ^{1}H NMR (300 MHz, CDCl$_3$) of **11b**.
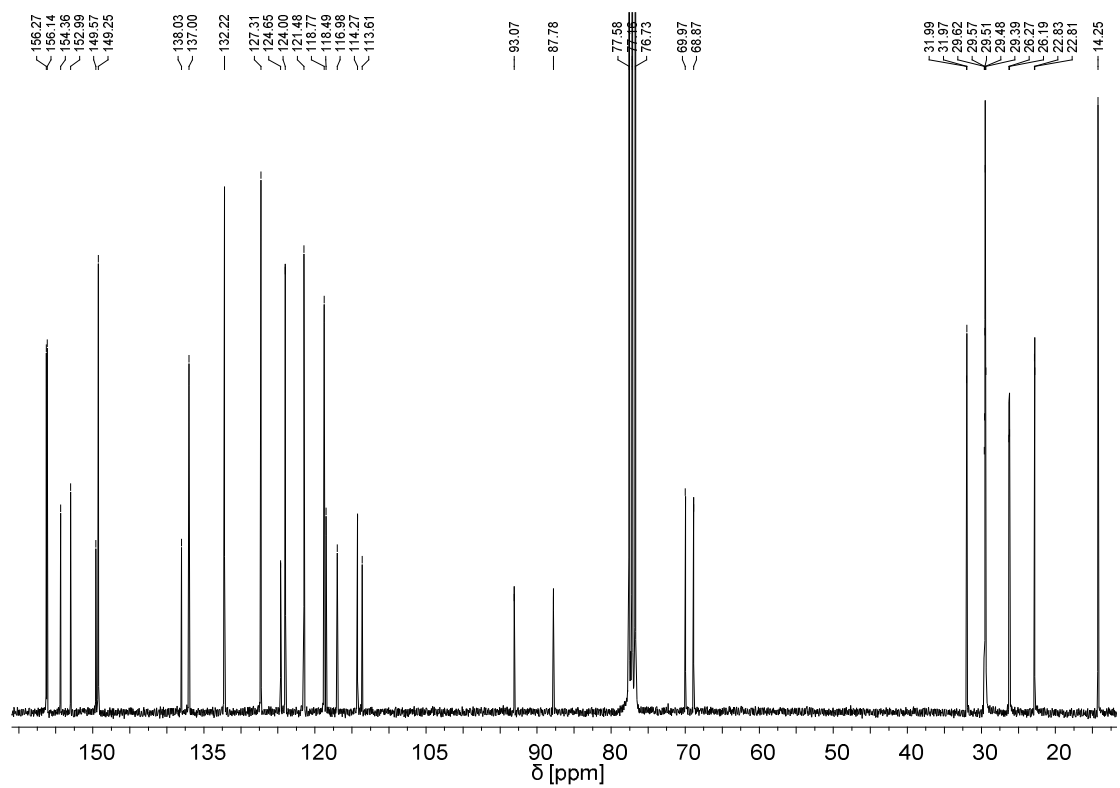
Figure S51. ^{13}C NMR (75 MHz, CDCl$_3$) of **11b**.
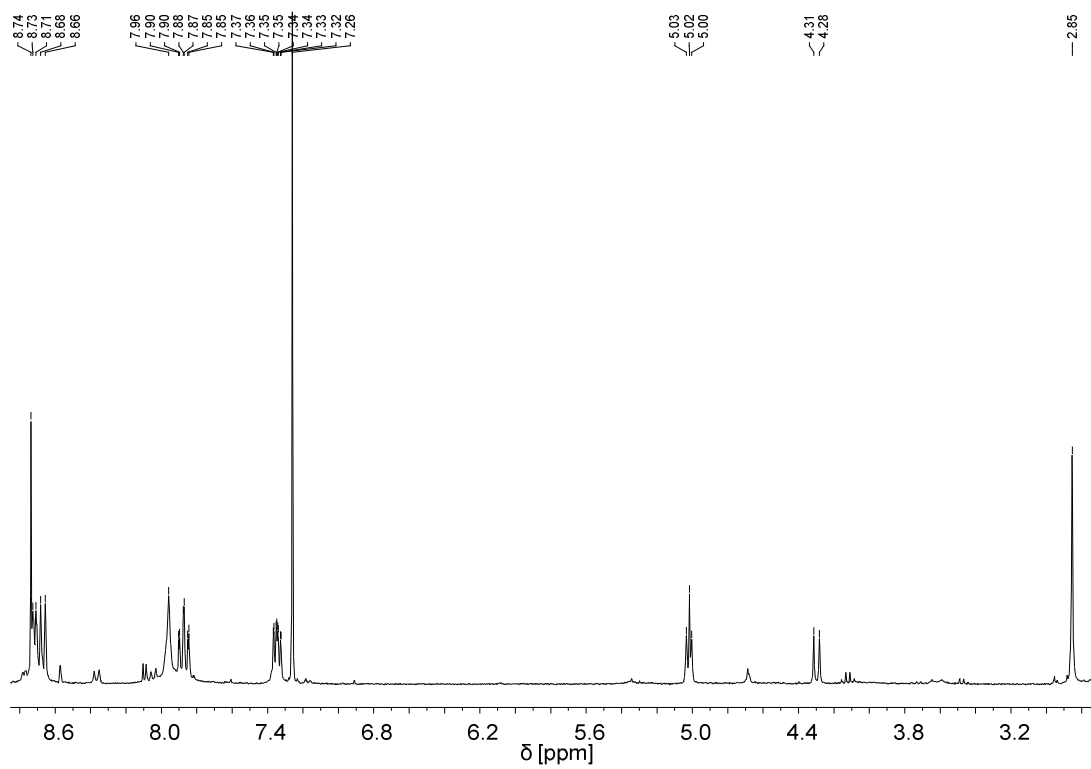
Figure S52. ^{1}H NMR (300 MHz, CDCl$_3$) of **10a**.

6. MS spectra
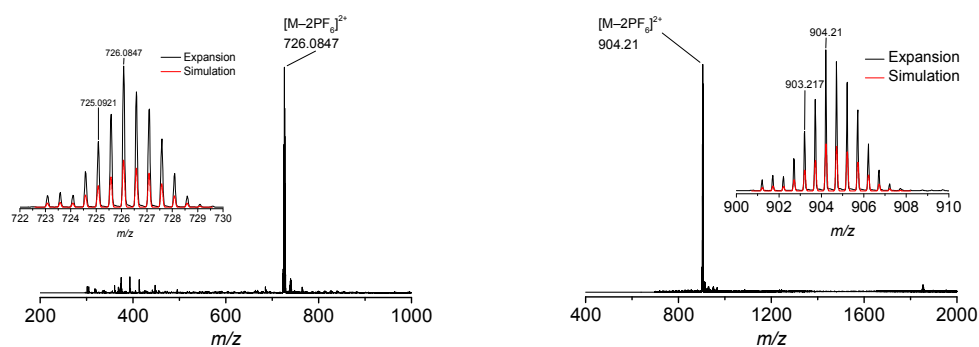
Figure S53. ESI-TOF MS spectra of **1a** (left) and **1b** (right) (solvent: acetonitrile).
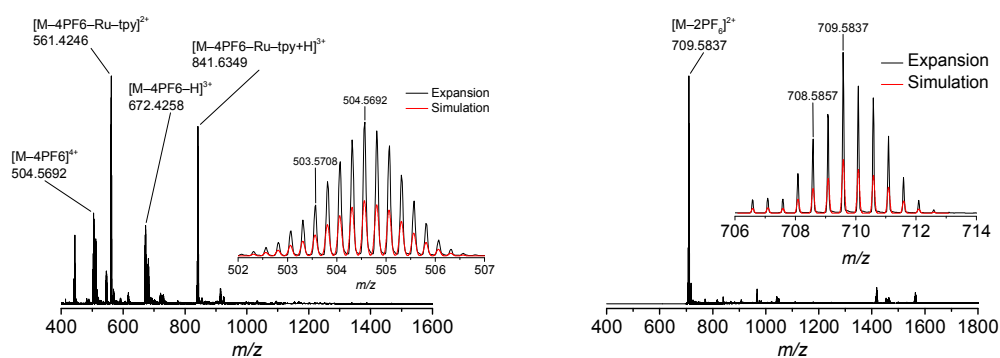
Figure S54. ESI-TOF MS spectra of **1c** (left) and **2a** (right) (solvent: acetonitrile).
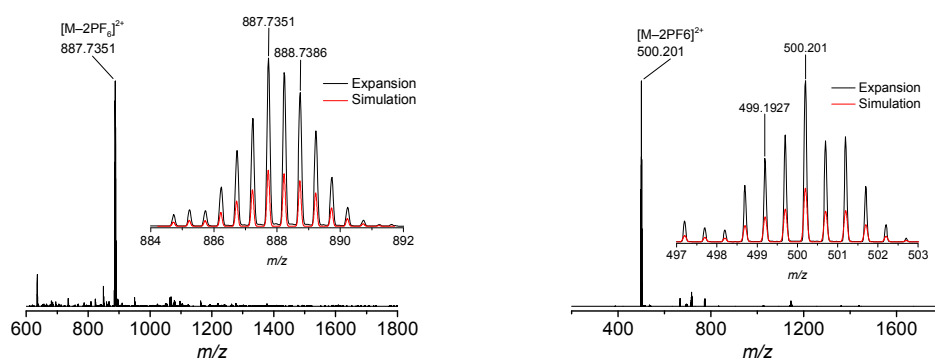
Figure S55. ESI-TOF MS spectra of **2b** (left) and **3b** (right) (solvent: acetonitrile).
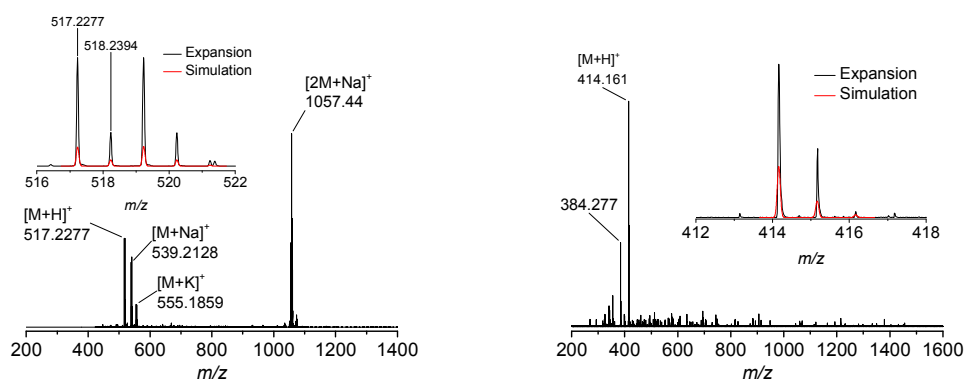
Figure S56. ESI-TOF MS spectrum of **5b** (left) (solvent: acetonitrile) and MALDI-TOF MS spectrum of **6a** (right) (Matrix: Dithranol).
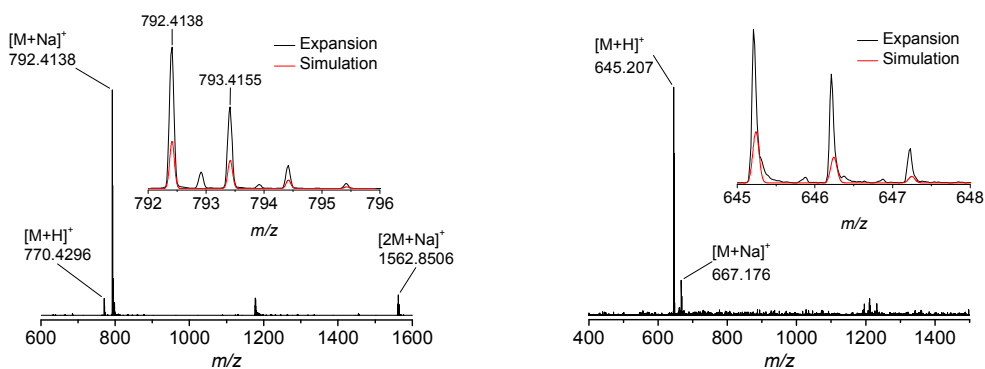
Figure S57. ESI-TOF MS spectrum of **6b** (left) (solvent: acetonitrile) and MALDI-TOF MS spectrum of **6c** (right) (Matrix: Dithranol).
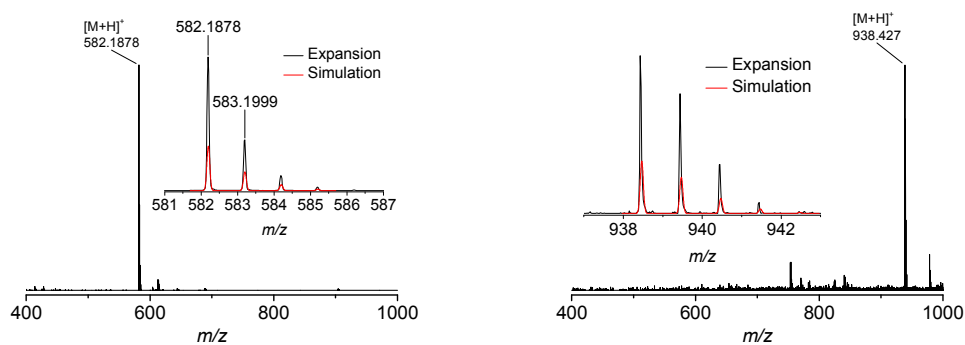
Figure S58. ESI-TOF MS spectrum of **7a** (left) (solvent: acetonitrile) and MALDI-TOF MS spectrum of **7b** (right) (Matrix: Dithranol).
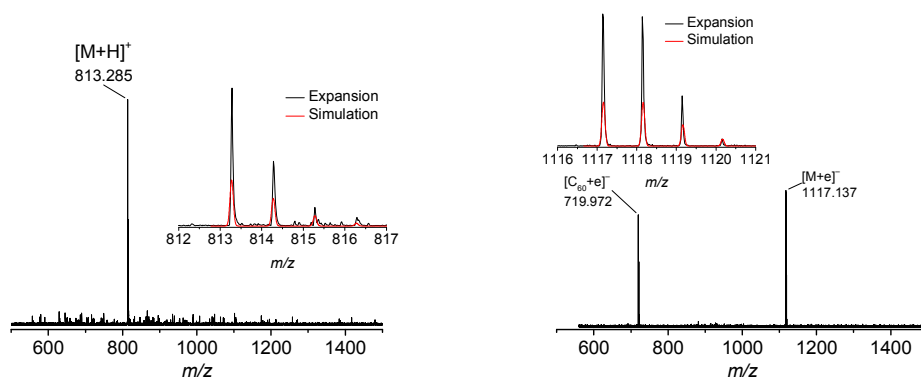
Figure S59. MALDI-TOF MS spectra of **7c** (left) (Matrix: Dithranol) and **8a** (right) (Matrix: terthiophene, negative mode).
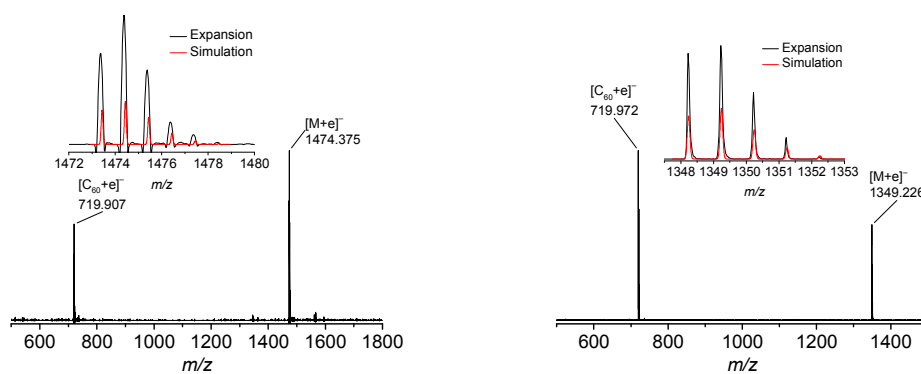
Figure S60. MALDI-TOF MS spectra of **8b** (left) and **8c** (right) (Matrix: terthiophene, negative mode).
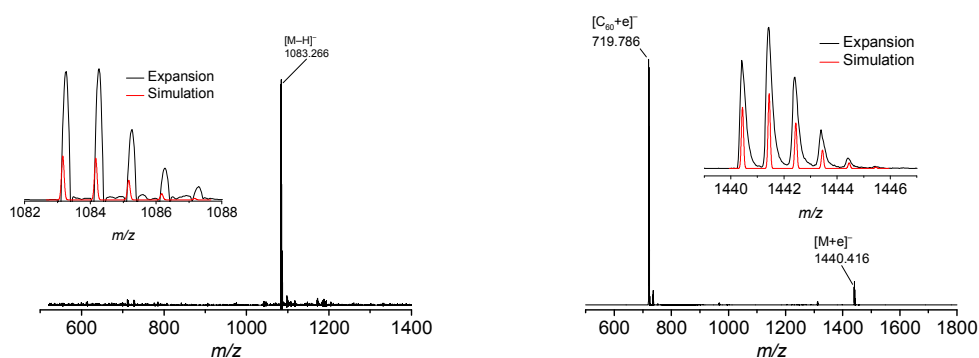
Figure S61. MALDI-TOF MS spectra of **10a** (left) and **10b** (right) (Matrix: terthiophene, negative mode).
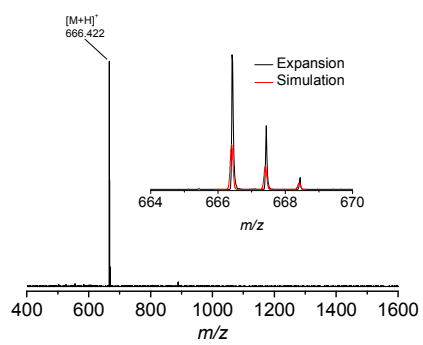
Figure S62. MALDI-TOF MS spectrum of **11b** (Matrix: Dithranol).

P3 - Structure–Property Relationships in an Iridium(III) Bis(Terpyridine) Complex with Extended Conjugated Side Chains

Structure−Property Relationships in an Iridium(III) Bis(Terpyridine) Complex with Extended Conjugated Side chains

Joachim Kübel,[†,‡] Andreas Winter,[§,⊥] Ulrich S. Schubert,[§,⊥] and Benjamin Dietzek*[,†,‡,⊥]

[†]Institute of Physical Chemistry and Abbe Center of Photonics, Friedrich Schiller University Jena, Helmholtzweg 4, 07743 Jena, Germany

[‡]Leibniz Institute of Photonic Technology (IPHT) Jena e.V., Albert-Einstein-Strasse 9, 07745 Jena, Germany

[§]Laboratory of Organic and Macromolecular Chemistry (IOMC), Friedrich Schiller University Jena, Humboldtstrasse 10, 07743 Jena, Germany

[⊥]Jena Center for Soft Matter (JCSM), Friedrich Schiller University Jena, Philosophenweg 7, 07743 Jena, Germany

S *Supporting Information*

ABSTRACT: Iridium(III) bis(terpyridine) complexes are known as excellent triplet emitters with emission lifetimes in the order of microseconds. We report the homoleptic complex $[IrL_2]^{3+}$ (L = 4′-(4−2,5-bis(octyloxy)-4-styrylphenyl)ethinyl)-phenyl)-2,2′:6′,2″-terpyridine) that shows no detectable phosphorescence at room temperature but shows fluorescence. Emission spectra of $[IrL_2]^{3+}$ depend on the excitation wavelength. The origin of this behavior is studied with the help of results from (TD-)DFT calculations and is attributed to the selective excitation of different rotamers and isomers. Femtosecond-transient absorption experiments give further support for this interpretation as the specific excited-state absorption features of *Z*- and *E*-stilbene motives can be identified.
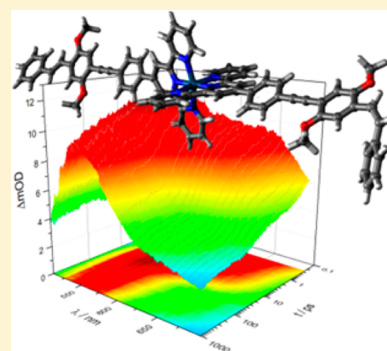
INTRODUCTION

Metal complexes of 2,2′:6′,2″-terpyridine (tpy)[1,2] and derived materials[3,4] hold great potential for applications in organic photovoltaics (OPV)[5,6] or organic light emitting devices (OLEDs).[7] The favorable structural features of such compounds in comparison with transition metal complexes based on bidentate ligands such as 2,2′-bipyridine (bpy) include the absence of diastereomers in multinuclear complexes[8] and the possibility to construct linear arrays,[9−11] which can be referred to as molecular wires.[12,13] There are, however, short comings of tpy-complexes compared to bpy-analogues such as the very short excited-state lifetimes[14] though these can be overcome, e.g., by introducing substituents in 4′-position of the tpy-unit.[15,16] Particularly successful attempts to increase the excited-state lifetimes of Ru^{II}-tpy complexes so far were combinations of complex fragments with secondary organic chromophores.[17,18] In such systems, ligand-centered triplet states can serve as reservoir for excitation energy and prolong the ^{3}MLCT emission lifetime by several orders of magnitude.[19−21] As an example, homoleptic complexes of the ligand 4′-(4−2,5-bis(octyloxy)-4-styrylphenyl)ethinyl)phenyl)-2,2′:6′,2″-terpyridine (L)[22,23] and the metal ions Fe^{II}, Ru^{II}, and Os^{II} (with $PF_6^−$ counterions, denoted as **Fe**, **Ru** and **Os**, respectively) were photophysically characterized.[24,25] The complex **Ru** shows a 150-fold increased lifetime as compared to the unsubstituted model compound $[Ru(tpy)_2]^{2+}$[14] of 36.5 ns in aerated solution.[25] Another remarkable property of the complexes **Ru** and **Os** is the observation of dual luminescence: Fluorescence emission of the ligand (centered at 470 nm) as well as a metal-based ^{3}MLCT phosphorescence (centered at 650 and 710 nm for **Ru** and **Os**, respectively) is found upon excitation of $\pi−\pi^*$ transitions in the ligand. The two emission bands observed for either **Ru** or **Os** extend over a large part of spectrum of visible light and render these compounds valuable lead-structures for single molecule white emitters.[24,25] This dual emission originates from an ultrafast branching of the excited-state relaxation pathway near the Franck−Condon-point of absorption. While most excited molecules undergo intersystem crossing, the triplet yield was found to be larger than 99%, a small fraction (<1%) of excited molecules remains in the singlet manifold of the potential energy surface and deactivates primarily via fluorescence.[25] It should be stressed that the observation of dual emission is due to the combination of specific electronic properties of the metal-coordination sphere of the complexes and of the organic chromophores present. Hence, it is intriguing to investigate the photophysical behavior of systems, in which the highly fluorescent organic chromophore attached to the 4′-position of the tpy-ligand is combined with an emissive metal-coordination center such as $[Ir(tpy)_2]^{3+}$. Already the emission properties of $[Ir(tpy)_2]^{3+}$ are

impressive: Emission lifetimes in the microsecond range are observed at quantum yields in the order of several percent.[26−29] Contrary to Ru^{II}-tpy-based complexes, emission in $[Ir(tpy)_2]^{3+}$ originates from $^3LC^{26}$ or ^3ILCT states[29,30] depending on the substituents in 4′-position.[31,32] The absence of low-lying ^3MLCT states in $[Ir(tpy)_2]^{3+}$ and its derivatives is due to the high oxidation potential[29] (i.e., low-lying $5d\pi$ orbitals) of the Ir^{III} ion as well as its electronic and atomic structure that cause the orbital overlap between the tpy-nitrogen lone pairs and the Ir^{III} d-orbitals to be very inefficient.[33]

Very impressive work demonstrated the feasibility of constructing a molecular dyad based on $[Ir(tpy)_2]^{3+}$ with a triphenylamine donor and naphthalene bisimide acceptor showing a charge-separated state lifetime of 120 μs at room temperature.[30] The favorable properties of Ir^{III} as central metal in tpy-based assemblies allow for significant alterations of complex properties[34] besides the usual way of introducing additional functionality due to substituents in 4′-position of the tpy-unit, which was extensively pursued for Ru^{II} complexes.

In this contribution we introduce the homoleptic complex $[IrL_2]^{3+}$, which is referred to as **Ir** in the remainder of this manuscript. Steady-state and time-resolved spectroscopy are applied in this study to detail the photophysics and light-induced processes in **Ir**.

■ EXPERIMENTAL SECTION

Synthesis. The synthesis of the terpyridine ligand (**L**) was published earlier.[35] For the synthesis of **Ir**, the general protocol for the preparation of Ir^{III}−terpyridine complexes[36,37] was applied. Characterization data for **Ir**. ^1H NMR (acetone-d_6, 300 MHz): δ = 9.61 (s, 4H), 9.18 (d, ^3J = 7.9 Hz, 4H), 8.42 (d, ^3J = 8.1 Hz, 4H), 8.29 (m_c, 2H), 7.94 (m, 4H), 7.71−7.22 (m, 28H), 4.15 (m_c, 8H), 1.92 (m_c, 8H), 1.66 (m_c, 8H), 1.55−1.22 (m, 32H), 0.91 (m_c, 12H). Anal. Calcd for $C_{106}H_{114}F_{18}N_6O_4P_3Ir$ (2163.23): C, 58.85; H, 5.31; N, 3.89. Found: C, 58.90; H, 5.28; N, 3.94. On the basis of the synthetic route molecules should be produced under thermodynamic control, i.e., with an E-configured double bond. Indeed, coupling constants (J > 15 Hz) derived from NMR data[35] of the related zinc complex $[ZnL_2]^{2+}$ suit well with E-configuration.

Spectroscopic Methods. The time-resolved transient absorption setup is based on an amplified Ti:sapphire oscillator (Legend-Elite, Coherent Inc.), which produces a pulse train of 35 fs, 3.5 mJ pulses centered at 795 nm with a pulse repetition rate of 1 kHz. One third (ca. 1.2 mJ) of the amplifier output is used to generate the pump pulses (λ_{pump} = 480 nm) in a collinear optical-parametric amplifier (TOPAS-C, LightConversion Ltd.). White light is used as the probe, which is generated by focusing a minor fraction of the amplifier output into a sapphire plate. The pump pulses are delayed with respect to the probe−pulses by means of an optical delay line, and their polarization is rotated by 54.7° (magic angle) with respect to the probe beam by using a Berek compensator. The probe pulses are sent to a double-stripe diode-array detection system (Pascher Instruments AB). The diode array is read out with the repetition rate of the laser and the ΔA signal is calculated for individual pairs of probe pulses corresponding to pump-on and pump-off conditions. The energy of a pump pulse is attenuated to 1 μJ, while typical probe intensities fall into the range of a few hundred nanojoules. Steady-state absorption spectra are frequently recorded to ensure sample integrity. The time-resolution of our setup is in the order of 80 fs estimated from

the width of the coherent artifact region. Prior to data analysis, the experimental differential absorption data is chirp corrected and afterward fitted with a global fitting routine.

Steady-state absorption spectra are recorded on a Jasco V-670 spectrophotometer. Steady-state fluorescence and phosphorescence spectra are recorded on a Jasco FP-6200 spectrofluorimeter and on a PerkinElmer LS-50B fluorescence spectrometer in phosphorescence mode, respectively.

The fluorescence quantum yield was determined from integrated, corrected emission spectra relative to $[Ir(ttpy)]^{3+}$ (ϕ = 0.029 in air saturated acetonitrile)[26] using a PerkinElmer LS-50B fluorescence spectrometer.

For fluorescence lifetime determination a Hamamatsu HPDTA streak camera is employed. A Ti:sapphire laser (Tsunami, Newport Spectra-Physics GmbH) is used as the light source. The repetition rate of the laser is reduced to 400 kHz by a pulse selector (Model 3980, Newport Spectra-Physics GmbH). Afterward the fundamental beam of the oscillator is frequency doubled to create the 355 nm pump beam. The emission is detected by the streak camera via a CHROMEX spectrograph.

Sample Preparation. For transient absorption measurements the sample is prepared to yield on optical density of 0.3 at the excitation wavelength. Absorption and emission spectra were recorded from dilute solutions (OD < 0.1) in various solvent. Since **Ir** is insoluble in toluene, the compound is first dissolved in THF and a few drops are added to an excess of pure toluene. All solvents utilized in this study are obtained from Sigma-Aldrich in spectroscopic grade.

Quantum-Chemical Calculations. Quantum chemical calculations were performed using density functional theory applying the exchange-correlation functionals B3-LYP[38−40] or PBE0[41,42] or the long-range corrected functional CAM-B3LYP.[43] Typically, 6-31G** basis sets[44] were used for all atoms except the metal ions which were described using appropriate pseudopotentials, namely MDF10 (iron), MWB28 (ruthenium) and MWB 60 (osmium and iridium).[45,46] Solvent interactions (THF) were included using the IEFPCM formalism.[47] All calculations were accomplished using the Gaussian 09 software.[48] In order to reduce computational cost without affecting the spectroscopic properties the octyl groups were replaced by methyl groups. For vertical excitation energies TD-DFT with CAM-B3LYP was applied starting from the B3LYP optimized ground state molecular structure. The analogous calculation with TD-B3LYP yields almost the same energies. In contrast, vertical excitation energies from the CAM-B3LYP optimized ground state molecular structure are significantly over- and underestimated by CAM-B3LYP and B3LYP, respectively. Orbital grids were visualized using Avogadro 1.1.0[49] and rendered using POV-Ray.[50]

■ RESULTS AND DISCUSSION

Steady-State Absorption and Emission. Chart 1 shows the molecular structure and Figure 1 the UV/vis absorption spectra of **Ir**, the free ligand **L** and $[Ir(ttpy)_2]^{3+}$ (ttpy = 4′-tolyl-2,2′:6′,2″-terpyridine). The absorption spectrum of **Ir**, which combines the $[Ir(ttpy)_2]^{3+}$ core and an ethinyl-linked dialkoxy-stilbene chromophore (see Chart 1), exhibits a maximum at 320 nm with shoulders at 248, 290, 375, and 475 nm. Notably, some of these absorption features can be directly attributed to the absorption spectrum of $[Ir(ttpy)_2]^{3+}$ with its shoulders and local maxima at 248, 310, 350, and 375 nm. This indicates only weak coupling of the electronic states of the molecular subunits.

Chart 1. Three Possible Isomers of 1-Ethynyl-2,5-bis(octyloxy)-4-styrylbenzene Relevant to This Work (in Blue)[a]
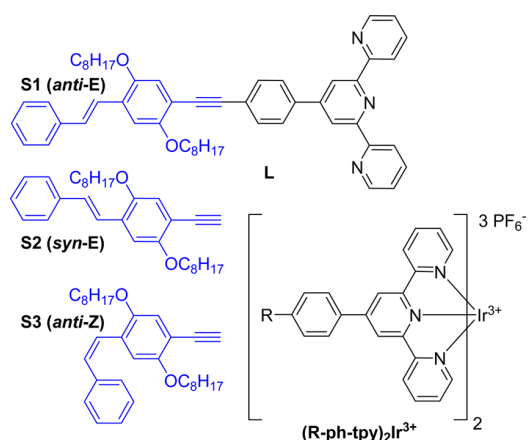
[a]They are labeled **S1** (anti-rotamer of *E*-isomer), **S2** (syn-rotamer of *E*-isomer) and **S3** (anti-rotamer of *Z*-isomer). **Ir** is the homoleptic complex of Ir[III] with the ligand **L** (4′-(4-2,5-bis(octyloxy)-4-styrylphenyl)ethinyl)phenyl)-2,2′:6′,2″-terpyridine). The possible symmetric isomers of **Ir** can be described as (R-ph-tpy)$_2$Ir^{3+} where R = (**S1, S2, S3**). The model compound [Ir(ttpy)$_2$]$^{3+}$ (ttpy =4′-tolyl-2,2′:6′,2″-terpyridine) is (R-ph-tpy)$_2$Ir^{3+} where R = methyl.
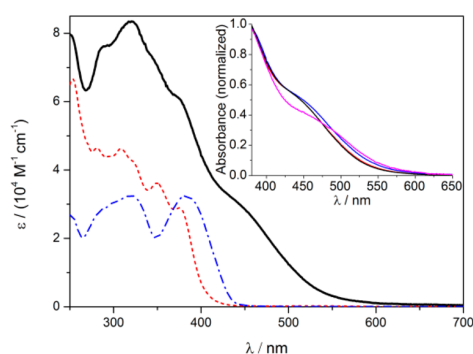
Figure 1. UV/vis absorption spectra of **Ir** (solid line), the free ligand **L** (blue dash-dotted line) and [Ir(ttpy)$_2$]$^{3+}$ (red dashed line) in THF. The inset shows absorption spectra of **Ir** in different solvents (normalized at 380 nm): tetrahydrofuran (THF, black curve), acetonitrile (ACN, red curve), *N,N*-dimethylpyrrolidine—urimid (DMPU, blue curve) and toluene (pink curve).

However, the red-most shoulder at 475 nm is characteristic for the **Ir** absorption spectrum; i.e., it is neither present in [Ir(ttpy)$_2$]$^{3+}$ nor **L** and suggests non-negligible electronic coupling of the stilbene chromophore and the complex fragment already in the electronic ground state.

The band at 475 nm undergoes a red-shift upon reducing the solvent polarity (see inset of Figure 1) by ca. 1400 cm^{-1} when changing the solvent from ACN (ε_{ACN} = 37.5) to toluene ($\varepsilon_{toluene}$ = 2.38; points of inflection at 474 and 507 nm, respectively). Such negative solvatochromism is typical for optical transitions inducing charge-transfer opposite to the direction of the ground-state dipole moment. Hence, upon photoexcitation the net-dipole moment is reduced and the ground-state is more efficiently stabilized in polar solvents than the excited state.[51]

However, it should be noticed (see Figure 1), that the lowest-energy band for **Ir** is slightly shifted bathochromically in DMPU (absorption at 480 nm) compared to ACN (absorption 474 nm), i.e., in two solvents with almost identical dielectric constants (ε_{ACN} = 37.5, ε_{DMPU} = 36.1). Furthermore, from THF to ACN the polarity changes significantly but the UV/vis absorption spectra of **Ir** in these solvents can be considered identical. These results show that the solvent-dependent absorption features of **Ir** are not solely due to different solvent polarities. One property that is clearly very different for DMPU and ACN is the dynamic viscosity (η_{ACN} = 0.38 mPa·s, η_{DMPU} = 3 mPa·s). However, in a static scenario viscosity should not have any influence on an UV/vis absorption spectrum. Nonetheless, when considering dynamic processes such as photoinduced excited-state decay viscosity may impact the outcome of the species formed.[52−54] For **Ir**, isomerization of the terminal stilbene unit is possible and will affect the UV/vis absorption spectrum of the sample: As isolated molecules both stilbene isomers have specific absorption features,[55] but also impact the electronic structure of **Ir** when used as a part of the extended ligand structure. This is supported by the density functional theory (DFT) calculations (*vide infra*).

Unlike in many transition-metal-polypyridine complexes[14] the lowest-energy transition for [Ir(tpy)$_2$]$^{3+}$ is not a ^{1}MLCT transition. In fact, for [Ir(tpy)$_2$]$^{3+}$ derivatives ^{3}MLCT states are located above 2.7 eV[26,29] and the lowest energy transition observed for **Ir** is an intraligand charge-transfer (ILCT) excitation.[31] In **Ir** the (ttpy)Ir^{3+}-complex fragment acts as strong acceptor and the ground-state dipole moment points toward the stilbene chromophore. Taking into account the negative solvatochromism of the lowest energy transition, it is concluded that photoinduced charge-transfer occurs from the stilbene chromophore directed toward the terpyridine moiety. This finding is in line with other literature reports on a related zinc complex, [ZnL$_2$]$^{2+}$,[35] in which charge density is shifted from the extended chromophore to the terpyridine unit upon light absorption. To corroborate this qualitatively, quantum chemical calculations on **Ir** were performed, which are presented in the following.

The structure of symmetrically *E*-configured and *anti*-rotated (i.e., the most stable isomer) **Ir** was fully optimized without symmetry constraints at DFT level. Subsequently the 75 lowest singlet excitations were calculated at the ground state molecular structure using TD-DFT (see Experimental Section for details). The energies of the lowest excited states are given in Table 1 together with the wavelength and the oscillator strength of the

Table 1. Vertical Excitation Energies of (*anti-E*)-Ir from the S$_0$ Ground State (B3LYP Optimized Structure of S$_0$) to the Lowest Excited Singlet States[a]

	E/eV	λ/nm	f		E/eV	λ/nm	f	assignment
S$_1$	2.60	477	3.24	S$_1$′	2.65	468	0.003	ILCT
S$_2$	3.14	394	0.0	S$_2$′	3.14	394	0.0	LLCT
S$_3$	3.25	381	0.0	S$_3$′	3.25	381	0.0	ILCT
S$_4$	3.37	368	1.79	S$_4$′	3.37	368	0.03	ILCT
S$_5$	3.61	343	0.0	S$_5$′	3.61	343	0.0	LLCT
S$_6$	3.70	336	0.71	S$_6$′	3.75	331	0.02	ILCT
S$_7$	3.90	318	0.08	S$_7$′	3.91	317	0.0	ILCT
S$_8$	4.00	310	0.11	S$_8$′	4.00	310	0.11	MLCT

[a]The left and right columns represent quasi-degenerate states that belong to different irreducible representations.

respective $S_0 \rightarrow S_n$ transition. The states (S_i and S_i') belong to either irreducible representation (A or B for the C_2 point group). It should be noted that the energy and the composition of these pairs of states in terms of the involved orbitals is almost identical, whereas the oscillator strength can differ significantly.

The $S_0 \rightarrow S_n$ excitations energies can be compared to the experimental UV/vis absorption spectrum even without a simulation of the vibronic progression of the electronic transitions. The excitation energies correspond well with the maxima and shoulders observed in the experimental spectrum. Nonetheless, at the particular level of theory the calculations fail to correctly predict the relative oscillator strengths, which is particularly noticeable for the $S_0 \rightarrow S_1$ transition (for the respective calculated UV/vis absorption spectra regarded to in this study *vide infra*).

From the calculations natural transition orbitals (NTOs)[56] can be derived, which allow for discussing the nature of the singlet excitations in some detail and are shown in Table 2 for

Table 2. Compositions of Selected Excited States Shown in Terms of Natural Transition Orbitals,[56] Where the Percentage of the Respective Hole/Particle Pair Quantifies the Contribution of the Transition[a]

	"hole"	"particle"
S_1 49%		
S_2 80%		
S_3 98%		
S_4 51%		
S_5 100%		
S_6 46%		
S_7 47%		
S_8 51%		

[a]For S_1, S_4, S_6, and S_7 a second major contribution with about the same percentage can be assigned to a similar transition on the other respective ligand.

representative transitions. The lowest excited singlet state is a $\pi-\pi^*$ transition with significant charge-transfer character as illustrated in the NTOs: Electron density is shifted toward the Ir(tpy)$_2$ moiety. This supports the qualitative discussion of the lowest-energy transition as an ^{1}ILCT band. The higher singlet states are $\pi-\pi^*$ transitions with varying amount of charge-transfer character. This holds true for S_2 to S_7 (S_2 and S_5 involve a transition between the two ligands) while S_8 exhibits significant MLCT character. The energy of this lowest ^{1}MLCT state (4 eV) is significantly higher than for other bis-(terpyridine) complexes, e.g. of Ru^{II}.

Vertical excitation energies to the lowest excited triplet states were also calculated and the results are presented in the Supporting Information. While singlet excitation energies can be compared to the band positions observed in an UV/vis absorption spectrum, for triplets the excitation energies describe the typically dark S_0-T_n transitions. Nevertheless, the prediction of triplet states helps understanding photo-induced (picosecond) dynamics. For **Ir** calculations predict energetically low-lying triplet states at the ground-state geometry with energies of 1.66 eV (T_1/T_1') and 2.28 eV (T_2/T_2') corresponding to delocalized $^3\pi-\pi^*$ and ^{3}ILCT transitions, respectively. While emission of Ir^{III}-bis-(terpyridine) complexes was reported to stem from ILCT states for a variety of substituents,[37,29] for **Ir** a similar emission is not detectable at room temperature using a commercial fluorimeter. Nonetheless, phosphorescence is detectable at low-temperature (see Supporting Information).

Atypical for transition metal terpyridine complexes,[14] **Ir** exhibits fluorescence after excitation at short wavelengths below 450 nm (2.76 eV). This emission (Figure 2) is centered at
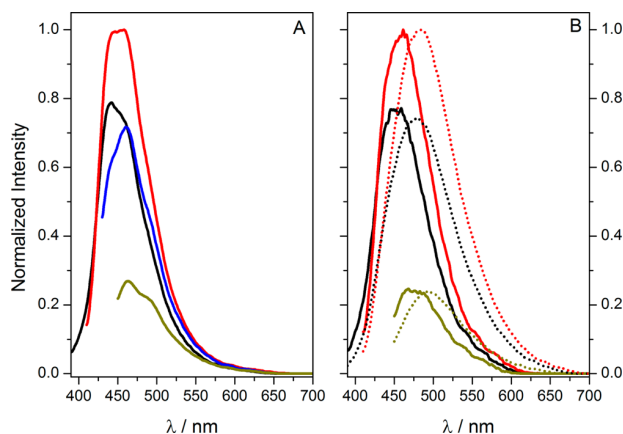
Figure 2. Emission spectra of **Ir** in nonpolar (panel A: toluene) and semipolar/polar solution (panel B: THF, solid lines; ACN, dotted lines) for selected excitation wavelength (black, 370 nm; red, 390 nm; blue, 410 nm; ochre, 430 nm).

around 460 nm, i.e. it overlaps with the ^{1}ILCT transition, shows a lifetime of 1.7 ns and a quantum yield of 0.02 in THF. Fluorescence excitation spectra (FES, Figure 4) show spectral features that correspond to bands in the UV/vis absorption spectrum. However, the lowest energy (^{1}ILCT) transition in the absorption spectrum is not visible in the FES.

Following 370 nm excitation, the emission band of **Ir** in toluene reveals a sharp rise on the blue-edge of the band and noticeable shoulders. Upon increasing the solvent polarity the emission band to becomes structure-less and its maximum shifts to longer wavelengths (see Figure 2, panel B): The bathochromic shift from 442 nm (toluene) to 455.5 nm (THF) to 479.5 nm (ACN) indicates an increased stabilization (in total 1250 cm^{-1}) of the relaxed (emissive) excited state in polar environments on top of the stabilization of the ground state at the Franck−Condon-point of absorption, which is responsible for the negative solvatochromism.[57]

Ir thus reveals emission properties, which are very similar to the ones observed for the free ligand **L**:[23] The emission band shape (sharp rise on the blue-edge of the band and noticeable shoulders on low-energy tail) upon 330 nm excitation and the

respective fluorescence lifetimes (1.58 ns[23]) are basically identical for **Ir** and **L**. However, the emission quantum yield of **Ir** (0.02) is reduced compared to the free ligand (0.74),[24] which is likely caused by an enhanced intersystem crossing rate in the presence of the Ir[III] ion. This behavior is in line with observations previously made for other [ML$_2$]$^{2+}$ complexes (M = Fe[II], Ru[II], Os[II]), which also show emission properties almost identical to those of **L**, although with reduced quantum yields.[24]

However, a remarkable feature of the **Ir** photophysics had not been reported for the related complexes of the iron group: The marked change of the emission band shape upon change of the excitation wavelength (see Figure 2). This effect is most pronounced in the least polar solvent in this study (toluene). Excitation of **Ir** dissolved in toluene at 370 nm yields a rather structured emission band with a maximum at 440 nm and a shoulder at 460 nm. The emission recorded upon 390 nm excitation shows an increased shoulder at 460 nm compared to the higher-energy excitation to an extent that both peaks have similar intensity. Excitation at 410 and 430 nm produces an emission spectrum with pronounced shoulders, which are bathochromically shifted compared to the emission spectrum recorded at 370 nm excitation. In line with the excitation-wavelength dependent emission, the FES recorded at different emission wavelengths differ (see Figure 4, panel A). Relative to the FES recorded at 440 nm, the FES maxima at 315 and 370 nm undergo a red-shift with increasing emission wavelength. In particular, the low-energy band at around 370 nm broadens with the maximum intensity increasing and red-shifting. The largest changes in the FES are observed at emission wavelengths 440, 460, and 480 nm, while the FES at 500 and 520 nm show a very similar band structure with only minor deviations in the red flank.

In polar solvents the excitation-wavelength dependence of the emission band shape is less pronounced (see Figure 4, panel B). This is presumably due to the fact, that emission band shapes generally become less structured in polar solvents.[58,57] However, we cannot exclude the possibility that the energies of the emissive excited states change with solvent polarity and hence affect the excitation-wavelength dependence of the emission.

The observation of excitation-wavelength dependent emission suggests the existence of two noninterconverting energetically close lying bright states separated by ca. 1100 cm^{-1} estimated from the positions of the emission band maxima in toluene at 435 and 459 nm for 370 and 410 nm excitation, respectively. These two states might be related to the overall symmetry of the molecule as already discussed in the context of the TD-DFT calculations, which show that two quasi degenerate excited states exist in **Ir** each belonging to one of the irreducible representations. Hence, the dual fluorescence might be caused by symmetry effects. However, one of both transitions would then be symmetry forbidden, but the relative intensity of both experimental bands does not differ significantly. Hence, a more likely explanation involves the stilbene unit of the molecule, which can be present either in *Z*- or *E*-configuration. The photophysics of both stilbene isomers[53,59−61] as well as stilbene derivatives is very well studied[62,63] and helps to rationalize the emission properties of **Ir**: The emission of *Z*-stilbene is broad and structureless with a maximum at ca. 420 to 440 nm (weakly depending on solvent polarity) and a quantum yield of less than 10^{-4} in acetonitrile.[64,65] On the other hand, the emission of *E*-stilbene has a maximum at 350 nm,[64] is structured and more intense

(quantum yield >0.02 in acetonitrile).[65] The qualitative agreement of the *E*-stilbene emission with the emission of **Ir** (the larger chromophore in **Ir** causes the red-shift of the emission) points toward the fact that the isomeric form of **L** determines the emission properties of **Ir**. To explore this theoretically, the S$_0$ structure of **L** was optimized and subsequently vertical excitation energies were calculated using TD-DFT. The S$_0$ → S$_1$ transition (382 nm) is mainly a HOMO−LUMO transition (see Figure 3) between strongly
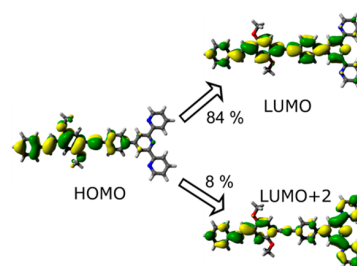
Figure 3. Main contributions (2c^2 values) to the S$_1$ state of **L** obtained from vertical excitations (25 singlets calculated using CAM-B3LYP) from the optimized ground state molecular structure (optimized using B3LYP).

delocalized orbitals indicating a highly conjugated and planar structure of the emitting state.[22] Furthermore, the high quantum yield of 0.74 suggests a rigid molecular structure. The KOHN-SHAM-Orbitals resembling the S$_0$ → S$_1$ transition (382 nm) of **L** (Figure 3) nicely compare with the S$_0$ → S$_4$ NTOs of **Ir** (see Table 2). It may be concluded from these similarities that the S$_1$ PES of **L** is closely related to the S$_4$ PES of **Ir** causing the similar emission.

Another argument supporting that emission of **Ir** (and **L**) stems from a rigid structure is that the emission band of both **Ir** and **L** is structured in nonpolar solution, while *Z*-stilbene emission is structureless even in nonpolar solution.[66,67] Therefore, the emitting structure in both **Ir** and **L** likely involves an *E*-configured terminal stilbene unit with strongly enhanced conjugation length as compared to an isolated stilbene molecule.

In order to explain the wavelength-dependence of the emission band the rotamers at the terminal stilbene unit are considered (see Chart 1), which are associated with the two possible orientations of the terminal styrene unit. The resulting *syn*- and *anti*-isomers are not energetically equivalent due to steric repulsion between the alkoxy substituents and the methine group hydrogen atoms of the stilbene double bond. Likely this repulsion also affects the energy of the fluorescent state and hence slightly different emission maxima for the *syn*- and *anti*-isomers are observed.

In addition to the *anti*-E isomer, the structures of the other two possible isomers of **Ir** considered in this article (*anti*-Z, *syn*-E) were optimized followed by the calculation of vertical excitations (see Experimental Section): Figure 4, panel B, contains the calculated absorption spectra for three (symmetric) isomers of **Ir**: *anti-Z*, *syn-E*, and *anti-E*.

From the data presented in Figure 4 panel B it is conceivable that the double bond configuration is of significance for the spectral position of the two bands in the UV/vis absorption spectrum at ca. 360 nm (3.44 eV, S$_4$ state) and 460 nm (2.70 eV, S$_1$ state). For these two electronic resonances the excitation energy is 126 (S$_4$) and 94 mV (S$_1$) lower for the *E*-isomer than
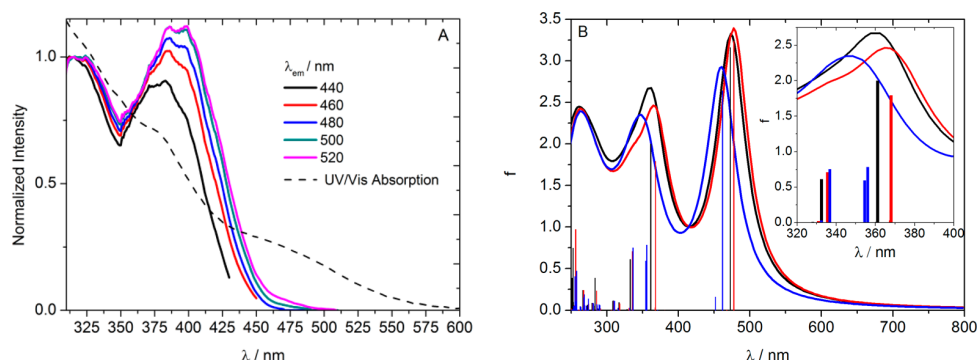
Figure 4. Panel A: Fluorescence−excitation spectra for **Ir** recorded in toluene for selected emission wavelengths shown in concert with the UV/vis-absorption spectrum (dashed line, arbitrarily scaled). The excitation spectra are cut 10 nm before the respective excitation wavelength to avoid the overlap region between the excitation spectra and scattered excitation light. All excitation spectra are normalized at 315 nm. Panel B: Simulated UV/vis absorption spectra for different isomers of **Ir**: *syn*-E (black curve), *anti*-E (red curve), *anti*-Z (blue curve). The spectra are obtained from 75 vertical singlet excitations calculated using TD-DFT with a 25 nm Lorentz convolution.
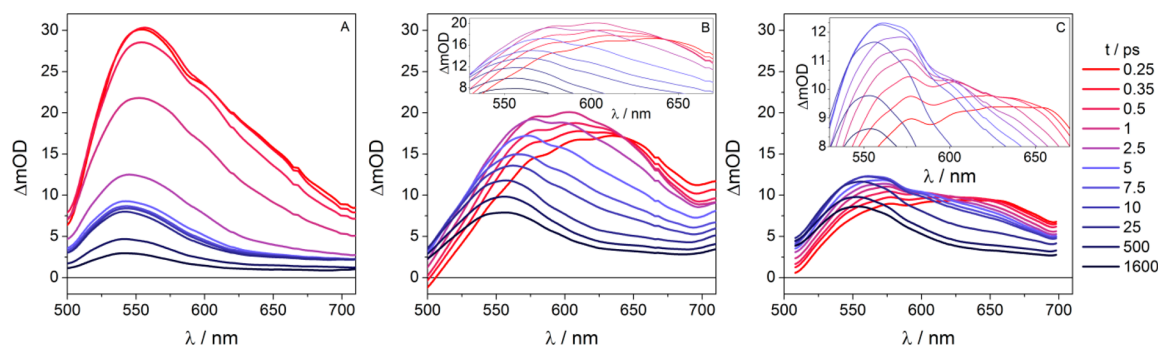
Figure 5. Transient absorption spectra for **Ir** in acetonitrile (ACN, panel A), tetrahydrofuran (THF, panel B) and *N,N*-dimethylpyrrolidineurimid (DMPU, panel C) after excitation at λ_{exc} = 480 nm at different delay times. The insets in panels B and C contain a more detailed representation of the spectra recorded in THF and DMPU, respectively. All spectra shown here were smoothed using a 15-point FFT filter to remove a systematic noise pattern (see Supporting Information).

for the *Z*-isomer. On the other hand, the two E-configured rotamers have more similar absorption spectra with only minor variations in excitation energies and oscillator strengths. Nevertheless, there is a distinctive difference in excitation energy for both rotamers that is most pronounced for the S_4 state. As discussed above, the calculated $S_0 \rightarrow S_4$ transition can be related to excitation of fluorescence. Therefore, the characteristic changes observed in the FES recorded for different emission wavelengths may be understood as the result of selective excitation of different rotamers. Because of the size of **Ir** and the cost of such computations, the emissive molecular structure could not be determined by (TD-)DFT calculations. Nevertheless, the specific change of the vertical excitation energy of both rotamers is striking and points to this interpretation of the excitation-wavelength-dependence of the fluorescence observed for **Ir**.

It should be noted that the spectral behavior observed here relates to the phenomenon of red-edge excitation shifts, which typically occur for frozen solutions or polymers when the rate constant for radiative decay is significantly larger than those for structural relaxation.[68,57] In the case of **Ir** the two rotamers at the periphery of the molecule are thought to cause a similar effect: Red-edge excitation of the S_4 band leads to the preferred excitation of molecules with a particular configuration. In the excited state this structural feature is preserved upon solvent relaxation and thus a specific emission structure with either

anti- or *syn*-configuration is formed. Depending on solvent polarity the emission band shape changes, which slightly masks the shift of the emission band position depending on the excitation wavelength. This however does not contradict the central role of the rotameric state for the emission properties of **L** and **Ir**.

Photoinduced Excited-State Dynamics. Transient absorption spectroscopy was performed on **Ir** in order to investigate the photoinduced dynamics upon excitation of the ^{1}ILCT transition (λ_{exc} = 480 nm) in dependence of both solvent polarity and viscosity. While the effect of increased solvent polarity is evaluated by the comparison of the data recorded in tetrahydrofuran (THF) and acetonitrile (ACN) (ε = 7.5 and 37.5, respectively), the influence of viscosity variation can be rationalized from the comparison between ACN and DMPU (0.38 and 3 dP, respectively). It should be noted that the difference in viscosity in the former pair as well as the difference in polarity for the latter solvent pair is small (ε(DMPU) = 36.1 and η(THF) = 0.55 dP).

Transient spectra for **Ir** recorded in ACN, THF, and DMPU are displayed in Figure 5. Already after a delay time of 250 fs the transient absorption for all three solvents is dominated by positive differential-absorption signals in the spectral range shown. The transient changes in the spectra are characteristic for each of the three solvents. Most obvious, the signal amplitude is the largest in ACN and decreases from THF to
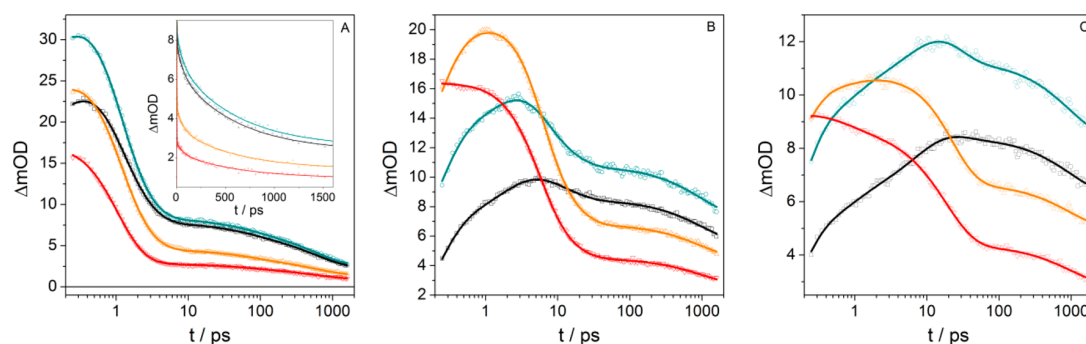
Figure 6. Selected kinetic traces (hollow symbols) for **Ir** in ACN (panel A), THF (panel B) and DMPU (panel C) after excitation at λ_{exc} = 480 nm for different wavelengths: 525 nm (black), 550 nm (cyan), 600 nm (orange), and 650 nm (red). The solid lines represent results from the respective multiexponential global fits. The inset in panel A contains the same data in linear scale.

DMPU—an effect that cannot be related to experimental parameters such as different optical densities of the samples in various solvents or the use of different pump-intensities or focus conditions. Interestingly, this trend does not follow the polarity variation of the solvents as ACN and DMPU are more polar than THF. However, the observed transient absorption intensities can be correlated with the solvent viscosity.

The time-dependent spectra for all three solvents evolve to be very similar after a solvent-specific delay time in the pump–probe measurements. In detail, the spectra at delay times >5 ps for ACN compared with the ones at delay times >25 ps for THF and >500 ps for DMPU have very similar shapes: The maxima for all differential absorption-spectra in the mentioned time range are located between 540 and 560 nm and rather weak absorption occurs between 600 and 700 nm. This is likely attributed to the same electronic state being populated. The weak polarity impact on the transient absorption spectra hints toward a locally excited state without significant charge-transfer contributions. Given the strong electronic coupling in **Ir** it is unlikely that photoinduced charges can be well separated within the molecule. In fact, according to the NTOs calculated for the ^{1}ILCT transition, the charges would not be well separated since electron density on the central phenyl ring is found in both the "hole" and the "particle" orbitals. Therefore, fast charge recombination can be considered a reasonable pathway yielding a delocalized triplet state. Nevertheless, the early photoinduced dynamics reflecting the population of the long-lived locally excited state differ for the different solvents:

(i) For ACN (Figure 5, panel A) the shape of the transient absorption spectra undergoes only minor changes on the time scale of our experiment: At early delay times (<1 ps) the maximum is located at ca. 555 nm. This maximum undergoes a weak blue-shift to about 542 nm within a few ps, which goes along with an overall signal decrease. This signal decrease in the first ps after photoexcitation is more pronounced in the red flank of the differential absorption spectrum causing a narrowing of the absorption band. The kinetic traces (Figure 6, panel A) reveal that the signal amplitude decreases by 90% over the entire probe range (500 to 710 nm) within the time-scale of our experiment. Specifically the ΔOD signal probed at 550 nm drops from about 30 mOD at 0.3 ps to 3 mOD at 1.4 ns.

(ii) For **Ir** dissolved in THF (Figure 5, panel B) the spectra change significantly during the monitored time range: At early delay times the spectra are dominated by a broad

absorption at 634 nm, which undergoes a blue-shift to 556 nm. The initial temporal evolution in THF between 0.25 and 1 ps involves an isosbestic point at 642 nm which is found in none of the other solvents. Afterward the absorption band narrows to a maximum at about 555 nm due to a strong signal decrease between 600 and 680 nm. The maximum signal amplitude (20 mOD) at a probe-wavelength of 600 nm is reached after 1 ps and the signal drops to 5 mOD at 1.5 ns (see Figure 6, panel B).

(iii) The photoinduced dynamics in DMPU (Figure 5, panel C and Figure 6, panel C) are similar to those observed in THF considering that all photoinduced processes occur more slowly due to the higher viscosity.

The spectral signatures observed are not clearly assignable to known data. A TA spectrum of the ^{3}LC state of $[Ir(ttpy)_2]^{3+}$ was reported,[26] showing intense excited state absorption between 600 and 900 nm with a maximum at ca. 700 nm. Despite the fact that the spectral window accessible in our experiment ends at around 700 nm, it is conceivable that the TA spectra of **Ir** are at least not dominated by a ^{3}LC-like absorption. On the other hand, the excited-state absorption spectrum of **L** was reported to show an absorption feature at around 550 nm, weakly depending on solvent polarity.[22]

More insight is provided by a quantitative analysis in terms of a global multiexponential fit routine applied to the transient absorption data: The kinetic traces in Figure 6 are overlapped by solid lines representing fitted curves obtained from global fitting with five exponentials (when fewer exponential functions were used in the fit, systematic noise patterns were observed which are eliminated in the fit presented here) and an offset corresponding to a process with a time constant exceeding the time scale of our experiment (2 ns).

The fit results in characteristic time constants (Table 3) and decay-associated spectra (DAS, see Figure 7). In line with the similarity of the transient absorption spectra at long delay times (vide supra), the three DAS corresponding to the long-lived state and two slowest processes are almost identical in all three solvents: The offset component resembles the transient absorption spectrum at long delay times (>1.5 ns) containing a broad maximum at ca. 550 nm and a positive, flat absorption in the red part of the spectrum. The shape of the DAS associated with τ_5 is similar to the long-lived spectrum for all three solvents, however, the relative amplitudes vary from solvent to solvent. The lifetimes τ_5 (1 ns in THF and DMPU and 0.6 ns in ACN) are in principle too large to be determined precisely using the applied experimental setup. It may be

Table 3. Time Constants (Inverse Rate Constants) as the Results from a Global Multi-Exponential Fit Applied to the Transient Absorption Data of Ir in the Three Solvents ACN, THF, and DMPU

	τ/ps		
	ACN	THF	DMPU
τ_1	<0.25	<0.25	<0.25
τ_2	0.84	1.8	0.68
τ_3	1.8	3.6	7.7
τ_4	65	11	15.9
τ_5	600	980	970

possible, that the real lifetime τ_5 is related to the emission lifetime (1.7 ns, vide supra). However, the deviation of τ_5 and the emission lifetime is significant anyhow and the DAS (τ_5) does not show an indication of stimulated emission (SE). The low fluorescence quantum yield (<3%) is probably determining a high triplet yield caused by increased ISC in the presence of the Ir^{III} ion (vide supra). Therefore, it is concluded that the photoinduced ps-dynamics probed in the transient absorption measurements are exclusively occurring in the triplet regime.

In the triplet manifold the slow process (τ_5) may be attributed to excited-state-equilibration: A large portion of molecules relax into another excited state with specific absorption features outside the probed spectral window, which has been observed for homodinuclear complexes of related ligands.[69] For Ir the triplet states discussed afore could contribute to the equilibration as locally excited triplet $^3\pi-\pi^*$ states of related conjugated compounds are expected to absorb in the NIR.[70,71] Likely the T_1 state in Ir shows similar absorption which is located outside the spectral window probed in our experiment.

The discussion of the ps-ns dynamics of Ir is exemplified for THF as solvent: The maximum of the DAS (τ_4) is bathochromically shifted compared to the DAS (τ_5). The signal reduction in the red shoulder of the transient absorption band caused by the process associated with τ_4 causes a blue-shift of this absorption band maximum. Another blue-shift is observed on the early ps-time scale (see Figure 5): τ_2 and τ_3 lead to a decrease (τ_2) and increase (τ_3) of ESA due the respective (negative) maximum in the DAS (τ_3) being blue-shifted as compared to the (positive) maximum of the DAS (τ_2) (see Figure 7, panel B). An ultrafast process with a time constant $\tau_1 < 250$ fs and similar DAS is found irrespective of the solvent. The negative signal amplitude in the respective DAS

between 500 and 650 nm describes either the depopulation of an emitting state, i.e., the loss of stimulated emission (SE), or the buildup of excited-state absorption. SE from the initially populated ^{1}ILCT state can occur, as long as ISC promotes molecules into the ^{3}ILCT.

The initial rise is described by the processes associated with τ_1 and τ_2, while the decay is due to the process with τ_3. For 600, 550, and 525 nm both rise and decay are clearly resolved, while at 650 nm the rise component is missing. Keeping this in mind, the transient absorption data recorded in the other solvents can be interpreted similarly: In ACN, the rise is too fast to be resolved and only the first three data points for 550 and 525 nm show a positive slope and, thus, the photoinduced dynamics on the ps-time scale primarily involve signal reduction. The blue-shifts appear only weakly in ACN. In DMPU, both rise and decay of the signal are slower indicating that major structural rearrangements are involved in the photoinduced dynamics that are significantly slowed down in viscous solution. The large signal amplitude directly after photoexcitation in the polar and fluid solvent ACN may be indicative of a charge-transfer state, which is associated with structural reorganization.

Therefore, deciphering the roles of solvent polarity and solvent viscosity requires knowledge of the electronic structure and the flexible parts of Ir: It is known for related compounds that the orientation of the phenyl ring bound to the 4'-position of the terpyridine can have strong impact on the electronic structure of the terpyridine moiety.[72,73] Both rings are twisted in the ground state. Upon photoexcitation the phenyl ring can undergo torsional motion and planarize into the plane of the terpyridine group. This process has been identified as barrierless for L.[23] For 4'-phenyl-substituted $[Ru(tpy)_2]^{2+}$ and $[Os(tpy)_2]^{2+}$ derivatives it is known that the energy of the emitting ^{3}MLCT state is lowered upon planarization by enhancing the electronic delocalization, thereby increasing the energy gap to the ^{3}MC state and consequently leading to increased excited-state lifetimes and emission quantum yields.[72] For 4'-phenyl-substitued $[Ir(tpy)_2]^{3+}$ derivatives, planarization leads to a stabilization of the emitting ^{3}LC state shown using temperature-dependent emission spectroscopy on $[Ir(ttpy)_2]^{3+}$.[26] Because of the high energy of deactivating ^{3}MC states in the latter, the stabilization of the emitting state does not cause a significant increase of the emission quantum yield contrary to what is observed for Ru-based ^{3}MLCT emitters. Therefore, the enhanced lifetime of the ^{3}LC in $[Ir(ttpy)_2]^{3+}$ is due to an increased energy gap in the Marcus inverted region. However, in Ir planarization will cause stronger electronic
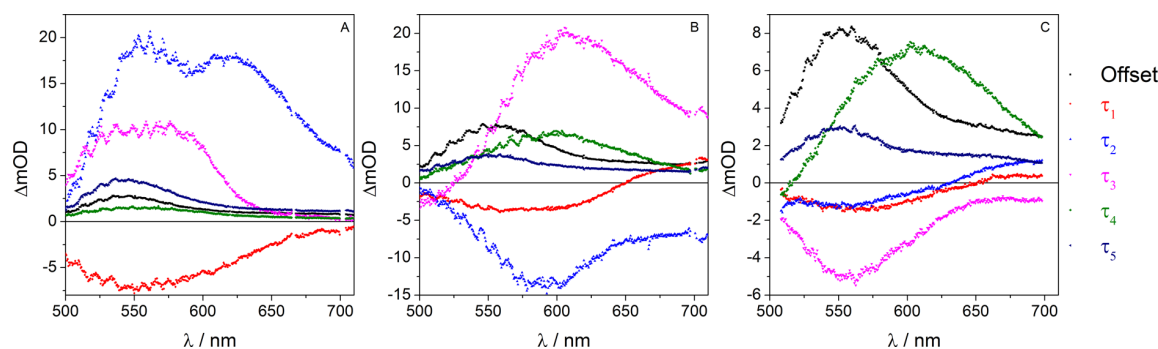
Figure 7. Decay-associated spectra (DAS) from global multiexponential fits of the transient absorption data recorded in different solvents. The time constants of the kinetic components are given in Table 3.

communication between the ligand backbone and the tpy group yielding a large and planar organic chromophore with low-lying $\pi-\pi^*$ states, lower in energy than a localized ^{3}LC state. Given the size of the chromophore in **Ir**, it seems unlikely that planarization will have such significant impact on the conjugation to explain the experimentally observed dynamic blue-shift of more than 2200 cm^{-1}. This argument is supported by theory in terms of selected parameters of optimized molecular structures for **Ir** as well as **Fe**, **Ru**, and **Os** for comparison.

Table 4. Structural Parameters for Ir as Well as Fe, Ru, and Os for Comparison from Optimized Ground State Structures (see Figure 8)^a

	r/Å	θ/deg
Ir	1.471	28.6
Fe	1.477	32.2
Ru	1.478	32.9
Os	1.478	32.7

^{a}The bond length (r) between the terpyridine unit and the adjacent phenyl ring is given as well as the respective dihedral angle (θ) between both rings.

Figure 8. Visualization of the structural parameters presented in Table 4. The dihedral angle (θ) between the plane of the complexing tpy unit (red) and the plane of the adjacent chromophore (cyan) and the bond length (r) of the bridging C–C-single bond are visualized.

The data in Table 3 shows that the dihedral angle between the terpyridine unit and the adjacent phenyl ring is decreased in **Ir** (28.6°) compared to the related compounds (between 32.2° to 32.9° for **Fe** and **Ru**, respectively). Together with the decreased bond length between the central pyridine ring and the phenyl ring 1.471 Å (compared to 1.478 Å for **Ru**, **Fe**, and **Os**), it can be concluded that already in the ground state the effective conjugation in **Ir** is stronger than in the analogues **Fe**, **Ru**, and **Os**. This can be caused by the weak electronic interaction between the tpy orbitals and the Ir^{III} orbitals, such that stabilization in the ligand is reached by a more planar structure and thus enhanced electronic communication within the (extended) ligand sphere, i.e. between the tpy and the phenyl ring. Therefore, the large dynamic blue-shift observed experimentally is unlikely to be caused solely by planarization. For comparison, the total blue-shift observed for **Ru** after 525 nm excitation is much less than 1000 cm^{-1} and should—based on the quantum chemical results—have more prominent contributions from planarization.[25]

Aside from the orientation of the bridging phenyl ring the terminal stilbene unit (either *E*- or *Z*-configuration) can take

part in sterical rearrangements. The transient absorption characteristics of both isomers can be identified in the data recorded for **Ir**: Transient absorption at around 630–650 nm, which is typical for *Z*-stilbene,[74,61] is observed in all three solvents. As the ESA features of **Ir** are more complex than in *Z*-stilbene, the typical *Z*-stilbene absorption at 640 nm appears convoluted with other spectral features. The *E*-stilbene absorption is located at ca. 570 nm,[74,61] which is close to the maximum of the transient absorption spectra observed for **Ir** after the initial blue-shift (vide supra).

Concerning the electronic structure of **Ir**, a comparison to the known and related analogues **Ru** and **Os** can be helpful. An obvious distinction between **Ir** and **Ru/Os** is the additional positive charge of the former (3+ vs 2+). The high charge in conjunction with the high oxidation potential of Ir^{3+} causes the ligand- (and ligand-periphery-) metal interaction to be primarily electrostatically driven. This interaction is represented, e.g., by the induction of an ILCT state (*vide supra*), and might also be a reason for the higher degree of planarity within the ttpy-unit. It should be noted that, in analogy to the observations made for the analogous [ZnL$_2$]$^{2+}$ complex,[35] it is likely that also for **Ru**, and **Os** the electrostatically induced ILCT state exists. This is supported by TD-DFT calculations (see Supporting Information) and,[25] where an ^{3}ILCT state equilibrating with the ^{3}MLCT state was suggested. Nevertheless, for **Ir**, due to the absence of the low-lying ^{3}MLCT state, the ^{3}ILCT state plays a more direct role in the photoinduced dynamics than in **Ru** and **Os**. In both cases the transient absorption spectra observed[25] are consistent with typical absorption spectra of respective polypyridine ^{3}MLCT states.[14] Therefore, the spectral signature of the ^{3}ILCT is not easily conceivable from the **Ru/Os** data sets. Also the excited-state absorption spectrum of [Ir(ttpy)$_2$]$^{3+}$, i.e., of its strongly emitting ^{3}LC state, might contribute to the transient absorption spectra of **Ir**.

Assuming that excited-state absorption above 670 nm is due to the excited Ir(ttpy)$^{3+}$ moiety, the signal reduction in this spectral region could be ascribed to a depopulation (loss of electron density) of the complex fragment toward ligand-centered states. Possibly also the ligand-centered excited-state extinction coefficients are higher than those of the tpy-related excited states (such as the ^{3}LC state in [Ir(ttpy)$_2$]$^{3+}$), which would also cause the latter to be hard to detect. At this point, it is concluded, that a polar ^{3}ILCT state will be significantly stabilized in a highly polar environment. Also, a different polarity of both (*Z/E*)-isomers seems probable. If so, due to a possible stabilization of the *E*-isomer in the ^{3}ILCT state, high solvent polarity (such as in ACN and DMPU) could speed up the isomerization, while a high solvent viscosity (as in DMPU) will decelerate the process involving structural rearrangements such as *Z–E*-isomerization. This would explain the major differences observed in the photoinduced dynamics of **Ir** in both solvents. In THF solution, despite the much lower polarity as compared to the other two solvents, the isomerization is faster than in DMPU due to the lower viscosity of the solvent. The pump–probe spectra of **Ir** at long delay-times are dominated by absorption features not observed for **Ru**, **Os**, [Ir(ttpy)$_2$]$^{3+}$ or its derivatives. However, the differential absorption spectra of **Ir** at long delay-times contain features observed for the free ligand **L**,[22] in particular the band at 550 nm. This points to the fact that metal–ligand-interactions in **Ir** dominate the photophysics only at short delay times, while the

slower photoinduced dynamics are determined by the properties of the extended ligand system.

CONCLUSION

The homoleptic complex **Ir** was synthesized and characterized using steady-state and time-resolved spectroscopy. The weak solvent dependence of the lowest-energy absorption band revealed negative solvatochromism and the respective transition was identified as an intramolecular charge-transfer (^{1}ILCT) with the help of TD-DFT calculations. While phosphorescence of **Ir** is too weak to be detected, fluorescence can be excited at wavelength below 450 nm. TD-DFT calculations showed that rotamers at the terminal dimethoxy-stilbene unit possess somewhat different absorption spectra. As the interconversion between the rotamers is hindered by a large barrier, both rotamers show fluorescence independently causing an excitation-wavelength-dependence of the emission spectra. Photoinduced dynamics after excitation of the ^{1}ILCT transition at 480 nm were probed using broadband femtosecond transient absorption spectroscopy in three different solvents. The processes occurring after photo excitation involve *Z−E*-isomerization of the stilbene unit and a planarization of the organic chromophore with respect to the central complex fragment. Impact of both solvent polarity and viscosity has to be considered in order to understand the relaxation processes. The present study contains a fascinating example of how the central Ir^{III} metal ion influences the photophysics of a chromophore as large as **L** mainly by electrostatic interactions. The importance of a detailed understanding of the interplay between electronic and structural aspects is highlighted and successfully attempted in order to explain the unusual photophysical properties of **Ir**. We believe that the study at hand provides helpful considerations when creating new functional materials based on Ir^{III} involving flexible organic ligands.

ASSOCIATED CONTENT

Ⓢ Supporting Information

Complete reference data for Gaussian 09, additional steady-state emission spectra, results from DFT calculations, and raw transient absorption data. This material is available free of charge via the Internet at http://pubs.acs.org.

AUTHOR INFORMATION

Corresponding Author
*(B.D.) E-mail: Benjamin.Dietzek@uni-jena.de.

Author Contributions

The manuscript was written through contributions of all authors. All authors have given approval to the final version of the manuscript.

Notes

The authors declare no competing financial interest.

ACKNOWLEDGMENTS

REFERENCES

(1) Schubert, U. S.; Eschbaumer, C.; Andres, P.; Hofmeier, H.; Weidl, C. H.; Herdtweck, E.; Dulkeith, E.; Morteani, A.; Hecker, N. E.; Feldmann, J. 2,2′:6′,2″-Terpyridine Metal Complexes as Building Blocks for Extended Functional Metallo-Supramolecular Assemblies and Polymers. *Synth. Met.* **2001**, *121*, 1249−1252.

(2) Schubert, U. S.; Hofmeier, H.; Newkome, G. R. *Modern Terpyridine Chemistry*; Wiley-VCH: Weinheim, Germany, 2006.

(3) Schubert, U. S.; Eschbaumer, C. Macromolecules Containing Bipyridine and Terpyridine Metal Complexes: Towards Metallosupramolecular Polymers. *Angew. Chem., Int. Ed.* **2002**, *41*, 2892−2926.

(4) Schubert, U. S.; Winter, A.; Newkome, G. R. *Terpyridine-Based Materials For Catalytic, Optoelectronic and Life Science Applications*; Wiley-VCH: Weinheim, Germany, 2011.

(5) Brabec, C. J., Scherf, U., Dyakonov, V., Eds. *Organic photovoltaics. Materials, Device Physics, and Manufacturing Technologies*; Wiley: New York, 2014.

(6) Günes, S.; Neugebauer, H.; Sariciftci, N. S. Conjugated Polymer-Based Organic Solar Cells. *Chem. Rev.* **2007**, *107*, 1324−1338.

(7) Müllen, K.; Scherf, U. *Organic Light-Emitting Devices. Synthesis, properties, and applications*; Wiley-VCH: Weinheim, Germany, 2006.

(8) Constable, E. C. 2,2′:6′,2″-Terpyridines: From Chemical Obscurity to Common Supramolecular Motifs. *Chem. Soc. Rev.* **2007**, *36*, 246−253.

(9) Sauvage, J. P.; Collin, J. P.; Chambron, J. C.; Guillerez, S.; Coudret, C.; Balzani, V.; Barigelletti, F.; Cola, L.; Flamigni, L. Ruthenium(II) and Osmium(II) Bis(terpyridine) Complexes in Covalently-Linked Multicomponent Systems: Synthesis, Electrochemical Behavior, Absorption Spectra, and Photochemical and Photophysical Properties. *Chem. Rev.* **1994**, *94*, 993−1019.

(10) Dobrawa, R.; Würthner, F. Photoluminescent Supramolecular Polymers: Metal-Ion Directed Polymerization of Terpyridine-Functionalized Perylene Bisimide Dyes. *Chem. Commun.* **2002**, 1878−1879.

(11) Tuccitto, N.; Delfanti, I.; Torrisi, V.; Scandola, F.; Chiorboli, C.; Stepanenko, V.; Würthner, F.; Licciardello, A. Supramolecular Self-Assembled Multilayers of Terpyridine-Functionalized Perylene Bisimide Metal Complexes. *Phys. Chem. Chem. Phys.* **2009**, *11*, 4033−4038.

(12) Kelch, S.; Rehahn, M. Synthesis and Properties in Solution of Rodlike, 2,2′:6′,2″-Terpyridine-Based Ruthenium(II) Coordination Polymers. *Macromolecules* **1999**, *32*, 5818−5828.

(13) Barigelletti, F.; Flamigni, L. Photoactive Molecular Wires Based on Metal Complexes. *Chem. Soc. Rev.* **2000**, *29*, 1−12.

(14) Balzani, V., Campagna, S., Eds. *Photochemistry and Photophysics of Coordination Compounds I*; Springer: Berlin and Heidelberg, Germany, 2007.

(15) Ng, W. Y.; Gong, X.; Chan, W. K. Electronic and Light-Emitting Properties of Some Polyimides Based on Bis(2,2′:6′,2″-terpyridine) Ruthenium(II) Complex. *Chem. Mater.* **1999**, *11*, 1165−1170.

(16) Mutai, T.; Cheon, J.-D.; Arita, S.; Araki, K. Phenyl-Substituted 2,2′:6′,2″-Terpyridine as a New Series of Fluorescent Compounds—Their Photophysical Properties and Fluorescence Tuning. *J. Chem. Soc., Perkin Trans. 2* **2001**, 1045−1050.

(17) Wang, X.; Del Guerzo, A.; Schmehl, R. H. Photophysical Behavior of Transition Metal Complexes Having Interacting Ligand Localized and Metal-to-Ligand Charge Transfer States. *J. Photochem. Photobiol. C: Photochem. Rev.* **2004**, *5*, 55−77.

(18) McClenaghan, N. D.; Leydet, Y.; Maubert, B.; Indelli, M. T.; Campagna, S. Excited-State Equilibration: A Process Leading to Long-Lived Metal-to-Ligand Charge Transfer Luminescence in Supramolecular Systems. *Coord. Chem. Rev.* **2005**, *249*, 1336−1350.

(19) Medlycott, E. A.; Hanan, G. S. Designing Tridentate Ligands for Ruthenium(II) Complexes with Prolonged Room Temperature Luminescence Lifetimes. *Chem. Soc. Rev.* **2005**, *34*, 133−142.

(20) Medlycott, E. A.; Hanan, G. S. Synthesis and Properties of Mono- and Oligo-Nuclear Ru(II) Complexes of Tridentate Ligands:

The Quest for Long-Lived Excited States at Room Temperature. *Coord. Chem. Rev.* **2006**, *250*, 1763−1782.

(21) Sun, Y.; El Ojaimi, M.; Hammitt, R.; Thummel, R. P.; Turro, C. Effect of Ligands with Extended π-System on the Photophysical Properties of Ru(II) Complexes. *J. Phys. Chem. B* **2010**, *114*, 14664−14670.

(22) Siebert, R.; Akimov, D.; Schmitt, M.; Winter, A.; Schubert, U. S.; Dietzek, B.; Popp, J. Spectroscopic Investigation of the Ultrafast Photoinduced Dynamics in π-Conjugated Terpyridines. *ChemPhysChem.* **2009**, *10*, 910−919.

(23) Siebert, R.; Winter, A.; Schubert, U. S.; Dietzek, B.; Popp, J. Excited-State Planarization as Free Barrierless Motion in a π-Conjugated Terpyridine. *J. Phys. Chem. C* **2010**, *114*, 6841−6848.

(24) Siebert, R.; Winter, A.; Dietzek, B.; Schubert, U. S.; Popp, J. Dual Emission from Highly Conjugated 2,2′:6′:2″-Terpyridine Complexes-A Potential Route to White Emitters. *Macromol. Rapid Commun.* **2010**, *31*, 883−888.

(25) Siebert, R.; Winter, A.; Schubert, U. S.; Dietzek, B.; Popp, J. The Molecular Mechanism of Dual Emission in Terpyridine Transition Metal Complexes—Ultrafast Investigations of Photoinduced Dynamics. *PCCP Phys. Chem. Chem. Phys.* **2011**, *13*, 1606−1617.

(26) Collin, J.-P.; Dixon, I. M.; Sauvage, J.-P.; Williams, J. A. Gareth; Barigelletti, F.; Flamigni, L. Synthesis and Photophysical Properties of Iridium(III) Bisterpyridine and Its Homologues: a Family of Complexes with a Long-Lived Excited State. *J. Am. Chem. Soc.* **1999**, *121*, 5009−5016.

(27) Licini, M.; Gareth Williams, J. A. Iridium(III) Bis-Terpyridine Complexes Displaying Long-Lived pH Sensitive Luminescence. *Chem. Commun.* **1999**, 1943−1944.

(28) Dixon, I. M.; Collin, J.-P.; Sauvage, J.-P.; Flamigni, L.; Encinas, S.; Barigelletti, F. A Family of Luminescent Coordination Compounds: Iridium(III) Polyimine Complexes. *Chem. Soc. Rev.* **2000**, *29*, 385−391.

(29) Flamigni, L.; Ventura, B.; Barigelletti, F.; Baranoff, E.; Collin, J.-P.; Sauvage, J.-P. Luminescent Iridium(III)-Terpyridine Complexes - Interplay of Ligand Centred and Charge Transfer States. *Eur. J. Inorg. Chem.* **2005**, *2005*, 1312−1318.

(30) Flamigni, L.; Baranoff, E.; Collin, J.-P.; Sauvage, J.-P. A Triad Based on an Iridium(III) Bisterpyridine Complex Leading to a Charge-Separated State with a 120-μs Lifetime at Room Temperature. *Chem.—Eur. J.* **2006**, *12*, 6592−6606.

(31) Baranoff, E.; Collin, J.-P.; Flamigni, L.; Sauvage, J.-P. From Ruthenium(II) to Iridium(III): 15 Years of Triads Based on Bis(terpyridine) Complexes. *Chem. Soc. Rev.* **2004**, *33*, 147−155.

(32) Baranoff, E.; Dixon, I. M.; Collin, J.-P.; Sauvage, J.-P.; Ventura, B.; Flamigni, L. Dyads Containing Iridium(III) Bis(terpyridine) as Photoactive Center: Synthesis and Electron Transfer Study. *Inorg. Chem.* **2004**, *43*, 3057−3066.

(33) Yoshikawa, N.; Yamabe, S.; Kanehisa, N.; Kai, Y.; Takashima, H.; Tsukahara, K. Synthesis, Characterization, and DFT Investigation of Ir(III) Tolylterpyridine Complexes. *Eur. J. Inorg. Chem.* **2007**, *2007*, 1911−1919.

(34) Flamigni, L.; Collin, J.-P.; Sauvage, J.-P. Iridium Terpyridine Complexes as Functional Assembling Units in Arrays for the Conversion of Light Energy. *Acc. Chem. Res.* **2008**, *41*, 857−871.

(35) Winter, A.; Friebe, C.; Chiper, M.; Schubert, U. S.; Presselt, M.; Dietzek, B.; Schmitt, M.; Popp, J. Synthesis, Characterization, and Electro-Optical Properties of Zn II Complexes with π-Conjugated Terpyridine Ligands. *ChemPhysChem.* **2009**, *10*, 787−798.

(36) Goodall, W.; Williams, J. A. Gareth Iridium(III) Bis-Terpyridine Complexes Incorporating Pendent N-Methylpyridinium Groups: Luminescent Sensors for Chloride Ions. *J. Chem. Soc., Dalton Trans.* **2000**, 2893−2895.

(37) Leslie, W.; Poole, R. A.; Murray, P. R.; Yellowlees, L. J.; Beeby, A.; Williams, J. G. Near Infra-Red Luminescence from Bis-Terpyridyl Iridium(III) Complexes Incorporating Electron-Rich Pendants. *Polyhedron.* **2004**, *23*, 2769−2777.

(38) Lee, C.; Yang, W.; Parr, R. G. Development of the Colle-Salvetti Correlation-Cnergy Formula into a Functional of the Electron Density. *Phys. Rev. B: Condens. Matter Mater. Phys.* **1988**, *37*, 785−789.

(39) Becke, A. D. Density-Functional Thermochemistry. III. The Role of Exact Exchange. *J. Chem. Phys.* **1993**, *98*, 5648−5652.

(40) Stephens, P. J.; Devlin, F. J.; Chabalowski, C. F.; Frisch, M. J. Ab Initio Calculation of Vibrational Absorption and Circular Dichroism Spectra Using Density Functional Force Fields. *J. Phys. Chem.* **1994**, *98*, 11623−11627.

(41) Perdew, J. P.; Burke, K.; Ernzerhof, M. Generalized Gradient Approximation Made Simple. *Phys. Rev. Lett.* **1996**, *77*, 3865−3868.

(42) Adamo, C.; Barone, V. Toward Reliable Density Functional Methods without Adjustable Parameters: The PBE0Model. *J. Chem. Phys.* **1999**, *110*, 6158−6170.

(43) Yanai, T.; Tew, D. P.; Handy, N. C. A New Hybrid Exchange—Correlation Functional Using the Coulomb-Attenuating Method (CAM-B3LYP). *Chem. Phys. Lett.* **2004**, *393*, 51−57.

(44) Hariharan, P. C.; Pople, J. A. The Influence of Polarization Functions on Molecular Orbital Hydrogenation Energies. *Theor. Chim. Acta.* **1973**, *28*, 213−222.

(45) Dolg, M.; Wedig, U.; Stoll, H.; Preuss, H. Energy-Adjusted ab initio Pseudopotentials for the First Row Transition Elements. *J. Chem. Phys.* **1987**, *86*, 866−872.

(46) Andrae, D.; Häußermann, U.; Dolg, M.; Stoll, H.; Preuß, H. Energy-Adjusted ab initio Pseudopotentials for the Second and Third Row Transition Elements. *Theor. Chim. Acta.* **1990**, *77*, 123−141.

(47) Tomasi, J.; Mennucci, B.; Cammi, R. Quantum Mechanical Continuum Solvation Models. *Chem. Rev.* **2005**, *105*, 2999−3094.

(48) Frisch, M. J.; Trucks, G. W.; Schlegel, H. B.; Scuseria, G. E.; Robb, M. A.; Cheeseman, J. R.; Scalmani, G.; Barone, V.; Mennucci, B.; Petersson, G. A.; et al. *Gaussian 09 Revision D.01*; Gaussian: Pittsburgh, PA, 2009.

(49) Hanwell, M. D.; Curtis, D. E.; Lonie, D. C.; Vandermeersch, T.; Zurek, E.; Hutchison, G. R. Avogadro: An Advanced Semantic Chemical Editor, Visualization, and Analysis Platform. *J. Cheminf.* **2012**, *4*, 4−17.

(50) Persistence of Vision Pty. Ltd. *Persistence of Vision Raytracer (Version 3.6)*; Persistence of Vision Pty. Ltd.: Williamstown, Australia, 2004.

(51) Reichardt, C. Solvatochromic Dyes as Solvent Polarity Indicators. *Chem. Rev.* **1994**, *94*, 2319−2358.

(52) Gegiou, D.; Muszkat, K. A.; Fischer, E. Temperature Dependence of Photoisomerization. VI. Viscosity Effect. *J. Am. Chem. Soc.* **1968**, *90*, 12−18.

(53) Waldeck, D. H. Photoisomerization Dynamics of Stilbenes. *Chem. Rev.* **1991**, *91*, 415−436.

(54) Dietzek, B.; Tarnovsky, A. N.; Yartsev, A. Visualizing Overdamped Wavepacket Motion: Excited-State Isomerization of Pseudocyanine in Viscous Solvents. *Chem. Phys.* **2009**, *357*, 54−62.

(55) Beveridge, D. L.; Jaffé, H. H. The Electronic Structure and Spectra of cis- and trans-Stibene 1. *J. Am. Chem. Soc.* **1965**, *87*, 5340−5346.

(56) Martin, R. L. Natural Transition Orbitals. *J. Chem. Phys.* **2003**, *118*, 4775−4777.

(57) Lakowicz, J. R. *Principles of Fluorescence Spectroscopy*, 3rd ed.; Springer: New York, 2006.

(58) Boldrini, B.; Cavalli, E.; Painelli, A.; Terenziani, F. Polar Dyes in Solution: A Joint Experimental and Theoretical Study of Absorption and Emission Band Shapes. *J. Phys. Chem. A* **2002**, *106*, 6286−6294.

(59) Syage, J. A.; Lambert, W.; Felker, P. M.; Zewail, A. H.; Hochstrasser, R. M. Picosecond Excitation and trans-cis Isomerization of Stilbene in a Supersonic Jet: Dynamics and Spectra. *Chem. Phys. Lett.* **1982**, *88*, 266−270.

(60) Weigel, A.; Ernsting, N. P. Excited Stilbene: Intramolecular Vibrational Redistribution and Solvation Studied by Femtosecond Stimulated Raman Spectroscopy. *J. Phys. Chem. B* **2010**, *114*, 7879−7893.

(61) Sension, R. J.; Repinec, S. T.; Szarka, A. Z.; Hochstrasser, R. M. Femtosecond Laser Studies of the cis-Stilbene Photoisomerization Reactions. *J. Chem. Phys.* **1993**, *98*, 6291−6315.

(62) Mazzucato, U.; Momicchioli, F. Rotational Isomerism in trans-1,2-Diarylethylenes. *Chem. Rev.* **1991**, *91*, 1679−1719.

(63) Quick, M.; Berndt, F.; Dobryakov, A. L.; Ioffe, I. N.; Granovsky, A. A.; Knie, C.; Mahrwald, R.; Lenoir, D.; Ernsting, N. P.; Kovalenko, S. A. Photoisomerization Dynamics of Stiff-Stilbene in Solution. *J. Phys. Chem. B* **2014**, *118*, 1389−1402.

(64) Nakamura, T.; Takeuchi, S.; Suzuki, N.; Tahara, T. Revised Steady-State Fluorescence Spectrum and Nature of the Reactive S1 State of cis-Stilbene in Solution. *Chem. Phys. Lett.* **2008**, *465*, 212−215.

(65) Sajadi, M.; Dobryakov, A. L.; Garbin, E.; Ernsting, N. P.; Kovalenko, S. A. Time-Resolved Fluorescence Spectra of cis-Stilbene in Hexane and Acetonitrile. *Chem. Phys. Lett.* **2010**, *489*, 44−47.

(66) Lewis, G. N.; Magel, T. T.; Lipkin, D. The Absorption and Re-emission of Light by cis- and trans-Stilbenes and the Efficiency of their Photochemical Isomerization. *J. Am. Chem. Soc.* **1940**, *62*, 2973−2980.

(67) Warshel, A. Calculation of Vibronic Structure of the $\pi \rightarrow \pi^*$ Transition of trans- and cis-Stilbene. *J. Chem. Phys.* **1975**, *62*, 214−221.

(68) Demchenko, A. P.; Sytnik, A. I. Solvent Reorganizational Red-Edge Effect in Intramolecular Electron Transfer. *Proc. Natl. Acad. Sci. U.S.A.* **1991**, *88*, 9311−9314.

(69) Siebert, R.; Hunger, C.; Guthmuller, J.; Schlütter, F.; Winter, A.; Schubert, U. S.; Gonzalez, L.; Dietzek, B.; Popp, J. Direct Observation of Temperature-Dependent Excited-State Equilibrium in Dinuclear Ruthenium Terpyridine Complexes Bearing Electron-Poor Bridging Ligands. *J. Phys. Chem. C* **2011**, *115*, 12677−12688.

(70) Frolov, S.; Liess, M.; Lane, P.; Gellermann, W.; Vardeny, Z.; Ozaki, M.; Yoshino, K. Exciton Dynamics in Soluble Poly(p-phenylene-vinylene): Towards an Ultrafast Excitonic Switch. *Phys. Rev. Lett.* **1997**, *78*, 4285−4288.

(71) Kraabel, B.; Klimov, V.; Kohlman, R.; Xu, S.; Wang, H.-L.; McBranch, D. Unified Picture of the Photoexcitations in Phenylene-Based Conjugated Polymers: Universal Spectral and Dynamical Features in Subpicosecond Transient Absorption. *Phys. Rev. B* **2000**, *61*, 8501−8515.

(72) Laine, P.; Campagna, S.; Loiseau, F. Conformationally Gated Photoinduced Processes Within Photosensitizer−Acceptor Dyads Based on Ruthenium(II) and Osmium(II) Polypyridyl Complexes With an Appended Pyridinium Group. *Coord. Chem. Rev.* **2008**, *252*, 2552−2571.

(73) Presselt, M.; Dietzek, B.; Schmitt, M.; Rau, S.; Winter, A.; Jäger, M.; Schubert, U. S.; Popp, J. A Concept to Tailor Electron Delocalization: Applying QTAIM Analysis to Phenyl−Terpyridine Compounds. *J. Phys. Chem. A* **2010**, *114*, 13163−13174.

(74) Yoshihara, K.; Namiki, A.; Sumitani, M.; Nakashima, N. Picosecond Flash Photolysis of cis- and trans-Stilbene. Observation of an Intense Intramolecular Charge-Resonance Transition. *J. Chem. Phys.* **1979**, *71*, 2892−2895.

Structure-Property Relationships in an Iridium(III) Bis-Terpyridine Complex with Extended Conjugated Sidechains

Joachim Kübel, [†,‡] Andreas Winter, [§,⊥] Ulrich S. Schubert, [§,⊥] and Benjamin Dietzek[,†,‡,⊥]*

[†] Institute of Physical Chemistry and Abbe Center of Photonics, Friedrich Schiller University Jena, Helmholtzweg 4, 07743 Jena, Germany

[‡] Leibniz Institute of Photonic Technology (IPHT) Jena e.V., Albert-Einstein-Str. 9, 07745 Jena, Germany

[§] Laboratory of Organic and Macromolecular Chemistry (IOMC), Friedrich Schiller University Jena, Humboldtstr. 10, 07743 Jena, Germany

[⊥] Jena Center for Soft Matter (JCSM), Friedrich Schiller University Jena, Philosophenweg 7, 07743 Jena, Germany

Supporting Information

The complete author list for Gaussian 09 is:

Frisch, M. J.; Trucks, G. W.; Schlegel, H. B.; Scuseria, G. E.; Robb, M. A.; Cheeseman, J. R.; Scalmani, G.; Barone, V.; Mennucci, B.; Petersson, G. A.;Nakatsuji, H.; Caricato, M.; Li, X.; Hratchian, H. P.; Izmaylov, A. F.; Bloino, J.; Zheng, G.; Sonnenberg, J. L.; Hada, M.; Ehara, M.; Toyota, K.; Fukuda, R.; Hasegawa, J.; Ishida, M.; Nakajima, T.; Honda, Y.; Kitao, O.; Nakai, H.; Vreven, T.; Montgomery, Jr. J. A.; Peralta, J. E.; Ogliaro, F.; Bearpark, M.; Heyd, J. J.; Brothers, E.; Kudin, K. N.; Staroverov, V. N.; Kobayashi, R.; Normand, J.; Raghavachari, K.; Rendell, A.; Burant, J. C.; Iyengar, S. S.; Tomasi, J.; Cossi, M.; Rega, N.; Millam, J. M.; Klene, M.; Knox, J. E.; Cross, J. B.; Bakken, V.; Adamo, C.; Jaramillo, J.; Gomperts, R.; Stratmann, R. E.; Yazyev, O.; Austin, A. J.; Cammi, R.; Pomelli, C.; Ochterski, J. W.; Martin, R. L.; Morokuma, K.; Zakrzewski, V. G.; Voth, G. A.; Salvador, P.; Dannenberg, J. J.; Dapprich, S.; Daniels, A. D.; Farkas, Ö.; Foresman, J. B.; Ortiz, J. V.; Cioslowski, J.; Fox, D. J. *Gaussian 09 Revision D.01*.
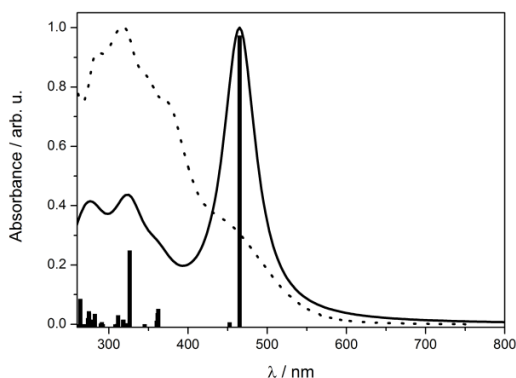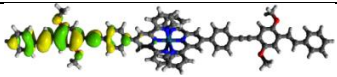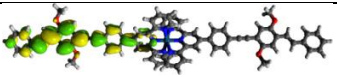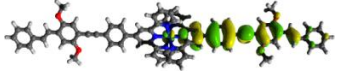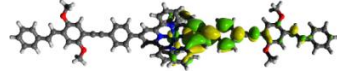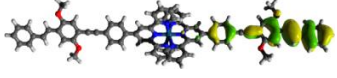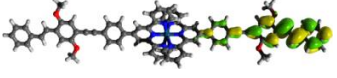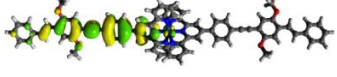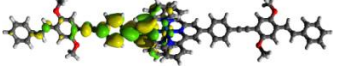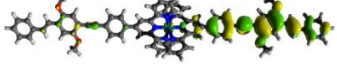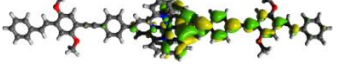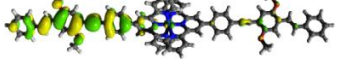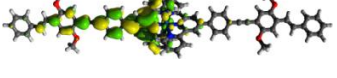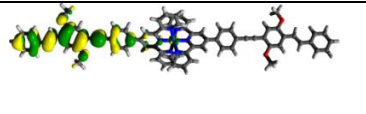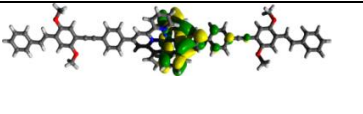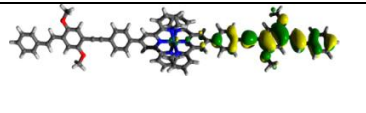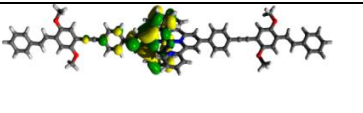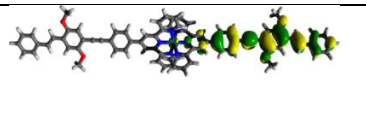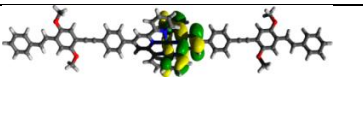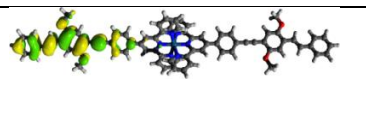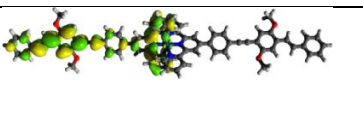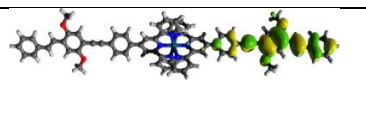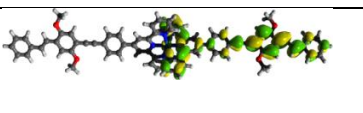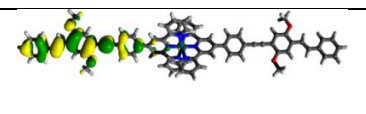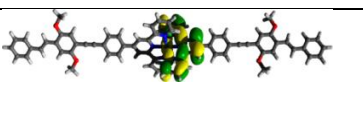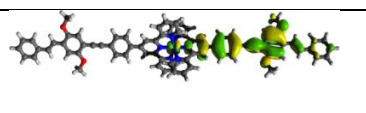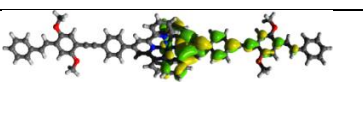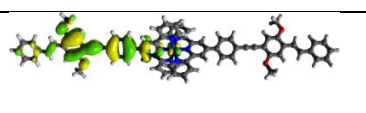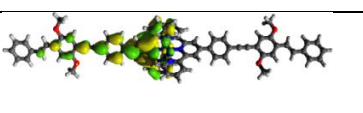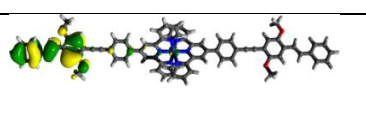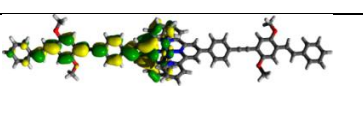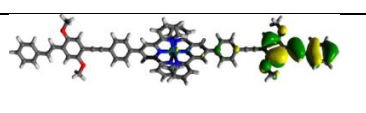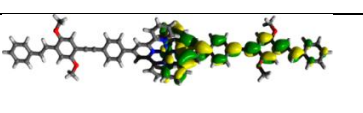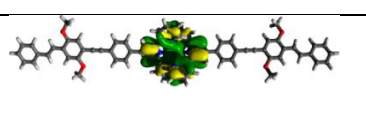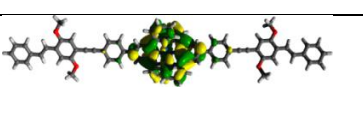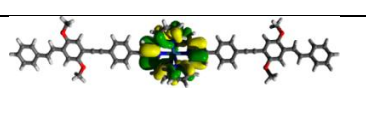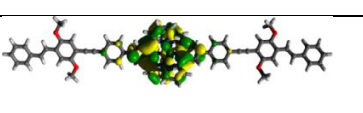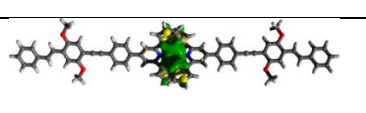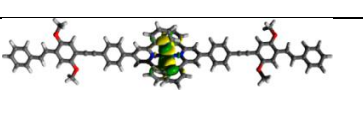
Figure S 1. UV/Vis absorption spectrum in THF (dotted line) and TD-DFT calculated absorption spectrum obtained from a lorentzian convolution (25 nm width) of the 75 lowest vertical excitations.

	E / eV	λ / nm	f		E / eV	λ / nm	f
T_1	1.66	745		T_1'	1.66	745	
T_2	2.28	544		T_2'	2.28	544	
S_1	2.60	477	3.24	S_1'	2.65	468	0.003
T_3	2.83	438		T_3'	2.83	438	
T_4	2.98	416		T_4'	2.98	416	
T_5	3.05	407		T_5'	3.05	407	
T_6	3.08	403		T_6'	3.08	403	
T_7	3.14	394		T_7'	3.14	394	
S_2	3.14	394	0.0	S_2'	3.14	394	0.0
S_3	3.25	381	0.0002	S_3'	3.25	381	0.0002
S_4	3.37	368	1.79	S_4'	3.37	368	0.03
S_5	3.61	343	0.0	S_5'	3.61	343	0.00
S_6	3.70	336	0.71	S_6'	3.75	331	0.02
S_7	3.90	318	0.08	S_7'	3.91	317	0.002
S_8	4.00	310	0.11	S_8'	4.00	310	0.11

Table S 1. The vertical excitation energies from the S_0 state to the lowest excited singlet and triplet states. The left and right columns represent quasi-degenerate states that belong to different irreducible representations.

	"hole"	"particle"
T_1 85%		
T_2 47.7%		
20.3%		
17.4%		
S_1 48.7%		
48.6%		

S₂ 79.5%		
20.5%		
S₃ 98%		
S₄ 50.6%		
45.4%		
S₅ 99.9%		
S₆ 46.3%		
46.0%		
S₇ 47.3%		
47.1%		
S₈ 51.0%		
28.1%		
S₉ 98.9%		
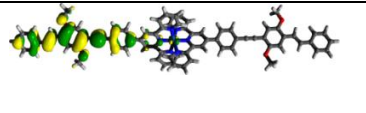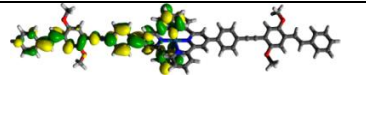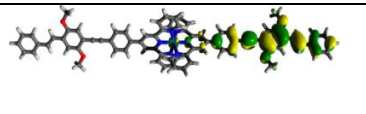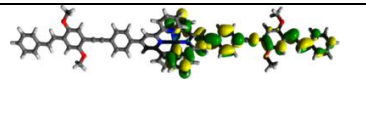
S$_{10}$ 37.1%		
35.1%		

Table S 2. Compositions of excited singlet states are shown in terms of natural transition orbitals, where the percentage of the respective hole/particle pair quantifies the contribution of the transition.

	B3LYP		CAM-B3LYP		PBE0	
	r / Å	Θ / °	r / Å	Θ / °	r / Å	Θ / °
Ir	1.471	28.6	1.474	32.9	1.466	29.7
Fe	1.477	32.2	1.478	35.8	1.472	33.9
Ru	1.478	32.9	1.479	36.9	1.473	33.5
Os	1.478	32.7	1.479	36.4	1.473	33.1

Table S 3. Structural parameters for **Ir** as well as **Fe**, **Ru** and **Os** for comparison from optimized ground state structures using three different functions (B3LYP, CAM-B3LYP, PBE0): The bond length (r) between the terpyridine unit and the adjacent phenyl ring is given as well as the respective dihedral angle (θ) between both rings.
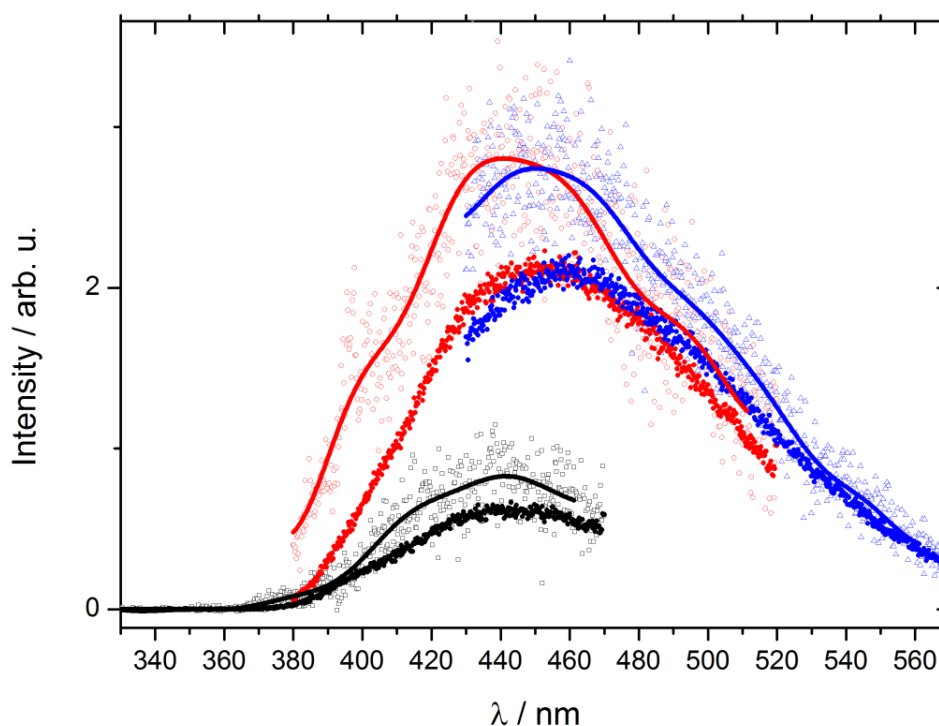
Figure S 2. Time-resolved streak camera data for **Ir** after 370 nm excitation in ACN: Evolution-associated spectra are obtained from global biexponential fits with convolution using a gaussian response function. The x-axis contains three different datasets each recorded in a 140-nm broad window around central wavelengths of 400 nm (black squares), 450 nm (red circles) and 500 nm (blue triangles). The amplitude of the black curves is smaller than for the other curves due to a reduced number of images taken. For all three time windows a fast component (hollow symbols) with time constants of 160 ps, 140 ps and 200 ps, respectively and a slower component (solid symbols) with time constants 1.71 ns, 1.74 ns and 1.77 ns are needed. The solid line represents a smoothed curve obtained via application of 50-point FFT filter to the noisy spectral data of the respective fast components. The deviation of the curve maxima between the different spectral windows is due to spectrograph calibration.
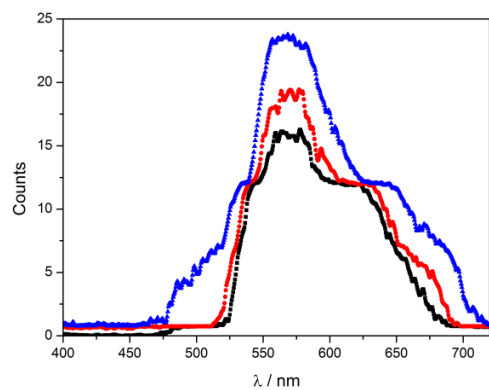
Figure S 3. Phosphorescence spectra of **Ir** in butyronitrile at 77 K at selected delay times: 30 µs (blue curve), 40 µs (red curve), 50 µs (black curve)
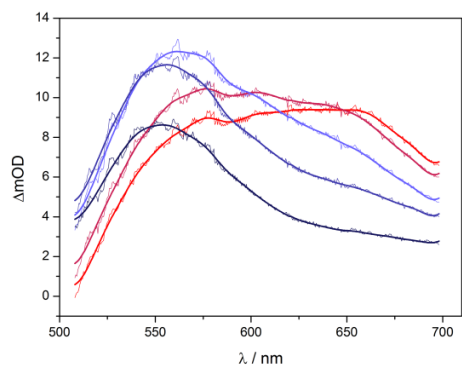
Figure S 4. Selected raw and smoothed transient absorption spectra obtained via a 15-point FFT filter. The spectra are recorded in *N,N*-dimethylpyrrolidineurimid (DMPU) after excitation at $\lambda_{exc} = 480$ nm at different delay times color coded from red to dark blue: 0.25 ps, 0.5 ps, 7.5 ps, 25 ps, 1600 ps.
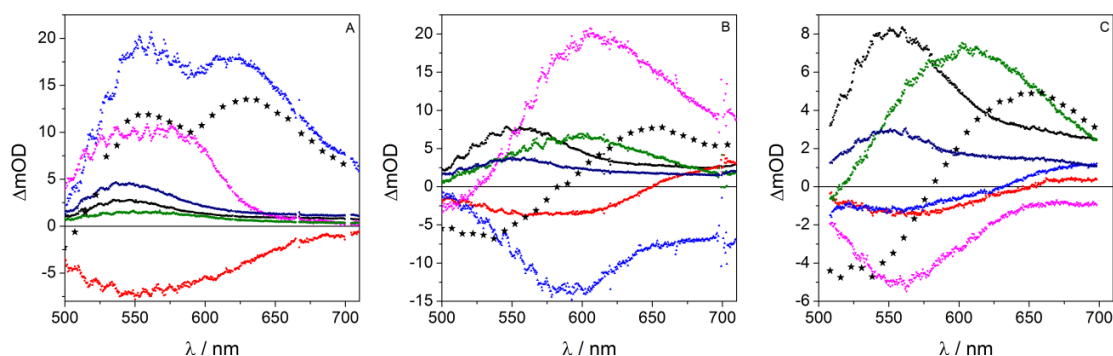
Figure S 5. The same data as in the manuscript is shown: Decay-associated spectra (DAS) from global multiexponential fits of the transient absorption data recorded in different solvents. The time constants of the kinetic components are characteristic for each solvent: Panel A (ACN): 240 fs (red), 840 fs (blue) 1.8 ps (pink), 65 ps (green), 600 ps (dark blue). Panel B (THF): 170 fs (red), 1.8 ps (blue) 3.6 ps (pink), 11 ps (green), 980 ps (dark blue). Panel C (DMPU): 120 fs (red), 680 fs (blue) 7.7 ps (pink), 15.9 ps (green), 970 ps (dark blue). The black curve corresponds to the spectral offset for all solvents, i.e. a process with a time-constant that is not completed on the time-scale of our experiment (< 2 ns). Additionally the black stars in each panel represent the respective sum of the DAS corresponding to τ_1, τ_2 and τ_3 (for ACN only the first two DAS were added).

	Ru			Os		
	E / eV	λ / nm	Assignment	E / eV	λ / nm	Assignment
T_1	1.72	720	π-π*	1.72	722	π-π*
T_2	2.26	549	π-π*/ILCT	1.99	622	π-π*/ILCT
T_3	2.66	467	MLCT/ILCT'	2.39	519	MLCT
T_4	2.73	454	MLCT	2.56	479	MLCT/ILCT'

Table S 4. The vertical excitation energies from the S_0 state to the lowest excited triplet states for **Ru** and **Os** are given with a respective assignment regarding the electronic nature of the transition. The quasi-degenerate states belonging to another irreducible representation (analogous to the calculations presented for **Ir**, see the paper) produced in the calculation are not listed here.

P4 - Energy transfer and formation of long-lived ^{3}MLCT states in multimetallic complexes coordinating extended highly conjugated bis-terpyridyl ligands
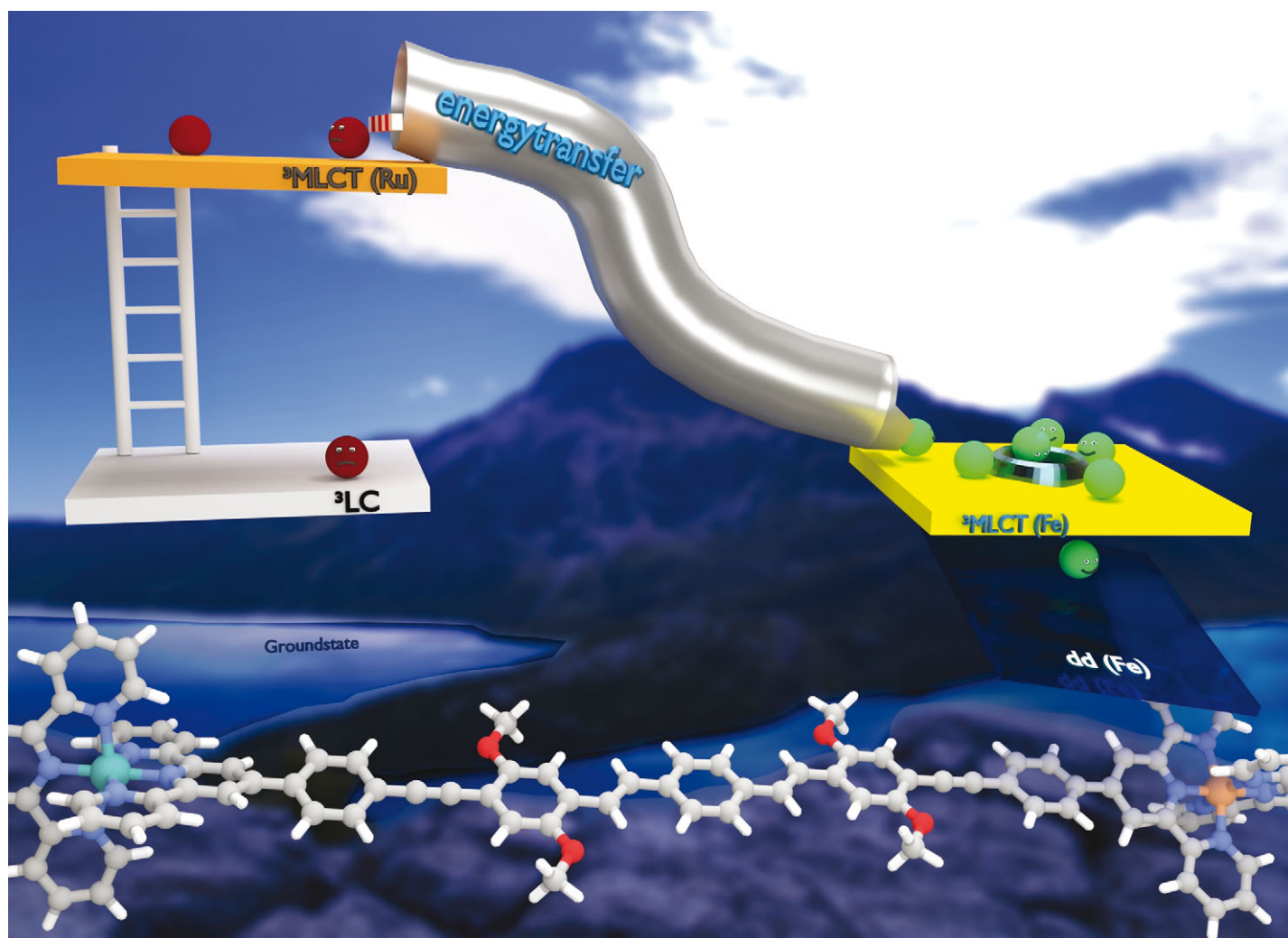
Showcasing research from the laboratory of Prof. Dr Benjamin Dietzek at the Leibniz Institute of Photonic Technology, Jena, Germany.

Title: Energy transfer and formation of long-lived ^{3}MLCT states in multimetallic complexes with extended highly conjugated bis-terpyridyl ligands

Heterometallic complexes in which metal centers are connected by functional bridging chromophores are components for light-harvesting antenna units in potential artificial photosynthetic model systems. The present work includes a trinuclear Ru(II)−Fe(II)−Ru(II) complex with extended and highly conjugated 2,2′:6′,2″-terpyridine ligands. The compound shows after photoexcitation of the Ru-based ^{1}MLCT band efficient, yet incomplete, energy transfer from the Ru- towards the Fe-based-^{3}MLCT state. This state is remarkably long-lived (23 ps) in view of the very fast spin-crossover (≪1 ps) typically observed in Fe(II)-polypyridine complexes.
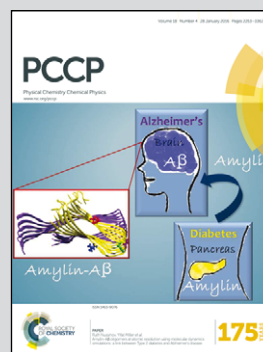
ROYAL SOCIETY OF CHEMISTRY

Energy transfer and formation of long-lived 3MLCT states in multimetallic complexes with extended highly conjugated bis-terpyridyl ligands†

Maria Wächtler,[a] Joachim Kübel,[ab] Kevin Barthelmes,[cd] Andreas Winter,[cd] Alexander Schmiedel,[e] Torbjörn Pascher,[f] Christoph Lambert,[e] Ulrich S. Schubert[cd] and Benjamin Dietzek*[abd]

Multimetallic complexes with extended and highly conjugated bis-2,2′:6′,2″-terpyridyl bridging ligands, which present building blocks for coordination polymers, are investigated with respect to their ability to act as light-harvesting antennae. The investigated species combine Ru(II)- with Os(II)- and Fe(II)-terpyridyl chromophores, the latter acting as energy sinks. Due to the extended conjugated system the ligands are able to prolong the lifetime of the 3MLCT states compared to unsubstituted terpyridyl species by delocalization and energetic stabilization of the 3MLCT states. This concept is applied for the first time to Fe(II) terpyridyl species and results in an exceptionally long lifetime of 23 ps for the Fe(II) 3MLCT state. While partial energy (>80%) transfer is observed between the Ru(II) and Fe(II) centers with a time-constant of 15 ps, excitation energy is transferred completely from the Ru(II) to the Os(II) center within the first 200 fs after excitation.

Introduction

The design of artificial antennae systems for efficient collection of solar radiation, *i.e.*, multicomponent systems in which several molecular components absorb the incident light and channel the energy to an acceptor unit, is an active field of research.[1–8] The ultimate goal is to build systems, which are capable of harvesting light over a large part of the visible spectrum. In this respect a number of systems containing transition metal complexes have been prepared and studied.[1,2,5,9–16] Multimetallic complexes containing several metal centers connected *via* large conjugated ligands can show photoinduced energy and/or electron transfer processes between the individual chromophoric centers.[13,16,17] A challenge in the design of such systems is to control the direction of the energy/electron transfer, to transport the

excitation over large distances, *e.g.*, in wirelike structures.[17–20] This can be achieved by structural and electronic variations of the bridging ligands and/or by changing metal centers and their coordination environment to create a gradient for energy or electron transport in the system.[13] In this respect, hierarchically structured coordination polymers are interesting systems for the design of artificial light-harvesting antennas. Especially, low-spin d⁶ polypyridyl transition metal complexes play an important role in this field due to their strong absorption of light in the visible spectral range and the favorable and tunable photophysical properties of their charge-transfer states.[13,17,21–23]

In this contribution bi- and trimetallic systems are investigated, which may serve as building blocks for coordination polymers. For this purpose a bis-2,2′:6′,2″-terpyridyl ligand **L** bearing a conjugated spacer, which is closely related to the widely used poly[phenylene–vinylene] and poly[phenylene–ethynylene] conjugated polymers (Fig. 1), is used.[24,25] The strong conjugation of the bridging ligand together with the tridentate coordination site enables to build linear, rodlike structures and no stereo-isomer mixtures are formed upon complexation, as it is the case for bidentate ligands.[13,17,20,26,27] The herein investigated species combine Ru(II) and Fe(II) (**RuFeRu**) or Ru(II) and Os(II) (**RuOs**) centers, which are coordinated by the terpyridyl units. This combination of metal centers in the supramolecular assembly is advantageous due to their complementary absorption features: both Fe(II) and Os(II) complexes absorb at wavelengths longer than the 1MLCT (metal-to-ligand charge transfer) absorption band of Ru(II)-terpyridyl centers: Fe(II) terpyridyl complexes possess a

ᵃ Leibniz Institute of Photonic Technology e.V., Albert-Einstein-Straße 9, 07745 Jena, Germany. E-mail: benjamin.dietzek@ipht-jena.de; Fax: +49 (0)3641 206-390; Tel: +49 (0)3641 206-332

ᵇ Institute of Physical Chemistry and Abbe Center of Photonics, Friedrich Schiller University Jena, Helmholtzweg 4, 07743 Jena, Germany

ᶜ Laboratory of Organic and Macromolecular Chemistry (IOMC), Friedrich Schiller University Jena, Humboldtstraße 10, 07743 Jena, Germany

ᵈ Jena Center for Soft Matter (JCSM), Friedrich Schiller University Jena, Philosophenweg 7, 07743 Jena, Germany

ᵉ Institut für Organische Chemie, Universität Würzburg, Wilhelm Conrad Röntgen Research Center for Complex Material Systems, Center for Nanosystems Chemistry, Am Hubland, 97074 Würzburg, Germany

ᶠ Pascher Instruments AB, Stora Råbybyaväg 24, 22478 Lund, Sweden

† Electronic supplementary information (ESI) available. See DOI: 10.1039/c5cp04447b

2350 | *Phys. Chem. Chem. Phys.*, 2016, **18**, 2350–2360

This journal is © the Owner Societies 2016
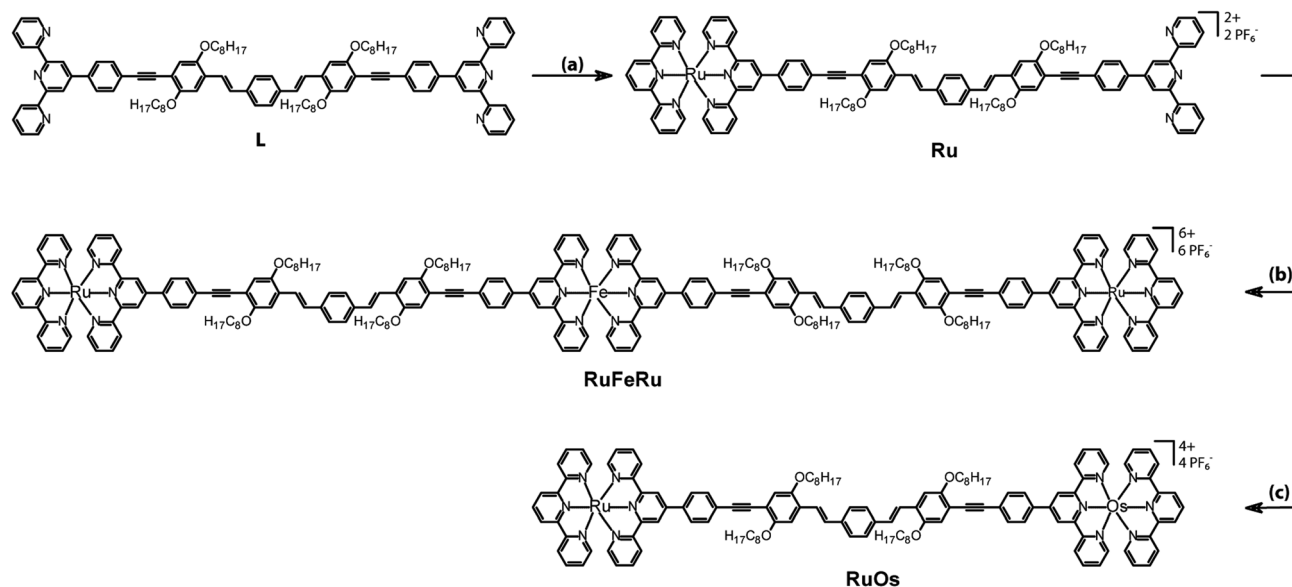
Fig. 1 Structures and synthesis of the investigated polynuclear complexes **RuFeRu** and **RuOs** and the mononuclear reference complex **Ru**. Legend: (a) [Ru(tpy)(acetonitrile)$_3$](PF$_6$)$_2$, DMF, 160 °C, 3 h; (b) FeSO$_4$·7H$_2$O, dichloromethane/methanol, room temperature, 2 h; (c) (i) Os(tpy)Cl$_3$, AgBF$_4$, acetone, 70 °C, 2 h, (ii) DMA/ethylene glycol, 160 °C, 24 h.

^{1}MLCT transition at *ca.* 560 nm$^{28–30}$ and the Os(II) terpyridyl chromophore shows, besides a ^{1}MLCT absorption band in the same wavelengths range as the Ru(II) ^{1}MLCT transitions, a ^{3}MLCT absorption band spanning the entire visible range of the absorption spectrum[17] extending the overall absorption spectrum of the assembly far into the red up to 700 nm. In these assemblies the Ru(II) centers are expected to serve as excitation energy donor while Os(II) and Fe(II) centers possess lower lying excited states and serve as potential energy accepting units.[13,15,17,18,24,28,31–33]

A critical property for future applicability of such structures is the excited state lifetime of the acceptor centers, which can be a crucial efficiency determining factor for subsequent reaction steps, *e.g.*, charge separation and generation of redox-equivalents. The ^{3}MLCT states of Os(II)-bis(terpyridyl) chromophores possess sufficiently long lifetimes in the range of 200 ns in aerated solution at room temperature.[17] Due to the high ligand-field strength in Os complexes the energy gap between ^{3}MLCT states and metal-centered (MC) ligand field states, which offer an efficient route for radiationless deactivation, is large.[17,28] This prevents deactivation of the ^{3}MLCT state *via* thermal population of the MC states.[34] In the order Os(II), Ru(II) and Fe(II) the ligand field strength decreases and, hence, the MC states are significantly closer in energy to the ^{3}MLCT states in comparable Ru(II) and Fe(II) complexes. Furthermore, in tridentate terpyridyl complexes additional weakening of the ligand field is observed due to the unfortunate bite angle of the terpyridyl ligand, which causes a distortion of the octahedral coordination sphere.[13,17] This further decreases the energetic separation between MC and MLCT states which is reflected in the short room-temperature lifetime of the ^{3}MLCT excitation in Ru(II)-terpyridyl complexes ([Ru(tpy)$_2$]$^{2+}$ τ = 124 ps)^{17,35} and Fe(II)-polypyridyl complexes in general ([Fe(tpy)$_2$]$^{2+}$, [Fe(bpy)$_3$]$^{2+}$ $\tau \leq 0.2$ ps).$^{36–43}$ This is also the reason why – in contrast to

Ru(II) and Os(II)-polypyridyl centers – Fe(II)-polypyridiyl complexes are not established in light-harvesting applications yet, despite its high abundance and low cost of production. Only ultrafast charge separation processes on the sub 100 fs timescale are able to compete with the ultrafast deactivation to the high spin quintet state (which is probably mediated by ligand field triplet states) in Fe(II)-polypyridyl complexes,$^{36–42}$ *e.g.*, ultrafast injection of electrons into TiO$_2$.^{37,44,45} Hence, to boost the applicability of Fe(II)-polypyridyl dyes in light-harvesting applications one important goal is to prolong the ^{3}MLCT lifetime.

One approach to prolong the lifetime of ^{3}MLCT states is to increase the relative energy of the MC states *via* coordination of ligands with high ligand field strength, *e.g.*, strong σ-donor ligands. Attractive candidates in this respect are cyclometallated ligands. In a first attempt ^{3}MLCT lifetimes in Ru(II) complexes were extended by four orders of magnitude$^{46–48}$ and in Fe(II) cyclometallated complexes ^{3}MLCT lifetimes of 9 ps and even 13 ps were achieved, which corresponds to an extension of the ^{3}MLCT lifetime by two orders of magnitude.$^{49–51}$ A second possibility to increase the energy gap between ^{3}MLCT and MC states is to coordinate stronger π-acceptor ligands, which also increases the ligand field strength, hence raises the energy of the MC states and further results in lower energies of the ^{3}MLCT state. This can be achieved by substitution in the 4′-position of the terpyridyl ligand and extending the conjugated system of the terpyridyl coordination sphere. Applying this approach the lifetimes in Ru(II) complexes were extended to reach tens of ns.[27] An additional prolongation of the lifetime of the ^{3}MLCT state can be achieved by applying highly extended conjugated 4′-terpyridyl ligands. In such systems low lying ^{3}LC (ligand-centered) states may form equilibria with the ^{3}MLCT state.^{27,30,52,53} Though structures fulfilling these preconditions are known in literature,$^{54–56}$ the Fe(II) ^{3}MLCT lifetimes in such systems have not been addressed yet.

A third approach was applied by Heinze *et al.*[57] by coordinating ligands with larger bite angle than the classical terpyridyl units, which increases the relative energy of MC states due to less distortion of the coordination polyhedron resulting in a stronger ligand field.[58–62] Additionally, ligands with strong electron withdrawing/electron donating character have been combined resulting in push–pull systems with low lying ^{3}MLCT states.[63–65] The first attempts following this approach for Fe(II) complexes, however, did not lead to formation of a long-lived CT (charge-transfer) states.[57]

In the here investigated systems the highly conjugated bis-2,2′:6′,2″-terpyridine ligands offer the possibility to stabilize the ^{3}MLCT states and additionally to form equilibria with low lying ^{3}LC states as was previously reported for Ru(II) coordinated by related ligands.[66] In the following the photoinduced processes in the multimetallic systems, especially with respect to possible energy transfer pathways between the specific metal centers, will be investigated by time-resolved spectroscopy. Special emphasis will be on the ^{3}MLCT lifetime of the Fe(II) ^{3}MLCT states in these systems.

Experimental section

For spectroscopic measurements all compounds were dissolved in aerated acetonitrile (spectrophotometric grade). Absorption spectra were recorded with a Lambda 750 (PerkinElmer) UV/VIS spectrometer in a cell with 1 cm pathlength. Emission spectra were recorded with a Jasco FP-6200 spectrofluorometer. For all time-resolved measurements the stability of the samples was verified by recording the absorption spectra before and after each measurement.

For the ns time-resolved transient absorption (TA) measurements the samples were excited by 5 ns pulses at 520 nm with a repetition rate of 10 Hz. The probe light is delivered by a pulsed 75 W Xe arc lamp and detected on a PMT after passing a monochromator. By switching off the probe light emission decay can be detected with ns-temporal resolution with the same set-up.

The fs time-resolved transient absorption measurements were performed in a cuvette with 1 mm path length. **Ru** and **RuFeRu** were excited by 140 fs pulses at 520 nm and 520/575 nm, respectively. A white light continuum generated in a CaF$_2$ crystal was used to probe the sample between 350 and 800 nm. The relative temporal delay between the pump and probe pulses was varied over a maximum range of 8 ns. The fs time-resolved measurements for **RuOs** were performed applying pump pulses centered at 520 and 670 nm with a duration of ∼80 fs and probed by a white-light continuum between 450 and 700 nm, which is produced in a sapphire crystal. The pump pulses are delayed with respect to the probe pulses by means of an optical delay stage over a maximum range of 2 ns. The mutual polarization of the pump and probe pulses was set to magic angle.

Prior to data analysis the experimental data from the fs time-resolved measurements were chirp corrected. To avoid prominent contributions from the coherent artifact the pulse overlap region

(±200 fs) around time zero was excluded in the data fitting procedure. The data were fitted with a global fitting routine applying a sum of exponential functions for data analysis. Additionally, the data for **RuFeRu** upon excitation at 520 nm were numerically fitted with a home-written algorithm for non-sequential (*e.g.*, including branching of the relaxation pathway) kinetic schemes.

For a more detailed description of the synthetic procedures, characterization, experimental set-ups and the fitting procedure the reader is referred to the ESI.†

Results and discussion

Synthesis

The synthesis of the bridging ligand **L**, which is used in this study, was reported recently.[67] In order to obtain heterometallic oligonuclear complexes, a two-step assembly approach had to be followed (Fig. 1). The first step was the preparation of the mononuclear Ru(II) bisterpyridyl complex **Ru** by reaction of [Ru(tpy)(acetonitrile)$_3$](PF$_6$)$_2$[68] with ligand **L** in DMF (tpy – 2,2′:6′,2″-terpyridine).[69] The trinuclear complex **RuFeRu** was prepared by addition of a methanolic Fe(II) sulphate solution to a solution of **Ru** in dichloromethane. The dinuclear complex **RuOs** was prepared by the reactions of **Ru** with silver-activated Os(tpy)Cl$_3$ in a DMAc/ethylene glycol mixture.[70]

Steady-state absorption and emission spectroscopy

The absorption spectra of **Ru**, **RuFeRu** and **RuOs** in acetonitrile are displayed in Fig. 2. The spectra show multiple electronic transitions in the visible and UV spectral region. $\pi\pi^*$ transitions, which are located at the terpyridine sphere, dominate at wavelengths shorter than 350 nm. At longer wavelengths the spectra contain a superposition of ligand-centered $\pi\pi^*$ transitions and transitions which appear upon coordination of the metal center and, according to literature, most likely are due to MLCT
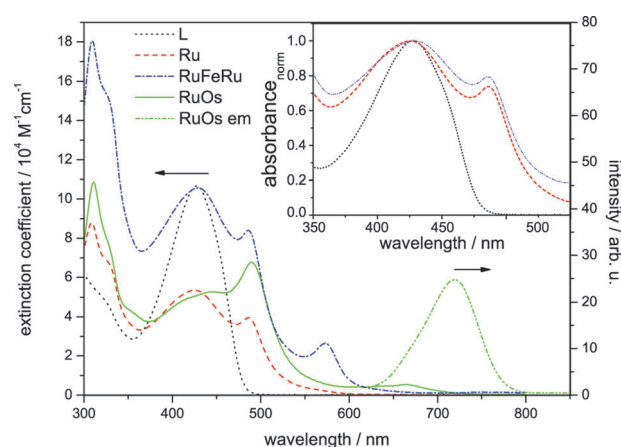
Fig. 2 Steady-state absorption spectra of **Ru**, **RuFeRu** and **RuOs** and emission spectrum of **RuOs** after excitation at 488 nm in aerated acetonitrile. For comparison the absorption spectrum of the bridging ligand **L** in dichloromethane is given. The inset shows the normalized absorption spectra of **L**, **Ru** and **RuFeRu** for comparison of the position of the LC absorption band.

transitions.[17,28–30,71] The ligand-centered $\pi\pi^*$ transitions of the extended bridging ligand can be identified by the comparison with the absorption spectrum of the pure ligand **L** (absorption maximum at 429 nm). No significant shifts are observed in the $\pi\pi^*$ transition upon coordination of one or two metal centers: for **Ru** the maximum of the $\pi\pi^*$ transition is at 426 nm and for **RuFeRu** at 429 nm. For **RuOs** no separate maximum of the $\pi\pi^*$ transition can be distinguished. The Ru(II) ^{1}MLCT transitions in **Ru** and **RuFeRu** peak at 486 nm while in **RuOs** the maximum of the superimposed ^{1}MLCT transitions of both the Ru(II) and Os(II) centers is at 490 nm. The ^{1}MLCT transitions at the Ru(II) and Os(II) center present a mixture of transitions to the terminal tpy ligand and the 4′-substituted bridging ligand with the extended chromophore. The torsional angle between the tpy unit and the adjacent phenyl ring, which is typically in the range of 30°,[72–74] reduces conjugation but does not inhibit it completely. Hence, the chromophore is delocalized over the tpy and the directly connected phenyl ring, but – on the other hand – does not extent over the ethynyl bond.[72] When comparing the absorption spectrum of **RuFeRu** to the one of **Ru** an additional band at 574 nm is observed, which is assigned to the Fe(II) ^{1}MLCT transition to the bridging ligand. Also the spectrum of **RuOs** is significantly broadened due to additional weak spin-forbidden ^{3}MLCT transitions spanning the visible spectral region up to 700 nm with a maximum at 665 nm.

Only for **RuOs** a weak triplet emission could be detected at room temperature in aerated solution. This emission peaks at 720 nm and is due to ^{3}MLCT phosphorescence from the Os(II) center. In all three investigated species, even the mononuclear complex **Ru**, phosphorescence from the Ru(II) ^{3}MLCT state is not detectable, hence no conclusions about energy transfer between the metal centers can be drawn from emission experiments. The missing emission could be an indication for a strong delocalization of the ^{3}MLCT state over the extended bridge in these systems, decreasing the oscillator strength for the radiative return to the ground state and open the competition with more prone non-radiative deactivation processes. Besides its probably low quantum yield, unambiguous detection of the Ru(II) ^{3}MLCT emission in **Ru** unfortunately is additionally hampered by residual fluorescence originating from LC states in the same spectral region where the emission of the ^{3}MLCT is expected (for further details see ESI,† Fig. S1 and S2). Such LC emission was reported earlier for related 2,2′:6′,2″-terpyridine complexes coordinating two highly conjugated 4′-(4-{[2,5-bis(octyloxy)-4-styrylphenyl]ethynyl}-phenyl)-2,2′:6′,2″-terpyridine ligands.[30,75] Emission originating from the Fe(II) ^{3}MLCT in **RuFeRu** is not expected due to the generally observed fast deactivation of the ^{3}MLCT states in Fe(II)-polypyridyl complexes either populating a non-luminescent high-spin quintet state[36–43] or rapidly repopulating the ground state *via* ^{3}MC states.[50,51]

Lifetime of long-lived excited states

The lifetime of the Os(II) ^{3}MLCT based phosphorescence of **RuOs** in aerated acetonitrile at room temperature was determined to 100 ns, which is in good agreement with the decay time of the excited-state absorption (ESA) signal in ns time-resolved transient absorption (TA) measurements ($\tau = 84$ ns) (Fig. 3).
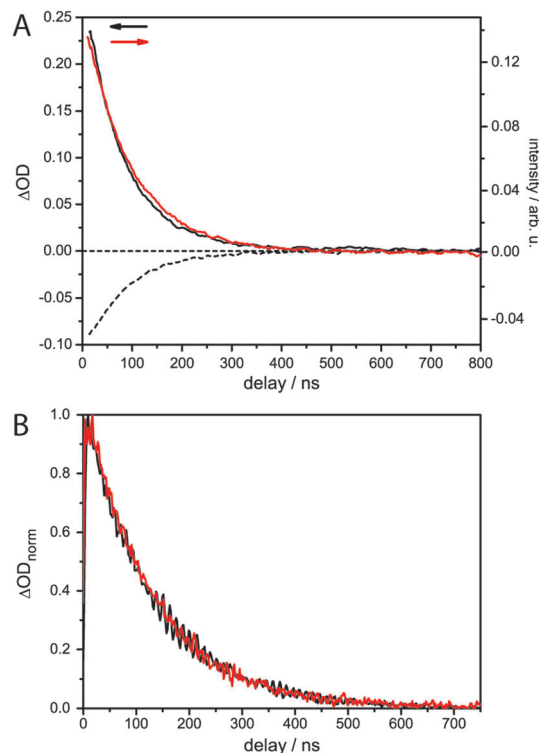
Fig. 3 (A) Transient absorption kinetics of **RuOs** at selected probe wavelengths: 450 nm (dash/black), 590 nm (solid/black) and emission decay at 750 nm (red solid). (B) Direct comparison of the decay kinetics at 600 nm probe wavelength for **Ru** (black) and **RuFeRu** (red).

For **Ru** and **RuFeRu**, although no Ru(II) ^{3}MLCT emission is detectable at room temperature, transient absorption spectroscopy with ns time-resolution reveals the presence of a long-lived excited state. The excited state lifetimes of **Ru** and **RuFeRu** are 132 and 129 ns, respectively (Fig. 3), which is in good agreement with the lifetime determined for the analogues homo-bimetallic Ru(II) complex (145 ns).[66] The nearly identical values of their lifetimes and spectral shapes of the transient spectra of the long-lived excited state in **Ru** and **RuFeRu** (see ESI,† Fig. S8) point to a similar origin of the signals, *i.e.* an excited state connected with the Ru(II) center. Contributions of an Fe(II) excited state to the transient spectra are not expected on the timescale of the experiment, as Fe(II)-terpyridyl species show typically lifetimes <10 ns (see below).[17,29,36,76–78] The observation of an excited Ru(II) state suggests that energy transfer between the Ru(II) and the Fe(II) metal centers in **RuFeRu** occurs with much less than 100% efficiency.

fs time-resolved spectroscopy

To identify and to follow possible energy transfer processes in the polynuclear systems **RuFeRu** and **RuOs** fs time-resolved TA spectroscopy was applied. To disentangle the contributions of the Ru(II) and Fe(II)/Os(II) centers to the observed photoinduced dynamics and to be able to identify possible interactions and transfer processes between the different metal centers, first the characteristic dynamics of each metal center is studied by selective excitation at carefully chosen excitation wavelengths.

In contrast to the Os(II) and the Fe(II) centers, selective excitation of the Ru(II) chromophore is not possible in the polymetallic species, hence the monometallic compound **Ru** serves as reference model for the Ru(II) intrinsic spectral signatures and dynamics.

Upon excitation at 520 nm, *i.e.*, in the Ru(II) [1]MLCT band of **Ru**, the transient spectra (Fig. 4) are dominated by excited-state absorption (ESA) at probe wavelengths longer than 520 nm with a maximum at 630 nm. Below 500 nm negative signal contributions due to ground-state bleach (GSB) dominate. Within the first 100 ps the signal intensity increases and the minimum in the GSB at 482 nm vanishes, while the second minimum shifts from 432 to 418 nm. After 1000 ps the overall intensity starts to decay (by approximately 8% up to 8 ns).

The data was globally fitted with a sequential relaxation scheme. To describe the data four rates and an additional long-lived component, with a lifetime exceeding the observation window, had to be taken into account (Table 1). A feasible assignment of the processes and the species associated spectra (SAS) corresponding to the excited states contributing to the relaxation processes (Fig. 5) is displayed in Scheme 1. The sub-ps process can be related to internal vibrational energy redistribution (IVR) and intersystem crossing (ISC), which leads to the population of the manifold of vibrationally hot Ru(II) [3]MLCT states within the first ~200 fs with a quantum yield close to unity.[53,79–83] The two components in the range of a few ps describe intramolecular relaxation processes: $\tau_2 = 2$ ps is assigned to vibrational cooling[23,53,71,82–86] and interligand electron transfer (ILET)[35] after which the lowest vibrationally relaxed Ru(II) [3]MLCT state in the system is populated and $\tau_3 = 15$ ps describes further structural relaxation, *i.e.*, planarization of the bridging ligand, and as a consequence delocalization of the Ru(II) [3]MLCT state beyond the terpyridine sphere of the bisterpyridine bridging ligand.[30,66] The slowest component τ_5 responsible for the slight decay of the signal amplitude at later delay times can be identified as equilibration with a [3]LC state (see ESI,† Fig. S10).[66] This equilibration is found to be approached much slower in the monometallic complex **Ru** than in the related homobimetallic complex **RuRu** (**Ru** $\tau_5 = 3100$ ps, **RuRu** $\tau = 361$ ps[66]). This could be an indication for changes in the relative energetic positions of the [3]MLCT and [3]LC states induced by the coordination of the
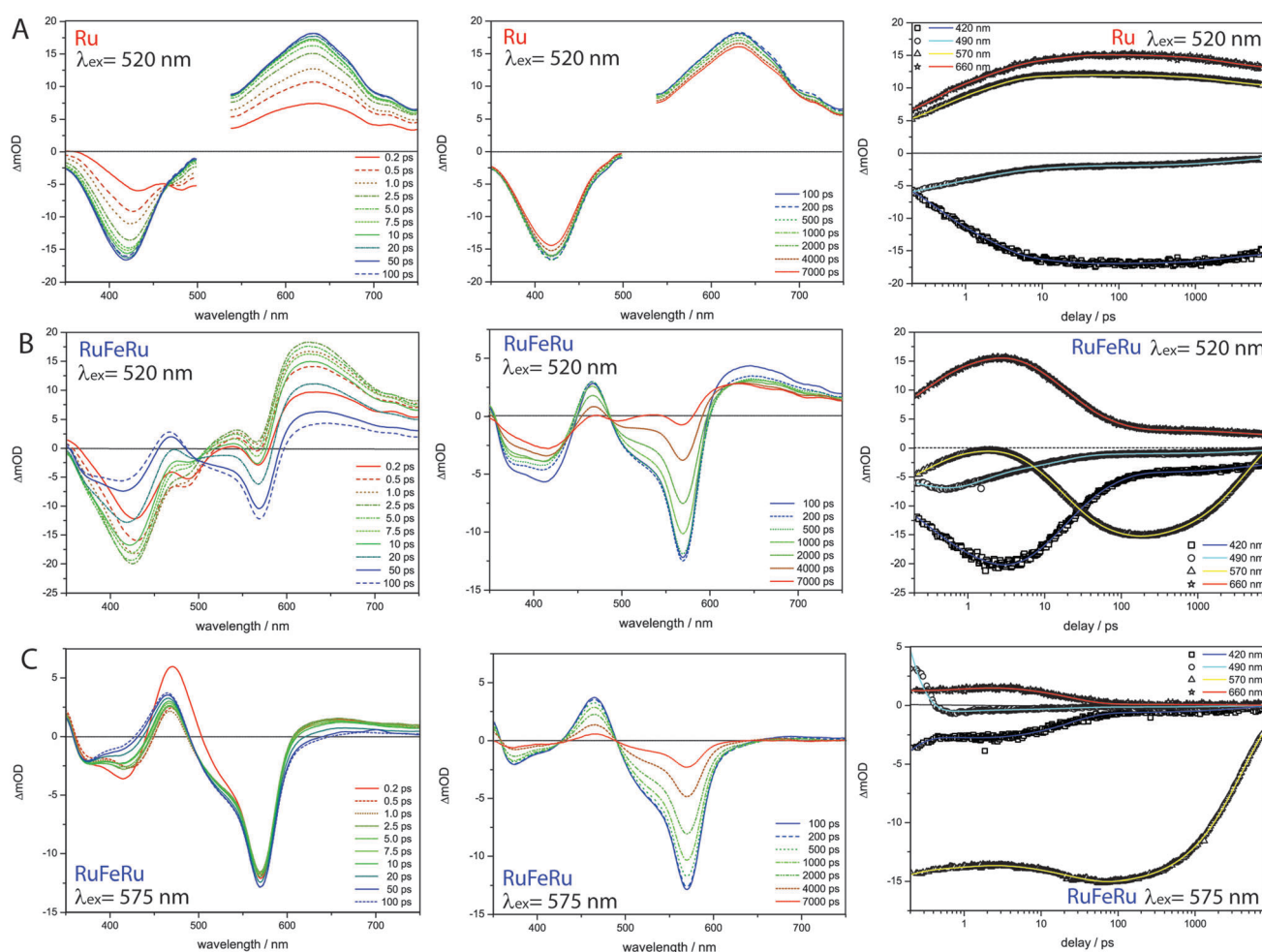
Fig. 4 Transient absorption spectra at selected delay times (left and middle) for (A) **Ru** following excitation at 520 nm, (B) **RuFeRu** upon excitation at 520 nm and (C) **RuFeRu** upon excitation at 575 nm in acetonitrile and the respective kinetics at selected probe wavelengths (right). The pump region for **Ru** is neglected in the data evaluation due to scattered pump.

Table 1 Fit results of fs and ns time-resolved transient absorption measurements in acetonitrile, k represents rate constant for a certain process, τ is the corresponding reciprocal value given for convenience

	λ_{ex}/nm	k_1/ps^{-1}	τ_1/ps	k_2/ps^{-1}	τ_2/ps	k_3/ps^{-1}	τ_3/ps	k_4/ps^{-1}	τ_4/ps	k_5/ps^{-1}	τ_5/ps	k_6/ns^{-1}	τ_6/ns	$k_{inf}{}^a$/ns^{-1}	$\tau_{inf}{}^a$/ns
Ru	520	3.1	≤0.3	0.48	2.0	0.066	15	—	—	0.00033	3100	—	—	0.0076	132
RuFeRu model^b	520	4.1	≤0.2	0.74	1.4	0.067	15	0.018	56	—	—	0.24	4.2	0.0077	129
RuFeRu	575	9.7	≤0.1	0.92	1.1	—	—	0.043	23	—	—	0.25	4.1	—	—
RuOs	670	—	—	1.3	0.8	0.11	9	—	—	0.0016	650	—	—	0.01	100
RuOs	520	4.8	≤0.2	0.63	1.6	0.090	11	—	—	0.0014	700	—	—		

^{a} Infinite component in the fs time-resolved measurements, rate/lifetime determined by ns time-resolved TA and emission measurements. ^{b} Numerical fit applying model described in Scheme 1.
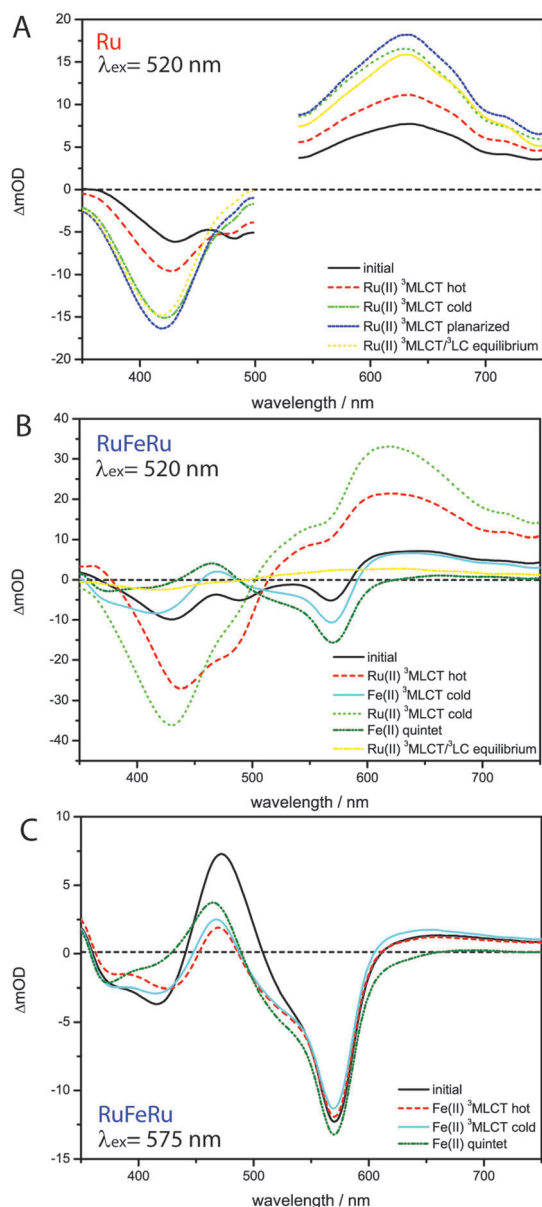
Fig. 5 SAS resulting from the global fit (A) **Ru** excitation 520 nm sequential model, (B) **RuFeRu** excitation 520 nm model with energy transfer according to Scheme 1, (C) **RuFeRu** excitation at 575 nm sequential model.

Scheme 1 Proposed relaxation schemes for **Ru** and **RuFeRu**, solid lines define energy levels with defined energetic positions, while dashed lines define excited states, the energy of which can only be indirectly inferred or depends on the excitation wavelength, processes in grey are not directly observable in the data.

second metal center leading to changes in the activation barriers impacting the equilibration process.

Upon selective excitation of **RuFeRu** into the Fe(II) ^{1}MLCT transition at 575 nm, the Fe(II) intrinsic dynamics is accessible (Fig. 4). Transient spectra show GSB at 570 nm corresponding to the maximum of the Fe(II) ^{1}MLCT transition. Three regions dominated by ESA are observed: at wavelength longer than 605 nm, between 490 and 430 nm and in the UV below 360 nm. The ESA feature in the red spectral region decays within 100 ps. On the same timescale the second ESA feature gains intensity and broadens, extending further to the blue spectral range. After 100 ps a global decay of the overall signal intensity occurs. This development can quantitatively be described by a multi-exponential fit corresponding to the sequential relaxation scheme presented in Scheme 1 applying four exponentials (see Table 1 and Fig. 5 for SAS). The sub-ps and 1.1 ps processes describe – in analogy to the processes at the Ru(II) center – population of the Fe(II) ^{3}MLCT manifold and vibrational cooling. Especially interesting is the process with a time constant of $\tau_4 = 23$ ps. This process is connected to the decay of the ESA feature in the red

This journal is © the Owner Societies 2016

Phys. Chem. Chem. Phys., 2016, **18**, 2350–2360 | **2355**

probe range (see also decay associated spectra (DAS) in the ESI,† Fig. S10), which is – according to literature – a characteristic feature of the Fe(II) ^{3}MLCT state.[37,38] Hence, the process associated with τ_4 probably describes the depopulation of the Fe(II) ^{3}MLCT state *via* ^{3}MC states resulting in population of the high-spin Fe(II) quintet state. From the decay of the overall signal representing repopulation of the ground state a Fe(II) quintet lifetime of τ_6 = 4.1 ns is determined, which is comparable to lifetimes reported for the quintet state of [Fe(tpy)$_2$]$^{2+}$.[17,29,36,76,77] Neither planarization nor formation of an equilibrium with an ^{3}LC state is observed upon excitation of the Fe(II) center. The latter is probably due to the lower energetic position of the excited states of the Fe(II) center compared to the Ru(II) center, preventing a thermal population of the ^{3}LC states, while the former might skip detection due to negligible spectral changes in the observation range. Nevertheless, from these results it can be concluded that the system at hand shows a lifetime of 23 ps for the Fe(II) ^{3}MLCT state, which is the longest reported in literature.[50,51] Hence, the strong conjugated and extended ligand system shows a similar stabilizing effect on the Fe(II) ^{3}MLCT state as for the Ru(II) ^{3}MLCT states.

In the next step the photoinduced processes in **RuFeRu** upon excitation at 520 nm, where simultaneously excitation of Ru(II) ^{1}MLCT and Fe(II) ^{1}MLCT transitions occurs, are investigated. Immediately after excitation the transient spectra (Fig. 4) can be described as a superposition of the spectral characteristics of both centers at early delay times. During the first 100 ps the spectral features characteristic for the excited states of the Ru(II) center decay (*e.g.*, the strong ESA signal in the red probe range) while the characteristic signatures of the Fe(II) excited states (*e.g.*, bleach at 570 nm) gain in intensity. In the following the signal amplitude is decaying on a similar timescale as observed for the ground-state repopulation from the Fe(II) quintet state. Nonetheless, a residual amplitude remains beyond the time-scale of the experiment (8 ns). This long-lived species shows positive and negative signal above and below 500 nm, respectively, and thus reflects the transient spectra of the photoexcited Ru(II)-subunit at long delay times (see ESI,† Fig. S14). A simple multi-exponential fit assuming a superposition of the characteristic Ru(II) and Fe(II) centered photoinduced dynamics was not sufficient to describe the observed temporal development of the signal (see ESI,† Table S1 and Fig. S9). Hence, changes of the values of the rates of the processes at the Ru(II) center due to coordination of the second metal center and additional processes like energy transfer between the Ru(II) and the Fe(II) centers need to be taken into account. A further complication is that by applying a sum of exponential functions to model the data only a strictly parallel or sequential relaxation scheme can be analytically described.[87] Hence, to describe the data exactly a numerical fit based on the relaxation scheme in Scheme 1 was performed (Table 1): due to the very similar time constants and close resemblance of the spectral contributions of the sub-ps τ_1 and cooling processes τ_2 at both metal centers, the applied model regards the initial excited state as weighted mixture of Ru(II) and Fe(II) ^{1}MLCT states. These states are decaying in parallel to the respective thermally relaxed ^{3}MLCT states,

described by a component $\tau_1 \leq 0.2$ ps representing population of the respective triplet manifolds. The component τ_2 mainly represents the vibrational cooling at the Ru(II) center, contributions from cooling at the Fe(II) center are neglected, this process probably is not detectable due only minor changes in the SAS (Fig. 5) between Fe(II) ^{3}MLCT$_{hot}$ and Fe(II) ^{3}MLCT$_{cold}$. From the development of the spectral signature with time (Fig. 4), *i.e.* decay of the Ru(II) features and increase of the Fe(II) signatures on a timescale up to 50 ps, it can be deduced that the energy transfer from the Ru(II) center to the Fe(II) center occurs in parallel to or even before further relaxation (planarization and equilibration) at the Ru(II) center. The time constant for the energy transfer τ_3 is found to be with 15 ps nearly identical to that describing the planarization in **Ru**. Further, a fraction of excitation remains at the Ru(II) center, which is indicated by the remaining residual Ru(II) signature beyond 8 ns. This suggests that in this system energy transfer might occur from a non-planarized state in parallel to planarization and a fraction of the excited molecules remains trapped in the energetically low-lying planarized Ru(II) excited state. From the intensity ratio of the long-lived component in the data of **Ru** and **RuFeRu** upon excitation at 520 nm the efficiency of the energy transfer from the Ru(II) center to the Fe(II) center is determined to be at least 80%, assuming that neither the extinction coefficient in the ground nor the excited state changes significantly upon coordination of the Fe(II) center (details see ESI†). In the model applied, equilibration at the Ru(II) center is not explicitly included. This process is expected to be slower than the energy transfer and occurs only in the residual fraction of the excited molecules remaining in the Ru(II) excited state, resulting in very weak contributions to the overall signal development, too low to be determined properly (see ESI,† Fig. S12). The final equilibrated Ru(II) state is considered in the fit by incorporation of a constant component. Hence, the further development of the signal represents Fe(II) centered kinetics only. The process associated with τ_4 probably is connected to the depopulation of the ^{3}MLCT state to form the Fe(II) quintet state. The reason for the observed deceleration of this process upon excitation at 520 nm compared to direct excitation at 575 nm remains unclear at the moment and is subject to further investigations. τ_6 describes ground-state repopulation originating from the quintet state. The description of the experimental data applying this model results in SAS for the involved excited states, which are in good agreement with the spectra determined for the respective states at the Ru(II) and Fe(II) center from the reference measurements described above (Fig. 5). This resemblance confirms the validity of the applied model.

In contrast to **RuFeRu**, **RuOs** shows only minor differences in the dynamic behavior upon direct excitation of the ^{3}MLCT of the Os(II) center at 670 nm and upon excitation at 520 nm, where ^{1}MLCT transitions of both the Ru(II) and the Os(II) center are excited (Fig. 6). Under both conditions the transient spectra show strong GSB below 510 nm and a broad ESA feature at wavelengths longer than 510 nm. The ESA intensity increases during the first 10 ps, while the GSB intensity remains constant. After 10 ps the overall signal amplitude decays reaching a plateau at 80% of the maximum value of signal amplitude. Assuming excitation of both Ru(II) and Os(II) ^{1}MLCT states at
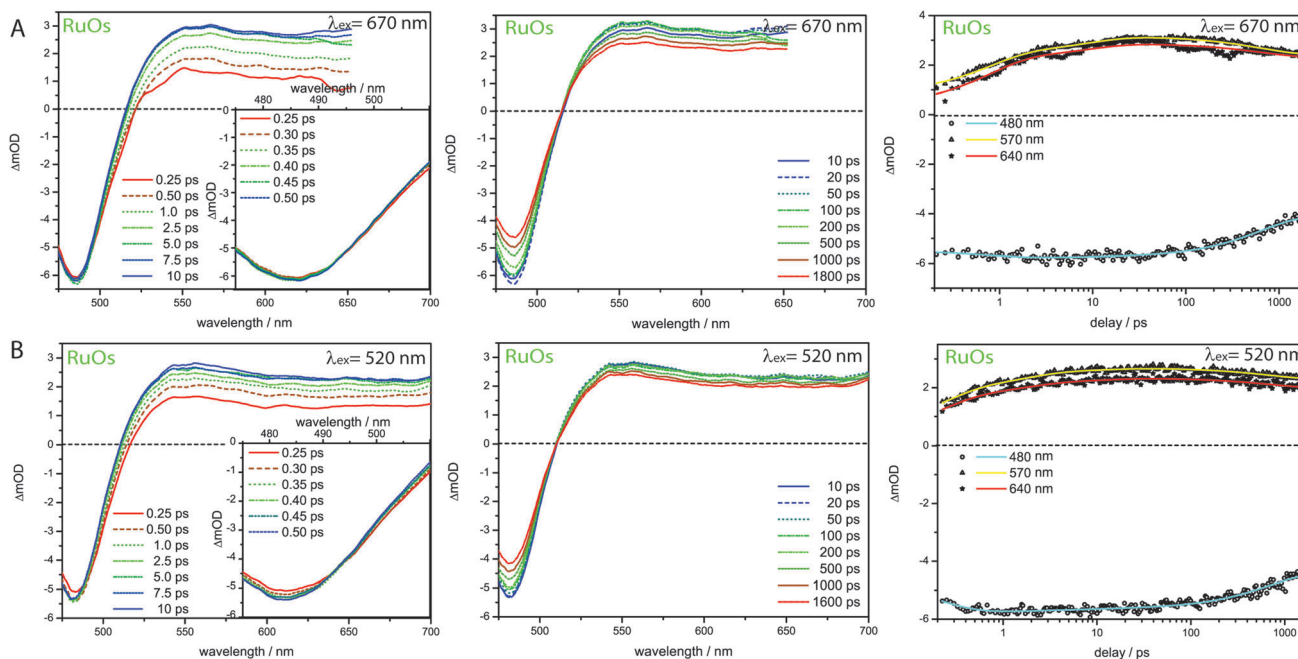
Fig. 6 Transient spectra and kinetic traces for **RuOs** upon excitation at (A) 670 nm and (B) 520 nm. The insets show a magnification of the ultrafast sub 0.5 ps development of the GSB region.

520 nm, the absence of signatures of Ru(II) excited states in the transient spectra suggests that the energy transfer from the Ru(II) to the Os(II) center occurs on an ultrafast timescale (<200 fs) with 100% efficiency and escapes detection due to the limited time-resolution of the experiment. Such highly efficient ultrafast energy transfer processes have been reported before for other multimetallic systems combining Ru(II) and Os(II) metal centers.[15,18,28,31,56,88–90] This assumption is corroborated by the results of the multi-exponential fit (Table 1): independent of the excitation conditions vibrational cooling (~ 1 ps), ligand planarization (~ 10 ps) and equilibration with the ^{3}LC state (~ 600–700 ps) are observed. Further, the SAS (Fig. 7) for the involved excited states match each other very closely for varying excitation conditions and hence, the observed processes are assigned to occur in the Os(II) excited states manifold. The equilibration in **RuOs** between the Os(II) ^{3}MLCT state and the ^{3}LC state is slower than the equilibration between the Ru(II) ^{3}MLCT states and the ^{3}LC states in the homobimetallic complex **RuRu**,[66] which is probably due to different relative energetic positions between the respective ^{3}MLCT state and the ^{3}LC state and altered activation barriers, the Os(II) ^{3}MLCT states are typically 0.20–0.3 eV lower in energy than the Ru(II) ^{3}MLCT states.[17] The only difference in the pump-wavelength dependent data can be found on timescales <0.5 ps: here, an increase in GSB intensity and a slight blueshift in the maximum is present upon excitation at 520 nm (Fig. 6), which is described by the sub-ps component τ_1 (Table 1). This component could be due to ^{3}MLCT population processes from the excited ^{1}MLCT states under these excitation conditions but could also show contributions of the energy transfer. However, to unambiguously assign these possible processes measurements with higher time resolution are necessary.
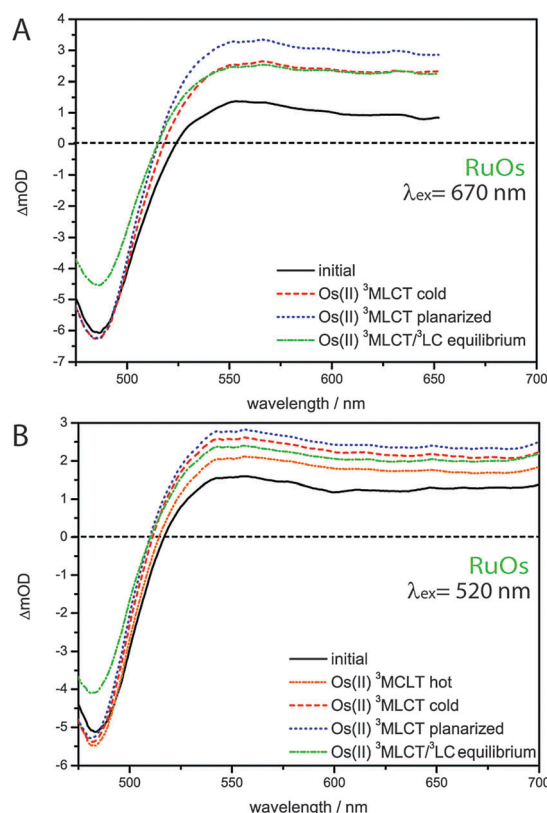
Fig. 7 SAS for **RuOs** resulting from a fit with a sequential model according to Scheme 2 upon excitation at (A) 670 nm and (B) 520 nm.

The effect that energy transfer occurs on the ultrafast time-scale and with 100% efficiency from Ru(II) to Os(II) centers while

This journal is © the Owner Societies 2016

Phys. Chem. Chem. Phys., 2016, **18**, 2350–2360 | **2357**
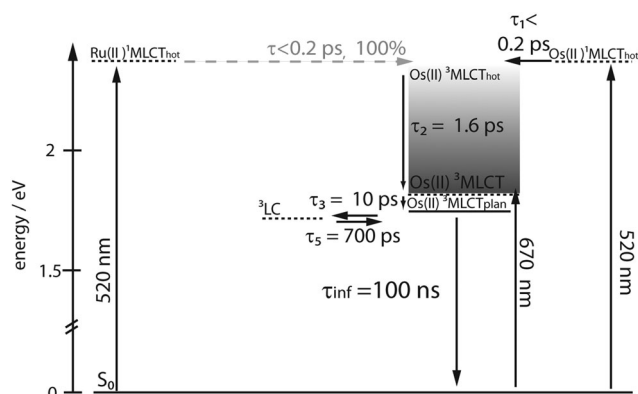
Scheme 2 Proposed relaxation scheme for **RuOs**, solid lines define energy levels with defined energetic positions, while dashed lines define excited states, the energy of which can only be indirectly inferred or depends on the excitation wavelength, processes in grey are not directly observable in the data.

in comparable systems combining Ru(II) and Fe(II) centers energy transfer to the lower lying Fe(II) centered states is slower and less efficient, has been observed before but no explanation was delivered.[56] In general, two mechanisms for energy transfer are distinguished: energy transfer *via* dipole–dipole inter-actions (Förster-type)[91] and energy transfer *via* electron-exchange mechanism (Dexter-type).[92] A precondition for the dipole mechanism to be efficient is that transitions with high oscillator strength at the donor and acceptor site are involved and spectral overlap between donor emission and acceptor absorption is necessary. Dexter transfer requires orbital overlap for efficient electron exchange and is usually discussed as short range mechanism, but the conjugated system of the ligand system can support long-range energy transfer of Dexter-type. The missing donor emission would rule out energy transfer by Förster-type in our systems, but the situation is more complicated, because the energy transfer originates from non-relaxed states. For the ultrafast energy transfer in **RuOs** two scenarios can be discussed:[15,88–90] singlet–singlet transfer and triplet–triplet transfer. For the triplet transfer mechanism, Dexter transfer might be favored, due to the low oscillator strength of the contributing triplet transitions though contributions of Förster transfer cannot be ruled out completely with the available data. For the transfer between the singlet states both Förster and Dexter mechanism could contribute, as the singlet states at both centers possess substantial oscillator strengths. Similar conclusions can be reached for the transfer mechanism in **RuFeRu**. As the oscillator strength of the radiative transitions from the non-relaxed [3]MLCT state is not assessable from the available data, it is not possible to completely rule out a transfer following Förster mechanism, but a number of reports in literature suggest Dexter-type energy transfer between Ru(II) and Fe(II)-polypyridyl centers to be the most probable pathway.[93–97] Unfortunately, no further insight in the mechanism is possible with the available data, but the observed differences in the rates might be determined by which of the proposed routes is followed and simply be based on differences in the relative energy of donor and acceptor states.

Summary and conclusion

In this investigation polymetallic complexes are investigated, which combine Ru(II) and Fe(II) (**RuFeRu**) or Os(II) (**RuOs**) bisterpyridine chromophores by coordination to an extended highly conjugated bis-4'-terpyridine bridging ligand. Due to their broad absorption range these mixed metal systems represent interesting candidates for light-harvesting antennae systems. Time-resolved spectroscopy reveals that energy transfer to the metal center with the lowest excited states in the assembly occurs in both systems with high efficiencies. While in **RuFeRu** an energy transfer of 80% occurs with a time constant of 15 ps from the Ru(II) to the Fe(II) center, the transfer from the Ru(II) to the Os(II) center in **RuOs** occurs on the ultrafast timescale ≤ 200 fs with unity quantum yield. These high efficiencies make these structures feasible candidates for incorporation into larger assemblies for long-range energy transfer.

The high conjugation of the bis-4'-terpyridyl ligand leads to a stabilization of the [3]MLCT states resulting in a prolonged lifetime. This is of special importance with respect to the lifetime of the [3]MLCT state at the Fe(II) center, which up to now limits the applicability of Fe(II) polypyridyl systems for collection of solar energy. The results presented in this study indicate that in these Fe(II)-terpyridyl structures with extended conjugated ligands an exceptional high [3]MLCT lifetime of 23 ps is achieved, which is the longest reported in literature.

In summary, the investigations presented in this work demon-strate that the compounds employed may be suitable building blocks for light-harvesting antennas. Future work will focus on the transfer of these structural motifs into oligomeric structures.

Acknowledgements

References

1 T. Zhang and W. B. Lin, *Chem. Soc. Rev.*, 2014, **43**, 5982–5993.
2 P. D. Frischmann, K. Mahata and F. Würthner, *Chem. Soc. Rev.*, 2013, **42**, 1847–1870.
3 B. Albinsson, J. K. Hannestad and K. Borjesson, *Coord. Chem. Rev.*, 2012, **256**, 2399–2413.
4 J. Yang, M. C. Yoon, H. Yoo, P. Kim and D. Kim, *Chem. Soc. Rev.*, 2012, **41**, 4808–4826.
5 F. Puntoriero, A. Sartorel, M. Orlandi, G. La Ganga, S. Serroni, M. Bonchio, F. Scandola and S. Campagna, *Coord. Chem. Rev.*, 2011, **255**, 2594–2601.
6 M. Kozaki and K. Okada, *J. Synth. Org. Chem., Jpn.*, 2011, **69**, 1145–1157.
7 D. Gust, T. A. Moore and A. L. Moore, *Acc. Chem. Res.*, 2009, **42**, 1890–1898.

8 M. R. Wasielewski, *Acc. Chem. Res.*, 2009, **42**, 1910–1921.

9 F. Puntoriero, F. Nastasi, M. Cavazzini, S. Quici and S. Campagna, *Coord. Chem. Rev.*, 2007, **251**, 536–545.

10 F. Puntoriero, S. Serroni, M. Galletta, A. Juris, A. Licciardello, C. Chiorboli, S. Carnpagna and F. Scandola, *ChemPhysChem*, 2005, **6**, 129–138.

11 G. Calzaferri and K. Lutkouskaya, *Photochem. Photobiol. Sci.*, 2008, **7**, 879–910.

12 F. Odobel and H. Zabri, *Inorg. Chem.*, 2005, **44**, 5600–5611.

13 V. Balzani, A. Juris, M. Venturi, S. Campagna and S. Serroni, *Chem. Rev.*, 1996, **96**, 759–833.

14 C. Chiorboli, C. A. Bignozzi, F. Scandola, E. Ishow, A. Gourdon and J. P. Launay, *Inorg. Chem.*, 1999, **38**, 2402–2410.

15 J. Larsen, F. Puntoriero, T. Pascher, N. McClenaghan, S. Campagna, E. Åkesson and V. Sundström, *ChemPhysChem*, 2007, **8**, 2643–2651.

16 V. Balzani, G. Bergamini, F. Marchioni and P. Ceroni, *Coord. Chem. Rev.*, 2006, **250**, 1254–1266.

17 J. P. Sauvage, J. P. Collin, J. C. Chambron, S. Guillerez, C. Coudret, V. Balzani, F. Barigelletti, L. Decola and L. Flamigni, *Chem. Rev.*, 1994, **94**, 993–1019.

18 S. Welter, N. Salluce, P. Belser, M. Groeneveld and L. De Cola, *Coord. Chem. Rev.*, 2005, **249**, 1360–1371.

19 S. Welter, N. Salluce, A. Benetti, N. Rot, P. Belser, P. Sonar, A. C. Grimsdale, K. Mullen, M. Lutz, A. L. Spek and L. De Cola, *Inorg. Chem.*, 2005, **44**, 4706–4718.

20 A. Wild, A. Winter, F. Schlütter and U. S. Schubert, *Chem. Soc. Rev.*, 2011, **40**, 1459–1511.

21 A. Juris, V. Balzani, F. Barigelletti, S. Campagna, P. Belser and A. Vonzelewsky, *Coord. Chem. Rev.*, 1988, **84**, 85–277.

22 V. Balzani, G. Bergamini, S. Campagna and F. Puntoriero, *Photochemistry and Photophysics of Coordination Compounds I*, 2007, vol. 280, pp. 1–36.

23 A. Vlcek, *Coord. Chem. Rev.*, 2000, **200**, 933–977.

24 D. A. M. Egbe, B. Carbonnier, E. Birckner and U. W. Grummt, *Prog. Polym. Sci.*, 2009, **34**, 1023–1067.

25 A. C. Grimsdale, K. L. Chan, R. E. Martin, P. G. Jokisz and A. B. Holmes, *Chem. Rev.*, 2009, **109**, 897–1091.

26 R. Siebert, Y. X. Tian, R. Camacho, A. Winter, A. Wild, A. Krieg, U. S. Schubert, J. Popp, I. G. Scheblykin and B. Dietzek, *J. Mater. Chem.*, 2012, **22**, 16041–16050.

27 E. A. Medlycott and G. S. Hanan, *Chem. Soc. Rev.*, 2005, **34**, 133–142.

28 X. Y. Wang, A. Del Guerzo, S. Baitalik, G. Simon, G. B. Shaw, L. X. Chen and R. Schmehl, *Photosynth. Res.*, 2006, **87**, 83–103.

29 H. Cho, M. L. Strader, K. Hong, L. Jamula, E. M. Gullikson, T. K. Kim, F. M. F. de Groot, J. K. McCusker, R. W. Schoenlein and N. Huse, *Faraday Discuss.*, 2012, **157**, 463–474.

30 R. Siebert, A. Winter, U. S. Schubert, B. Dietzek and J. Popp, *Phys. Chem. Chem. Phys.*, 2011, **13**, 1606–1617.

31 C. Chiorboli, M. T. Indelli, F. Scandola, *Molecular Wires: From Design to Properties*, 2005, vol. 257, pp. 63–102.

32 C. Chiorboli, M. A. J. Rodgers and F. Scandola, *J. Am. Chem. Soc.*, 2003, **125**, 483–491.

33 L. Y. Zhu, A. Widom and P. M. Champion, *J. Chem. Phys.*, 1997, **107**, 2859–2871.

34 P. S. Wagenknecht and P. C. Ford, *Coord. Chem. Rev.*, 2011, **255**, 591–616.

35 J. T. Hewitt, P. J. Vallett and N. H. Damrauer, *J. Phys. Chem. A*, 2012, **116**, 11536–11547.

36 C. Creutz, M. Chou, T. L. Netzel, M. Okumura and N. Sutin, *J. Am. Chem. Soc.*, 1980, **102**, 1309–1319.

37 J. E. Monat and J. K. McCusker, *J. Am. Chem. Soc.*, 2000, **122**, 4092–4097.

38 W. Gawelda, A. Cannizzo, V. T. Pham, F. van Mourik, C. Bressler and M. Chergui, *J. Am. Chem. Soc.*, 2007, **129**, 8199–8206.

39 A. L. Smeigh, M. Creelman, R. A. Mathies and J. K. McCusker, *J. Am. Chem. Soc.*, 2008, **130**, 14105–14107.

40 C. Bressler, C. Milne, V. T. Pham, A. ElNahhas, R. M. van der Veen, W. Gawelda, S. Johnson, P. Beaud, D. Grolimund, M. Kaiser, C. N. Borca, G. Ingold, R. Abela and M. Chergui, *Science*, 2009, **323**, 489–492.

41 W. K. Zhang, R. Alonso-Mori, U. Bergmann, C. Bressler, M. Chollet, A. Galler, W. Gawelda, R. G. Hadt, R. W. Hartsock, T. Kroll, K. S. Kjaer, K. Kubicek, H. T. Lemke, H. Y. W. Liang, D. A. Meyer, M. M. Nielsen, C. Purser, J. S. Robinson, E. I. Solomon, Z. Sun, D. Sokaras, T. B. van Driel, G. Vanko, T. C. Weng, D. L. Zhu and K. J. Gaffney, *Nature*, 2014, **509**, 345–348.

42 C. Sousa, C. de Graaf, A. Rudavskyi, R. Broer, J. Tatchen, M. Etinski and C. M. Marian, *Chem. – Eur. J.*, 2013, **19**, 17541–17551.

43 G. Auböck and M. Chergui, *Nat. Chem.*, 2015, **7**, 629–633.

44 S. Ferrere and B. A. Gregg, *J. Am. Chem. Soc.*, 1998, **120**, 843–844.

45 D. N. Bowman, J. H. Blew, T. Tsuchiya and E. Jakubikova, *Inorg. Chem.*, 2013, **52**, 8621–8628.

46 D. G. Brown, N. Sanguantrakun, B. Schulze, U. S. Schubert and C. P. Berlinguette, *J. Am. Chem. Soc.*, 2012, **134**, 12354–12357.

47 S. U. Son, K. H. Park, Y. S. Lee, B. Y. Kim, C. H. Choi, M. S. Lah, Y. H. Jang, D. J. Jang and Y. K. Chung, *Inorg. Chem.*, 2004, **43**, 6896–6898.

48 L. Mercs and M. Albrecht, *Chem. Soc. Rev.*, 2010, **39**, 1903–1912.

49 Y. Z. Liu, T. Harlang, S. E. Canton, P. Chabera, K. Suarez-Alcantara, A. Fleckhaus, D. A. Vithanage, E. Goransson, A. Corani, R. Lomoth, V. Sundström and K. Wärnmark, *Chem. Commun.*, 2013, **49**, 6412–6414.

50 L. A. Fredin, M. Papai, E. Rozsalyi, G. Vanko, K. Warnmark, V. Sundstrom and P. Persson, *J. Phys. Chem. Lett.*, 2014, **5**, 2066–2071.

51 Y. Liu, K. S. Kjær, L. A. Fredin, P. Chábera, T. Harlang, S. E. Canton, S. Lidin, J. Zhang, R. Lomoth, K.-E. Bergquist, P. Persson, K. Wärnmark and V. Sundström, *Chem. – Eur. J.*, 2015, **21**, 3628–3639.

52 P. P. Laine, S. Campagna and F. Loiseau, *Coord. Chem. Rev.*, 2008, **252**, 2552–2571.

53 X. Y. Wang, A. Del Guerzo and R. H. Schmehl, *J. Photochem. Photobiol., C*, 2004, **5**, 55–77.

54 S. Baitalik, X. Y. Wang and R. H. Schmehl, *J. Am. Chem. Soc.*, 2004, **126**, 16304–16305.

55 D. Maity, S. Mardanya, S. Karmakar and S. Baitalik, *Dalton Trans.*, 2015, **44**, 10048–10059.

56 D. Maity, C. Bhaumik, S. Mardanya, S. Karmakar and S. Baitalik, *Chem. – Eur. J.*, 2014, **20**, 13242–13252.

This journal is © the Owner Societies 2016

Phys. Chem. Chem. Phys., 2016, **18**, 2350–2360 | 2359

57 A. K. C. Mengel, C. Forster, A. Breivogel, K. Mack, J. R. Ochsmann, F. Laquai, V. Ksenofontov and K. Heinze, *Chem. – Eur. J.*, 2015, **21**, 704–714.

58 L. Hammarström and O. Johansson, *Coord. Chem. Rev.*, 2010, **254**, 2546–2559.

59 M. Abrahamsson, M. Jager, T. Osterman, L. Eriksson, P. Persson, H. C. Becker, O. Johansson and L. Hammarstrom, *J. Am. Chem. Soc.*, 2006, **128**, 12616–12617.

60 M. Abrahamsson, M. Jager, R. J. Kumar, T. Osterman, P. Persson, H. C. Becker, O. Johansson and L. Hammarstrom, *J. Am. Chem. Soc.*, 2008, **130**, 15533–15542.

61 R. J. Kumar, S. Karlsson, D. Streich, A. R. Jensen, M. Jager, H. C. Becker, J. Bergquist, O. Johansson and L. Hammarstrom, *Chem. – Eur. J.*, 2010, **16**, 2830–2842.

62 F. Schramm, V. Meded, H. Fliegl, K. Fink, O. Fuhr, Z. R. Qu, W. Klopper, S. Finn, T. E. Keyes and M. Ruben, *Inorg. Chem.*, 2009, **48**, 5677–5684.

63 A. Breivogel, C. Forster and K. Heinze, *Inorg. Chem.*, 2010, **49**, 7052–7056.

64 A. Breivogel, C. Kreitner and K. Heinze, *Eur. J. Inorg. Chem.*, 2014, 5468–5490.

65 A. Breivogel, M. Meister, C. Forster, F. Laquai and K. Heinze, *Chem. – Eur. J.*, 2013, **19**, 13745–13760.

66 R. Siebert, C. Hunger, J. Guthmuller, F. Schlütter, A. Winter, U. S. Schubert, L. Gonzalez, B. Dietzek and J. Popp, *J. Phys. Chem. C*, 2011, **115**, 12677–12688.

67 A. Winter, C. Friebe, M. D. Hager and U. S. Schubert, *Eur. J. Org. Chem.*, 2009, 801–809.

68 B. Schulze, D. Escudero, C. Friebe, R. Siebert, H. Görls, S. Sinn, M. Thomas, S. Mai, J. Popp, B. Dietzek, L. Gonzalez and U. S. Schubert, *Chem. – Eur. J.*, 2012, **18**, 4010–4025.

69 K. Barthelmes, J. Kübel, A. Winter, M. Wächtler, C. Friebe, B. Dietzek and U. S. Schubert, *Inorg. Chem.*, 2015, **54**, 3159–3171.

70 F. Barigelletti, L. Flamigni, V. Balzani, J. P. Collin, J. P. Sauvage, A. Sour, E. C. Constable and A. M. W. C. Thompson, *J. Am. Chem. Soc.*, 1994, **116**, 7692–7699.

71 S. Campagna, F. Puntoriero, F. Nastasi, G. Bergamini and V. Balzani, *Photochemisty and Photophysics of Coordination Compounds I: Ruthenium*, Springer, Berlin, 2007.

72 R. Siebert, F. Schlutter, A. Winter, M. Presselt, H. Gorls, U. S. Schubert, B. Dietzek and J. Popp, *Cent. Eur. J. Chem.*, 2011, **9**, 990–999.

73 M. Presselt, B. Dietzek, M. Schmitt, S. Rau, A. Winter, M. Jager, U. S. Schubert and J. Popp, *J. Phys. Chem. A*, 2010, **114**, 13163–13174.

74 M. Presselt, B. Dietzek, M. Schmitt, J. Popp, A. Winter, M. Chiper, C. Friebe and U. S. Schubert, *J. Phys. Chem. C*, 2008, **112**, 18651–18660.

75 R. Siebert, A. Winter, B. Dietzek, U. S. Schubert and J. Popp, *Macromol. Rapid Commun.*, 2010, **31**, 883–888.

76 J. K. Mccusker, K. N. Walda, R. C. Dunn, J. D. Simon, D. Magde and D. N. Hendrickson, *J. Am. Chem. Soc.*, 1993, **115**, 298–307.

77 A. Hauser, C. Enachescu, M. L. Daku, A. Vargas and N. Amstutz, *Coord. Chem. Rev.*, 2006, **250**, 1642–1652.

78 G. Vankó, A. Bordage, M. Pápai, K. Haldrup, P. Glatzel, A. M. March, G. Doumy, A. Britz, A. Galler, T. Assefa, D. Cabaret, A. Juhin, T. B. van Driel, K. S. Kjær, A. Dohn, K. B. Møller, H. T. Lemke, E. Gallo, M. Rovezzi, Z. Németh, E. Rozsályi, T. Rozgonyi, J. Uhlig, V. Sundström, M. M. Nielsen, L. Young, S. H. Southworth, C. Bressler and W. Gawelda, *J. Phys. Chem. C*, 2015, **119**, 5888–5902.

79 J. N. Demas and D. G. Taylor, *Inorg. Chem.*, 1979, **18**, 3177–3179.

80 J. N. Demas and G. A. Crosby, *J. Am. Chem. Soc.*, 1971, **93**, 2841–2847.

81 A. I. Baba, J. R. Shaw, J. A. Simon, R. P. Thummel and R. H. Schmehl, *Coord. Chem. Rev.*, 1998, **171**, 43–59.

82 N. H. Damrauer, G. Cerullo, A. Yeh, T. R. Boussie, C. V. Shank and J. K. McCusker, *Science*, 1997, **275**, 54–57.

83 J. K. McCusker, *Acc. Chem. Res.*, 2003, **36**, 876–887.

84 M. Chergui, *Dalton Trans.*, 2012, **41**, 13022–13029.

85 A. C. Bhasikuttan, M. Suzuki, S. Nakashima and T. Okada, *J. Am. Chem. Soc.*, 2002, **124**, 8398–8405.

86 W. R. Browne, W. Henry, C. G. Coates, C. Brady, K. L. Ronayne, P. Matousek, M. Towrie, S. W. Botchway, A. W. Parker, J. G. Vos and J. J. McGarvey, *J. Phys. Chem. A*, 2008, **112**, 4537–4544.

87 I. H. M. van Stokkum, D. S. Larsen and R. van Grondelle, *Biochim. Biophys. Acta*, 2004, **1658**, 262.

88 H. B. Baudin, J. Davidsson, S. Serroni, A. Juris, V. Balzani, S. Campagna and L. Hammarström, *J. Phys. Chem. A*, 2002, **106**, 4312–4319.

89 J. Andersson, F. Puntoriero, S. Serroni, A. Yartsev, T. Pascher, T. Polivka, S. Campagna and V. Sundstrom, *Faraday Discuss.*, 2004, **127**, 295–305.

90 J. Andersson, F. Puntoriero, S. Serroni, A. Yartsev, T. Pascher, T. Polivka, S. Campagna and V. Sundstrom, *Chem. Phys. Lett.*, 2004, **386**, 336–341.

91 T. Förster, *Discuss. Faraday Soc.*, 1959, 7–17.

92 D. L. Dexter, *J. Chem. Phys.*, 1953, **21**, 836–850.

93 J. Lombard, J. C. Lepretre, J. Chauvin, M. N. Collomb and A. Deronzier, *Dalton Trans.*, 2008, 658–666.

94 J. Lombard, S. Romain, S. Dumas, J. Chauvin, M. N. Collomb, D. Daveloose, A. Deronzier and J. C. Lepretre, *Eur. J. Inorg. Chem.*, 2005, 3320–3330.

95 R. H. Schmehl, R. A. Auerbach, W. F. Wacholtz, C. M. Elliott, R. A. Freitag and J. W. Merkert, *Inorg. Chem.*, 1986, **25**, 2440–2445.

96 S. L. Larson, S. M. Hendrickson, S. Ferrere, D. L. Derr and C. M. Elliott, *J. Am. Chem. Soc.*, 1995, **117**, 5881–5882.

97 F. Lafolet, J. Chauvin, M. Collomb, A. Deronzier, H. Laguitton-Pasquier, J. C. Lepretre, J. C. Vial and B. Brasme, *Phys. Chem. Chem. Phys.*, 2003, **5**, 2520–2527.

Supporting information

Energy transfer and formation of long-lived [3]MLCT states in multimetallic complexes with extended highly conjugated bis-terpyridyl ligands

Dr. Maria Wächtler,[a] Joachim Kübel,[a,b] Kevin Barthelmes,[c,d] Dr. Andreas Winter,[c,d] Alexander Schmiedel,[e] Dr. Torbjörn Pascher,[f] Prof. Christoph Lambert,[e] Prof. Ulrich S. Schubert,[c,d] Prof. Benjamin Dietzek [a,b,d] *

AFFILIATIONS

a Leibniz Institute of Photonic Technology e.V., Albert-Einstein-Straße 9, 07745 Jena, Germany

b Institute of Physical Chemistry and Abbe Center of Photonics, Friedrich Schiller University Jena, Helmholtzweg 4, 07745 Jena, Germany

c Laboratory of Organic and Macromolecular Chemistry (IOMC), Friedrich Schiller University Jena, Humboldtstraße 10, 07743 Jena, Germany

d Jena Center for Soft Matter (JCSM), Friedrich Schiller University Jena, Philosophenweg 7, 07743 Jena, Germany

e Institut für Organische Chemie, Universität Würzburg, Wilhelm Conrad Röntgen Research Center for Complex Material Systems, Center for Nanosystems Chemistry, Am Hubland, 97074 Würzburg, Germany

f Pascher Instruments AB, Stora Råbybyaväg 24, 22478 Lund, Sweden

*corresponding author:

benjamin.dietzek@ipht-jena.de, phone +49 (0)3641 206-332, fax +49 (0)3641 206-390

Synthesis and characterization

All reagents were purchased from commercial sources and used without further purification unless specified. Chromatographic separation was performed with standardized silica gel 60 (Merck) and aluminum oxide 90 neutral (Molekula). The reaction progress was controlled by thin layer chromatography (TLC) using aluminum sheets precoated with silica gel 60 F254 and aluminum oxide 60 F254 neutral (Merck). Nuclear magnetic resonance (NMR) spectra were recorded on a AC 300 MHz (Bruker) spectrometer at 298 K. Chemical shifts are reported in parts per million (ppm, δ scale) relative to the residual signal of the deuterated solvent. Coupling constants are given in Hz. High resolution (HR) ESI-TOF MS was performed on an ESI-(Q)-TOF-MS MICROTOF II (Bruker Daltonics) mass spectrometer.

The Ligand **L**,[1] [Ru(tpy)(acetonitrile)$_3$](PF$_6$)$_2$,[2] and Os(tpy)Cl$_3$[3] were prepared according to literature procedures.

Compound Ru

A microwave vial (20 mL) was charged with [Ru(tpy)(acetonitrile)$_3$](PF$_6$)$_2$ (44 mg, 59 µmol), ditopic ligand **L** (103 mg, 71 µmol) and DMF (10 mL). The vial was capped and purged with nitrogen for 20 min. The suspension was heated to 160 °C for 3 h in an oil bath. After cooling to room temperature, the reaction mixture was filtrated to remove the unreacted ligand. The filtrate was added to an aqueous ammonium hexafluorophosphate solution. The red precipitate was collected by filtration, washed with water, then methanol and diethyl ether. Subsequently, the solid was dissolved in acetone and loaded on a alumina column (dichloromethane/methanol, 95:5 ratio). The first dark red fraction was collected, concentrated *in vacuo* and precipitated in *n*-hexane. The compound was obtained as red solid (43 mg, 35%).

^{1}H NMR (300 MHz, CD$_2$Cl$_2$, ppm): δ 8.91 (s, 2H), 8.80 (s, 2H), 8.74 (d, J = 6.2 Hz, 2H), 8.73 (d, J = 7.9 Hz, 2H), 8.70 (d, J = 8.4 Hz, 2H), 8.60 (d, J = 8.2 Hz, 2H), 8.47 (d, J = 8.1 Hz, 2H), 8.44 (t, J = 8.2 Hz, 1H), 8.18 (d, J = 8.1 Hz, 2H), 8.01–7.80 (m, 10H), 7.70 (d, J = 7.9 Hz, 2H), 7.58 (s, 4H), 7.55 (d, J = 16.1 Hz, 1H), 7.53 (d, J = 16.2 Hz, 1H), 7.44–7.36 (m, 4H), 7.33 (d, J = 5.5 Hz, 2H), 7.25 (d, J = 16.3 Hz, 2H), 7.24–7.18 (m, 6H), 7.12 (s, 1H), 7.08 (s, 1H), 4.24–3.97 (m, 8H), 2.06–1.77 (m, 8H), 1.72–1.15 (m, 40H), 1.01–0.71 (m, 12H) ppm.

HRMS (ESI-TOF, CH$_3$CN, m/z): 895.9145, C$_{115}$H$_{119}$N$_9$O$_4$Ru ([M–2PF$_6$]$^{2+}$) requires 895.9211.

Compound RuOs

A microwave vial (2 mL) was charged with Os(tpy)Cl$_3$ (3.5 mg, 6.63 µmol) and silver(I)-tetrafluoroborate (3.9 mg, 20 µmol) in acetone (3 mL). The vial was capped and purged with nitrogen for 20 min. The mixture was heated to 70 °C for 2 h. After cooling and filtration, DMAc/ethylene glycol (3:1, 2 mL) was added to the filtrate and the acetone was removed *in vacuo*. The resulting black solution was added to a microwave vial (2 mL) charged with **Ru** (11.5 mg, 5.52 µmol). The vial was capped and purged with nitrogen for 20 min. The mixture was heated to 160 °C for 24 h. Subsequently, the solution was cooled to room temperature and precipitated from an aqueous ammonium hexafluorophosphate solution. After filtration and washing with water, the crude product was purified by column chromatography (silica, CH$_3$CN/H$_2$O/sat. aq. KNO$_3$ 70:4:1 then 40:4:1 ratio). The dark brown fraction was concentrated and precipitated by adding an aqueous ammonium hexafluorophosphate solution to obtain a dark brown solid (8 mg, 51%).

^{1}H NMR (300 MHz, CD$_3$CN, ppm): δ 9.05 (s, 2H), 9.03 (s, 2H), 8.77 (d, J = 8.6 Hz, 2H), 8.76 (d, J = 7.9 Hz, 2H), 8.65 (d, J = 7.0 Hz, 2H), 8.63 (d, J = 7.0 Hz, 2H), 8.50 (d, J = 7.6 Hz, 2H), 8.48 (d, J = 7.6 Hz, 2H), 8.42 (t, J = 8.2 Hz, 1H), 8.24 (d, J = 8.0 Hz, 2H), 8.21 (d, J

= 8.5 Hz, 2H), 7.99–7.87 (m, 9H), 7.82 (d, J = 8.5 Hz, 2H), 7.77 (d, J = 8.5 Hz, 2H), 7.66–7.49 (m, 6H), 7.44 (d, J = 5.7 Hz, 2H), 7.39–7.34 (m, 2H), 7.35 (d, J = 5.3 Hz, 2H), 7.31 (d, J = 5.9 Hz, 2H), 7.23 (d, J = 5.6 Hz, 2H), 7.20 (s, 1H), 7.18 (d, J = 6.2 Hz, 4H), 7.16 (s, 1H), 7.13 (s, 1H), 7.11 (d, J = 6.8 Hz, 4H), 7.08 (s, 1H), 4.26–3.93 (m, 8H), 2.06–1.77 (m, 8H), 1.70–1.13 (m, 40H), 1.02–0.71 (m, 12H).

HRMS (ESI-TOF, CH$_3$CN, m/z): 554.2261, C$_{130}$H$_{130}$N$_{12}$O$_4$OsRu ([M–4PF$_6$]$^{4+}$) requires 554.2252.

Compound RuFeRu

A microwave vial (2 mL) was charged with **Ru** (11.8 mg, 5.67 µmol) and dichloromethane (1.5 mL). The vial was capped and purged with nitrogen for 20 min. To the stirring solution was added iron(II)-sulfate heptahydrate (0.87 mg, 3.12 µmol) in methanol (0.5 mL) via a syringe. The resulting mixture continued stirring for 2 h. Subsequently, the solvents were removed by a stream of nitrogen and ammonium hexafluorophosphate (30 mg, 187 µmol), acetonitrile (3 mL) was added. After 15 min stirring at room temperature, water (30 mL) was added, to precipitate the complex. Subsequently, the suspension was filtrated and intensively washed with water to obtain a dark red-brown solid (12 mg, 85%).

^{1}H NMR (300 MHz, CD$_3$CN, ppm): δ 9.21 (s, 4H), 9.02 (s, 4H), 8.76 (d, J = 8.1 Hz, 4H), 8.69–8.60 (m, 8H), 8.50 (d, J = 8.9 Hz, 4H), 8.42 (t, J = 7.6 Hz, 2H), 8.38 (d, J = 7.8 Hz, 4H), 8.26 (d, J = 7.8 Hz, 4H), 8.01–7.84 (m, 20H), 7.64 (s, 8H), 7.57 (d, J = 16.6 Hz, 4H), 7.46–7.32 (m, 12H), 7.24–7.14 (m, 20H), 7.10 (dd, J = 7.8, 7.1 Hz, 4H), 4.25–4.16 (m, 8H), 4.15–4.06 (m, 8H), 2.05–1.82 (m, 16H), 1.69–1.16 (m, 80H), 1.03–0.76 (m, 24H).

HRMS (ESI-TOF, CH$_3$CN, m/z): 606.6051, C$_{230}$H$_{238}$FeN$_{18}$O$_8$Ru$_2$ ([M–6PF$_6$]$^{6+}$) requires 606.6043.

Experimental Section

The pump pulses for the ns time-resolved transient absorption measurements of **Ru** and **RuFeRu** at 520 nm were delivered by an OPO (OPO-PLUS, Continuum) pumped by a ND:YAG (Surelite S10 II, Continuum) laser at 10 Hz resulting in pulses with a duration of 5 ns. Probe light is delivered by a pulsed 75 W Xe arc lamp. The sample is probed in 90° geometry. Spherical concave mirrors were used to focus the probe light at the sample position and to refocus the light on the entrance slit of a monochromator (Acton, Princeton Instruments). Probe light is detected by a PMT (Hamamatsu R928) mounted on a fivestage base and the signal was processed by a commercially available detection system (Pascher Instruments AB). By switching off the probe light, emission decay can be detected with ns-temporal resolution.

For **Ru** and **RuFeRu** fs time-resolved transient absorption spectroscopy was performed on an experimental setup with maximum delay between pump and probe pulses of 8 ns. The laser system consists of an ultrafast Ti:sapphire amplifier (Newport-Spectra-Physics, Solstice) with a central wavelength of 800 nm, pulse lengths of 100 fs and a repetition rate of 1 kHz. One part of the output beam was used to seed an optical parametric amplifier (Newport-Spectra-Physics, TOPAS-C) as the source for the pump pulse with an attenuated energy of 200 nJ at wavelengths 520 and 575 nm and a pulse length of 140 fs. A small fraction of the Ti:sapphire output was focused into a moving calcium fluoride plate to produce a white light continuum between 350 nm and 800 nm, which acted as the probe pulse. Pump and probe were set to magic angle and spatially overlapped in the sample. After passing the sample the probe pulses were detected via a transient absorption spectrometer with a CMOS sensor (Ultrafast Systems, Helios). Part of the probe light pulse was used to correct for intensity fluctuations of the white light continuum. The relative temporal delay between pump and probe pulses was with a motorized, computer-controlled linear stage.

The fs time-resolved measurements for **RuOs** were performed on as system consisting of a Ti:sapphire amplifier (Legend-Elite, Coherent inc.), producing 35 fs pulses centred at 795 nm with a repetition rate of 1 kHz. The pump pulses centered at 520 and 670 nm were generated in a collinear optical-parametric amplifier (TOPAS-C, LightConversion Ltd.). The white light continuum between 450 and 700 nm to probe the sample is generated by focussing a part of the fundamental of the amplifier output into a sapphire plate. The pump pulses are delayed with respect to the probe pulses by means of an optical delay stage (maximum delay: 2 ns) and focused into the sample by a lens (f = 1 m), the energy of the pump pulses is attenuated to 1 μJ. Probe intensities fall into the range of a few hundred nJ. The repetition rate of the pump pulses is reduced to 500 Hz by a mechanical chopper and the polarization of the pump with respect to the probe pulses is set to the magic angle (54.7 °) using a Berek compensator and a polarizer. The white light continuum is split into probe and reference. The probe pulse is focused onto the sample by a concave mirror (f = 500 mm) and spatially overlapped with the pump pulse. Probe and reference are collected by a detection system (Pascher Instruments, AB) consisting of a spectrograph (Acton, Princeton Instruments) equipped with a double-stripe diode array detector. The diode array is read out with the laser repetition rate and the signal (ΔA) is calculated from two consecutive probe pulses, corresponding to pump-on and pump-off conditions.

The chirp-corrected two-dimensional TA data matrix was fitted globally using a number of exponential functions, corresponding to a reaction scheme of consecutive first-order reactions. The wavelength-dependent preexponential factors correspond to the decay associated spectra (DAS). Global fitting of a more appropriate reaction scheme for the data of **RuFeRu** upon excitation at 520 nm was carried out using a home-written algorithm applying the Nelder-Mead algorithm[4] as implemented in the fminsearch function in Scilab.[5] The rate-constants are optimized via fminsearch. During fitting, the temporal evolution of the species concentrations

according to the reaction scheme is calculated iteratively, and the evolution associated spectra

(species spectra, i.e. SAS) are calculated in a second step.

Steady-State Emission
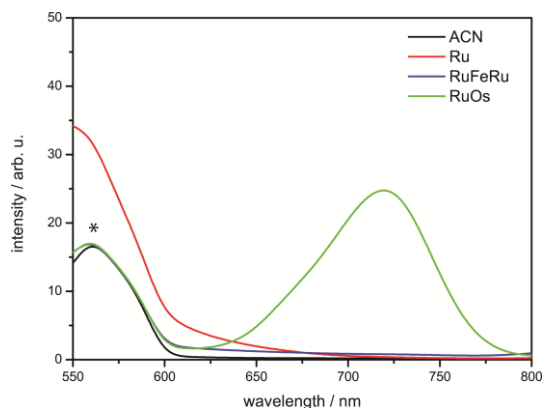
Figure S1: Emission spectra (solutions with identical optical density at the excitation wavelength) upon excitation at 488 nm. For comparison the background signal of the solvent is given additionally. Only **RuOs** displays clear ^{3}MLCT emission at room temperature in aerated acetonitrile. The weak signal for Ru below 700 nm is probably due to residual emission from LC states, which are also excited at 488 nm excitation[6, 7] (see Figure S2). The solvent Raman peak is marked with an asterisk.
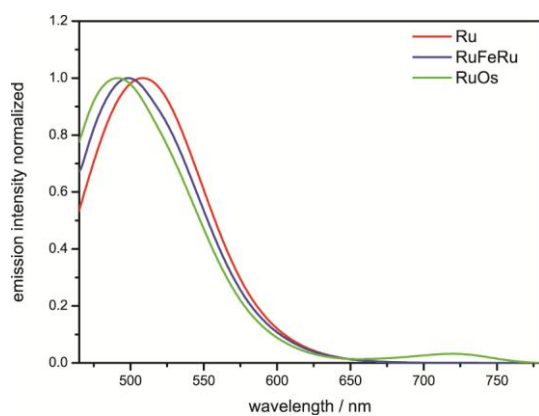
Figure S2: LC emission (spectra are normalized to the emission maximum) in aerated acetonitrile upon excitation at 425 nm (corresponding to the maximum of the LC absorption band). Only for **RuOs** weak ^{3}MLCT emission at 740 nm is observed additionally.

Absorption and Emission spectra of related Fe, Ru and Os complexes[7]

Fe: M = Fe^{2+}; Ru: M = Ru^{2+};
Os: M = Os^{2+}
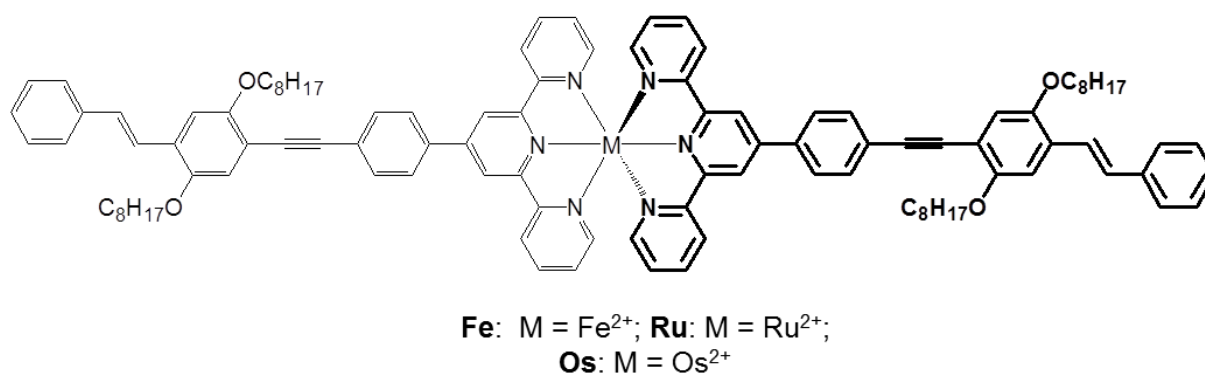
Figure S3: Structure of Ru, Fe and Os
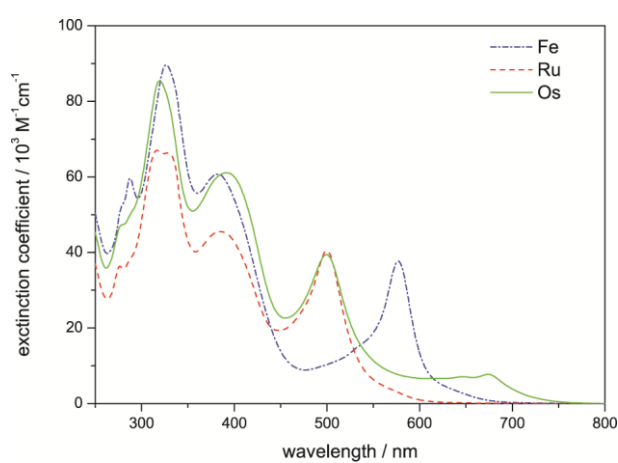
Figure S4: Absorption spectra of Fe, Ru and Os in THF
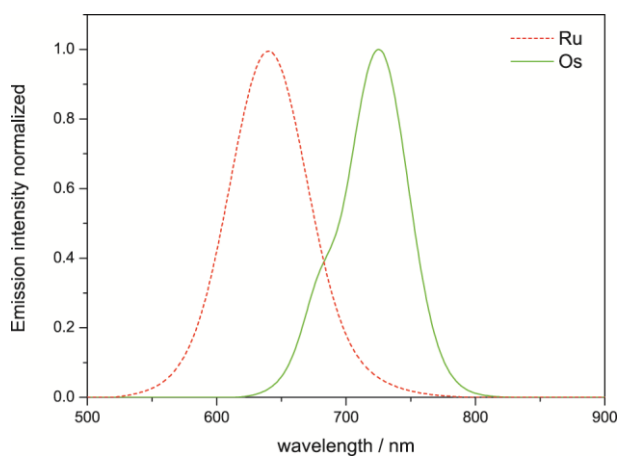
Figure S5: Emission spectra of Fe, Ru and Os in THF at room temperature, Fe shows no emission

Transient absorption measurements – ns regime
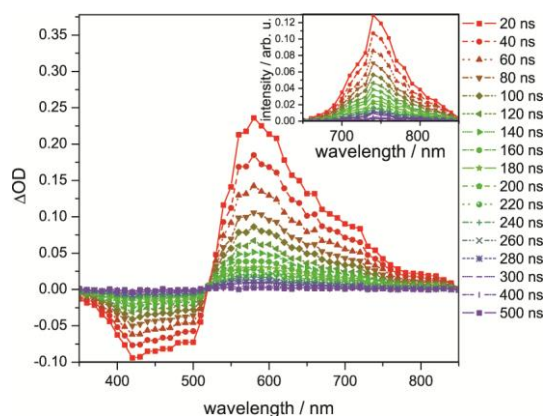
Figure S6: Transient spectra of **RuOs** upon excitation at 520 nm at selected delay times, the inset shows the emission spectra at chosen delay times.
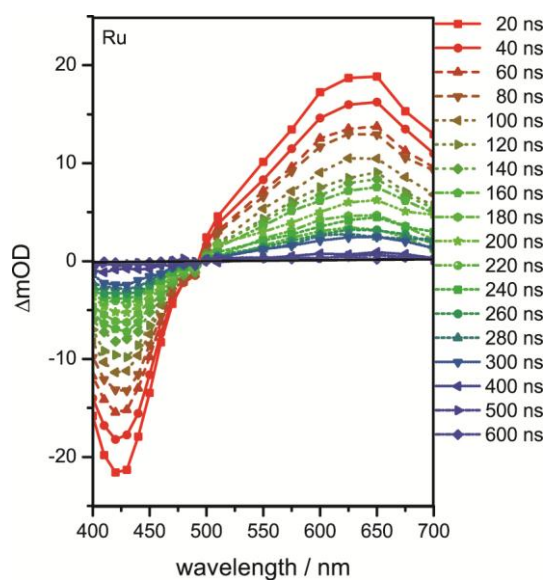
Figure S7: Transient spectra of **Ru** upon excitation at 520 nm at selected delay times.
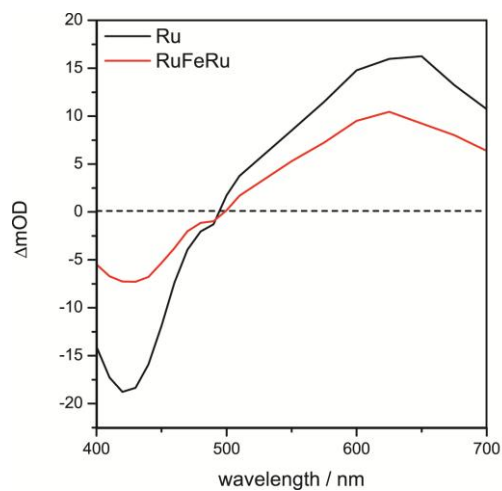
Figure S8: Comparison of the transient spectra of **Ru** and **RuFeRu** averaged between 20 and 60 ns after excitation at 520 nm.

Transient absorption measurements – fs regime

A straight-forward fit of the data collected for **RuFeRu** with the kinetic components determined for the single metal centers, assuming a simple superposition of Ru(II) and Fe(II) centered photoinduced dynamics, was not sufficient to describe the observed temporal development of the signal (see Table S1 and Figure S9).

By applying a sum of exponential functions to describe the data at least 5 components and an additional infinite component are necessary (Figure S9 and Tale S1). The two fastest processes τ_1 and τ_2 are superpositions of the ^{3}MLCT population and vibrational cooling at both the Fe(II) and the Ru(II) centers. Further, the processes corresponding to τ_6 and the infinite component can be easily identified by their spectral characteristics of their decay associated spectra (DAS) (Figure S11) by comparing with the DAS for the photoinduced processes of **Ru** and **RuFeRu** upon selective excitation of the Fe(II) center(Figure S10): τ_6 describes the decay of the quintet to the ground state. The infinite component represents the long-lived excited state at the Ru(II) center, which can also be observed in the ns time-resolved experiments (Figure S8 and S14). The very weak amplitude of this component compared to the data obtained for **Ru** is a first indication for the presence of an additional pathway depopulating the Ru(II) excited states in the presence of the Fe(II) center. These processes are probably faster than the equilibration between the Ru(II) ^{3}MLCT and the ^{3}LC state, hence the equilibration process escapes detection due to its very low amplitude (Figure S9 and S12). In contrast, the interpretation of the processes associated with $\tau_3 = 13$ ps and $\tau_4 = 44$ ps is not as straight forward. τ_3 is in the same temporal range as ligand planarization, which follows excitation at the Ru(II) center, but shows a completely different spectral shape for **RuFeRu** than for **Ru**. This component describes the decay of the Ru(II) spectral contributions parallel to a build-up of Fe(II) GSB, represented by the maximum in the DAS at 570 nm (Figure S11). Hence, this process can be interpreted as energy transfer between both centers. This transfer does not take place with unity quantum yield, i.e., some spectral

10

contributions from the Ru(II) excited states remain apparent at longer delay times. τ_4 could be assigned to the population of the Fe(II) quintet state, but it would be significantly decelerated (44 ps) compared to direct excitation of the iron center (23 ps). Further, it shows a rather high relative amplitude compared to excitation of only the Fe(II) center. There is no explanation for the seemingly deceleration of this process under changed excitation conditions at this point. Investigations addressing this matter are on the way.

The multi-exponential description is only correct for cascade kinetics or independent parallel relaxation at both centers.[8] A comparison of the species associated spectra (SAS) of the photoinduced dynamics at the isolated Ru(II) and Fe(II) centers with the SAS for **RuFeRu** upon excitation at 520 nm resulting from the multi-exponential fit reveals, that while the sequential reaction model gives reasonable results for the kinetics at the single centers, for **RuFeRu** upon excitation at 520 nm the fit with the sequential model results in SAS, which correspond to a mixture of the different excited species, which are present (see Figure S13 and Figure 5 in the main text).[8] Due to energy transfer depopulating the Ru(II) ^{3}MLCT state and transferring population to Fe(II) ^{3}MLCT states, the description with a sequential reaction scheme is not valid anymore. Hence, a modified model based on the processes and their respective timescales discussed above including the energy transfer between the metal centers was fitted numerically to the data (Scheme S1).
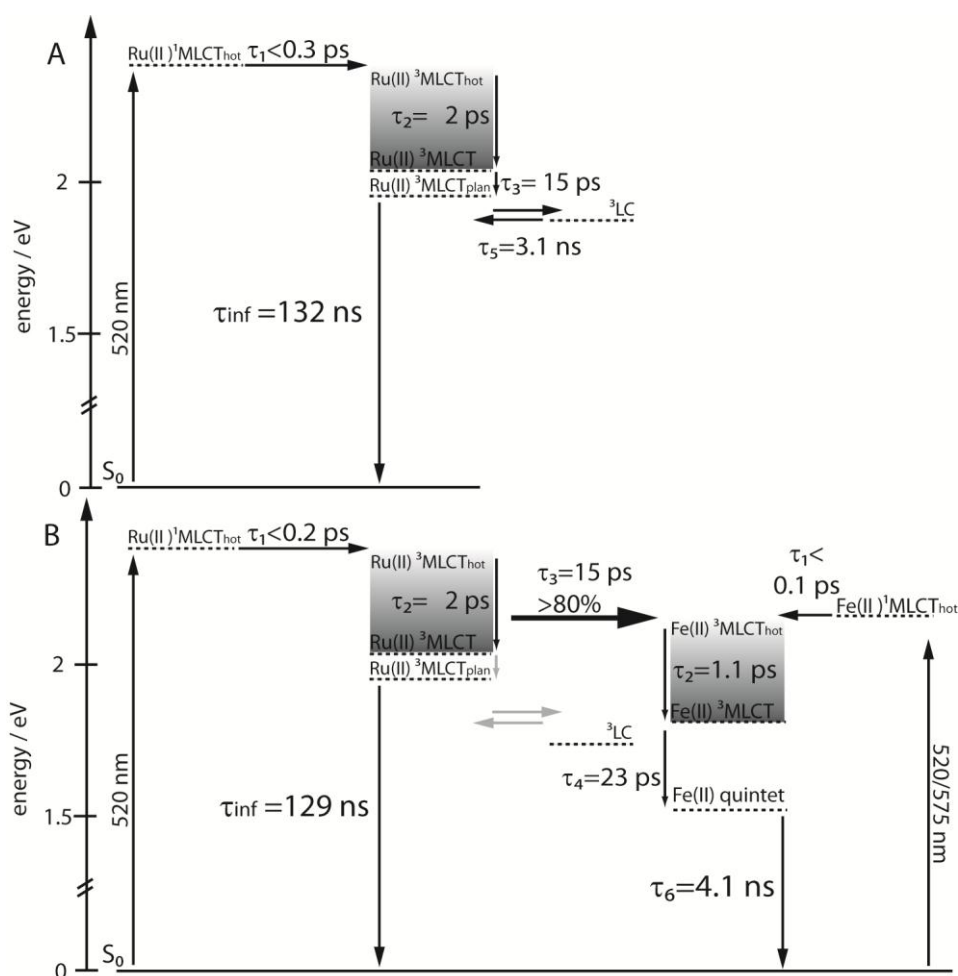
Scheme S1: Proposed relaxation schemes for **Ru** and **RuFeRu**, processes marked in gray are not directly observable, solid lines define energy levels with defined energetic positions, while dashed lines define excited states, the energy of which can only be indirectly inferred or depends on the excitation wavelength, processes in grey are not directly observed in the data

Table S1: global fit results of RuFeRu upon excitation at 520 nm with increasing number of exponentials

	τ_{1Fe}/ ps	τ_{1Ru}/ ps	τ_{2Fe}/ ps	τ_{2Ru}/ ps	τ_3/ ps	τ_4/ ps	τ_5/ ps	τ_6/ ps	
RuFeRu_520 nm									
1 component					35				Inf
2 components	0.9				23				Inf
3 components	0.8				26			4100	Inf
4 components	0.8				12	44		4300	Inf
5 components	0.2		1.3		13	44		4300	Inf
6 components	0.2		1.4		13	44	230	4100	Inf
Fixed[a]	0.1	0.3	1.1	2.0	15	23	3100	4100	Inf
Model[b]	0.2		1.4		15	56		4200	Inf
RuFeRu_570 nm	0.1		1.1			23		4100	
Ru_520 nm		0.3		2.0	15		3100		Inf

a) fit with the kinetic components determined for the single metal centers (**RuFeRu** excitation 570 nm, **Ru** excitation 520 nm), assuming a simple superposition of Ru(II) and Fe(II) centered photoinduced dynamics

b) numerical fit, model described in the main text (Scheme 1, and Scheme S1)
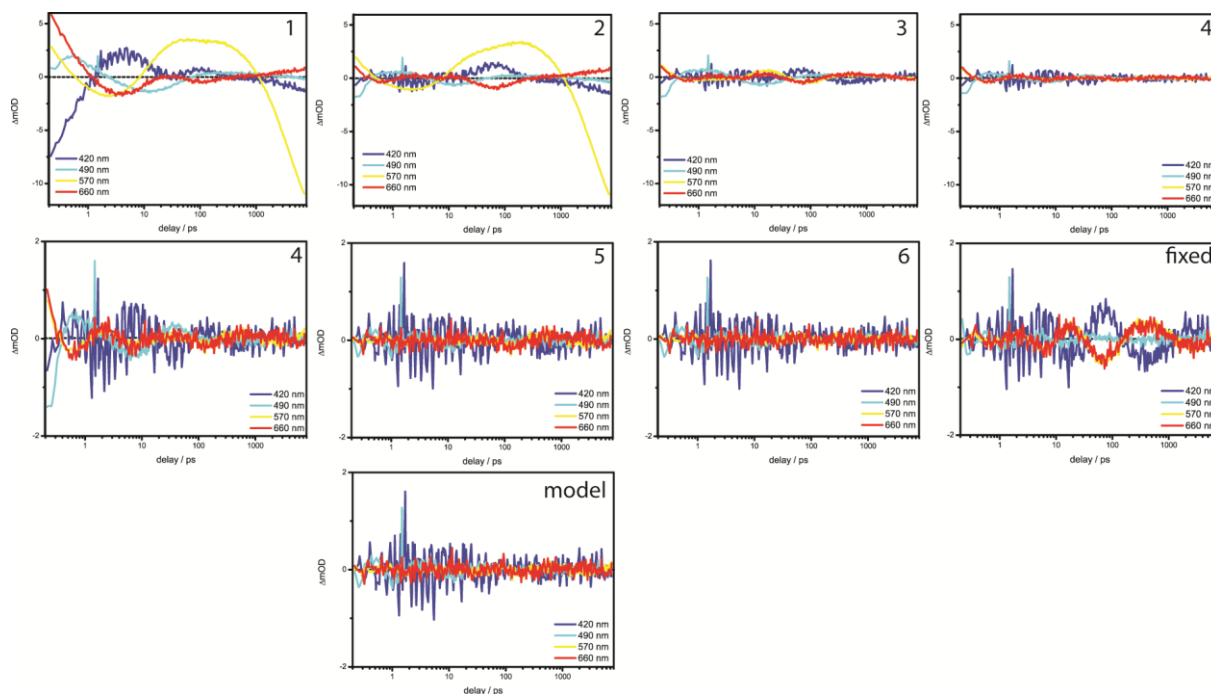
Figure S9: Residuals of the global fit with varying number of exponentials (see table S1) for **RuFeRu** excited at 520 nm, also the residuals of the fit with fixed time constants determined for **Ru** and upon selective excitation of the Fe(II) center of **RuFeRu** and the fit with the modified model are included.
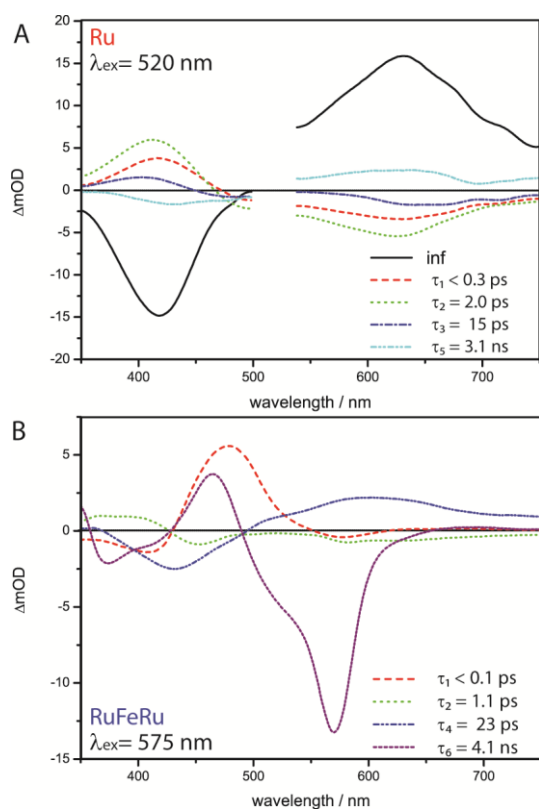
Figure S10: Decay associated spectra (DAS) and respective time constants resulting from a multi-exponential global fit of (A) **Ru** upon excitation at 520 nm and (B) **RuFeRu** upon excitation 575 nm, representing the characteristic photoinduced dynamics and spectral characteristics at the Ru(II) and the Fe(II) center, respectively. Planarization and equilibration processes with the ^{3}LC states can be identified by comparison to related structures by their characteristic DAS[7, 9]
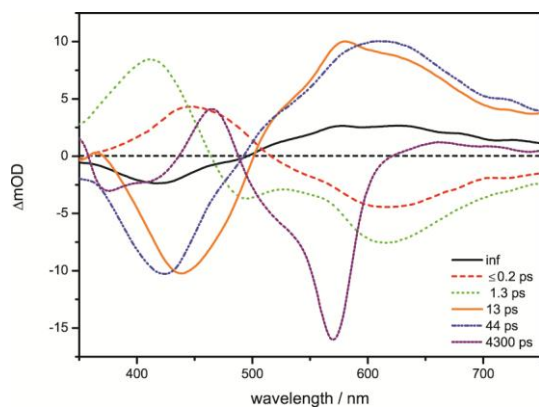
Figure S11: DAS of the multi-exponential fit of **RuFeRu** with 5 exponentials upon excitation at 520 nm.
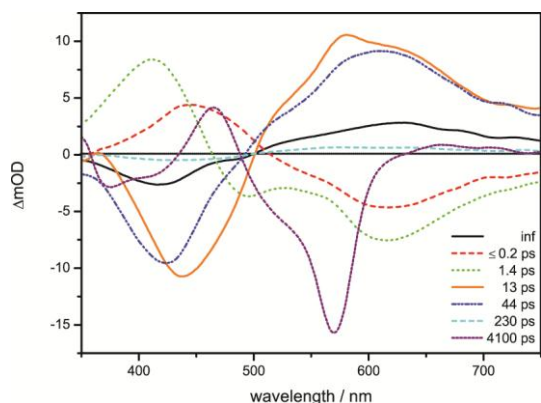
Figure S12: DAS of the multi-exponential fit with 6 exponentials of **RuFeRu** upon excitation at 520 nm. The component with a time constant of 230 ps fits spectrally to the equilibration process, but shows only very weak contributions, hence can only be determined with high inaccuracy.
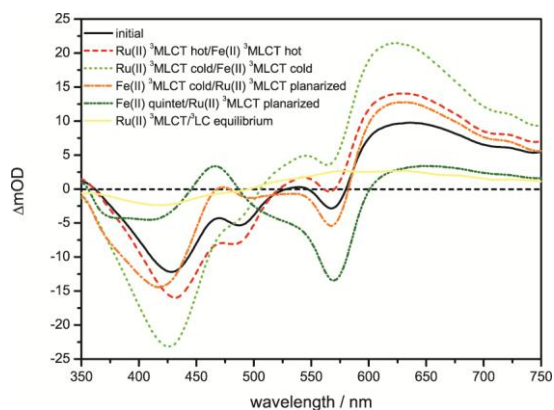
Figure S13: SAS from the multi-exponential fit (sequential model) with 5 exponentials of **RuFeRu** upon excitation at 520 nm. From comparison with the SAS resulting from a sequential fit of the dynamics of the centers selectively excited it is apparent, that the SAS determined from the multi-exponential fit are superpositions of these SAS of the single centers. This indicates that the model needs to be modified.
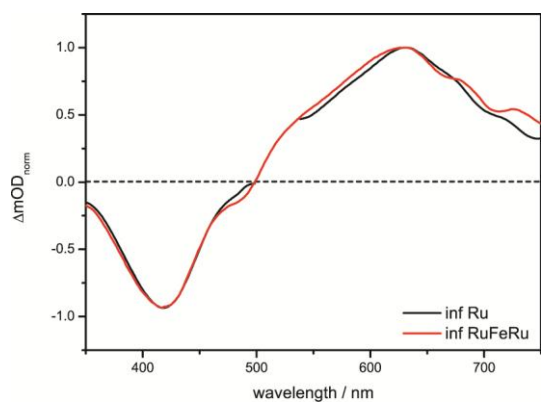
Figure S14: Comparison of the long-lived components (normalized representation) in the fs time-resolved measurements of **Ru** and **RuFeRu** upon excitation at 520 nm illustrating the identity of the long-lived state in **Ru** and **RuFeRu**.

15

Estimation of the energy transfer efficiency in RuFeRu

The fs time-resolved measurements were performed under identical excitation conditions (wavelength and intensity).

Assumption 1: extinction coefficients of the Ru(II) [1]MLCT transitions in the ground state are not significantly changed upon coordination of the Fe(II) center.

Then the part of Ru(II) excitation in **RuFeRu** can be determined by regarding the absorption spectrum of **RuFeRu** as sum of two times the absorptions spectrum of **Ru** plus the unknown absorption spectrum of the iron center. This leads to an initial excitation ratio at 520 nm of approximately 3(Ru):1(Fe).

Assumption 2: Excited state extinction coefficients are also not changed significantly upon coordination of the Fe(II) center.

The ratio of signal intensity of the long-lived component is determined to 1(**Ru**):0.16(**RuFeRu**). This means that 84% of signal intensity is quenched by energy transfer from the Ru to the Fe center. This value would hold true if the optical intensities of the samples were adjusted in a way that both show equal optical density of the Ru [1]MLCT transition. The optical densities at 520 nm were 0.12 for **Ru** and 0.21 for **RuFeRu**. Regarding the excitation ratio determined above this leaves an optical density for the Ru [1]MLCT transitions of 0.15 in **RuFeRu**, which is slightly too high. Assuming that a sample of higher optical density gives a higher transient signal, the determined value for the efficiency of energy transfer defines a lower limit, as the signal detected for **RuFeRu** is even too high.

From this short estimation we conclude that we can state that energy transfer occurs with at least 80 % efficiency in **RuFeRu**.
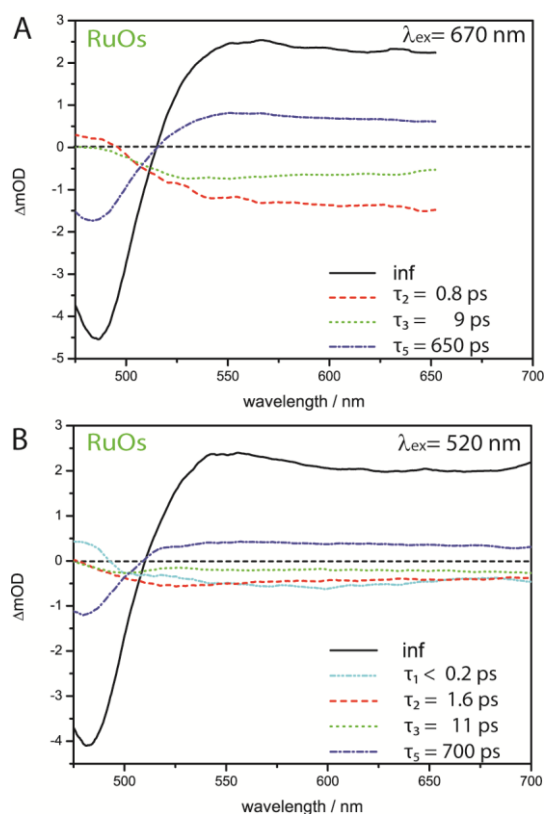
Figure S15: DAS and respective time constants resulting from a multi-exponential global fit for **RuOs** (A) upon excitation at 670 nm and (B) 520 nm.

References

1. A. Winter, C. Friebe, M. D. Hager and U. S. Schubert, *Eur. J. Org. Chem.*, 2009, 801-809.
2. B. Schulze, D. Escudero, C. Friebe, R. Siebert, H. Görls, S. Sinn, M. Thomas, S. Mai, J. Popp, B. Dietzek, L. Gonzalez and U. S. Schubert, *Chem.-Eur. J.*, 2012, 18, 4010-4025.
3. D. F. Zigler, M. T. Mongelli, M. Jeletic and K. J. Brewer, *Inorg. Chem. Commun.*, 2007, 10, 295-298.
4. J. A. Nelder and R. Mead, *The Computer Journal*, 1965, 7, 308-313.
5. S. E. (2012). *Scilab: Free and Open Source software for numerical computation (OS, Version 5.XX) [Software].* , Available from: http://www.scilab.org.
6. R. Siebert, A. Winter, B. Dietzek, U. S. Schubert and J. Popp, *Macromol. Rapid Commun.*, 2010, 31, 883-888.
7. R. Siebert, A. Winter, U. S. Schubert, B. Dietzek and J. Popp, *Phys. Chem. Chem. Phys.*, 2011, 13, 1606-1617.
8. I. H. M. van Stokkum, D. S. Larsen and R. van Grondelle, *Biochim. Biophys. Acta*, 2004, 1658, 262-262.
9. R. Siebert, C. Hunger, J. Guthmuller, F. Schlütter, A. Winter, U. S. Schubert, L. Gonzalez, B. Dietzek and J. Popp, *J. Phys. Chem. C*, 2011, 115, 12677-12688.

P5 - Excitation-power modulates energy-transfer dynamics in a supramolecular RuII-FeII-RuII triad

J. Kübel, M. Wächtler, B. Dietzek: Excitation-power modulates energy-transfer dynamics in a supramolecular Ru(II)-Fe(II)-Ru(II) triad. *ChemPhysChem*. 2017. *Volume*. Page(s). Copyright Wiley-VCH Verlag GmbH & Co. KGaA./ submitted/not yet published - Reproduced with permission. Manuscript submitted May 22nd 2017. Submission confirmed

June 26th 2017.

Reply   **Forward**   **Delete**

For your information: Manuscript number: cphc.201700710 submitted to ChemPhysChem - [EMID:1f74b6b98e95cb91]

Date: 06/26/2017 (08:53:47 AM CEST)

From: ChemPhysChem

To: Joachim Kübel

Reply-To: ChemPhysChem

📄 Text (1 KB)

Manuscript number: cphc.201700710
Title: "Excitation-power modulates energy-transfer dynamics in a supramolecular RuII-FeII-RuII triad"

_____

Dear Mr Kübel,

This is to inform you that the above-mentioned Article has just been submitted to ChemPhysChem by Prof. Dr. Benjamin Dietzek including Joachim Kübel; Maria Wächtler; Benjamin Dietzek, Prof. and you are listed as a co-author.

Yours sincerely,
Editorial Office Staff

_____

WILEY-VCH
Boschstrasse 12
69469 Weinheim
Germany
phone: +49-6201-606-200
fax: +49-6201-606-331 /-328
e-mail: chemphyschem@WILEY-VCH.de
http:\\www.chemphyschem.org

A journal of ChemPubSoc Europe
Published by Wiley-VCH: www.wiley-vch.de

_____

(Impact Factor 2015: 3.138)

Now open for submission: Covering the entire spectrum of photochemistry - ChemPhotoChem! New sister journal to Angewandte Chemie and ChemElectroChem. A ChemPubSoc Europe journal.

*****
Wiley-VCH Verlag GmbH & Co. KGaA - A company of John Wiley& Sons, Inc. - Location of the Company: Weinheim - Trade Register: Mannheim, HRB 432833. Chairman of the Supervisory Board: Mark Allin. General Partner: John Wiley & Sons GmbH, Location: Weinheim - Trade Register Mannheim, HRB 432296 - Managing Directors: Sabine Steinbach, Dr. Guido F. Herrmann.
*****

ARTICLE WILEY-VCH

Excitation-power modulates energy-transfer dynamics in a supramolecular Ru^{II}-Fe^{II}-Ru^{II} triad

Joachim Kübel,[a,b,c] Dr. Maria Wächtler[a] and Prof. Dr. Benjamin Dietzek*[a,b,d]

Abstract: Multichromophoric arrays are key to light-harvesting in natural and artificial photosynthesis. A trinuclear, symmetric Ru^{II}-Fe^{II}-Ru^{II} triad may resemble a light-harvesting model system, in which excitation energy from donor units (Ru-terpyridine-fragments) is efficiently transferred to the acceptor (an Fe-terpyridine-fragment). The photoinduced dynamics after simultaneous excitation of more than a single chromophoric unit (donor/acceptor) at varying excitation fluence is investigated in this contribution. Data suggests that energy transfer is decelerated if the acceptor states (on the Fe^{II} unit) are not depopulated fast enough. As a consequence the lifetime of a high-lying excited state (centered on either of the Ru^{II} units) is prolonged. A kinetic model is suggested to account for this effect. While the model proposed is specifically adopted to account for the experimental data reported here, it might be generalized to other situations, in which multiple energy or electron donors are covalently linked to a single acceptor site – a situation of interest in contemporary artificial photosynthesis.

Introduction

Natural light harvesting relies on specialized chromophores in spatially and energetically well-organized arrangements.[1] Many of the working principles have been identified and rationalized[2] and could conceptually be transferred to artificial photosynthesis. Remarkable implementations of natural working principles into molecular science concern, e.g., the photosynthetic Z-scheme in a semiconductor-based[3] and a purely molecular approach.[4] Here, the absorption of more than one photon during a full charge transfer cycle is essential for photocatalytic function. However, at increased photon flux, side reactions may occur. In the case of natural photosynthesis, singlet-singlet-annihilation (SSA) in light harvesting complex II of green plants was identified as a major decay channel at elevated photon densities (exceeding the photon flux available under natural irradiation conditions).[5] Such annihilation reduces the overall population of excited states. Though typical sunlight irradiance does not lead to SSA, plants have developed mechanisms to cope with high irradiance situations in order to protect natural systems from oxidative damage. Such strategies to control the number of photoexcited states include, e.g., energy transfer to carotenoids.[6]
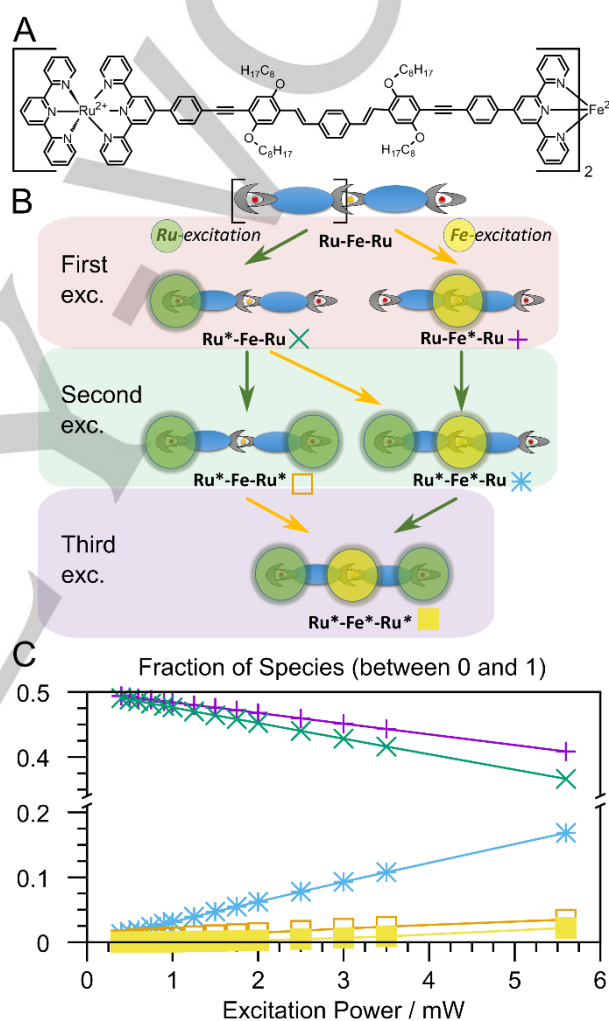
Figure 1. Panel A: Molecular structure of **RuFeRu**. Panel B: Schematic presentation of the generation of multiply excited species. Circles illustrate excited metal center(s) (green: Ru, yellow: Fe). Panel C: The fraction of the multiply excited species resulting from a simulation of the excitation (see SI) are given relative to the overall number of excited molecules for each pump power.

Artificial photosynthesis generally focuses on fast and directional charge separation, the stability of the catalytic center, introduction of molecular groups for substrate handling and efficient energy transfer to a reaction center. To this end one

[a] Joachim Kübel, Dr. Maria Wächtler and Prof. Dr. Benjamin Dietzek*
     Research Department Functional Interfaces
     Leibniz Institute of Photonic Technology (IPHT) Jena e.V.
     Albert-Einstein-Str. 9, 07745 Jena, Germany.
     E-mail: benjamin.dietzek@uni-jena.de
[b] Joachim Kübel, Prof. Dr. Benjamin Dietzek*
     Institute of Physical Chemistry and Abbe Center of Photonics
     Friedrich Schiller University Jena
     Helmholtzweg 4, 07743 Jena, Germany
[c] Joachim Kübel
     Department of Chemistry and Molecular Biology
     University of Gothenburg
     40530 Gothenburg, Sweden
[d] Prof. Dr. Benjamin Dietzek
     Center for Energy and Environmental Chemistry (CEEC)
     Friedrich Schiller University Jena
     Philosophenweg 7, 07743 Jena, Germany

     Supporting information for this article is given via a link at the end of the document.

successful strategy has been to arrange multiple light-absorbing units within a (supra)molecular structure (e.g. metal-complex based structures[7], organic chromophore arrays[8] or dendrimers[9]). Spectroscopic studies on molecules and materials under high irradiance have revealed effects of multiple excited states on the photoinduced dynamics e.g. in semi-conductors[10] and conducting polymers,[11] where multiple excitons can be produced in close spatial distance. While the bleaching or breakup of artificial light harvesting systems (e.g. [12]) has been reported under intense irradiation, few studies focus on the alteration of photophysics under high fluence in molecular species.[13]

Thus, here we report the photoinduced dynamics under high-fluence conditions in the tri-nuclear complex, **RuFeRu**[14] (see Figure 1). We show that increased excitation power can have specific impact on the photoinduced dynamics of this model system for an artificial photosynthetic antenna system. In this model complex, which however lacks a reaction center analogue to which photoinduced electron transfer can occur, energy is transferred from the peripheral Ru-units to the central Fe[II] part. Via the Fe-center excited-states are deactivated by internal conversion to the ground state.[14]
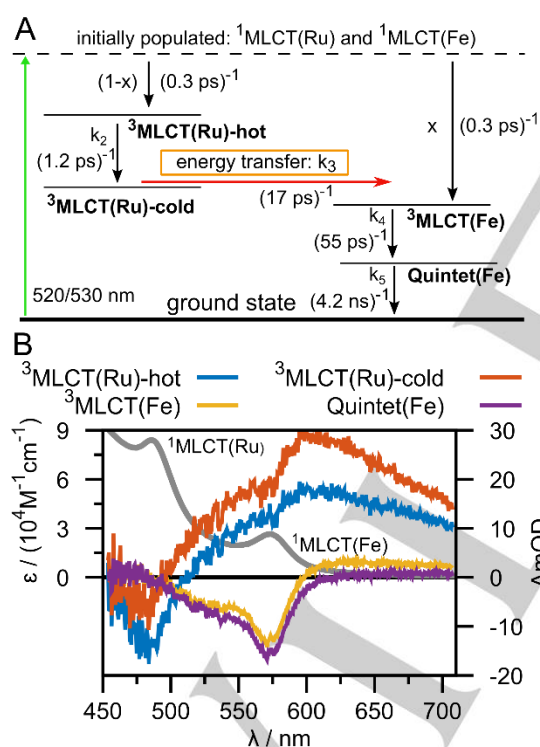
Figure 2. Panel A: The photophysical model ("low-P", *vide infra*) to account for the data measured at low pump intensities.[14] The variable parameter x (0 ≤ x ≤ 1) has to be adapted for the respective excitation wavelength due to a varied ratio of the numbers of the singly excited species **Ru*FeRu** and **RuFe*Ru** (see SI, Figures S13-S15). Panel B: Ground-state absorption spectrum of **RuFeRu** in Acetonitrile (gray, left scale) and species spectra from a fit of the dataset measured at P = 0.4 mW to the low-P model.

Results and Discussion

The light absorption of **RuFeRu** in the visible region is dominated by two singlet metal-to-ligand charge-transfer transition bands centered at ca. 488 and 575 nm for Ru ("^{1}MLCT(Ru)") and Fe ("^{1}MLCT(Fe)"), respectively (Figure 2B) which overlap in the spectral region chosen for excitation (530 nm). There is no detectable emission from the triplet states in the molecule.[14] In the low-pump fluence regime,[14] where only one chromophor per molecule is excited, excitation of a Ru-based singlet metal-to-ligand charge-transfer transition ("^{1}MLCT(Ru)") leads to intramolecular energy transfer towards the Fe-fragment likely via ligand-centered triplet states[14] (see Figure 2, further details on the model as reported previously are summarized in the SI).

By increasing the pump intensity the probabilities for double- and triple-excitation (Figure 1) of **RuFeRu** are increased, while – at the same time – the relative weight of single-excitations decrease. The relevant parameters of the measurements are given in Table 1. Based on the approximation that only the ^{1}MLCT(Ru) and ^{1}MLCT(Fe) contribute to the absorption of **RuFeRu** at the pump wavelength, we simulated the multiple absorption events (see Figure 1 and the corresponding chapter in the SI). This simulation suggests that the only multiply excited species that is formed substantially under the experimental conditions is **Ru*Fe*Ru**, *i.e.* one ^{1}MLCT(Ru) and the ^{1}MLCT(Fe) are excited. The impact of these multiple excited states on the photoinduced dynamics of **RuFeRu** is monitored via femtosecond transient absorption spectroscopy.

Table 1. Measurement parameters in terms of power P, fluence F (beam diameter at sample position of 940 µm), photon density N and the average number of photons per molecule in the sample volume for excitation at 530 nm.

Index	P / mW	F / (mJ cm^{-2})	N / (10^{15} photons cm^{-2})	Photons per molecule
1	0.4	0.12	0.3	8
2	0.5	0.14	0.4	10
3	0.6	0.17	0.5	12
4	0.75	0.22	0.6	15
5	0.9	0.26	0.7	18
6	1	0.29	0.8	20
7	1.25	0.36	1.0	26
8	1.5	0.43	1.1	31
9	1.75	0.50	1.3	36
10	2	0.58	1.5	41
11	2.5	0.72	1.9	51
12	3	0.87	2.3	61
13	3.5	1.01	2.7	72

14	5.6	1.61	4.3	115

In order to understand the pump-intensity dependent transient absorption data, we will resort to the spectral characteristics of individually excited sub-units, *i.e.* Ru- or Fe-centered states (see Figure 2B). The identification of the characteristic spectroscopic signatures is based on the data measured in the low-pump fluence regime:

1. Negative signal between 470 and 490 nm (bleach of the ^{1}MLCT(Ru) band) is indicative of population in the ^{3}MLCT(Ru) states. Fe-centered states do not significantly contribute in this spectral region.
2. Above 600 nm the excited-state absorption (ESA) of ^{3}MLCT(Ru) states dominates the weak ESA from ^{3}MLCT(Fe).
3. The negative peak at 577 nm (bleach of the ^{1}MLCT(Fe)) is the dominant feature of both the ^{3}MLCT(Fe) and the Quintet(Fe) state. However, also ^{3}MLCT(Ru) states contribute to this spectral region with a positive ΔOD signal.
4. The two Fe-centered states can be distinguished based on their transient absorption: the Quintet(Fe) (contrary to the ^{3}MLCT(Fe)) does not show considerable signal above 600 nm (Figure 2B).[15]

Raw transient absorption spectra for four exemplary datasets measured at different pump fluences are shown in **Error! Reference source not found.**. The apparent deviations in the spectra with increasing pump power include a different ratio between the signal intensity below 500 nm (region of the ^{1}MLCT(Ru) bleach) as compared to the signal intensity at around 577 nm (bleach of the ^{1}MLCT(Fe) bleach).

Figure 4 summarizes the pump fluence induced changes of the transient absorption spectra from a different perspective, *i.e.* in plotting selected spectral characteristics, *e.g.* band intensities, the spectral position of a zero crossing or the pump-probe delay time, at which the kinetics pass through an extremum, as a function of the pump intensity. The characteristic observations made from the data shown in Figure 3 and summarized in Figure 4 are:

- *Observation 1* (Figure 4A): The negative signal amplitude at 577 nm, i.e. the ^{1}MLCT(Fe) ground-state bleach, decreases with increasing pump fluence;
- *Observation 2* (Figure 4A/B): The ESA of ^{3}MLCT(Ru) and ^{3}MLCT(Fe) above 600 nm decreases with increasing fluence. This is most pronounced at early delay times (10 ps). At longer delay times (100 and 1600 ps) the amplitude above 600 nm varies only slightly with increasing fluence, yet there is a blue shift of the zero-crossing from ca. 605 to 590 nm at 100 ps;
- *Observation 3* (Figure 4C): Maximum and minimum of the kinetic trace at 577 nm are shifting to longer delay times with increasing fluence.

Figure 3. Raw transient absorption spectra at selected delay times for four datasets (each measured at a specific pump power).
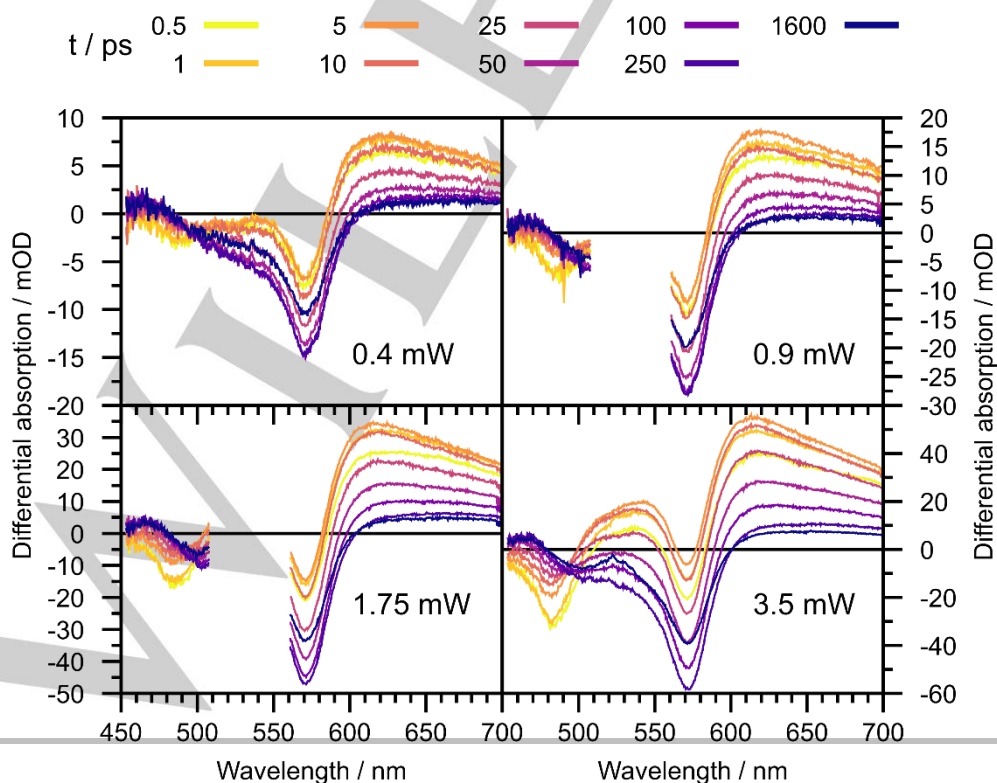
Figure 4. Panel A: Spectral integrals of the GSB-band (between 561 nm (17829 cm⁻¹) and the respective zero-crossing, see boxes in panel A,) and ESA-bands (between the respective zero-crossing and 707 nm (14136 cm⁻¹), see boxes in Figure 4A) at selected time delays (see legend in inset). Panel B: Wavelength of the zero-crossing between GSB- and ESA signatures. Panel C: Delay time at which the minimum in the kinetic traces at 577 nm is reached in dependence of pump power. The different symbols (square, stars, and crosses) in panels A and B refer to transient absorption spectra recorded at different pump-probe delay times as indicated in the Figure's legend adjacent to panel A.
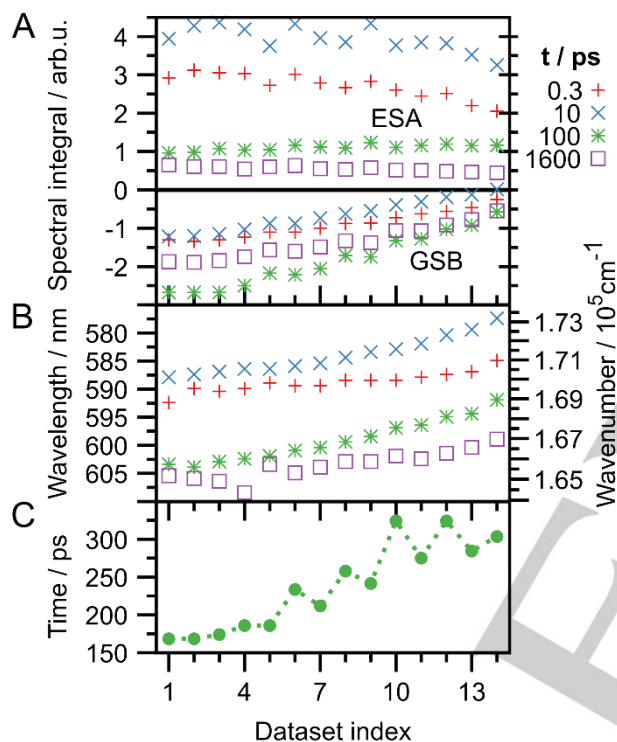
These experimental findings can be related to the spectral characteristic of the electronically excited states associated with the individual sub-units of **RuFeRu** as shown in Figure 2B:

Ad *Observation 1*: Relative changes of the negative ΔOD signal at 577 nm are caused by a combination of both a relative reduction of population in the iron-centered states (³MLCT(Fe) and Quintet(Fe)) and by an relative increase of the ³MLCT(Ru) excitation, the latter one contributing with ESA at this spectral position.

Ad *Observation 2*: A reduced signal amplitude >600 nm at delay times <100 ps is indicative of a relatively reduced population in ³MLCT(Ru) states as these carry the largest signal at the respective probe wavelengths.

Ad *Observation 3*: The normalized kinetics at 577 nm (recording GSB, see Figure 5c) exhibits identical behaviors at long delay times. This indicates that all pump-intensity induced deviations in the excited-state relaxation concern processes, which take place before reaching the minimum. After that – irrespective of the nature of the (intermediately populated) excited state(s) – all systems relax to the ground state in an identical manner, *i.e.* via the Quintet(Fe) state.

Before considering a photophysical molecular model to account for the key observables, it should be noticed that both inter-molecular and intra-molecular processes might be responsible for the pump-fluence dependent behavior reported here.[13, 16] However, inter-molecular processes in solution are typically diffusion controlled, *i.e.* the observed kinetic window of less than 500 ps, in which the pump-fluence induced differences in the kinetics of **RuFeRu** are most prominently visible, is too short to account for diffusion-controlled processes. Furthermore, the long alkoxy chains on the backbone of the chromophore are expected to hinder intermolecular π-π-stacking in solution. Thus, we conclude that the afore described pump-intensity dependent kinetics route in intramolecular effects, *i.e.* the relative increase in multiple excited species and the relative decrease in singly excited species upon increasing the pump fluence has to be considered to explain the experimental results. While a kinetic model for the low-pump-power-regime exists (Figure 2 and reference [14]), a kinetic model for multiply excited species of **RuFeRu** will be developed below. To account for the experimental data, which will originate from a mixture of **Ru*FeRu** and **RuFe*Ru** (*i.e.* represented in the low-pump-power model) and **Ru*Fe*Ru** (*i.e.* represented in the high-pump-power model), we will consider a linear combination of both the low- and the high-pump-power model. The respective weight factors of the individual models in the linear combination will be a function of the pump-power.
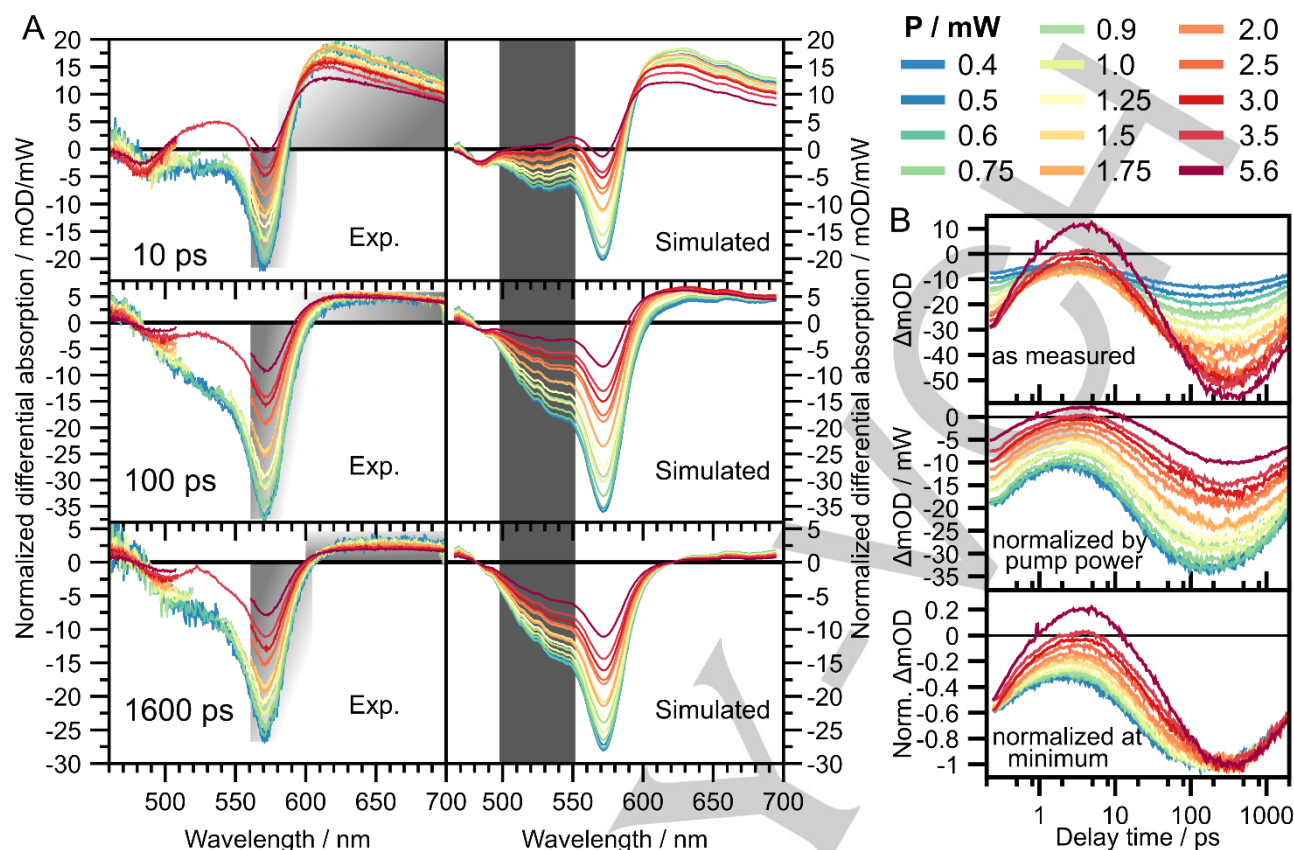
Figure 5. Pump-intensity normalized transient absorption data color-coded from blue (low excitation powers) to dark red (highest excitation powers). Panel A: Transient absorption spectra (normalized to the respective excitation power, experimental and simulated) for selected delay times. The spectral region between 500 and 550 nm (or an interval as needed), is ignored for most measurements due to overlap with pump scatter and marked with a dark gray box in the simulated data. The gray shading in the experimental data marks the intervals in which the integrals for GSB- and ESA-bands were calculated (see **Error! Reference source not found.**A). Panel B: Kinetic traces at 577 nm in differently normalized representations.

The kinetic model developed for **Ru*Fe*Ru** (*high-P* model) is based on the kinetic model for the low-pump-power-regime (*low-P* model), *i.e.* we assume that the rate constants which are associated with relaxation within one of the subunits of the triad, *i.e.* k_1, k_2, k_4 and k_5 (see Figure 2) are unaffected by photoexcitation of the neighboring unit. Within this assumption the respective rate constants are considered identical for the low- and the high-pump-power model. However, the effective energy transfer rate from the ^{3}MLCT(Ru)-cold to the ^{3}MLCT(Fe) is considered to depend on the pump-fluence. The rationale behind this pump-intensity dependence is that in **Ru*Fe*Ru** the energy transfer from ^{3}MLCT(Ru)-states to ^{3}MLCT(Fe) might be impaired if the Fe^{II}-center is already in its excited state, *i.e.* if the acceptor states of the intramolecular energy transfer are already occupied. Numerically we account for this hindered energy transfer by modulating k_3 by an acceptor state occupation

(denoted o) dependent parameter, *ffac(o)* (Figure 6A, and SI). The functional form of *ffac* is inspired by the Fermi distribution, *i.e.* below a certain threshold (in our case representing the occupancy of the acceptor states, *o*) *ffac* = 1 and the apparent rate of the $Ru^{II} \rightarrow Fe^{II}$ energy transfer, *ffac*·k_3, equals the transfer rate obtained in the low-pump-intensity regime, *i.e.* k_3. Above the threshold *ffac* approaches zero and the apparent rate of energy transfer diminishes. The characteristic parameter in the model, which determines the regime of *ffac* is o_{full} (taking over the function of the Fermi energy and representing the occupancy of the acceptor states). Thus, o_{full} determines the turning point of the function, *i.e.* to which extent the acceptor state has to be populated in order for the rate to be modified. The parameter w determines the increase of the kinetic hindrance and with that the width of the concentration/population interval in which the rate is modified. The resulting dependence of *ffac* on the acceptor state occupancy is shown in Figure 6A. The values of 1 and 0.2 for the *ffac* parameters o_{full} and w, respectively, have been determined in a global fit as described below.

It should be noted that the apparent rate of $Ru^{II} \rightarrow Fe^{II}$ energy transfer, *i.e. ffac*·k_3, is temporally dependent as the occupancy of the ^{3}MLCT(Fe) state is a function of time: Upon double excitation of the complex, *i.e.* formation of **Ru*Fe*Ru,** the ^{3}MLCT(Fe) state becomes fully populated (*o* = 1) and $Ru^{II} \rightarrow Fe^{II}$ energy transfer is hindered. At later times the initially formed ^{3}MLCT(Fe) relaxes to the Quintet(Fe) state and eventually back to the ground state liberating the excited state decay pathway for Ru-centered excitation. In the context of the numerical modeling this

translates into a decreasing acceptor state occupancy upon increasing the pump-probe delay time, *i.e.* $o=o(t)$. With the occupancy decreasing, *ffac* increases, causing the effective rate constant for energy transfer (*ffac*·k_3) to increase and allowing energy transfer to occur.

The kinetic profiles, i.e. the time-dependent occupation of the relevant states according to the *low-P* and *high-P* model, are numerically modeled to cover the time points recorded in the experiment (see Figure 7A, B). In other words, the sets of differential equations describing each kinetic scheme are numerically solved in sufficiently small time-steps to yield the temporal dependence of the states within each kinetic model. In the *high-P* model *ffac* is part of the differential expressions. To obtain *ffac* for each individual time point the acceptor occupancy $o(t)$ is calculated as the sum of the populations in the ^{3}MLCT(Fe) and the Quintet(Fe). Thus, for every time-step in the *high-P* model *ffac* is calculated and hence the effective energy transfer rate ffac*k_3 is determined.

Notably, *ffac* causes an upper limit for the population in the ^{3}MLCT(Fe). The actual limit depends on the rates of forming the Fe^{II}-centered states, i.e. *ffac*·k_3, and k_4 and k_5, *i.e.* the interconversion and depopulation dynamics of the ^{3}MLCT(Fe) and Quintet(Fe).

This kinetic model is capable of accounting for the pump-intensity dependent kinetics recorded at 577 nm (Figure 7C), which show a prolongation of the delay time at which the minimum of the kinetics is observed (Observation 3, Figures 4C and 5). This can be rationalized considering that Ru^{II}→Fe^{II} energy transfer leads to the build-up of a bleach of the Fe^{II} MLCT transitions at 577 nm. Hence, upon increasing the pump-intensity energy transfer is slowed.

Having discussed the kinetic consequences of the model to rationalize Observation 3, we will now include spectral information into the model in order to account for Observations 1 and 2. In doing so the experimental data is simulated (Figure 5A and Figure 7) by a linear combination of the low-pump-intensity and the high-pump-intensity model with relative weights (a and b for the low-P and high-P model, respectively, see Figure 6B) that are determined by a fit.

The fitted weights (a and b) are consistent with increased double excitations at elevated pump powers. The combined kinetics are calculated for each pump power: The individual kinetics obtained for **Ru*FeRu/RuFe*Ru** via the low-P model and **Ru*Fe*Ru** via the high-P model are shown in Figure 7B for P = 3 mW. In order to model the full transient absorption data (and not only kinetics of individual components) the differential absorption signals of the individual excited-state species as obtained within the low-pump-intensity limit (see Figure 2B) are combined with the kinetic profiles (see Figure 7A). The thus simulated transient absorption data is depicted in Figures 5A and 7. It is apparent that the model is able to reproduce the three key experimental observations as outlined above:

Ad Observation 1: The reduced bleach of the ^{1}MLCT(Fe) band with increasing pump fluence is accounted for by a power-dependent relative decrease of Fe- with respect to Ru-population. This is resembled by different x-values (Figure 2A) in both kinetic models (x_{low-P}≈0.75 while x_{high-P}≈0.5). Thus, in the

model accounting for intermediate pump fluences x changes with the pump intensity.

Ad Observation 2: The reduced ESA above 600 nm – previously associated with a decreased contribution of Ru-MLCT states – according to the fitting model results mainly from the overall reduced (relative) number of excited states at increased fluences. This can be inferred from considering the sum, a+2*b, of the linear coefficients which describe the weight of the low-P (a) and the high-P (b) kinetic model contributing at a given pump intensity. Thus, the sum a+2*b can be considered a representation of the overall number of excited states (see Figure 6B/C). Hence, its overall decrease as a function of increasing pump power explains the relative decrease of the ESA probed at 1.6 ns at probe wavelength above 600 nm (see Figure 5A).

The blue-shifted zero-crossing upon increasing the pump-intensity (see Figure 4B) is mainly a consequence of the power-dependent variation of the relative population in Ru- and Fe-centered states, *i.e.* x=x(P). Upon increasing the pump-power the relative weight of excited Ru-centers increases and the ESA of ^{3}MLCT(Ru) states contributes more to the observed transient absorption data. As a consequence the increased ESA at wavelengths above 600 nm starts to overlap with the ground-state bleach features of the Fe^{II}-centers and thus pushing the observed zero crossing in the transient absorption spectra to shorter probe wavelengths. This opposes the shift of the observed zero crossing in the transient absorption spectra to longer wavelengths as a consequence of the overall relaxation of photoexcited states towards the Fe^{II} centered states with increasing the pump-probe delay.

Ad Observation 3: As already detailed before, the increased delay time, at which the minimum of the 577-nm kinetics is observed, correlates with an increased contribution of **Ru*Fe*Ru** and hence a larger weight of the high-P model in fitting the data.

A

energy transfer rate: k_{EnT}

low-P model: $k_{EnT,low-P} = k_3 = const.$

high-P model: $k_{EnT,high-P} = k_3 * ffac$

$ffac = 1 / (exp((o - o_{full}) / w) + 1)$

with: $o_{full} = 1.0$ and $w = 0.2$

B

C
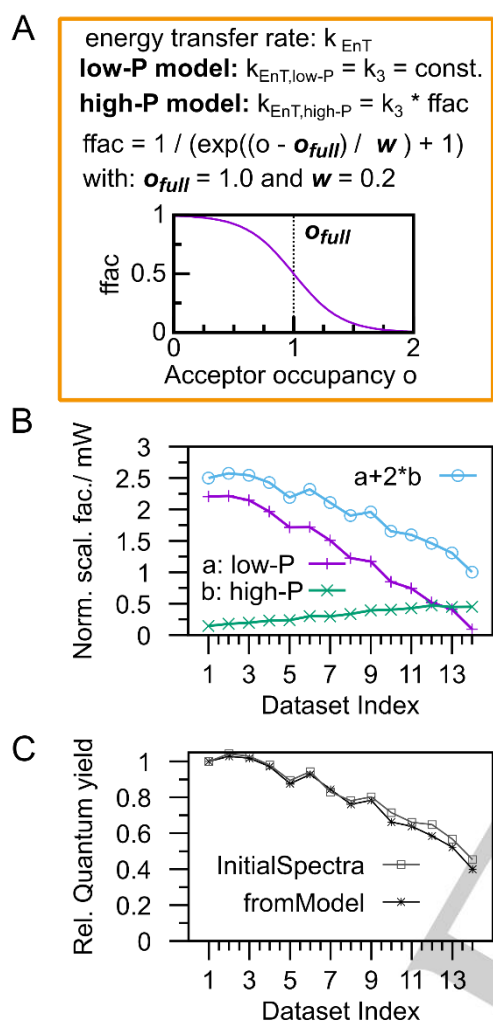
Figure 6. Photophysical model at high pump power: The energy transfer rate (k_{EnT}) constant is modulated with a function called "*ffac*" (panel A) producing an acceptor state occupancy dependent energy transfer rate. For the simulation a linear combination of the low pump fluence ("low-P model") model (see **Error! Reference source not found.**) and the one described here ("high-P model") is considered. The weights of the kinetic models (a and b referring to the low-P model and the high-P model, respectively, see panel B) were fitted for all datasets, i.e. the pump-probe data recorded at different pump fluences. However, the individual kinetic models remain unaltered, i.e. the rates of the individual models are not modified for different pump powers (see Figure 7A,B). Panel C: A relative quantum yield for the total number of excited states was determined with two different methods: Firstly, the weighted sum (a+2*b, see panel B) which represents the overall number of excited metal centers divided by the pump power can be interpreted as a quantum yield which is fitted based on the suggested model. On the other hand, a fit of the initial spectra (sub 500-fs, see Figure S9-11) has been performed. In both cases, the quantum yield decreases to less than 0.5 at the highest powers. This may be an indication of ultrafast (singlet-singlet) annihilation.

While the model proposed correctly reproduces the key observations laid out before, it fails to account for the long-lived excited state absorption at probe-wavelengths above 600 nm (see Figure 5 A, data recorded at a delay-time of 1600 ps). This is likely due to an equilibrated state (^{3}MLCT(Ru)-^{3}LC state), which was neglected in our model and is responsible for only ca. 10% of the overall signal amplitude at the lowest pump power (SI and reference [14]). Furthermore, the model does not explicitly include annihilation effects, which are frequently observed, *e.g.* in conjugated polymers,[10-11] but have also been reported for dinuclear coordination compounds[13] or Ru-complexes embedded into membranes.[16c] It is likely that annihilation also plays a role in the high-pump-power photophysics of **RuFeRu**.

However, the simple kinetic model proposed here based on kinetically hindered Ru^{II}→Fe^{II} energy transfer is capable of accounting for the sub-ns data with the specific experimental signal-to-noise ratio quite well. Therefore, an inclusion of another kinetic component carries the danger of overfitting and overinterpretation the experimentally accessible data. However, the diminishing overall number of excited metal centers, which is reflected in the sum a+2*b (see Figure 6B) might implicitly indicate the presence of fast annihilation upon elevated pump powers. As a consequence of annihilation the overall number of excited states becomes reduced and hence is not captured in our fit, which is concerned with the experimental data recorded at delay times longer than 500 fs. Hence, these numbers indicate a loss of excited states within the first some-100 fs after excitation and hence the presence of rapid annihilation, likely singlet-singlet annihilation. Nonetheless, we do not believe that our experimental data is detailed enough in order to explicitly treat annihilation in the kinetic model.

It should be noticed that *o(t)* is calculated as the sum of the populations in the ^{3}MLCT(Fe) and the Quintet(Fe). If only the population in the ^{3}MLCT(Fe) state was considered in the calculation of *o(t)*, ffac*k_3 would approach k_3 quickly because the ^{3}MLCT(Fe) relaxes to the Quintet(Fe) with the fixed rate k_4 (55 ps)$^{-1}$. Further, in the kinetic profiles resulting from our model (Figure 7B) a relative concentration of the Quintet(Fe) rising above 1 is observed, which is physically not meaningful and routes in the neglection of possible hindrances of the decay pathways following the energy transfer steps and additional decay pathways, e.g. annihilation. However, the model describes the data well within the limitations of our experimental signal-to-noise ratio, as discussed above.

Such kinetic blockage of energy transfer in multi-center transition metal complexes has not been reported yet to the best of our knowledge. This effect could, be of considerable interest when designing artificial light harvesting antenna systems. Particularly interesting model systems for further studies could be organic light harvesting arrays where the energy transfer dynamics may more conveniently be probed using time-resolved emission spectroscopy, and on the other hand, systems with a longer intrinsic lifetime as compared to the Fe-terpy fragment. In such situation, also triplet-triplet annihilation might take place on time-scales comparable to the energy transfer processes. Therefore, the system at hand proved particularly useful in identifying the role of occupied acceptor states in the excited-

state $Ru^{II} \rightarrow Fe^{II}$ energy transfer and the resultant kinetic blockade of excitation transfer.

A Data simulation based on bilinear model:
C: kinetic profiles, n*5 matrix
S: species spectra, m*5 matrix
n timepoints, m spectral datapoints

pump powers. While data recorded at low pump power is consistent with results from an earlier study[14], there are distinctive effects of increased pump powers on the
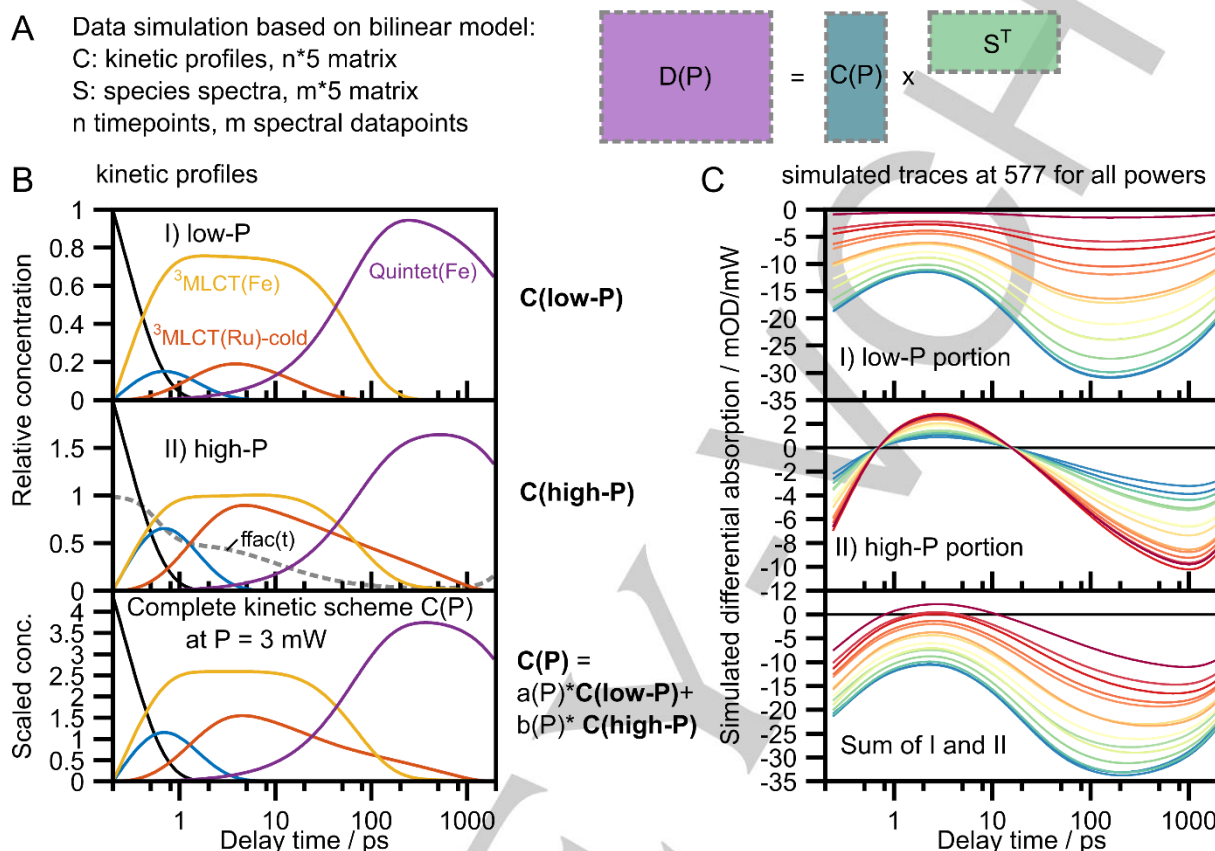
Figure 7. Panel A: Schematic presentation of the data simulation approach. The two-dimensional (time-wavelength) data matrix D is calculated as the matrix product of a matrix C containing the kinetic profiles of the 5 states considered here (see description of the low-P model and Figure 2) with the matrix S containing the species spectra as shown in Figure 2B. Panel B: The kinetic profiles of the low-P (for **Ru*FeRu/RuFe*Ru**) and the high-P (for **Ru*Fe*Ru**) model are shown with the state color code introduced in Figure 2B. The set of differential equations for each model is solved numerically. In the case of the high-P model, the *ffac* modulation factor for k_3 is calculated for each time-step and affects the temporal profiles. By calculating the sum of the low-P and high-P model weighted by the parameters a and b (see Figure 6B), which were fitted for each dataset measured at a specific pump power, a combined model is obtained. This is shown exemplarily for dataset 12 (P = 3 mW). Panel C: Simulated pump-power-normalized traces at 577 nm for all pump powers, from blue (low excitation powers) to dark red (highest excitation powers, with the same color code as in Figure 5). Shown are the individual contributions of the low-P model, that of the high-P model and the combined data providing the simulated traces at 577 nm, which are comparable to the respective experimental data shown in **Error! Reference source not found.**B.

Conclusions

We have performed broadband transient absorption spectroscopy on the trinuclear complex **RuFeRu** for different

photoinduced dynamics probed. The observation sticking out most is a temporal delay of the ^{3}MLCT(Ru) to ^{3}MLCT(Fe) energy transfer that becomes more significant at higher fluences. A tempting explanation for this behavior is that energy transfer is decelerated if acceptor states are already occupied. This observation possibly is of fundamental importance for artificial photosynthetic light harvesting, which attempts to combine multiple donor units with a single (limited number of) acceptor(s). A decelerated energy transfer causes an increased lifetime of a high-lying triplet states. Thereby *e.g.* previously inaccessible and unwanted side reactions might occur.

This observation could add another challenge to the efficient design of molecular artificial photosynthetic systems combining multi-chromophoric antennas with individual reaction centers.

Experimental Section

The time-resolved transient absorption setup has been described earlier.[17] For further experimental details and details on the data evaluation the reader is referred to the supporting information.

Acknowledgements

References

[1]   a) H. Dau, *Photochem. Photobiol.* **1994**, *60*, 1-23; b) R. van Grondelle, J. P. Dekker, T. Gillbro, V. Sundstrom, *BBA-Bioenergetics* **1994**, *1187*, 1-65; c) V. Sundström, T. Pullerits, R. van Grondelle, *J. Phys. Chem. B* **1999**, *103*, 2327-2346.

[2]   G. D. Scholes, G. R. Fleming, A. Olaya-Castro, R. van Grondelle, *Nat. Chem.* **2011**, *3*, 763-774.

[3]   H. Tada, T. Mitsui, T. Kiyonaga, T. Akita, K. Tanaka, *Nat. Mater.* **2006**, *5*, 782-786.

[4]   L. Favereau, A. Makhal, Y. Pellegrin, E. Blart, J. Petersson, E. Göransson, L. Hammarström, F. Odobel, *J. Am. Chem. Soc.* **2016**, *138*, 3752-3760.

[5]   a) M. Vos, R. van Grondelle, F. W. van der Kooij, D. van de Poll, J. Amesz, L. N. M. Duysens, *BBA-Bioenergetics* **1986**, *850*, 501-512; b) V. Barzda, V. Gulbinas, R. Kananavicius, V. Cervinskas, H. van Amerongen, R. van Grondelle, L. Valkunas, *Biophys. J.* **2001**, *80*, 2409-2421; c) G. Trinkunas, J. L. Herek, T. Polívka, V. Sundström, T. Pullerits, *Phys. Rev. Lett.* **2001**, *86*, 4167-4170.

[6]   a) A. V. Ruban, R. Berera, C. Ilioaia, I. H. M. van Stokkum, J. T. M. Kennis, A. A. Pascal, H. van Amerongen, B. Robert, P. Horton, R. van Grondelle, *Nature* **2007**, *450*, 575-578; b) P. Jahns, A. R. Holzwarth, *BBA-Bioenergetics* **2012**, *1817*, 182-193; c) I. Szabó, E. Bergantino, G. M. Giacometti, *EMBO reports* **2005**, *6*, 629-634; d) A. A. Pascal, Z. Liu, K. Broess, B. van Oort, H. van Amerongen, C. Wang, P. Horton, B. Robert, W. Chang, A. Ruban, *Nature* **2005**, *436*, 134-137.

[7]   a) Z. A. Morseth, L. Wang, E. Puodziukynaite, G. Leem, A. T. Gilligan, T. J. Meyer, K. S. Schanze, J. R. Reynolds, J. M. Papanikolas, *Acc. Chem. Res.* **2015**, *48*, 818-827; b) M. Orazietti, M. Kuss-Petermann, P. Hamm, O. S. Wenger, *Angew. Chem. Int. Ed.* **2016**, *55*, 9407-9410; c) A. G. Bonn, O. Yushchenko, E. Vauthey, O. S. Wenger, *Inorg. Chem.* **2016**, *55*, 2894-2899.

[8]   a) R. Ziessel, A. Harriman, *Chem. Commun.* **2011**, *47*, 611-631; b) A. Harriman, *Chem. Commun.* **2015**, *51*, 11745-11756; c) J. Iehl, J. F. Nierengarten, A. Harriman, T. Bura, R. Ziessel, *J. Am. Chem. Soc.* **2012**, *134*, 988-998.

[9]   a) J. Andersson, F. Puntoriero, S. Serroni, A. Yartsev, T. Pascher, T. Polívka, S. Campagna, V. Sundstrom, *Faraday Discuss.* **2004**, *127*, 295-305; b) F. Puntoriero, F. Nastasi, M. Cavazzini, S. Quici, S. Campagna, *Coord. Chem. Rev.* **2007**, *251*, 536-545; c) Y. Zeng, Y.-Y. Li, J. Chen, G. Yang, Y. Li, *Chem. Asian. J.* **2010**, *5*, 992-1005.

[10]   J. Piris, T. E. Dykstra, A. A. Bakulin, P. H. M. v. Loosdrecht, W. Knulst, M. T. Trinh, J. M. Schins, L. D. A. Siebbeles, *J. Phys. Chem. C* **2009**, *113*, 14500-14506.

[11]   T. W. Kee, *J. Phys. Chem. Lett.* **2014**, *5*, 3231-3240.

[12]   M. A. Alamiry, A. s. Harriman, A. Haefele, R. Ziessel, *ChemPhysChem* **2015**, *16*, 1867-1872.

[13]   C. Kuhnt, M. Karnahl, M. Schmitt, S. Rau, B. Dietzek, J. Popp, *Chem. Commun.* **2011**, *47*, 3820-3821.

[14]   M. Wächtler, J. Kübel, K. Barthelmes, A. Winter, A. Schmiedel, T. Pascher, C. Lambert, U. S. Schubert, B. Dietzek, *Phys. Chem. Chem. Phys.* **2015**, *18*, 2350-2360.

[15]   a) J. E. Monat, J. K. McCusker, *J. Am. Chem. Soc.* **2000**, *122*, 4092-4097; b) W. Gawelda, A. Cannizzo, V.-T. Pham, F. van Mourik, C. Bressler, M. Chergui, *J. Am. Chem. Soc.* **2007**, *129*, 8199–8206.

[16]   a) R. E. Kellogg, *J. Chem. Phys.* **1964**, *41*, 3046-3047; b) A. N. Tarnovsky, W. Gawelda, M. Johnson, C. Bressler, M. Chergui, *J. Phys. Chem. B* **2006**, *110*, 26497-26505; c) A. De la Cadena, T. Pascher, D. Davydova, D. Akimov, F. Herrmann, M. Presselt, M. Wächtler, B. Dietzek, *Chem. Phys. Lett.* **2016**, *644*, 56-61.

[17]   J. Kübel, A. Winter, U. S. Schubert, B. Dietzek, *J. Phys. Chem. A* **2014**, *118*, 12137-12148.

Supporting Information
©Wiley-VCH 2016
69451 Weinheim, Germany

Excitation-power variations modulate energy-transfer in a supramolecular Ru^{II}-Fe^{II}-Ru^{II}

Joachim Kübel, Dr. Maria Wächtler and Prof. Dr. Benjamin Dietzek*

Abstract: Multichromophoric arrays are key to light-harvesting in natural and artificial photosynthesis. A trinuclear, symmetric Ru^{II}-Fe^{II}-Ru^{II} triad may resemble a light-harvesting model system, in which excitation energy from donor units (Ru-terpyridine-fragments) is efficiently transferred to the acceptor (an Fe-terpyridine-fragment). The photoinduced dynamics after simultaneous excitation of more than a single chromophoric unit (donor/acceptor) at varying excitation fluence is investigated in this contribution. Data suggests that energy transfer is decelerated if the acceptor states (on the Fe^{II} unit) are not depopulated fast enough. As a consequence the lifetime of a high-lying excited state (centered on either of the Ru^{II} units) is prolonged. A kinetic model is suggested to account for this effect. While the model proposed is specifically adopted to account for the experimental data reported here, it might be generalized to other situations, in which multiple energy or electron donors are covalently linked to a single acceptor site – a situation of interest in contemporary artificial photosynthesis.

Table of Contents

Experimental Procedures

Notes on the data set in general

The dataset acquired contains complete two-dimensional transient absorption data (spectral range ca. 460 to 710 nm, delay time range 0 to 1900 ps) for 14 different excitation powers. The complexity of the complete dataset hampers a readily accessible presentation of the data. Nevertheless, within the manuscript, different normalizations of the raw data are introduced which should aid interpretability. Furthermore, different representations of the dataset using kinetic traces, transient spectra and absolute intensities are discussed within the manuscript.

Time-resolved spectroscopy

The time-resolved transient absorption setup (based on a Legend-Elite, Coherent Inc.) has been described earlier.[1] The polarization of the pump-pulses is rotated by 54.7° (magic angle) with respect to the probe beam by using a Berek compensator. The excitation power is varied by adjusting the Berek relative to a polarizer at fixed angle. A thermal sensor (Thorlabs S302C) is used to measure the average beam power. Per time point, 500 individual laser shots are collected. For each excitation power, two scans (delay-line runs) were performed. Before and after a measurement a steady-state absorption spectrum was recorded to ensure sample integrity. If necessary, a fresh sample solution was prepared. The samples were prepared in acetonitrile to yield an optical density of 0.18 at 520 nm in a 1 mm cuvette. The beam diameter of the pump beam at the sample position was determined using the Knife-edge technique, i.e. by laterally moving a razorblade across the beam whilst monitoring the intensity of the increasingly clipped beam with a photodiode.
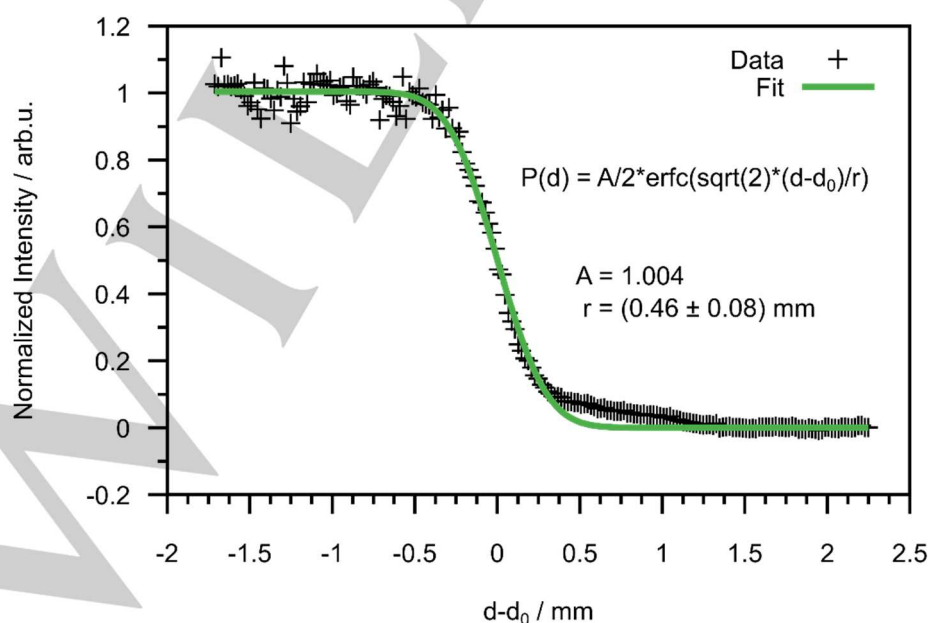
Figure S1. Knife-edge measurement of the pump beam at the sample position (erfc is the complementary error function).

The plot shows:

$$P(d) = A/2 \cdot \mathrm{erfc}(\mathrm{sqrt}(2) \cdot (d-d_0)/r)$$

$$A = 1.004$$
$$r = (0.46 \pm 0.08)\ \mathrm{mm}$$

Data handling

All data manipulation is performed using Scilab.[2] The data sets are corrected for a slightly varied timing by overlapping the coherent artifact regions. The same chirp correction is applied to all datasets and a time interval of ca. 450 fs around time zero is ignored due to strong contributions of the coherent artifact in this temporal window. Most graphic representations are created using Gnuplot (http://www.gnuplot.info) and Inkscape (http://www.inkscape.org).

Results and Discussion

Raw data

Table S1. Measurement parameters in terms of power P, fluence F (beam diameter at sample position of 940 μm, see Figure S1), photon density N and the respective color code used throughout the manuscript.

P / mW	P(rel.)	F / (mJ cm^{-2})	N / (10^{15} photons cm^{-2})	Color Code
0.4	1.0	0.12	0.4	
0.5	1.3	0.14	0.6	
0.6	1.5	0.17	0.7	
0.75	1.9	0.22	0.8	
0.9	2.3	0.26	1.0	
1	2.5	0.29	1.1	
1.25	3.1	0.36	1.4	
1.5	3.8	0.43	1.7	
1.75	4.4	0.50	1.9	
2	5.0	0.58	2.2	
2.5	6.3	0.72	2.8	
3	7.5	0.87	3.3	
3.5	8.8	1.01	3.9	
5.6	14.0	1.61	6.2	
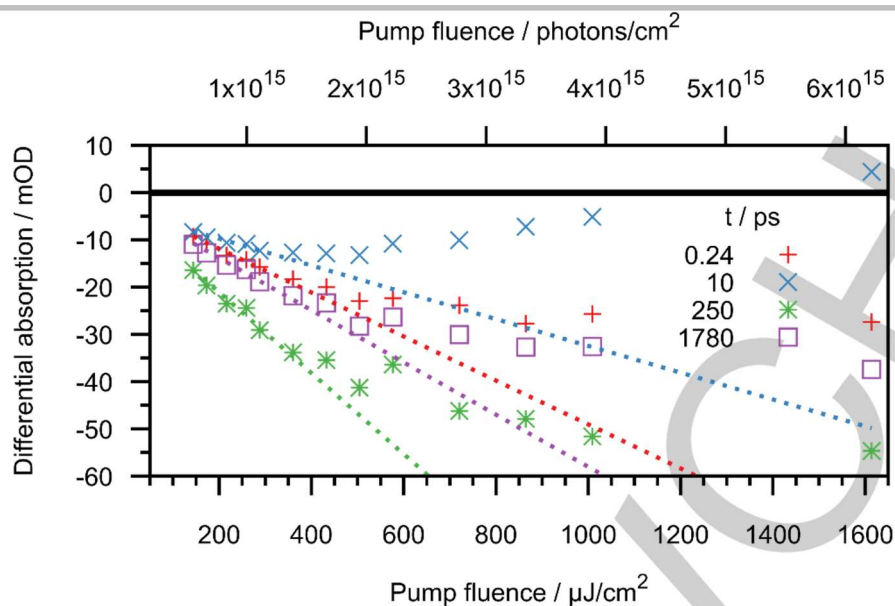
Figure S2. Absolute signal intensities at 577 nm as a function of excitation power (averaged over three consecutive time points and ca. 8 nm spectral bandwidth) are shown as symbols for four different delay times being   0.24 (red) , 10 (blue), 250 (green), 1780 ps (violet). The dashed lines represent linear fits of the first six data points (powers up to 1 mW or a fluence of 0.29 mJ/cm²). Note: The range of the linear fit to cover the first six data points has been arbitrarily chosen.

Figure S2 contains raw signal amplitudes as a function of the excitation power at the central wavelength (577 nm) of the [1]MLCT(Fe)-bleach signature for selected delay times. Up to ca. 0.29 mJ/cm² the *absolute value* of experimental signal intensity (symbols) at the delay times shown increases. The first six data points can be well fitted to a linear dependence (shown as dashed lines). For the data points recorded at pump fluences higher than 0.29 mJ/cm² there are clear deviations from the linear function that well describes the data points recorded at pump fluences up to 0.29 mJ/cm². In detail, the experimental signal values are smaller (i.e. less negative) than expected. Furthermore, the signal value at a delay time of 10 ps even becomes positive, which suggests a rather significant change of the photo-induced dynamics at the highest pump fluence probed: The change of sign indicates the presence of a species that causes excited-state absorption in contrast to the species that causes the negative signal contribution probably due to ground-state bleach. Deviations from a linear dependence of the measured signal intensity on the pump fluence are observable over the whole delay range probed and indicate non-linear signal contributions at elevated pump powers.
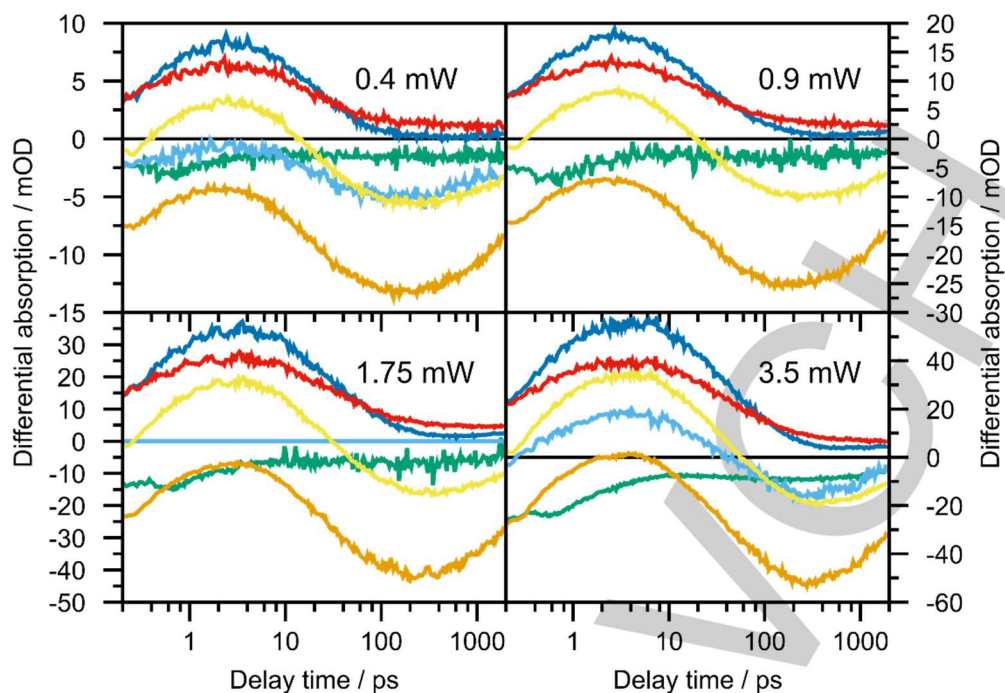
Figure S3. Raw kinetic traces at selected wavelengths for four selected powers. The legend is given below.
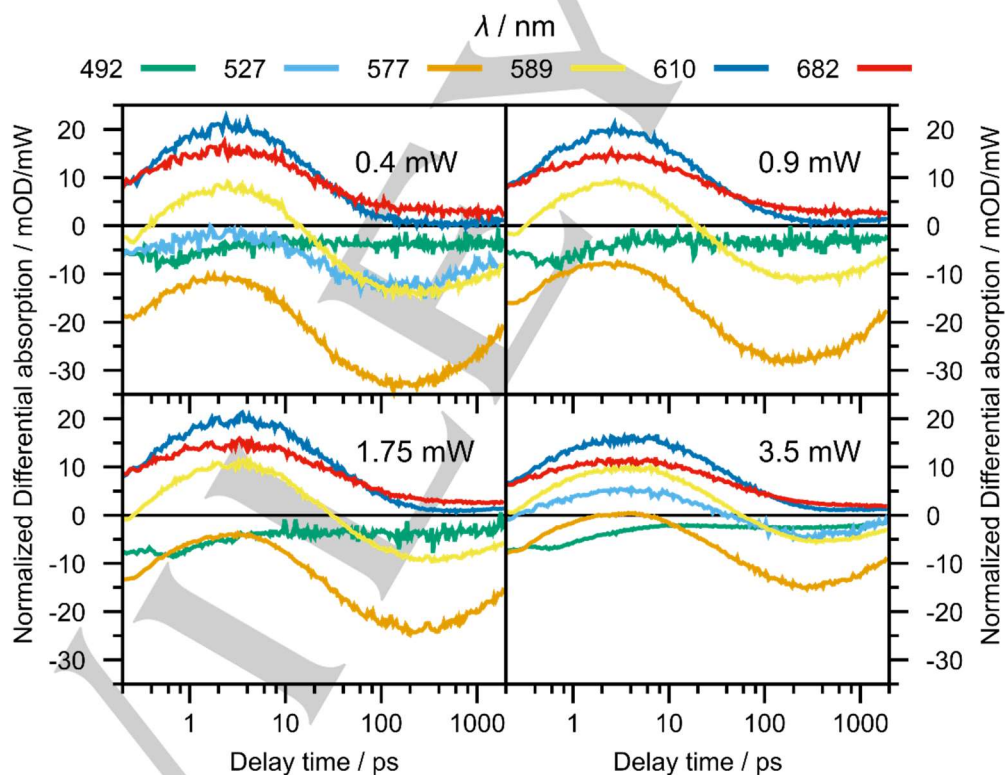
Figure S4. Pump-power normalized kinetic traces at selected wavelengths for four selected powers.
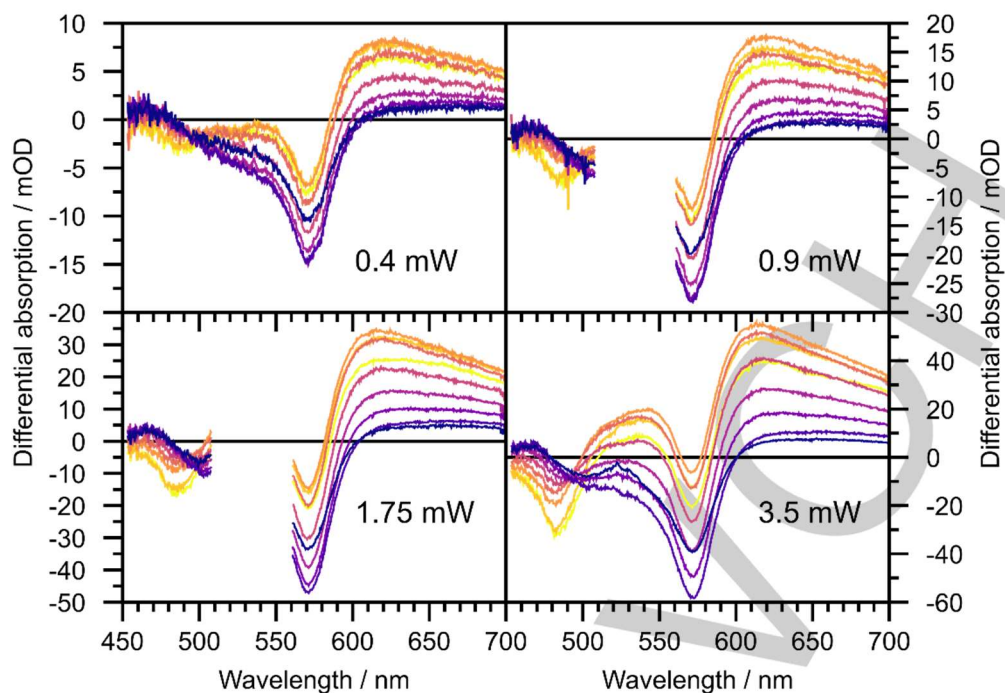
Figure S5. Raw transient spectra at selected delay times for four selected powers. The legend is given below.
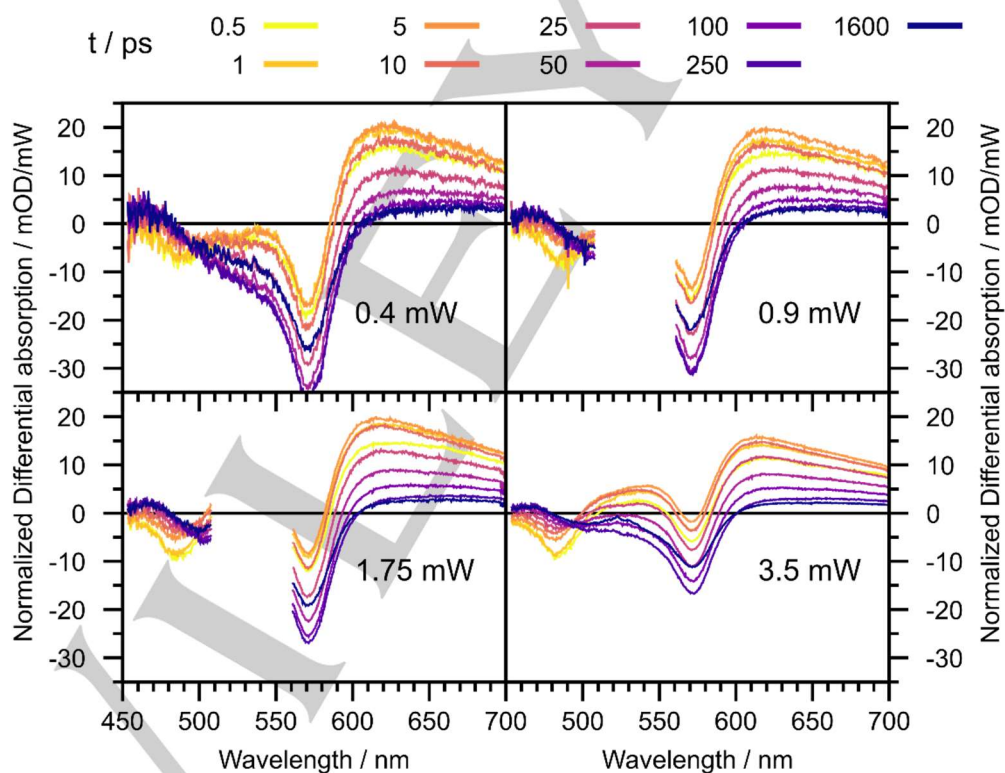
Figure S6. Pump-power normalized transient spectra at selected delay times for four selected powers.

A careful look into dynamics in the first picosecond
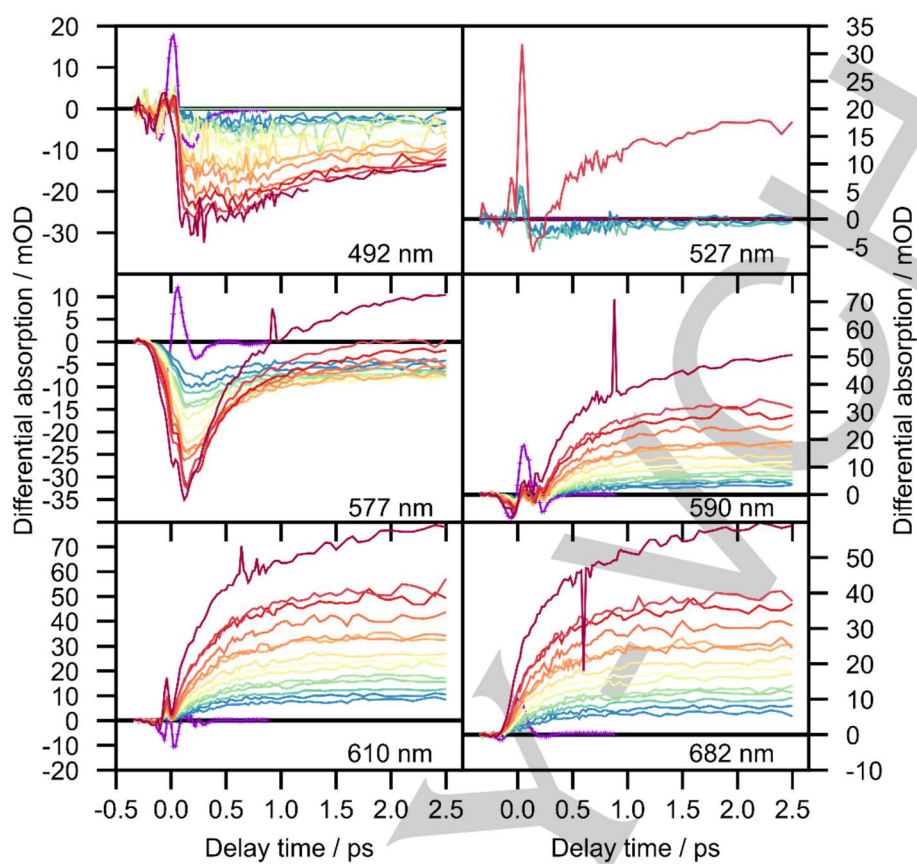
Figure S7. Raw kinetic traces at selected wavelengths. The color-code from blue (low excitation powers) to dark red (highest excitation powers) is given in Table S1. The violet curve in all panels is the coherent artifact in pure solvent, which was separately measured with a power of 5 mW.
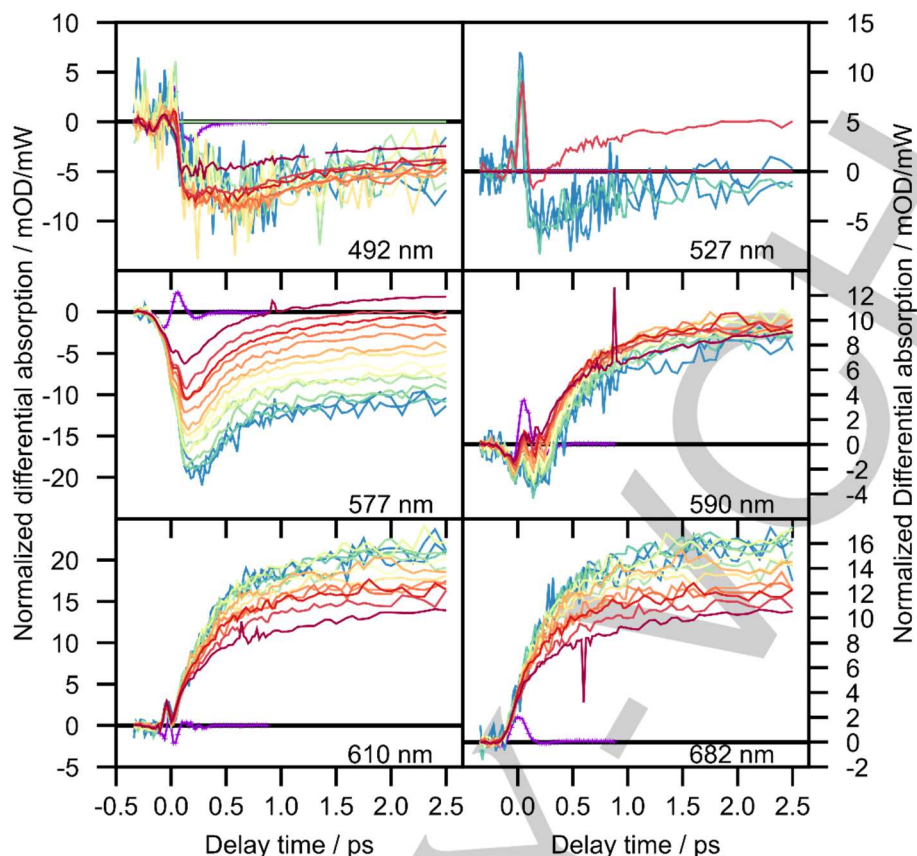
Figure S8. Pump-power normalized kinetic traces at selected wavelengths. The color-code from blue (low excitation powers) to dark red (highest excitation powers) is given in Table S1. The violet curve in all panels is the coherent artifact in pure solvent, which was separately measured with a power of 5 mW.

Firstly, by inspecting the pump-power normalized kinetic traces (Figure S8), particularly those at 610 nm, it can be concluded that the normalization by pump is valid, as the coherent artifacts in all curves line up (at least at 610 nm). The (very) early rising edge fits well e.g. for 610 and 682 nm. Thus, at these wavelengths the early signal rise is dominated by pulse characteristics, including the solvent interaction, which gives rise to the coherent artifact. However, at some wavelengths there are clear deviations already on the sub 200 fs timescale. Prominently, this is the case for 527, 577 and 590 nm (and probably for 492 nm, but the S/N ratio for the lower powers is rather bad). At these wavelengths, signatures of the ^{1}MLCT states are expected. Therefore, possible variations of the photoinduced dynamics in dependence of the pump power may indeed be due to singlet-singlet annihilation. Unfortunately, due to the limited temporal resolution of our experiment, we are not able to provide deeper insight at this stage.
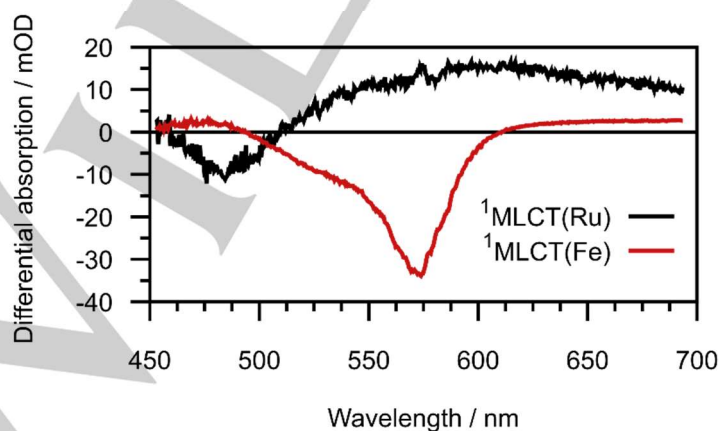
Figure S9. Average spectrum of the initially excited state after excitation of **RuFeRu** at 575 nm (^{1}MLCT(Fe)). This spectrum was scaled and subtracted from the average transient absorption spectrum (between 0.24 and 0.42 ps) measured after excitation at 530 nm (dataset measured at 0.6 mW). The scaling factor was chosen based on the elimination of ^{1}MLCT(Fe) features in the remaining spectrum, which should roughly describe the ^{1}MLCT(Ru).

8
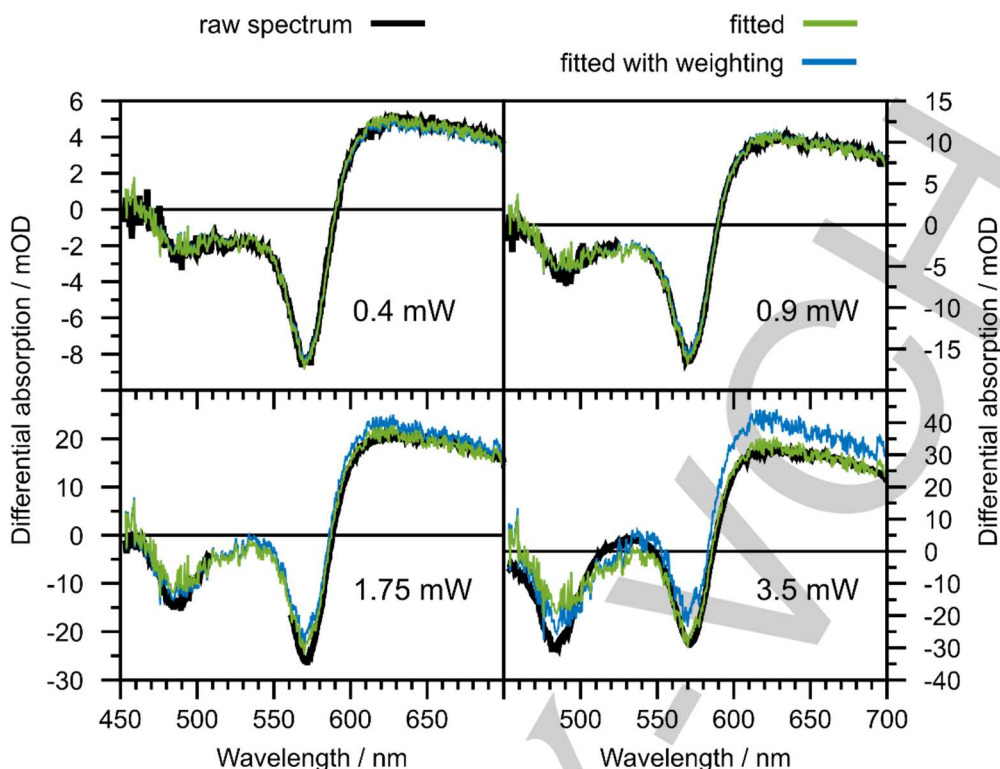
Figure S10. Initial spectra (0.24-0.42 ps) fitted as a linear combination of the spectra from Figure S9. The fits are perfect for the lower powers, but show some weaknesses at the highest powers. This is addressed by performing the fit both unweighted and with particular weighting of the region of [1]MLCT(Ru)-bleach (from 453 to 497.4 nm). The fitted parameters are plotted in Figure S11.
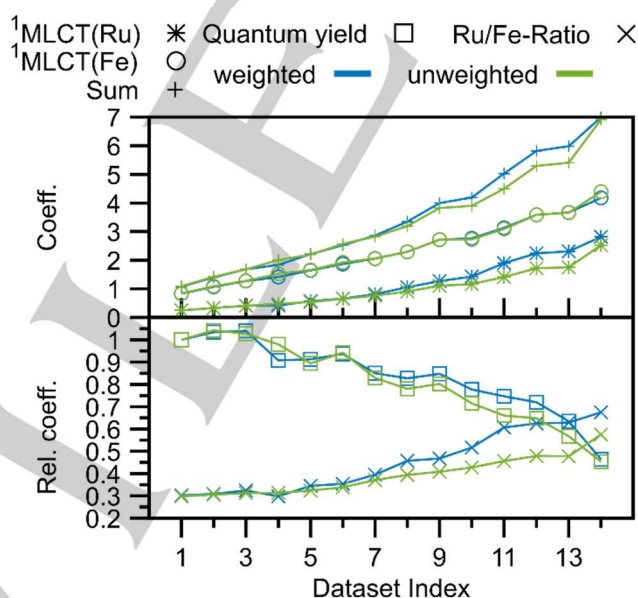
Figure S11. Results from the fit of the initial spectra performed weighted and unweighted in the [1]MLCT(Ru) region. The coefficients "[1]MLCT(Ru)" and "[1]MLCT(Fe)" have been normalized to the initial value at the lowest pump power (0.25 for [1]MLCT(Ru) and 0.75 for [1]MLCT(Fe)). The sum of these coefficients ("sum") is a measure of the overall number of excited states. "Ru/Fe-Ratio" is the ratio of the coefficients "[1]MLCT(Ru)" and "[1]MLCT(Fe)". This ratio is ca. 0.3 for the lowest powers and increases for the data recorded at higher pump powers. The quantum yield ("Sum" divided by the excitation power) decreases with increasing excitation power, suggesting non-linear effects, such as singlet-singlet annihilation, already on the sub 200 fs-timescale.

Raw transient absorption spectra at selected delay times for all pump powers
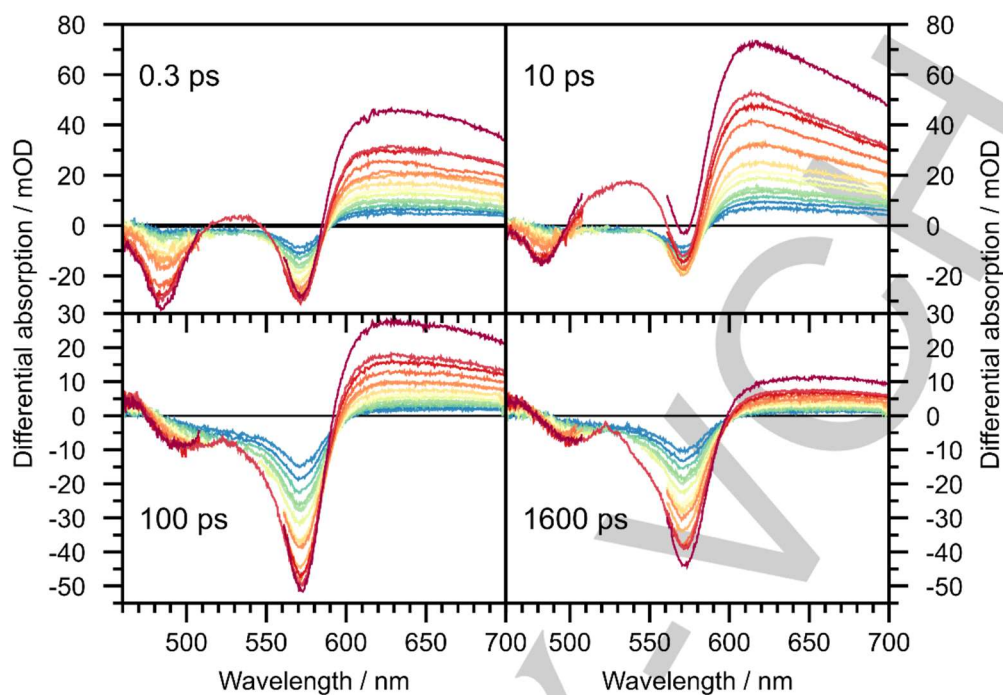
Figure S12. Transient absorption spectra for four selected delay times (0.3, 10, 100 and 1600 ps). The spectral region between 500 and 550 nm (or an interval as needed), is ignored for most measurements due to overlap with pump scatter. The color-code from blue (low excitation powers) to dark red (highest excitation powers) is given in Table S1.

Absorption spectra, role of the split ratio and other details of the low-P kinetic model
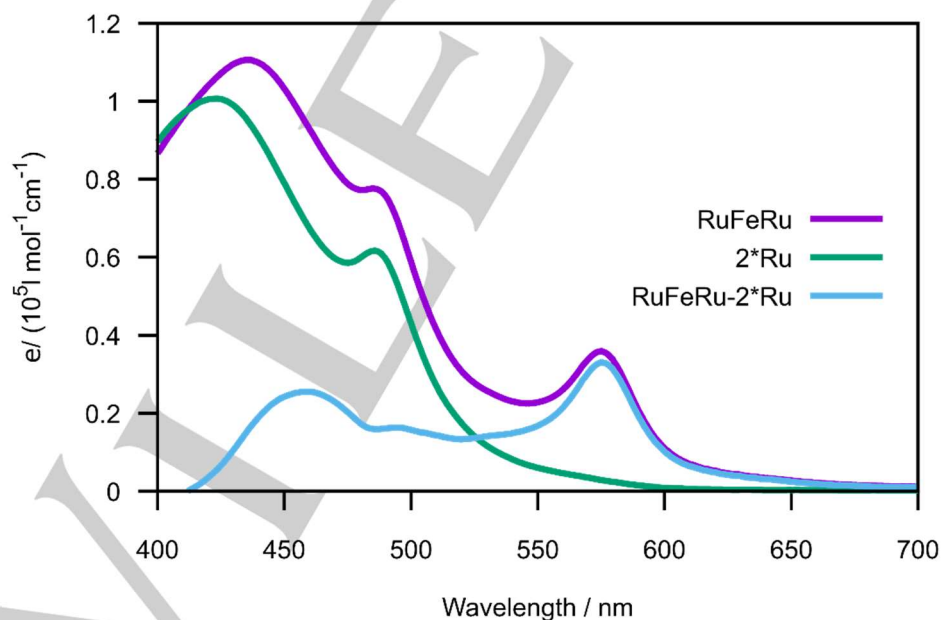
Figure S13. Absorption spectra in acetonitrile solution of **RuFeRu** (violet line) as well as twice the absorption spectrum of the mononuclear Ru-complex with the same ligands ("2*Ru", green line). The absorption spectrum of the hypothetic molecule "Fe" (light blue line) is calculated by subtracting the "2*Ru" spectrum from the absorption spectrum of **RuFeRu**.
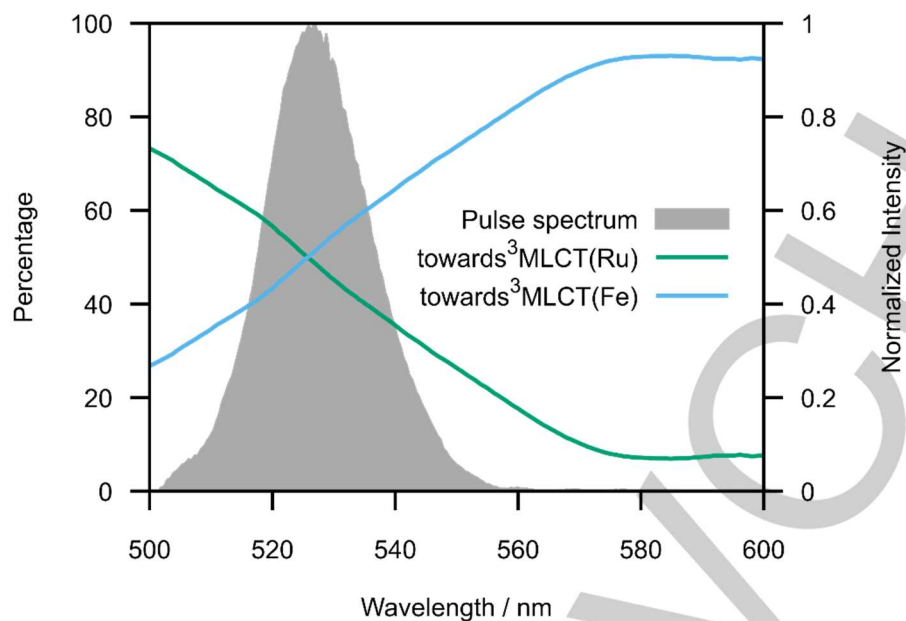
Figure S14. Wavelength-dependent excitation probabilities (left axis) for ^{1}MLCT(Ru) (green line) and ^{1}MLCT(Fe) (light blue line) based on the assumption that only these two transitions give rise to absorbance of **RuFeRu** at wavelengths longer than 500 nm. For the calculation of the fractions, the spectra shown in Figure S3 are used. The averaged pump pulse spectrum recorded as scatter in the measurements is shown in grey (right axis).

The parameter that allows the flexibility to adjust the kinetic model for low excitation intensities according to the excitation wavelength is the initial ratio of for Ru- vs. Fe-^{1}MLCT excitation. This number is not readily available from UV/Vis-absorption data due to the larger number of optically allowed transitions in the spectral region of interest. However, assuming a linear combination of the absorption spectrum of **Ru**, i.e. the model compound containing no iron center, with the unknown spectrum of a Fe(II)-terpy unit, the ratio for Ru/Fe-^{1}MLCT excitation can be estimated to be roughly 1 to 1 at 530 nm (see Figure S14). This ratio is a crucial parameter in order to obtain reasonable species spectra from the fit. The split ratio is included in the fit via the parameter dvra, which is defined as dvra = (1-x)/x (x is the fraction that initially populates the ^{1}MLCT(Fe)). The influence of dvra on the fit results is shown in Figure S15. There is a discrepancy between the estimation based on the UV/Vis absorption spectra suggesting a 1:1 ratio (Ru/ Fe-excitation) to a 1:3 ratio (based on dvra of ca 0.3, see Figure S15). An explanation for that could be ultrafast singlet energy transfer (between the ^{1}MLCT(Ru) and the ^{1}MLCT(Fe)) transferring 50 % of the initial population in the ^{1}MLCT(Ru) state to the ^{1}MLCT(Fe).
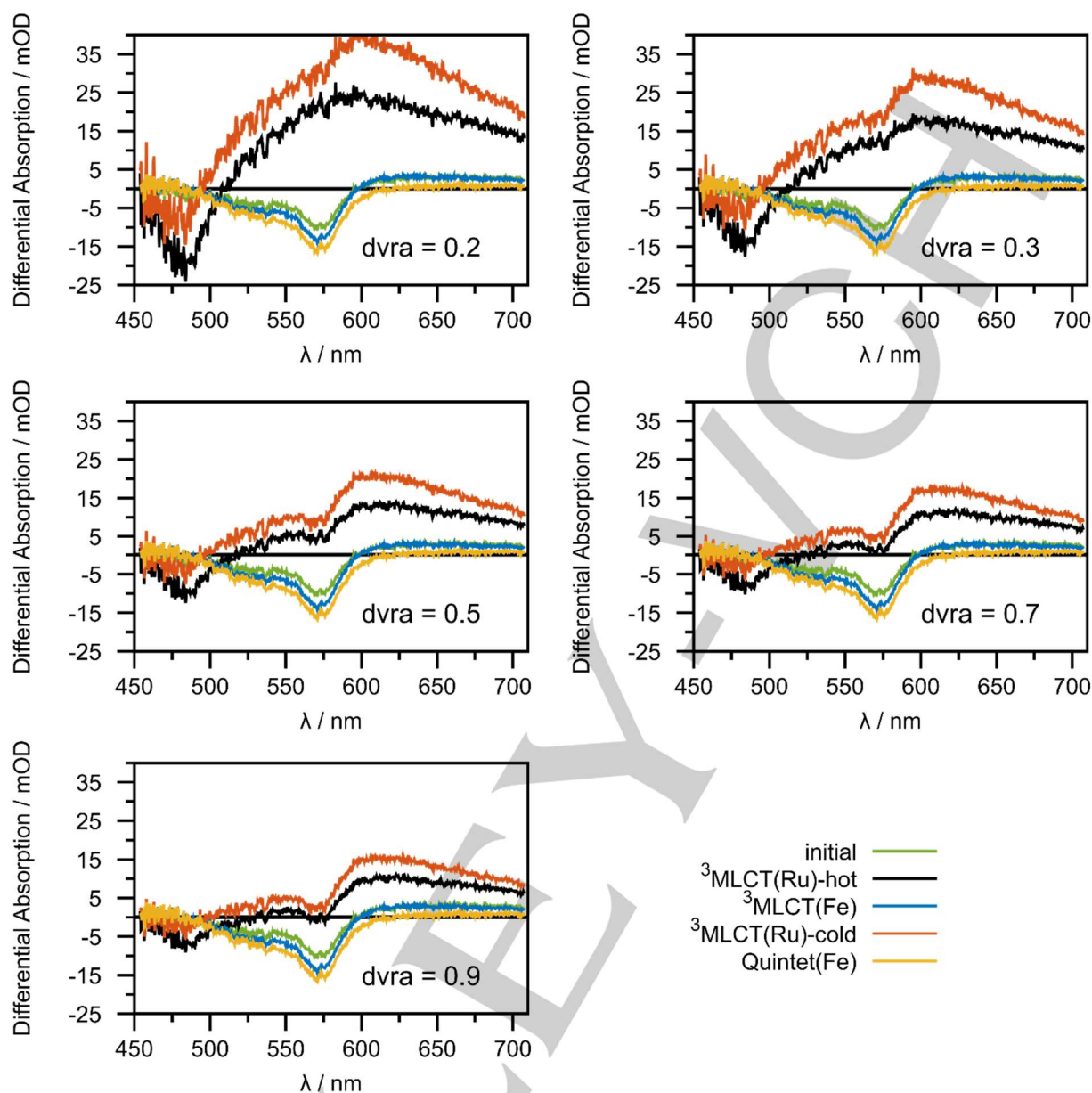
Figure S15. Species spectra from fits of the data acquired at P = 0.4 mW according to the photophysical model for **RuFeRu** in the low-pump-power regime (see manuscript and reference 2) for different split-ratios (parameter dvra). Changing this parameter does not influence the error that is minimized in the fit routine, yet the resulting species spectra are clearly dependent on this parameter. At dvra > 0.7 the bleach signature of the [1]MLCT(Fe) band is clearly present also in the spectra for Ru-based states, and still visible at dvra = 0.5. On the other hand, at dvra = 0.2 the bleach of the [1]MLCT(Ru) band below 500 nm in the spectrum of the [3]MLCT(Ru)-hot state has an amplitude that seems too large given the fact that the extinction coefficients of the [1]MLCT(Fe) and the [1]MLCT(Ru) bands are rather similar. Due to these observations, the optimal split-ratio should be larger than 0.2 and smaller than 0.5.

In contrast to previous work,[3] the species spectrum of the equilibrated state ([3]LC) could not be extracted from the dataset recorded at the lowest pump power. This is due to its inherently low amplitude and the fact that its weight becomes more significant only at delay times > 4-5 ns,[3] when the major portion of the Quintet(Fe) state is already depopulated (k_5 = (4.2 ns)$^{-1}$). The experimental setup employed in this study allowed maximal pump probe delays of ca. 2 ns.

Simulation of multiple absorption events

The possible multiple absorption events have been simulated based on

$N_{events} = \sigma_{abs.} * N_{molecules} * N_{photons} / A$,

where $\sigma_{abs.}$ is the absorption cross section and A is the area of the focal spot. We assume that the total absorption cross section at the given excitation wavelength is the sum of two parts σ_{abs}([1]MLCT(Ru)) and one part σ_{abs}([1]MLCT(Fe)) in the ground state (estimated from absorption spectra, see above). For the multiply excited species, depending on the first absorption event, the total absorption cross section is reduced by either σ_{abs}([1]MLCT(Ru)) or σ_{abs}([1]MLCT(Fe)).

Since there are two Ru-moieties, the probability for excitation of the ^{1}MLCT(Ru) is roughly the same as that for excitation of the ^{1}MLCT(Fe). Once either transition is excited, the absorption of the respective excited-species will be reduced due to ground-state bleach, which is likely the dominant contribution at early delay times.

A simulation of the multiple excitation events was carried out, considering that upon Ru (or Fe)-excitation the absorption cross section is reduced by σ(Ru), green arrows, or σ(Fe), yellow arrows (see Figure 1).

The results of this simulation are included as bar plot in Figure 1 in the manuscript (normalized to the overall number of excited molecules at the corresponding excitation power). Further they are shown in Figure S16 (normalized to the overall number of excited molecules at the corresponding excitation power) as well as in Figure S17 (fractions of the possible excited species for all pump powers normalized to the number of excited molecules at the lowest pump power). The largest portion is for all conditions that of the singly excited species, whereas their relative portion decreases for higher fluences due to multiple excitation processes. The only multiply excited species, which is formed in substantial amounts is the mixed-doubly excited species **Ru*Fe*Ru**. The yield for the species with two-fold ^{1}MLCT(Ru)-excitation (**Ru*FeRu***) is below 5 percent even for the highest fluences probed. Likewise, the portion of triply excited **Ru*Fe*Ru*** is quite low even for the highest powers.

A somewhat subtle aspect is the different probability for double excitation in **Ru*FeRu** as compared to that of **RuFe*Ru**. This eventually causes a power-dependent ratio of the number of the singly excited species. Since the Fe/Ru-excitation probability from the ground-state to form either **RuFe*Ru** or **Ru*FeRu** (or the identically treated **RuFeRu***) is constant, the declining ratio N(**Ru*FeRu**)/N(**RuFe*Ru**) produced in the simulation is due to the absorption of a second photon: accompanied with the formation of doubly-excited species is the depletion of singly-excited species.
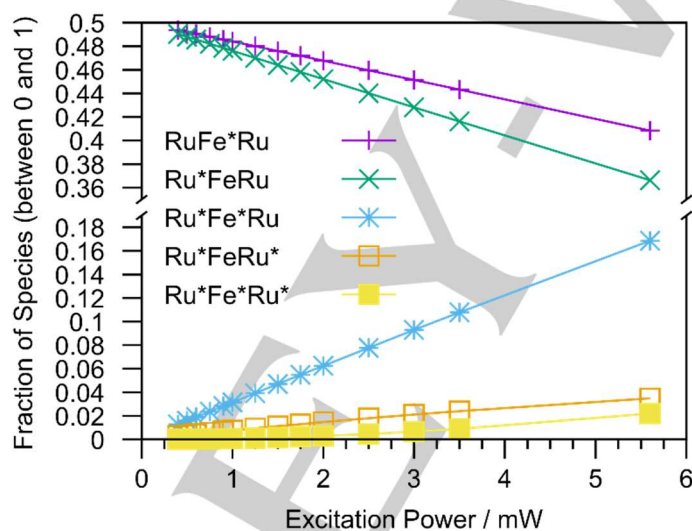
Figure S16. Results from the excitation simulation under the experimental parameters used. For each excitation-power value, the number (amount) of each excited species was divided by the sum of all excited species at that excitation power. The y-axis is interrupted from 0.19 to 0.35.
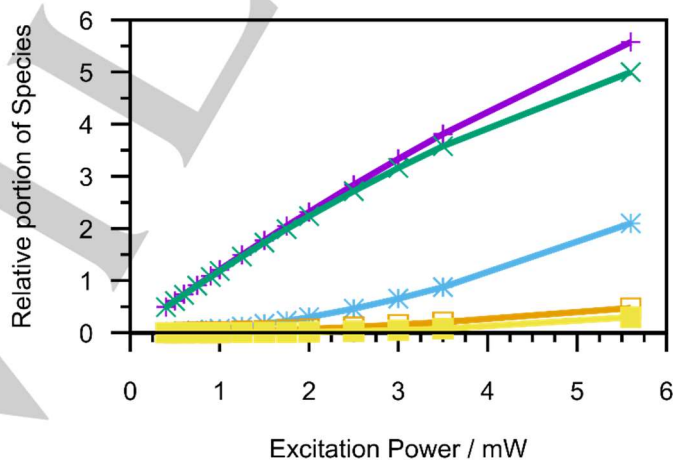
Figure S17. Results from the excitation simulation under the experimental parameters used. For each excitation-power value, the number (amount) of each excited species was divided by the sum of all excited species at the lowest excitation power. The legend is the same as that in Figure S6.

13

Scilab-Code for the excitation simulation

```
//datasetnumbers contains pump powers in mW
datasetnumbers = [0.4 0.5
// for the generation of random numbers between 0 and 1
rand('seed',getdate('s'));
rand('uniform');
tic();


AbsCrossStotal=9.79E-21; //m^2/molecule (total CrossS at ca. 530 nm)
AbsCrossSFe=0.5*AbsCrossStotal;
AbsCrossSRu=0.25*AbsCrossStotal;
// focal spot size: radius 0.47 µm
Apump=6.93978E-07; // pumped area in m^2,
MoleculesInFocus=2.59106E+13 // molecules 0.062 mol/m^3.
wavelength=527; // in nm
// Ephoton = h*c/lambda
Ephoton=6.626E-34*299792458/(wavelength*0.000000001) // in J
// Calculation of Energy per pulse for all powers. 500 Hz rep.-rate
Epuls=datasetnumbers ./ (500/1E-3);

Nph=Epuls ./ Ephoton;

groundstates = MoleculesInFocus;

f=scf(25);
clf;

NRu1Fe0list=zeros(1,14);
NRu0Fe1list=zeros(1,14);
NRu1Fe1list=zeros(1,14);
NRu2Fe0list=zeros(1,14);
NRu2Fe1list=zeros(1,14);

for j=1:14
    photons=Nph(j);
    groundstates = MoleculesInFocus;
    NRu0Fe1=0;
    NRu1Fe0=0;
    NRu1Fe1=0;

    // Ru1Fe1 can be created in two different channels (a and b)
    NRu1Fe1a=0;
    NRu1Fe1b=0;

    NRu2Fe0=0;
    NRu2Fe1=0;

    // Ru2Fe1 can be created in two different channels (a and b)
    NRu2Fe1a=0;
    NRu2Fe1b=0;

    mprintf("Dataset %i - %i s\n",j, toc());
    photonsabsorbed=0;

    // Number of photons that hit molecules at the same time,
    // i.e. with identical absorption probability
    stepsize=1E8;

    steps=round(groundstates/stepsize);

    for i=1:steps
        pAbs=stepsize*(2*AbsCrossSRu+AbsCrossSFe)/Apump;

        // Numbers of singly excited species
        excitedstates=(photons-photonsabsorbed)*pAbs;
        photonsabsorbed=photonsabsorbed+excitedstates;

        // reduction of number of groundstates
        groundstates=groundstates-excitedstates;

        // percentage of Ru1Fe0 and Ru0Fe1 of those
        Feportion = AbsCrossSFe/(2*AbsCrossSRu+AbsCrossSFe);
        Ruportion = 1-Feportion;

        NRu0Fe1=NRu0Fe1+Feportion*excitedstates;
        NRu1Fe0=NRu1Fe0+Ruportion*excitedstates;

        // Double excitation -> from NRu1Fe0
        pAbs2a = Ruportion*excitedstates*(AbsCrossSRu+AbsCrossSFe)/Apump;

        // Double excitation -> from NRu0Fe1
        pAbs2b = Feportion*excitedstates*(2*AbsCrossSRu)/Apump;

        // now the 2nd excitation of Ru1Fe0 and Ru0Fe1 has to be
        // treated separately. Since absorption will reduce the total
```

```
// number of available photons, there will be a 50:50 chance
// which 2nd excitation is treated first

fe=0;
if rand() < 0.5 then
    fe=1; // i.e. Ru0Fe1 has been treated.
    excitedstates2b=(photons-photonsabsorbed)*pAbs2b;
    photonsabsorbed=photonsabsorbed+excitedstates2b;
end

excitedstates2a=(photons-photonsabsorbed)*pAbs2a;
NRu1Fe1a=NRu1Fe1a+AbsCrossSFe/(AbsCrossSFe+AbsCrossSRu)*excitedstates2a;
NRu2Fe0=NRu2Fe0+AbsCrossSRu/(AbsCrossSFe+AbsCrossSRu)*excitedstates2a;
photonsabsorbed=photonsabsorbed+excitedstates2a;

if fe == 0 then // if Ru0Fe1 has been not been treated yet
    excitedstates2b=(photons-photonsabsorbed)*pAbs2b;
    photonsabsorbed=photonsabsorbed+excitedstates2b;
end

// reduction of number of singly excited species
NRu1Fe0=NRu1Fe0-excitedstates2a;
NRu0Fe1=NRu0Fe1-excitedstates2b;

NRu1Fe1b=NRu1Fe1b+excitedstates2b;

NRu1Fe1=NRu1Fe1a+NRu1Fe1b;

// from Ru1Fe1
pAbs3a=(AbsCrossSFe/(AbsCrossSFe+AbsCrossSRu)*excitedstates2a+excitedstates2b)*AbsCrossSRu/Apump;
// from Ru2Fe0
pAbs3b=AbsCrossSRu/(AbsCrossSFe+AbsCrossSRu)*excitedstates2a*AbsCrossSFe/Apump;

fe=0;
if rand() < 0.5 then
    fe=1;
    excitedstates3b=(photons-photonsabsorbed)*pAbs3b;
    photonsabsorbed=photonsabsorbed+excitedstates3b;
end

excitedstates3a=(photons-photonsabsorbed)*pAbs3a;
photonsabsorbed=photonsabsorbed+excitedstates3a;

if fe == 0 then
    excitedstates3b=(photons-photonsabsorbed)*pAbs3b;
    photonsabsorbed=photonsabsorbed+excitedstates3b;
end

// reduction of number of doubly excited species
NRu1Fe1=NRu1Fe1-excitedstates3a;
NRu2Fe0=NRu2Fe0-excitedstates3b;

NRu2Fe1=NRu2Fe1+excitedstates3a+excitedstates3b;
end

mprintf("Exc. Power: %f mW - %i percent of photons absorbed. %f Photons per molecule\n",datasetnumbers(j),
(photonsabsorbed/photons)*100,round((photonsabsorbed)/MoleculesInFocus*100)/100 );
mprintf(" NRu1Fe0: %f \n",NRu1Fe0);
mprintf(" NRu0Fe1: %f \n",NRu0Fe1);
mprintf(" NRu1Fe1: %f \n",NRu1Fe1);
mprintf(" NRu2Fe0: %f \n",NRu2Fe0);
mprintf(" NRu2Fe1: %f \n",NRu2Fe1);

end
```

Modeling of the experimental data (global fit based on the low-P model)
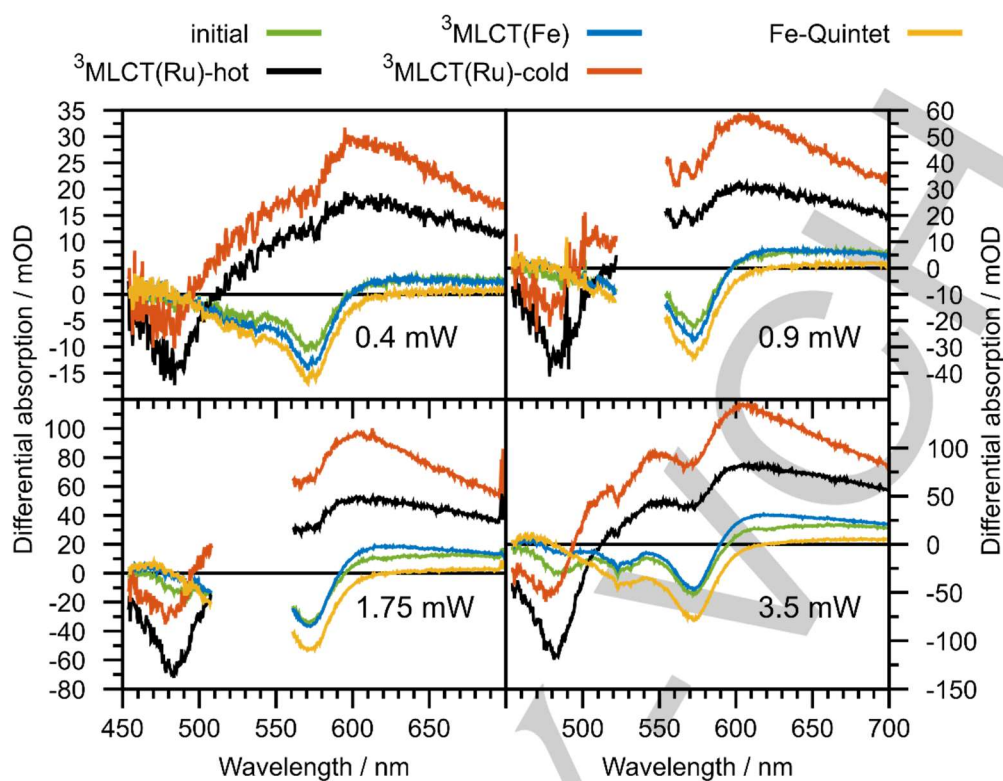
Figure S18. Species spectra from global multiexponential fits of the pump-power dependent datasets based on the kinetic scheme for **RuFeRu** (Figure 2 in the manuscript). The fits have been performed individually for all datasets optimizing both spectra and rates (see Figure S19). Shown here are the species spectra for four selected datasets. The fits describe the data well (Figure S20), but there are power-dependent changes of the species spectra: For both the ^{3}MLCT(Ru)-hot and the ^{3}MLCT(hot) the ratio between the negative signal amplitude around 480 nm and the positive signal at around 600 nm changes. Also, the ratio between the negative signal in the spectra of the ^{3}MLCT(Fe) to the positive signal above 600 nm changes. These observations are explained by mixing of the species spectra, and indicate that the kinetic scheme is incorrect.
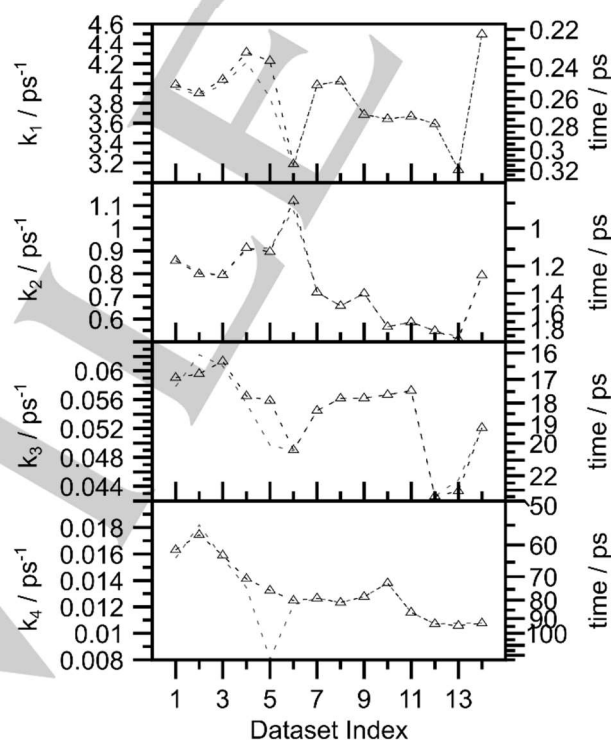
Figure S19. Rate constants from a global multiexponential fit based on the kinetic scheme for **RuFeRu** (Figure 2 in the manuscript). The fits have been performed individually for all datasets optimizing both spectra and rates (the rate k_5 has been kept constant at $(4200 \text{ ns})^{-1}$). Except for k_1 there is a tendency of decreasing rates (increasing time constants) for the processes, which resemble the temporal delay of the minimum in the kinetics at 577 nm at increased pump powers, which is best visible in the plots with kinetic traces at all pump powers, e.g. Figure 5B in the manuscript.

16
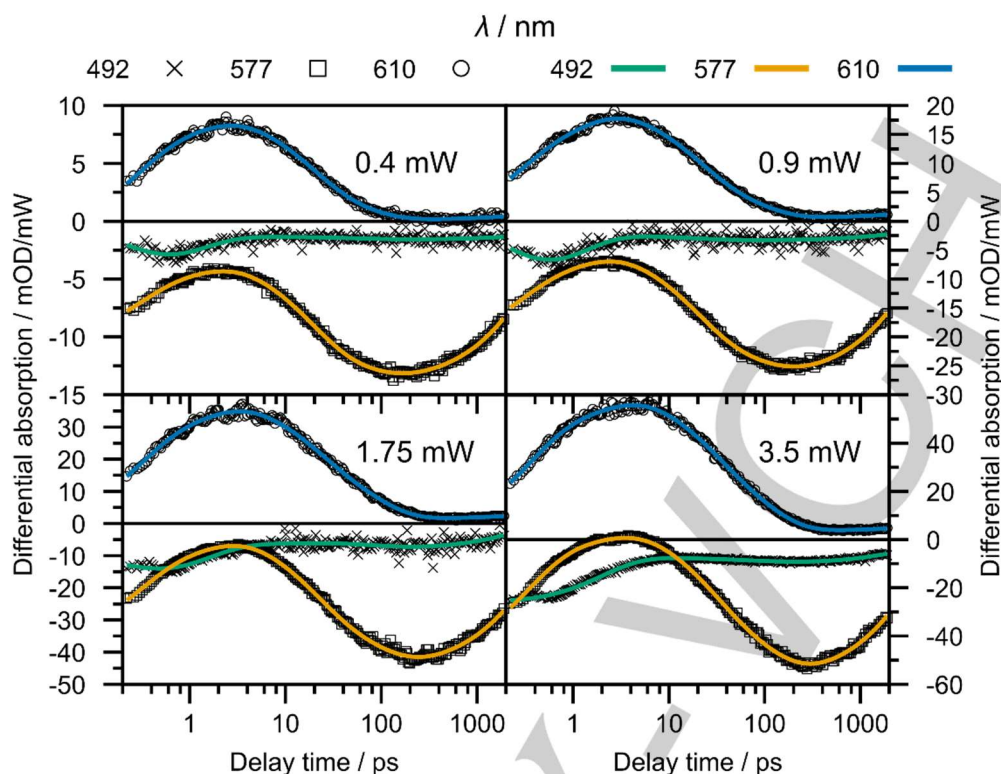
Figure S20. Experimental kinetic traces and respective fit results from a global multiexponential fit based on the kinetic scheme for **RuFeRu** (Figure 2 in the manuscript).

Common approaches to data analysis such as singular value decomposition are not conclusive in the present case, because there is a linear dependence of the individual spectra, such that the characteristics of ^{3}MLCT(Ru) and ^{3}MLCT(Fe) occur mix in the species spectra. This mutual dependence is also reflected in the fact that variation of the split ratio dvra does not influence the fit quality, but has significant impact on the resulting species spectra (Figure S15).

A description of the power-dependent datasets based on the known kinetic scheme as described (**Fehler! Verweisquelle konnte nicht gefunden werden.**) is problematic concerning the physical interpretability. This is because such approach may only generate an overall description of the datasets with common spectra and kinetic behavior. Therefore, this may give an idea of the average contribution of all molecules in the sample volume. However, the gradual influence of increasing excitation power on the photoinduced dynamics points towards the increasing influence of additional species. Nevertheless, a global fit optimizing both spectra and time constants has been performed for completeness. The respective results are discussed above ("Modeling of the experimental data model", Figure S18-19).

Modeling of the experimental data (scheme combining low-P and high-P model)

To model the experimental data, the two kinetic schemes corresponding to low-P and high-P model, respectively, are kept constant (i.e. the time constants are not varied), but are scaled and added up (see Figures 6 and 7 in the manuscript). The two-dimensional (time, wavelength) data matrix **A** is calculated as the matrix product of the n*k time-dependent matrix **C** with and the k*m matrix **S** containing the spectra of the k individual components.[4] Here, the time-dependent matrix **C** is treated as the weighted sum of the individual matrices **C**(low-P) and **C**(high-P). The matrix **S** contains the species spectra shown in Figure 2B (obtained using the low-P model and the dataset recorded at lowest pump power).

The scaling factors (weights) of the individual matrices C1 and C2 as well as the ffac-parameters o_{full} and w were fitted in a two-step routine. The two ffac parameters were fitted globally for all datasets (i.e. such that the parameter values minimize the error for all datasets at the same time), while the scaling factors are optimized for each dataset (i.e. recorded at a specific pump power).

References

[1]   J. Kübel, A. Winter, U. S. Schubert, B. Dietzek, *J. Phys. Chem. A* **2014**, *118*, 12137-12148.
[2]   S. Enterprises, (64-bit Windows, Version 5.52) ed., **2012**.
[3]   M. Wächtler, J. Kübel, K. Barthelmes, A. Winter, A. Schmiedel, T. Pascher, C. Lambert, U. S. Schubert, B. Dietzek, *Phys. Chem. Chem. Phys.* **2015**, *18*, 2350-2360.
[4]   C. Ruckebusch, M. Sliwa, P. Pernot, A. de Juan, R. Tauler, *J. Photochem. Photobiol., C* **2012**, *13*, 1-27.

Author Contributions

JK, MW and BD conceived the work. MW and BD supervised the work. JK performed the experiments and processed the data. All authors contributed to data analysis and interpretation. JK wrote the manuscript with input from MW and BD.

P6 - Efficient Energy Transfer and Metal Coupling in Cyanide-Bridged Heterodinuclear Complexes Based on (Bipyridine)(terpyridine)ruthenium(II) and (Phenylpyridine)iridium(III) Complexes

Efficient Energy Transfer and Metal Coupling in Cyanide-Bridged Heterodinuclear Complexes Based on (Bipyridine)(terpyridine)ruthenium(II) and (Phenylpyridine)iridium(III) Complexes

Kevin Barthelmes,[†,‡] Michael Jäger,[†,‡] Joachim Kübel,[§,⊥] Christian Friebe,[†,‡] Andreas Winter,[†,‡] Maria Wächtler,[§] Benjamin Dietzek,[§,⊥,‡] and Ulrich S. Schubert*,[†,‡]

[†]Laboratory of Organic and Macromolecular Chemistry, Friedrich Schiller University Jena, Humboldtstraße 10, 07743 Jena, Germany
[‡]Center for Energy and Environmental Chemistry, Friedrich Schiller University Jena, Philosophenweg 7a, 07743 Jena, Germany
[§]Leibniz Institute of Photonic Technology, Albert-Einstein-Straße 9, 07745 Jena, Germany
[⊥]Institute of Physical Chemistry and Abbe Center of Photonics, Friedrich Schiller University Jena, Helmholtzweg 4, 07743 Jena, Germany

S *Supporting Information*

ABSTRACT: We report a series of cyanide-bridged, hetero-dinuclear iridium(III)−ruthenium(II) complexes with the generalized formula $[Ir((R_2)_2\text{-ppy})_2(CN)(\mu\text{-CN})Ru(bpy)(tpy\text{-}R_1)]PF_6$ (ppy = 2-phenylpyridine, bpy = 2,2′-bipyridine, and tpy = 2,2′:6′,2″-terpyridine). The structural, spectroscopic, and electrochemical properties were analyzed in the context of variation of the electron-withdrawing (e.g., −F, −Br, −CHO) and -donating (e.g., −Me) and extended π-conjugated groups at several positions. In total, ten dinuclear complexes and the appropriate model complexes have been prepared. The iridium(III)-based emission is almost fully quenched in these complexes, and only the ruthenium(II)-based emission is observed, which indicates an efficient energy transfer toward the Ru center. Upon oxidation of the Ru center, the fluorinated complexes **2** exhibit a broad intervalence charge-transfer transition in the near-infrared region. The complexes are assigned to a weakly coupled class II system according to the Robin−Day classification. The electronic structure was evaluated by density functional theory (DFT) and time-dependent DFT calculations to corroborate the experimental data.
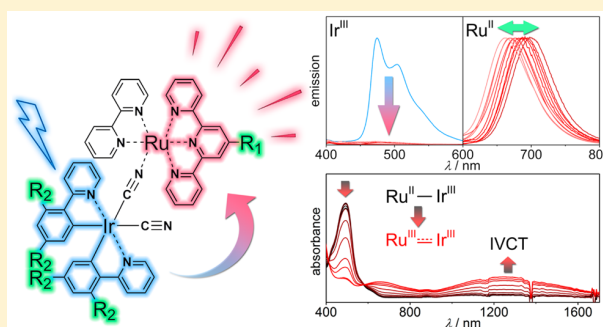
■ INTRODUCTION

During the last decades, polypyridyl complexes of d^6 transition metals have been intensively studied regarding their potential in light-driven devices.[1] The presence of relatively long excited-state lifetimes and sufficiently high quantum yields is the basis for further photoinduced processes that play an important role in the development of light-harvesting antennae or artificial photosynthetic systems. Polypyridyl transition-metal complexes, e.g., of ruthenium(II)[2] and iridium(III),[3] are well-known for their readily tunable photophysical and electrochemical properties. In a covalently bridged multinuclear assembly, the metal's individual properties can be combined. Thereby, the geometry, length, and nature of the bridging ligand are crucial parameters for controlling electronic communication and, thus, the energy- and/or electron-transfer processes between the components.[4] Recently, efficient energy transfer between polypyridyliridium(III) and -ruthenium(II) complexes, i.e., bridged by either *p*-diphenylene,[5] 7,7′-diphenylnorbornane,[6] 3,5-bis(2-pyridyl)-1,2,4-triazole,[7] or

2,3,5,6-tetrakis(2-pyridyl)pyrazine[8] units, was shown. In these heterometallic complexes, the iridium(III)-based emission is strongly quenched by the Ru^{II} center. In contrast, triphenylene units in a meta arrangement lead to weak coupling between the metals and result in two independent metal-based emissions at room temperature.[9] Dual emission is also observed for an ion pair based on anionic $[Ir(ppy)_2(CN)_2]^-$ complexes (ppy = 2-phenylpyridine) and a cationic $[Ru(bpy)_3]^{2+}$ complex (bpy = 2,2′-bipyridine) in a 2:1 stoichiometric mixture.[10] These ion pairs were studied as light-emitting devices and electroluminescent materials.[11]

In the last three decades, research on the very short ambidentate cyanide ligand focused on its use as a bridging unit because it is able to simultaneously bind two metal ions and to promote strong electronic as well as magnetic coupling between them.[12] For example, multinuclear homometallic
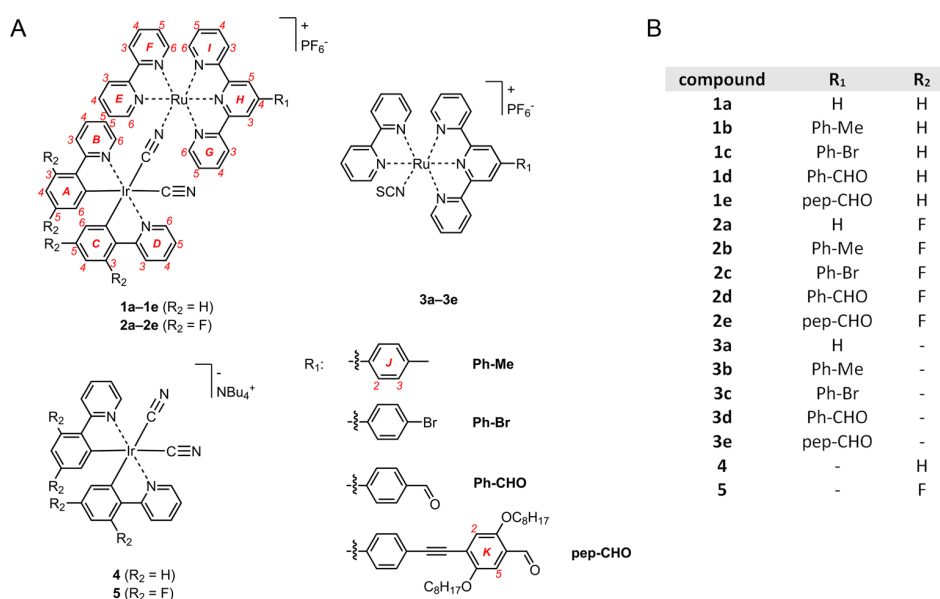
Figure 1. Schematic representation of the cyanide-bridged iridium(III)−ruthenium(II) complexes **1a−1e** and **2a−2e** and their model complexes **3a−3e**, **4**, and **5** (panel A), along with a numbering scheme for the complexes (the numbering is analogous for **3−5**). Panel B lists an overview of the complexes.

ruthenium(II/III) complexes in their mixed-valence (MV) form exhibit a broad intervalence charge-transfer (IVCT) absorption in the near-infrared (NIR) region, which reflects the electronic interactions between both metal centers.[13] Furthermore, related heterometallic ruthenium(II/III) complexes containing Os$^{II/III}$,[12d,13a] Rh$^{I/III}$,[12e,14] Fe^{II},[15] Cr^{III},[12e,15c] or Ln^{III} [16] centers were discussed in the same context of metal coupling. On the other hand, there are a limited number of cyanide-bridged iridium(III) complexes containing Ln^{III},[17] Re^{I},[17] or Ir^{III} [18] centers. However, to the best of our knowledge, a dinuclear system based on cyanide-bridged Ir^{III} and Ru^{II} centers has not yet been established.

Herein, we present the synthesis of such close-coupled heterodinuclear iridium(III)−ruthenium(II) complexes and analyzed the electrochemical and spectroscopic properties with respect to their electronic coupling as well as their capability for light-harvesting antennae. The assemblies consist of [Ru(bpy)(tpy-R$_1$)]$^{2+}$ and [Ir((R$_2$)$_2$-ppy)$_2$(CN)] moieties (tpy = 2,2′:6′,2″-terpyridine) linked by a cyanide group. To gain detailed information about the influence of the ancillary tpy and ppy ligands on the photophysical and electrochemical properties, a systematic variation of the substituents—electron-withdrawing (e.g., −F, −Br, −CHO) and -donating (e.g., −Me) groups—as well as extension of the ligand via π-conjugated groups has been performed. Related mononuclear model complexes based on [Ru(bpy)(tpy-R$_1$)(SCN)]PF$_6$ and anionic Bu$_4$N[Ir((R$_2$)$_2$-ppy)$_2$(CN)$_2$] complexes[19] were used as reference to analyze the photophysical and electrochemical properties of the individual metal centers. The cyanide fragment in the ruthenium model complexes was chosen as the isothiocyanato ligand because the S atom can mimic the electron-withdrawing effect of the Ir^{III} center. On the other hand, the iridium model complexes were chosen because the cyanide group can be protonated to simulate a Coloumbic contribution by the Ru^{II} center.

■ RESULTS AND DISCUSSION

Synthesis. An overview of the synthesized complexes is shown in Figure 1. The dinuclear iridium(III)−ruthenium(II) complexes are denoted with **1** for pristine ppy ligands (R$_2$ = H) and **2** for fluorinated ppy ligands (R$_2$ = F). The functionalization pattern on the tpy ligand in **1** and **2** is additionally labeled by **a−e**, i.e., **a** for pristine tpy, **b**, **c**, and **d** for phenyl-substituted tpy's, and **e** for tpy functionalized with an extended π-conjugated group. The same labeling scheme is used for the isothiocyanatoruthenium(II) complexes [Ru(bpy)-(tpy-R$_1$)(SCN)]PF$_6$ (**3a−3e**). The iridium(III) model complexes Bu$_4$N[Ir((R$_2$)$_2$-ppy)$_2$(CN)$_2$] are denoted as **4** for pristine ppy ligands (R$_2$ = H) and **5** for fluorinated ppy ligands (R$_2$ = F). They were prepared according to literature procedures.[19]

An overview of the synthetic route is shown in Scheme 1. The chloro complexes **6a−6e** (Scheme 1) of the general formula [Ru(bpy)(tpy-R$_1$)(Cl)]$^+$ represent the key molecule

Scheme 1. Schematic Representation of the Synthetic Route^a
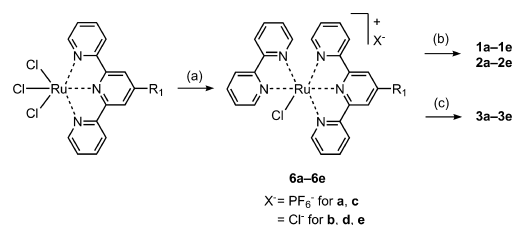
^{a}(a) (i) 2,2′-Bipyridine, LiCl, N-ethylmorpholine, methanol/water, 3 h, 75 °C, for **a** and **c**; (ii) excess NH$_4$PF$_6$. (b) (i) **4** or **5**, methanol/water, 120 °C, microwave, 30 min; (ii) excess NH$_4$PF$_6$, for **d** and **e**; (iii) 1 M HCl, DMSO, rt, 3 h; (iv) excess NH$_4$PF$_6$. (c) (i) KSCN, methanol/water, 120 °C, microwave, 30 min; (ii) excess NH$_4$PF$_6$; (iii) DMSO, 80 °C, 3 h, for **d** and **e**; (iv) 1 M HCl, DMSO, rt, 3 h; (v) excess NH$_4$PF$_6$.
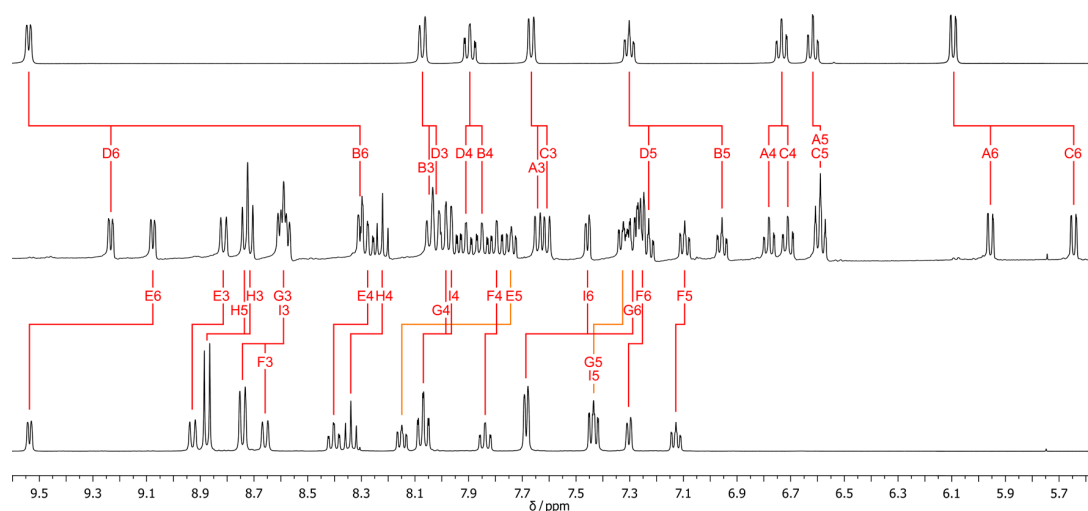
Figure 2. ^{1}H NMR spectra (DMSO-d_6, 400 MHz) of the model complexes **4** (top) and **3a** (bottom) and the dinuclear complex **1a** (middle). See Figure 1 for the numbering.

for the synthesis of heterodinuclear complexes **1** and **2**. These polypyridylruthenium(II) compounds were prepared as their chloride salts by heating the respective ruthenium(III) precursors Ru(tpy-R$_1$)Cl$_3$ with stoichiometric amounts of bpy in a methanol/water mixture.[20] Compounds **6a** and **6c** had to be purified by column chromatography and were isolated as hexafluorophosphate salts. Compounds **6d** and **6e** were isolated as an acetal/aldehyde mixture and used without deprotection for subsequent reactions. Finally, **1** and **2** were prepared by the reaction of **6** with an excess of **4** and **5**, respectively. The synthesis was performed in a methanol/water mixture at 120 °C under microwave irradiation for 30 min. The reddish complexes were obtained in moderate-to-good yields after column chromatography. The solubility in organic solvents (e.g., acetonitrile, dichloromethane) was increased for complexes **2**, which contain fluoro groups, compared to the parent compounds **1**. The ruthenium(II) model complexes **3** were prepared in an analogous manner, using an excess of potassium thiocyanate. Because of the ambient nature of the thiocyanate anion, a small fraction of complexes with S-coordinated thiocyanate was observed; isomerization toward the thermodynamically more stable N-coordinated thiocyanate in >97% purity could be achieved by heating the mixture in DMSO for 3 h at 80 °C (for kinetic studies on compound **3e**, see Figures S2−S4).[21] Compounds **1d**, **1e**, **2d**, **2e**, **3d**, and **3e**, which contained aldehyde/acetal mixtures after the reaction, were treated with aqueous HCl (1 M) in DMSO, as a final purification step, in order to cleave all acetal entities.

NMR Spectroscopy. The heterodinuclear complexes were thoroughly studied by ^{1}H, ^{13}C, and ^{19}F NMR spectroscopy in DMSO-d_6 (for **1**) and CD$_3$CN (for **2**). The assignment of the resonances was accomplished with the help of the model compounds and 2D NMR techniques. The ^{1}H NMR spectra of **4**, **1a**, and **3a** are exemplarily shown in Figure 2. The iridium compound **4** shows eight well-resolved signals in the aromatic region arising from the two equal ppy ligands. The ruthenium compound **3a** possesses eight bpy-related (denoted as E and F) and six tpy-related signals. Because of the decreased symmetry in the dinuclear complex **1a**, the signals of the two ppy units (denoted as A−D) as well as the tpy signals (denoted as G−I) become unequal and are, consequently, split up in the

respective spectrum. Significant shifts are observed for those signals that are in proximity to the newly formed μ-CN group. Namely, atoms B6 and E6 are more shielded, and the signals are thus shifted upfield. ^{13}C NMR analysis showed that the chemical shift for the carbon in the CN group is at 131 ppm in the iridium model complex **4**. The chemical shift for the ^{13}C signal of the SCN group in **3a** is at 134 ppm. The carbon in the bridging CN group features less electron density and is more deshielded than the terminal CN group. Consequently, the chemical shifts for the CN groups in the heterodinuclear complex are at 143 ppm for the bridging CN and at 130 ppm for the terminal CN. The ^{19}F NMR spectrum of **2** shows four well-resolved resonances in the range between −110 and −112 ppm, which are assigned to the four unequal fluorine substituents on the two ppy units. Moreover, a doublet at −73 ppm is assigned to the PF$_6^-$ counterion, and the integral ratio of 4:6 for the signals of the aromatic fluorine substituents and the counterion matches the monocationic nature of the assembly.

Electrochemistry. Cyclic voltammetry (CV) for all compounds was performed in dichloromethane using a potential window between −2.5 and +1.5 V against ferrocene as the reference. The model compound **4** shows an irreversible process in the anodic region at 0.53 V (peak potential) assigned to an Ir^{IV}/Ir^{III} oxidation.[22] For the fluorinated compound **5**, this process is anodically shifted by 0.3 V because of the electron-withdrawing substituents. The ruthenium model complexes **3** show a reversible signal in the anodic region with a half-wave potential of around 0.5 V, assigned to a Ru^{III}/Ru^{II} couple.[15c] Here, functionalization on the tpy moiety has a negligible influence. For the complex **3e**, a second reversible process at 1.09 V is observed. This process is assigned to oxidation of the bis(octyloxy)phenylene groups in the extended π-conjugated substituent. In the cathodic region, two redox processes at around −1.7 and −2.2 V are present, ascribed to tpy and bpy reduction. For the complexes containing an aldehyde function, a further reversible redox process is observed at around −2.0 V.

In the case of the nonfluorinated dinuclear complexes **1**, the first oxidation is observed at around 0.68 V (Figure 3). Because of its irreversible nature, this process is assigned to the Ir^{IV}/Ir^{III} oxidation. The process is shifted anodically by 0.15 V versus **4**
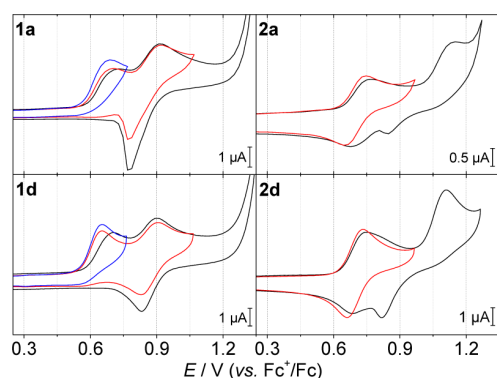
Figure 3. Cyclic voltammograms of selected dinuclear complexes in dichloromethane/0.1 M Bu$_4$NPF$_6$ at a 0.2 V/s scan rate (the fifth cycle is shown; different colors illustrate different potential ranges).

because of the electron-withdrawing effect of the Ru center to the iridium oxidation. The second process at around 0.83 V (half-wave potential) is assigned to a Ru^{III}/Ru^{II} redox couple. In contrast, the order of metal center oxidation is inverted for the fluorinated compounds **2** because the fluorine substituents have a strong influence on the iridium oxidation potential, as was already seen for the model compounds. Here, the first process at around 0.7 V is related to the reversible Ru^{III}/Ru^{II} redox couple and is shifted anodically by 0.2 V versus **3** because of the influence of the iridium metal. The second process at around 1.13 V is the irreversible Ir^{IV}/Ir^{III} oxidation. The functionalization pattern on the tpy fragment in **1** and **2** results in minor shifts of the Ru^{III}/Ru^{II} redox couple, as for the abovementioned complexes **3**. The potential splitting (ΔE_{PS}) between the anodic Ir^{IV}/Ir^{III} and Ru^{III}/Ru^{II} peak potentials is, on average, 0.22 and 0.37 V for **1** and **2**, respectively (Table 1). Moreover, the ΔE_{PS} value for the fluorinated compounds **2** is increased when using acetonitrile as the solvent. This implies that electronic coupling between the metal centers becomes

more pronounced in more polar solvents and is analyzed in more detail by spectroelectrochemistry (SEC; vide infra).

UV–Vis Spectroscopy. The absorption spectra of the dinuclear complex **1d** and the corresponding model complexes **3d** and **4** are exemplarily shown in Figure 4. The iridium model
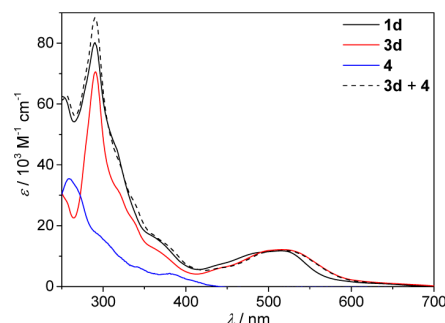
Figure 4. Room-temperature UV−vis absorption spectra of **1d**, **3d**, and **4** and superposition of **3d** and **4** in dichloromethane.

complex **4** exhibits a distinct absorption band in the UV region (λ_{max} = 259 nm), which mainly arises from ligand-centered (LC) transitions of the ppy moiety. Weaker absorption bands up to 400 nm correspond to iridium-based metal−ligand-to-ligand charge-transfer (MLLCT) transitions, with the longest-wavelength absorption maximum at 380 nm. For the fluorinated compound **5**, the longest-wavelength absorption maximum is shifted hypsochromically to 365 nm. A protonation experiment was performed on **4** and **5** to mimic the Coloumbic contribution by a Ru^{II} center (Figures S5 and S6). Upon protonation of the cyano group, a hypsochromic shift of the longest-wavelength absorption maximum is observed. A similar behavior has been shown recently for compound **4** versus related isocyanoboratoiridium(III) complexes.[23]

Complex **3d** features the characteristic absorption bands known from polypyridylruthenium(II) complexes.[24] In the UV

Table 1. Electrochemical Properties[a]

compound	E_{pa}(Ir^{IV}/Ir^{III})^{irr}/V[b]	E_{pa}(Ru^{III}/Ru^{II})/V[b]	$E_{1/2}$(Ru^{III}/Ru^{II})/V[c]	ΔE_{PS}/V[d]	$E_{1/2}$(ox$_3$)/V[c]	$E_{1/2}$(red$_1$)/V[c]	$E_{1/2}$(red$_2$)/V[c]	$E_{1/2}$(red$_3$)/V[c]
1a	0.70 (1.02)	0.92 (1.24)	0.85 (1.17)	0.22 (0.22)		−1.79		−2.18
1b	0.68	0.89	0.82	0.21		−1.77		−2.17
1c	0.68	0.90	0.83	0.22		−1.72		−2.15
1d	0.65	0.91	0.85	0.26		−1.64	−1.95	−2.20
1e	0.69	0.90	0.83	0.21	1.07	−1.70	−1.98	−2.17
2a	1.14 (1.31)	0.77 (0.71)	0.72 (0.67)	0.37 (0.60)		−1.77		−2.15
2b	1.12 (1.30)	0.73 (0.70)	0.69 (0.64)	0.39 (0.60)		−1.75		−2.15
2c	1.14 (1.24)	0.76 (0.71)	0.71 (0.67)	0.38 (0.53)		−1.71		−2.16
2d	1.11 (1.31)	0.75 (0.72)	0.70 (0.68)	0.36 (0.59)		−1.60	−1.95	−2.17
2e	1.12 (1.18)	0.75 (0.71)	0.72 (0.67)	0.37 (0.47)	1.09	−1.67	−1.98	−2.14
3a		0.56	0.51			−1.77		−2.12
3b		0.55	0.50			−1.75		−2.12
3c		0.54	0.50			−1.72		−2.12
3d		0.54	0.49			−1.63	−1.94	−2.15
3e		0.54	0.51		1.09	−1.69	−1.99	−2.16
4	0.53							
5	0.83							

[a]Conditions: differential pulse voltammetry (DPV) and CV potentials are given, and a deaerated dichloromethane solution is used as the solvent (a deaerated acetonitrile solution is used as the solvent for values in parentheses), 0.1 M Bu$_4$NPF$_6$, scan rate = 0.2 V/s, referenced against Fc$^+$/Fc^0; irr = irreversible process. [b]The anodic peak potential from the cyclic voltammogram is shown. [c]The half-wave potentials were determined with DPV. [d]Potential splitting between E_{pa}(Ir^{IV}/Ir^{III}) and E_{pa}(Ru^{III}/Ru^{II}).
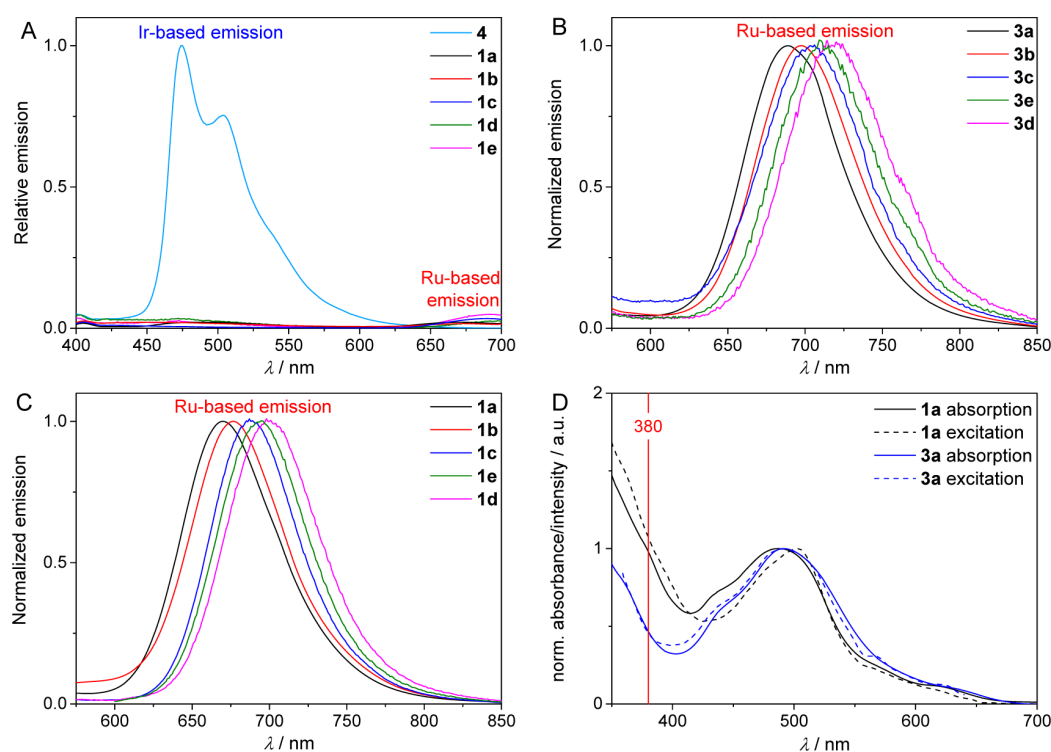
Figure 5. Room-temperature emission spectra of **4** (panel A, λ_{exc} = 380 nm), the ruthenium(II) model complexes **3** (panel B, λ_{exc} = 500 nm), and the dinuclear complexes **1** (panel A, λ_{exc} = 380 nm; panel C, λ_{exc} = 500 nm). Panel D shows the normalized absorption and excitation spectra of **1a** (λ_{det} = 670 nm) and **3a** (λ_{det} = 689 nm). The red line indicates the longest-wavelength absorption maximum of **4**. All spectra were recorded in dichloromethane.

region, a sharp absorption band (λ_{max} = 291 nm) arises from LC transitions of the bpy and the functionalized tpy moieties. The visible region exhibits broad absorption bands up to 600 nm (λ_{max} = 516 nm), which are assigned to ruthenium-based metal-to-ligand charge-transfer (MLCT) transitions. When the individual absorption spectra of complexes **3a**−**3e** are compared with each other, a shift of the long-wavelength absorption maximum is observed. In fact, for the nonfunctionalized complex **3a**, the maximum is located at 492 nm. Upon functionalization on the tpy fragment, a bathochromic shift of the absorption maximum at the longest wavelength is observed in the following order: **3b**/**3c**, **3d**, and **3e**.

The absorption spectrum of dinuclear complex **1d** correspond, in principle, to the spectra of the respective model complexes, i.e., intensive absorption in the UV region and broad absorption in the visible region. Deviations are found for the broad absorption band between 400 and 700 nm, i.e., the maximum in **3d** is slightly bathochromically shifted versus **1d**. This spectral region is governed by the ruthenium(II)-based MLCT transitions because the iridium model complex shows no contribution. On the other hand, a superposition of the spectra of the model complex (**3d** + **4**) matches very well with that of **1d**, in particular for the UV region, while a superposition of the protonated species of **4** and **3d** resulted in a hypsochromic shift and a worse match. This indicates that the dinuclear spectra are a result of compensation of the deviations found in the model complexes, i.e., a hypsochromic shift by the protonated iridium(III) model complex and a bathochromic shift by the isothiocyanatoruthenium(II) model complex. In the analogous series of fluorinated complexes **2**, the

longest-wavelength absorption maximum is hypsochromically shifted compared to the nonfluorinated species **1**. This obvious influence of fluorination on the visible-region absorption maximum indicates a contribution of the Ir[III] d orbitals to the Ru[II] MLCT-dominated transitions and is discussed in more detail in the computational section (vide infra).

Emission Spectroscopy. The emission spectra of the dinuclear and reference complexes, as measured in dichloromethane, are depicted in Figure 5 and summarized in Table 2. The excitation wavelengths were chosen according to the longest-wavelength MLCT absorption maxima of **4** (λ_{exc} = 380 nm) and the ruthenium(II) model complexes **3** (λ_{exc} = 500 nm). The iridium(III) model complex **4** exhibits a vibronically structured emission band with a maximum at 474 nm and shoulders at 503 and 540 nm, which indicates the emission from [3]LC states (Figure 5, panel A).[25] In comparison, the fluorinated complex **5** (λ_{exc} = 360 nm) shows a similar emission structure, although hypsochromically shifted by 20 nm. The ruthenium model complexes **3** exhibit a [3]MLCT-based emission at around 704 nm, and the tpy substituent likewise has a distinct influence on the energy of the emission (Figure 5, panel B). In fact, the complex **3a**, with the nonfunctionalized tpy moiety, exhibits the shortest emission wavelength within their series. Complexes with functionalized tpy units show an increasing bathochromic shift in the following order: Ph-Me (**3b**), Ph-Br (**3c**), pep-CHO (**3e**), and Ph-CHO (**3d**). This is known for ruthenium(II) complexes and stems from delocalization of the electron density over the increasing conjugated system.[4b] When the dinuclear complexes **1** are excited at 380 nm (λ_{exc} = 360 nm for **2**), virtually no iridium-based emission is observed (see Figure 5, panel A, Figure S10

Table 2. Photophysical Properties[a]

compound	absorption			emission	
	λ_{abs}/nm[b] (ε/10^3 M^{-1} cm^{-1})	$\varepsilon_{365\ nm}$[c]/ 10^3 M^{-1} cm^{-1}	$\varepsilon_{380\ nm}$[d]/ 10^3 M^{-1} cm^{-1}	$\lambda_{max,\ em}$/nm	lifetime/ ns
1a	488 (8.8)		8.6	670[e]	n.d.
1b	496 (10.8)		8.6	677[e]	n.d.
1c	509 (15.6)		12.5	688[e]	n.d.
1d	515 (11.8)		12.0	700[e]	71,[e,g] 39[f,g]
1e	518 (16.7)		35.3	694[e]	45,[e,g] 39[f,g]
2a	487 (8.2)	8.6		663[e]	n.d.
2b	501 (12.5)	11.6		669[e]	n.d.
2c	503 (9.3)	8.8		677[e]	n.d.
2d	508 (14.6)	16.7		691[e]	53,[e,g] 60[f,g]
2e	511 (18.0)	33.7		684[e]	55,[e,g] 33[f,g] (347)[f,h]
3a	492 (11.1)	7.9	5.2	689[e]	n.d.
3b	503 (10.1)	7.7	4.9	698[e]	n.d.
3c	501 (12.8)	9.6	6.0	705[e]	n.d.
3d	516 (12.1)	12.0	8.9	718[e]	50[e,g]
3e	516 (16.5)	31.6	32.4	711[e]	32[e,g]
4	380 (4.3)			474, 503 (sh), 540 (sh)[f]	90[f,g] (93)[f,h]
5	365 (7.1)			453, 480 (sh), 515 (sh)[f]	183[f,g] (163)[f,h]

[a]Conditions: an aerated dichloromethane solution, room temperature. [b]Longest-wavelength absorption maxima. [c]Extinction coefficients at 365 nm given for fluorinated complexes. [d]Extinction coefficients at 380 nm given for nonfluorinated complexes. [e]Ruthenium-based emission. [f]Iridium-based emission. [g]Measured in an aerated acetonitrile solution. [h]Measured in an aerated dichloromethane solution.

for **2**, and Table 2). However, for some of the dinuclear complexes, a weak residual emission is visible, which is ascribed as inefficient quenching, and is discussed in more detail in the time-resolved spectroscopy section (vide infra). To mimic a Coulombic contribution by a Ru^{II} center on the model compounds **4** and **5**, the above-mentioned protonation experiment was applied to investigate the influence on their emission spectra. No quenching of the iridium-based emission was observed upon protonation of the cyano ligand with a hexafluorophosphoric acid solution, although there were hypsochromically shifted emission maxima for the protonated species of **4** ($\lambda_{max,em}$ = 453 nm) and **5** ($\lambda_{max,em}$ = 441 nm). A similar, but weaker hypsochromic shift is observed for related isocyanoboratoiridium(III) complexes.[23] In contrast, the residual iridium-based emission in **1** and **2** is only slightly hypsochromically shifted compared to those of **4** and **5**, respectively (Figures S11 and S12). This indicates that an additional contribution by the Ru^{II} center leads to a compensation and, thus, to the less pronounced hypsochromic shift.

Direct excitation of **1** and **2** at 500 nm leads to the occurrence of a ruthenium-based emission (Figure 5, panel C) similar to the ruthenium model complexes **3**. The emission of **1** is generally shifted hypsochromically (on average, $\lambda_{max,em}$ = 686 nm) versus **3**, while the trend on the emission energy upon tpy functionalization is the same. It is also worth noting that the fluoro substitution (**2**) on the ppy moiety leads to a hypsochromic shift (on average, $\lambda_{max,em}$ = 677 nm) versus **1** (Figure S10), confirming the effect of the peripheral substitution of the iridium(III) fragment (R$_2$) on the Ru-tpy-based emission.

A rough estimate based on the extinction coefficients at 365 and 380 nm of the model and dinuclear complexes shows that there is significant absorption of the ruthenium model complexes present over the whole range of iridium-based absorption (Table 2). Hence, selective excitation of the Ir^{III} center is not possible for these complexes. Therefore, considering the emission spectra alone, it is not possible to conclude about the presence of intramolecular energy transfer between the Ir^{III} and Ru^{II} centers. However, the fact that the iridium-based absorption bands contribute to the ruthenium-based emission can serve as an indication for the presence of energy transfer. To investigate this matter, the origin of the ruthenium-based emission was analyzed by the corresponding excitation spectra and compared to the respective absorption profiles. The excitation spectra match very well in the visible region of the absorption spectra (exemplarily shown for **1a** in Figure 5, panel D, and Figures S17−S21). More importantly, the excitation spectra of the dinuclear complexes below 400 nm also fit to the absorption profiles and clearly show the additive contribution of the iridium fragment to the ruthenium-based emission. This finding is corroborated in a similar analysis for the ruthenium model complexes **3**, which show significantly
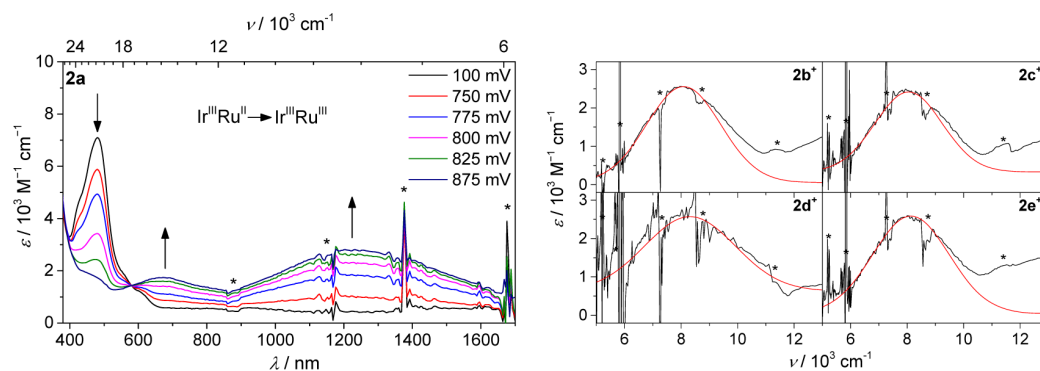
Figure 6. Left: Vis−NIR SEC spectra of **2a**, during the first ruthenium-based oxidation. Right: NIR absorptions showing the IVCT transitions (black curve) and Gaussian fittings (red curve) of **2b**−**2e$^+$**. Solvent and spectrometer artifacts are marked with asterisks. All spectra are recorded in a 0.1 M Bu$_4$NPF$_6$ solution of acetonitrile.

less intensity in the UV region (exemplarily shown for **3a** in Figure 5, panel D, and Figures S17−S21).

SEC and IVCT Analysis. The dinuclear complexes **1a** and **2a** (Figure S22) were analyzed by UV−vis−NIR SEC in acetonitrile (for **2b−2e**, see Figures S23−S25). For this purpose, stepwise oxidations were performed, and the related spectral changes were recorded. The first iridium-based oxidation process of **1a** shows a hypsochromic shift of the MLCT band (Figure S22, left). The oxidation product is tentatively denoted as $Ir^{IV}Ru^{II}$ species. However, it should be noted that the irreversible process destroys or changes the chemical structure of the complex. This could also be the reason for the absent absorption in the NIR region, typically observed for an electronically coupled system in the MV state (vide infra). The second, ruthenium-based oxidation (formally labeled as $[Ir^{IV}Ru^{III}]$) leads to a depletion of the MLCT band, associated with a weak absorption at around 700 nm, assigned to LMCT transitions of the ruthenium(III) species.[26] Surprisingly, the re-reduction (labeled as $[Ir^{III}Ru^{II}]_{rered}$) of the double-oxidized species reproduces qualitatively the initial spectrum with only minor spectral changes. As discussed before, the reaction order for **2a** is inversed, rendering the first oxidation process reversible, with a formal $Ir^{III}Ru^{III}$ character of the formed **2a⁺** species. As a result, the long-wavelength MLCT band is fully depleted and associated with a weak absorption at around 700 nm (Figure 6, left) assigned to the LMCT transition because it is also present in double-oxidized species ($Ir^{IV}Ru^{III}$; Figure S22, right). Surprisingly, subsequent computational studies suggest an IVCT character (vide infra). Furthermore, a very broad band in the NIR region with a flat maximum at 1220 nm ($E_{IT} = 8200$ cm⁻¹) arises. This band is ascribed to a $Ru^{III} \leftarrow Ir^{III}$ IVCT transition because it is absent in the initial ($Ir^{III}Ru^{II}$) and the double-oxidized species ($Ir^{IV}Ru^{III}$), as well as in the fully re-reduced species ($[Ir^{III}Ru^{II}]_{rered}$) (Figure S22, right). The re-reduction, furthermore, shows qualitatively the reappearance of the MLCT transition, which is hypsochromically shifted and less intense, with respect to the initial state, caused by the irreversibility of the iridium oxidation. Compounds **2b⁺−2e⁺** exhibit IVCT transition energies similar to those observed for **2a⁺** (Figure 6, right, and Table 3). Additionally, an IVCT absorption band for **2d⁺** in dichloromethane is not observed (Figure S23, right), which could be ascribed to a less intense IVCT absorption in

nonpolar solvents, as seen in other compounds.[13a] The generalized Mulliken−Hush expression was applied to calculate the electronic coupling matrix element (H_{ab}), where ε_{IT} is the extinction coefficient, $\Delta\tilde{v}_{1/2}$ is the bandwidth, and r_{ab} is the metal-to-metal distance (Table 3).[27] The distance between the metal centers is provided by the density functional theory (DFT)-optimized structure (vide infra) and was calculated as $r_{ab} = 5.3$ Å. Similar metal-to-metal distances were found by X-ray crystal structure analysis in related cyanide-bridged complexes.[13a,15c] Consequently, H_{ab} values of approximately 1000 cm⁻¹ for **2a⁺−2e⁺** were obtained. Additionally, the interaction parameter α^2, which gives an estimate for the degree of electronic coupling between the metal ions, was calculated (Table 3). The average value for α^2 is 1.5% in the series of **2a−2e⁺**. These values and the solvent dependency are typical for weakly coupled Robin−Day class II systems.[28] For related cyanide-bridged bimetallic ruthenium(II) complexes with the simplified formula trans-$[(NC)Ru(R-py)_4(\mu-CN)Ru(py)_4Cl]PF_6$ (py = pyridine),[13b] similar E_{IT} values but higher values for H_{ab} and α^2 are reported (Table 3).

Time-Resolved Spectroscopy. The quenching of the iridium-based emission in the dinuclear complexes is apparent from the steady-state emission data presented above. Along with a reduced emission quantum yield, quenching, in general, is governed by a decrease of the donor emission lifetime. As a consequence, the respective measurements were carried out in aerated acetonitrile for the selected dinuclear complexes **1d**, **1e**, **2d**, and **2e** and their respective monometallic model compounds, i.e., **3d**, **3e**, **4**, and **5** (Table 2). The lifetime of the iridium-based emission is reduced in the dinuclear complexes compared to the respective model complexes: For the nonfluorinated complexes **1d** and **1e** versus **4**, lifetimes of 39 versus 90 ns were determined, respectively, and for the fluorinated complexes **2d** and **2e** versus **5**, lifetimes of 60 and 33 versus 183 ns were obtained, respectively. Similar lifetimes of 93 and 163 ns for **4** and **5**, respectively, were obtained in aerated dichloromethane and differ from previously reported lifetimes.[22b] In contrast, the lifetime of the residual iridium-based emission in **2e** becomes 10 times longer (347 ns) when the solvent is changed from acetonitrile to dichloromethane. It should be noted that the apparent solvent dependence and the lifetime differences in the dinuclear complexes compared to the model complexes contradict an assignment of the residual iridium-based emission to impurities of **4** or **5**. The fact that emission from energetically significantly higher-lying iridium-based states ($^3MLLCT/^3LC$) is strong enough to be measured is remarkable but is a known feature for a number of related iridium(III) complexes.[29]

Thermal deactivation of the iridium-based ^3LC state is energetically favorable in light of the lower-lying ruthenium-based MLCT states, but time-resolved emission spectroscopy with ca. 120 ps time resolution enables no clear indication of emission quenching via this pathway (Figures S26 and S27). This motivated us to look closer into the early events occurring after photoexcitation using transient absorption (TA) spectroscopy. Unfortunately, no isolated excitation of an iridium-based transition is possible because of the omnipresent overlap with various $\pi-\pi^*$ transitions of the ruthenium(II) fragment. Therefore, all TA experiments were carried out using 200 fs pump pulses centered at 355 nm. Selected TA spectra of isoabsorbing solutions with optical densities of ca. 0.6 for **1d**, **1e**, **2d**, and **2e** and ca. 0.3 for **3d** and **3e** at the excitation wavelengths are shown in Figure 7.

Table 3. IVCT Transition Energy and Electronic Coupling Parameter for Oxidized Complexes 2a−2e⁺ in Acetonitrile

compound	$E_{IT}/$ cm⁻¹	$\varepsilon_{IT}/$ M⁻¹ cm⁻¹	$\Delta\tilde{v}_{1/2}/$ cm⁻¹	$H_{ab}/$ cm⁻¹	α^2
2a⁺	8200	2300	3420	990[b]	0.014[c]
2b⁺	8100	2500	3180	990[b]	0.015[c]
2c⁺	8050	2400	2810	910[b]	0.013[c]
2d⁺	8320	2600	3780	1110[b]	0.018[c]
2e⁺	8140	2500	3180	990[b]	0.015[c]
trans-$[(NC)Ru(py)_4(\mu$-$CN)Ru(py)_4Cl]PF_6$[a]	8400	6000	3400	1700	0.039
trans-$[(NC)Ru(MeOpy)_4(\mu$-$CN)Ru(py)_4Cl]PF_6$[a]	7200	8500	3100	1800	0.066

[a]Taken from ref 13b. [b]Calculated as $H_{ab} = 0.0206\frac{(\Delta\tilde{v}_{1/2}\varepsilon_{IT}E_{IT})^{1/2}}{r_{ab}}$. [c]Calculated as $\alpha^2 = 0.00042\frac{\Delta\tilde{v}_{1/2}\varepsilon_{IT}}{E_{IT}r_{ab}^2}$.
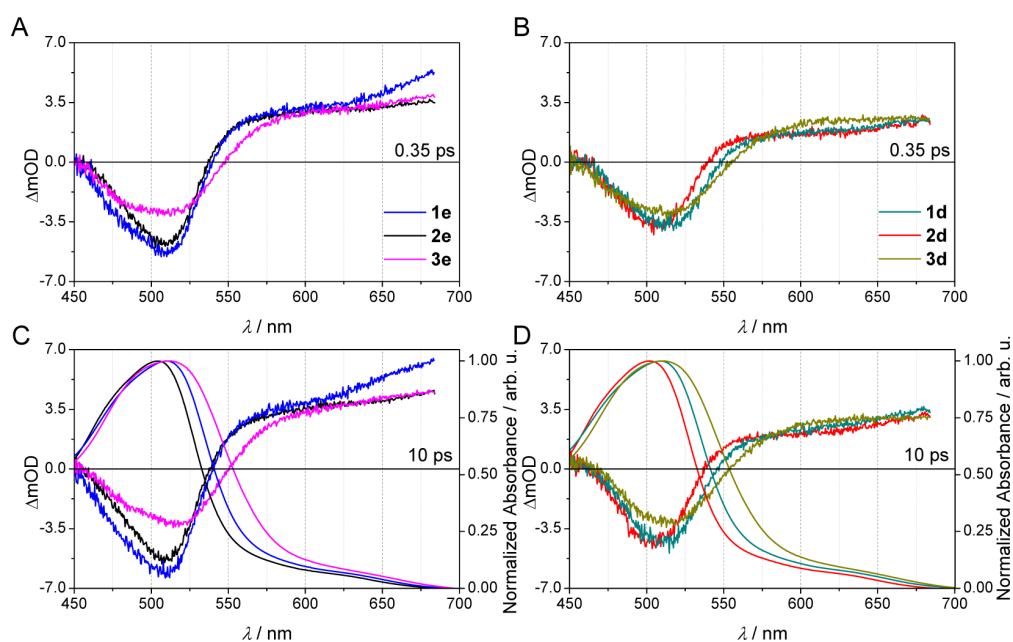
Figure 7. TA data (λ_{exc} = 355 nm) for selected molecular species measured in acetonitrile. Raw TA spectra at 0.35 ps (10 ps) delay time are plotted in panels A (C) and B (D). The data in panels A and C belong to **1e**, **2e**, and **3e**, while the data in panels B and D belong to **1d**, **2d**, and **3d**. The ground-state absorption spectra (normalized to the MLCT band maximum) of the respective compounds are shown in panels C and D for comparison (right scale).

Already at early delay times (0.35 ps; Figure 7, panels A and B), the TA spectra contain the typical characteristics of ruthenium-based [3]MLCT states regardless of the actual compound: Ground-state bleach below 535−550 nm and excited-state absorption (ESA) at longer wavelengths are observed. Those observations are consistent with the SEC data, which show that oxidation from Ru[II] to Ru[III] causes the MLCT band to vanish, which is typical for such types of transition-metal complexes.[30] Within the first 10 ps, i.e., a typical time scale for cooling and solvent relaxation, the spectra undergo only very minor changes. This indicates that no significant changes regarding the nature of the excited state or the molecular structure are occurring on this time scale. The positions of the respective minimum and the zero-crossing depend on the actual compound investigated and are consistent with the spectral positions of their individual ground-state absorption bands (Figure 7). The absolute signal intensities do not seem to be determined by the absorbance at the excitation wavelength for the respective samples only, i.e., specific molecular features for each compound may play a role. It should be emphasized that the very similar TA spectra, particularly for the compounds with smaller tpy ligands (**1d−3d**; Figure 7, panels B and D), reflect very similar excited states, considering that the differences, e.g., regarding the zero-crossing, correspond to the differences also found in the ground-state absorption. These observations suggest that the electronic structure of the ground state is more strongly influenced by the presence of the Ir center than it is the case for the excited state (at least the one probed in the TA measurements). The slightly different ESA signatures, e.g., the rise of the positive band above 630 nm observed for **2e** (Figure 7, panels A and C), which is not as pronounced in the nonfluorinated analogue or the model complex, may be attributed to a somewhat different extent of mixing between the [3]MLCT state and the orbitals of the extended ligand including the alkoxyphenyl unit, which is known to shift the ESA band toward 690 nm.[31]

When the observations from emission spectroscopy are related with the TA data, it is intriguing to note that while iridium-based [3]LC emission is observed, no iridium-specific signatures are observed in the TA data. On the one hand, the oscillator strength (based on their extinction coefficients; see Figure 4 and Table 2) of iridium-based [1]MLLCT transitions is much lower than that for the ruthenium-based [1]MLCT transitions. This trend might be the same in the excited state (also for triplet−triplet transitions), i.e., the iridium-based population will lead to lower TA signals compared to the ruthenium-based population. On the other hand, in emission spectroscopy, even small populations of iridium-based [3]LC states can be identified: Because of the absence of low-lying [3]MC states, emitters based on iridium typically possess significantly higher quantum yields than the ruthenium analogues, for which deactivation via [3]MC states provides an efficient decay channel from [3]MLCT states.[32] There are numerous examples for iridium(III) complexes described in the literature with quantum yields in the order of 90%.[19,33] The presented analysis suggests that there is a fast (within 0.35 ps), yet incomplete, deactivation of iridium-based states toward ruthenium-based [3]MLCT states in all compounds investigated here.

Computational Investigation. Selected representative model and dinuclear complexes (**1a−3a**, **1d−3d**, **1e−3e**, **4**, and **5**) were investigated by DFT and its time-dependent formalism (TD-DFT). In order to shorten the computational efforts, the flexible octyl chains (**1e−3e**) were replaced by methyl groups. For each complex, the geometry was first optimized for its singlet ground state (S_0), which served as the basis for the TD-DFT calculation as well as for a later optimization of the triplet (T_1) and formally oxidized (D^+) states. In all cases, the true minimum nature of the optimized
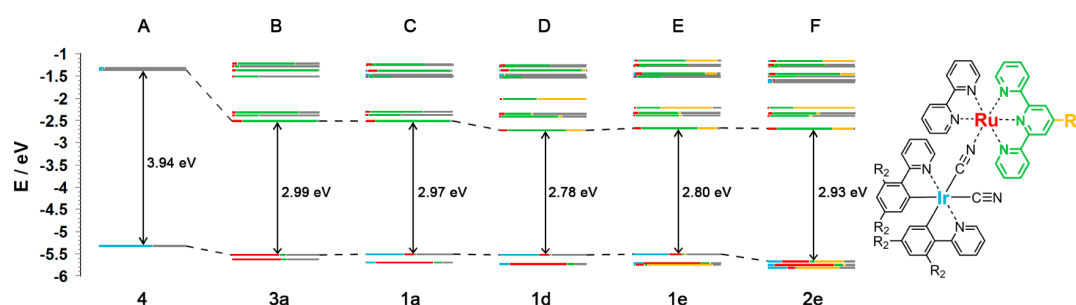
Figure 8. Energy diagram of the frontier MOs for selected complexes, including a color code for the spatial localization (legend: iridium, blue; ruthenium, red; tpy, green; tpy substituent, orange; rest of the compound, gray).
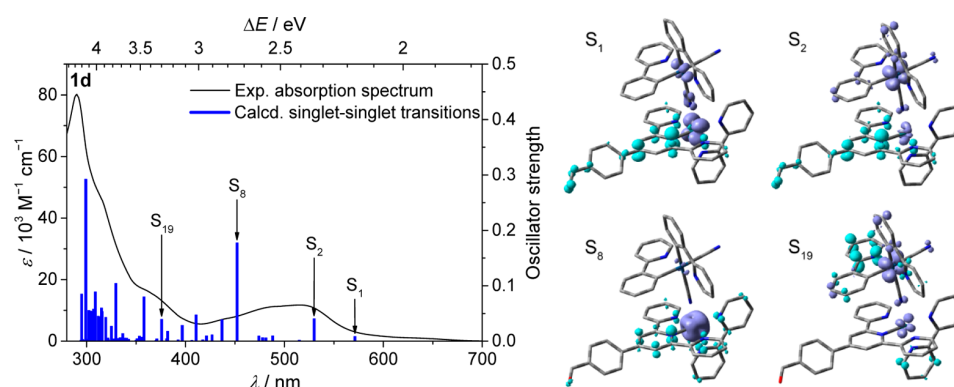
Figure 9. Experimental absorption spectra and calculated singlet−singlet transition energies with selected EDDM plots (plum-blue = depletion of electron density; cyan = accumulation of electron density; isovalue = 0.004) of **1d**. H atoms are omitted for clarity.

geometries was confirmed by vibrational analysis. The obtained ground-state geometries of the model complexes match the crystallographic data, i.e., the quasi-octahedral geometry of the Ir^{III} (**4**)[22b] and Ru^{II} (**3a**)[15c] centers. In the case of dinuclear complexes, the intervening cyanide bridge adapts a quasi-linear arrangement with a net Ru−Ir distance of approximately 5.3 Å (Figure S29). Hence, the ligands of the Ir and Ru centers, namely, the ppy and tpy moieties, are nearly coplanar with a large spatial interannular separation (>5 Å) and inferior contribution of π stacking. In addition, the effect of rotation around the Ru−Ir axis is expected to lead to minor changes in the electronic structure, in analogy to a recent report for related Ru−C≡N−Ru complexes.[34]

The electronic structures of representative complexes were analyzed in terms of molecular orbitals (MOs). Figure 8 displays the energy diagram of the frontier MOs, complemented by a color code to describe the spatial localization of the respective MO. First, two selected iridium (**4**; Figure 8, panel A) and ruthenium (**3a**; Figure 8, panel B) model complexes were analyzed. They represent the dominating contribution of the metal centers to the highest occupied molecular orbitals (HOMOs), while the lowest occupied molecular orbitals (LUMOs) are LC. The HOMO energies suggest that **4** (−5.3 eV) is more easily oxidized than **3a** (−5.5 eV), while the LUMO energies differ significantly between **4** (−1.4 eV) and **3a** (−2.5 eV), caused by the electron-rich ppy ligands versus electron-poor bpy and tpy units. In the case of **3a**, the LUMO is primarily localized on the tpy fragment. The results of **4** agree very well with reported data,[22b] while no computational data are available for complex **3a**. The corresponding dinuclear complex **1a** (Figure 8, panel C) reveals the generally preserved properties of its constituents,

i.e., the HOMO is dominated by the Ir^{III} center, and the LUMO is tpy-localized. The lower HOMO energy of **1a** versus **4** is attributed to the electron-withdrawing effect of the ruthenium(II) fragment mediated by the cyanide bridge, while the LUMO stays tpy-localized and its energy level is not affected. These assignments are corroborated by the electrochemical data, i.e., the observed anodic shift of the oxidation and the maintained reduction potential. Next, the effect of delocalization by the tpy substituent is explored for representative complexes **1a** (R$_1$ = H; Figure 8, panel C), **1d** (R$_1$ = Ph−CHO; Figure 8, panel D), and **1e** (R$_1$ = pep-CHO; Figure 8, panel E). In all three cases, the HOMOs remain Ir^{III}-centered at the same energy, while the LUMO of the aryl-decorated complexes (**1d** and **1e**) exhibit an additional contribution of R$_1$, which further leads to a stabilization by approximately 150 meV. Finally, the influence of fluorination is exemplified for **1e** (Figure 8, panel E) versus **2e** (Figure 8, panel F). In line with the previous assignments, the character and energy levels of the LUMOs are retained, while the fluoro groups stabilize the ppy-based orbitals and lead to lower energies of the Ir^{III} d orbitals. As a consequence, the HOMOs are now dominated by Ru^{II} d orbitals, in excellent agreement with the assignments derived from the electrochemical data. The corresponding optical gap can be easily estimated from the color-coded HOMOs and LUMOs, i.e., a proper localization upon taking interacting fragments into account. For example, the optical gap of complex **1e** (panel E) is governed by LUMO and HOMO−1 because the donating Ir^{III}-localized HOMO has a very small spatial overlap with the tpy-localized LUMO. A consistent behavior was found for the remaining studied complexes (see the Supporting Information), which supports the generalized conclusions.
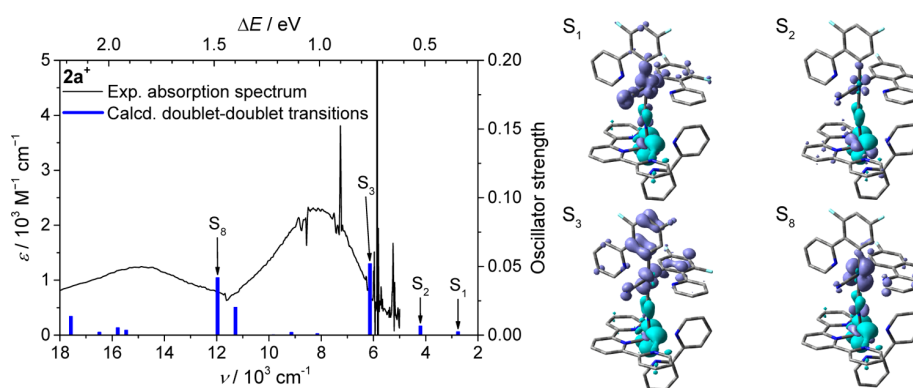
Figure 10. Experimental absorption spectra and calculated doublet−doublet transition energies with selected EDDM plots (plum-blue = depletion of electron density; cyan = accumulation of electron density; isovalue = 0.002) of **2a**$^+$. H atoms are omitted for clarity.

TD-DFT calculations were performed to detail the absorption properties of selected complexes (Figures S30− S40). The calculated singlet−singlet transitions (S_n) fit qualitatively very well with the experimental absorption spectrum, as exemplified for the dinuclear complex **1d** (Figure 9). Characteristic electronic transitions are visualized by their electron density difference maps (EDDMs), which share similarities with natural transition orbitals but compact all contributing MO pairs into a single plot of redistributed electron density. The longest-wavelength transition (S_1) reveals the depletion of the electron density at the Ru−N≡C−Ir fragment and the increase of the electron density at the tpy fragment and the aldehyde group. The donating fragment is dominated by a Ru^{II} d orbital, which is coupled through aligned p orbitals of the cyanide bridge with the corresponding Ir^{III} d orbital. The low oscillator strength of S_1 is reflected by the improper alignment (symmetry) of the accepting fragment, i.e., the central pyridine's N p orbital. Consequently, the S_2 transition is more intense because of the proper orbital symmetry between Ru^{II} d and N p orbitals and is best described as MLCT with tpy(π^*) ← Ru(d) character, with admixed Ir d and cyanide p donor contributions. All further transitions >400 nm are of similar MLCT character. The calculated transition S_8 consists of more than one contributing Ru^{II} d orbital and an extended delocalization across the bpy and tpy fragments, which can explain the high oscillator strength and energetic stabilization (red shift vs experimental data) due to the known deficiencies of the B3LYP functional to describe delocalized and/or charge-transfer states.[35] The S_{19} transition of **1d** is the first transition with a sizable ppy(π^*) ← Ir(d) contribution, in excellent agreement with the model complex (Figures S30 and S31) and the experimental absorption data. The remaining complexes exhibit qualitatively similar transitions in the visible region and show the effect of delocalization by the tpy substituent (R_1), i.e., a similar absorption profile for **1e** (R_1 = pep-CHO) but a hypsochromic shift for **1a** (R_1 = H). In addition, a blue-shifted absorption upon fluorination of the ppy-Ir fragment (**1d** vs **2d**) was found. The excellent agreement with the experimental data demonstrates that TD-DFT calculations satisfyingly reproduce the experimental absorption spectra, thus assisting the future design of complexes with enhanced charge transfer:[35] For example, the darkness of S_1 can be traced to the improper orbital symmetry of the Ru^{II} d and N p orbitals, whose spatial orientation is dictated by the interaction with cyanide−Ir^{III} orbitals and the extended π system of R_1, respectively. Hence, this symmetry constraint

would be overcome if the R_1 substituent was placed onto a peripheral pyridine instead (cf. S_1 in Figure 9). In order to further test the influence of selected functionals qualitatively, the two popular functionals PBE0[36] and MPWB1K from the Minnesota suite of functionals[37] were chosen for TD-DFT calculations on **2d**. When the B3LYP-optimized nuclear geometry is employed, the calculated set of vertical transitions for PBE0 and MPWB1K agrees well with the B3LYP-derived transitions. In the case of MPWB1K, a sizable blue shift of the entire spectrum was noticed, as was also reported for range-separated functionals. The EDDM plots (see Figure S36) confirm the similar nature of the corresponding transitions among the tested functionals. As stated above, the EDDM representation simplifies an elaborate analysis based on MOs and thereby assists the qualitative comparison between different computational methods. In summary, no profound difference between the functionals was found with regard to the MLCT nature of the low-energy transitions.

The triplet- and single-oxidized doublet states of selected complexes were optimized to exemplify the emission and electrochemical properties (Figures S41−S44). In all studied cases, the spin-density plots of the triplet state reveal the localization on the ruthenium(II) and tpy fragments without a significant iridium(III) contribution and corroborate the previous assignment as the emissive ^{3}MLCT excited state. In contrast, the single-oxidized states exhibit distinct differences upon fluorination, i.e., the nonfluorinated complexes are best described by a diphenyliridium-based oxidation, while the fluorinated congeners reveal the dominant spin localization on the ruthenium fragment (Figures S41−S43). In both cases, the corresponding d orbitals are aligned to promote coupling over the cyanide bridge. The vertical doublet−doublet transitions were calculated for **2a**$^+$, **2d**$^+$, and **2e**$^+$ on the basis of TD-DFT calculations employing the B3LYP functional. Pieslinger et al. recently analyzed a series of Ru−C≡N−Ru MV complexes using the same functional,[13f] and our results qualitatively follow the drawn conclusions. In the following analysis, compound **2a**$^+$ was chosen for reasons similar to those in Pieslinger's work. Figure 10 displays the calculated transitions with characteristic EDDM plots for visualization. The transition energies are shifted to lower wavenumbers by approximately 2000 cm^{-1} with correct oscillator strengths. The nature of most of the low-energy transitions (<12000 cm^{-1}) is best described as IVCT transitions. In all cases, admixing of interconfigurational (IC) contributions is observed, which is particularly expressed for S_2. The LMCT transitions are hypsochromically shifted with

respect to the Ru−C≡N−Ru MV complexes,[13f] which is tentatively attributed to the higher electron deficiency of our iridium(III) fragment. It is worth noting that complexes **2d**$^+$ and **2e**$^+$ bearing π-conjugated substituents also exhibit IVCT character of the low-energy transitions (Figure S45). However, the large deviation of the calculated transition energies and corresponding oscillator strengths with respect to the experimentally observed values indicate the weakness of the employed computational methodology as discussed before for the ground-state transitions. A further assessment of the functionals is beyond the scope of this work. More importantly, the assignment of the low-energy transitions consistently reveals the IVCT nature with some admixing of IC contributions.

CONCLUSION

The reported dinuclear complexes, a combination of cyanide-bridged $(ppy)_2Ir^{III}$ and $(bpy)(tpy)Ru^{II}$ building blocks, were readily synthesized and subsequently analyzed regarding their photophysical and electrochemical properties. The series, featuring different substituents, reveals a strong influence upon fluorination of the ppy unit, while functionalization on the tpy fragment resulted only in minor changes. A different spectral behavior is observed for complexes **1a−1e** and **2a−2e** in their MV form upon first oxidation. The fluorinated **2a**$^+$**−2e**$^+$ exhibit broad $Ru^{III} \leftarrow Ir^{III}$ IVCT bands in the NIR region that indicate slight electronic interaction between the two metal centers (weakly coupled class II system). For the non-fluorinated analogues **1a−1e**, the first irreversible iridium oxidation changes or destroys the complex structures and could explain the absence of an IVCT band. However, an efficiently quenched iridium emission and an observable ruthenium emission are present for all heterodinuclear complexes. DFT and TD-DFT calculations support that the short cyanide bridge mediates electronic contribution from the Ir center to the Ru moiety. Time-resolved spectroscopy indicates that a fast energy transfer (<350 fs after photoexcitation) from the excited states of iridium toward lower-lying ruthenium ^{3}MLCT states takes place. For future works, the reported heterometallic complexes are considered as effective donor (i.e., the Ir center) and acceptor (i.e., the Ru center) systems that can be further extended over the bromine or aldehyde functionality by either chromophores or other acceptor units to generate assemblies that offer directional, cascade-like energy transfer.

EXPERIMENTAL SECTION

Materials and Instrumentation. Compounds **4**[22b] and **5**,[22b] the ligands tpy-Ph-Me,[38] tpy-Ph-Br,[38] tpy-Ph-CHO,[39] and tpy-pep-CHO,[39] and the ruthenium(III) precursor complexes $Ru(tpy-R_1)Cl_3$[40] were prepared according to analogous literature procedures. All other chemicals were purchased from commercial suppliers and used as received. All reactions were monitored by thin-layer chromatography (silica gel on aluminum sheets with fluorescent dye F254, Merck KGaA). Microwave-assisted reactions were carried out using a Biotage Initiator Microwave synthesizer. NMR spectra were recorded on a Bruker AVANCE (250, 300, 400, or 600 MHz) instrument in deuterated solvents (Euriso-Top) at 25 °C. ^{1}H and ^{13}C NMR resonances were assigned using appropriate 2D correlation spectra. Chemical shifts are reported in ppm using the solvent as the internal standard. ^{19}F NMR spectra were referenced to −73.3 ppm for the resonance of the hexafluorophosphate anion. High-resolution electrospray ionization time-of-flight mass spectrometry (ESI-TOF HRMS) was performed on a Bruker Daltonics ESI-(Q)-TOF MS microTOF II mass spectrometer. UV−vis absorption spectra were recorded on a

PerkinElmer Lambda 750 UV−vis−NIR spectrophotometer and emission spectra on a Jasco FP6500 instrument. Measurements were carried out using $10^{-5}–10^{-6}$ M solutions of the respective solvents (spectroscopy grade) in 1 cm quartz cuvettes at room temperature. CV measurements were performed on a Metrohm Autolab PGSTAT30 potentiostat with a standard three-electrode configuration using a glassy-carbon-disk working electrode, a platinum-rod auxiliary electrode, and a AgCl/Ag reference electrode; a scan rate of 0.2 V/s was applied. The experiments were carried out in deaerated CH_3CN or CH_2Cl_2 (spectroscopy grade) containing 0.1 M Bu_4NPF_6 salt. At the end of each measurement, ferrocene was added as an internal standard. Spectroelectrochemical experiments were carried out in a quartz cuvette (1 mm optical path length) containing 0.1 M Bu_4NPF_6 in a CH_3CN or CH_2Cl_2 solution, a platinum-grid working electrode, a platinum-wire auxiliary electrode, and a $AgNO_3/Ag/CH_3CN$ reference electrode. The potential was controlled using a Metrohm Autolab PGSTAT30 potentiostat. The redox process was monitored by UV−vis−NIR spectroscopy using a PerkinElmer Lambda 750 UV−vis−NIR spectrophotometer and considered complete when there was no further spectral change.

Time-Resolved Spectroscopy. Spectrally resolved emission decay curves were determined employing a Hamamatsu HPDTA streak camera. Emission is excited by pulses centered at 355−370 nm created by frequency-doubling the output of a Ti:sapphire laser (Tsunami, Newport Spectra-Physics GmbH). The repetition rate of the fundamental is reduced to 400 kHz by a pulse selector (model 3980, Newport Spectra-Physics GmbH). Emission is collected from a 1 cm cuvette in a 90° angle and spectrally dispersed on the detector using a CHROMEX spectrograph. Measurements with and without a polarizer (set to magic angle) in the detection path were performed, but no contributions from rotational diffusion were observed on the time scales probed.

The time-resolved TA measurements were performed on a setup described earlier.[41] The setup is based on an amplified Ti:sapphire oscillator (800 nm, 1 kHz; Libra, Coherent Inc.). The pump beam (355 nm) is created in a noncollinear optical−parametric amplifier (TOPASwhite, Lightconverison Ltd.) and overlapped on the sample position with the white-light probe (created in a sapphire plate) in a close-to-collinear geometry. The mutual polarization of the linearly polarized beam was set to magic angle using a Berek compensator in the pump path. The pulse duration of the pump pulses at the sample position was determined as 200 fs via difference-frequency generation at the sample position. The pulse energy of the pump pulses was ca. 150 nJ, and the optical density of the sample at the pump wavelength was 0.6 in a 1 mm cuvette.

Computational Methods. The theoretical calculations are based on DFT or TD-DFT. All calculations were performed with the *Gaussian09* program package (version A.02).[42] The hybrid functional B3LYP[43] was selected in combination with the 6-31G* basis set for all atoms except Ru and Ir, which were described by an effective core potential and the associated orbitals (mwb). For all calculations, the solvent environment was modeled for acetonitrile using the implemented polarization continuum model.[44] The geometries of the singlet ground state (S_0) were optimized and serve as the starting point for the optimization of the corresponding triplet states (T_1) and singly oxidized doublet states (D^+). In cases of difficult self-consistent-field convergence, additional quadratic (qc) or extra quadratic (xqc) functions were used. The true nature of all minima structures was confirmed by vibrational analysis, showing no imaginary frequencies. TD-DFT calculations were performed on the same level of theory. *Chemissian3.3* was used for Mulliken population analysis and visualization of the MO composition. The EDDMs were obtained by *GaussSum2.2*.[45] The graphical visualizations were generated by *GaussView5.0.8*,[46] i.e., the isovalues were drawn at 0.002 or 0.004 (EDDM), 0.04 (Kohn−Sham MOs), or 0.004 (spin-density calculations).

Synthesis. *General Procedure for the Synthesis of Monochloro-Containing (bpy)(tpy)Ru^{II} Complexes* **6**; *[Ru(bpy)(tpy-R₁)Cl]Cl/ PF₆.*[20a] $Ru(tpy-R_1)Cl_3$ and 2,2′-bipyridine were combined with LiCl and *N*-ethylmorpholine (3 drops) in a methanol/water mixture (5:1

ratio). The mixture was then heated at reflux for 3 h. The solvent was removed and the residue redissolved in dichloromethane and washed with water. Subsequently, the solvent was dried over Na_2SO_4 and removed. The remaining solid was washed with diethyl ether and dried in vacuo. The complexes were isolated as chloride or hexafluorophosphate salt. When applicable, deviations from this general protocol are given below.

[Ru(bpy)(tpy)Cl]PF₆ (6a). According to the general procedure, $Ru(tpy-R_1)Cl_3$ (R_1 = H; 309.2 mg, 0.7 mmol), 2,2′-bipyridine (109.3 mg, 0.7 mmol), and LiCl (297 mg, 7 mmol) were reacted in 24 mL of methanol/water. Further purification by column chromatography (silica, 40:4:1 acetonitrile/water/saturated aqueous KNO_3 solution), followed by precipitation in an aqueous NH_4PF_6 solution, was carried out. A dark-purple solid was obtained (107 mg, 0.159 mmol, 23%).

^{1}H NMR (250 MHz, CD_3OD): δ 10.20 (dd, ^4J = 0.9 Hz, ^3J = 5.7 Hz, 1H, H^{E6}), 8.76 (d, ^3J = 8.3 Hz, 1H, H^{E3}), 8.65 (d, ^3J = 8.1 Hz, 2H, H^{H3}), 8.53 (d, ^3J = 8.1 Hz, 2H, H^{G3}), 8.48 (d, ^3J = 8.4 Hz, 1H, H^{F3}), 8.31 (td, ^4J = 1.4 Hz, ^3J = 7.8 Hz, 1H, H^{E4}), 8.16 (t, ^3J = 8.1 Hz, 1H, H^{H4}), 8.05−7.88 (m, 3H, H^{E5}, H^{G4}), 7.79−7.66 (m, 3H, H^{F4}, H^{G6}), 7.40−7.28 (m, 3H, H^{F6}, H^{G5}), 7.04 (ddd, ^4J = 1.2 Hz, ^3J = 5.9 Hz, ^3J = 7.2 Hz, 1H, H^{F5}).

[Ru(bpy)(tpy-Ph-Me)Cl]Cl (6b). According to the general procedure, $Ru(tpy-R_1)Cl_3$ (R_1 = Ph-Me; 100 mg, 0.188 mmol), 2,2′-bipyridine (29.4 mg, 0.188 mmol), and LiCl (80 mg, 1.88 mmol) were reacted in 12 mL of methanol/water to obtain a dark-purple solid (65 mg, 0.100 mmol, 53%).

^{1}H NMR (400 MHz, CD_3OD): δ 10.27 (dd, ^4J = 1.5 Hz, ^3J = 5.8 Hz, 1H, H^{E6}), 8.83 (s, 2H, H^{H3}), 8.78 (dt, ^4J = 1.0 Hz, ^3J = 8.3 Hz, 1H, H^{E3}), 8.60 (d, ^3J = 8.1 Hz, 2H, H^{G3}), 8.48 (d, ^3J = 8.1 Hz, 1H, H^{F3}), 8.33 (td, ^4J = 1.6 Hz, ^3J = 7.9 Hz, 1H, H^{E4}), 8.08−7.98 (m, 3H, H^{E5}, H^{J2}), 7.85 (td, ^4J = 1.5 Hz, ^3J = 7.9 Hz, 2H, H^{G4}), 7.75−7.66 (m, 3H, H^{F4}, H^{G6}), 7.41 (d, ^3J = 8.0 Hz, 2H, H^{J3}), 7.37 (dd, ^4J = 1.2 Hz, ^3J = 5.8 Hz, 1H, H^{F6}), 7.30 (ddd, ^4J = 1.2 Hz, ^3J = 5.5 Hz, ^3J = 7.3 Hz, 2H, H^{G5}), 7.02 (dd, ^4J = 1.4 Hz, ^3J = 5.8 Hz, ^3J = 7.4 Hz, 1H, H^{F5}), 2.49 (s, 3H, CH_3). ^{13}C{^{1}H} NMR (63 MHz, CD_3OD): δ 160.4, 160.3, 159.4, 157.8, 153.7, 153.3, 152.9, 148.2, 141.7, 138.2, 137.9, 136.8, 135.0, 131.2, 128.8, 128.4, 128.0, 127.5, 125.4, 124.8, 124.6, 121.4, 21.4.

[Ru(bpy)(tpy-Ph-Br)Cl]PF₆ (6c). The synthesis was performed according to a literature procedure.[20b]

In a two-necked flask, 2,2′-bipyridine (44.6 mg, 0.285 mmol) was added to a solution of LiCl (66.5 mg, 1.570 mmol) dissolved in ethanol (18 mL) and water (6 mL) and deaerated with nitrogen for 15 min. Triethylamine (0.1 mL) and $Ru(tpy-R_1)Cl_3$ (R_1 = Ph-Br; 170 mg, 0.285 mmol) was added to the solution, and the mixture was heated to reflux for 4 h. After cooling to room temperature, the solution was evaporated and the remaining solid purified by column chromatography (silica, 40:4:1 acetonitrile/water/saturated aqueous KNO_3 solution). The purple fraction was collected, and an excess of NH_4PF_6 was added; the mixture was concentrated in vacuo, and water was added. The fine precipitate was collected by filtration, washed with water, and rinsed with dichloromethane (around 200 mL) until the filtrate was only slightly purple. The solvent was evaporated and the residue dried in vacuo to obtain a dark-purple solid (134 mg, 0.162 mmol, 57% yield).

^{1}H NMR (300 MHz, CD_3CN): δ 10.24 (dd, ^4J = 1.6 Hz, ^3J = 5.7 Hz, 1H, H^{E6}), 8.70 (s, 2H, H^{H3}), 8.60 (dt, ^4J = 0.9 Hz, ^3J = 8.1 Hz, 1H, H^{E3}), 8.48 (dt, ^4J = 1.0 Hz, ^3J = 8.1 Hz, 2H, H^{G3}), 8.33−8.23 (m, 2H, H^{F3}, H^{E4}), 8.05−7.95 (m, 3H, H^{J2}, H^{E5}), 7.90−7.77 (m, 4H, H^{G4}, H^{J3}), 7.72−7.62 (m, 3H, H^{G6}, H^{F4}), 7.35−7.22 (m, 3H, H^{F6}, H^{G5}), 6.93 (ddd, ^4J = 1.3 Hz, ^3J = 5.8 Hz, ^3J = 7.3 Hz, 1H, H^{F5}).

[Ru(bpy)(tpy-Ph-CHO)Cl]Cl (6d). According to the general procedure, $Ru(tpy-R_1)Cl_3$ (R_1 = Ph-CHO; 100 mg, 0.184 mmol), 2,2′-bipyridine (28.7 mg, 0.184 mmol), and LiCl (78 mg, 1.84 mmol) were reacted in 12 mL of methanol/water to obtain a dark-purple solid as an acetal/aldehyde mixture (108 mg, 0.149 mmol, 81%). ^{1}H NMR signals of the acetal are given.

^{1}H NMR (300 MHz, CD_3OD): δ 10.23 (d, ^3J = 5.7 Hz, 1H, H^{E6}), 8.95 (s, 2H, H^{H3}), 8.78 (d, ^3J = 8.2 Hz, 1H, H^{E3}), 8.69 (d, ^3J = 7.9 Hz, 2H, H^{G3}), 8.50 (d, ^3J = 7.7 Hz, 1H, H^{F3}), 8.35−8.28 (m, 1H, H^{E4}),

8.18 (d, ^3J = 8.0 Hz, 2H, H^{J2}), 8.07−7.99 (m, 1H, H^{E5}), 7.98−7.88 (m, 2H, H^{G4}), 7.80−7.67 (m, 5H, H^{F4}, H^{J3}, H^{G6}), 7.45 (d, ^3J = 5.8 Hz, 1H, H^{F6}), 7.40−7.29 (m, 2H, H^{G5}), 7.04 (t, ^3J = 6.6 Hz, 1H, H^{F5}), 5.49 (s, 1H, $CH(OCH_3)_2$), 3.42 (s, 6H, $CH(OCH_3)_2$).

[Ru(bpy)(tpy-pep-CHO)Cl]Cl (6e). According to the general procedure, $Ru(tpy-R_1)Cl_3$ (R_1 = pep-CHO; 125 mg, 0.139 mmol), 2,2′-bipyridine (21.7 mg, 0.139 mmol), and LiCl (59 mg, 1.39 mmol) were reacted in 19 mL of methanol/water to obtain a dark-purple solid as an acetal/aldehyde mixture (130 mg, 0.122 mmol, 88%). ^{1}H NMR signals of the acetal are given.

^{1}H NMR (300 MHz, CD_3OD): δ 10.23 (d, ^3J = 5.6 Hz, 1H, H^{E6}), 8.99 (s, 2H, H^{H3}), 8.79 (d, ^3J = 8.2 Hz, 1H, H^{E3}), 8.70 (d, ^3J = 8.0 Hz, 2H, H^{G3}), 8.50 (d, ^3J = 8.2 Hz, 1H, H^{F3}), 8.33 (t, ^3J = 7.9 Hz, 1H, H^{E4}), 8.24 (d, ^3J = 8.2 Hz, 2H, H^{J2}), 8.02 (t, ^3J = 6.7 Hz, 1H, H^{E5}), 7.93 (t, ^3J = 7.8 Hz, 2H, H^{G4}), 7.81−7.73 (m, 3H, H^{J3}, H^{F4}), 7.71 (d, ^3J = 5.4 Hz, 2H, H^{G6}), 7.44 (d, ^3J = 5.7 Hz, 1H, H^{F6}), 7.34 (t, ^3J = 6.6 Hz, 2H, H^{G5}), 7.15 (s, 1H, H^{K2}), 7.13 (s, 1H, H^{K5}), 7.05 (t, ^3J = 6.6 Hz, 1H, H^{F5}), 5.62 (s, 1H, $CH(OCH_3)_2$), 4.09 (t, ^3J = 6.2 Hz, 2H, α-OCH_2), 4.03 (t, ^3J = 6.3 Hz, 2H, α-OCH_2), 3.41 (s, 6H, $CH(OCH_3)_2$), 1.94−1.75 (m, 4H, β-CH_2), 1.70−1.50 (m, 4H, γ-CH_2), 1.50−1.23 (m, 16H, δ-η-CH_2), 0.99−0.81 (m, 6H, CH_3).

General Procedure for Thiocyanate-Containing (bpy)(tpy)Ru^{II} Complexes 3; [Ru(bpy)(tpy-R₁)SCN]PF₆. A microwave vial (5 mL) was charged with $[Ru(bpy)(tpy-R_1)Cl]Cl/PF_6$ (**6a−6e**; 0.028 mmol) and KSCN (26.8 mg, 0.28 mmol) in 2.2 mL of methanol/water (10:1). The vial was capped, and the mixture was deaerated with nitrogen for 15 min. The purple solution was heated under microwave irradiation for 30 min at 120 °C. Acetonitrile (5 mL) and NH_4PF_6 (225 mg, 1.378 mmol, 50 equiv) were added, and the solution was stirred for 5 min. Subsequently, water (50 mL) was added, and the formed precipitate was filtered, washed with water, and rinsed with acetonitrile. The solvent was removed and the residue redissolved in DMSO (3 mL) and heated for 3 h at 80 °C. After cooling to room temperature, NH_4PF_6 (excess) and water (50 mL) were added. The dark-red complex was collected by filtration.

For the complexes containing an aldehyde group (**6d** and **6e**), an additional, final step was performed. The complex was dissolved in DMSO (3 mL), and a 1 M HCl solution (1 mL) was added. The solution was stirred for 3 h at room temperature. Subsequently, NH_4PF_6 (excess) and water (50 mL) were added to the stirred solution, and the solid was collected by filtration.

[Ru(bpy)(tpy)SCN]PF₆ (3a). Yield: 39%. ^{1}H NMR (400 MHz, DMSO-d_6): δ 9.54 (dd, ^4J = 1.4 Hz, ^3J = 5.6 Hz, 1H, H^{E6}), 8.93 (dt, ^4J = 1.1 Hz, ^3J = 8.3 Hz, 1H, H^{E3}), 8.88 (d, ^3J = 8.1 Hz, 2H, H^{H3}), 8.74 (dt, ^4J = 1.1 Hz, ^3J = 8.0 Hz, 2H, H^{G3}), 8.66 (d, ^3J = 8.1 Hz, 1H, H^{F3}), 8.40 (td, ^4J = 1.6 Hz, ^3J = 7.9 Hz, 1H, H^{E4}), 8.34 (t, ^3J = 8.1 Hz, 1H, H^{H4}), 8.15 (ddd, ^4J = 1.3 Hz, ^3J = 5.6 Hz, ^3J = 7.4 Hz, 1H, H^{E5}), 8.07 (td, ^4J = 1.5 Hz, ^3J = 7.8 Hz, 2H, H^{G4}), 7.84 (td, ^4J = 1.5 Hz, ^3J = 7.8 Hz, 1H, H^{F4}), 7.69 (dd, ^4J = 1.4 Hz, ^3J = 5.6 Hz, 2H, H^{G6}), 7.43 (ddd, ^4J = 1.3 Hz, ^3J = 5.5 Hz, ^3J = 7.1 Hz, 2H, H^{G5}), 7.30 (ddd, ^4J = 1.3 Hz, ^3J = 5.7 Hz, 1H, H^{F6}), 7.13 (ddd, ^4J = 1.3 Hz, ^3J = 5.7 Hz, ^3J = 7.3 Hz, 1H, H^{F5}). ^{13}C{^{1}H} NMR (100 MHz, DMSO-d_6): δ 158.0 (2C, C^{G2}), 157.6 (C^{F2}), 157.1 (2C, C^{H2}), 155.4 (C^{E2}), 152.2 (2C, C^{G6}), 151.4 (C^{E6}), 151.1 (C^{F6}), 137.9 (2C, C^{G4}), 137.2 (C^{E4}), 136.5 (C^{F4}), 135.3 (C^{H4}), 133.6 (SCN), 128.0 (2C, C^{G5}), 127.7 (C^{E5}), 126.7 (C^{F5}), 124.2 (2C, C^{G3}), 124.2 (C^{E3}), 123.6 (C^{F3}), 123.3 (2C, C^{H3}). HRMS (ESI-TOF). Calcd for $C_{26}H_{19}N_6RuS$ ([M − PF_6]$^+$): m/z 549.0429. Found: m/z 549.0435. IR (KBr): $\tilde{\nu}_{CN}$ 2104 cm^{-1}.

[Ru(bpy)(tpy-Ph-Me)SCN]PF₆ (3b). Yield: 87%. ^{1}H NMR (300 MHz, DMSO-d_6): δ 9.56 (dd, ^4J = 1.3 Hz, ^3J = 5.6 Hz, 1H, H^{E6}), 9.21 (s, 2H, H^{H3}), 8.98 (d, ^3J = 8.1 Hz, 2H, H^{G3}), 8.94 (d, ^3J = 8.8 Hz, 1H, H^{E3}), 8.66 (d, ^3J = 8.2 Hz, 1H, H^{F3}), 8.41 (t, ^3J = 7.8 Hz, 1H, H^{E4}), 8.27 (d, ^3J = 7.9 Hz, 2H, H^{J2}), 8.16 (t, ^3J = 6.7 Hz, 1H, H^{E5}), 8.09 (td, ^4J = 1.5 Hz, ^3J = 7.8 Hz, 2H, H^{G4}), 7.84 (t, ^3J = 7.7 Hz, 1H, H^{F4}), 7.69 (dd, ^4J = 1.4 Hz, ^3J = 5.6 Hz, 2H, H^{G6}), 7.52 (d, ^3J = 7.9 Hz, 2H, H^{J3}), 7.49−7.37 (m, 3H, H^{G5}, H^{F6}), 7.13 (t, ^3J = 6.6 Hz, 1H, H^{F5}), 2.48 (s, 3H, CH_3). ^{13}C{^{1}H} NMR (63 MHz, DMSO-d_6): δ 158.2 (2C, C^{G2}), 157.7 (C^{F2}), 157.2 (2C, C^{H2}), 155.4 (C^{E2}), 152.2 (2C, C^{G6}), 151.4 (C^{E6}), 151.2 (C^{F6}), 146.5 (C^{J4}), 140.2 (C^{J1}), 137.8 (2C, C^{G4}), 137.1 (C^{E4}), 136.4 (C^{H4}), 133.8 (SCN), 133.2 (C^{F4}), 129.9 (2C, C^{J3}), 127.9

(2C, C^{G5}), 127.7 (C^{E5}), 127.6 (2C, C^{J2}), 126.7 (C^{F5}), 124.5 (2C, C^{G3}), 124.18 (C^{E3}), 123.6 (C^{F3}), 120.2 (2C, C^{H3}), 21.0 (CH_3). HRMS (ESI-TOF). Calcd for $C_{33}H_{25}N_6RuS$ ([M − PF_6]$^+$): m/z 639.0896. Found: m/z 639.0905. IR (KBr): $\tilde{\nu}_{CN}$ 2098 cm^{-1}.

[Ru(bpy)(tpy-Ph-Br)SCN]PF$_6$ (3c). Yield: 51%. ^{1}H NMR (400 MHz, DMSO-d_6): δ 9.56 (dd, ^4J = 1.5 Hz, ^3J = 5.7 Hz, 1H, H^{E6}), 9.24 (s, 2H, H^{H3}), 8.97 (dt, ^4J = 1.0 Hz, ^3J = 8.3 Hz, 2H, H^{G3}), 8.94 (dt, ^4J = 1.0 Hz, ^3J = 8.4 Hz, 1H, H^{E3}), 8.66 (dt, ^4J = 1.1 Hz, ^3J = 8.3 Hz, 1H, H^{F3}), 8.41 (td, ^4J = 1.5 Hz, ^3J = 7.9 Hz, 1H, H^{E4}), 8.32 (d, ^3J = 8.7 Hz, 2H, H^{J2}), 8.16 (ddd, ^4J = 1.3 Hz, ^3J = 5.6 Hz, ^3J = 7.3 Hz, 1H, H^{E5}), 8.11 (td, ^4J = 1.6 Hz, ^3J = 7.9 Hz, 2H, H^{G4}), 7.93 (d, ^3J = 8.6 Hz, 2H, H^{J3}), 7.84 (td, ^4J = 1.5 Hz, ^3J = 7.9 Hz, 1H, H^{F4}), 7.70 (dd, ^4J = 1.4 Hz, ^3J = 5.5 Hz, 2H, H^{G6}), 7.45 (ddd, ^4J = 1.3 Hz, ^3J = 5.5 Hz, ^3J = 7.2 Hz, 2H, H^{G5}), 7.39 (dd, ^4J = 1.4 Hz, ^3J = 5.7 Hz, 1H, H^{F6}), 7.12 (ddd, ^4J = 1.3 Hz, ^3J = 5.7 Hz, ^3J = 7.2 Hz, 1H, H^{F5}). $^{13}C\{^1H\}$ NMR (100 MHz, DMSO-d_6): δ 158.1 (2C, C^{G2}), 157.6 (C^{F2}), 157.4 (2C, C^{H2}), 155.4 (C^{E2}), 152.2 (2C, C^{G6}), 151.4 (C^{E6}), 151.2 (C^{F6}), 145.2 (C^{J1}), 137.9 (2C, C^{G4}), 137.2 (C^{E4}), 136.5 (C^{H4}), 135.4 (C^{J4}), 133.8 (SCN), 132.2 (2C, C^{J3}), 129.8 (2C, C^{J2}), 128.1 (2C, C^{G5}), 127.7 (C^{E5}), 126.7 (C^{F5}), 124.6 (2C, C^{G3}), 124.2 (C^{E3}), 124.0 (C^{J4}), 123.6 (C^{F3}), 120.5 (2C, C^{H3}). HRMS (ESI-TOF). Calcd for $C_{32}H_{22}BrN_6RuS$ ([M − PF_6]$^+$): m/z 702.9826. Found: m/z 702.9853. IR (KBr): $\tilde{\nu}_{CN}$ 2098 cm^{-1}.

[Ru(bpy)(tpy-Ph-CHO)SCN]PF$_6$ (3d). Yield: 77%. ^{1}H NMR (400 MHz, DMSO-d_6): δ 10.19 (s, 1H, CHO), 9.57 (dd, ^4J = 1.4 Hz, ^3J = 5.7 Hz, 1H, H^{E6}), 9.30 (s, 2H, H^{H3}), 8.99 (d, ^3J = 8.1 Hz, 2H, H^{G3}), 8.95 (d, ^3J = 8.2 Hz, 1H, H^{E3}), 8.67 (d, ^3J = 8.2 Hz, 1H, H^{F3}), 8.57 (d, ^3J = 8.1 Hz, 2H, H^{J2}), 8.42 (td, ^4J = 1.6 Hz, ^3J = 7.9 Hz, 1H, H^{E4}), 8.23 (d, ^3J = 8.3 Hz, 2H, H^{J3}), 8.17 (ddd, ^4J = 1.3 Hz, ^3J = 5.6 Hz, ^3J = 7.3 Hz, 1H, H^{E5}), 8.11 (td, ^4J = 1.5 Hz, ^3J = 7.8 Hz, 2H, H^{G4}), 7.85 (td, ^4J = 1.5 Hz, ^3J = 7.9 Hz, 1H, H^{F4}), 7.72 (dd, ^4J = 1.4 Hz, ^3J = 5.5 Hz, 2H, H^{G6}), 7.47 (ddd, ^4J = 1.3 Hz, ^3J = 5.5 Hz, ^3J = 7.2 Hz, 2H, H^{G5}), 7.40 (dd, ^4J = 1.3 Hz, ^3J = 5.8 Hz, 1H, H^{F6}), 7.13 (ddd, ^4J = 1.3 Hz, ^3J = 5.7 Hz, ^3J = 7.3 Hz, 1H, H^{F5}). $^{13}C\{^1H\}$ NMR (100 MHz, DMSO-d_6): δ 192.9 (CHO), 158.1 (2C, C^{G2}), 157.6 (C^{F2}), 157.6 (2C, C^{H2}), 155.4 (C^{E2}), 152.3 (2C, C^{G6}), 151.4 (C^{E6}), 151.2 (C^{F6}), 144.9 (C^{J4}), 141.7 (C^{J1}), 137.9 (2C, C^{G4}), 137.4 (C^{E4}), 136.9 (C^{H4}), 136.6 (C^{F4}), 133.9 (SCN), 130.3 (2C, C^{J3}), 128.5 (2C, C^{J2}), 128.2 (2C, C^{G5}), 127.8 (C^{E5}), 126.8 (C^{F5}), 124.6 (2C, C^{G3}), 124.3 (C^{E3}), 123.7 (C^{F3}), 121.0 (2C, C^{H3}). HRMS (ESI-TOF). Calcd for $C_{33}H_{23}N_6ORuS$ ([M − PF_6]$^+$): m/z 653.0674. Found: m/z 653.0697. IR (KBr): $\tilde{\nu}_{CN}$ 2102 cm^{-1}.

[Ru(bpy)(tpy-pep-CHO)SCN]PF$_6$ (3e). Yield: 68%. ^{1}H NMR (400 MHz, DMSO-d_6): δ 10.36 (s, 1H, CHO), 9.57 (d, ^3J = 5.3 Hz, 1H, H^{E6}), 9.27 (s, 2H, H^{H3}), 8.99 (d, ^3J = 8.0 Hz, 2H, H^{G3}), 8.94 (d, ^3J = 8.2 Hz, 1H, H^{E3}), 8.67 (d, ^3J = 8.3 Hz, 1H, H^{F3}), 8.47 (d, ^3J = 8.5 Hz, 2H, H^{J2}), 8.41 (td, ^4J = 1.5 Hz, ^3J = 7.9 Hz, 1H, H^{E4}), 8.16 (ddd, ^4J = 1.2 Hz, ^3J = 5.7 Hz, ^3J = 7.4 Hz, 1H, H^{E5}), 8.11 (td, ^4J = 1.5 Hz, ^3J = 7.8 Hz, 2H, H^{G4}), 7.88−7.81 (m, 3H, H^{J3}), 7.71 (dd, ^4J = 1.5 Hz, ^3J = 5.6 Hz, 2H, H^{G6}), 7.46 (ddd, ^4J = 1.3 Hz, ^3J = 5.6 Hz, ^3J = 7.4 Hz, 2H, H^{G5}), 7.44 (s, 1H, H^{K2}), 7.39 (dd, ^4J = 1.3 Hz, ^3J = 5.7 Hz, 1H, H^{F6}), 7.28 (s, 1H, H^{K5}), 7.13 (ddd, ^4J = 1.3 Hz, ^3J = 5.7 Hz, ^3J = 7.3 Hz, 1H, H^{F5}), 4.15 (t, ^3J = 6.4 Hz, 2H, α-OCH$_2$), 4.10 (t, ^3J = 6.2 Hz, 2H, α-OCH$_2$), 1.87−1.72 (m, 4H, β-CH$_2$), 1.54 (quint, ^3J = 7.1 Hz, 2H, γ-CH$_2$), 1.49−1.16 (m, 18H, γ-η-CH$_2$), 0.86 (t, ^3J = 6.7 Hz, 3H, CH$_3$), 0.81 (t, ^3J = 6.8 Hz, 3H, CH$_3$). ^{13}C-$\{^1H\}$ NMR (100 MHz, DMSO-d_6): δ 188.4 (CHO), 158.2 (2C, C^{G2}), 157.7 (C^{F2}), 157.5 (2C, C^{H2}), 155.4 (C^{E2}), 155.1 (C^{K6}), 153.3 (C^{K3}), 152.2 (2C, C^{G6}), 151.4 (C^{E6}), 151.1 (C^{F6}), 145.1 (C^{H4}), 137.9 (2C, C^{G4}), 137.3 (2C, C^{E4}), 136.6 (C^{J1}), 136.5 (C^{F4}), 133.9 (SCN), 132.1 (2C, C^{J3}), 128.1 (4C, C^{J2}, C^{G5}), 127.7 (C^{E5}), 126.7 (C^{F5}), 124.8 (C^{K4}), 124.6 (2C, C^{G3}), 124.2 (C^{E3}), 123.8 (C^{J4}), 123.7 (C^{F3}), 120.5 (2C, C^{H3}), 119.2 (C^{K1}), 118.2 (C^{K2}), 109.8 (C^{K5}), 96.4 (C^{alkyne}), 87.9 (C^{alkyne}), 69.2 (α-OCH$_2$), 68.8 (α-OCH$_2$), 31.29 (β-CH$_2$), 31.26 (β-CH$_2$), 28.82 (γ-CH$_2$), 28.73 (2C, γ-CH$_2$, δ-CH$_2$), 28.70 (δ-CH$_2$), 28.65 (ε-CH$_2$), 28.59 (ε-CH$_2$), 25.6 (ζ-CH$_2$), 25.5 (ζ-CH$_2$), 22.16 (η-CH$_2$), 22.15 (η-CH$_2$), 14.01 (CH$_3$), 14.00 (CH$_3$). HRMS (ESI-TOF). Calcd for $C_{57}H_{59}N_6O_3RuS$ ([M − PF_6]$^+$): m/z 1009.3363. Found: m/z 1009.3413. IR (KBr): $\tilde{\nu}_{CN}$ 2094 cm^{-1}.

General Procedure for Dinuclear Cyanide-Bridged Iridium(III)− Ruthenium(II) Complexes 1 and 2; [Ir((R$_2$)$_2$-ppy)$_2$(CN)(μ-CN)Ru-(bpy)(R$_1$-tpy)]PF$_6$. A microwave vial (5 mL) was charged with [Ru(bpy)(tpy-R$_1$)Cl]Cl/PF$_6$ (**6a−6e**; 0.039 mmol) and Bu$_4$N[Ir-

((R$_2$)$_2$-ppy)$_2$(CN)$_2$] (**4 and 5**; 0.059 mmol) in 2.2 mL of methanol/ water (10:1). The vial was capped, and the mixture was deaerated with nitrogen for 15 min. The purple solution was heated under microwave irradiation for 30 min at 120 °C. The solvent was evaporated, and the residue was purified by column chromatography (silica, 40:4:1 acetonitrile/water/saturated aqueous KNO$_3$ solution). The red fraction was collected, and an excess of NH$_4$PF$_6$ was added; the mixture was concentrated in vacuo, and water was added. The fine precipitate was collected by filtration and further purified by preparative size-exclusion chromatography (Bio-Beads S-X3 Beads, dichloromethane) to obtain a dark-red complex.

For the complexes containing an aldehyde group, an additional, final step was performed. The complex was dissolved in DMSO (3 mL), and a 1 M HCl solution (1 mL) was added. The solution was stirred for 3 h at room temperature. Subsequently, NH$_4$PF$_6$ (excess) and water (50 mL) were added to the stirred solution, and the solid was collected by filtration.

[Ir(ppy)$_2$(CN)(μ-CN)Ru(bpy)(tpy)]PF$_6$ (1a). Yield: 66%. ^{1}H NMR (400 MHz, DMSO-d_6): δ 9.23 (dd, ^4J = 1.2 Hz, ^3J = 5.9 Hz, 1H, H^{D6}), 9.08 (dd, ^4J = 1.1 Hz, ^3J = 5.7 Hz, 1H, H^{E6}), 8.81 (d, ^3J = 8.0 Hz, 1H, H^{E3}), 8.72 (t, ^3J = 7.8 Hz, 2H, H^{H5}, H^{H3}), 8.64−8.55 (m, 3H, H^{G3}, H^{I3}, H^{F3}), 8.33−8.25 (m, 2H, H^{B6}, H^{E4}), 8.22 (t, ^3J = 8.1 Hz, 1H, H^{H4}), 8.09−7.94 (m, 4H, H^{B3}, H^{D3}, H^{G4}, H^{I4}), 7.91 (td, ^4J = 1.6 Hz, ^3J = 7.9 Hz, ^3J = 8.3 Hz, 1H, H^{D4}), 7.85 (td, ^4J = 1.6 Hz, ^3J = 8.0 Hz, ^3J = 8.4 Hz, 1H, H^{B4}), 7.80 (td, ^4J = 1.5 Hz, ^3J = 7.8 Hz, 1H, H^{F4}), 7.74 (ddd, ^4J = 1.2 Hz, ^3J = 5.6 Hz, ^3J = 7.1 Hz, 1H, H^{E5}), 7.64 (dd, ^4J = 1.2 Hz, ^3J = 7.9 Hz, 1H, H^{A3}), 7.61 (dd, ^4J = 1.2 Hz, ^3J = 7.9 Hz, 1H, H^{C3}), 7.46 (dd, ^4J = 1.1 Hz, ^3J = 5.5 Hz, 1H, H^{G6}), 7.36−7.20 (m, 5H, H^{G5}, H^{I5}, H^{I6}, H^{F6}, H^{D5}), 7.09 (ddd, ^4J = 1.3 Hz, ^3J = 5.7 Hz, ^3J = 7.3 Hz, 1H, H^{F5}), 6.96 (ddd, ^4J = 1.5 Hz, ^3J = 5.8 Hz, ^3J = 7.3 Hz, 1H, H^{B5}), 6.78 (td, ^4J = 1.3 Hz, ^3J = 7.4 Hz, 1H, H^{A4}), 6.71 (td, ^4J = 1.3 Hz, ^3J = 7.5 Hz, 1H, H^{C4}), 6.63−6.55 (m, 2H, H^{A5}, H^{C5}), 5.96 (dd, ^4J = 1.2 Hz, ^3J = 7.6 Hz, 1H, H^{A6}), 5.65 (dd, ^4J = 1.2 Hz, ^3J = 7.4 Hz, 1H, H^{C6}). $^{13}C\{^1H\}$ NMR (150 MHz, DMSO-d_6): δ 167.7 (C^{B2}), 167.5 (C^{D2}), 161.24 (C^{C1}), 161.16 (C^{A1}), 157.7 (C^{G2}), 157.6 (C^{I2}), 157.3 (C^{F2}), 156.70 (C^{H2}), 156.67 (C^{H6}), 155.4 (C^{E2}), 153.0 (C^{D6}), 151.8 (C^{G6}), 151.6 (C^{I6}), 151.5 (C^{B6}), 150.93 (C^{E6}), 150.85 (C^{F6}), 144.1 (C^{C2}), 143.9 (C^{A2}), 142.9 (μ-CN), 137.7 (C^{G4}), 137.6 (C^{I4}), 136.9 (C^{D4}), 136.8 (C^{E4}), 136.6 (C^{B4}), 136.5 (C^{F4}), 135.2 (C^{H4}), 130.4 (C^{A6}), 130.2 (C^{C6}), 129.7 (CN), 129.0 (C^{C5}), 128.6 (C^{A5}), 127.89 (C^{G5}), 127.85 (C^{I5}), 127.0 (C^{E5}), 126.6 (C^{F5}), 124.08 (C^{G3}), 124.05 (C^{I3}), 123.92 (C^{E3}), 123.90 (C^{A3}), 123.86 (C^{C3}), 123.5 (C^{F3}), 123.1 (C^{H3}), 123.0 (C^{H5}), 122.9 (C^{D5}), 122.4 (C^{B5}), 120.7 (C^{A4}), 120.6 (C^{C4}), 119.4 (C^{B3}), 119.2 (C^{D3}). HRMS (ESI-TOF). Calcd for $C_{49}H_{35}IrN_9Ru$ ([M − PF_6]$^+$): m/z 1044.1640. Found: m/z 1044.1688. IR (KBr): $\tilde{\nu}_{CN}$ 2101, 2116 cm^{-1}.

[Ir(F$_2$-ppy)$_2$(CN)(μ-CN)Ru(bpy)(tpy)]PF$_6$ (2a). Yield: 35%. ^{1}H NMR (600 MHz, CD$_3$CN): δ 9.46 (ddd, ^5J = 0.8 Hz, ^4J = 1.5 Hz, ^3J = 5.5 Hz, 1H, H^{E6}), 9.32 (ddd, ^5J = 0.8 Hz, ^4J = 1.7 Hz, ^3J = 5.8 Hz, 1H, H^{D6}), 8.59 (ddd, ^5J = 0.8 Hz, ^4J = 1.7 Hz, ^3J = 5.8 Hz, 1H, H^{B6}), 8.55 (dt, ^4J = 1.1 Hz, ^3J = 8.2 Hz, 1H, H^{E3}), 8.32 (dd, ^5J = 0.8 Hz, ^3J = 8.1 Hz, 1H, H^{H3}), 8.30−8.26 (m, 2H, H^{H5}, H^{F3}), 8.25−8.21 (m, 2H, H^{E4}, H^{G3}), 8.18−8.14 (m, 2H, H^{B3}, H^{I3}), 8.11−8.05 (m, 2H, H^{D3}, H^{H4}), 7.94−7.80 (m, 5H, H^{D4}, H^{G4}, H^{B4}, H^{E5}, H^{I4}), 7.70 (ddd, ^4J = 1.5 Hz, ^3J = 7.5 Hz, ^3J = 8.2 Hz, 1H, H^{F4}), 7.56 (ddd, ^5J = 0.8 Hz, ^4J = 1.5 Hz, ^3J = 5.5 Hz, 1H, H^{G6}), 7.39 (ddd, ^5J = 0.7 Hz, ^4J = 1.6 Hz, ^3J = 5.5 Hz, 1H, H^{I6}), 7.27−7.22 (m, 2H, H^{G5}, H^{F6}), 7.19 (ddd, ^4J = 1.5 Hz, ^3J = 5.8 Hz, ^3J = 7.4 Hz, 1H, H^{D5}), 7.15 (ddd, ^4J = 1.3 Hz, ^3J = 5.5 Hz, ^3J = 7.5 Hz, 1H, H^{I5}), 7.01 (ddd, ^4J = 1.5 Hz, ^3J = 5.8 Hz, ^3J = 7.4 Hz, 1H, H^{B5}), 6.96 (ddd, ^4J = 1.3 Hz, ^3J = 5.8 Hz, ^3J = 7.3 Hz, 1H, H^{F5}), 6.42 (ddd, ^4J = 2.4 Hz, $^3J_{HF}$ = 9.3 Hz, $^3J_{HF}$ = 12.9 Hz, 1H, H^{C4}), 6.37 (ddd, ^4J = 2.4 Hz, $^3J_{HF}$ = 9.3 Hz, $^3J_{HF}$ = 13.0 Hz, 1H, H^{A4}), 5.53 (dd, ^4J = 2.4 Hz, $^3J_{HF}$ = 8.4 Hz, 1H, H^{A6}), 5.13 (dd, ^4J = 2.4 Hz, $^3J_{HF}$ = 8.2 Hz, 1H, H^{C6}). $^{19}F\{^1H\}$ NMR (188 MHz, CD$_3$CN): δ −73.30 (d, $^1J_{FP}$ = 706.4 Hz, 6F), −110.43 (d, ^4J = 8.7 Hz, 1F), −111.05 (d, ^4J = 8.9 Hz, 1F), −111.34 (d, ^4J = 8.6 Hz, 1F), −111.93 (d, ^4J = 8.5 Hz, 1F). HRMS (ESI-TOF). Calcd for $C_{49}H_{31}F_4IrN_9Ru$ ([M − PF_6]$^+$): m/z 1116.1226. Found: m/z 1116.1311. IR (KBr): $\tilde{\nu}_{CN}$ 2112, 2121 cm^{-1}.

[Ir(ppy)$_2$(CN)(μ-CN)Ru(bpy)(tpy-Ph-Me)]PF$_6$ (1b). Yield: 81%. ^{1}H NMR (600 MHz, DMSO-d_6): δ 9.24 (d, ^3J = 5.7 Hz, 1H, H^{D6}), 9.18 (d, ^3J = 5.4 Hz, 1H, H^{E6}), 9.04 (s, 1H, H^{H5}), 9.02 (s, 1H, H^{H3}), 8.86–8.79 (m, 3H, H^{G3}, H^{E3}, H^{I3}), 8.58 (d, ^3J = 8.5 Hz, 1H, H^{F3}), 8.37 (d, ^3J = 5.5 Hz, 1H, H^{B6}), 8.29 (td, ^4J = 1.4 Hz, ^3J = 8.1 Hz, 1H, H^{E4}), 8.24 (d, ^3J = 7.9 Hz, 2H, H^{J2}), 8.03–7.93 (m, 4H, H^{B3}, H^{G4}, H^{D3}, H^{I4}), 7.86–7.76 (m, 4H, H^{D4}, H^{B4}, H^{F4}, H^{E5}), 7.59 (d, ^3J = 7.7 Hz, 1H, H^{A3}), 7.55 (d, ^3J = 7.7 Hz, 1H, H^{C3}), 7.50 (d, ^3J = 8.0 Hz, 2H, H^{J3}), 7.48 (d, ^3J = 5.0 Hz, 1H, H^{G6}), 7.35–7.27 (m, 4H, H^{G5}, H^{F6}, H^{I6}, H^{I5}), 7.17 (td, ^4J = 1.5 Hz, ^3J = 5.8 Hz, ^3J = 7.4 Hz, 1H, H^{D5}), 7.10 (td, ^4J = 1.2 Hz, ^3J = 5.9 Hz, ^3J = 7.3 Hz, 1H, H^{F5}), 6.94 (td, ^4J = 1.4 Hz, ^3J = 5.7 Hz, ^3J = 7.3 Hz, 1H, H^{B5}), 6.72–6.66 (m, 2H, H^{A4}, H^{C4}), 6.57 (td, ^4J = 1.2 Hz, ^3J = 7.4 Hz, 1H, H^{A5}), 6.51 (td, ^4J = 1.2 Hz, ^3J = 7.3 Hz, 1H, H^{C5}), 5.93 (d, ^3J = 7.3 Hz, 1H, H^{A6}), 5.64 (d, ^3J = 7.3 Hz, 1H, H^{C6}), 2.49 (s, 3H, CH_3). ^{13}C{^{1}H} NMR (150 MHz, DMSO-d_6): δ 167.7 (C^{B2}), 167.5 (C^{D2}), 161.21 (C^{C1}), 161.17 (C^{A1}), 158.0 (C^{G2}), 157.9 (C^{I2}), 157.4 (C^{F2}), 156.91 (C^{H2}), 156.88 (C^{E2}), 153.0 (C^{D6}), 151.8 (C^{G6}), 151.7 (C^{I6}), 151.5 (C^{B6}), 150.96 (C^{E6}), 150.95 (C^{F6}), 146.2 (C^{H4}), 144.1 (C^{C2}), 143.9 (C^{A2}), 143.0 (μ-CN), 140.2 (C^{J4}), 137.63 (C^{G4}), 137.56 (C^{I4}), 136.9 (C^{D4}), 136.8 (C^{E4}), 136.6 (C^{B4}), 136.5 (C^{F4}), 133.0 (C^{J1}), 130.4 (C^{A6}), 130.2 (C^{C6}), 129.9 (2C, C^{J3}), 129.8 (CN), 128.9 (C^{C5}), 128.6 (C^{A5}), 127.9 (C^{G5}), 127.8 (C^{I5}), 127.5 (2C, C^{J2}), 127.1 (C^{E5}), 126.6 (C^{F5}), 124.4 (C^{G3}), 124.3 (C^{I3}), 124.1 (C^{E3}), 123.9 (C^{A3}), 123.8 (C^{C3}), 123.5 (C^{F3}), 122.9 (C^{D5}), 122.4 (C^{B5}), 120.7 (C^{C4}), 120.6 (C^{A4}), 120.0 (C^{H3}), 119.8 (C^{H5}), 119.4 (C^{B3}), 119.1 (C^{D3}), 21.0 (CH_3). HRMS (ESI-TOF). Calcd for C$_{56}$H$_{41}$IrN$_9$Ru ([M − PF$_6$]$^+$): m/z 1134.2171. Found: m/z 1134.2158. IR (KBr): $\tilde{\nu}_{CN}$ 2102 cm^{-1}.

[Ir(F$_2$-ppy)$_2$(CN)(μ-CN)Ru(bpy)(tpy-Ph-Me)]PF$_6$ (2b). Yield: 83%. ^{1}H NMR (600 MHz, CD$_3$CN): δ 9.62 (d, ^3J = 5.4 Hz, 1H, H^{E6}), 9.37 (d, ^3J = 5.5 Hz, 1H, H^{D6}), 8.66 (d, ^3J = 5.5 Hz, 1H, H^{B6}), 8.55 (d, ^3J = 8.2 Hz, 1H, H^{E3}), 8.52 (s, 1H, H^{H5}), 8.46 (s, 1H, H^{H3}), 8.36 (d, ^3J = 8.1 Hz, 1H, H^{G3}), 8.29–8.20 (m, 3H, H^{I3}, H^{F3}, H^{E4}), 8.07 (d, ^3J = 8.6 Hz, 1H, H^{B3}), 7.96–7.90 (m, 3H, H^{J2}, H^{D3}), 7.87 (t, ^3J = 6.5 Hz, 1H, H^{E5}), 7.83 (t, ^3J = 7.7 Hz, 1H, H^{G4}), 7.78–7.69 (m, 3H, H^{B4}, H^{D4}, H^{I4}), 7.67 (t, ^3J = 7.8 Hz, 1H, H^{F4}), 7.59 (d, ^3J = 5.5 Hz, 1H, H^{G6}), 7.45–7.41 (m, 3H, H^{J3}, H^{I6}), 7.24–7.19 (m, 2H, H^{G5}, H^{F6}), 7.13–7.06 (m, 2H, H^{I5}, H^{D5}), 6.99–6.92 (m, 2H, H^{B5}, H^{F5}), 6.29 (ddd, ^4J = 2.4 Hz, $^3J_{HF}$ = 9.2 Hz, $^3J_{HF}$ = 12.2 Hz, 1H, H^{A4}), 6.23 (ddd, ^4J = 2.4 Hz, $^3J_{HF}$ = 9.1 Hz, $^3J_{HF}$ = 12.1 Hz, 1H, H^{C4}), 5.47 (dd, ^4J = 2.4 Hz, $^3J_{HF}$ = 8.4 Hz, 1H, H^{A6}), 5.18 (dd, ^4J = 2.4 Hz, $^3J_{HF}$ = 8.2 Hz, 1H, H^{C6}), 2.49 (s, 3H, CH_3). ^{19}F{^{1}H} NMR (188 MHz, CD$_3$CN): δ −73.30 (d, $^1J_{FP}$ = 706.8 Hz, 6F), −110.25 (d, ^4J = 9.5 Hz, 1F), −110.94 (d, ^4J = 9.7 Hz, 1F), −111.34 (d, ^4J = 9.6 Hz, 1F), −111.80 (d, ^4J = 9.7 Hz, 1F). HRMS (ESI-TOF). Calcd for C$_{56}$H$_{37}$F$_4$IrN$_9$Ru ([M − PF$_6$]$^+$): m/z 1206.1738. Found: m/z 1206.1781. IR (KBr): $\tilde{\nu}_{CN}$ 2111, 2124 cm^{-1}.

[Ir(ppy)$_2$(CN)(μ-CN)Ru(bpy)(tpy-Ph-Br)]PF$_6$ (1c). Yield: 64%. ^{1}H NMR (400 MHz, DMSO-d_6): δ 9.23 (d, ^3J = 4.9 Hz, 1H, H^{D6}), 9.19 (d, ^3J = 5.3 Hz, 1H, H^{E6}), 9.07 (s, 1H, H^{H5}), 9.05 (s, 1H, H^{H3}), 8.84 (d, ^3J = 7.6 Hz, 1H, H^{E3}), 8.82 (d, ^3J = 7.2 Hz, 2H, H^{G3}, H^{I3}), 8.59 (d, ^3J = 8.2 Hz, 1H, H^{F3}), 8.36 (d, ^3J = 4.9 Hz, 1H, H^{B6}), 8.34–8.24 (m, 3H, H^{E4}, H^{J2}), 8.01 (d, ^3J = 8.1 Hz, 2H, H^{G4}, H^{I4}), 7.97 (d, ^3J = 8.2 Hz, 2H, H^{D3}, H^{B3}), 7.89 (d, ^3J = 7.7 Hz, 2H, H^{J3}), 7.87–7.76 (m, 4H, H^{B4}, H^{D4}, H^{E5}, H^{F4}), 7.59 (d, ^3J = 7.8 Hz, 1H, H^{C3}), 7.56 (d, ^3J = 7.8 Hz, 1H, H^{A3}), 7.49 (d, ^3J = 5.0 Hz, 1H, H^{G6}), 7.39–7.26 (m, 4H, H^{G5}, H^{I5}, H^{I6}, H^{F6}), 7.17 (t, ^3J = 6.6 Hz, 1H, H^{D5}), 7.10 (t, ^3J = 7.1 Hz, 1H, H^{F5}), 6.95 (t, ^3J = 6.6 Hz, 1H, H^{B5}), 6.69 (t, ^3J = 7.4 Hz, 2H, H^{A4}, H^{C4}), 6.57 (t, ^3J = 7.4 Hz, 1H, H^{A5}), 6.52 (t, ^3J = 7.3 Hz, 1H, H^{C5}), 5.92 (d, ^3J = 7.5 Hz, 1H, H^{A6}), 5.64 (d, ^3J = 6.6 Hz, 1H, H^{C6}). ^{13}C{^{1}H} NMR (150 MHz, DMSO-d_6): δ 167.7 (C^{B2}), 167.4 (C^{D2}), 161.13 (C^{C1}), 161.06 (C^{A1}), 157.8 (C^{G2}), 157.7 (C^{I2}), 157.3 (C^{F2}), 157.1 (C^{H2}), 157.0 (C^{H6}), 155.4 (C^{E2}), 153.0 (C^{D6}), 151.8 (C^{G6}), 151.7 (C^{I6}), 151.4 (C^{B6}), 150.9 (2C, C^{E6}, C^{F6}), 144.7 (C^{H4}), 144.1 (C^{C2}), 143.9 (C^{A2}), 143.2 (μ-CN), 137.6 (C^{G4}), 137.6 (C^{I4}), 136.8 (C^{D4}), 136.60 (C^{E4}), 136.55 (C^{F4}), 135.0 (C^{J1}), 132.2 (2C, C^{J3}), 130.3 (C^{A6}), 130.2 (C^{C6}), 129.7 (CN), 129.6 (2C, C^{J2}), 128.8 (C^{C5}), 128.6 (C^{A5}), 127.94 (C^{G5}), 127.90 (C^{I5}), 127.1 (C^{E5}), 126.6 (C^{F5}), 124.4 (C^{I3}), 124.3 (C^{G3}), 124.1 (C^{E3}), 123.93 (C^{J4}), 123.85 (C^{A3}), 123.8 (C^{C3}), 123.5 (C^{F3}), 122.9 (C^{D5}), 122.4 (C^{B5}), 120.7 (C^{C4}), 120.6 (C^{A4}), 120.1 (C^{H3}), 119.9

(C^{H5}), 119.4 (C^{B3}), 119.1 (C^{D3}). HRMS (ESI-TOF). Calcd for C$_{55}$H$_{38}$BrIrN$_9$Ru ([M − PF$_6$]$^+$): m/z 1198.1125. Found: m/z 1198.1106. IR (KBr): $\tilde{\nu}_{CN}$ 2106, 2117 cm^{-1}.

[Ir(F$_2$-ppy)$_2$(CN)(μ-CN)Ru(bpy)(tpy-Ph-Br)]PF$_6$ (2c). Yield: 76%. ^{1}H NMR (600 MHz, CD$_3$CN): δ 9.61 (d, ^3J = 5.5 Hz, 1H, H^{E6}), 9.35 (d, ^3J = 5.6 Hz, 1H, H^{D6}), 8.65 (d, ^3J = 5.6 Hz, 1H, H^{B6}), 8.56 (d, ^3J = 8.2 Hz, 1H, H^{E3}), 8.54 (s, 1H, H^{H5}), 8.48 (s, 1H, H^{H3}), 8.37 (d, ^3J = 8.0 Hz, 1H, H^{G3}), 8.28 (d, ^3J = 8.2 Hz, 2H, H^{F3}, H^{I3}), 8.25 (t, ^3J = 7.9 Hz, 1H, H^{E4}), 8.05 (d, ^3J = 8.6 Hz, 1H, H^{B3}), 7.97 (d, ^3J = 8.3 Hz, 2H, H^{J2}), 7.94 (d, ^3J = 8.7 Hz, 1H, H^{D3}), 7.88 (t, ^3J = 6.6 Hz, 1H, H^{E5}), 7.85 (t, ^3J = 8.0 Hz, 1H, H^{G4}), 7.78 (d, ^3J = 8.2 Hz, 2H, H^{J3}), 7.75 (t, ^3J = 7.9 Hz, 3H, H^{I4}, H^{D4}, H^{B4}), 7.68 (t, ^3J = 7.5 Hz, 1H, H^{F4}), 7.60 (d, ^3J = 5.3 Hz, 1H, H^{G6}), 7.44 (d, ^3J = 5.4 Hz, 1H, H^{I6}), 7.23 (t, ^3J = 6.6 Hz, 1H, H^{G5}), 7.19 (d, ^3J = 5.7 Hz, 1H, H^{F6}), 7.14 (t, ^3J = 6.5 Hz, 1H, H^{I5}), 7.09 (t, ^3J = 6.6 Hz, 1H, H^{D5}), 6.98–6.92 (m, 2H, H^{B5}, H^{F5}), 6.32–6.19 (m, 2H, H^{A4}, H^{C4}), 5.46 (dd, ^4J = 2.4 Hz, $^3J_{HF}$ = 8.2 Hz, 1H, H^{A6}), 5.16 (dd, ^4J = 2.3 Hz, $^3J_{HF}$ = 8.2 Hz, 1H, H^{C6}). ^{19}F{^{1}H} NMR (188 MHz, CD$_3$CN): δ −73.30 (d, $^1J_{FP}$ = 706.8 Hz, 6F), −110.24 (d, ^4J = 9.5 Hz, 1F), −110.88 (d, ^4J = 9.7 Hz, 1F), −111.30 (d, ^4J = 9.6 Hz, 1F), −111.74 (d, ^4J = 9.7 Hz, 1F). HRMS (ESI-TOF). Calcd for C$_{55}$H$_{34}$BrF$_4$IrN$_9$Ru ([M − PF$_6$]$^+$): m/z 1270.0686. Found: m/z 1270.0729. IR (KBr): $\tilde{\nu}_{CN}$ 2111 cm^{-1}.

[Ir(ppy)$_2$(CN)(μ-CN)Ru(bpy)(tpy-Ph-CHO)]PF$_6$ (1d). Yield: 82%. ^{1}H NMR (600 MHz, DMSO-d_6): δ 10.18 (s, 1H, CHO), 9.26 (d, ^3J = 5.2 Hz, 1H, H^{E6}), 9.24 (d, ^3J = 5.1 Hz, 1H, H^{D6}), 9.09 (s, 1H, H^{H5}), 9.07 (s, 1H, H^{H3}), 8.84 (d, ^3J = 8.4 Hz, 1H, H^{E3}), 8.81 (d, ^3J = 8.4 Hz, 1H, H^{G3}), 8.80 (d, ^3J = 8.6 Hz, 1H, H^{I3}), 8.59 (d, ^3J = 8.3 Hz, 1H, H^{F3}), 8.50 (d, ^3J = 8.0 Hz, 2H, H^{J2}), 8.39 (d, ^3J = 5.4 Hz, 1H, H^{B6}), 8.31 (dd, ^3J = 8.2 Hz, ^4J = 1.3 Hz, 1H, H^{E4}), 8.18 (d, ^3J = 8.1 Hz, 2H, H^{J3}), 8.03–7.90 (m, 4H, H^{B3}, H^{G4}, H^{D3}, H^{I4}), 7.86–7.77 (m, 4H, H^{D4}, H^{F4}, H^{B4}, H^{E5}), 7.58 (d, ^3J = 7.8 Hz, 1H, H^{A3}), 7.53 (d, ^3J = 7.7 Hz, 1H, H^{C3}), 7.51 (d, ^3J = 5.2 Hz, 1H, H^{G6}), 7.37–7.27 (m, 4H, H^{G5}, H^{F6}, H^{I5}, H^{I6}), 7.14 (t, ^3J = 6.4 Hz, 1H, H^{D5}), 7.10 (t, ^3J = 6.6 Hz, 1H, H^{F5}), 6.96 (t, ^3J = 6.6 Hz, 1H, H^{B5}), 6.70–6.63 (m, 2H, H^{A4}, H^{C4}), 6.56 (t, ^3J = 7.4 Hz, 1H, H^{A5}), 6.51 (t, ^3J = 7.2 Hz, 1H, H^{C5}), 5.91 (d, ^3J = 7.5 Hz, 1H, H^{A6}), 5.66 (d, ^3J = 7.3 Hz, 1H, H^{C6}). ^{13}C{^{1}H} NMR (150 MHz, DMSO-d_6): δ 192.8 (CHO), 167.7 (C^{B2}), 167.5 (C^{D2}), 161.1 (C^{C1}), 161.0 (C^{A1}), 157.8 (C^{G2}), 157.7 (C^{I2}), 157.3 (C^{F2}), 157.23 (C^{H2}), 157.20 (C^{H6}), 155.3 (C^{E2}), 153.0 (C^{D6}), 151.9 (C^{G6}), 151.7 (C^{I6}), 151.5 (C^{B6}), 151.0 (2C, C^{E6}, C^{F6}), 144.4 (C^{H4}), 144.1 (C^{C2}), 143.9 (C^{A2}), 143.3 (μ-CN), 141.3 (C^{J1}), 137.7 (C^{G4}), 137.6 (C^{I4}), 137.0 (C^{E4}), 136.9 (C^{D4}), 136.8 (C^{J4}), 136.7 (2C, C^{B4}, C^{F4}), 130.3 (C^{A6}), 130.24 (C^{C6}), 130.22 (2C, C^{J3}), 129.8 (CN), 128.9 (C^{C5}), 128.7 (C^{A5}), 128.3 (2C, C^{J2}), 128.03 (C^{G5}), 127.99 (C^{I5}), 127.2 (C^{E5}), 126.7 (C^{F5}), 124.5 (C^{I3}), 124.4 (C^{G3}), 124.1 (C^{E3}), 123.9 (C^{A3}), 123.8 (C^{C3}), 123.6 (C^{F3}), 122.9 (C^{D5}), 122.5 (C^{B5}), 120.8 (C^{C4}), 120.7 (C^{A4}), 120.6 (C^{H3}), 120.5 (C^{H5}), 119.5 (C^{B3}), 119.2 (C^{D3}). HRMS (ESI-TOF). Calcd for C$_{56}$H$_{39}$IrN$_9$ORu ([M − PF$_6$]$^+$): m/z 1148.1917. Found: m/z 1148.1950. IR (KBr): $\tilde{\nu}_{CN}$ 2099, 2115 cm^{-1}.

[Ir(F$_2$-ppy)$_2$(CN)(μ-CN)Ru(bpy)(tpy-Ph-CHO)]PF$_6$ (2d). Yield: 69%. ^{1}H NMR (600 MHz, CD$_3$CN): δ 10.18 (s, 1H, CHO), 9.55 (d, ^3J = 5.3 Hz, 1H, H^{E6}), 9.34 (d, ^3J = 5.5 Hz, 1H, H^{D6}), 8.67–8.63 (m, 2H, H^{B6}, H^{H3}), 8.61 (s, 1H, H^{H5}), 8.57 (d, ^3J = 8.2 Hz, 1H, H^{E3}), 8.42 (d, ^3J = 8.0 Hz, 1H, H^{G3}), 8.35 (d, ^3J = 8.0 Hz, 1H, H^{I3}), 8.31–8.23 (m, 4H, H^{F3}, H^{J2}, H^{E4}), 8.18 (d, ^3J = 7.9 Hz, 2H, H^{J3}), 8.11 (d, ^3J = 8.4 Hz, 1H, H^{B3}), 7.98 (d, ^3J = 8.8 Hz, 1H, H^{D3}), 7.93–7.85 (m, 2H, H^{G4}, H^{E5}), 7.83 (t, ^3J = 7.7 Hz, 1H, H^{I4}), 7.79 (t, ^3J = 7.9 Hz, 2H, H^{B4}, H^{D4}), 7.70 (td, ^4J = 1.5 Hz, ^3J = 8.4 Hz, 1H, H^{F4}), 7.60 (d, ^3J = 4.9 Hz, 1H, H^{G6}), 7.44 (d, ^3J = 4.9 Hz, 1H, H^{I6}), 7.26 (t, ^3J = 6.4 Hz, 1H, H^{G5}), 7.23 (d, ^3J = 5.5 Hz, 1H, H^{F6}), 7.17 (t, ^3J = 6.5 Hz, 1H, H^{I5}), 7.13 (t, ^3J = 6.5 Hz, 1H, H^{D5}), 7.01–6.93 (m, 2H, H^{B5}, H^{F5}), 6.32 (ddd, ^4J = 2.3 Hz, $^3J_{HF}$ = 9.4 Hz, $^3J_{HF}$ = 12.2 Hz, 1H, H^{A4}), 6.28 (ddd, ^4J = 2.4 Hz, $^3J_{HF}$ = 9.2 Hz, $^3J_{HF}$ = 12.1 Hz, 1H, H^{C4}), 5.48 (dd, ^4J = 2.4 Hz, $^3J_{HF}$ = 8.4 Hz, 1H, H^{A6}), 5.16 (dd, ^4J = 2.4 Hz, $^3J_{HF}$ = 8.2 Hz, 1H, H^{C6}). ^{19}F{^{1}H} NMR (188 MHz, CD$_3$CN): δ −73.30 (d, $^1J_{FP}$ = 706.5 Hz, 6F), −110.24 (d, ^4J = 9.6 Hz, 1F), −110.96 (d, ^4J = 9.7 Hz, 1F), −111.28 (d, ^4J = 9.4 Hz, 1F), −111.83 (d, ^4J = 9.7 Hz, 1F). HRMS (ESI-TOF). Calcd for C$_{56}$H$_{35}$F$_4$IrN$_9$ORu ([M − PF$_6$]$^+$): m/z 1220.1530. Found: m/z 1220.1574. IR (KBr): $\tilde{\nu}_{CN}$ 2108, 2125 cm^{-1}.

[Ir(ppy)$_2$(CN)(μ-CN)Ru(bpy)(tpy-pep-CHO)]PF$_6$ (1e). Yield: 60%.
^{1}H NMR (600 MHz, DMSO-d_6): δ 10.37 (s, 1H, CHO), 9.24 (d, ^3J = 5.6 Hz, 1H, H^{D6}), 9.21 (d, ^3J = 5.9 Hz, 1H, H^{E6}), 9.13 (s, 1H, H^{H3}), 9.12 (s, 1H, H^{H5}), 8.92–8.80 (m, 3H, H^{G3}, H^{I3}, H^{E3}), 8.60 (d, ^3J = 8.2 Hz, 1H, H^{F3}), 8.47 (d, ^3J = 7.9 Hz, 2H, H^{J2}), 8.37 (d, ^3J = 5.4 Hz, 1H, H^{B6}), 8.30 (td, ^4J = 1.5 Hz, ^3J = 7.9 Hz, 1H, H^{E4}), 8.08–7.97 (m, 3H, H^{G4}, H^{I4}, H^{B3}), 7.96 (d, ^3J = 8.0 Hz, 1H, H^{D3}), 7.86 (d, ^3J = 7.9 Hz, 2H, H^{J3}), 7.84–7.78 (m, 4H, H^{D4}, H^{E5}, H^{B4}, H^{F4}), 7.58 (d, ^3J = 8.3 Hz, 1H, H^{A3}), 7.56 (d, ^3J = 7.9 Hz, 1H, H^{C3}), 7.51 (d, ^3J = 5.4 Hz, 1H, H^{G6}), 7.45 (s, 1H, H^{K2}), 7.37–7.30 (m, 4H, H^{G5}, H^{I5}, H^{I6}, H^{F6}), 7.30 (s, 1H, H^{K5}), 7.17 (t, ^3J = 6.5 Hz, 1H, H^{D5}), 7.10 (t, ^3J = 6.7 Hz, 1H, H^{F5}), 6.94 (ddd, ^4J = 1.4 Hz, ^3J = 5.6 Hz, ^3J = 7.2 Hz, 1H, H^{B5}), 6.72–6.65 (m, 2H, H^{C4}, H^{A4}), 6.57 (t, ^3J = 7.4 Hz, 1H, H^{A5}), 6.53 (t, ^3J = 7.2 Hz, 1H, H^{C5}), 5.94 (d, ^3J = 7.5 Hz, 1H, H^{A6}), 5.66 (d, ^3J = 7.3 Hz, 1H, H^{C6}), 4.16 (t, ^3J = 6.4 Hz, 2H, α-OCH$_2$), 4.11 (t, ^3J = 6.3 Hz, 2H, α-OCH$_2$), 1.87–1.74 (m, 4H, β-CH$_2$), 1.55 (quint, ^3J = 6.5 Hz, 2H, γ-CH$_2$), 1.46 (quint, ^3J = 7.6 Hz, 2H, γ-CH$_2$), 1.42–1.19 (m, 16H, δ-η-CH$_2$), 0.86 (t, ^3J = 6.8 Hz, 3H, CH$_3$), 0.80 (t, ^3J = 7.0 Hz, 3H, CH$_3$).
^{13}C{^{1}H} NMR (150 MHz, DMSO-d_6): δ 188.4 (CHO), 167.7 (C^{B2}), 167.4 (C^{D2}), 161.11 (C^{C1}), 161.10 (C^{A1}), 157.9 (C^{G2}), 157.8 (C^{I2}), 157.3 (C^{F2}), 157.10 (C^{H2}), 157.07 (C^{H6}), 155.3 (C^{E2}), 155.0 (C^{K3}), 153.2 (C^{K6}), 153.0 (C^{D6}), 151.8 (C^{G6}), 151.6 (C^{I6}), 151.5 (C^{B6}), 150.92 (C^{E6}), 150.89 (C^{F6}), 144.7 (C^{H4}), 144.0 (C^{C2}), 143.9 (C^{A2}), 143.0 (μ-CN), 137.7 (C^{G4}), 137.6 (C^{I4}), 136.9 (C^{E4}), 136.8 (C^{D4}), 136.5 (2C, C^{B4}, C^{F4}), 136.4 (C^{J1}), 132.1 (2C, C^{J3}), 130.3 (C^{A6}), 130.2 (C^{C6}), 129.6 (CN), 128.8 (C^{C5}), 128.6 (C^{A5}), 128.0 (3C, C^{J2}, C^{G5}), 127.9 (C^{I5}), 127.1 (C^{E5}), 126.6 (C^{F5}), 124.8 (C^{K4}), 124.5 (C^{I3}), 124.3 (C^{G3}), 124.1 (C^{E3}), 123.83 (C^{C3}), 123.77 (2C, C^{J4}, C^{A3}), 123.5 (C^{F3}), 122.8 (C^{D5}), 122.3 (C^{B5}), 120.7 (C^{C4}), 120.5 (C^{A4}), 120.2 (C^{H5}), 120.0 (C^{H3}), 119.4 (C^{B3}), 119.2 (C^{K1}), 119.1 (C^{D3}), 118.2 (C^{K2}), 109.8 (C^{K5}), 96.4 (C^{alkyne}), 87.8 (C^{alkyne}), 69.1 (α-OCH$_2$), 68.8 (α-OCH$_2$), 31.3 (β-CH$_2$), 31.2 (β-CH$_2$), 28.77 (γ-CH$_2$), 28.71 (γ-CH$_2$), 28.70 (δ-CH$_2$), 28.67 (δ-CH$_2$), 28.63 (ε-CH$_2$), 28.57 (ε-CH$_2$), 25.53 (ζ-CH$_2$), 25.49 (ζ-CH$_2$), 22.1 (2C, η-CH$_2$), 13.97 (CH$_3$), 13.96 (CH$_3$). HRMS (ESI-TOF): Calcd for C$_{80}$H$_{75}$IrN$_9$O$_3$Ru ([M − PF$_6$]$^+$): m/z 1504.4621. Found: m/z 1504.4666. IR (KBr): $\tilde{\nu}_{CN}$ 2100, 2116 cm^{-1}.

[Ir(F$_2$-ppy)$_2$(CN)(μ-CN)Ru(bpy)(tpy-pep-CHO)]PF$_6$ (2e). Yield: 50%.
^{1}H NMR (600 MHz, CD$_3$CN): δ 10.43 (s, 1H, CHO), 9.63 (d, ^3J = 5.3 Hz, 1H, H^{E6}), 9.36 (d, ^3J = 5.5 Hz, 1H, H^{D6}), 8.65 (d, ^3J = 5.7 Hz, 1H, H^{B6}), 8.59 (s, 1H, H^{H3}), 8.56–8.51 (m, 2H, H^{E3}, H^{H5}), 8.41 (d, ^3J = 8.1 Hz, 1H, H^{G3}), 8.30 (d, ^3J = 8.1 Hz, 1H, H^{I3}), 8.27 (d, ^3J = 8.2 Hz, 1H, H^{F3}), 8.22 (td, ^4J = 1.4 Hz, ^3J = 7.9 Hz, 1H, H^{E4}), 8.14 (d, ^3J = 7.8 Hz, 2H, H^{J2}), 8.05 (d, ^3J = 8.5 Hz, 1H, H^{B3}), 7.94 (d, ^3J = 8.2 Hz, 1H, H^{D3}), 7.91–7.85 (m, 2H, H^{E5}, H^{G4}), 7.79 (d, ^3J = 8.1 Hz, 2H, H^{J3}), 7.78–7.70 (m, 3H, H^{I4}, H^{D4}, H^{B4}), 7.69 (td, ^4J = 1.2 Hz, ^3J = 7.7 Hz, 1H, H^{F4}), 7.62 (d, ^3J = 5.2 Hz, 1H, H^{G6}), 7.44 (d, ^3J = 5.2 Hz, 1H, H^{I6}), 7.33 (s, 1H, H^{K5}), 7.29–7.24 (m, 2H, H^{K2}, H^{G5}), 7.22 (d, ^3J = 5.6 Hz, 1H, H^{F6}), 7.15 (t, ^3J = 6.5 Hz, 1H, H^{I5}), 7.10 (t, ^3J = 6.5 Hz, 1H, H^{D5}), 6.99–6.91 (m, 2H, H^{F5}, H^{B5}), 6.29 (ddd, ^4J = 2.4 Hz, $^3J_{HF}$ = 9.3 Hz, $^3J_{HF}$ = 12.1 Hz, 1H, H^{A4}), 6.25 (ddd, ^4J = 2.4 Hz, $^3J_{HF}$ = 9.1 Hz, $^3J_{HF}$ = 12.0 Hz, 1H, H^{C4}), 5.48 (dd, ^3J = 2.3 Hz, $^3J_{HF}$ = 8.5 Hz, 1H, H^{A6}), 5.18 (dd, ^4J = 2.4 Hz, $^3J_{HF}$ = 8.2 Hz, 1H, H^{C6}), 4.13–4.04 (m, 4H, α-OCH$_2$), 1.85–1.76 (m, 4H, β-CH$_2$), 1.54 (quint, ^3J = 7.5 Hz, 2H, γ-CH$_2$), 1.48 (quint, ^3J = 7.3 Hz, 2H, γ-CH$_2$), 1.42–1.20 (m, 16H, δ-η-CH$_2$), 0.88 (t, ^3J = 6.9 Hz, 3H, CH$_3$), 0.82 (t, ^3J = 6.9 Hz, 3H, CH$_3$). ^{19}F{^{1}H} NMR (188 MHz, CD$_3$CN): δ −73.30 (d, $^1J_{FP}$ = 706.7 Hz), −110.19 (d, ^4J = 9.3 Hz), −110.87 (d, ^4J = 9.4 Hz), −111.28 (d, ^4J = 9.4 Hz), −111.71 (d, ^4J = 9.4 Hz). HRMS (ESI-TOF). Calcd for C$_{80}$H$_{71}$F$_4$IrN$_9$O$_3$Ru ([M − PF$_6$]$^+$): m/z 1576.4230. Found: m/z 1576.4289. IR (KBr): $\tilde{\nu}_{CN}$ 2109, 2125 cm^{-1}.

■ ASSOCIATED CONTENT

⑤ Supporting Information

The Supporting Information is available free of charge on the ACS Publications website at DOI: 10.1021/acs.inorgchem.5b02919.

> NMR spectra, CV, SEC spectra, kinetic studies on the thiocyanate isomerism, absorption, excitation, and emission spectra, and additional experimental and computational details (PDF)

■ AUTHOR INFORMATION

Corresponding Author

*E-mail: ulrich.schubert@uni-jena.de.

Notes

The authors declare no competing financial interest.

■ REFERENCES

(1) (a) Balzani, V.; Bergamini, G.; Marchioni, F.; Ceroni, P. *Coord. Chem. Rev.* **2006**, *250*, 1254−1266. (b) Frischmann, P. D.; Mahata, K.; Würthner, F. *Chem. Soc. Rev.* **2013**, *42*, 1847−1870. (c) Balzani, V.; Juris, A.; Venturi, M.; Campagna, S.; Serroni, S. *Chem. Rev.* **1996**, *96*, 759−833. (d) Puntoriero, F.; Sartorel, A.; Orlandi, M.; La Ganga, G.; Serroni, S.; Bonchio, M.; Scandola, F.; Campagna, S. *Coord. Chem. Rev.* **2011**, *255*, 2594−2601. (e) Zanoni, K. P. S.; Coppo, R. L.; Amaral, R. C.; Murakami Iha, N. Y. *Dalton Trans.* **2015**, *44*, 14559.

(2) (a) Tschierlei, S.; Karnahl, M.; Presselt, M.; Dietzek, B.; Guthmuller, J.; González, L.; Schmitt, M.; Rau, S.; Popp, J. *Angew. Chem., Int. Ed.* **2010**, *49*, 3981−3984. (b) Pfeffer, M. G.; Kowacs, T.; Wächtler, M.; Guthmuller, J.; Dietzek, B.; Vos, J. G.; Rau, S. *Angew. Chem., Int. Ed.* **2015**, *54*, 6627−6631. (c) Pfeffer, M. G.; Schäfer, B.; Smolentsev, G.; Uhlig, J.; Nazarenko, E.; Guthmuller, J.; Kuhnt, C.; Wächtler, M.; Dietzek, B.; Sundström, V.; Rau, S. *Angew. Chem., Int. Ed.* **2015**, *54*, 5044−5048.

(3) Kübel, J.; Winter, A.; Schubert, U. S.; Dietzek, B. *J. Phys. Chem. A* **2014**, *118*, 12137−12148.

(4) (a) De Cola, L.; Belser, P. *Coord. Chem. Rev.* **1998**, *177*, 301−346. (b) Medlycott, E. A.; Hanan, G. S. *Coord. Chem. Rev.* **2006**, *250*, 1763−1782.

(5) Sabatini, C.; Barbieri, A.; Barigelletti, F.; Arm, K. J.; Williams, J. A. G. *Photochem. Photobiol. Sci.* **2007**, *6*, 397−405.

(6) Osio Barcina, J. O.; Herrero-García, N.; Cucinotta, F.; De Cola, L.; Contreras-Carballada, P.; Williams, R. M.; Guerrero-Martínez, A. *Chem. - Eur. J.* **2010**, *16*, 6033−6040.

(7) Van Diemen, J. H.; Hage, R.; Haasnoot, J. G.; Lempers, H. E. B.; Reedijk, J.; Vos, J. G.; De Cola, L.; Barigelletti, F.; Balzani, V. *Inorg. Chem.* **1992**, *31*, 3518−3522.

(8) Vogler, L. M.; Scott, B.; Brewer, K. J. *Inorg. Chem.* **1993**, *32*, 898−903.

(9) Cavazzini, M.; Pastorelli, P.; Quici, S.; Loiseau, F.; Campagna, S. *Chem. Commun.* **2005**, 5266−5268.

(10) Sandroni, M.; Zysman-Colman, E. *Dalton Trans.* **2014**, *43*, 3676−3680.

(11) Swanick, K. N.; Sandroni, M.; Ding, Z. F.; Zysman-Colman, E. *Chem. - Eur. J.* **2015**, *21*, 7435−7440.

(12) (a) Vahrenkamp, H.; Geiß, A.; Richardson, G. N. *J. Chem. Soc., Dalton Trans.* **1997**, 3643−3652. (b) Tanase, S.; Reedijk, J. *Coord. Chem. Rev.* **2006**, *250*, 2501−2510. (c) Baraldo, L. M.; Forlano, P.; Parise, A. R.; Slep, L. D.; Olabe, J. A. *Coord. Chem. Rev.* **2001**, *219*, 881−921. (d) Macatangay, A. V.; Endicott, J. F. *Inorg. Chem.* **2000**, *39*, 437−446. (e) Watzky, M. A.; Macatangay, A. V.; Van Camp, R. A.; Mazzetto, S. E.; Song, X. Q.; Endicott, J. F.; Buranda, T. *J. Phys. Chem. A* **1997**, *101*, 8441−8459. (f) Ward, M. D. *Dalton Trans.* **2010**, *39*, 8851−8867.

(13) (a) Cadranel, A.; Aramburu Troselj, B. M.; Yamazaki, S.; Albores, P.; Kleiman, V. D.; Baraldo, L. M. *Dalton Trans.* **2013**, *42*,

16723−16732. (b) Pieslinger, G. E.; Albores, P.; Slep, L. D.; Coe, B. J.; Timpson, C. J.; Baraldo, L. M. *Inorg. Chem.* **2013**, *52*, 2906−2917. (c) Cutin, E. H.; Katz, N. E. *Polyhedron* **1993**, *12*, 955−960. (d) Scandola, F.; Argazzi, R.; Bignozzi, C. A.; Chiorboli, C.; Indelli, M. T.; Rampi, M. A. *Coord. Chem. Rev.* **1993**, *125*, 283−292. (e) Pieslinger, G. E.; Albores, P.; Slep, L. D.; Baraldo, L. M. *Angew. Chem., Int. Ed.* **2014**, *53*, 1293−1296. (f) Pieslinger, G. E.; Aramburu-Troselj, B. M.; Cadranel, A.; Baraldo, L. M. *Inorg. Chem.* **2014**, *53*, 8221−8229.

(14) Varshavsky, Y. S.; Cherkasova, T. G.; Galding, M. R.; Khrustalev, V. N.; Podkorytov, I. S.; Gindin, V. A.; Smirnov, S. N.; Nikol'skii, A. B. *J. Organomet. Chem.* **2009**, *694*, 2917−2922.

(15) (a) Dowling, N.; Henry, P. M.; Lewis, N. A.; Taube, H. *Inorg. Chem.* **1981**, *20*, 2345−2348. (b) Ma, X.; Lin, C. S.; Hu, S. M.; Tan, C. H.; Wen, Y. H.; Sheng, T. L.; Wu, X. T. *Chem. - Eur. J.* **2014**, *20*, 7025−7036. (c) Cadranel, A.; Albores, P.; Yamazaki, S.; Kleiman, V. D.; Baraldo, L. M. *Dalton Trans.* **2012**, *41*, 5343−5350.

(16) Baca, S. G.; Adams, H.; Sykes, D.; Faulkner, S.; Ward, M. D. *Dalton Trans.* **2007**, 2419−2430.

(17) Ali, N. M.; MacLeod, V. L.; Jennison, P.; Sazanovich, I. V.; Hunter, C. A.; Weinstein, J. A.; Ward, M. D. *Dalton Trans.* **2012**, *41*, 2408−2419.

(18) Baranoff, E.; Orselli, E.; Allouche, L.; Di Censo, D.; Scopelliti, R.; Gratzel, M.; Nazeeruddin, M. K. *Chem. Commun.* **2011**, *47*, 2799−2801.

(19) Nazeeruddin, M. K.; Humphry-Baker, R.; Berner, D.; Rivier, S.; Zuppiroli, L.; Graetzel, M. *J. Am. Chem. Soc.* **2003**, *125*, 8790−8797.

(20) (a) Wasylenko, D. J.; Ganesamoorthy, C.; Koivisto, B. D.; Henderson, M. A.; Berlinguette, C. P. *Inorg. Chem.* **2010**, *49*, 2202−2209. (b) Gerken, J. B.; Rigsby, M. L.; Ruther, R. E.; Pérez-Rodriguez, R. J.; Guzei, I. A.; Hamers, R. J.; Stahl, S. S. *Inorg. Chem.* **2013**, *52*, 2796−2798.

(21) (a) Brewster, T. P.; Ding, W. D.; Schley, N. D.; Hazari, N.; Batista, V. S.; Crabtree, R. H. *Inorg. Chem.* **2011**, *50*, 11938−11946. (b) Hue, R.; Mann, K. R.; Gladfelter, W. L. *J. Coord. Chem.* **2014**, *67*, 17−28.

(22) (a) Li, J.; Djurovich, P. I.; Alleyne, B. D.; Yousufuddin, M.; Ho, N. N.; Thomas, J. C.; Peters, J. C.; Bau, R.; Thompson, M. E. *Inorg. Chem.* **2005**, *44*, 1713−1727. (b) Di Censo, D.; Fantacci, S.; De Angelis, F.; Klein, C.; Evans, N.; Kalyanasundaram, K.; Bolink, H. J.; Grätzel, M.; Nazeeruddin, M. K. *Inorg. Chem.* **2008**, *47*, 980−989.

(23) Chan, K.-C.; Chu, W.-K.; Yiu, S.-M.; Ko, C.-C. *Dalton Trans.* **2015**, *44*, 15135−15144.

(24) Juris, A.; Balzani, V.; Barigelletti, F.; Campagna, S.; Belser, P.; Vonzelewsky, A. *Coord. Chem. Rev.* **1988**, *84*, 85−277.

(25) Chi, Y.; Chou, P. T. *Chem. Soc. Rev.* **2010**, *39*, 638−655.

(26) Hewitt, J. T.; Vallett, P. J.; Damrauer, N. H. *J. Phys. Chem. A* **2012**, *116*, 11536−11547.

(27) (a) Mulliken, R. S. *J. Am. Chem. Soc.* **1952**, *74*, 811−824. (b) Hush, N. S. *Prog. Inorg. Chem.* **1967**, *8*, 391−444. (c) Hush, N. S. *Electrochim. Acta* **1968**, *13*, 1005−1023. (d) Brunschwig, B. S.; Creutz, C.; Sutin, N. *Chem. Soc. Rev.* **2002**, *31*, 168−184. (e) D'Alessandro, D. M.; Keene, F. R. *Chem. Soc. Rev.* **2006**, *35*, 424−440.

(28) Robin, M. B.; Day, P. *Adv. Inorg. Chem. Radiochem.* **1968**, *10*, 247−422.

(29) (a) Rommel, S. A.; Sorsche, D.; Rockstroh, N.; Heinemann, F. W.; Kübel, J.; Wächtler, M.; Dietzek, B.; Rau, S. *Eur. J. Inorg. Chem.* **2015**, *2015*, 3730−3739. (b) Happ, B.; Kübel, J.; Pfeffer, M. G.; Winter, A.; Hager, M. D.; Dietzek, B.; Rau, S.; Schubert, U. S. *Macromol. Rapid Commun.* **2015**, *36*, 671−677. (c) King, K. A.; Watts, R. J. *J. Am. Chem. Soc.* **1987**, *109*, 1589−1590.

(30) (a) Brown, A. M.; McCusker, C. E.; McCusker, J. K. *Dalton Trans.* **2014**, *43*, 17635−17646. (b) Zhang, Y.; Kupfer, S.; Zedler, L.; Schindler, J.; Bocklitz, T.; Guthmuller, J.; Rau, S.; Dietzek, B. *Phys. Chem. Chem. Phys.* **2015**, *17*, 29637−29646.

(31) (a) Chaignon, F.; Torroba, J.; Blart, E.; Borgström, M.; Hammarström, L.; Odobel, F. *New J. Chem.* **2005**, *29*, 1272−1284. (b) Barthelmes, K.; Kübel, J.; Winter, A.; Wächtler, M.; Friebe, C.; Dietzek, B.; Schubert, U. S. *Inorg. Chem.* **2015**, *54*, 3159−3171.

(32) Meyer, T. J. *Pure Appl. Chem.* **1986**, *58*, 1193−1206.

(33) Puntoriero, F.; Nastasi, F.; Galletta, M.; Campagna, S. Photophysics and Photochemistry of Non-Carbonyl-Containing Coordination and Organometallic Compounds. In *Comprehensive Inorganic Chemistry II*, 2nd ed.; Poeppelmeier, J. R., Ed.; Elsevier: Amsterdam, The Netherlands, 2013; pp 255−337.

(34) Tsai, C.-N.; Allard, M. M.; Lord, R. L.; Luo, D.-W.; Chen, Y.-J.; Schlegel, H. B.; Endicott, J. F. *Inorg. Chem.* **2011**, *50*, 11965−11977.

(35) Jaeger, M.; Freitag, L.; González, L. *Coord. Chem. Rev.* **2015**, *304−305*, 146−165.

(36) Adamo, C.; Barone, V. *J. Chem. Phys.* **1999**, *110*, 6158−6170.

(37) Zhao, Y.; Truhlar, D. G. *J. Phys. Chem. A* **2004**, *108*, 6908−6918.

(38) Wang, J.; Hanan, G. S. *Synlett* **2005**, 1251−1254.

(39) Winter, A.; Egbe, D. A. M.; Schubert, U. S. *Org. Lett.* **2007**, *9*, 2345−2348.

(40) Sullivan, B. P.; Calvert, J. M.; Meyer, T. J. *Inorg. Chem.* **1980**, *19*, 1404−1407.

(41) Kübel, J.; Schroot, R.; Wächtler, M.; Schubert, U. S.; Dietzek, B.; Jäger, M. *J. Phys. Chem. C* **2015**, *119*, 4742−4751.

(42) Frisch, M. J.; Trucks, G. W.; Schlegel, H. B.; Scuseria, G. E.; Robb, M. A.; Cheeseman, J. R.; Scalmani, G.; Barone, V.; Mennucci, B.; Petersson, G. A.; Nakatsuji, H.; Caricato, M.; Li, X.; Hratchian, H. P.; Izmaylov, A. F.; Bloino, J.; Zheng, G.; Sonnenberg, J. L.; Hada, M.; Ehara, M.; Toyota, K.; Fukuda, R.; Hasegawa, J.; Ishida, M.; Nakajima, T.; Honda, Y.; Kitao, O.; Nakai, H.; Vreven, T.; Montgomery, J. A., Jr.; Peralta, J. E.; Ogliaro, F.; Bearpark, M.; Heyd, J. J.; Brothers, E.; Kudin, K. N.; Staroverov, V. N.; Kobayashi, R.; Normand, J.; Raghavachari, K.; Rendell, A.; Burant, J. C.; Iyengar, S. S.; Tomasi, J.; Cossi, M.; Rega, N.; Millam, N. J.; Klene, M.; Knox, J. E.; Cross, J. B.; Bakken, V.; Adamo, C.; Jaramillo, J.; Gomperts, R.; Stratmann, R. E.; Yazyev, O.; Austin, A. J.; Cammi, R.; Pomelli, C.; Ochterski, J. W.; Martin, R. L.; Morokuma, K.; Zakrzewski, V. G.; Voth, G. A.; Salvador, P.; Dannenberg, J. J.; Dapprich, S.; Daniels, A. D.; Farkas, Ö.; Foresman, J. B.; Ortiz, J. V.; Cioslowski, J.; Fox, D. J. *Gaussian 09*, revision A.02; Gaussian, Inc.: Wallingford, CT, 2010.

(43) (a) Becke, A. D. *J. Chem. Phys.* **1993**, *98*, 5648−5652. (b) Lee, C. T.; Yang, W. T.; Parr, R. G. *Phys. Rev. B: Condens. Matter Mater. Phys.* **1988**, *37*, 785−789.

(44) (a) Cancès, E.; Mennucci, B.; Tomasi, J. *J. Chem. Phys.* **1997**, *107*, 3032−3041. (b) Tomasi, J.; Mennucci, B.; Cammi, R. *Chem. Rev.* **2005**, *105*, 2999−3093.

(45) (a) O'Boyle, N. M.; Tenderholt, A. L.; Langner, K. M. *J. Comput. Chem.* **2008**, *29*, 839−845. (b) O'Boyle, N. M.; Vos, J. G. *GaussSum*, version 2.2.5; Dublin City University: Dublin, 2009.

(46) Dennington, R.; Keith, T.; Millam, J. *GaussView*, version 5.0.8; Semichem Inc.: Shawnee Mission, KS, 2009.

■ NOTE ADDED AFTER ASAP PUBLICATION

This paper was published ASAP on May 23, 2016. The Supporting Information was updated. The revised paper was reposted on May 26, 2016.

Supporting Information for:

Efficient energy transfer and metal coupling in cyanide-bridged heterodinuclear complexes based on (bipyridine)(terpyridine)ruthenium(II) and (phenylpyridine)iridium(III) complexes

Kevin Barthelmes,[†,§] Michael Jäger,[†,§] Joachim Kübel,[‡,⊥] Christian Friebe,[†,§] Andreas Winter,[†,§] Maria Wächtler,[‡] Benjamin Dietzek,[‡,⊥,§] Ulrich S. Schubert*[,†,§]

[†] Laboratory of Organic and Macromolecular Chemistry (IOMC), Friedrich Schiller University Jena, Humboldtstr. 10, 07743 Jena, Germany

[§] Center for Energy and Environmental Chemistry Jena (CEEC Jena), Friedrich Schiller University Jena, Philosophenweg 7a, 07743 Jena, Germany

[‡] Leibniz Institute of Photonic Technology (IPHT) Jena e.V., Albert-Einstein-Str. 9, 07745 Jena, Germany

[⊥] Institute of Physical Chemistry and Abbe Center of Photonics, Friedrich Schiller University Jena, Helmholtzweg 4, 07743 Jena, Germany

E-mail: ulrich.schubert@uni-jena.de

Table of Contents:

Figure S1. Schematic representation of the cyanide-bridged iridium(III)–ruthenium(II) complexes **1a–1e** and **2a–2e** and their model complexes **3a–3e**, **4**, and **5** (panel A), along with a numbering scheme for the complexes (the numbering is analogous for **3–5**). Panel B lists an overview of the complexes.

1. Equilibrium process for [SCN(bpy)(tpy-R₁)Ru]PF₆ complexes

Equilibrium process for [SCN(bpy)(tpy-R_1)Ru]PF$_6$ complexes
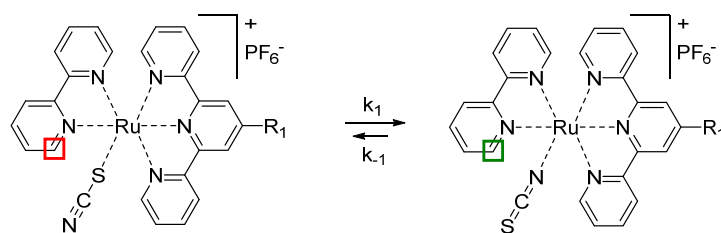
Figure S2. Equilibrium process between *S*- and *N*-coordinated thiocyanate ligand.
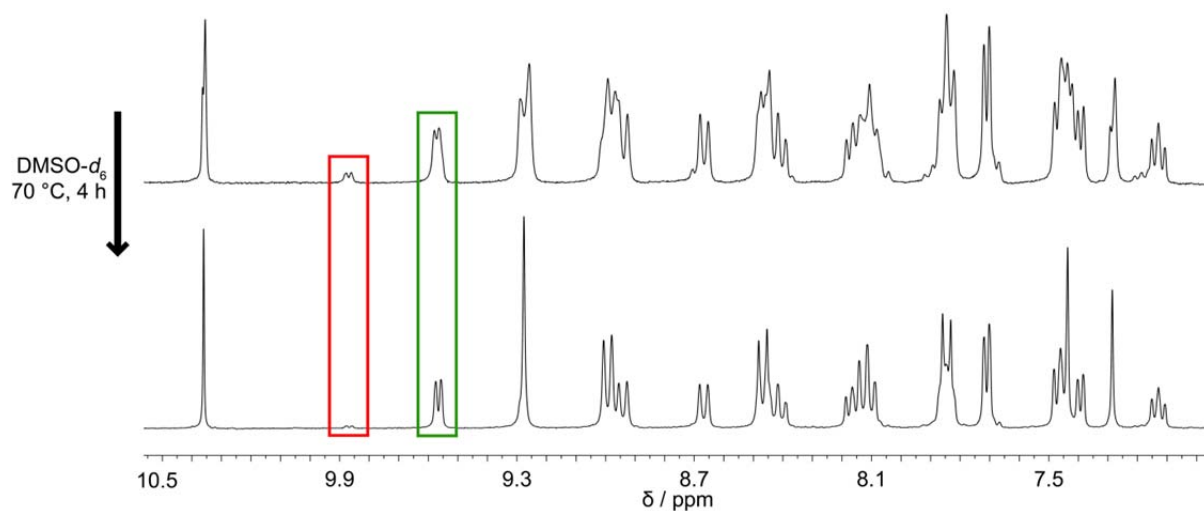
Figure S3. Stacked ^{1}H NMR (400 MHz, DMSO-d_6, aromatic region) spectra for **3e** before and after heating at 70 °C in DMSO-d_6. Red and green framed resonances belong to the bpy signal (see Figure S2) for *S*- and *N*-coordinated thiocyanate ligand, respectively.
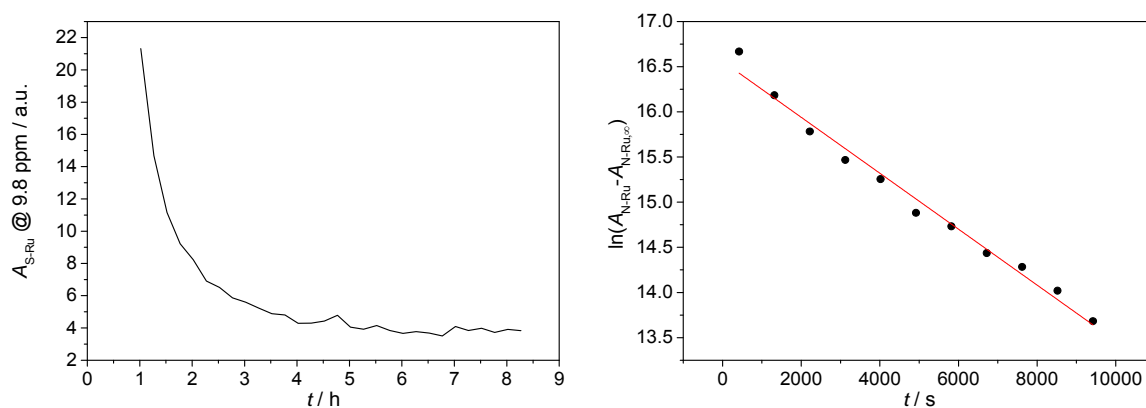
Figure S4. Decay of the *S*-coordinated thiocyanate bpy signal (left) and kinetic plot up to 2.6 h for the equilibrium reaction (right) for **3e** obtained from ^{1}H NMR integrals.

The following kinetic equation 1 for an equilibrium process was applied.

$$\ln\!\left(A_{\mathrm{N-Ru}} - A_{\mathrm{N-Ru},\infty}\right) = -(k_1 + k_{-1})\left(A_{\mathrm{N-Ru}} - A_{\mathrm{N-Ru},\infty}\right)t + X \qquad (1)$$

The kinetic fit results are $k_1 + k_{-1} = 3.097 \times 10^{-4}\ \mathrm{s}^{-1}$ and $X = 16.559$. The equilibrium constant K at 70 °C was calculated with the final signal area of *S*- and *N*-coordinated thiocyanate anion ($A_{\mathrm{N/S-Ru},\infty}$) according to equation 2. The value is around 25, which was used to calculate the rate constants.

$$K_{70\,°C} = \frac{A_{\text{N-Ru},\infty}}{A_{\text{S-Ru},\infty}} \approx 25 = \frac{k_1}{k_{-1}} \tag{2}$$

The obtained rate constant for forward (k_1) and backward (k_{-1}) reaction are in the same order of magnitude for [Ru(bpy-R)$_2$(NCS)$_2$] reported recently.[1] The values are $k_1 = 2.98 \times 10^{-4}$ s^{-1} and $k_{-1} = 1.19 \times 10^{-5}$ s^{-1}.

2. Protonation/Deprotonation experiments on iridium model complexes
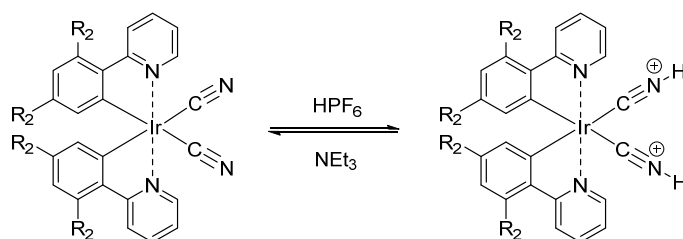
Figure S5. Schematic representation of the possible process for protonation and deprotonation in the iridium model complexes.
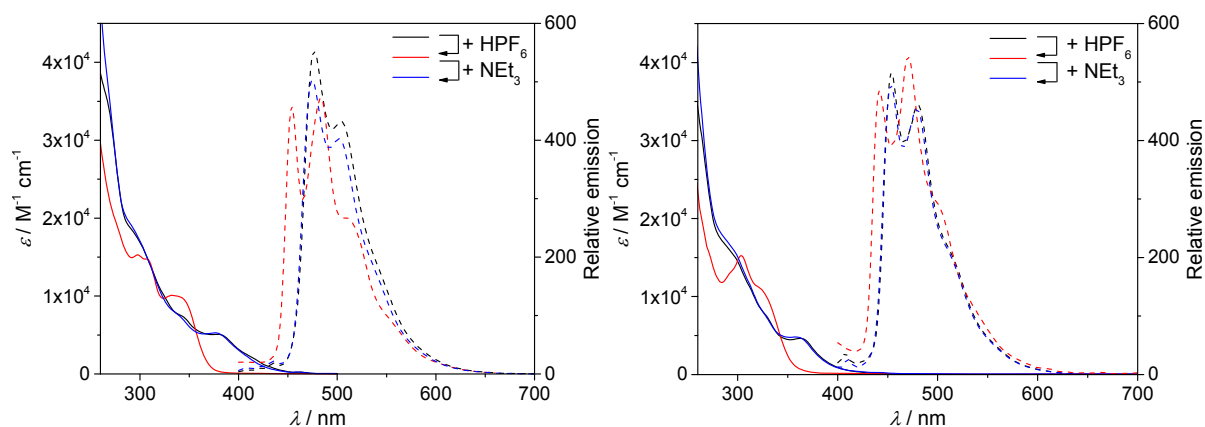
Figure S6. Room-temperature UV-vis absorption (solid line) and emission (dashed line, λ_{exc} = longest-wavelength maxima) spectral changes of iridium model complexes **4** (left) and **5** (right) upon protonation (red) and deprotonation (blue) in acetonitrile.

3. Cyclic voltammetry
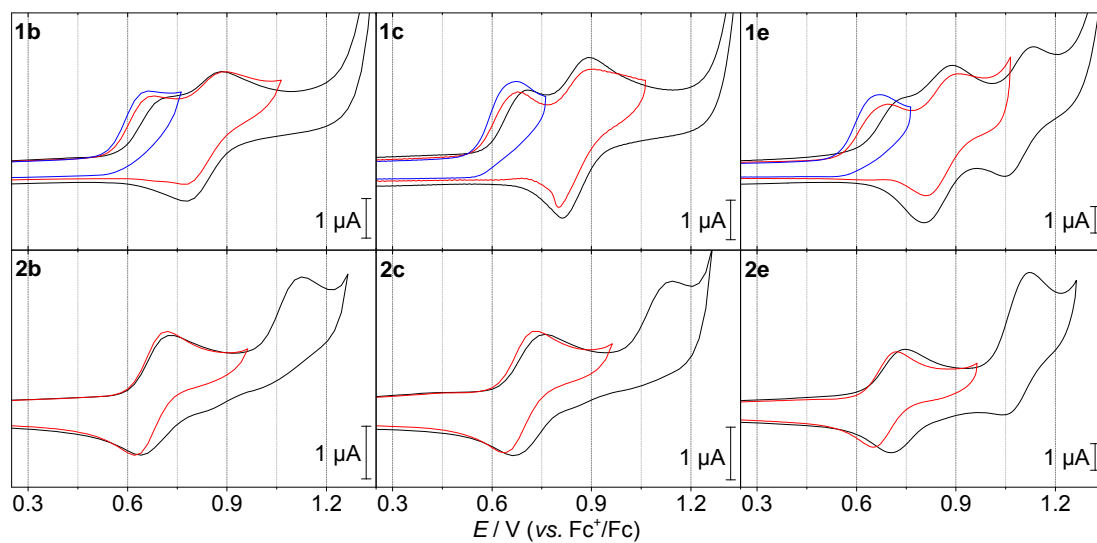
Figure S7. Cyclic voltammograms of the dinuclear complexes **1b**, **1c**, **1e**, **2b**, **2c**, and **2e** in dichloromethane/0.1 M Bu$_4$NPF$_6$ at 0.2 V/s scan rate in several potential ranges (5th cycle is shown).
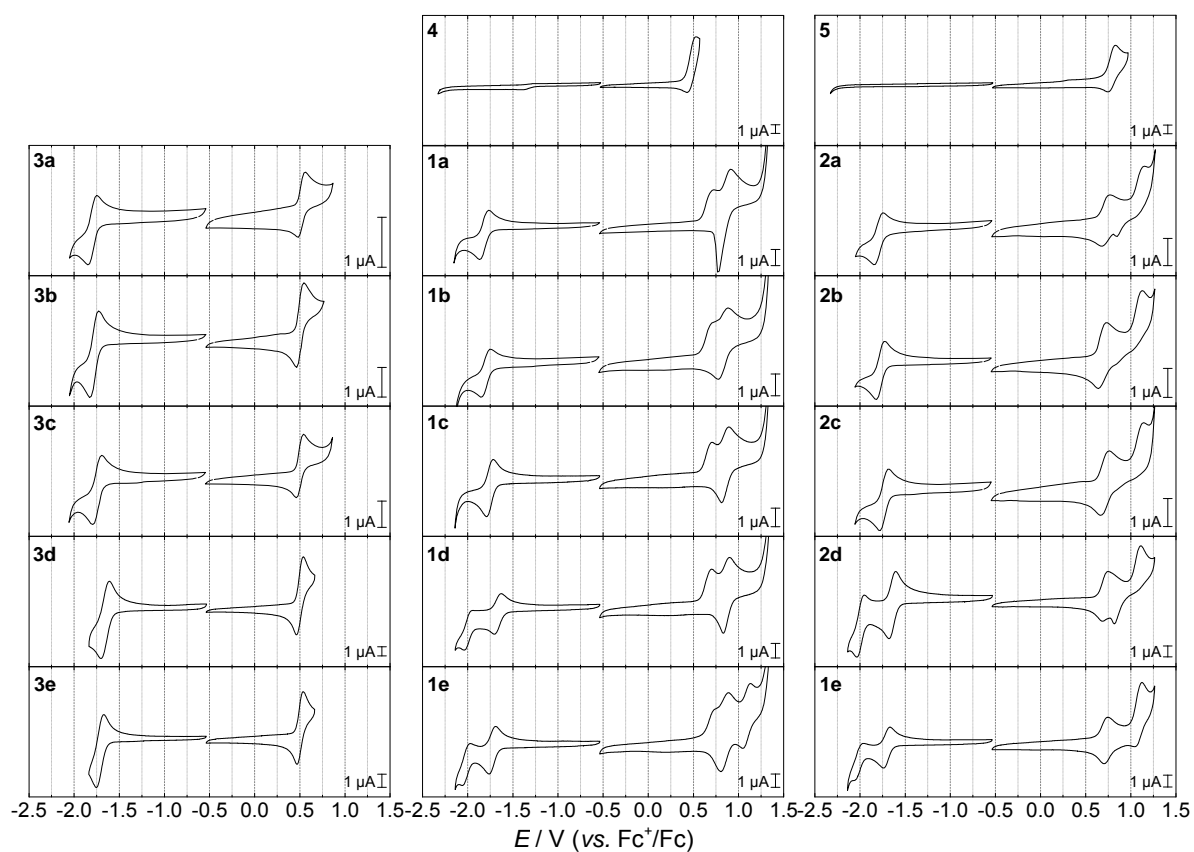
Figure S8. Cyclic voltammograms of **1–5** in dichloromethane/0.1 M Bu$_4$NPF$_6$ at 0.2 V/s scan rate (5th cycle is shown).

4. Absorption spectra
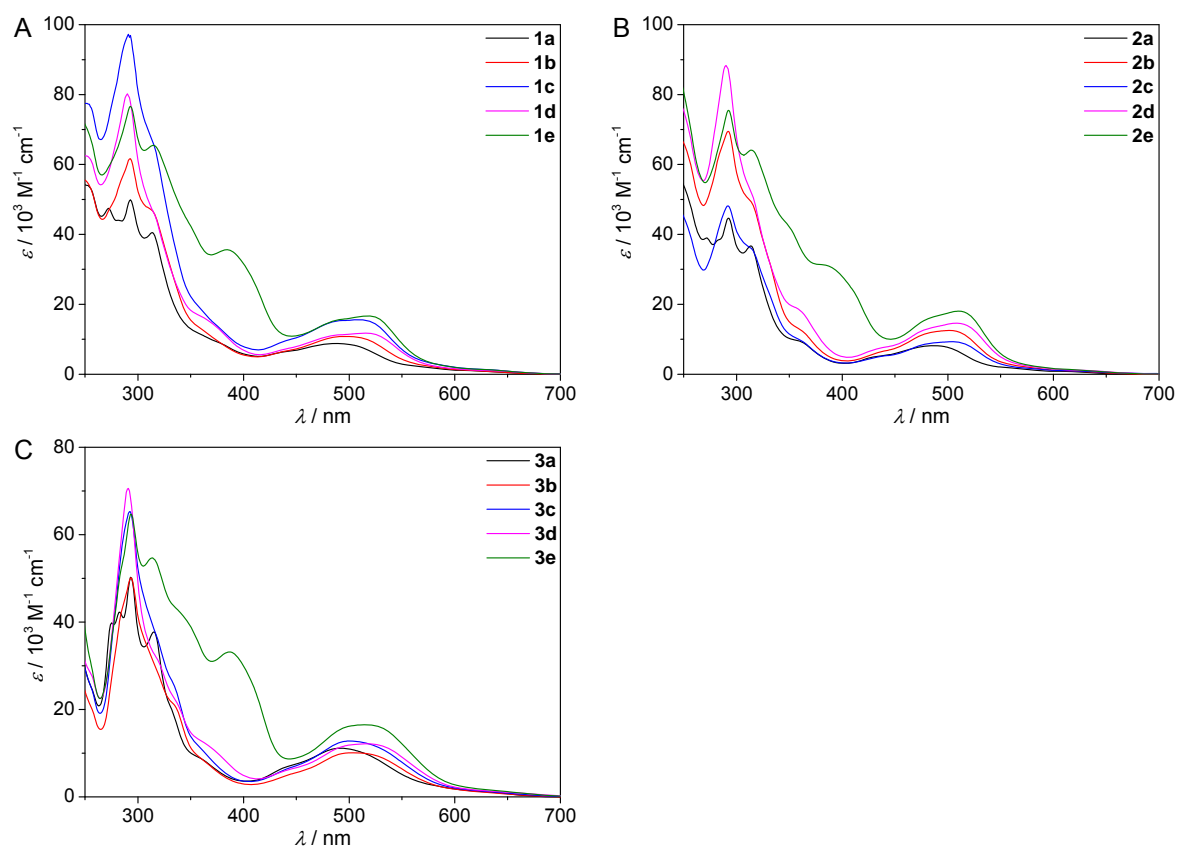
Figure S9. Absorption spectra of **1**−**3** in dichloromethane.

5. Emission spectra
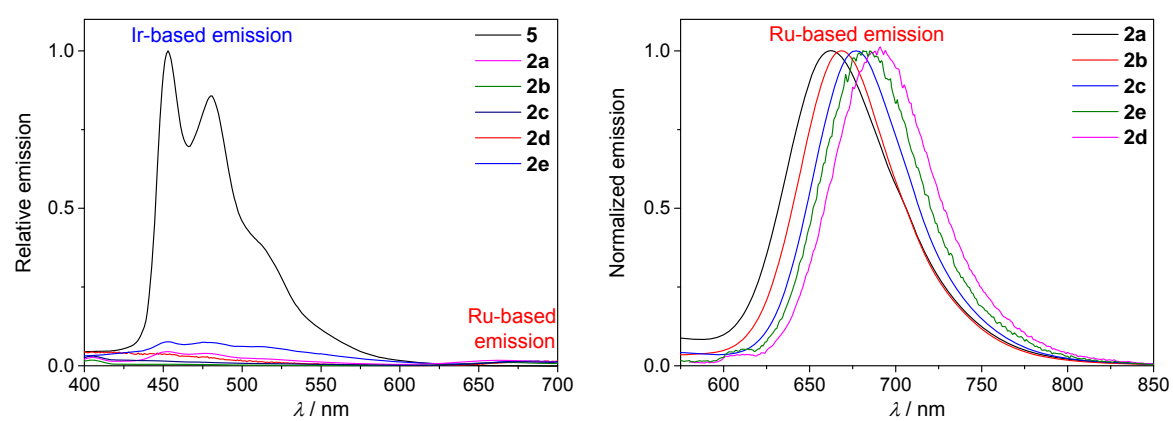
Figure S10. Room-temperature emission spectra (left, λ_{exc} = 365 nm; right, λ_{exc} = 500 nm) of **5** and fluorinated, dinuclear complexes **2a**−**2e** in dichloromethane.

6. Emission decay curves
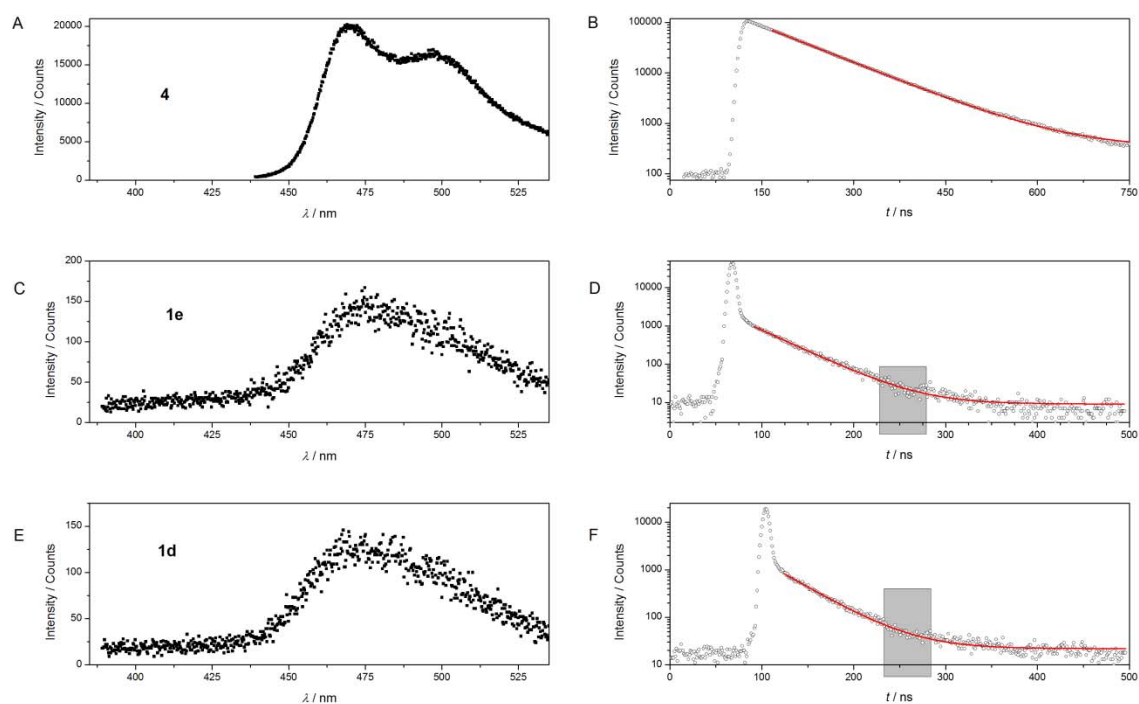
Figure S11. Streakcamera data for iridium-based emission of **4** (panels A, B), **1e** (panels C, D), **1d** (panels E, F) in aerated acetonitrile: Horizontal Cuts (i.e. emission spectra) are given in panels A, C, E and decay curves (hollow symbols) with respective mono-exponential tail fits are given in panels B, D, F. The region of the response function in the decay curves is dominated by Raman scatter and ligand fluorescence for **1e** and **1d**. The grey box (panels D, F) marks a region with faulty pixels in the detection system (ignoring those data points in the fit does not influence the result notably). The absolute signal intensity (counts) is not significant.
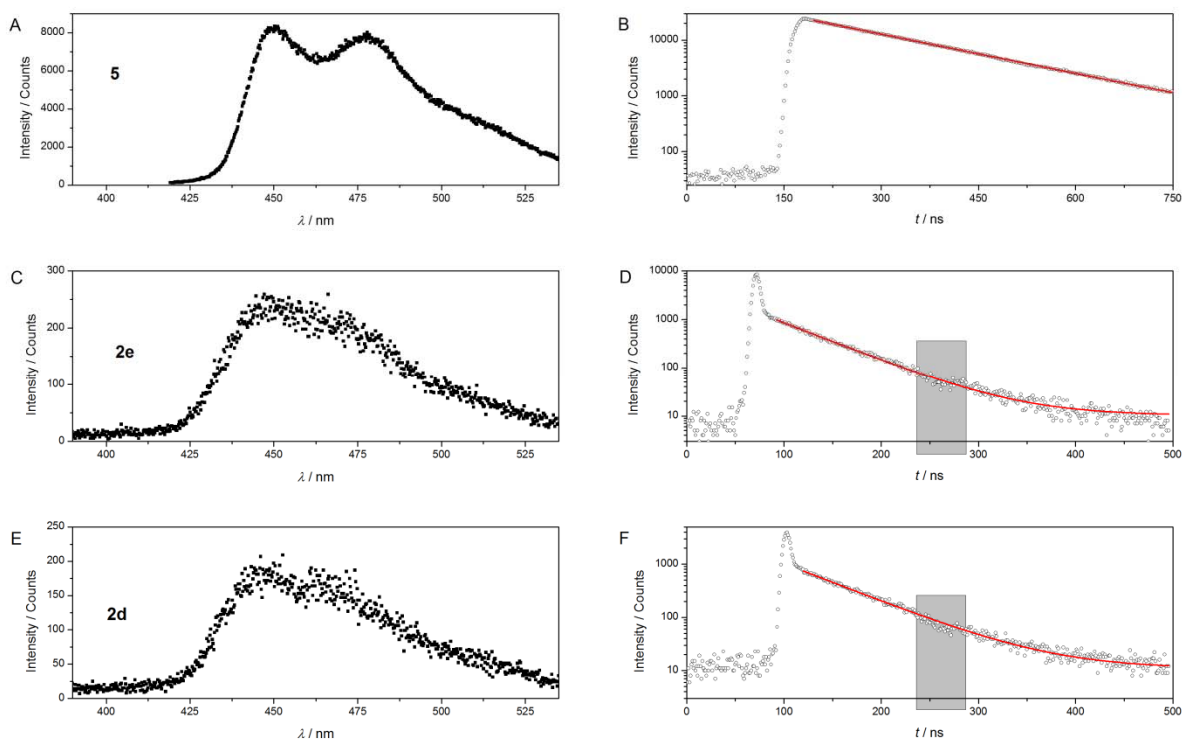
Figure S12. Streakcamera data for iridium-based emission of **5** (panels A, B), **2e** (panels C, D), **2d** (panels E, F) in aerated acetonitrile: Horizontal Cuts (i.e. emission spectra) are given in panels A, C, E and decay curves (hollow symbols) with respective mono-exponential tail fits are given in panels B, D, F. The region of the response function in the decay curves is dominated by Raman scatter and ligand fluorescence for **2e** and **2d**. The grey box (panels D, F) marks a region with faulty pixels in the detection system (ignoring those data points in the fit does not influence the result notably). The absolute signal intensity (counts) is not significant.
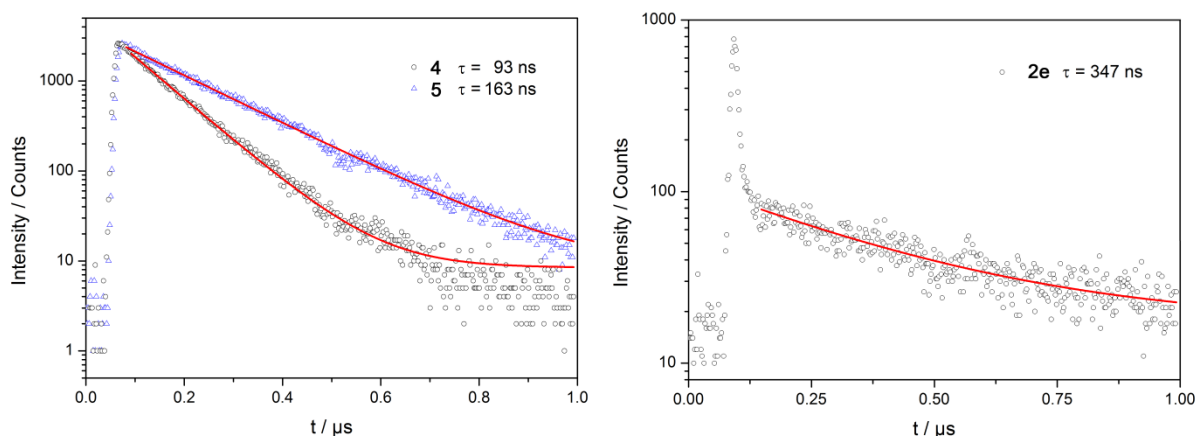
Figure S13. Streakcamera data for iridium-based emission of **4**, **5** (left) and **2e** (right) in aerated dichloromethane with respective mono-exponential tail fits.
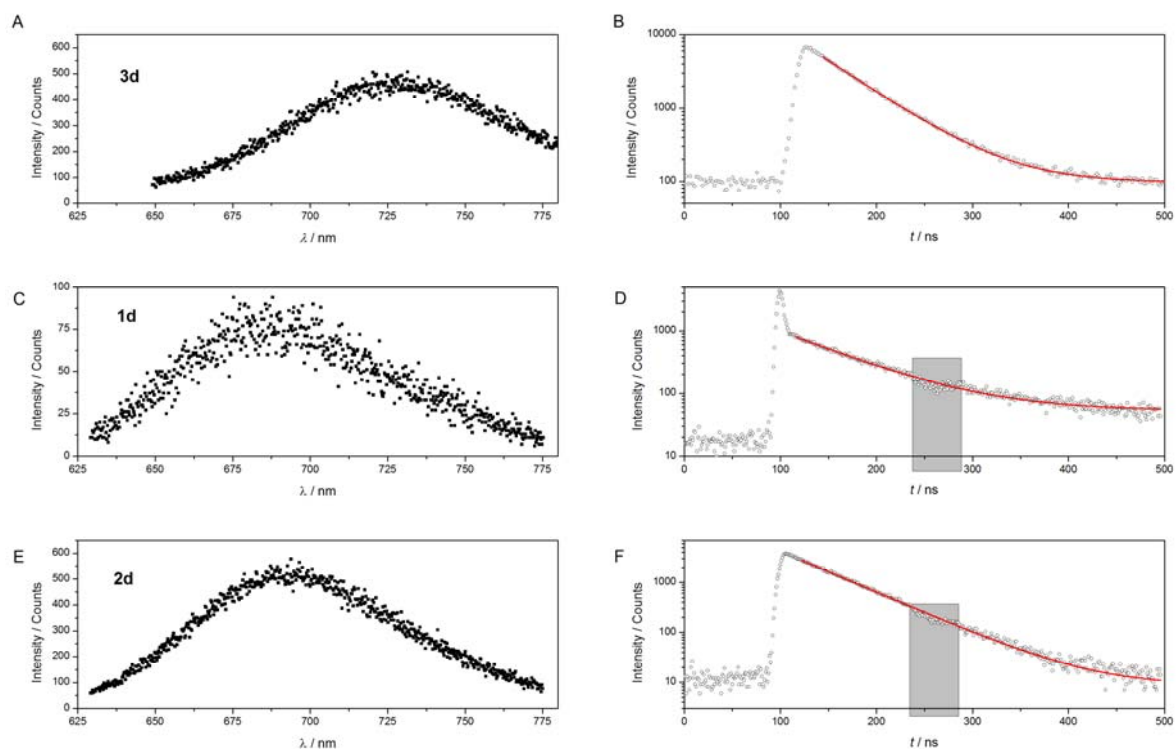
Figure S14. Streakcamera data for ruthenium-based emission of **3d** (panels A, B), **1d** (panels C, D), **2d** (panels E, F) in aerated acetonitrile: Horizontal Cuts (i.e. emission spectra) are given in panels A, C, E and decay curves (hollow symbols) with respective mono-exponential tail fits are given in panels B, D, F. The region of the response function in the decay curve is dominated by scatter for **1d**. The grey box (panels D, F) marks a region with faulty pixels in the detection system (ignoring those data points in the fit does not influence the result notably). The absolute signal intensity (counts) is not significant.
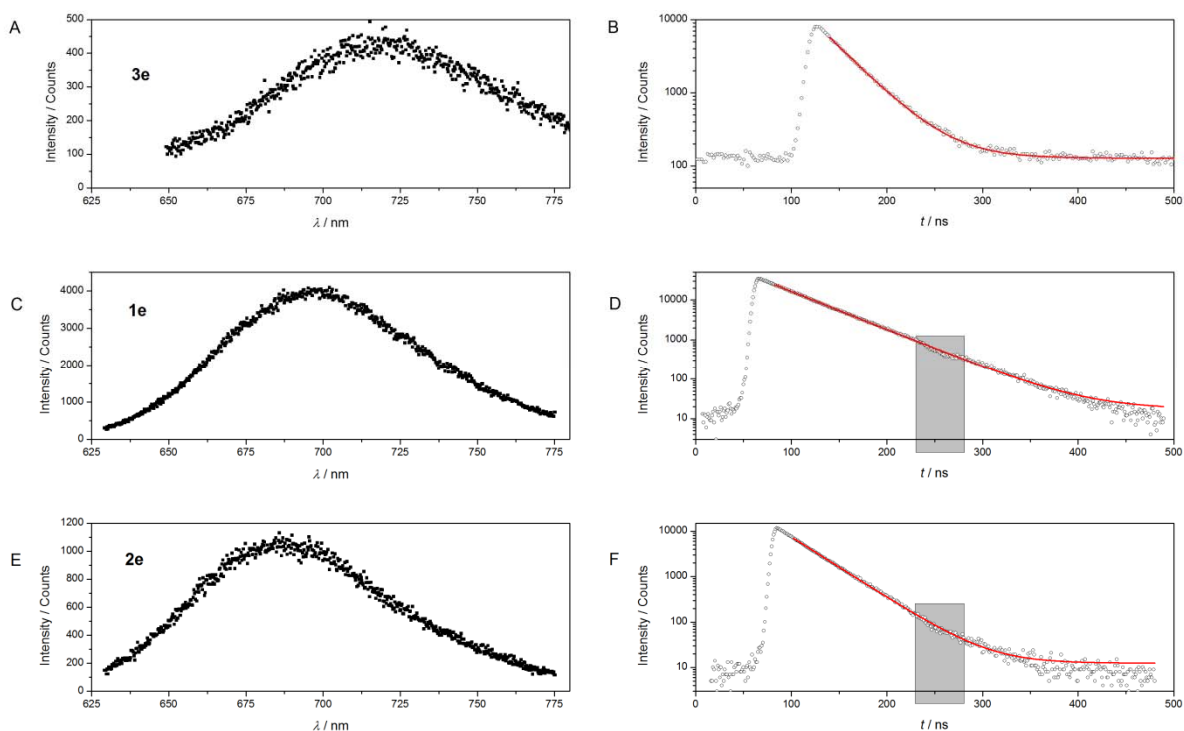
Figure S15. Streakcamera data for ruthenium-based emission of **3e** (panels A, B), **1e** (panels C, D), **2e** (panels E, F) in aerated acetonitrile: Horizontal Cuts (i.e. emission spectra) are given in panels A, C, E and decay curves (hollow symbols) with respective mono-exponential tail fits are given in panels B, D, F. The grey box (panels D, F) marks a region with faulty pixels in the detection system (ignoring those data points in the fit does not influence the result notably). The absolute signal intensity (counts) is not significant.

7. Excitation spectra

Excitation spectra of the ruthenium-based emission were corrected by the characteristic line of the emission spectrometer. Since direct measurement of this line is difficult, the one of the dinuclear complexes was used as reference. Starting with the assumption that in principle every absorption band contributes to the ruthenium-based emission, we could obtain the characteristic line as follows: First the absorption and uncorrected excitation spectra were normalized to the ruthenium-based MLCT transition at around 500 nm. Subsequently, the normalized absorption spectrum was divided by the normalized excitation spectrum of **2b**. Using this method a characteristic line of the spectrometer was obtained, which considers the lamp spectrum and filter effects (Figure S16).
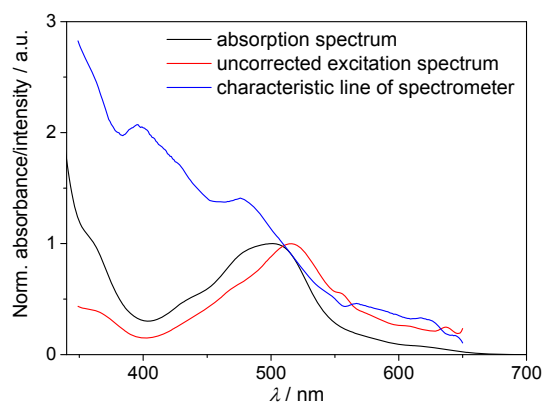
Figure S16. Normalized absorption and uncorrected excitation spectrum and of **2b** in dichloromethane. The characteristic line was obtained by dividing absorption by excitation spectrum.

The characteristic line spectrum was applied for the correction of the excitation spectra of all other complexes. By this approach we obtained corrected excitation spectra for the visible region which follow very well the absorption profile. The absorption and excitation spectra of the dinuclear complexes were compared to the corresponding ruthenium model complexes and are depicted in Figure S17-S21. The red marked wavelength describe the longest-wavelength absorption of the iridium model complexes **5** (360 nm) or **4** (380 nm). In every case amplification of the emission in this region is observed compared to the reference complexes. This allow us to assert that energy transfer from the Ir(III) to the Ru(II) center take place.
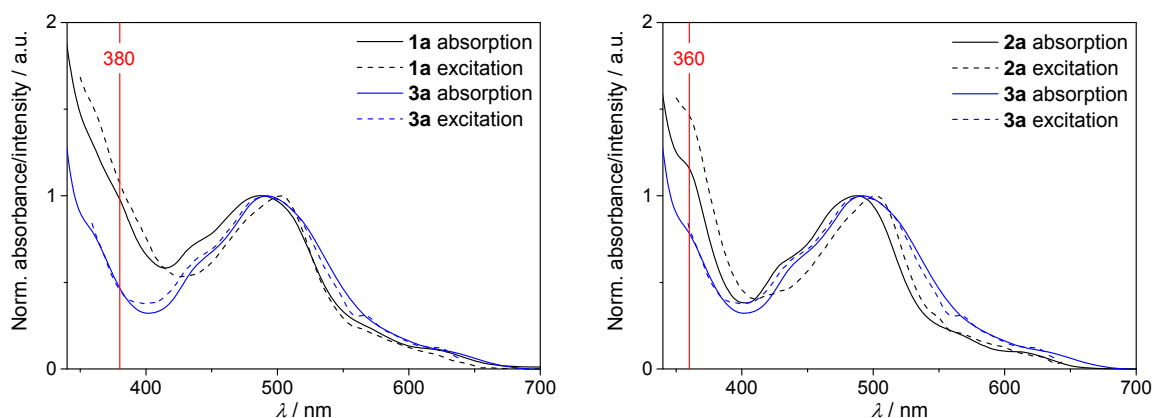
Figure S17. Absorption and corrected excitation spectra of **1a**, **2a** and **3a** in dichloromethane.
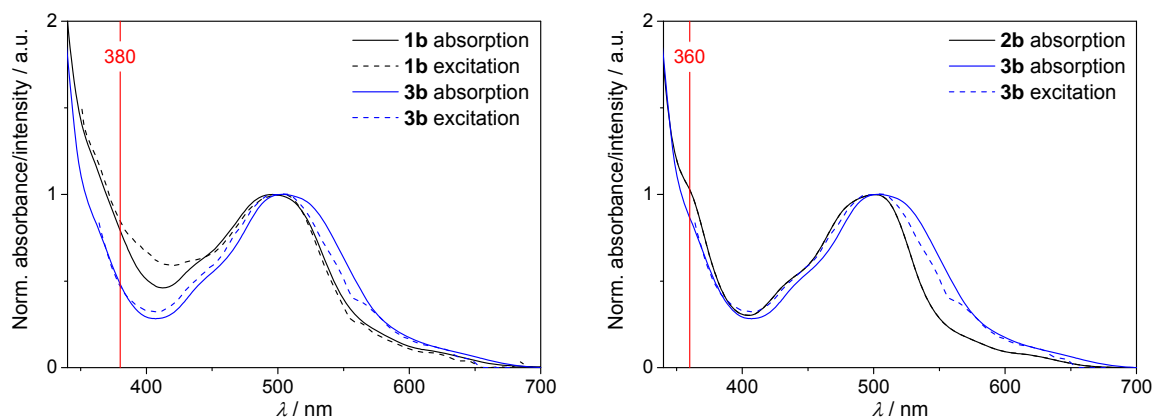
Figure S18. Absorption and corrected excitation spectra of **1b**, **2b** and **3b** in dichloromethane.
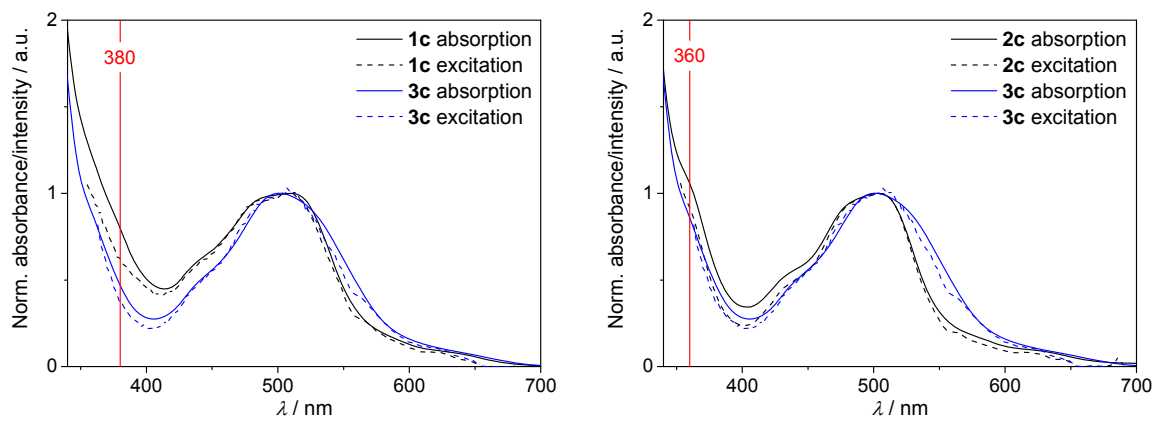
Figure S19. Absorption and corrected excitation spectra of **1c**, **2c** and **3c** in dichloromethane.
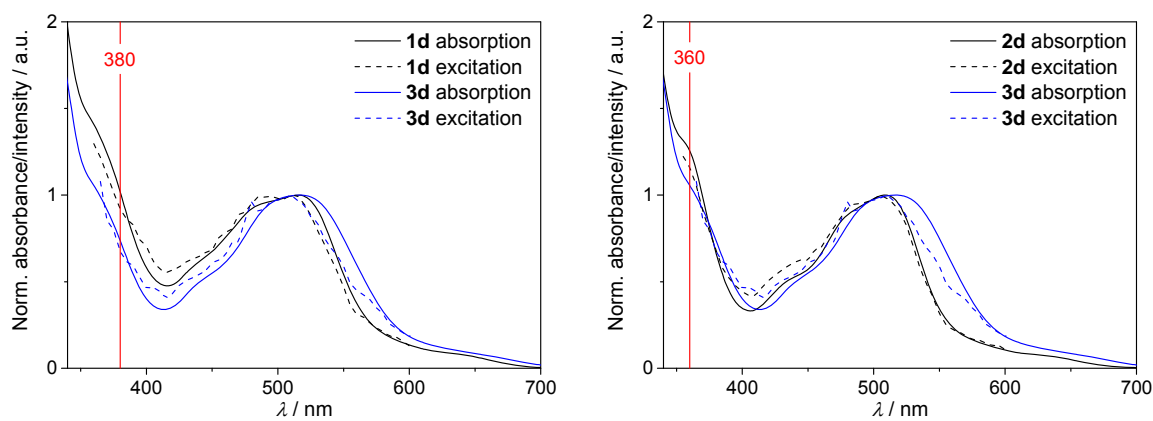
Figure S20. Absorption and corrected excitation spectra of **1d**, **2d** and **3d** in dichloromethane.
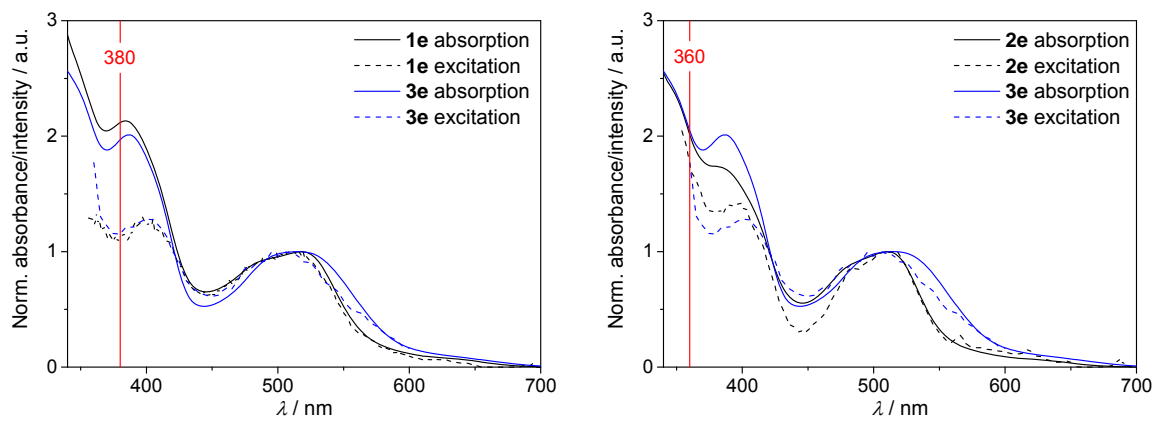
Figure S21. Absorption and corrected excitation spectra of **1e**, **2e** and **3e** in dichloromethane.

8. Spectroelectrochemistry
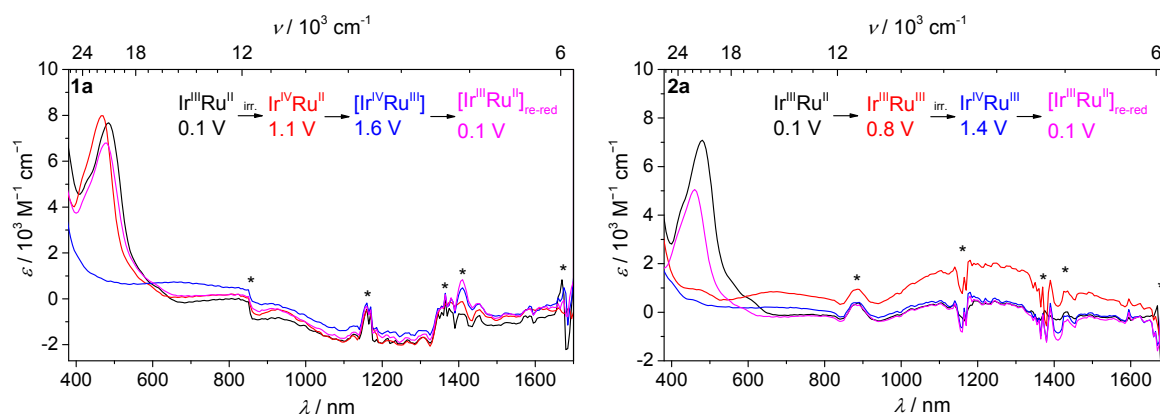
Figure S22. Vis-NIR spectroelectrochemistry of **1a** (left) and **2a** (Panel B) in 0.1 M Bu$_4$NPF$_6$ solution of acetonitrile, during the first (red curve) and second (blue curve) metal oxidation, and re-reduction (magenta curve) processes.
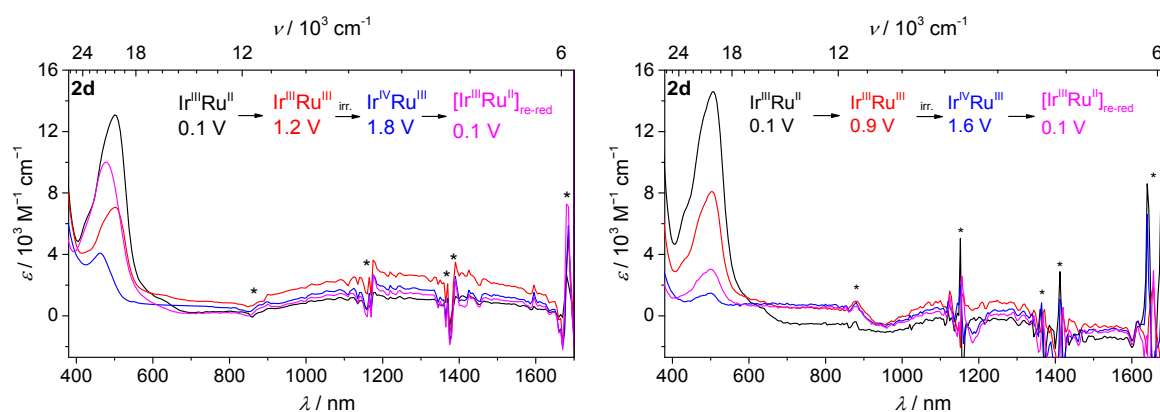
Figure S23. Vis-NIR Spectroelectrochemistry of **2d** in 0.1 M Bu$_4$NPF$_6$ solution of acetonitrile (left) or dichloromethane (right), during the first (red) and second (blue) metal oxidation, and re-reduction (magenta) processes. Solvent and spectrometer artifacts are marked with an asterisk.
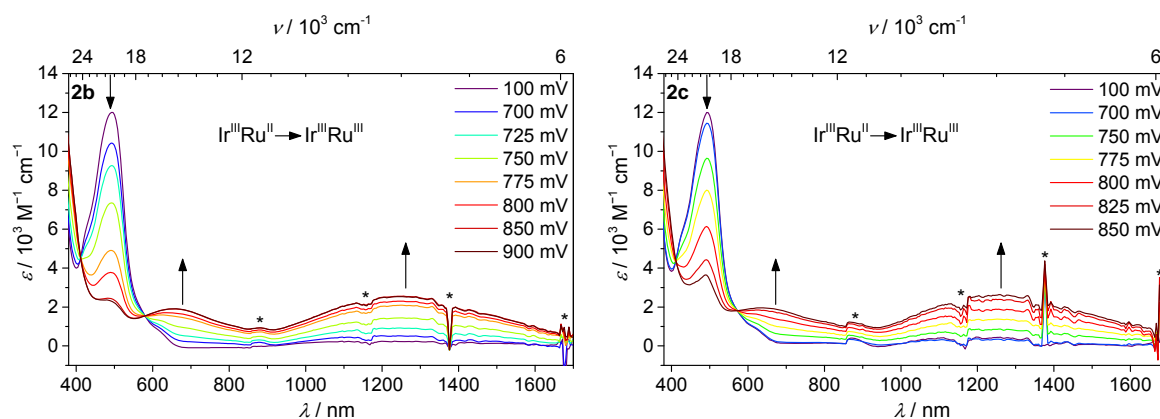
Figure S24. Vis-NIR Spectroelectrochemistry of **2b** (left) and **2c** (right) in 0.1 M Bu$_4$NPF$_6$ solution of acetonitrile, during the first ruthenium-based oxidation. Solvent and spectrometer artifacts are marked with an asterisk.
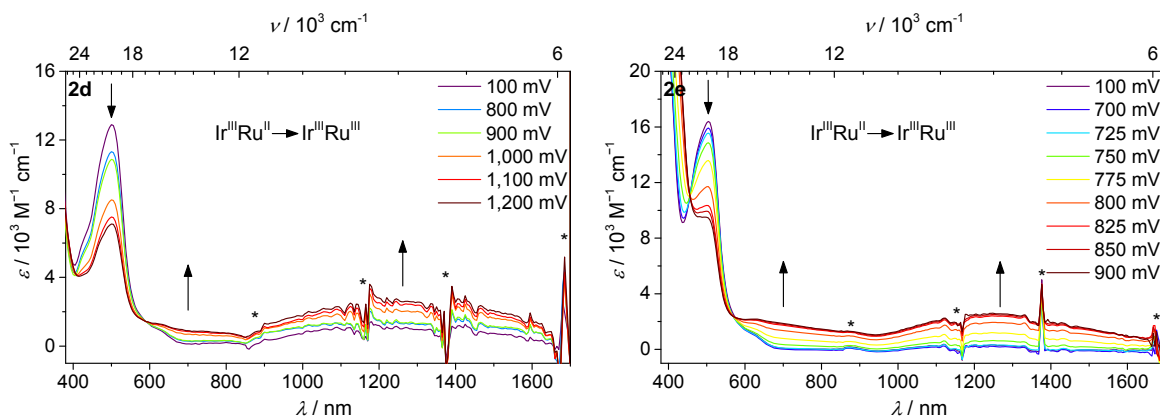
Figure S25. Vis-NIR Spectroelectrochemistry of **2d** (left) and **2e** (right) in 0.1 M Bu$_4$NPF$_6$ solution of acetonitrile, during the first ruthenium-based oxidation. Solvent and spectrometer artifacts are marked with an asterisk.

The bandwidth ($\Delta\tilde{\nu}_{1/2}$ (calcd)) of the IVCT transition was predicted by the Hush expression (Eq. 3), where R is the gas constant, T is the temperature and λ is the reorganization energy the term $16RT\ln 2$ takes a value of 2310 cm^{-1} at 298 K.[2-4]

$$\Delta\tilde{\nu}_{1/2}\ (\text{calcd}) = [16RT\ln2(\lambda)]^{1/2} = [2310(\lambda)]^{1/2} \tag{3}$$

For asymmetric redox systems, the energy of the IVCT transition (E_{IT}) is the sum of the reorganization energy (λ) and the energy change (ΔG^0) between the initial and the final state of the electron-transfer process ($E_{IT} = \lambda + \Delta G^0$).[5,6] An upper limit for ΔG^0 can be estimated from the potential splitting (ΔE_{PS}) between the Ru^{III}/Ru^{II} and Ir^{IV}/Ir^{III} wave, which is on average 0.56 V ($\approx$ 4500 cm^{-1}), for **2a-e**. Thus, values for $\Delta\tilde{\nu}_{1/2}$ (calcd) were determined and are presented in Table S1. The theoretical values fit to the experimental values, but are in general underestimated.

Table S1. Calculated and experimental bandwidths of the IVCT transition in **2a-e$^+$**.

compound	ΔE_{PS} / V	ΔG^0 / cm^{-1}	E_{IT} / cm^{-1}	$\Delta\tilde{\nu}_{1/2}$ (calcd) / cm^{-1}	$\Delta\tilde{\nu}_{1/2}$ / cm^{-1}
2a$^+$	0.60	4800	8200	2800	3420
2b$^+$	0.60	4900	8100	2700	3180
2c$^+$	0.53	4300	8050	2900	2810
2d$^+$	0.59	4800	8320	2900	3780
2e$^+$	0.47	3800	8140	3200	3180

9. Two-dimensional streakcamera images
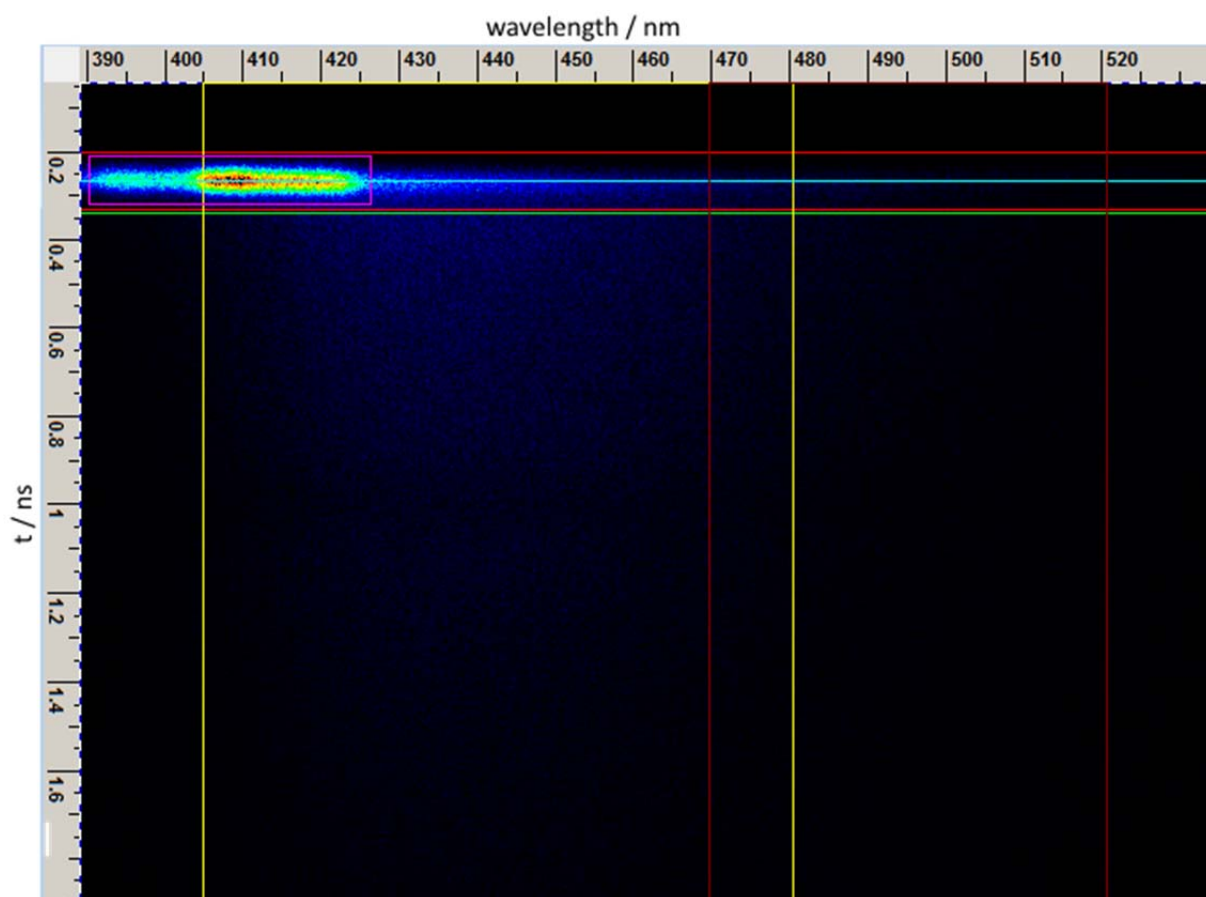
Figure S26. Two-dimensional streakcamera image recorded for **1e** (aerated acetonitrile solution) in a 2-ns time window. The colored boxes mark profiles (*vide infra*). The image is dominated by Raman-scatter at ca. 0.25 to 0.3 ns and after that an emission is observed, that does not fit with the iridium-based phosphorescence (see Figure S11, Figure S12 and Figure S28).
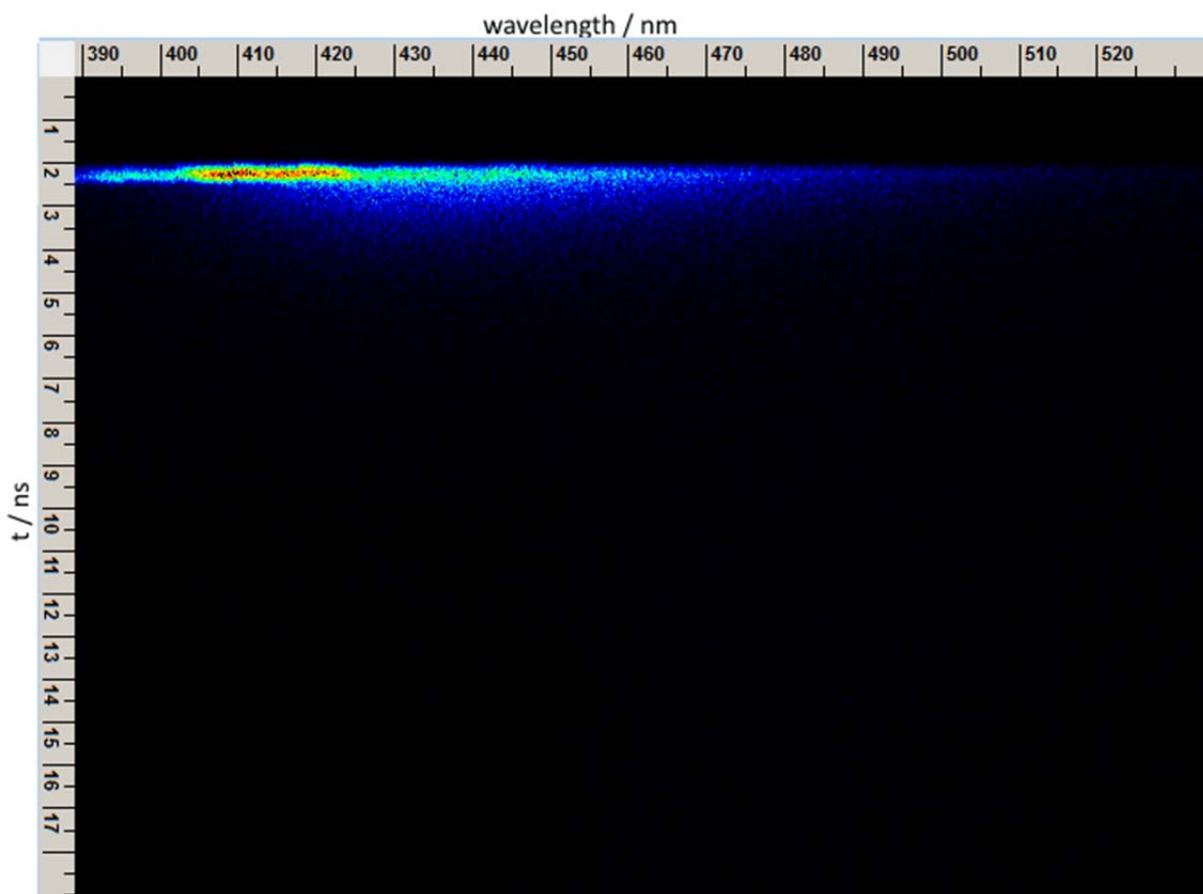
Figure S27. Two-dimensional streakcamera image recorded for **1e** (aerated acetonitrile solution) in a 20-ns time window. The image is dominated by Raman-scatter between 2 to 2.5 ns and after that an emission is observed, that does not fit with the iridium-based phosphorescence (see Figure S11, Figure S12 and Figure S28).
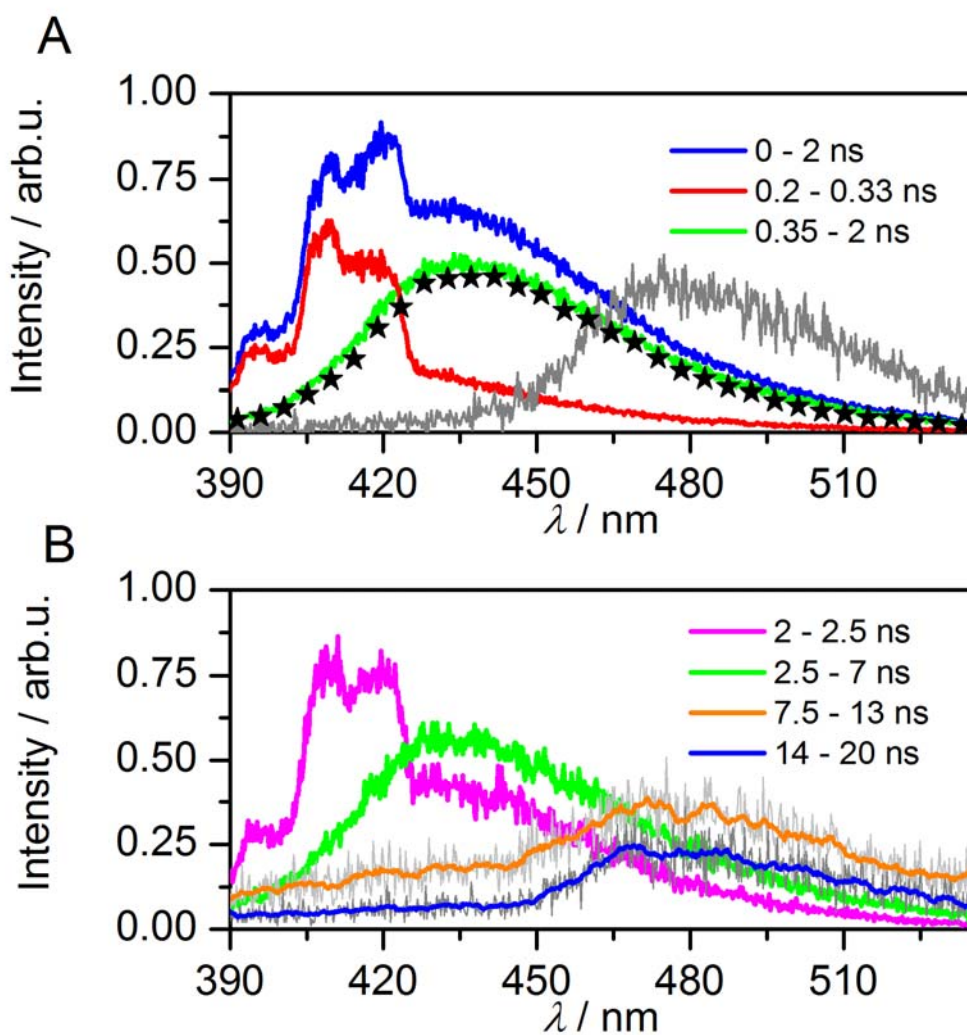
Figure S28. Streakcamera data recorded for **1e** (aerated acetonitrile solution) in a 2 ns (panel A, data from Figure S26 and 20 ns time window (panel B, data from Figure S27): Horizontal profiles of selected temporal intervals (i.e. temporally integrated time-resolved emission spectra) are shown as colored curves. Panel A: The gray curve represents the emission spectrum of **4** and the black stars display a species emission spectrum (lifetime ca. 0.8 ns) which was obtained from a global fit routine. At no time there is a signature in the spectra that fits with iridium emission, such that it can be concluded that there is no indication of quenching of the iridium emission. Panel B: The raw data for the two late intervals is scaled by a factor of 10 and shown in gray tones and the respective colored curves (orange and blue) are showing the respective 15-pt adjacent average. The iridium-based emission is weakly pronounced in the two spectra at late delay times and only visible when there is no more additional fast emission component. The lifetime of the iridium-based emission in **1e** is given in the main text. The green curve in panels A and B is assigned as ligand (tpy-based) fluorescence.

10. Geometry optimized structure
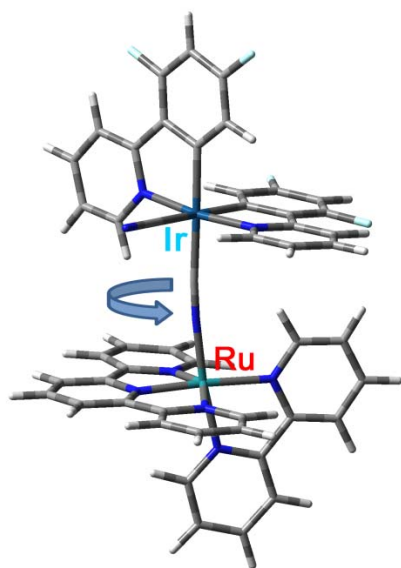
Figure S29. Three-dimensional structure of **2a** with possible conformers upon rotation along the Ru–C≡N–Ir axis.

11. Calculated singlet-singlet transitions energies and spin-density distributions
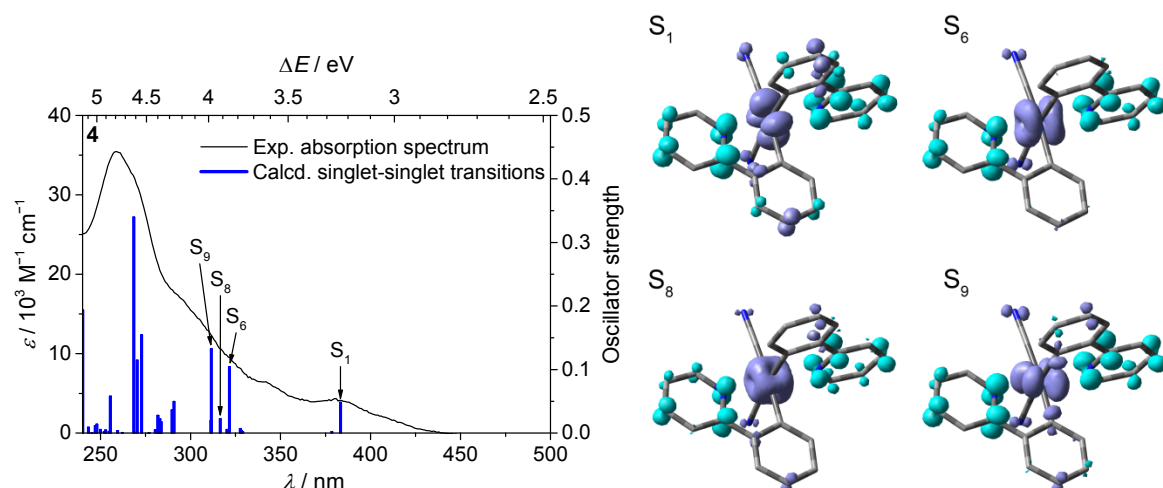
Figure S30. Experimental absorption spectra and B3LYP calculated singlet-singlet transitions energies with selected EDDM plots (plum-blue = depletion of electron density; cyan = accumulation of electron density; isovalue = 0.004) of **4**.

Table S2. B3LYP calculated electronic singlet-singlet transition energies ΔE with corresponding oscillator strengths f and contribution for **4**.

state	λ / nm	ΔE / eV	f	major contribution
S_1	383	3.24	0.0484	HOMO->LUMO (98%)
S_2	378	3.28	0.0023	HOMO->L+1 (97%)
S_3	329	3.77	0.002	H-3->L+1 (21%), H-2->LUMO (48%), H-1->L+1 (25%)
S_4	328	3.78	0.0042	H-3->LUMO (33%), H-2->L+1 (22%), H-1->LUMO (40%)
S_5	328	3.78	0.0071	HOMO->L+2 (89%)
S_6	322	3.85	0.1045	H-2->LUMO (46%), H-1->L+1 (39%)
S_7	320	3.87	0.0056	H-2->L+1 (31%), HOMO->L+3 (58%)
S_8	317	3.91	0.0225	H-2->L+1 (23%), H-1->LUMO (42%), HOMO->L+3 (25%)
S_9	312	3.97	0.1329	H-3->L+1 (53%), H-1->L+1 (25%)
S_{10}	311	3.99	0.0196	H-3->LUMO (46%), H-2->L+1 (13%), HOMO->L+3 (13%)
S_{11}	291	4.26	0.0496	H-4->LUMO (44%), H-2->L+2 (29%)
S_{12}	290	4.28	0.0363	H-5->LUMO (14%), H-4->L+1 (29%), H-1->L+2 (36%)
S_{13}	284	4.37	0.0174	H-5->L+1 (11%), H-4->LUMO (23%), H-2->L+2 (41%), H-1->L+3 (13%)
S_{14}	283	4.38	0.0224	H-6->L+1 (14%), H-5->LUMO (12%), H-3->L+2 (24%), H-2->L+3 (28%)
S_{15}	282	4.40	0.0014	H-5->LUMO (48%), H-4->L+1 (45%)
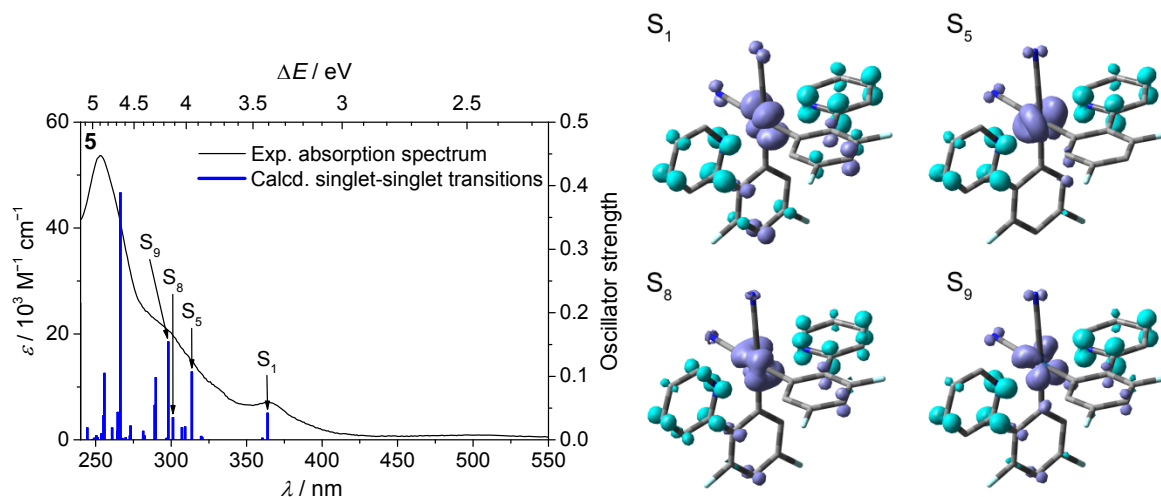
Figure S31. Experimental absorption spectra and B3LYP calculated singlet-singlet transitions energies with selected EDDM plots (plum-blue = depletion of electron density; cyan = accumulation of electron density; isovalue = 0.004) of **5**.

Table S3. B3LYP calculated electronic singlet-singlet transition energies ΔE with corresponding oscillator strengths f and contribution for **5**.

state	λ / nm	ΔE / eV	f	major contribution
S_1	364	3.41	0.042	HOMO->LUMO (97%)
S_2	360	3.44	0.0027	HOMO->L+1 (97%)
S_3	321	3.86	0.0035	H-3->L+1 (17%), H-2->LUMO (29%), H-1->L+1 (49%)
S_4	320	3.87	0.0054	H-3->LUMO (18%), H-2->L+1 (21%), H-1->LUMO (56%)
S_5	314	3.95	0.107	H-2->LUMO (59%), H-1->L+1 (25%)
S_6	309	4.01	0.0201	H-2->L+1 (60%), H-1->LUMO (16%)
S_7	307	4.04	0.0192	HOMO->L+2 (87%)
S_8	301	4.12	0.0349	H-3->LUMO (35%), H-1->LUMO (19%), HOMO->L+3 (39%)
S_9	298	4.16	0.154	H-3->L+1 (68%), H-1->L+1 (16%)
S_{10}	297	4.17	0.0024	H-3->LUMO (37%), HOMO->L+3 (48%)
S_{11}	290	4.28	0.0978	H-4->LUMO (77%)
S_{12}	289	4.29	0.0541	H-4->L+1 (71%), H-1->L+2 (10%)
S_{13}	283	4.38	0.0062	H-5->LUMO (86%)
S_{14}	281	4.41	0.0133	H-5->L+1 (86%)
S_{15}	273	4.54	0.0217	H-3->L+2 (18%), H-2->L+3 (18%), H-1->L+2 (45%)
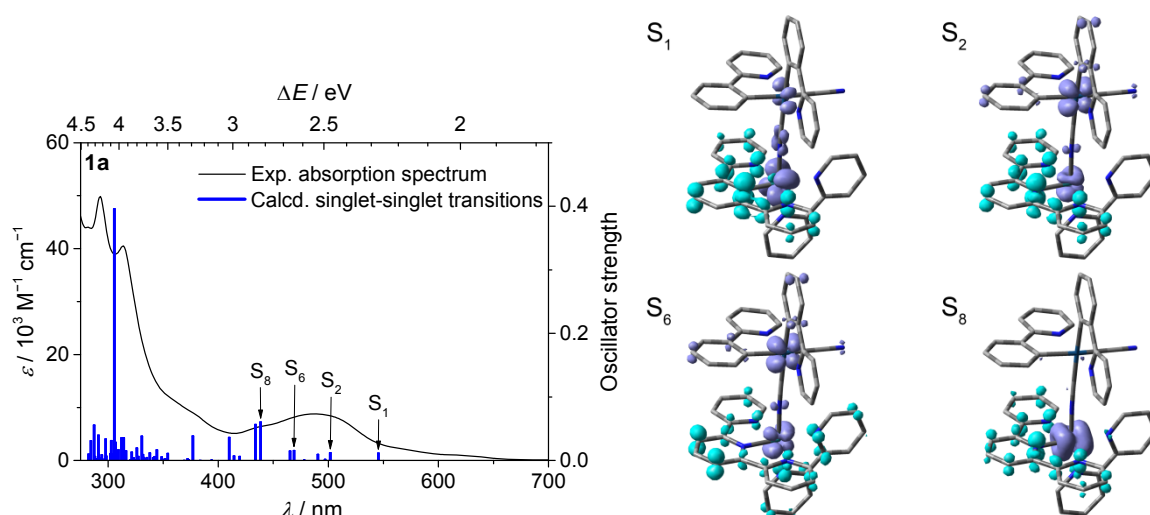
Figure S32. Experimental absorption spectra and B3LYP calculated singlet-singlet transitions energies with selected EDDM plots (plum-blue = depletion of electron density; cyan = accumulation of electron density; isovalue = 0.004) of **1a**.

Table S4. B3LYP calculated electronic singlet-singlet transition energies ΔE with corresponding oscillator strengths f and contribution for **1a**.

state	λ / nm	ΔE / eV	f	major contribution
S_1	545	2.27	0.0115	H-1->LUMO (93%)
S_2	502	2.47	0.0122	H-2->LUMO (10%), H-1->L+2 (10%), HOMO->LUMO (72%)
S_3	497	2.49	0.002	H-3->LUMO (90%)
S_4	491	2.53	0.0096	H-1->L+1 (67%), H-1->L+2 (23%)
S_5	478	2.59	0.0006	H-2->L+1 (22%), HOMO->L+1 (55%)
S_6	469	2.64	0.0158	H-2->L+2 (14%), HOMO->L+1 (13%), HOMO->L+2 (53%)
S_7	465	2.67	0.015	H-1->L+1 (16%), H-1->L+2 (39%), HOMO->LUMO (15%), HOMO->L+2 (10%)
S_8	439	2.82	0.0604	H-3->L+2 (37%), H-2->LUMO (50%)
S_9	434	2.86	0.0569	H-3->L+1 (77%), H-3->L+2 (11%)
S_{10}	419	2.96	0.0064	H-2->L+1 (71%), HOMO->L+1 (23%)
S_{11}	414	2.99	0.0071	H-2->L+2 (67%), HOMO->L+2 (26%)
S_{12}	410	3.02	0.0365	H-3->L+1 (16%), H-3->L+2 (39%), H-2->LUMO (20%), H-1->L+2 (14%)
S_{13}	394	3.15	0.0004	H-4->LUMO (96%)
S_{14}	383	3.24	0.0001	H-5->LUMO (97%)
S_{15}	377	3.29	0.0385	HOMO->L+3 (86%), HOMO->L+4 (10%)
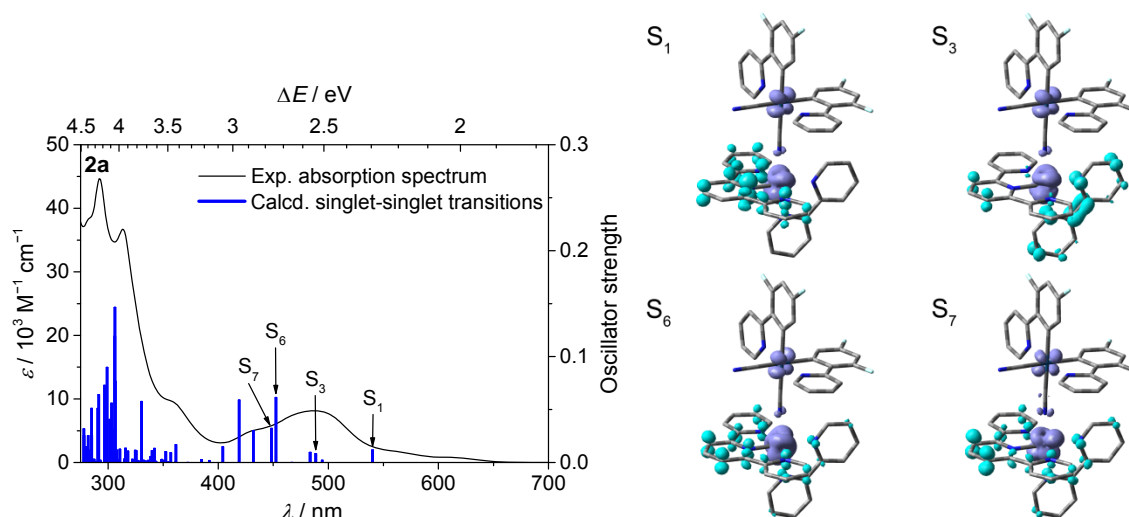
Figure S33. Experimental absorption spectra and B3LYP calculated singlet-singlet transitions energies with selected EDDM plots (plum-blue = depletion of electron density; cyan = accumulation of electron density; isovalue = 0.004) of **2a**.

Table S5. B3LYP calculated electronic singlet-singlet transition energies ΔE with corresponding oscillator strengths f and contribution for **2a**.

state	λ / nm	ΔE / eV	f	major contribution
S_1	540	2.30	0.0118	H-1->LUMO (38%), HOMO->LUMO (57%)
S_2	495	2.50	0.0022	H-2->LUMO (91%)
S_3	489	2.54	0.0084	H-1->L+1 (27%), HOMO->L+1 (47%), HOMO->L+2 (12%)
S_4	483	2.57	0.0095	H-3->LUMO (11%), H-1->LUMO (33%), H-1->L+2 (11%), HOMO->LUMO (17%), HOMO->L+2 (16%)
S_5	467	2.65	0.0001	H-3->L+1 (19%), H-1->L+1 (40%), HOMO->L+1 (17%)
S_6	452	2.74	0.0614	H-2->L+2 (15%), H-1->LUMO (14%), HOMO->LUMO (10%), HOMO->L+1 (14%), HOMO->L+2 (39%)
S_7	448	2.77	0.0321	H-3->L+2 (14%), H-1->L+1 (16%), H-1->L+2 (52%)
S_8	432	2.87	0.0299	H-2->L+1 (66%), H-2->L+2 (31%)
S_9	419	2.96	0.059	H-3->LUMO (26%), H-2->L+1 (18%), H-2->L+2 (30%)
S_{10}	404	3.07	0.0148	H-3->LUMO (54%), H-2->L+2 (17%)
S_{11}	392	3.16	0.0019	H-3->L+1 (73%), H-1->L+1 (11%), HOMO->L+1 (13%)
S_{12}	385	3.22	0.0028	H-3->L+2 (73%), H-1->L+2 (13%), HOMO->L+2 (10%)
S_{13}	372	3.33	0.0001	H-4->LUMO (95%)
S_{14}	362	3.43	0.0168	H-1->L+3 (14%), HOMO->L+3 (76%)
S_{15}	361	3.43	0.0004	H-5->LUMO (93%)
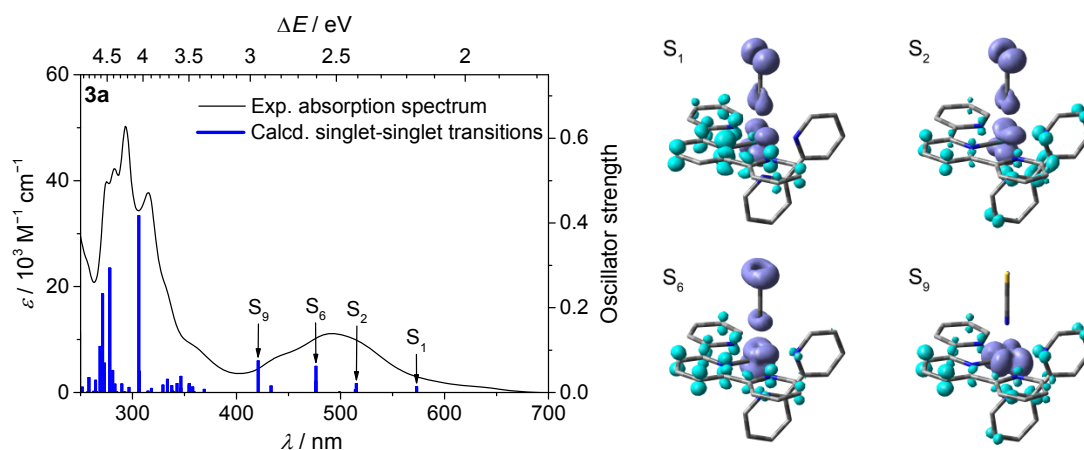
Figure S34. Experimental absorption spectra and B3LYP calculated singlet-singlet transitions energies with selected EDDM plots (plum-blue = depletion of electron density; cyan = accumulation of electron density; isovalue = 0.004) of **3a**.

Table S6. B3LYP calculated electronic singlet-singlet transition energies ΔE with corresponding oscillator strengths f and contribution for **3a**.

state	λ / nm	ΔE / eV	f	major contribution
S_1	573	2.16	0.0134	HOMO->LUMO (96%)
S_2	515	2.41	0.0207	H-1->LUMO (12%), HOMO->L+1 (56%), HOMO->L+2 (27%)
S_3	514	2.41	0.0062	H-1->LUMO (51%), HOMO->L+1 (32%), HOMO->L+2 (13%)
S_4	499	2.48	0.0009	H-2->LUMO (48%), H-1->L+1 (39%), H-1->L+2 (10%)
S_5	491	2.53	0.0	H-2->LUMO (49%), H-1->L+1 (43%)
S_6	476	2.60	0.0616	H-1->LUMO (31%), HOMO->L+2 (51%)
S_7	476	2.60	0.0266	H-1->L+1 (16%), H-1->L+2 (81%)
S_8	433	2.86	0.0152	H-2->L+1 (55%), H-2->L+2 (43%)
S_9	421	2.95	0.0746	H-2->L+1 (37%), H-2->L+2 (46%)
S_{10}	369	3.36	0.0073	HOMO->L+3 (91%)
S_{11}	369	3.36	0.0001	H-3->LUMO (95%)
S_{12}	359	3.45	0.0015	H-1->L+3 (67%), HOMO->L+4 (21%)
S_{13}	358	3.46	0.0129	H-1->L+3 (26%), HOMO->L+4 (28%), HOMO->L+8 (16%), HOMO->L+9 (18%)
S_{14}	355	3.49	0.0209	HOMO->L+4 (46%), HOMO->L+8 (20%), HOMO->L+9 (20%)
S_{15}	355	3.49	0.0176	H-4->LUMO (73%), HOMO->L+6 (15%)
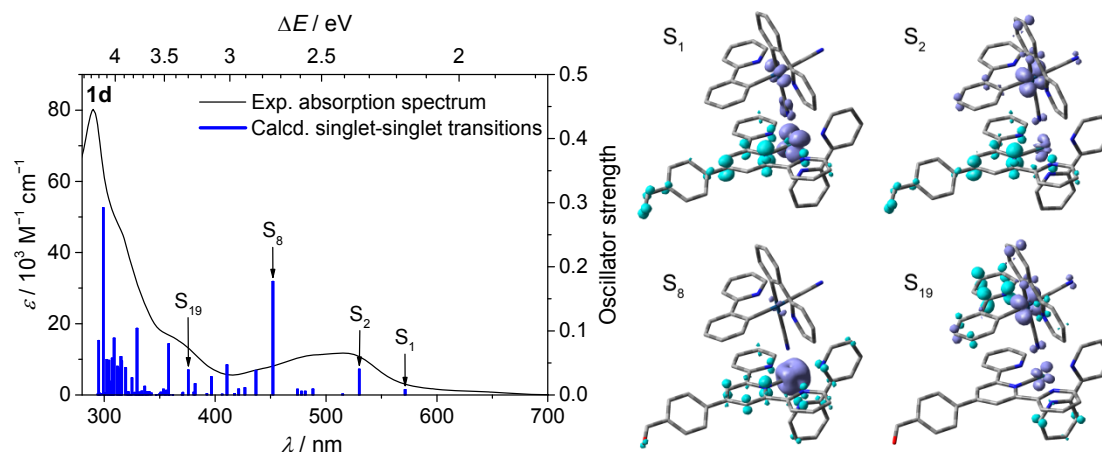
Figure S35. Experimental absorption spectra and B3LYP calculated singlet-singlet transitions energies with selected EDDM plots (plum-blue = depletion of electron density; cyan = accumulation of electron density; isovalue = 0.004) of **1d**.

Table S7. B3LYP calculated electronic singlet-singlet transition energies ΔE with corresponding oscillator strengths f and contribution for **1d**.

state	λ / nm	ΔE / eV	f	major contribution
S_1	571	2.17	0.0083	H-1->LUMO (88%)
S_2	530	2.34	0.0401	HOMO->LUMO (85%)
S_3	515	2.41	0.0013	H-3->LUMO (89%)
S_4	488	2.54	0.0091	H-1->L+1 (41%), H-1->L+2 (45%)
S_5	481	2.58	0.0056	H-2->LUMO (25%), H-1->L+1 (16%), H-1->L+2 (24%), HOMO->L+1 (18%)
S_6	478	2.59	0.0057	H-2->L+1 (15%), H-1->L+1 (13%), HOMO->L+1 (53%)
S_7	474	2.62	0.0089	H-2->L+2 (24%), HOMO->L+2 (57%)
S_8	452	2.74	0.1771	H-3->L+2 (23%), H-2->LUMO (43%), H-1->L+1 (21%)
S_9	437	2.84	0.0382	H-3->L+1 (85%)
S_{10}	427	2.90	0.0111	H-2->L+1 (68%), H-2->L+2 (11%), HOMO->L+1 (13%)
S_{11}	421	2.95	0.0091	H-4->LUMO (89%)
S_{12}	417	2.97	0.0019	H-2->L+2 (53%), HOMO->L+2 (30%)
S_{13}	411	3.02	0.047	H-3->L+2 (55%), H-1->L+2 (10%)
S_{14}	406	3.05	0.001	H-5->LUMO (96%)
S_{15}	397	3.12	0.0281	HOMO->L+3 (93%)
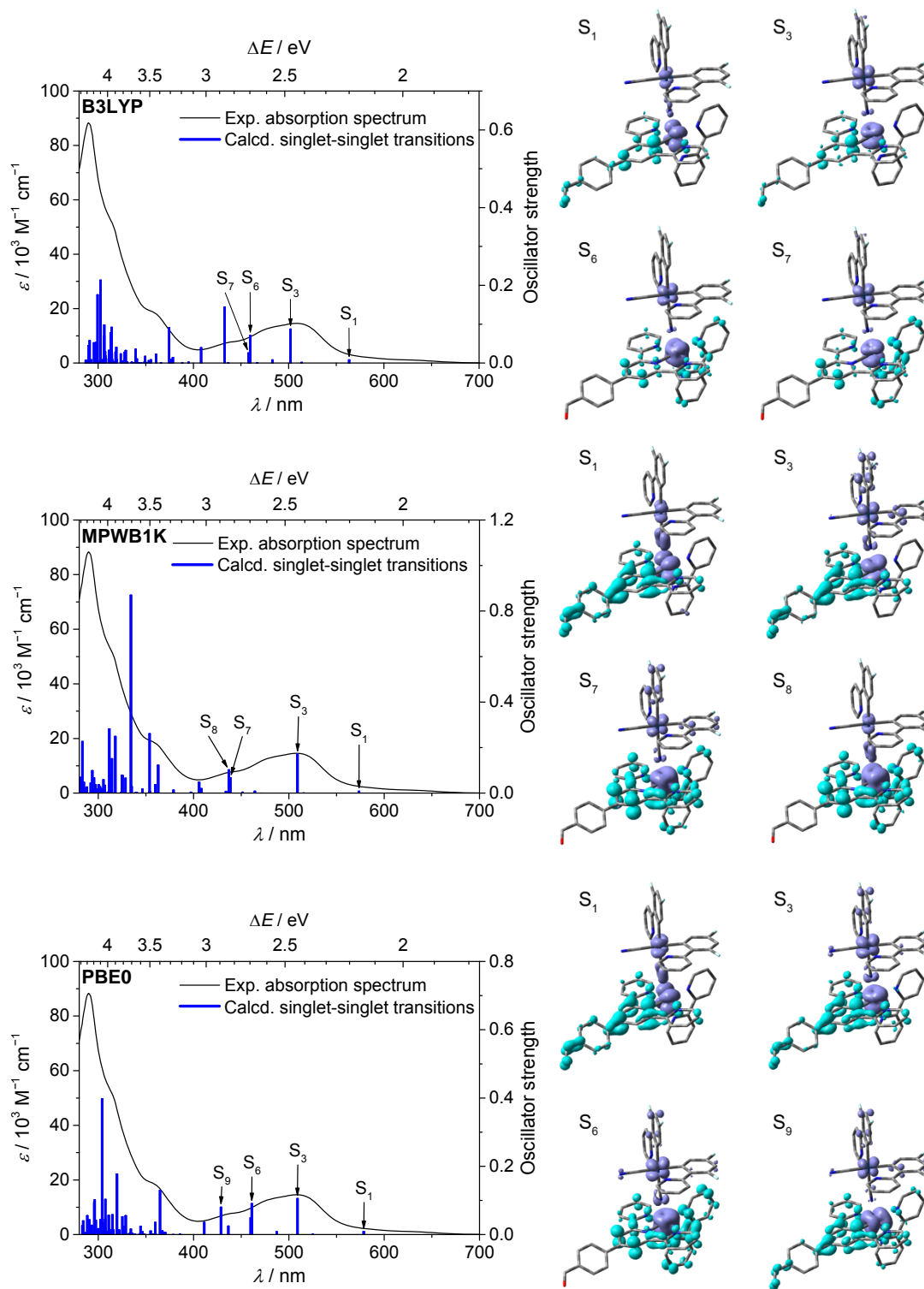
Figure S36. Comparison of different hybrid functionals: B3LYP (top), MPWB1K (middle) and PBE0 (bottom). The calculated singlet-singlet transitions energies using the MPWB1 and PBE0 functional were shifted that the S_3 transition is at the MLCT maximum. Experimental absorption spectra and calculated singlet-singlet transitions energies with selected EDDM plots (plum-blue = depletion of electron density; cyan = accumulation of electron density; isovalue = 0.004) of **2d**.

Table S8. B3LYP calculated electronic singlet-singlet transition energies ΔE with corresponding oscillator strengths f and contribution for **2d**.

state	λ / nm	ΔE / eV	f	major contribution
S$_1$	563	2.20	0.0082	H-1->LUMO (81%), HOMO->LUMO (11%)
S$_2$	514	2.41	0.0016	H-2->LUMO (88%)
S$_3$	502	2.47	0.0874	H-1->LUMO (10%), HOMO->LUMO (58%)
S$_4$	483	2.57	0.008	H-1->L+1 (38%), H-1->L+2 (43%)
S$_5$	467	2.65	0.0004	H-3->L+1 (11%), H-3->L+2 (12%), HOMO->L+1 (33%), HOMO->L+2 (29%)
S$_6$	460	2.70	0.0709	H-2->L+2 (12%), H-1->L+1 (23%), H-1->L+2 (15%), HOMO->LUMO (16%), HOMO->L+1 (15%), HOMO->L+2 (13%)
S$_7$	458	2.71	0.0262	H-3->L+2 (10%), H-1->L+1 (16%), H-1->L+2 (14%), HOMO->L+1 (24%), HOMO->L+2 (24%)
S$_8$	436	2.84	0.0002	H-3->LUMO (17%), H-2->L+1 (54%), H-2->L+2 (20%)
S$_9$	433	2.86	0.1443	H-3->LUMO (48%), H-2->L+1 (34%)
S$_{10}$	408	3.04	0.0397	H-3->LUMO (15%), H-2->L+2 (53%)
S$_{11}$	395	3.14	0.0025	H-3->L+1 (70%), HOMO->L+1 (17%)
S$_{12}$	392	3.16	0	H-4->LUMO (88%)
S$_{13}$	388	3.20	0.0003	H-3->L+2 (71%), HOMO->L+2 (22%)
S$_{14}$	379	3.27	0.014	H-5->LUMO (42%), H-1->L+3 (37%), HOMO->L+3 (13%)
S$_{15}$	377	3.29	0.0098	H-5->LUMO (53%), H-1->L+3 (30%), HOMO->L+3 (10%)

Table S9. MPWB1K calculated electronic singlet-singlet transition energies ΔE with corresponding oscillator strengths f and contribution for **2d**.

state	λ / nm	ΔE / eV	f	major contribution
S$_1$	574	2.16	0.0086	H-1->LUMO (81%)
S$_2$	516	2.40	0.0008	H-4->LUMO (82%)
S$_3$	509	2.44	0.1706	H-2->LUMO (46%), HOMO->LUMO (30%)
S$_4$	471	2.63	0.0002	H-1->L+18 (16%), H-1->L+22 (16%), H-1->L+23 (23%)
S$_5$	464	2.67	0.0086	H-1->L+1 (21%), H-1->L+2 (57%)
S$_6$	451	2.75	0.0042	H-2->L+2 (53%), HOMO->L+2 (31%)
S$_7$	439	2.82	0.0673	H-2->L+1 (31%), H-1->L+1 (11%), HOMO->L+1 (28%)
S$_8$	437	2.84	0.1024	H-4->L+2 (15%), H-2->L+1 (15%), H-1->L+1 (49%)
S$_9$	434	2.86	0.0078	H-4->L+18 (11%), H-4->L+22 (12%), H-4->L+23 (18%), H-4->L+25 (16%)
S$_{10}$	408	3.04	0.0197	H-4->L+1 (33%), H-4->L+2 (39%)
S$_{11}$	406	3.05	0.0491	H-4->L+1 (61%), H-4->L+2 (18%)
S$_{12}$	400	3.10	0.0001	H-15->LUMO (29%), H-15->L+3 (49%)
S$_{13}$	397	3.12	0.0047	H-2->L+25 (16%), H-2->L+27 (10%)
S$_{14}$	379	3.27	0.0135	H-2->LUMO (38%), HOMO->LUMO (52%)
S$_{15}$	363	3.42	0.1231	H-3->L+5 (11%), HOMO->L+4 (51%), HOMO->L+5 (18%)

Table S10. PBE0 calculated electronic singlet-singlet transition energies ΔE with corresponding oscillator strengths f and contribution for **2d**.

state	λ / nm	ΔE / eV	f	major contribution
S$_1$	579	2.14	0.009	H-1->LUMO (77%), HOMO->LUMO (14%)
S$_2$	525	2.36	0.0014	H-3->LUMO (14%), H-2->LUMO (77%)
S$_3$	509	2.44	0.1057	H-3->LUMO (12%), H-1->LUMO (11%), HOMO->LUMO (50%)
S$_4$	487	2.55	0.0083	H-1->L+1 (32%), H-1->L+2 (44%)
S$_5$	469	2.64	0	H-3->L+2 (17%), HOMO->L+1 (18%), HOMO->L+2 (36%)
S$_6$	461	2.69	0.0907	H-2->L+2 (14%), H-1->L+1 (14%), HOMO->L+1 (32%), HOMO->L+2 (15%)
S$_7$	460	2.70	0.0492	H-3->L+1 (10%), H-1->L+1 (34%), H-1->L+2 (15%), HOMO->L+1 (16%)
S$_8$	437	2.84	0.0252	H-3->L+1 (12%), H-2->L+1 (76%)
S$_9$	429	2.89	0.0804	H-3->LUMO (44%), H-2->L+2 (18%), HOMO->LUMO (19%)
S$_{10}$	411	3.02	0.0358	H-3->LUMO (23%), H-2->L+2 (40%)
S$_{11}$	386	3.21	0.0018	H-4->LUMO (10%), H-3->L+1 (54%), HOMO->L+1 (20%)
S$_{12}$	382	3.25	0	H-4->LUMO (82%)
S$_{13}$	378	3.28	0.0003	H-3->L+2 (57%), HOMO->L+2 (27%)
S$_{14}$	370	3.35	0.0063	H-1->L+3 (17%), H-1->L+14 (24%), H-1->L+15 (20%)
S$_{15}$	369	3.36	0.0058	H-5->LUMO (54%), H-1->L+3 (14%)
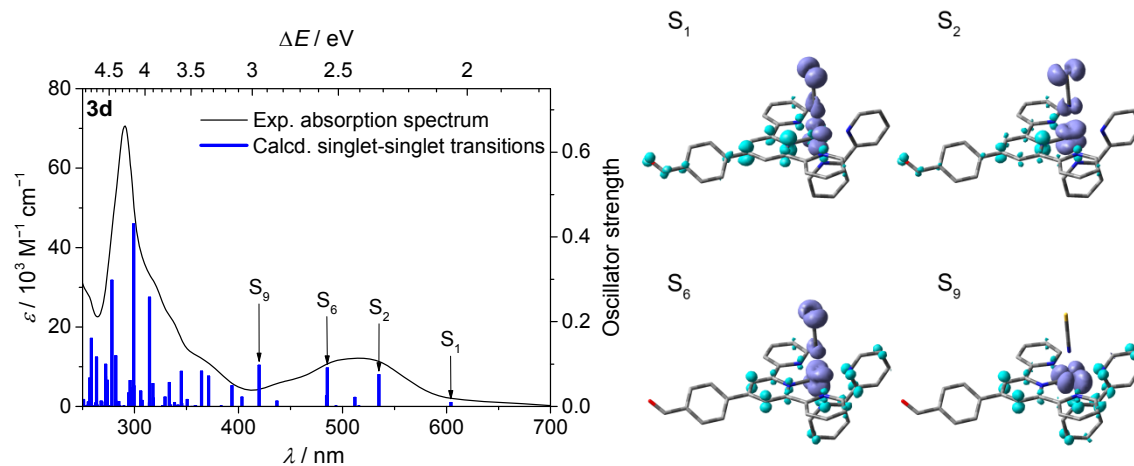
Figure S37. Experimental absorption spectra and B3LYP calculated singlet-singlet transitions energies with selected EDDM plots (plum-blue = depletion of electron density; cyan = accumulation of electron density; isovalue = 0.004) of **3d**.

Table S11. B3LYP calculated electronic singlet-singlet transition energies ΔE with corresponding oscillator strengths f and contribution for **3d**.

state	λ / nm	ΔE / eV	f	major contribution
S_1	604	2.05	0.009	HOMO->LUMO (93%)
S_2	535	2.32	0.0748	H-1->LUMO (76%), HOMO->L+2 (12%)
S_3	516	2.40	0.0006	H-2->LUMO (90%)
S_4	512	2.42	0.0211	HOMO->L+1 (64%), HOMO->L+2 (30%)
S_5	494	2.51	0.001	H-1->L+1 (62%), H-1->L+2 (31%)
S_6	485	2.56	0.0908	H-1->LUMO (17%), HOMO->L+1 (24%), HOMO->L+2 (46%)
S_7	485	2.56	0.0253	H-1->L+1 (32%), H-1->L+2 (60%)
S_8	437	2.84	0.0123	H-2->L+1 (77%), H-2->L+2 (22%)
S_9	420	2.95	0.0973	H-2->L+1 (20%), H-2->L+2 (64%)
S_{10}	403	3.08	0.0221	HOMO->L+3 (89%)
S_{11}	394	3.15	0.0487	H-1->L+3 (92%)
S_{12}	383	3.24	0.0008	H-3->LUMO (90%)
S_{13}	371	3.34	0.0716	H-4->LUMO (55%), HOMO->L+4 (32%)
S_{14}	364	3.41	0.0831	H-4->LUMO (28%), HOMO->L+4 (63%)
S_{15}	359	3.45	0.0015	H-1->L+4 (95%)
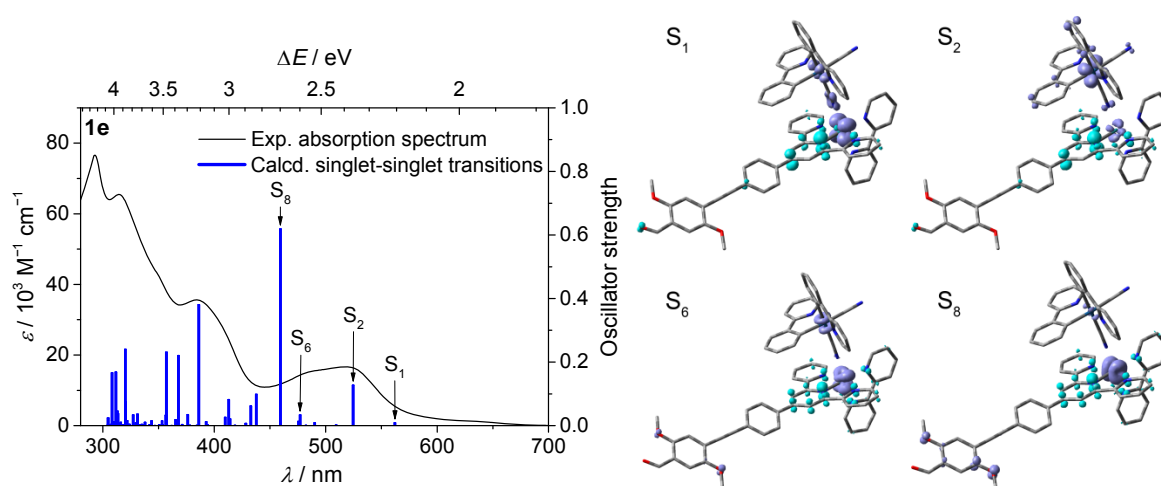
Figure S38. Experimental absorption spectra and B3LYP calculated singlet-singlet transitions energies with selected EDDM plots (plum-blue = depletion of electron density; cyan = accumulation of electron density; isovalue = 0.004) of **1e**.

Table S12. B3LYP calculated electronic singlet-singlet transition energies ΔE with corresponding oscillator strengths f and contribution for **1e**.

state	λ / nm	ΔE / eV	f	major contribution
S_1	562	2.21	0.009	H-1->LUMO (86%)
S_2	525	2.36	0.1276	HOMO->LUMO (83%)
S_3	509	2.44	0.002	H-4->LUMO (85%)
S_4	490	2.53	0.0091	H-1->L+1 (56%), H-1->L+2 (36%)
S_5	482	2.57	0.0012	H-3->L+1 (16%), HOMO->L+1 (57%), HOMO->L+2 (10%)
S_6	477	2.60	0.0335	H-3->LUMO (17%), H-2->LUMO (19%), H-1->L+1 (16%), H-1->L+2 (25%), HOMO->LUMO (12%)
S_7	476	2.60	0.0136	H-3->L+2 (13%), HOMO->L+1 (18%), HOMO->L+2 (56%)
S_8	459	2.70	0.619	H-4->L+2 (12%), H-2->LUMO (47%), H-1->L+1 (17%), H-1->L+2 (16%)
S_9	438	2.83	0.0986	H-4->L+1 (50%), H-4->L+2 (28%), H-3->LUMO (11%)
S_{10}	433	2.86	0.0619	H-4->L+1 (30%), H-3->LUMO (38%), H-2->LUMO (21%)
S_{11}	428	2.90	0.0069	H-3->L+1 (30%), H-2->L+1 (34%), HOMO->L+1 (13%)
S_{12}	419	2.96	0.001	H-3->L+2 (27%), H-2->L+2 (25%), HOMO->L+2 (25%)
S_{13}	414	2.99	0.021	H-5->LUMO (66%), H-4->L+2 (17%)
S_{14}	413	3.00	0.0818	H-5->LUMO (12%), H-4->L+2 (11%), HOMO->L+3 (63%)
S_{15}	410	3.02	0.026	H-5->LUMO (17%), H-4->L+2 (22%), H-3->LUMO (13%), HOMO->L+3 (29%)
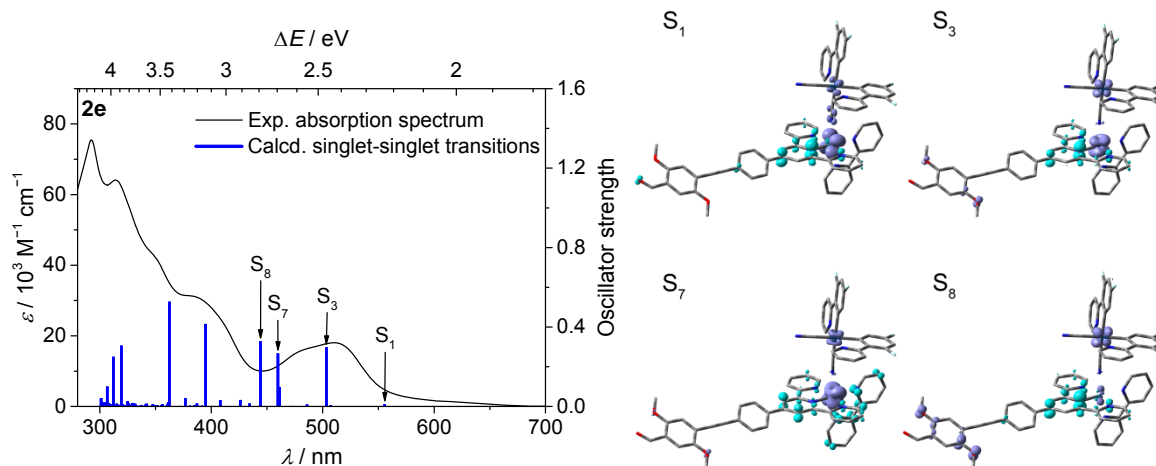
Figure S39. Experimental absorption spectra and B3LYP calculated singlet-singlet transitions energies with selected EDDM plots (plum-blue = depletion of electron density; cyan = accumulation of electron density; isovalue = 0.004) of **2e**.

Table S13. B3LYP calculated electronic singlet-singlet transition energies ΔE with corresponding oscillator strengths f and contribution for **2e**.

state	λ / nm	ΔE / eV	f	major contribution
S_1	556	2.23	0.009	H-1->LUMO (85%)
S_2	507	2.45	0.0044	H-3->LUMO (85%)
S_3	503	2.46	0.2946	H-1->L+2 (10%), HOMO->LUMO (65%)
S_4	486	2.55	0.0071	H-1->L+1 (58%), H-1->L+2 (33%)
S_5	473	2.62	0.0001	H-4->L+1 (11%), HOMO->L+1 (44%), HOMO->L+2 (23%)
S_6	461	2.69	0.0951	HOMO->L+1 (23%), HOMO->L+2 (38%)
S_7	460	2.70	0.2644	H-1->L+1 (23%), H-1->L+2 (30%), HOMO->LUMO (12%)
S_8	444	2.79	0.3255	H-2->LUMO (85%)
S_9	434	2.86	0.0125	H-3->L+1 (66%), H-3->L+2 (25%)
S_{10}	426	2.91	0.0297	H-4->LUMO (52%), H-3->L+1 (16%), H-3->L+2 (15%), HOMO->LUMO (10%)
S_{11}	408	3.04	0.0286	H-4->LUMO (25%), H-3->L+1 (11%), H-3->L+2 (39%), H-1->L+2 (12%)
S_{12}	400	3.10	0.0001	H-2->L+1 (69%), H-2->L+2 (17%)
S_{13}	395	3.14	0.4123	HOMO->L+3 (89%)
S_{14}	392	3.16	0.0008	H-4->L+1 (28%), H-2->L+2 (49%)
S_{15}	388	3.20	0.0005	H-4->L+1 (22%), H-4->L+2 (16%), H-1->L+3 (32%), HOMO->L+1 (10%)
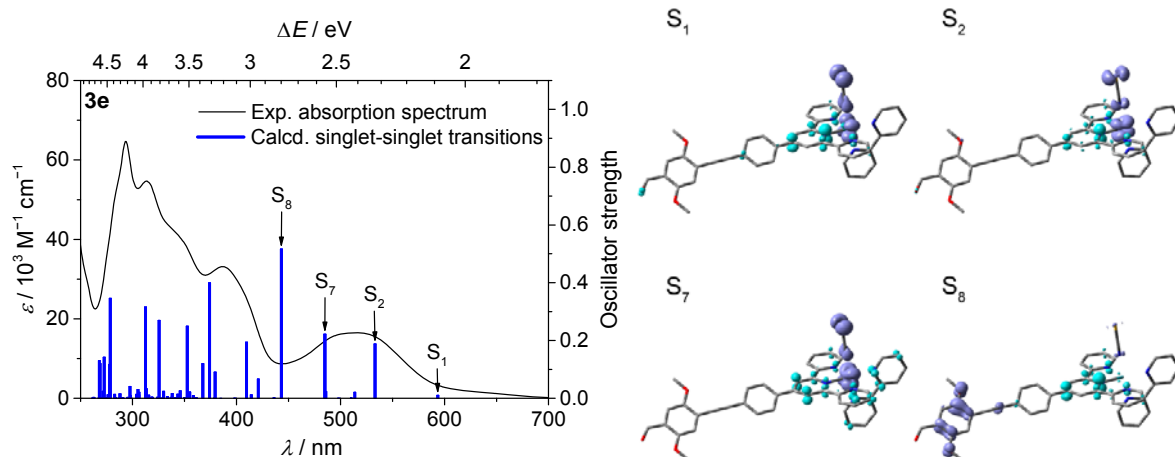
Figure S40. Experimental absorption spectra and B3LYP calculated singlet-singlet transitions energies with selected EDDM plots (plum-blue = depletion of electron density; cyan = accumulation of electron density; isovalue = 0.004) of **3e**.

Table S14. B3LYP calculated electronic singlet-singlet transition energies ΔE with corresponding oscillator strengths f and contribution for **3e**.

state	λ / nm	ΔE / eV	f	major contribution
S_1	593	2.09	0.0099	HOMO->LUMO (90%)
S_2	533	2.33	0.188	H-1->LUMO (73%), HOMO->L+2 (14%)
S_3	514	2.41	0.0206	HOMO->L+1 (75%), HOMO->L+2 (19%)
S_4	510	2.43	0.0008	H-3->LUMO (77%)
S_5	498	2.49	0.0004	H-3->LUMO (12%), H-1->L+1 (61%), H-1->L+2 (18%)
S_6	486	2.55	0.0234	H-1->L+1 (24%), H-1->L+2 (68%)
S_7	485	2.56	0.2219	H-1->LUMO (16%), HOMO->L+1 (18%), HOMO->L+2 (56%)
S_8	443	2.80	0.5163	H-2->LUMO (90%)
S_9	436	2.84	0.001	H-3->L+1 (65%), H-3->L+2 (30%)
S_{10}	421	2.95	0.0665	H-3->L+1 (27%), H-3->L+2 (56%)
S_{11}	414	2.99	0.0118	HOMO->L+3 (88%)
S_{12}	410	3.02	0.1941	H-1->L+3 (90%)
S_{13}	398	3.12	0.0004	H-2->L+1 (69%), H-2->L+2 (24%)
S_{14}	385	3.22	0.0001	H-2->L+1 (25%), H-2->L+2 (68%)
S_{15}	379	3.27	0.0905	H-2->L+3 (90%)
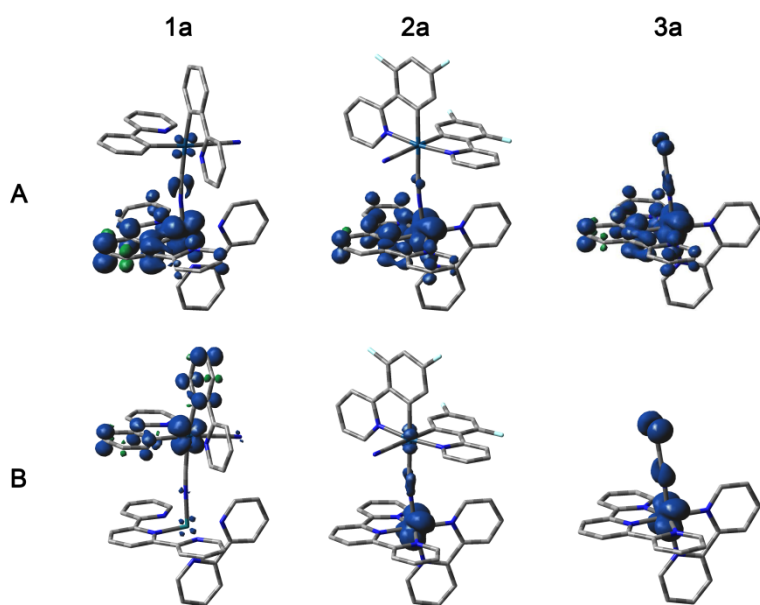
Figure S41. Spin-density distribution for **1a–3a** of the lowest triplet excited state (Panel A) and the one-electron oxidized state (Panel B) (isovalue = 0.004).
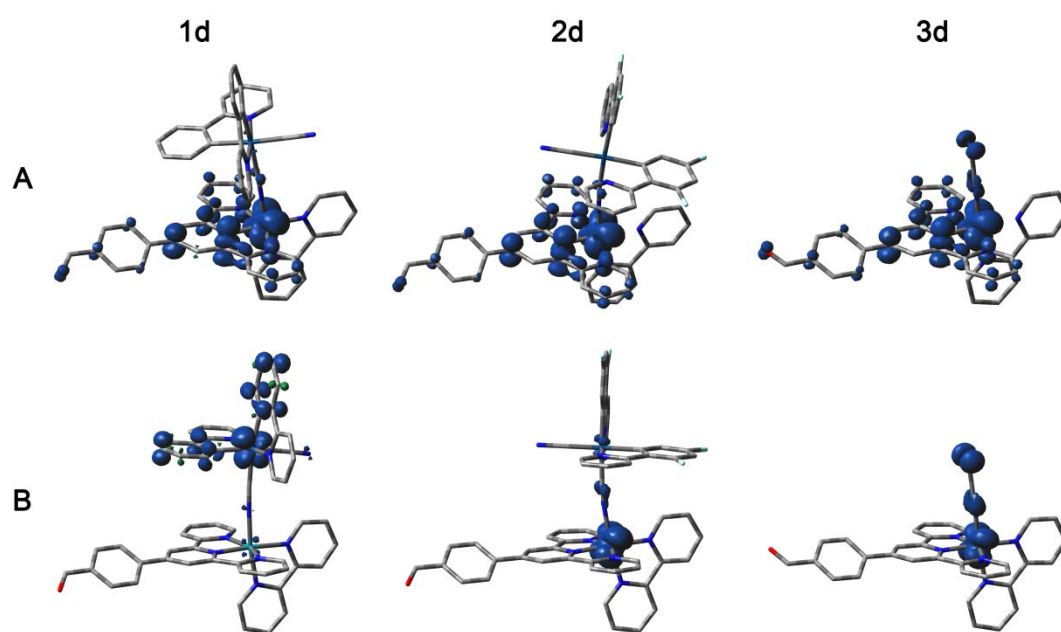
Figure S42. Spin-density distribution for **1d–3d** of the lowest triplet excited state (Panel A) and the one-electron oxidized state (Panel B) (isovalue = 0.004).
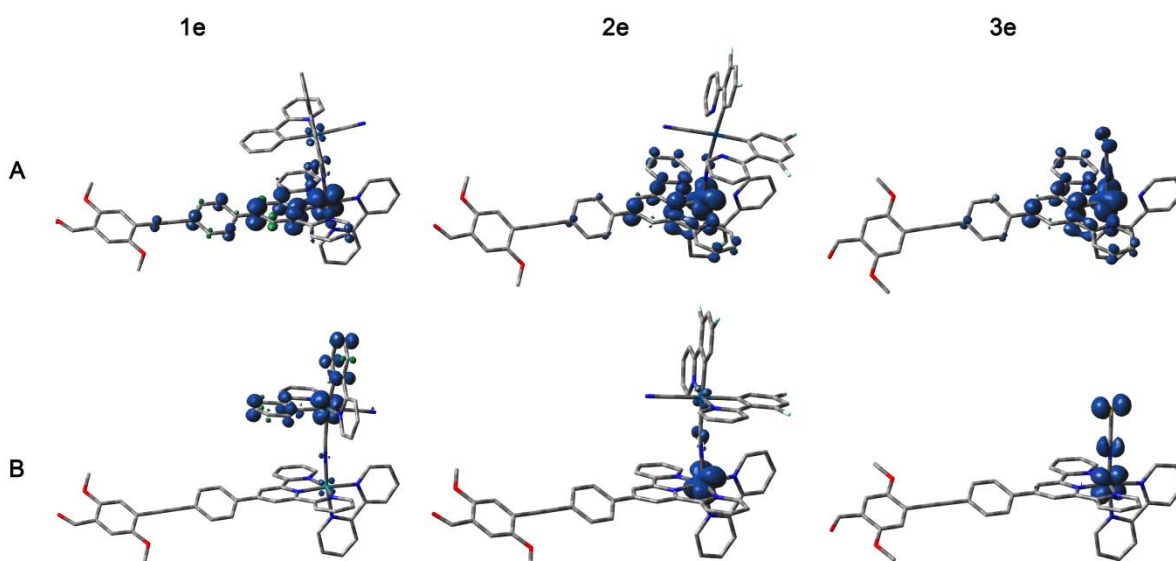
Figure S43. Spin-density distribution for **1e–3e** of the lowest triplet excited state (Panel A) and the one-electron oxidized state (Panel B) (isovalue = 0.004).
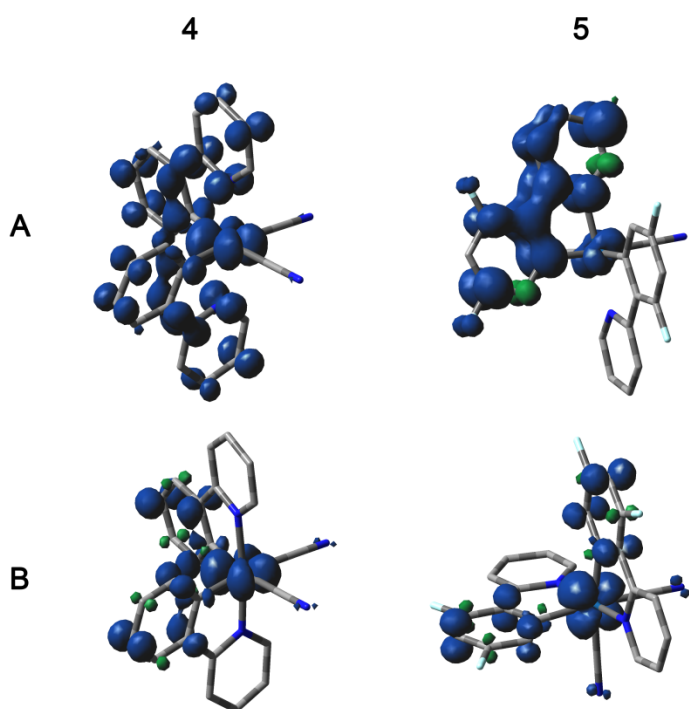
Figure S44. Spin-density distribution for **4** and **5** of the lowest triplet excited state (Panel A) and the one-electron oxidized state (Panel B) (isovalue = 0.004).
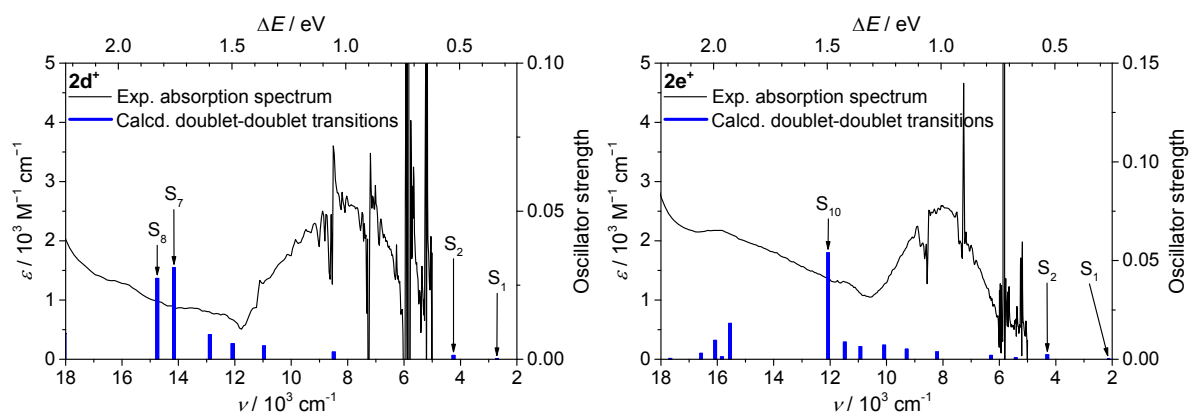
Figure S45. Experimental absorption spectra and B3LYP calculated doublet-doublet transitions energies of **2d⁺** (left) and **2e⁺** (right).

Table S15. B3LYP calculated electronic doublet-doublet transition energies ΔE with corresponding oscillator strengths f and contribution for **2a⁺**.

state	ν / cm^{-1}	ΔE / eV	f	major contribution
S$_1$	2763	0.34	0.0023	H-6(B)->LUMO(B) (33%), H-5(B)->LUMO(B) (16%), HOMO(B)->LUMO(B) (17%)
S$_2$	4205	0.52	0.0065	H-7(B)->LUMO(B) (62%), H-5(B)->LUMO(B) (12%)
S$_3$	6134	0.76	0.0519	H-6(B)->LUMO(B) (10%), HOMO(B)->LUMO(B) (74%)
S$_4$	8147	1.01	0.001	H-1(B)->LUMO(B) (93%)
S$_5$	9143	1.13	0.0019	H-4(B)->LUMO(B) (12%), H-3(B)->LUMO(B) (14%), H-2(B)->LUMO(B) (71%)
S$_6$	9834	1.22	0.0001	H-3(B)->LUMO(B) (69%), H-2(B)->LUMO(B) (18%)
S$_7$	11281	1.40	0.0202	H-4(B)->LUMO(B) (78%)
S$_8$	11965	1.48	0.0417	H-5(B)->LUMO(B) (66%)
S$_9$	15463	1.92	0.0035	H-11(B)->LUMO(B) (10%), H-9(B)->LUMO(B) (28%), H-8(B)->LUMO(B) (12%), H-6(B)->LUMO(B) (37%)
S$_{10}$	15788	1.96	0.0053	H-9(B)->LUMO(B) (34%), H-8(B)->LUMO(B) (46%)
S$_{11}$	16489	2.04	0.002	H-10(B)->LUMO(B) (88%), H-9(B)->LUMO(B) (10%)
S$_{12}$	17585	2.18	0.0136	H-11(B)->LUMO(B) (67%), H-8(B)->LUMO(B) (26%)
S$_{13}$	20232	2.51	0.0008	HOMO(B)->L+1(B) (98%)
S$_{14}$	20650	2.56	0.0002	HOMO(A)->LUMO(A) (98%)
S$_{15}$	20958	2.60	0.0065	H-13(B)->LUMO(B) (11%), H-12(B)->LUMO(B) (85%)

Table S16. B3LYP calculated electronic doublet-doublet transition energies ΔE with corresponding oscillator strengths *f* and contribution for **2d⁺**.

state	*v* / cm⁻¹	Δ*E* / eV	*f*	major contribution
S$_1$	2707	0.34	0.0001	H-14(B)->LUMO(B) (25%), H-6(B)->LUMO(B) (31%), H-5(B)->LUMO(B) (11%), HOMO(B)->LUMO(B) (14%)
S$_2$	4248	0.53	0.0013	H-13(B)->LUMO(B) (29%), H-9(B)->LUMO(B) (35%)
S$_3$	8496	1.05	0.0024	HOMO(B)->LUMO(B) (83%)
S$_4$	10965	1.36	0.0045	H-1(B)->LUMO(B) (93%)
S$_5$	12077	1.50	0.0052	H-4(B)->LUMO(B) (10%), H-2(B)->LUMO(B) (84%)
S$_6$	12882	1.60	0.0083	H-3(B)->LUMO(B) (84%)
S$_7$	14158	1.76	0.0309	H-5(B)->LUMO(B) (17%), H-4(B)->LUMO(B) (58%)
S$_8$	14753	1.83	0.0273	H-5(B)->LUMO(B) (58%), H-4(B)->LUMO(B) (25%)
S$_9$	18049	2.24	0.0087	H-13(B)->LUMO(B) (30%), H-9(B)->LUMO(B) (42%), H-8(B)->LUMO(B) (14%)
S$_{10}$	18382	2.28	0.0159	H-13(B)->LUMO(B) (24%), H-8(B)->LUMO(B) (54%)
S$_{11}$	18705	2.32	0.0023	H-12(B)->LUMO(B) (95%)
S$_{12}$	19851	2.46	0.0001	H-14(B)->LUMO(B) (13%), H-11(B)->LUMO(B) (40%), H-8(B)->LUMO(B) (11%), H-6(B)->LUMO(B) (25%)
S$_{13}$	20732	2.57	0.0003	H-14(B)->LUMO(B) (32%), H-11(B)->LUMO(B) (45%)
S$_{14}$	20821	2.58	0.0016	HOMO(A)->LUMO(A) (30%), HOMO(B)->L+1(B) (40%)
S$_{15}$	21075	2.61	0.0039	HOMO(A)->LUMO(A) (60%), HOMO(B)->L+1(B) (37%)

Table S17. B3LYP calculated electronic doublet-doublet transition energies ΔE with corresponding oscillator strengths *f* and contribution for **2e⁺**.

state	*v* / cm⁻¹	Δ*E* / eV	*f*	major contribution
S$_1$	2126	0.26	1E-4	H-10(B)->LUMO(B) (11%), H-9(B)->LUMO(B) (22%), H-1(B)->LUMO(B) (25%)
S$_2$	4300	0.53	0.0022	H-15(B)->LUMO(B) (11%), H-12(B)->LUMO(B) (25%), H-10(B)->LUMO(B) (30%), H-9(B)->LUMO(B) (11%)
S$_3$	5421	0.67	0.0007	H-1(B)->LUMO(B) (29%), HOMO(B)->LUMO(B) (68%)
S$_4$	6295	0.78	0.0019	H-9(B)->LUMO(B) (11%), H-1(B)->LUMO(B) (43%), HOMO(B)->LUMO(B) (25%)
S$_5$	8207	1.02	0.0037	H-2(B)->LUMO(B) (94%)
S$_6$	9284	1.15	0.0051	H-5(B)->LUMO(B) (10%), H-4(B)->LUMO(B) (82%)
S$_7$	10085	1.25	0.0071	H-5(B)->LUMO(B) (82%), H-4(B)->LUMO(B) (11%)
S$_8$	10928	1.35	0.0064	H-3(B)->LUMO(B) (74%)
S$_9$	11481	1.42	0.0087	H-6(B)->LUMO(B) (75%)
S$_{10}$	12074	1.50	0.0539	H-10(B)->LUMO(B) (12%), H-7(B)->LUMO(B) (70%)
S$_{11}$	15052	1.87	0	H-8(B)->LUMO(B) (100%)
S$_{12}$	15550	1.93	0.0181	H-12(B)->LUMO(B) (39%), H-9(B)->LUMO(B) (35%)
S$_{13}$	15839	1.96	0.0012	HOMO(A)->LUMO(A) (25%), HOMO(A)->L+3(A) (14%), HOMO(B)->L+1(B) (24%), HOMO(B)->L+4(B) (15%)
S$_{14}$	16079	1.99	0.0096	H-15(B)->LUMO(B) (39%), H-14(B)->LUMO(B) (30%), H-10(B)->LUMO(B) (11%)
S$_{15}$	16575	2.06	0.003	H-15(B)->LUMO(B) (38%), H-14(B)->LUMO(B) (60%)

12. NMR spectra
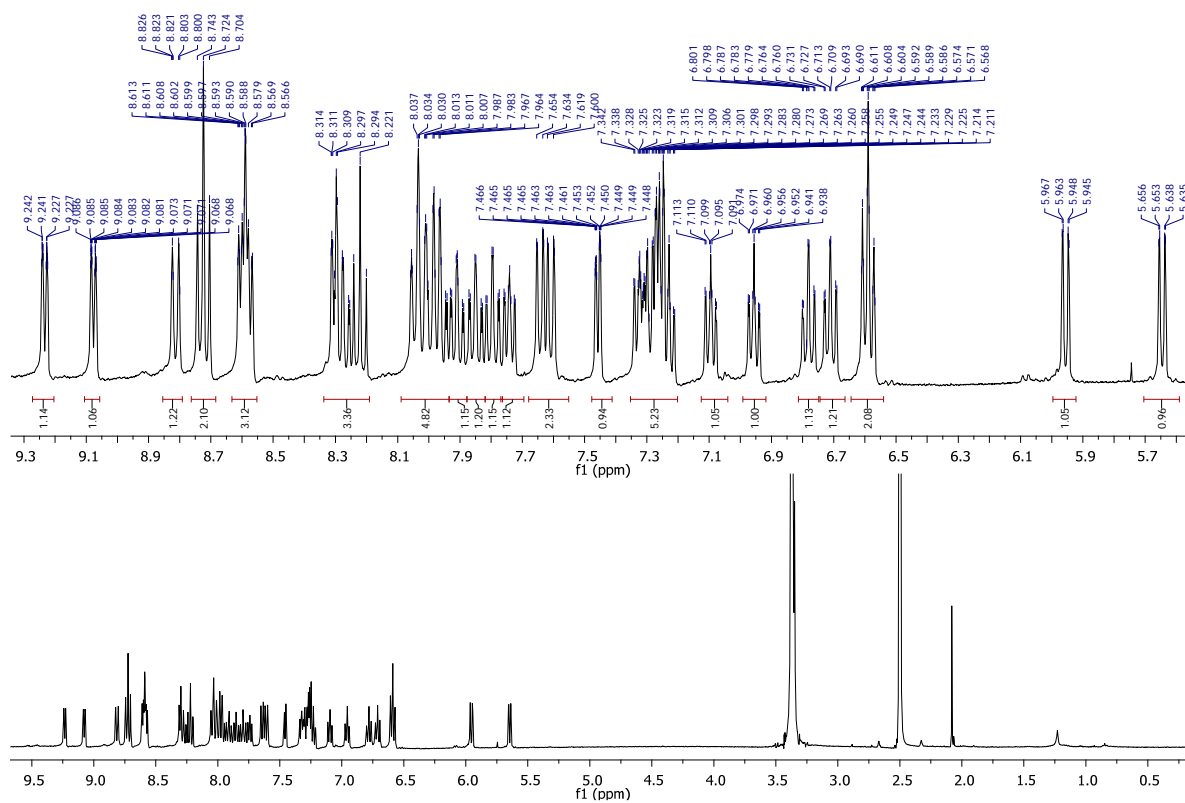
Figure S46. ^{1}H NMR (400 MHz, DMSO-d_6) spectrum of **1a**.
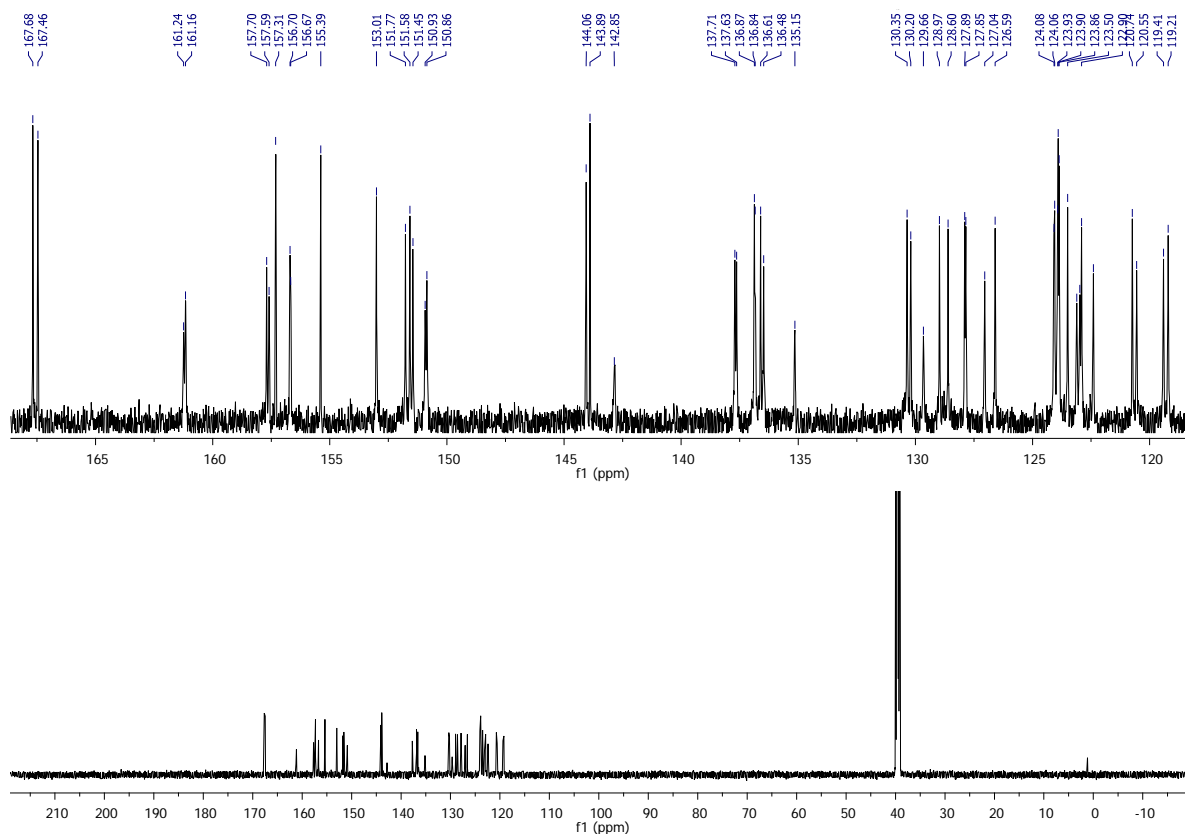
Figure S47. ^{13}C-{^{1}H} NMR (150 MHz, DMSO-d_6) spectrum of **1a**.
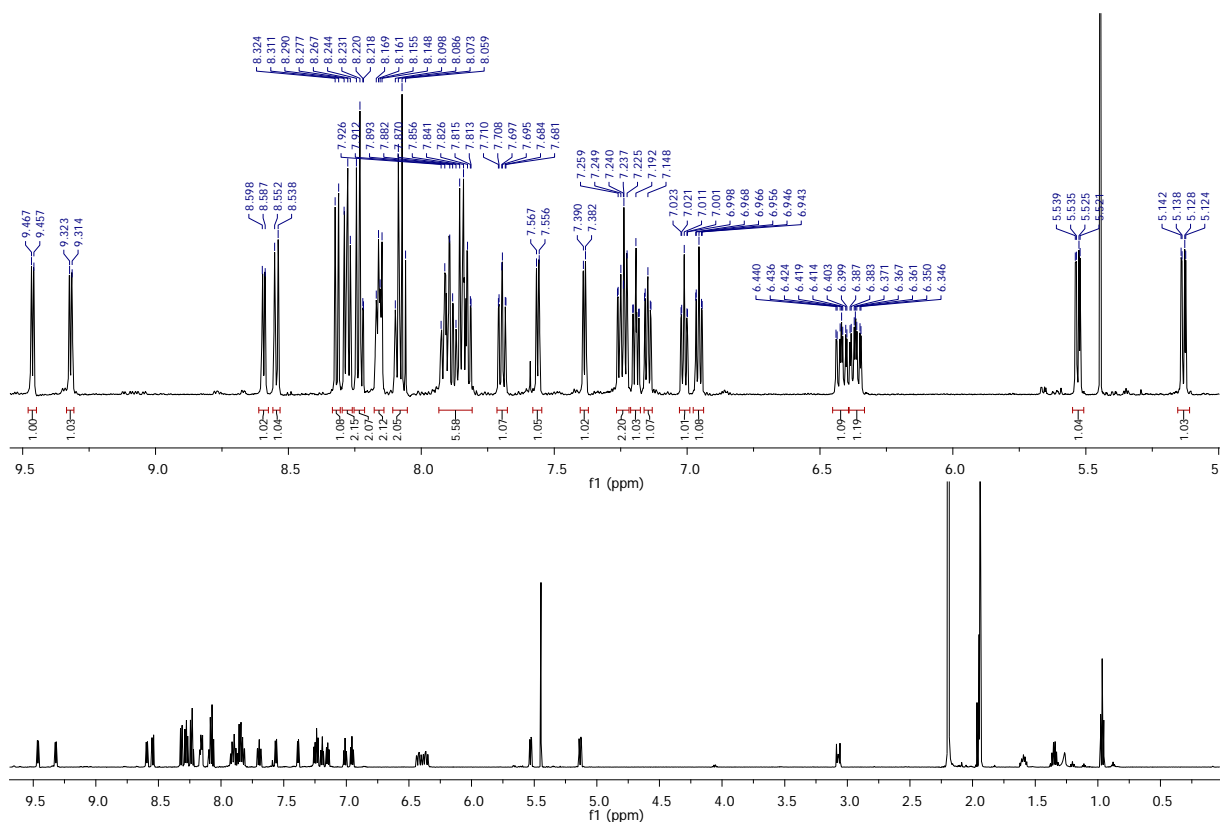
Figure S48. ^{1}H NMR (600 MHz, CD$_3$CN) spectrum of **2a**.
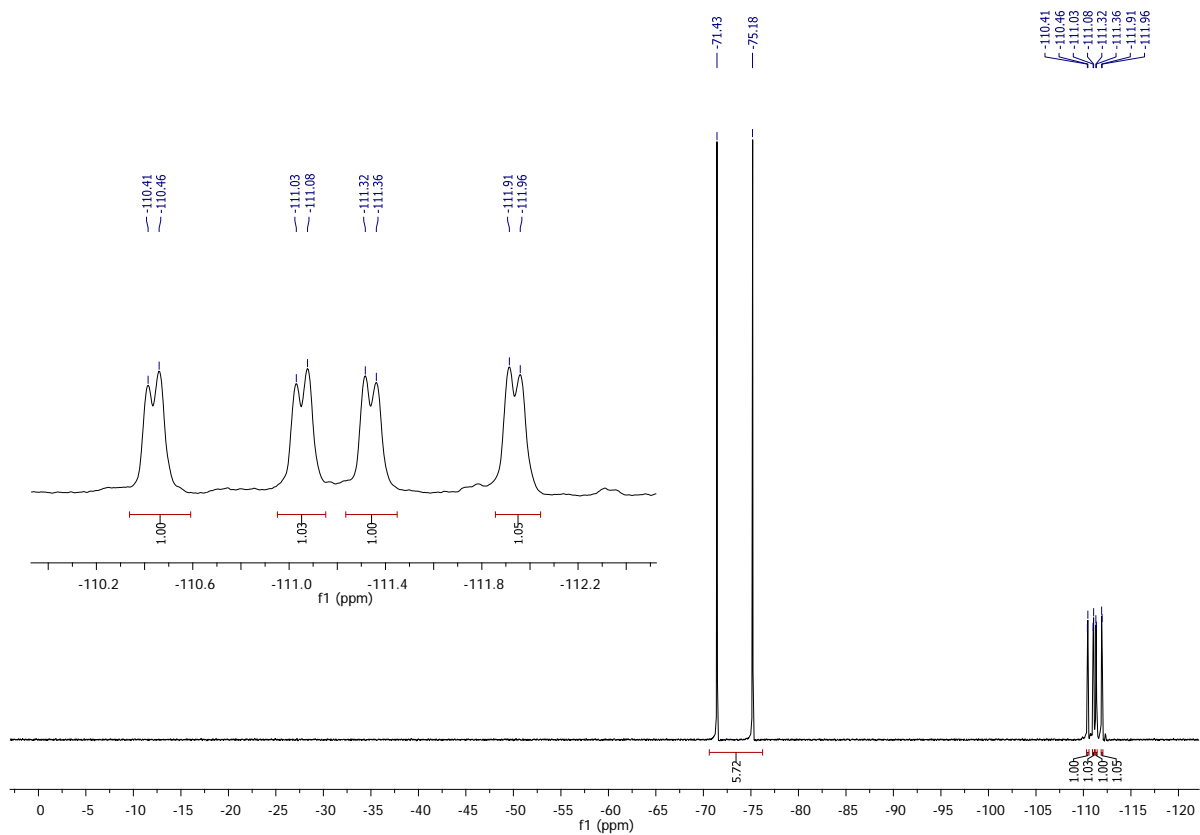
Figure S49. ^{19}F-{^{1}H} NMR (188 MHz, CD$_3$CN) spectrum of **2a**.
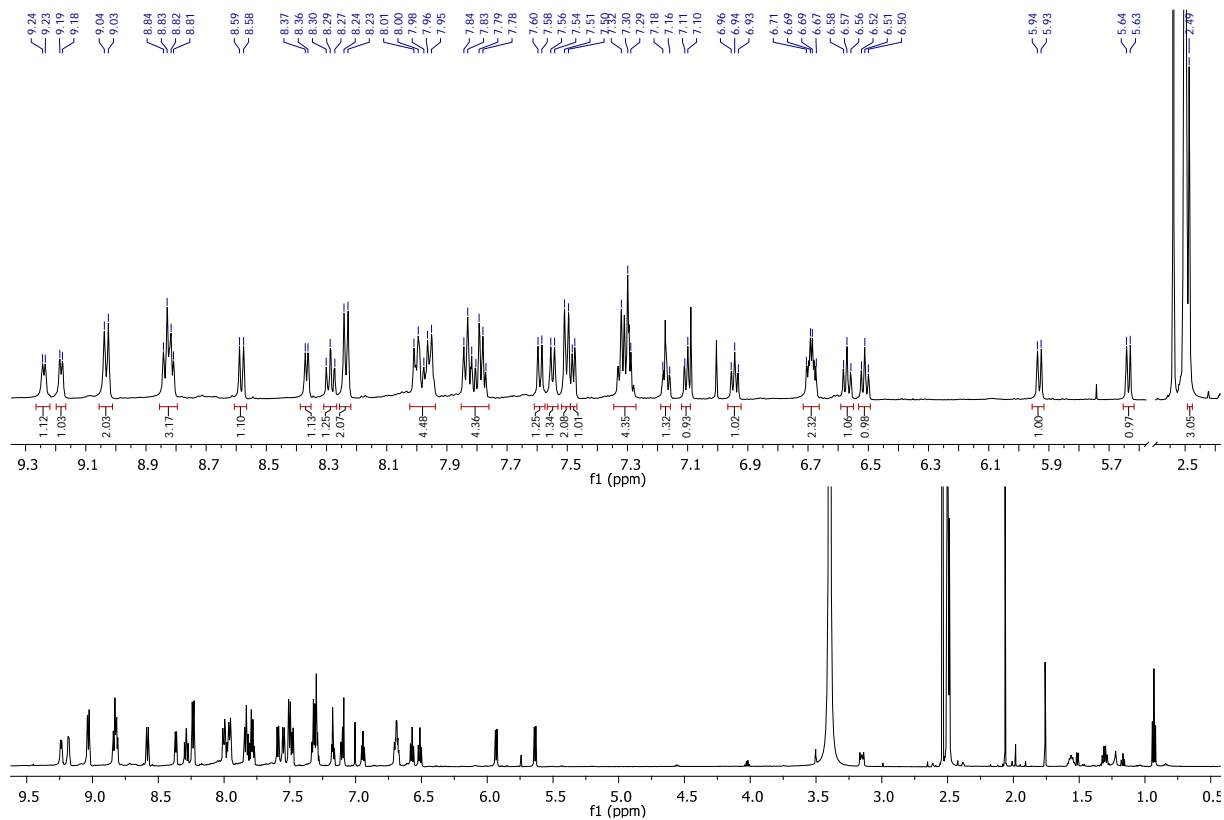
Figure S50. ^{1}H NMR (600 MHz, DMSO-d_6) spectrum of **1b**.
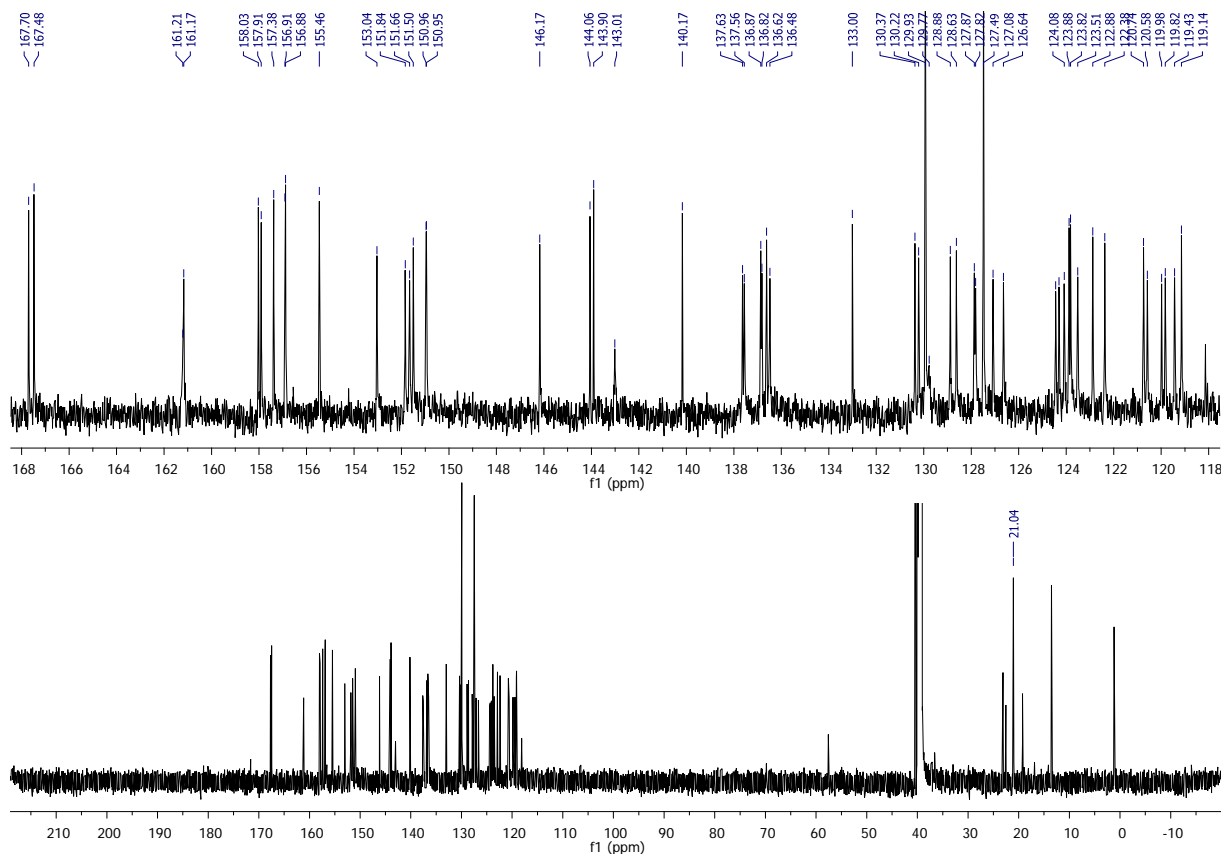
Figure S51. ^{13}C-{^{1}H} NMR (150 MHz, DMSO-d_6) spectrum of **1b**.
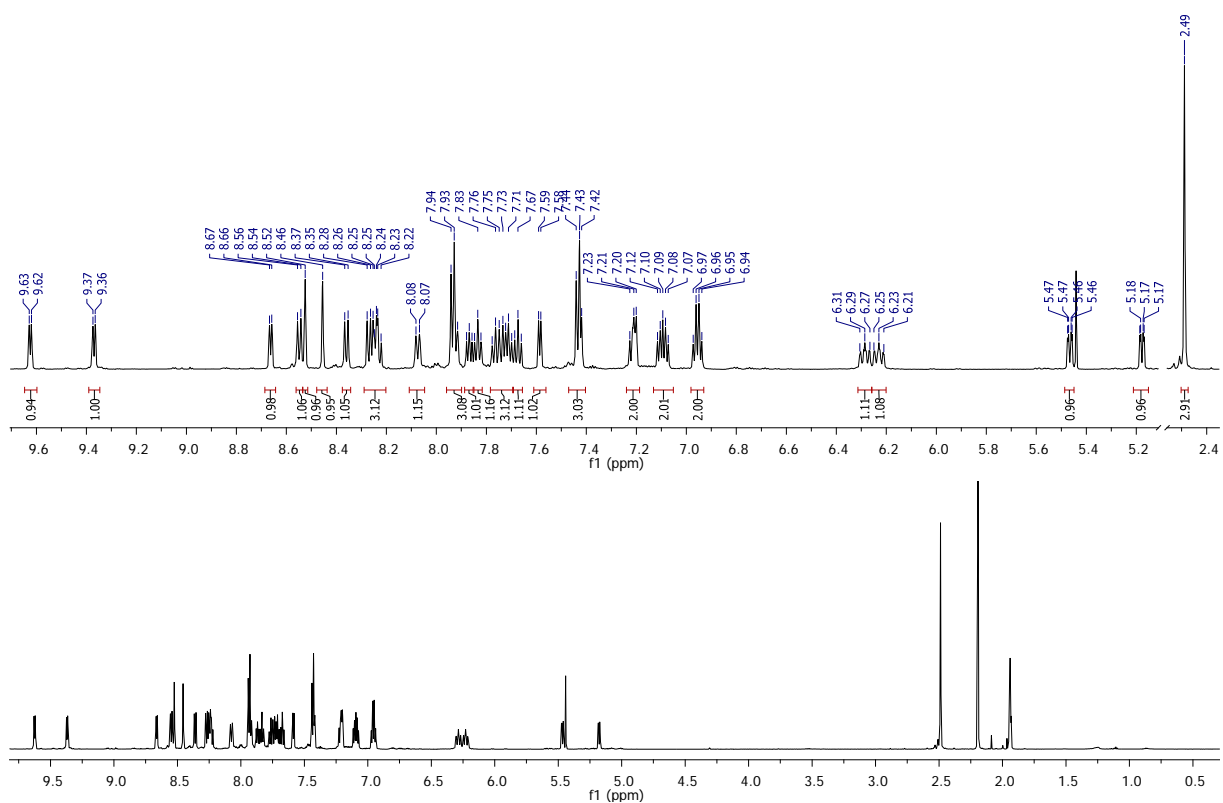
Figure S52. ^{1}H NMR (600 MHz, CD$_3$CN) spectrum of **2b**.
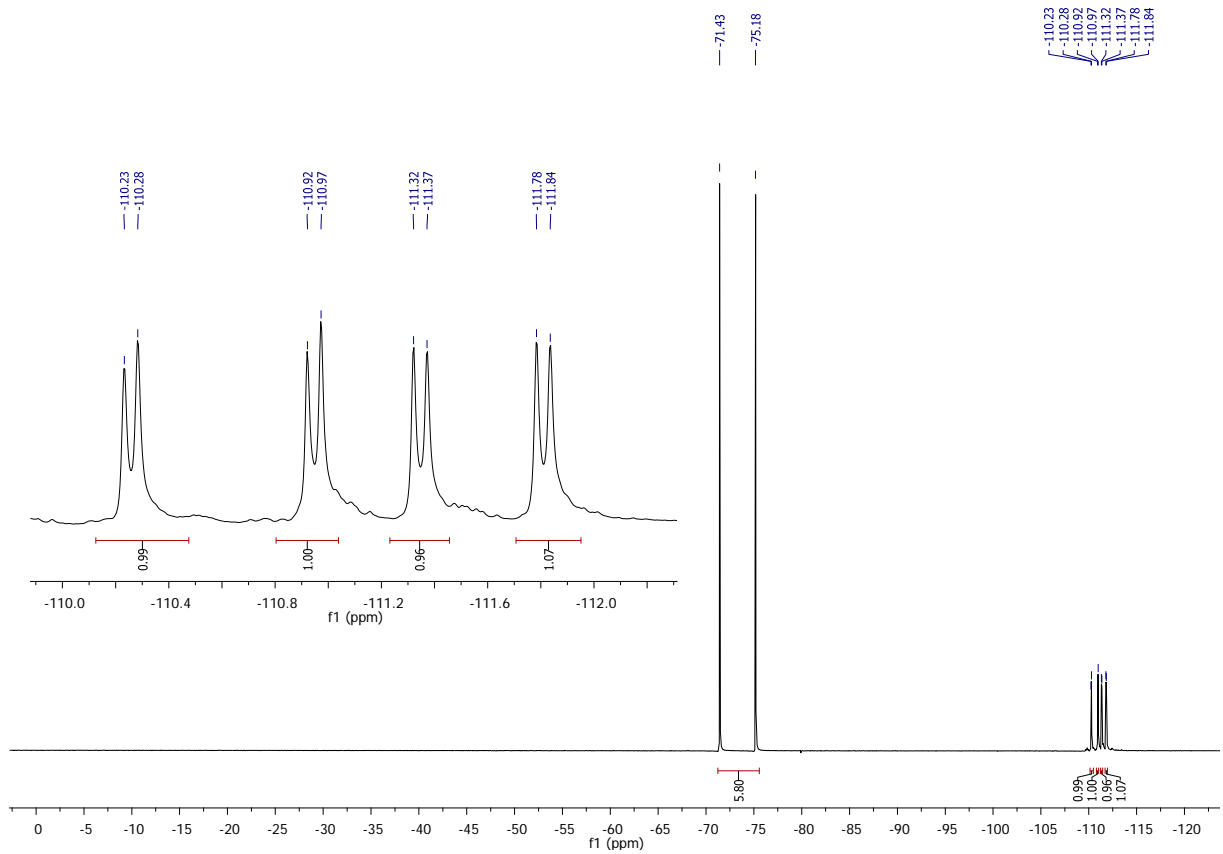
Figure S53. ^{19}F-{^{1}H} NMR (188 MHz, CD$_3$CN) spectrum of **2b**.
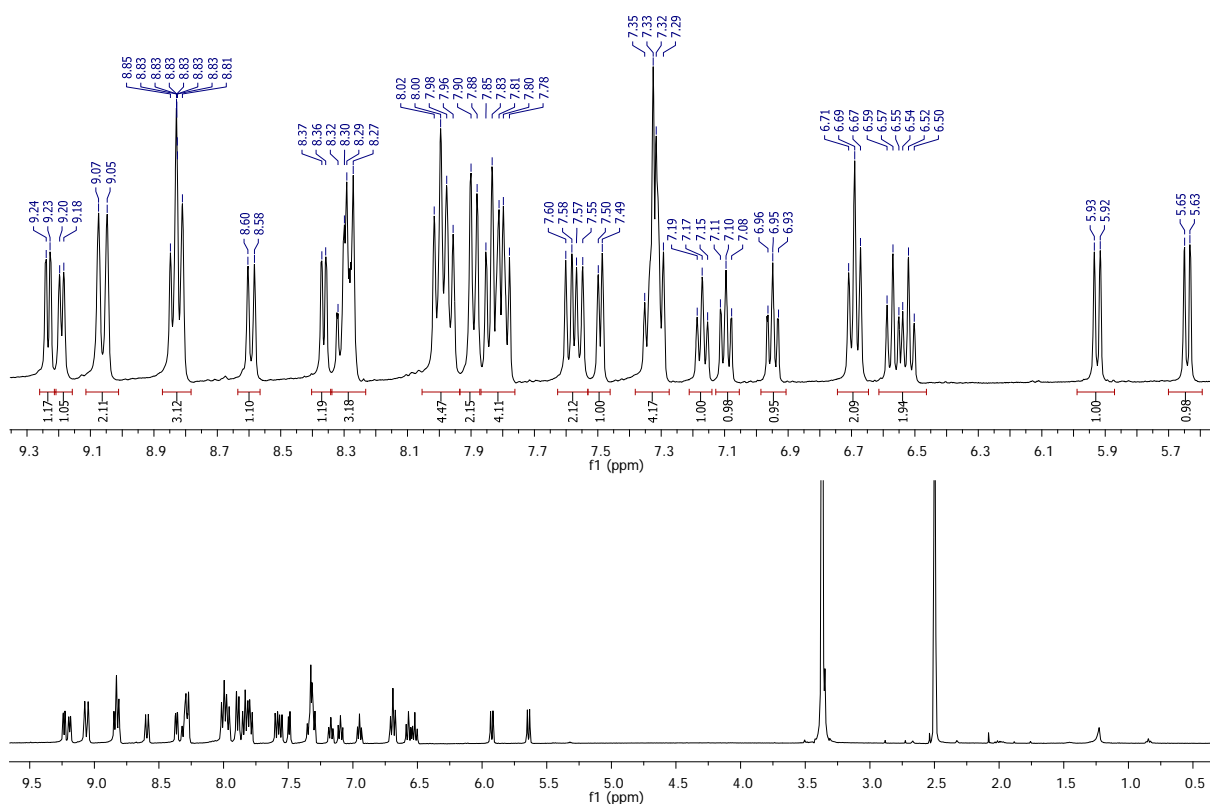
Figure S54. ^{1}H NMR (400 MHz, DMSO-d_6) spectrum of **1c**.
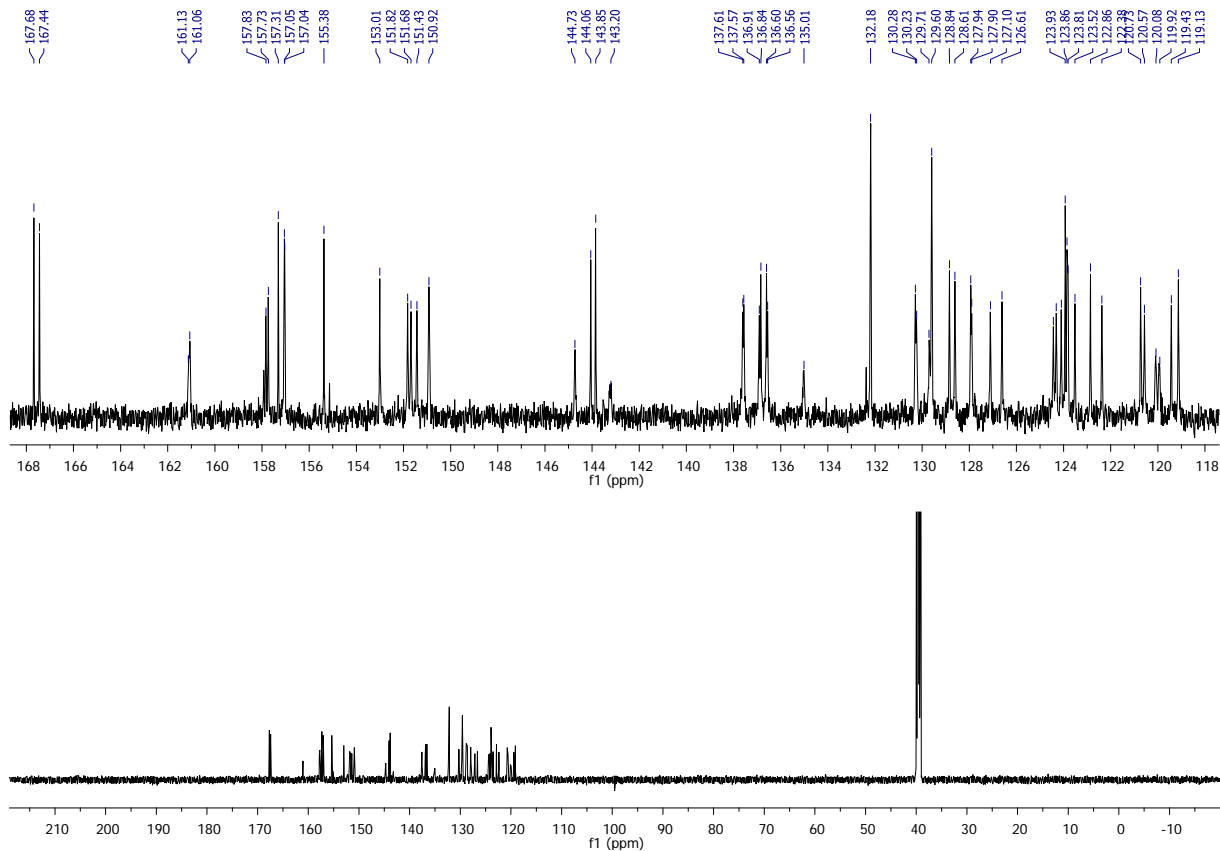
Figure S55. ^{13}C-{^{1}H} NMR (150 MHz, DMSO-d_6) spectrum of **1c**.
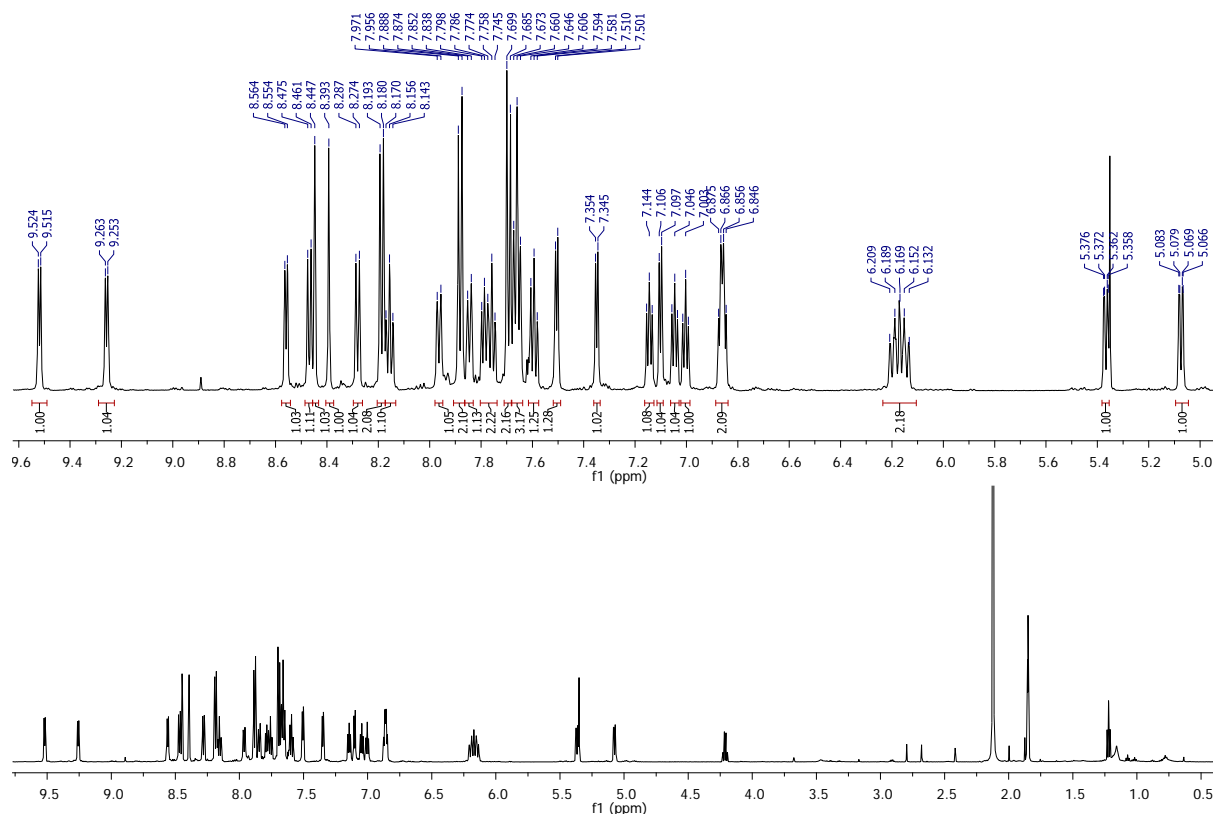
Figure S56. ^{1}H NMR (600 MHz, CD$_3$CN) spectrum of **2c**.
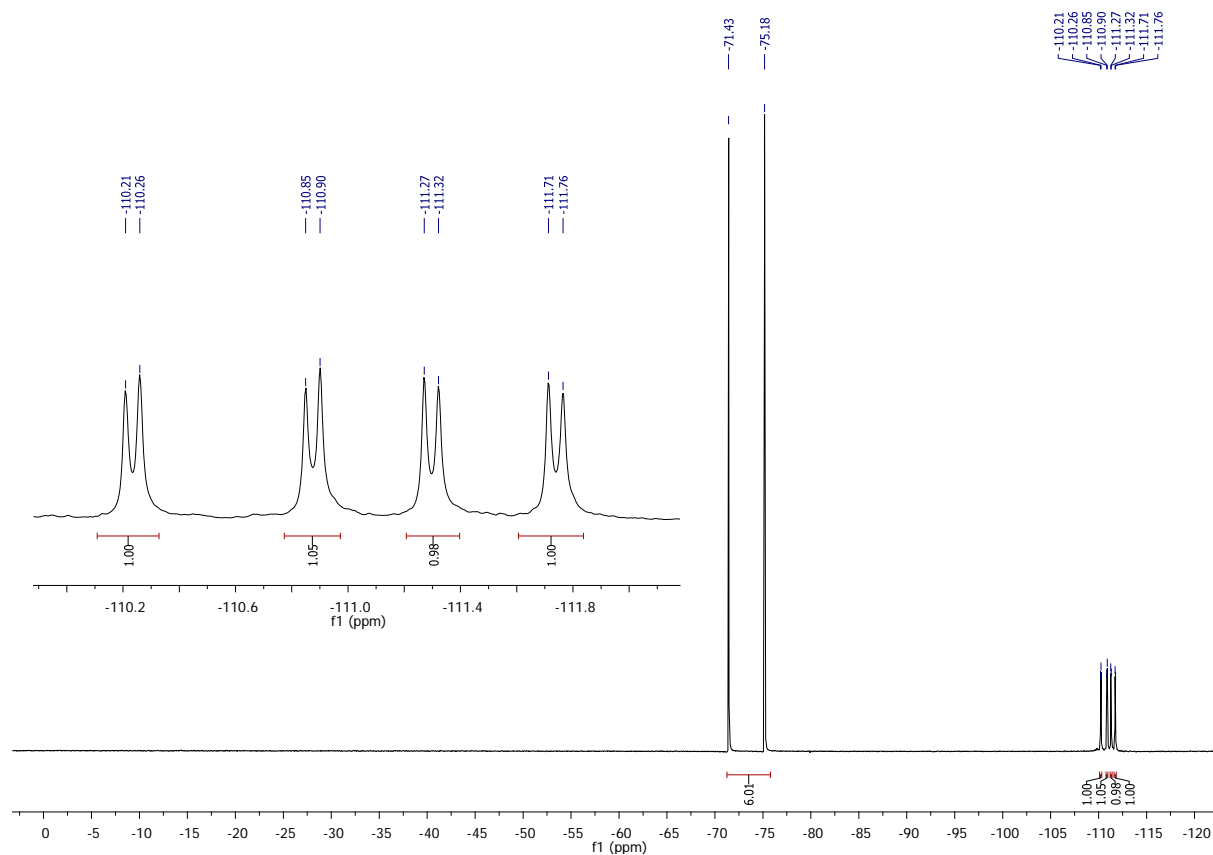
Figure S57. ^{19}F-{^{1}H} NMR (188 MHz, CD$_3$CN) spectrum of **2c**.
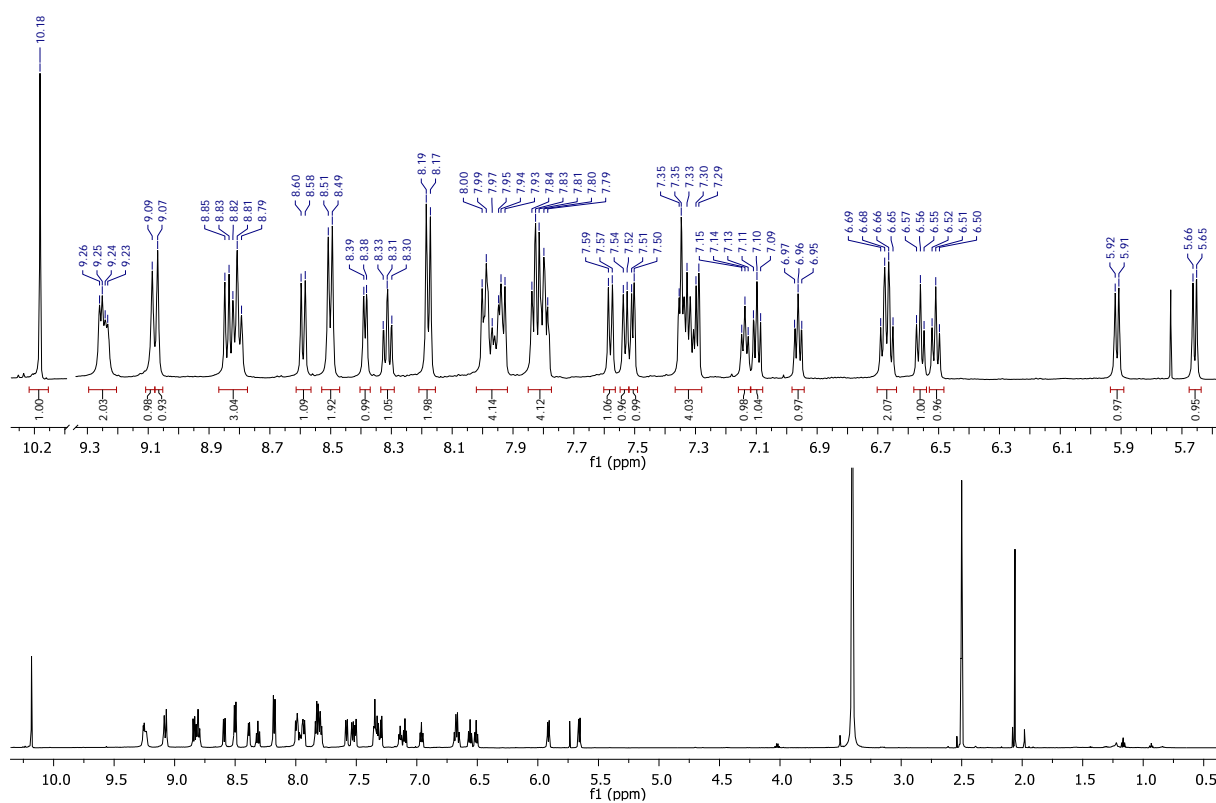
Figure S58. ^{1}H NMR (600 MHz, DMSO-d_6) spectrum of **1d**.
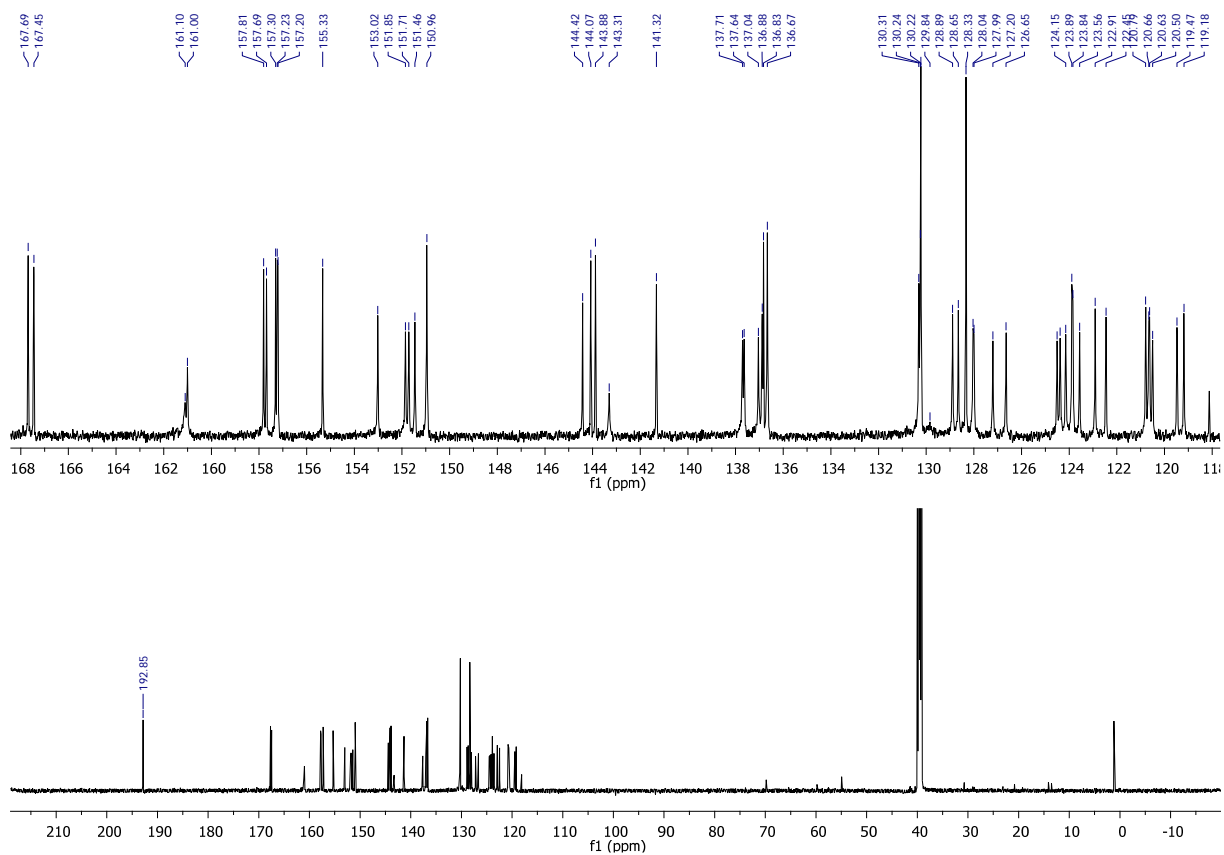
Figure S59. ^{13}C-{^{1}H} NMR (150 MHz, DMSO-d_6) spectrum of **1d**.
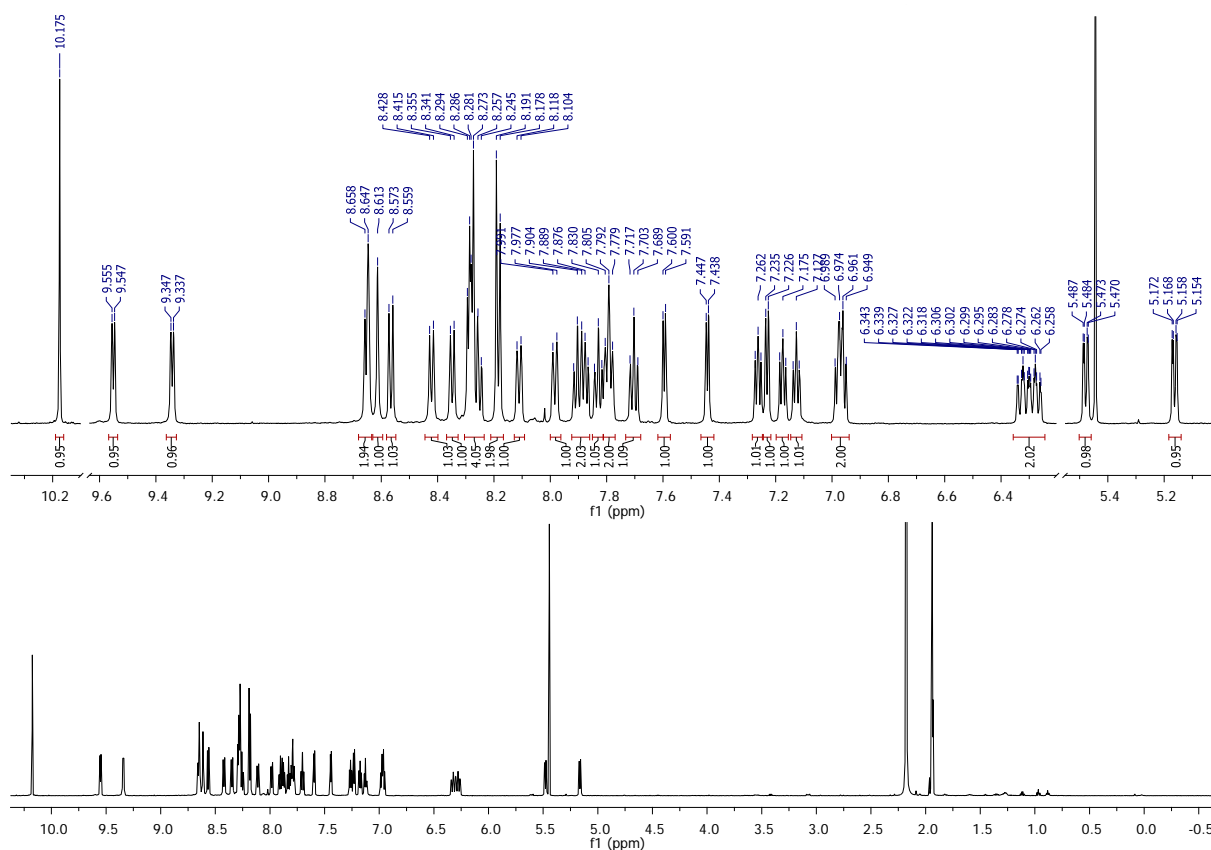
Figure S60. ^{1}H NMR (600 MHz, CD$_3$CN) spectrum of **2d**.
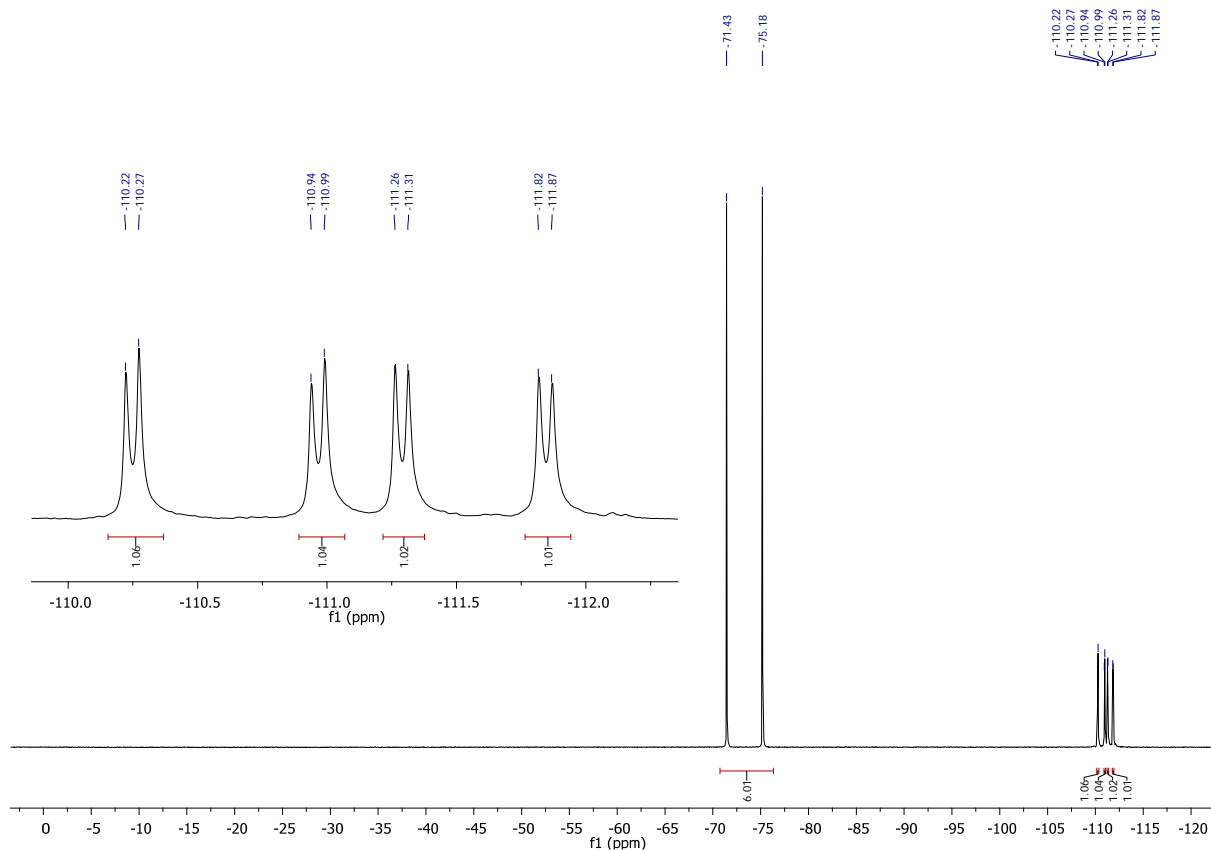
Figure S61. ^{19}F-{^{1}H} NMR (188 MHz, CD$_3$CN) spectrum of **2d**.
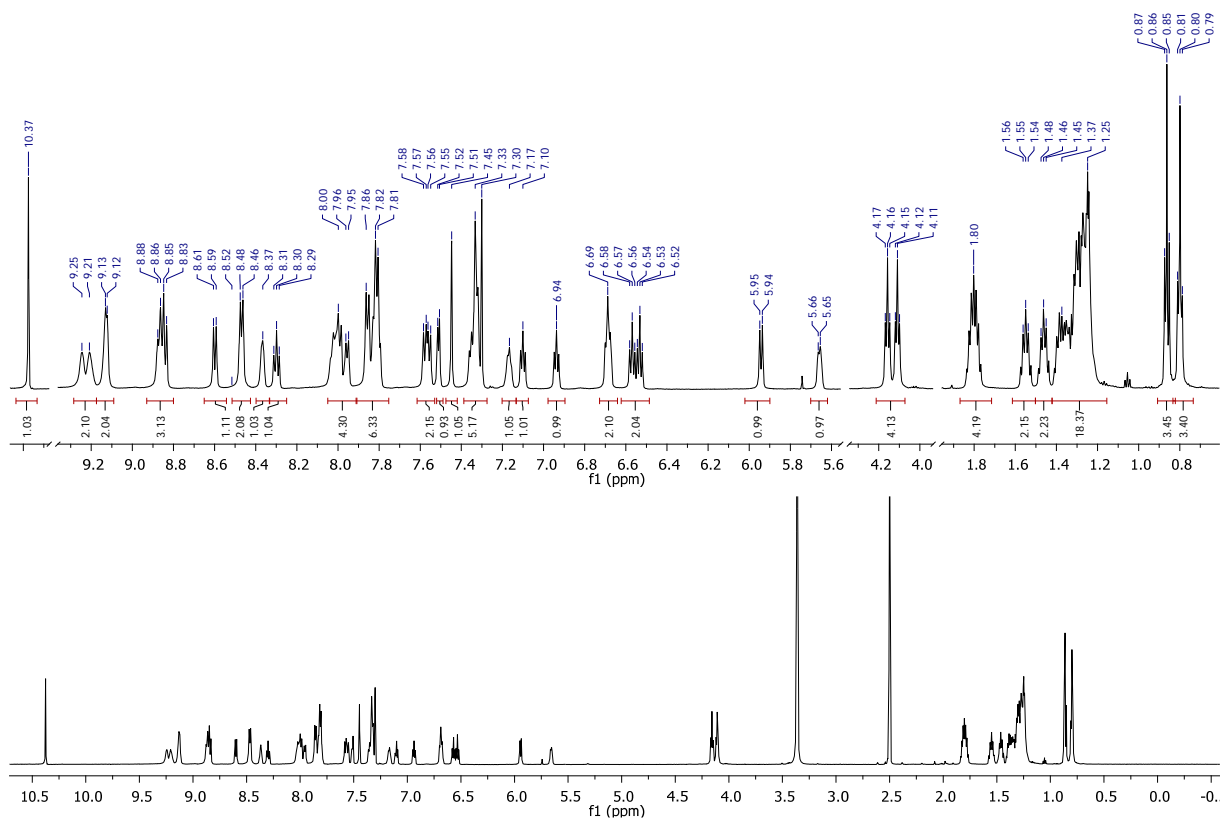
Figure S62. ^{1}H NMR (600 MHz, DMSO-d_6) spectrum of **1e**.
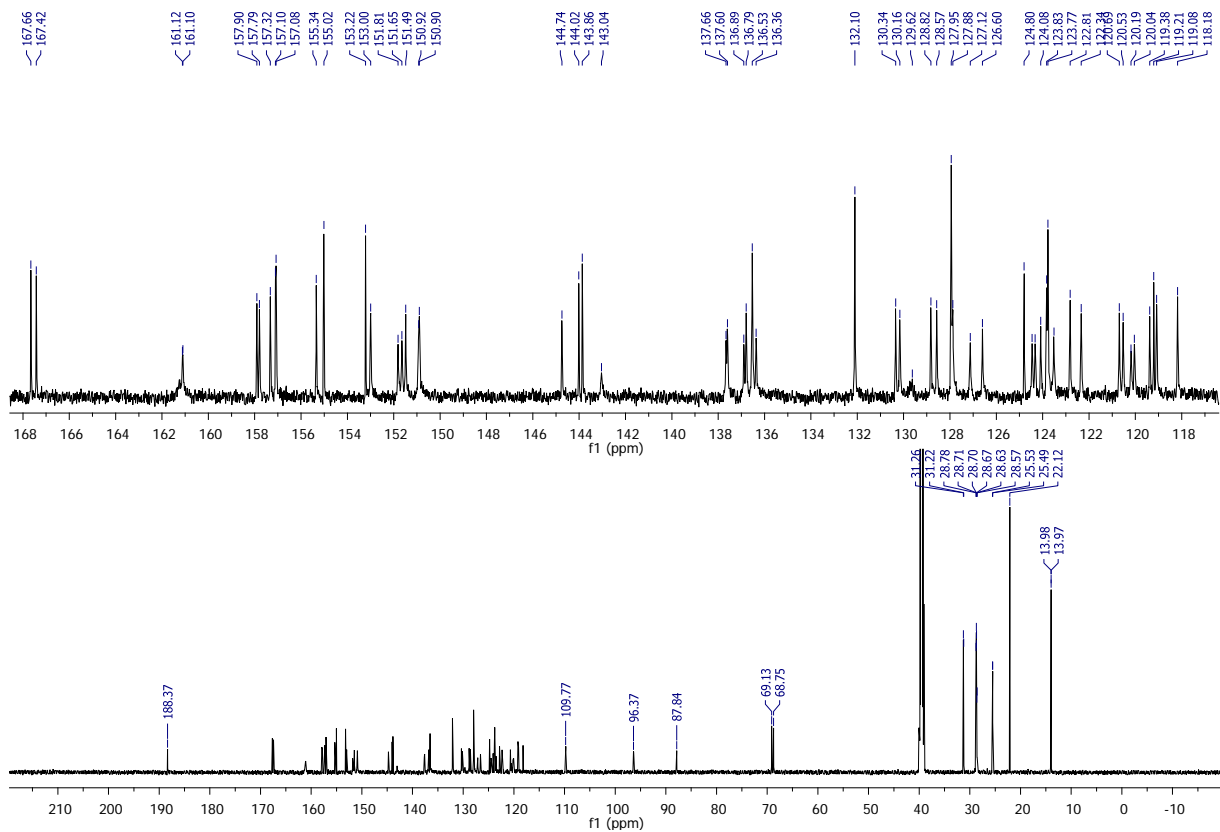
Figure S63. ^{13}C-{^{1}H} NMR (150 MHz, DMSO-d_6) spectrum of **1e**.
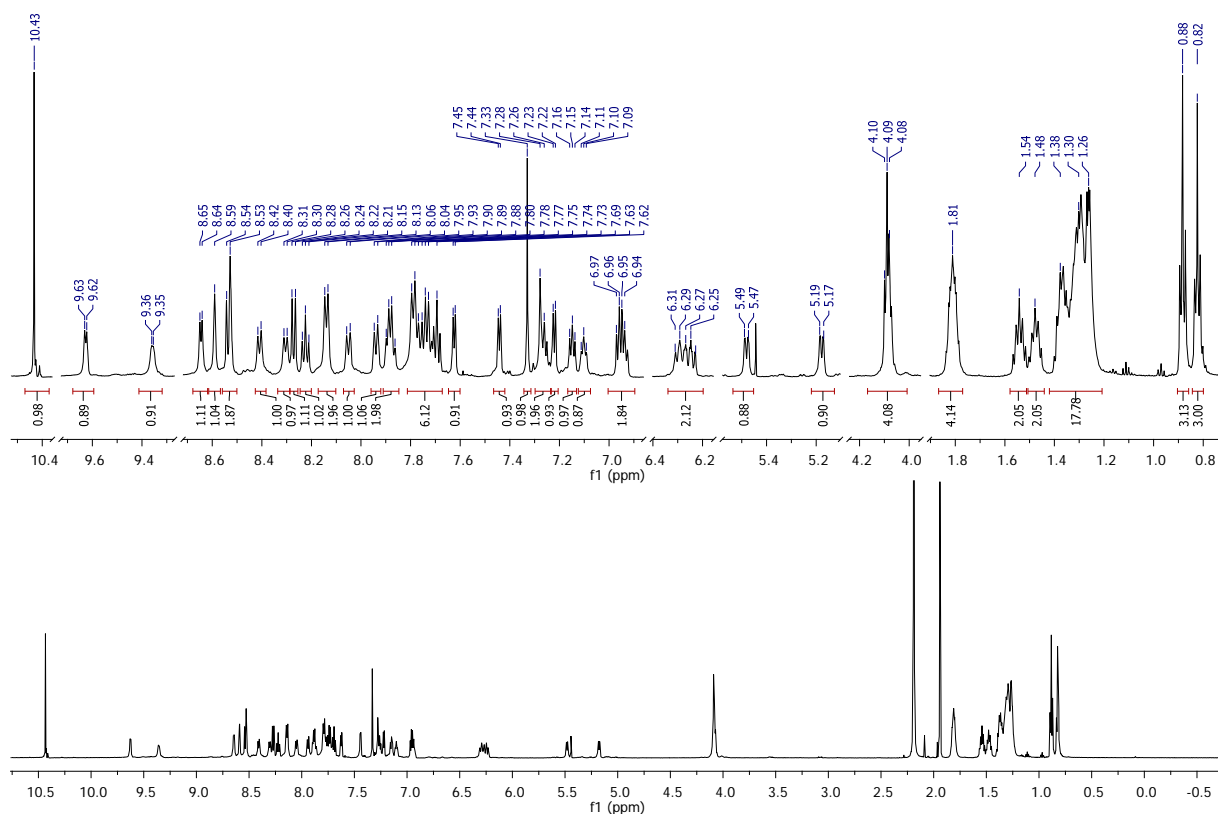
Figure S64. ^{1}H NMR (600 MHz, CD$_3$CN) spectrum of **2e**.
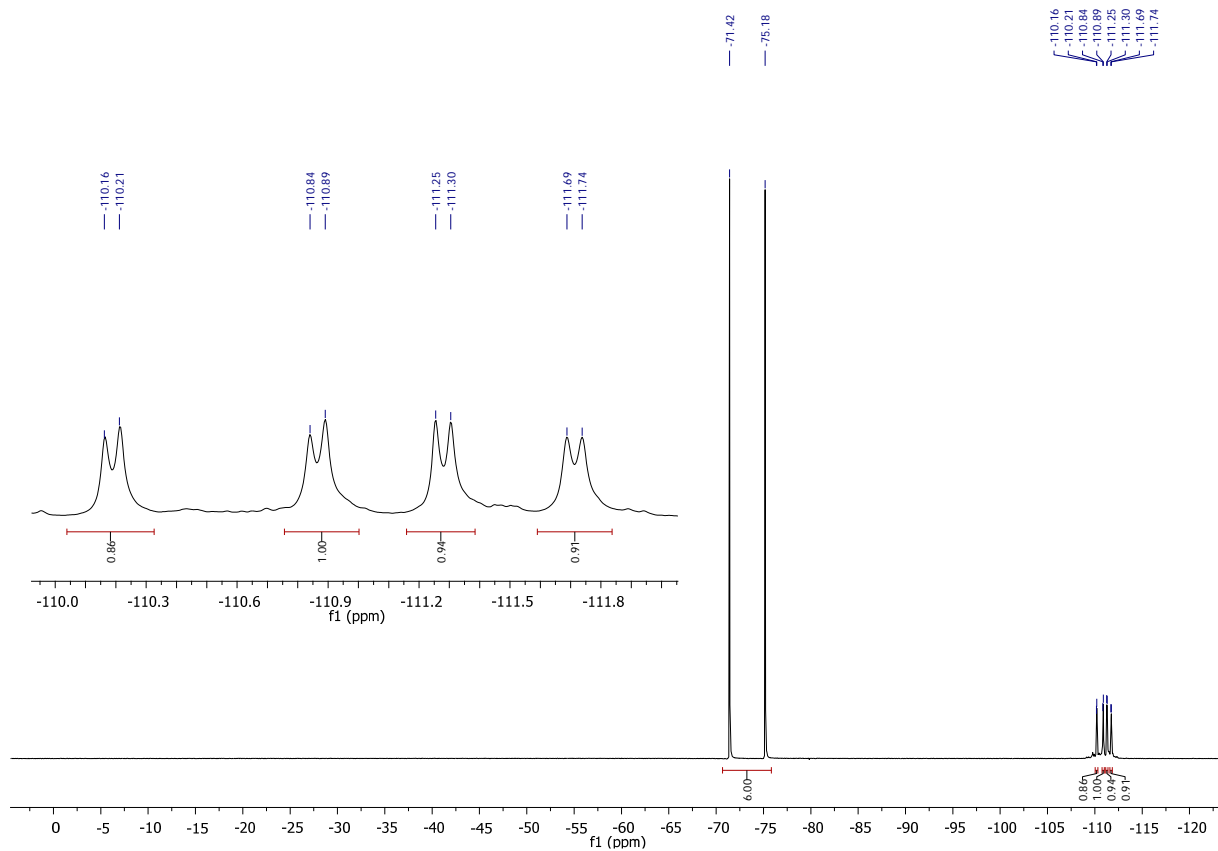
Figure S65. ^{19}F-{^{1}H} NMR (188 MHz, CD$_3$CN) spectrum of **2e**.
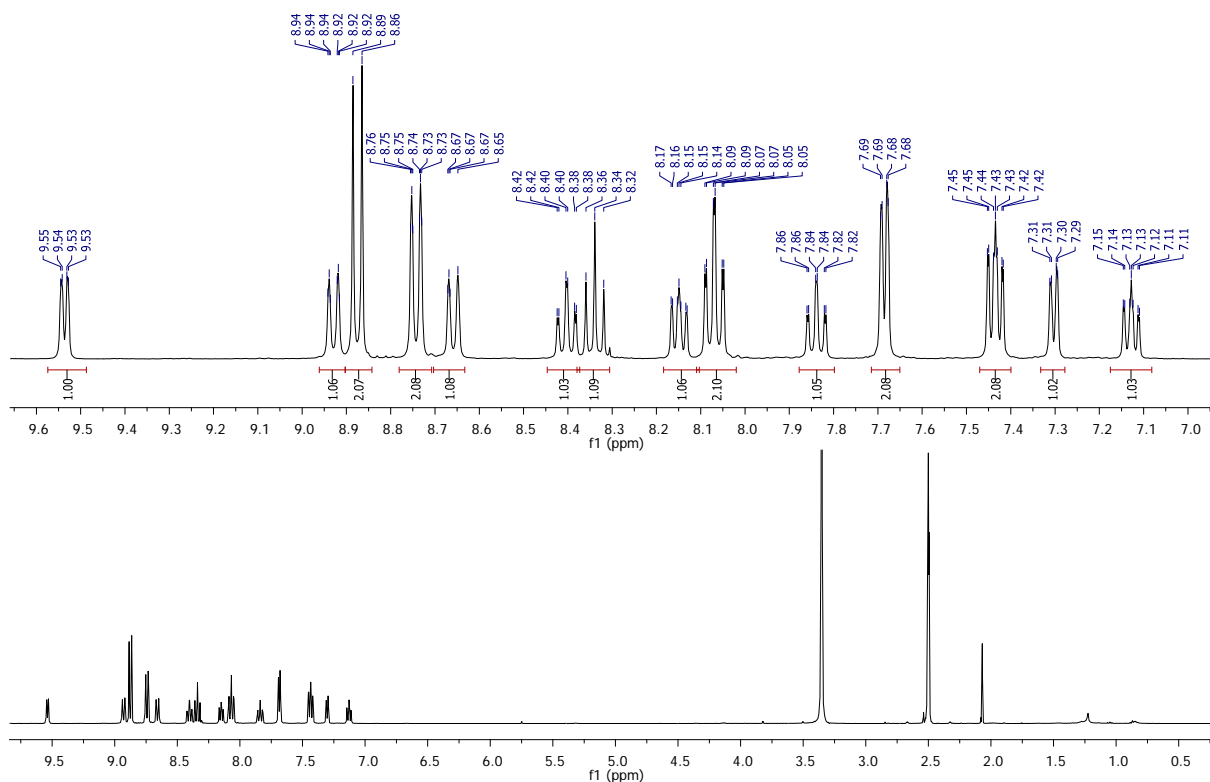
Figure S66. ^{1}H NMR (400 MHz, DMSO-d_6) spectrum of **3a**.
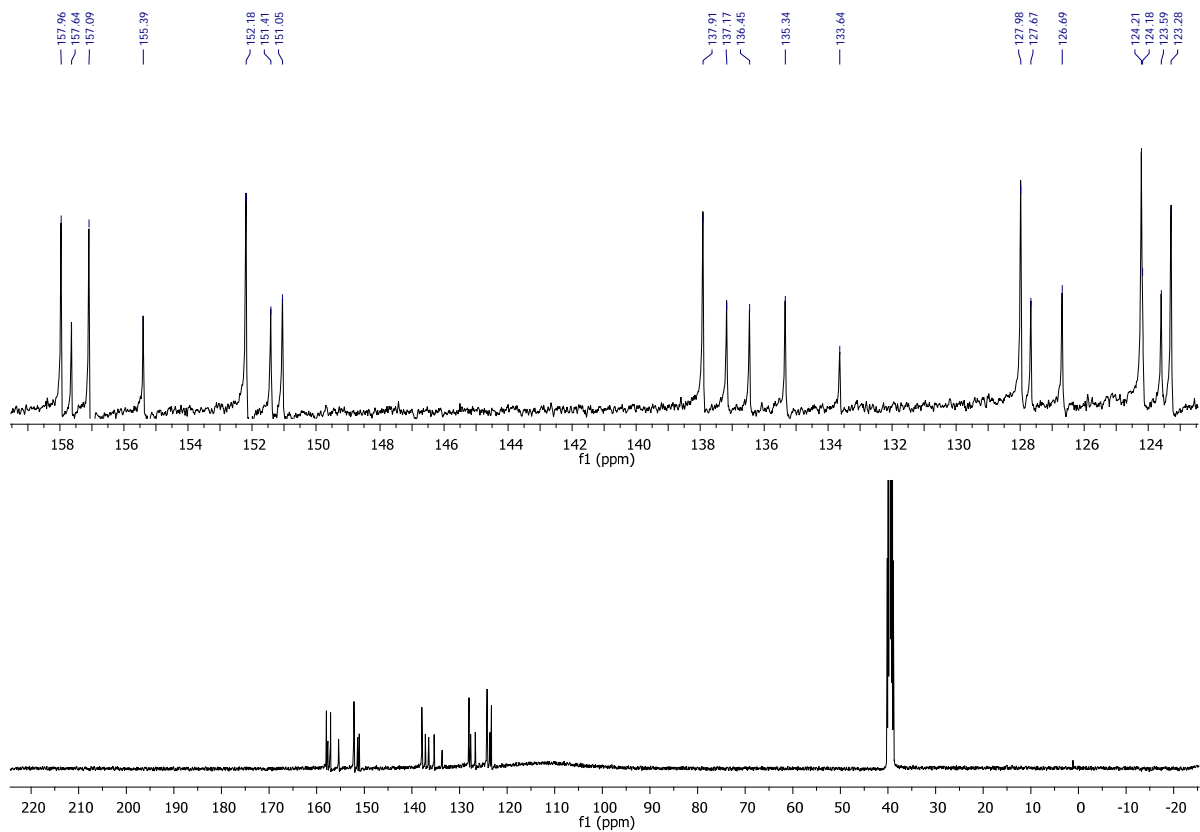
Figure S67. ^{13}C-{^{1}H} NMR (100 MHz, DMSO-d_6) spectrum of **3a**.
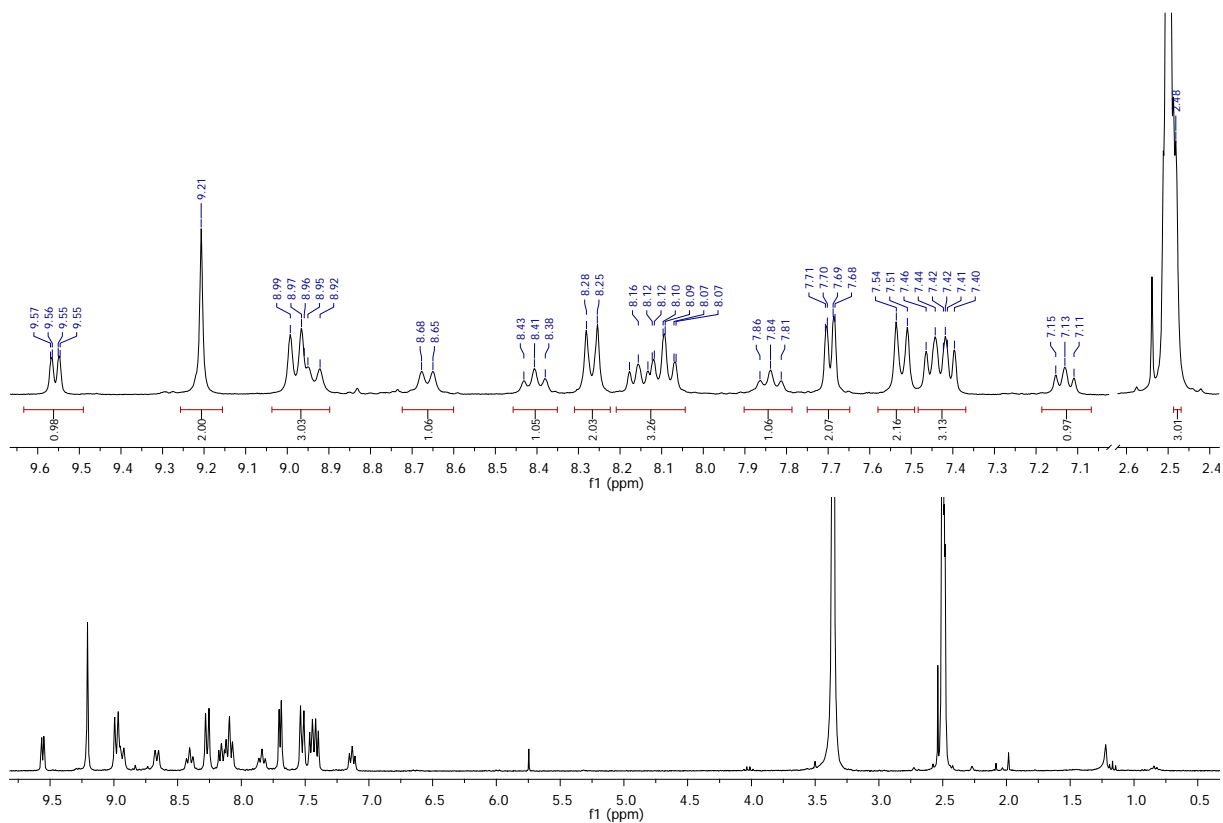
Figure S68. ^{1}H NMR (300 MHz, DMSO-d_6) spectrum of **3b**.
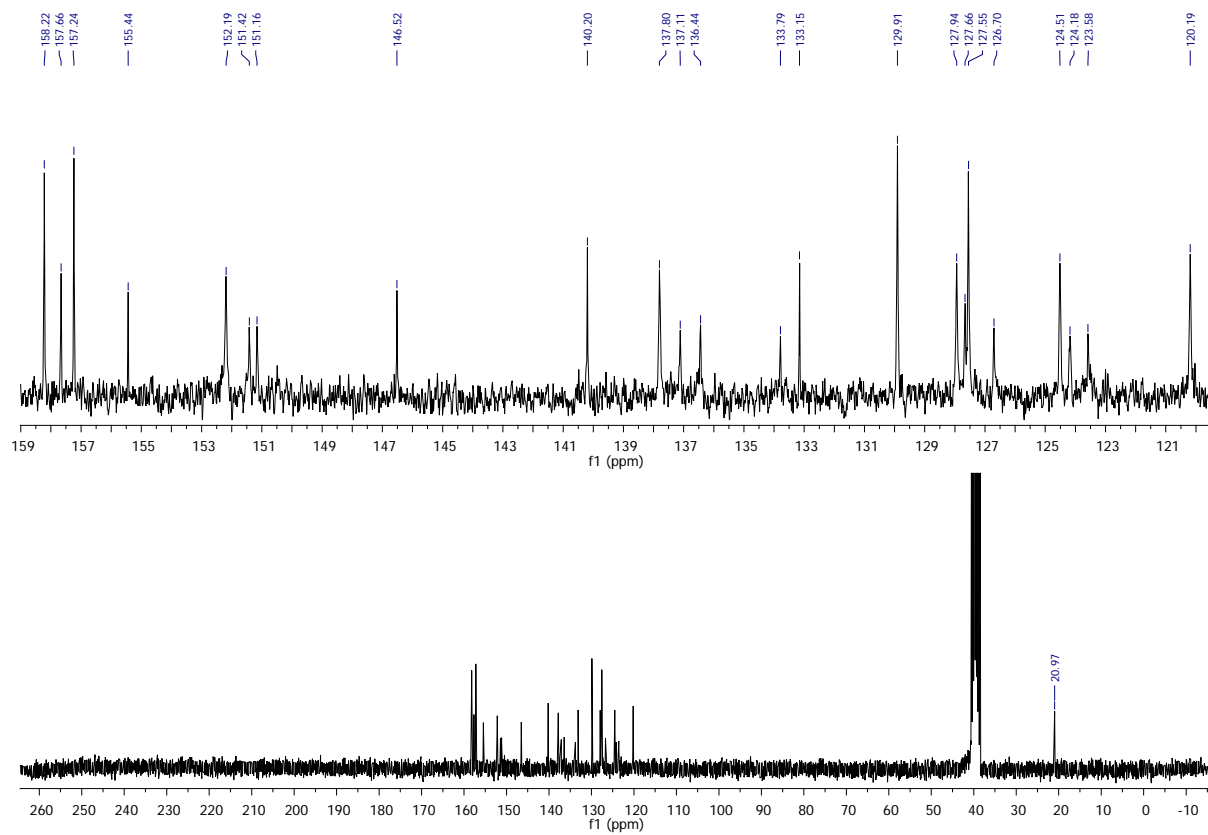
Figure S69. ^{13}C-{^{1}H} NMR (63 MHz, DMSO-d_6) spectrum of **3b**.
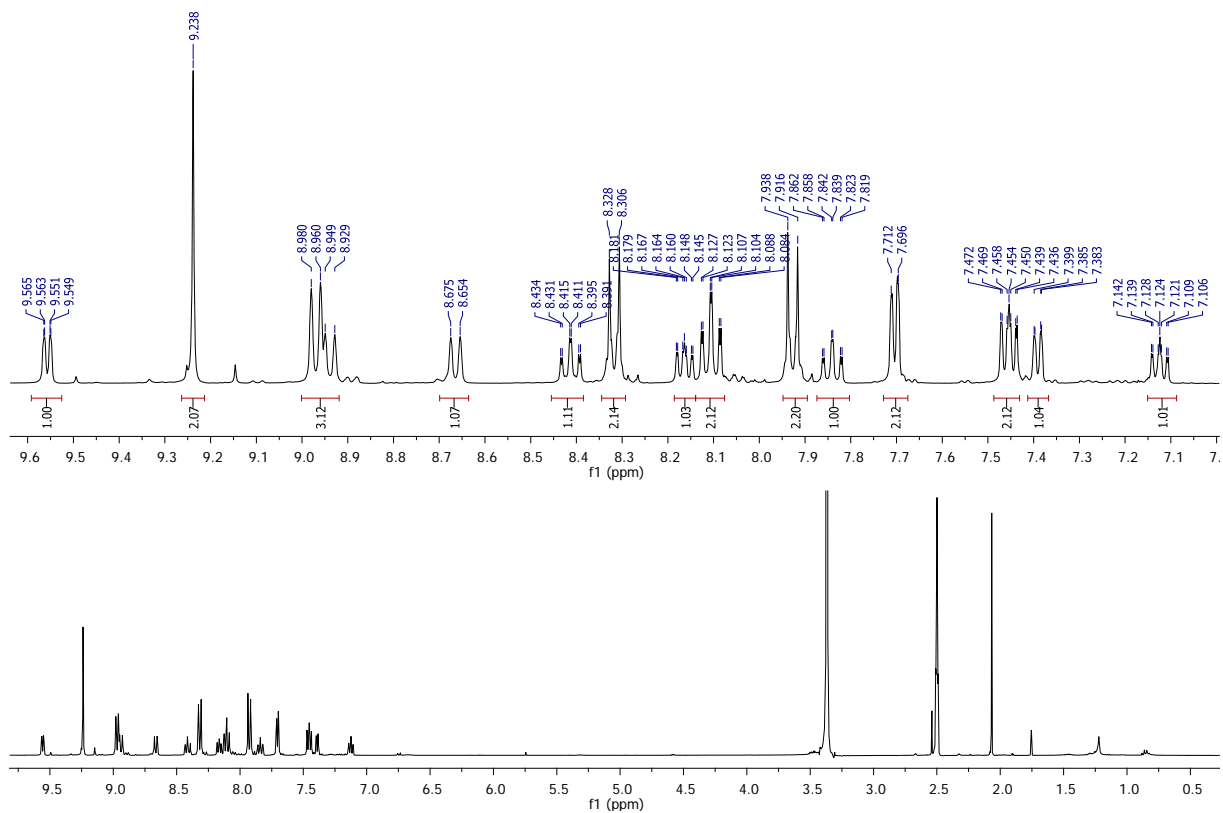
Figure S70. ¹H NMR (400 MHz, DMSO-d_6) spectrum of **3c**.
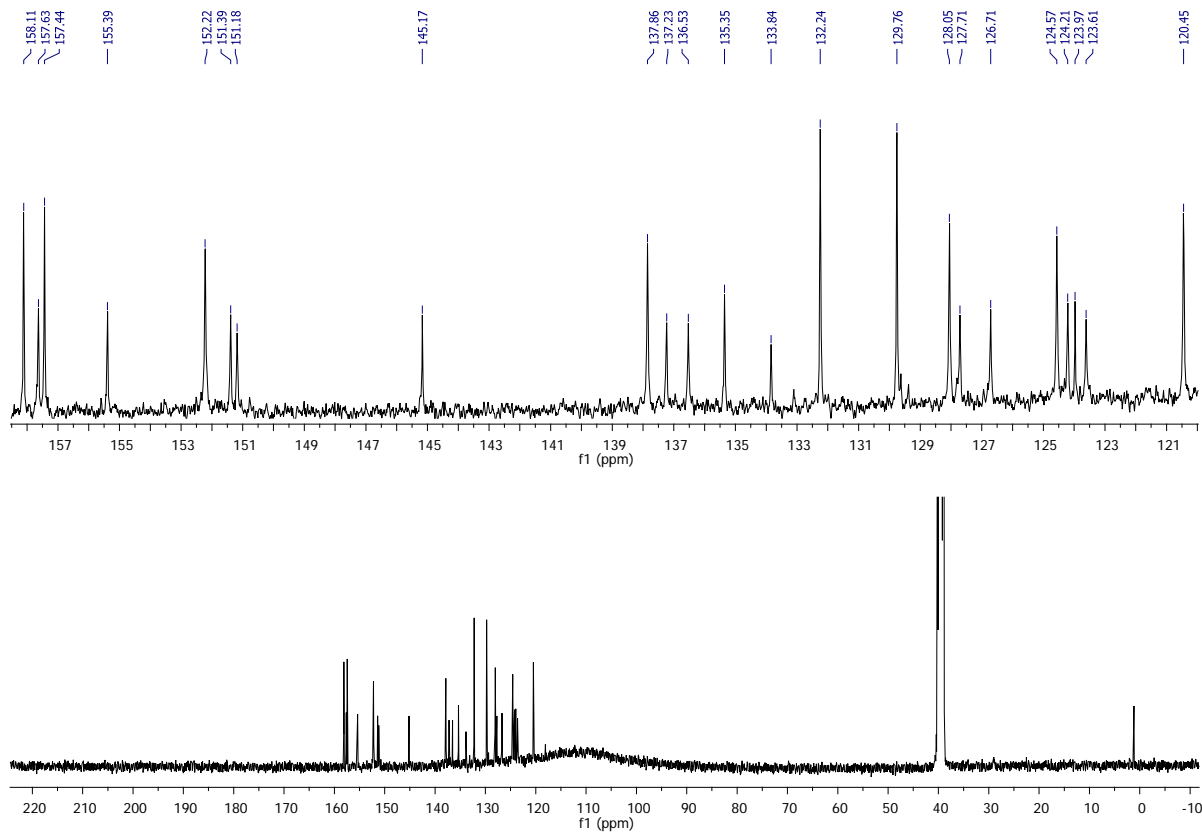
Figure S71. ¹³C-{¹H} NMR (100 MHz, DMSO-d_6) spectrum of **3c**.
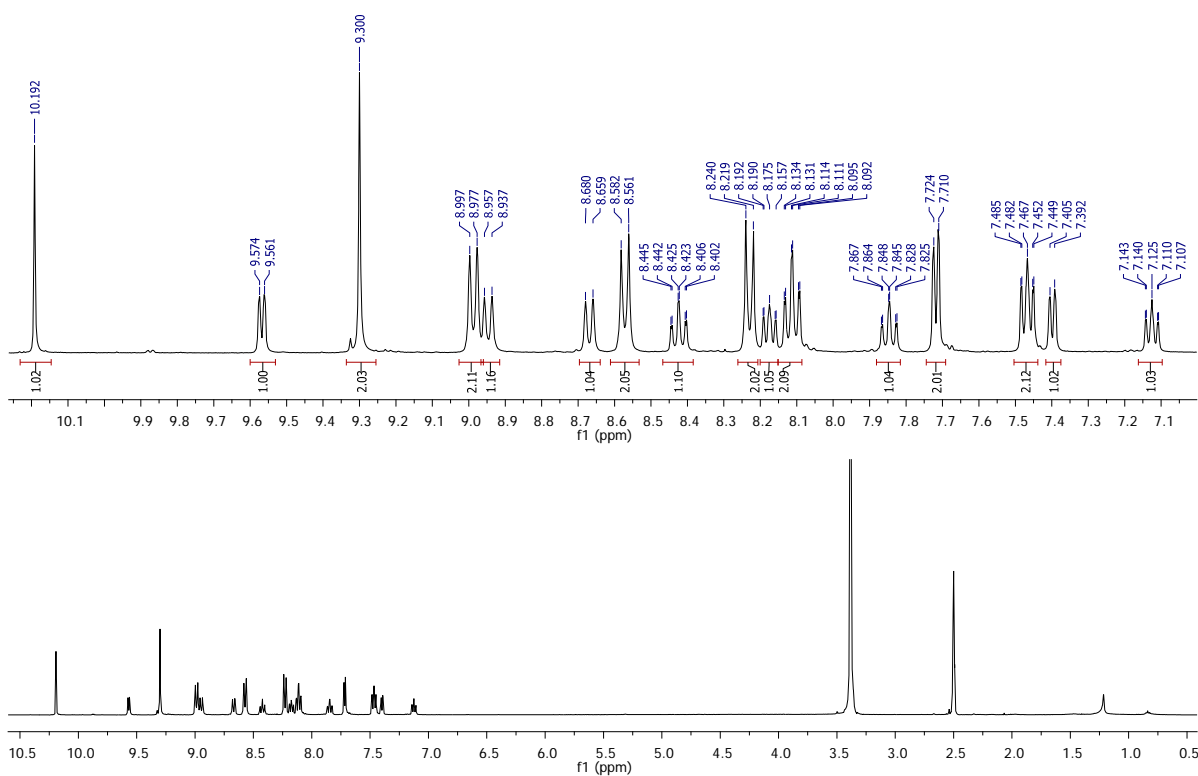
Figure S72. ^{1}H NMR (400 MHz, DMSO-d_6) spectrum of **3d**.
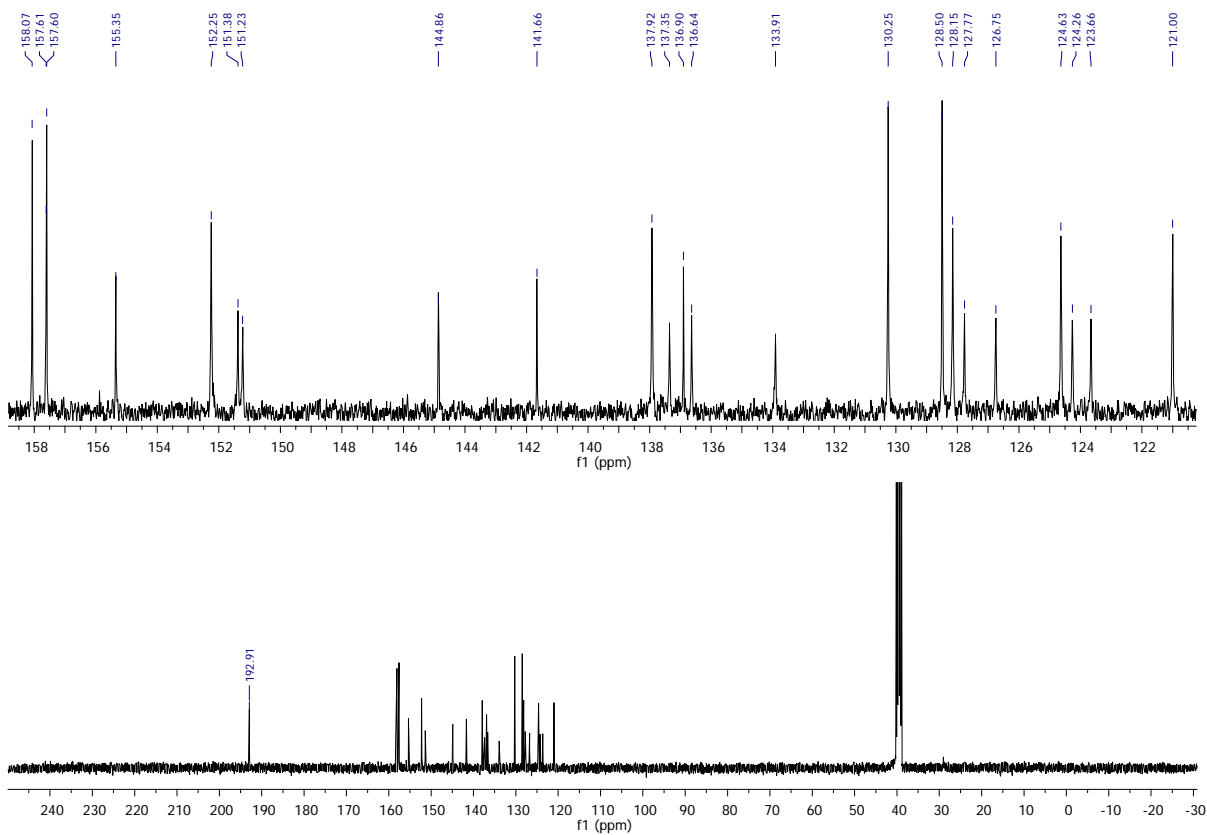
Figure S73. ^{13}C-{^{1}H} NMR (100 MHz, DMSO-d_6) spectrum of **3d**.
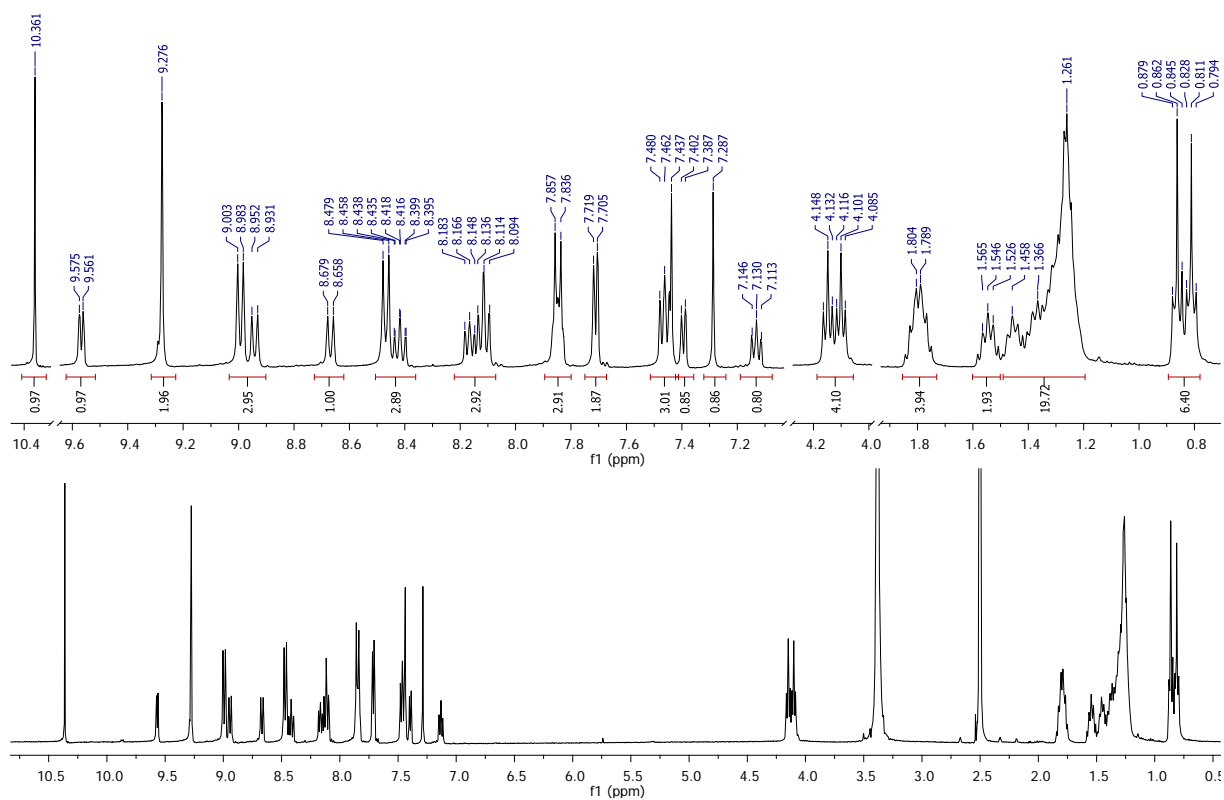
Figure S74. ^{1}H NMR (400 MHz, DMSO-d_6) spectrum of **3e**.
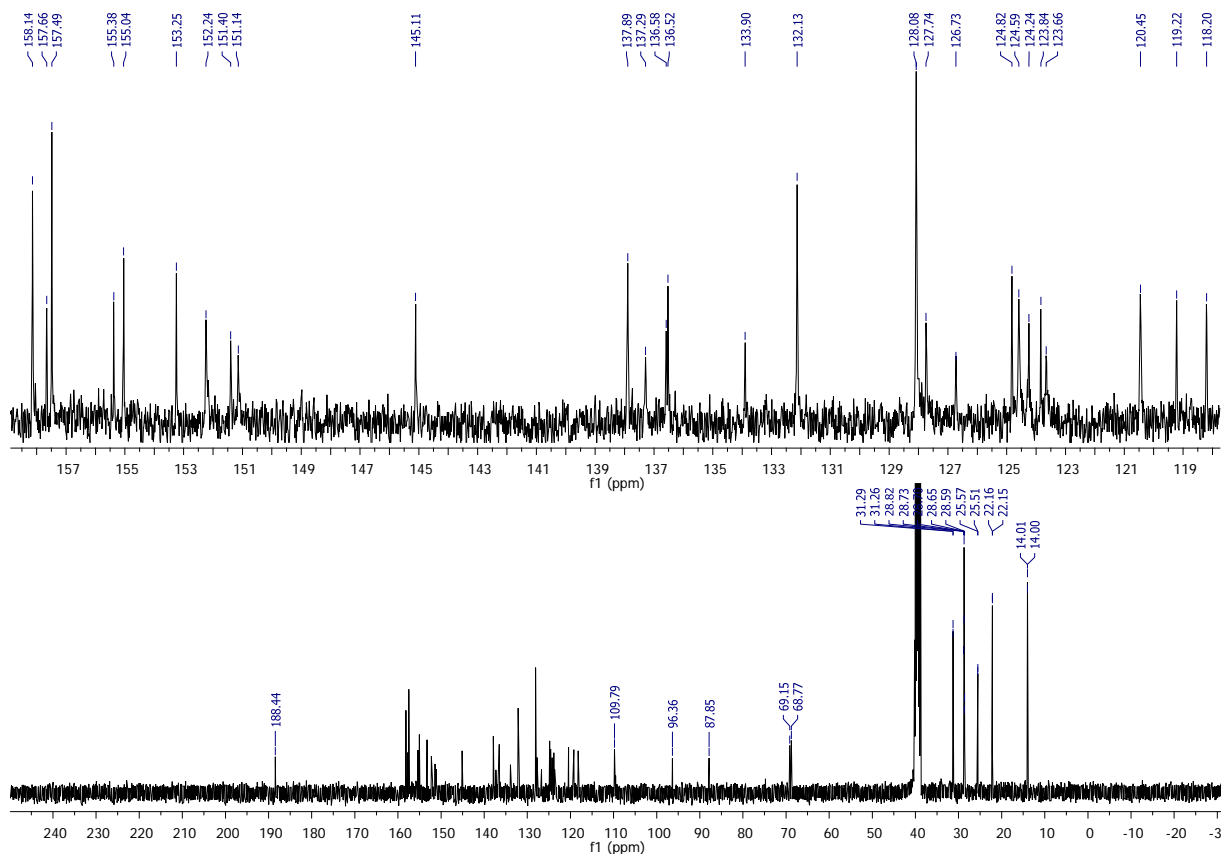
Figure S75. ^{13}C-{^{1}H} NMR (100 MHz, DMSO-d_6) spectrum of **3e**.

13. Coordinates for geometry optimized states

1a	S₀ (-2580.54560455 hartree)			D⁺ (-2580.35274776 hartree)			T₁ (-2580.4751639 hartree)		
	x	y	z	x	y	z	x	y	z
Ir	2.56534	-0.08721	-0.49339	2.62334	-0.07137	-0.36761	2.51944	-0.08236	-0.42216
C	4.62476	-0.22865	-0.70768	4.59344	-0.3185	-0.79366	4.55806	-0.33309	-0.74818
C	2.84867	0.69819	1.41207	2.79303	0.80583	1.46888	2.97606	0.76894	1.4217
C	5.15873	-1.50242	-0.37149	5.12113	-1.58913	-0.39877	5.04812	-1.6174	-0.39071
C	5.5371	0.75466	-1.12599	5.47012	0.60126	-1.4083	5.48393	0.58661	-1.26549
C	0.51203	-0.08983	-0.22807	0.53112	-0.03766	-0.13643	0.51019	0.00418	-0.0893
C	2.29713	-0.70338	-2.46631	2.16735	-0.8362	-2.2792	2.13905	-0.776	-2.35745
C	2.85587	2.11915	1.45921	2.82439	2.23421	1.42807	3.06652	2.18655	1.39803
C	3.03284	0.02068	2.62926	2.89014	0.17643	2.7265	3.209	0.13187	2.6509
C	6.53916	-1.76183	-0.45167	6.48031	-1.87669	-0.56191	6.40597	-1.94926	-0.54729
C	4.17981	-2.50718	0.05441	4.15988	-2.52689	0.18932	4.05212	-2.55316	0.14025
C	6.90843	0.49752	-1.20593	6.82001	0.30629	-1.56877	6.83331	0.25733	-1.42061
H	5.17483	1.74438	-1.39639	5.09387	1.56069	-1.74957	5.15192	1.58109	-1.55545
N	-0.6555	-0.09148	-0.12549	-0.636	-0.05046	-0.09429	-0.66161	0.019	0.02121
N	2.1329	-1.03694	-3.58033	1.87642	-1.24966	-3.33512	1.90052	-1.15303	-3.44307
C	3.03973	2.8113	2.67019	3.01153	2.97603	2.60033	3.37603	2.91742	2.55934
C	2.65773	2.79767	0.17383	2.67032	2.84266	0.10237	2.81333	2.81919	0.09917
C	3.21658	0.70711	3.83295	3.07457	0.92087	3.8885	3.51715	0.85777	3.80513
H	3.0353	-1.06753	2.64362	2.83884	-0.90625	2.7943	3.15099	-0.95263	2.71542
C	7.4143	-0.76341	-0.8678	7.32637	-0.93178	-1.14426	7.29813	-1.01312	-1.06101
H	6.93811	-2.73857	-0.19102	6.89328	-2.82811	-0.24208	6.77414	-2.93372	-0.27164
C	4.4795	-3.82806	0.42224	4.44764	-3.83331	0.60044	4.31411	-3.86916	0.55078
N	2.8803	-2.07716	0.07741	2.88981	-2.03871	0.31423	2.77786	-2.06057	0.223
H	7.5874	1.28214	-1.53339	7.48503	1.0336	-2.0257	7.52626	0.99252	-1.82397
C	3.22036	2.10697	3.8567	3.1366	2.32091	3.82579	3.60177	2.25435	3.7618
H	3.04406	3.89783	2.69573	3.06223	4.05998	2.57365	3.44322	4.00166	2.53342
C	2.62523	4.18815	-0.01346	2.6269	4.21688	-0.15965	2.84441	4.19947	-0.15095
N	2.49344	1.96744	-0.90197	2.55251	1.95145	-0.92694	2.52541	1.95517	-0.92222
H	3.3576	0.15065	4.75731	3.16985	0.41841	4.84706	3.6924	0.33434	4.74258
H	8.48028	-0.96417	-0.92942	8.37934	-1.162	-1.27447	8.34674	-1.2701	-1.18178
C	3.46918	-4.6971	0.80942	3.44307	-4.63254	1.1341	3.29166	-4.67038	1.03925
H	5.50818	-4.16772	0.40175	5.45398	-4.22044	0.4982	5.32305	-4.25817	0.4845
C	1.90123	-2.9265	0.4507	1.91583	-2.81435	0.82523	1.78666	-2.84356	0.69578
H	3.36287	2.64199	4.79153	3.27591	2.90065	4.73318	3.84139	2.81948	4.65815
C	2.42843	4.72269	-1.27925	2.46386	4.6724	-1.46302	2.58402	4.68876	-1.42352
H	2.75543	4.84516	0.8382	2.71836	4.92352	0.65618	3.07368	4.88401	0.65689
C	2.29948	2.49019	-2.1302	2.38777	2.39154	-2.18862	2.26919	2.43339	-2.15707
C	2.1497	-4.23842	0.82482	2.15245	-4.11584	1.24839	1.99829	-4.14825	1.11447
H	3.70521	-5.71798	1.09376	3.66444	-5.64574	1.45334	3.49851	-5.68784	1.35634
H	0.89776	-2.5206	0.44168	0.93251	-2.36659	0.88883	0.80349	-2.39268	0.73213
C	2.26138	3.85706	-2.36299	2.34009	3.74476	-2.49776	2.28889	3.78879	-2.4504
H	2.40486	5.79893	-1.42035	2.43134	5.73754	-1.66791	2.60966	5.75731	-1.61355
H	2.17549	1.77119	-2.9301	2.29434	1.62762	-2.94993	2.04818	1.68929	-2.9117
H	1.32429	-4.8778	1.11749	1.3355	-4.70149	1.6539	1.16419	-4.73242	1.48673
H	2.10444	4.22591	-3.37051	2.20817	4.05303	-3.52851	2.07806	4.12242	-3.46026
N	-2.60867	0.38527	1.88786	-2.67428	0.65301	1.77063	-2.92123	0.58142	1.83858
C	-2.55441	1.69538	2.22679	-2.68402	1.99882	1.9166	-2.81864	1.95582	2.0465
C	-2.52565	-0.60797	2.80492	-2.61048	-0.19598	2.82322	-2.72716	-0.34197	2.86451
Ru	-2.70943	-0.10001	-0.04234	-2.68056	-0.10833	-0.07504	-2.65852	-0.06355	-0.00425
C	-2.43586	2.05786	3.5703	-2.64468	2.55439	3.19732	-2.69082	2.42437	3.3449
C	-2.62623	2.6105	1.06793	-2.73602	2.7354	0.63498	-2.83397	2.74114	0.82291
C	-2.40322	-0.29011	4.15943	-2.57095	0.31695	4.12167	-2.59848	0.12506	4.16329
C	-2.57311	-1.96318	2.2158	-2.58737	-1.6233	2.43494	-2.65725	-1.72241	2.4131
C	-2.3634	1.05294	4.53543	-2.59089	1.7007	4.29952	-2.61113	1.50966	4.41025
H	-2.39367	3.09975	3.86376	-2.65198	3.62813	3.33958	-2.62443	3.48856	3.54213
C	-2.60961	4.00121	1.18274	-2.77747	4.1273	0.54963	-2.91217	4.1441	0.78051
N	-2.70978	2.00554	-0.15911	-2.74168	1.95972	-0.49495	-2.76185	2.01897	-0.3518

H	-2.33369	-1.06792	4.91026	-2.52208	-0.34137	4.98028	-2.46078	-0.56762	4.98608
C	-2.53219	-3.13442	2.97346	-2.54023	-2.67034	3.35596	-2.63244	-2.83699	3.26961
N	-2.66073	-2.01114	0.84867	-2.61345	-1.87146	1.08705	-2.60843	-1.90318	1.04464
H	-2.26889	1.31701	5.58311	-2.56028	2.11566	5.30103	-2.50593	1.87519	5.42553
C	-2.67636	4.78852	0.03534	-2.8213	4.74022	-0.70097	-2.907	4.80131	-0.43897
H	-2.54434	4.46624	2.15933	-2.77701	4.72903	1.45065	-2.98226	4.70584	1.70497
C	-2.77004	2.77339	-1.2599	-2.78054	2.55962	-1.69612	-2.75686	2.67063	-1.52986
C	-2.57474	-4.37143	2.334	-2.51603	-3.98754	2.90199	-2.54617	-4.11475	2.74131
H	-2.46805	-3.08262	4.05383	-2.52284	-2.46219	4.4191	-2.68635	-2.69056	4.3424
C	-2.69853	-3.20894	0.24114	-2.58737	-3.14449	0.65905	-2.52404	-3.15055	0.54504
C	-2.75713	4.16454	-1.20777	-2.82143	3.94366	-1.84367	-2.82678	4.0525	-1.62309
H	-2.6641	5.87043	0.11472	-2.8544	5.8219	-0.77687	-2.96754	5.88426	-0.4741
H	-2.82805	2.24431	-2.20404	-2.77793	1.90023	-2.55628	-2.69055	2.04798	-2.41514
C	-2.65776	-4.41026	0.94365	-2.53908	-4.22969	1.53041	-2.4886	-4.28048	1.34866
H	-2.54332	-5.28691	2.91526	-2.48002	-4.80776	3.61114	-2.52711	-4.97658	3.40052
H	-2.76185	-3.18956	-0.84064	-2.60544	-3.28474	-0.4155	-2.48104	-3.22589	-0.53579
H	-2.80871	4.73593	-2.12779	-2.85298	4.37585	-2.83747	-2.81876	4.52761	-2.59737
H	-2.69186	-5.34919	0.4025	-2.52136	-5.23729	1.13059	-2.4207	-5.26245	0.89467
N	-4.79079	-0.17159	-0.24009	-4.75169	-0.27447	-0.31398	-4.75593	-0.25884	-0.34657
C	-5.67292	0.06753	0.75025	-5.66733	0.08274	0.60738	-5.69376	0.04129	0.57054
C	-5.26349	-0.48235	-1.48222	-5.17791	-0.78782	-1.50423	-5.13982	-0.71683	-1.56934
C	-7.04854	0.01384	0.5633	-7.03468	-0.05048	0.4004	-7.05353	-0.09841	0.31948
H	-5.24938	0.30873	1.71753	-5.27974	0.48676	1.5344	-5.32522	0.40048	1.52316
C	-6.63771	-0.54954	-1.7308	-6.54149	-0.94612	-1.76878	-6.49268	-0.87783	-1.87893
C	-4.23482	-0.73378	-2.508	-4.11249	-1.14747	-2.45799	-4.04375	-1.01804	-2.50875
C	-7.54063	-0.30017	-0.70263	-7.48012	-0.57585	-0.81125	-7.4597	-0.56658	-0.92811
H	-7.71055	0.21602	1.39776	-7.72601	0.25376	1.17808	-7.76891	0.15725	1.0927
H	-7.00213	-0.79431	-2.72064	-6.87079	-1.35622	-2.71525	-6.79149	-1.24341	-2.8531
C	-4.52422	-1.07436	-3.83286	-4.35282	-1.68413	-3.7263	-4.23928	-1.49474	-3.80755
N	-2.94681	-0.61453	-2.07715	-2.84168	-0.9173	-2.02063	-2.79166	-0.79874	-2.02586
H	-8.60818	-0.35058	-0.88886	-8.53969	-0.69608	-1.01047	-8.51206	-0.68879	-1.16132
C	-3.48376	-1.29501	-4.72973	-3.28097	-1.98953	-4.55936	-3.13726	-1.75006	-4.6188
H	-5.55098	-1.16862	-4.16388	-5.36604	-1.86213	-4.06426	-5.23932	-1.66588	-4.18544
C	-1.94375	-0.83009	-2.95193	-1.80843	-1.21403	-2.83413	-1.72744	-1.04622	-2.81406
C	-2.16958	-1.17031	-4.28041	-1.98529	-1.74919	-4.10457	-1.859	-1.52196	-4.11346
H	-3.6981	-1.55994	-5.75981	-3.45789	-2.40664	-5.54515	-3.27927	-2.12067	-5.62848
H	-0.94099	-0.72205	-2.55674	-0.81882	-1.01212	-2.44392	-0.75139	-0.85565	-2.38697
H	-1.32429	-1.33274	-4.93989	-1.1156	-1.96801	-4.7138	-0.96584	-1.70329	-4.7004

2a	S$_0$ (-2977.48330415 hartree)			D$^+$ (-2977.28809896 hartree)			T$_1$ (-2977.41497486000 hartree)		
	x	y	z	x	y	z	x	y	z
Ru	2.50058	-2.91514	-0.00995	2.90802	-0.13595	0.03729	2.90641	-0.13624	0.03384
N	2.01217	-0.93984	-0.30932	0.91325	-0.28063	0.25761	0.90289	-0.2788	0.31594
N	1.48225	-2.88784	1.83679	3.21698	0.25565	2.08394	3.30131	0.34563	2.0456
N	0.65958	-3.41974	-0.58536	3.00831	-2.00645	0.79825	3.05297	-1.95542	0.89645
N	2.77785	-3.13781	-2.08998	2.90186	-1.30409	-1.71104	2.89577	-1.40773	-1.62466
N	3.24668	-4.83262	0.36332	4.94518	0.23364	-0.29026	4.94688	0.20507	-0.35881
N	4.47758	-2.51142	0.61273	2.88093	1.81648	-0.75675	2.8857	1.77812	-0.87604
C	1.98076	-2.60926	3.05288	3.35085	1.4651	2.65414	3.45397	1.59342	2.54565
C	1.20142	-2.62325	4.20643	3.47117	1.62174	4.03108	3.56934	1.84025	3.9009
C	-0.15175	-2.93668	4.09783	3.45889	0.48679	4.83832	3.52962	0.75211	4.79091
C	-0.67922	-3.22404	2.84086	3.3284	-0.77058	4.24907	3.38347	-0.53083	4.28953
C	0.15145	-3.19416	1.71993	3.20802	-0.87017	2.86564	3.27498	-0.73612	2.90573
C	-0.31945	-3.48035	0.34805	3.08497	-2.14951	2.13776	3.14972	-2.033	2.26129
C	-1.62596	-3.78672	-0.03906	3.05515	-3.42998	2.69356	3.13451	-3.27833	2.87661
C	-1.89242	-4.01508	-1.38938	2.94424	-4.52768	1.83945	3.0054	-4.43342	2.08522
C	-0.8695	-3.92995	-2.33438	2.87051	-4.34922	0.45801	2.8891	-4.32849	0.69911
C	0.42236	-3.62008	-1.90339	2.90257	-3.0494	-0.05137	2.90516	-3.06652	0.09683
C	1.62434	-3.47089	-2.75121	2.84912	-2.65297	-1.47246	2.79517	-2.75879	-1.30583
C	1.61587	-3.64591	-4.13567	2.77346	-3.55513	-2.53048	2.61756	-3.70244	-2.33697
C	2.79472	-3.4788	-4.85922	2.75224	-3.07704	-3.84028	2.56433	-3.29208	-3.65436

C	3.96198	-3.13851	-4.17863	2.81243	-1.70408	-4.06757	2.68971	-1.91786	-3.95964
C	3.90919	-2.97746	-2.79675	2.88977	-0.84698	-2.97467	2.85254	-1.0221	-2.92347
C	2.5514	-5.97725	0.21382	5.93316	-0.64095	-0.02231	5.92843	-0.66534	-0.06496
C	3.09541	-7.22863	0.47531	7.26899	-0.34649	-0.26183	7.26286	-0.40138	-0.3491
C	4.41702	-7.30648	0.91175	7.59314	0.89801	-0.79917	7.58913	0.80769	-0.96152
C	5.14244	-6.1302	1.0695	6.57469	1.80485	-1.07744	6.57477	1.71006	-1.26726
C	4.54143	-4.89913	0.79018	5.24871	1.45597	-0.81511	5.25065	1.3907	-0.95567
C	5.23094	-3.60327	0.92746	4.09974	2.34064	-1.07341	4.10362	2.27356	-1.23693
C	6.55811	-3.46757	1.34605	4.20608	3.6281	-1.60303	4.21406	3.53453	-1.82808
C	7.12294	-2.19991	1.44416	3.05355	4.38072	-1.81373	3.06655	4.29076	-2.05166
C	6.3447	-1.08874	1.12115	1.81329	3.83294	-1.49019	1.82592	3.7729	-1.68155
C	5.03146	-1.28647	0.71155	1.76922	2.54817	-0.96285	1.77923	2.51328	-1.09697
C	1.75743	0.18847	-0.49305	-0.25639	-0.30158	0.38038	-0.26435	-0.29839	0.43469
Ir	1.41165	2.207	-0.79336	-2.28215	-0.18538	0.5305	-2.30983	-0.18318	0.55366
C	3.41623	2.57851	-0.39293	-2.31333	0.9498	-1.21387	-2.29054	0.95834	-1.1852
N	1.35123	2.47499	1.28332	-2.06479	1.74599	1.31846	-2.09799	1.7435	1.35435
C	4.47653	2.61768	-1.30886	-2.46025	0.48868	-2.5274	-2.40888	0.50478	-2.50509
C	5.76889	2.86918	-0.86596	-2.40081	1.38588	-3.58737	-2.31739	1.40492	-3.55989
C	6.07808	3.08839	0.47243	-2.17842	2.74755	-3.41058	-2.09007	2.76431	-3.37285
C	5.02389	3.04911	1.37229	-2.03776	3.19326	-2.10678	-1.97799	3.20339	-2.06385
C	3.69612	2.80135	0.98826	-2.116	2.34427	-0.99084	-2.0871	2.35113	-0.95329
C	2.54651	2.74431	1.89819	-2.00959	2.77033	0.40941	-2.00839	2.7706	0.45134
C	2.57745	2.93628	3.28958	-1.8739	4.09077	0.86832	-1.86685	4.08771	0.91811
C	1.40787	2.85475	4.0346	-1.7943	4.35356	2.23019	-1.81758	4.34552	2.28245
C	0.20297	2.57834	3.38791	-1.84689	3.29426	3.13664	-1.90646	3.28395	3.18316
C	0.22063	2.39409	2.01331	-1.98231	2.00691	2.6387	-2.04489	2	2.67679
C	-0.62649	1.87614	-1.03227	-2.2867	-1.17411	2.36281	-2.33857	-1.17837	2.37914
N	-1.7795	1.69713	-1.15818	-2.29474	-1.72111	3.3999	-2.36259	-1.72875	3.41481
F	6.77909	2.90214	-1.76485	-2.54582	0.92444	-4.84831	-2.43595	0.94921	-4.82662
F	5.33976	3.26354	2.6756	-1.77616	4.5191	-1.94733	-1.71163	4.52846	-1.89507
C	1.14661	4.21355	-1.23261	-4.35668	-0.13379	0.56256	-4.38207	-0.13525	0.54257
N	1.63217	2.1799	-2.87389	-2.72942	-2.00516	-0.40431	-2.73289	-1.9935	-0.40574
C	0.88937	5.25578	-0.33158	-5.17079	0.87999	1.08136	-5.21149	0.86974	1.05634
C	0.75064	6.55712	-0.79694	-6.55328	0.7577	1.01465	-6.59166	0.7482	0.95398
C	0.85514	6.89279	-2.14236	-7.18605	-0.34177	0.44564	-7.21041	-0.34306	0.35435
C	1.10862	5.85675	-3.02695	-6.37141	-1.33907	-0.06592	-6.38212	-1.33237	-0.15091
C	1.25863	4.52083	-2.62126	-4.9688	-1.27704	-0.02829	-4.98103	-1.27023	-0.07876
C	1.52079	3.38751	-3.51335	-4.05987	-2.30129	-0.55039	-4.05887	-2.28786	-0.59141
C	1.65629	3.44273	-4.91095	-4.43344	-3.51086	-1.15954	-4.4156	-3.48854	-1.22794
C	1.9003	2.2853	-5.63834	-3.4646	-4.39782	-1.60925	-3.43473	-4.36888	-1.66496
C	2.00652	1.06651	-4.96746	-2.11635	-4.07686	-1.44843	-2.09143	-4.05069	-1.46252
C	1.86373	1.06028	-3.58833	-1.79453	-2.87381	-0.83979	-1.78675	-2.8565	-0.82773
F	0.50269	7.54973	0.08797	-7.32503	1.74423	1.52093	-7.37695	1.72791	1.45545
F	1.20902	6.19731	-4.33793	-7.00114	-2.40555	-0.61929	-6.99804	-2.39211	-0.73434
H	3.03681	-2.36822	3.08809	3.35091	2.31635	1.98465	3.47385	2.39878	1.82067
H	1.65589	-2.39113	5.16311	3.57171	2.6164	4.4491	3.69017	2.85811	4.25328
H	-0.78995	-2.95745	4.97486	3.55259	0.5729	5.91539	3.61569	0.91232	5.86048
H	-1.72926	-3.46918	2.73402	3.32264	-1.66256	4.86319	3.35415	-1.38136	4.96086
H	-2.42441	-3.84131	0.69097	3.11572	-3.57505	3.76487	3.22264	-3.36379	3.95349
H	-1.08157	-4.09639	-3.38362	2.79088	-5.20518	-0.20017	2.78951	-5.22229	0.09305
H	0.69685	-3.9096	-4.64546	2.73418	-4.62029	-2.33846	2.52605	-4.75329	-2.08576
H	2.7975	-3.61335	-5.93572	2.69309	-3.77283	-4.67018	2.43065	-4.02058	-4.44732
H	4.90243	-2.99696	-4.69932	2.80022	-1.29174	-5.06958	2.66295	-1.55887	-4.98196
H	4.79083	-2.70998	-2.22595	2.93476	0.22777	-3.0984	2.94606	0.04237	-3.10596
H	1.52837	-5.87277	-0.12644	5.63453	-1.59493	0.39397	5.61859	-1.58913	0.40864
H	2.48814	-8.11603	0.33681	8.02933	-1.08282	-0.02966	8.02108	-1.13256	-0.0937
H	4.87754	-8.265	1.12648	8.62555	1.1626	-1.00053	8.61976	1.04783	-1.20013
H	6.17005	-6.17252	1.4082	6.81332	2.77367	-1.49693	6.81461	2.65111	-1.74566
H	7.14819	-4.34134	1.59293	5.17502	4.04328	-1.84949	5.1828	3.92741	-2.11005
H	8.1523	-2.0848	1.76712	3.12717	5.38116	-2.22623	3.14378	5.27143	-2.50902
H	6.73843	-0.08008	1.18044	0.88889	4.37906	-1.6403	0.9056	4.32508	-1.83481
H	4.38623	-0.45674	0.44998	0.83378	2.0739	-0.69706	0.84411	2.0607	-0.79236

H	4.31449	2.45379	-2.36997	-2.61641	-0.56311	-2.74606	-2.56678	-0.54516	-2.73185
H	7.09019	3.2869	0.80335	-2.11173	3.43181	-4.24747	-1.99909	3.4516	-4.20496
H	3.51812	3.14968	3.77403	-1.84086	4.89966	0.15439	-1.80432	4.89819	0.20787
H	1.43872	3.00568	5.10927	-1.69334	5.3766	2.57882	-1.71147	5.36605	2.63706
H	-0.73456	2.50478	3.92752	-1.78808	3.4521	4.20754	-1.87177	3.43713	4.25586
H	-0.68088	2.17577	1.45545	-2.03103	1.14454	3.29098	-2.11819	1.13576	3.32436
H	0.79215	5.07334	0.73415	-4.75101	1.768	1.54278	-4.80344	1.75152	1.54021
H	0.74502	7.91249	-2.49044	-8.26516	-0.42246	0.3998	-8.28803	-0.42364	0.28132
H	1.56784	4.39381	-5.41366	-5.48104	-3.74411	-1.27353	-5.45976	-3.72002	-1.37337
H	2.00415	2.3354	-6.71784	-3.76021	-5.33055	-2.07931	-3.71742	-5.2944	-2.15688
H	2.19377	0.13578	-5.49119	-1.3249	-4.73801	-1.78261	-1.29046	-4.7065	-1.78454
H	1.93229	0.1439	-3.01687	-0.76462	-2.57812	-0.68764	-0.76199	-2.56276	-0.64148
H	-2.90173	-4.253	-1.70717	2.91821	-5.5292	2.25394	2.9968	-5.41017	2.556

3a	S_0 (-1823.8628925 hartree)			D^+ (-1823.67285673 hartree)			T_1 (-1823.79664642 hartree)		
	x	y	z	x	y	z	x	y	z
Ru	0.05553	-3.3E-5	0.19152	-0.0497	-0.00717	0.2262	-0.04782	-6E-6	0.23555
N	-0.93879	-2.9E-4	1.99863	0.93136	-0.03592	1.95423	0.97659	-7.4E-5	1.96248
N	-0.29968	-2.07129	0.00747	0.2648	2.0627	-0.0247	0.26125	2.04934	-0.10434
N	-1.70609	8E-5	-0.74042	1.73937	0.011	-0.70078	1.7173	1.4E-5	-0.73084
N	-0.29971	2.07127	0.00805	0.26746	-2.06796	-0.10346	0.26123	-2.04934	-0.10448
N	1.2895	2.41E-4	-1.49172	-1.30023	0.03248	-1.45674	-1.31227	6.6E-5	-1.44838
N	1.98171	-1.56E-4	1.05302	-1.97024	-0.02795	1.10446	-1.97815	-3.1E-5	1.11447
C	0.48166	-3.08506	0.41661	-0.5689	3.05451	0.33069	-0.57952	3.05448	0.23553
C	0.13201	-4.42165	0.24207	-0.23092	4.39557	0.17502	-0.24096	4.38673	0.09851
C	-1.07746	-4.7228	-0.38109	1.01085	4.71491	-0.36949	1.03084	4.71106	-0.41662
C	-1.89611	-3.67867	-0.80669	1.87746	3.68835	-0.74405	1.89777	3.69451	-0.77505
C	-1.49295	-2.35799	-0.60327	1.48872	2.36276	-0.56501	1.51161	2.35025	-0.626
C	-2.29683	-1.1875	-1.01464	2.32378	1.20357	-0.94208	2.32091	1.20662	-0.9919
C	-3.55241	-1.2106	-1.62636	3.59826	1.24032	-1.51234	3.58879	1.2157	-1.57034
C	-4.17475	2.27E-4	-1.93306	4.23115	0.03384	-1.81429	4.22235	3.7E-5	-1.86053
C	-3.55243	1.21097	-1.62602	3.60022	-1.18409	-1.55728	3.58877	-1.21564	-1.57042
C	-2.29685	1.18773	-1.01431	2.32644	-1.1708	-0.98461	2.3209	-1.20658	-0.99198
C	-1.49297	2.35812	-0.60263	1.49494	-2.34511	-0.6481	1.51158	-2.35022	-0.62616
C	-1.89614	3.67885	-0.80572	1.89149	-3.66233	-0.86694	1.89772	-3.69448	-0.77531
C	-1.07751	4.72287	-0.37985	1.02828	-4.70468	-0.52995	1.03078	-4.71105	-0.41695
C	0.13196	4.42157	0.24326	-0.21808	-4.40877	0.01711	-0.24101	-4.38673	0.0982
C	0.48162	3.08493	0.41746	-0.56317	-3.07503	0.21446	-0.57956	-3.05449	0.23532
C	0.85777	4.68E-4	-2.76873	-0.86934	0.06842	-2.73222	-0.8785	1.25E-4	-2.7214
C	1.72273	6.88E-4	-3.85629	-1.74343	0.09941	-3.81108	-1.75167	1.88E-4	-3.80258
C	3.09697	6.82E-4	-3.62015	-3.1147	0.09517	-3.55965	-3.12368	1.9E-4	-3.55297
C	3.55186	4.49E-4	-2.3054	-3.5644	0.05967	-2.24265	-3.57506	1.29E-4	-2.23629
C	2.63366	2.23E-4	-1.25072	-2.63993	0.0276	-1.19643	-2.64946	6.6E-5	-1.18874
C	3.02168	-3.2E-5	0.1713	-3.01472	-0.01121	0.22841	-3.02276	-2E-6	0.23827
C	4.34675	-1.49E-4	0.61859	-4.33374	-0.03053	0.68724	-4.34258	-3.5E-5	0.69783
C	4.61167	-3.79E-4	1.9846	-4.58261	-0.06488	2.05674	-4.59212	-9.4E-5	2.06735
C	3.54133	-4.88E-4	2.8794	-3.50654	-0.07977	2.94277	-3.51591	-1.19E-4	2.95438
C	2.24607	-3.74E-4	2.37492	-2.21516	-0.06112	2.42823	-2.22524	-8.6E-5	2.43851
C	-1.54055	-4.08E-4	3.01248	1.59135	-0.04445	2.94198	1.6238	-1.12E-4	2.95415
S	-2.36469	-5.75E-4	4.438	2.46099	-0.05731	4.30255	2.4929	-1.65E-4	4.32907
H	1.41061	-2.80327	0.89863	-1.51959	2.756	0.75476	-1.54225	2.75392	0.63266
H	0.80013	-5.20067	0.59168	-0.9332	5.16292	0.47875	-0.9503	5.15466	0.38459
H	-1.38288	-5.75248	-0.53425	1.30603	5.7498	-0.50474	1.32866	5.74785	-0.53377
H	-2.84098	-3.89108	-1.29261	2.84508	3.92055	-1.17159	2.87889	3.92675	-1.17371
H	-4.04292	-2.14878	-1.85579	4.09098	2.18222	-1.7187	4.08329	2.15339	-1.79787
H	-4.04296	2.14921	-1.85518	4.094	-2.11682	-1.79966	4.08326	-2.15332	-1.79802
H	-2.841	3.89137	-1.29161	2.86315	-3.87597	-1.29499	2.87884	-3.92671	-1.17398
H	-1.38293	5.75258	-0.53275	1.32971	-5.73331	-0.69572	1.32858	-5.74784	-0.53417
H	0.80007	5.2005	0.59307	-0.91833	-5.18863	0.29233	-0.95036	-5.15467	0.38423
H	1.41056	2.80302	0.89942	-1.51718	-2.79541	0.64378	-1.54229	-2.75394	0.63246
H	-0.21594	4.71E-4	-2.90886	0.20313	0.07276	-2.87863	0.19622	1.22E-4	-2.85659

H	1.3177	8.64E-4	-4.86193	-1.34841	0.12705	-4.81974	-1.35688	2.35E-4	-4.81197
H	3.80396	8.57E-4	-4.44299	-3.82813	0.11992	-4.37632	-3.83606	2.4E-4	-4.37114
H	4.61557	4.52E-4	-2.10295	-4.62669	0.05856	-2.03534	-4.63788	1.32E-4	-2.03037
H	5.16575	-6.7E-5	-0.0899	-5.16012	-0.01955	-0.01178	-5.16902	-1.5E-5	-0.00146
H	5.6361	-4.71E-4	2.34182	-5.60338	-0.07989	2.42323	-5.61316	-1.2E-4	2.43381
H	3.6988	-6.63E-4	3.95217	-3.65455	-0.10617	4.01609	-3.66493	-1.64E-4	4.02803
H	1.37924	-4.58E-4	3.02435	-1.34422	-0.07316	3.07117	-1.35281	-1.06E-4	3.08048
H	-5.15029	2.85E-4	-2.40698	5.22115	0.04286	-2.25648	5.20749	4.6E-5	-2.31363

1d	S₀ (-2924.93101136 hartree)			D⁺ (-2924.73786385 hartree)			T₁ (-2924.86620737 hartree)		
	x	y	z	x	y	z	x	y	z
Ru	0.69305	-2.4054	0.98193	0.73195	-2.25279	0.81228	0.7139	-2.42786	1.03387
N	1.21936	-0.51999	1.6168	1.23994	-0.3379	1.32271	1.18029	-0.53436	1.58468
N	-1.24382	-1.69495	0.53559	-1.21784	-1.59924	0.32417	-1.30198	-1.95361	0.68479
N	0.94034	-1.77553	-0.88923	0.95559	-1.78853	-1.11231	0.75243	-1.75767	-0.86531
N	2.72881	-2.86233	0.66897	2.77222	-2.71284	0.52021	2.68531	-2.86202	0.44091
N	0.12494	-4.37967	0.58974	0.18696	-4.25862	0.56899	0.23044	-4.43868	0.65343
N	0.40166	-3.18048	2.92359	0.45597	-2.88657	2.81051	0.65219	-3.25668	2.98156
C	-2.32977	-1.69917	1.32668	-2.2932	-1.53212	1.12617	-2.32157	-2.15204	1.5505
C	-3.56053	-1.19263	0.91752	-3.53199	-1.07312	0.68556	-3.60594	-1.70711	1.29777
C	-3.67342	-0.65923	-0.36471	-3.66346	-0.66608	-0.64007	-3.85887	-1.02936	0.09183
C	-2.55292	-0.64914	-1.19265	-2.55325	-0.7303	-1.47984	-2.8252	-0.83148	-0.80808
C	-1.34506	-1.16912	-0.72628	-1.33733	-1.19797	-0.98116	-1.53514	-1.30142	-0.51248
C	-0.10252	-1.19532	-1.52811	-0.10502	-1.29753	-1.79432	-0.38067	-1.18181	-1.385
C	0.06822	-0.67898	-2.81094	0.03764	-0.93619	-3.13203	-0.32987	-0.56905	-2.62796
C	1.32736	-0.7475	-3.43028	1.28417	-1.07593	-3.76568	0.88508	-0.50183	-3.35099
C	2.38724	-1.34219	-2.72573	2.36213	-1.5774	-3.01649	2.03615	-1.08156	-2.75724
C	2.17136	-1.85134	-1.44696	2.17606	-1.92598	-1.68045	1.95633	-1.69642	-1.51956
C	3.17639	-2.49539	-0.57362	3.20108	-2.46193	-0.75738	3.03879	-2.33616	-0.78619
C	4.49699	-2.72914	-0.95895	4.52311	-2.70409	-1.13065	4.36025	-2.45746	-1.24072
C	5.37709	-3.34048	-0.06875	5.4228	-3.20741	-0.19314	5.30364	-3.11058	-0.46382
C	4.9147	-3.70567	1.19364	4.97857	-3.45679	1.10312	4.92357	-3.64984	0.7763
C	3.58634	-3.44828	1.5213	3.64756	-3.1949	1.41766	3.61054	-3.50594	1.18668
C	1.53617	-0.19424	-4.78986	1.45753	-0.69934	-5.18924	0.95499	0.15559	-4.66377
C	0.53774	-0.3234	-5.7757	0.42273	-0.92503	-6.11896	-0.17592	0.21097	-5.51398
C	0.73314	0.19137	-7.04967	0.58316	-0.57631	-7.45252	-0.11241	0.83066	-6.75052
C	1.93022	0.852	-7.36769	1.78116	0.01075	-7.88884	1.08546	1.42298	-7.19191
C	2.92587	0.98735	-6.3908	2.8133	0.24097	-6.96955	2.21421	1.37483	-6.35715
C	2.73272	0.46845	-5.11424	2.65502	-0.1119	-5.63294	2.15209	0.75371	-5.1172
C	0.00607	-4.9219	-0.63805	0.07629	-4.89263	-0.61464	0.03252	-4.95011	-0.57443
C	-0.37864	-6.2408	-0.84477	-0.28855	-6.22897	-0.72139	-0.28139	-6.28827	-0.77806
C	-0.6546	-7.03949	0.26393	-0.55117	-6.9463	0.44427	-0.3935	-7.12484	0.33143
C	-0.53465	-6.48816	1.53532	-0.43838	-6.29989	1.67073	-0.18988	-6.5978	1.60326
C	-0.14276	-5.15413	1.68126	-0.06767	-4.95273	1.71594	0.12286	-5.24369	1.74698
C	0.01281	-4.48565	2.98613	0.07991	-4.18754	2.96767	0.35636	-4.58651	3.0462
C	-0.21183	-5.11318	4.21517	-0.14101	-4.72624	4.23862	0.28782	-5.24356	4.27675
C	-0.03609	-4.39736	5.39512	0.02666	-3.92595	5.36449	0.52466	-4.53021	5.4485
C	0.36271	-3.06301	5.32151	0.41364	-2.59759	5.19437	0.82556	-3.17103	5.36993
C	0.5706	-2.49352	4.0709	0.61733	-2.11769	3.90602	0.88004	-2.57048	4.11815
C	1.5098	0.57526	1.91716	1.52322	0.74643	1.65148	1.46137	0.57481	1.85155
Ir	2.01733	2.52446	2.39723	2.02027	2.6487	2.406	1.96587	2.51375	2.27737
C	2.42205	2.90335	0.39081	2.45265	3.24143	0.49942	2.93139	2.67052	0.43732
N	4.04753	2.01131	2.30292	4.04794	2.11041	2.31228	3.90345	1.89868	2.79713
C	1.55557	3.36677	-0.61371	1.5821	3.81087	-0.45181	2.40667	3.06817	-0.8028
C	1.99187	3.56869	-1.92615	2.05309	4.23487	-1.69156	3.20001	3.12014	-1.95289
C	3.3223	3.30953	-2.27807	3.40602	4.07194	-2.02447	4.5545	2.77045	-1.89503
C	4.2084	2.84789	-1.30899	4.28682	3.48122	-1.11793	5.10677	2.36923	-0.68212
C	3.76756	2.64539	0.01165	3.81989	3.0504	0.12954	4.30755	2.31796	0.47434
C	4.64578	2.15683	1.08043	4.67339	2.40695	1.134	4.82217	1.89858	1.78269
C	6.00513	1.84102	0.93274	6.02385	2.08131	0.96272	6.14436	1.51058	2.04801
C	6.74259	1.38428	2.01646	6.72566	1.45839	1.98852	6.52139	1.129	3.32826

C	6.11167	1.24142	3.25461	6.06567	1.1602	3.18103	5.56649	1.13456	4.34794
C	4.76626	1.56416	3.35311	4.7248	1.50074	3.30374	4.27178	1.52472	4.03964
C	1.79602	2.13115	4.43007	1.64889	1.74638	4.27506	1.1725	2.35767	4.19844
N	1.68445	1.90948	5.57787	1.44512	1.20792	5.29441	0.73967	2.27052	5.28605
C	2.37135	4.52677	2.81297	2.33547	4.40692	3.37109	2.35753	4.52839	2.6041
N	0.06657	3.28538	2.34166	0.06054	3.40148	2.42147	0.17242	3.37336	1.616
C	3.59449	5.17245	3.05979	3.54926	4.90531	3.8915	3.51381	5.12459	3.13269
C	3.66208	6.54495	3.31438	3.61584	6.16966	4.4675	3.6222	6.51039	3.27856
C	2.49711	7.32128	3.33086	2.46118	6.96131	4.56585	2.56734	7.34797	2.89758
C	1.26807	6.71453	3.09174	1.23831	6.48547	4.09046	1.40581	6.78978	2.37313
C	1.20074	5.33292	2.8352	1.162	5.21436	3.51177	1.29704	5.39496	2.22642
C	-0.0584	4.62825	2.57648	-0.0818	4.63103	3.00023	0.10184	4.73839	1.68875
C	-1.33089	5.22014	2.55656	-1.34735	5.22379	3.07545	-1.06345	5.39565	1.26484
C	-2.45925	4.45426	2.29937	-2.45754	4.56205	2.56333	-2.14089	4.67164	0.77433
C	-2.30975	3.08534	2.06408	-2.29072	3.30519	1.9817	-2.04938	3.27914	0.71152
C	-1.03343	2.54431	2.09681	-1.0152	2.75787	1.93164	-0.87915	2.67361	1.14262
C	2.14955	1.40616	-8.71991	1.964	0.38664	-9.30668	1.1667	2.08289	-8.50102
O	1.34609	1.33503	-9.63609	1.12614	0.22337	-10.17894	0.24276	2.1752	-9.30008
H	-2.19442	-2.12224	2.31522	-2.14369	-1.85786	2.14893	-2.07388	-2.67463	2.46687
H	-4.40493	-1.22189	1.59702	-4.36782	-1.04096	1.37535	-4.38988	-1.8869	2.02414
H	-4.61668	-0.25701	-0.71893	-4.61318	-0.30389	-1.01921	-4.85613	-0.6685	-0.13737
H	-2.61974	-0.24032	-2.19381	-2.635	-0.41848	-2.51425	-3.00615	-0.3193	-1.74605
H	-0.7557	-0.19258	-3.31851	-0.80106	-0.52242	-3.67768	-1.22185	-0.10427	-3.0303
H	3.36529	-1.41469	-3.18491	3.32865	-1.71108	-3.48604	2.97914	-1.07008	-3.28969
H	4.83644	-2.43876	-1.94617	4.85005	-2.50243	-2.14374	4.63687	-2.04092	-2.20227
H	6.40553	-3.52636	-0.35981	6.45276	-3.39919	-0.47468	6.32545	-3.20657	-0.81575
H	5.56326	-4.18198	1.92032	5.64276	-3.84683	1.86613	5.63072	-4.17189	1.41032
H	3.18357	-3.71284	2.49212	3.2577	-3.37094	2.41345	3.26821	-3.89991	2.13629
H	-0.382	-0.85299	-5.54674	-0.49858	-1.40082	-5.79753	-1.10206	-0.26706	-5.21026
H	-0.02928	0.08496	-7.81478	-0.2077	-0.7582	-8.17319	-0.98149	0.85781	-7.40074
H	3.85023	1.50693	-6.63034	3.73911	0.70373	-7.30181	3.14245	1.83897	-6.68249
H	3.49818	0.60691	-4.35727	3.45313	0.09481	-4.92697	3.02815	0.76412	-4.4767
H	0.22868	-4.267	-1.47153	0.28967	-4.30145	-1.4965	0.13252	-4.25607	-1.40021
H	-0.4572	-6.62341	-1.85614	-0.3615	-6.68715	-1.70121	-0.43192	-6.65678	-1.78616
H	-0.95808	-8.07408	0.14382	-0.83824	-7.9916	0.40252	-0.63664	-8.17518	0.21161
H	-0.74518	-7.09414	2.40761	-0.63673	-6.84337	2.58596	-0.27433	-7.23682	2.47294
H	-0.52035	-6.15049	4.25444	-0.44215	-5.7601	4.35199	0.05285	-6.2993	4.32538
H	-0.20778	-4.87536	6.35385	-0.14248	-4.33549	6.35481	0.4736	-5.03186	6.40901
H	0.51288	-2.4652	6.21357	0.55849	-1.93137	6.03733	1.01559	-2.57887	6.25768
H	0.88076	-1.46183	3.95739	0.91726	-1.09212	3.73147	1.10791	-1.51839	3.99698
H	0.51558	3.57665	-0.37138	0.53066	3.94004	-0.21289	1.35707	3.3444	-0.87946
H	1.29431	3.92932	-2.67927	1.37272	4.69253	-2.40429	2.76225	3.43097	-2.89898
H	3.6632	3.4675	-3.29745	3.77142	4.39961	-2.99298	5.17275	2.81184	-2.78748
H	5.23973	2.64917	-1.58837	5.32988	3.36463	-1.39493	6.15841	2.09808	-0.64513
H	6.47876	1.95752	-0.03481	6.51898	2.31377	0.02783	6.87316	1.51193	1.24632
H	7.79445	1.14238	1.89883	7.77308	1.20673	1.85766	7.54571	0.83088	3.52968
H	6.64445	0.88816	4.13046	6.57064	0.6723	4.00674	5.81246	0.84506	5.36348
H	4.22434	1.47377	4.28602	4.16194	1.29064	4.20426	3.48946	1.55074	4.78752
H	4.51742	4.59632	3.05541	4.45049	4.30321	3.83052	4.35027	4.50059	3.43954
H	4.62623	7.01316	3.50155	4.56233	6.54617	4.84496	4.53221	6.9406	3.69133
H	2.54864	8.38831	3.52884	2.51423	7.94602	5.02001	2.6509	8.42526	3.0105
H	0.36737	7.32249	3.10622	0.35744	7.11348	4.1778	0.59003	7.44547	2.08089
H	-1.42838	6.2829	2.74374	-1.45888	6.1975	3.5367	-1.11805	6.4761	1.32328
H	-3.4417	4.91605	2.28386	-3.4396	5.02003	2.62051	-3.04038	5.18392	0.44713
H	-3.15893	2.44282	1.85944	-3.12627	2.74861	1.5732	-2.86305	2.66675	0.33925

2d	S$_0$ (-3321.86945832 hartree)			D$^+$ (-3321.67256259 hartree)			T$_1$ (-3321.80365533 hartree)		
	x	y	z	x	y	z	x	y	z
Ru	2.44879	-2.64208	0.21267	2.52685	-2.65389	0.20451	2.5191	-2.63485	0.2122
N	1.98723	-0.67894	-0.19467	2.00489	-0.74211	-0.17685	1.97492	-0.71607	-0.16767
N	2.19456	-2.26324	2.27304	2.28328	-2.42982	2.28431	2.25404	-2.43824	2.28721
N	0.50878	-3.02308	0.4328	0.54998	-3.0133	0.43317	0.55946	-3.0423	0.43893
N	1.91478	-3.16785	-1.76044	1.97499	-3.29289	-1.72686	1.96783	-3.2887	-1.70877
N	3.18758	-4.56269	0.58966	3.29271	-4.57314	0.55855	3.28423	-4.55943	0.56821
N	4.53585	-2.37158	6.83E-4	4.60057	-2.35076	-0.01805	4.60833	-2.34366	-0.00634
C	3.12201	-1.87171	3.16263	3.25583	-2.15614	3.17073	3.22914	-2.161	3.18199
C	2.82871	-1.64675	4.50496	2.98391	-1.93273	4.51652	2.96254	-1.92332	4.51776
C	1.52053	-1.83341	4.946	1.66353	-2.00158	4.95442	1.62888	-1.97891	4.95864
C	0.55034	-2.23553	4.0306	0.65308	-2.29317	4.03852	0.62366	-2.27335	4.05266
C	0.90363	-2.44425	2.6971	0.98022	-2.50647	2.70243	0.9387	-2.51005	2.70562
C	-0.05621	-2.86355	1.65263	-0.00187	-2.84131	1.65167	-0.01924	-2.85769	1.66957
C	-1.42209	-3.08169	1.81925	-1.37666	-2.9897	1.81485	-1.38791	-3.01817	1.81511
C	-2.21096	-3.45483	0.71808	-2.18025	-3.31001	0.70708	-2.20005	-3.34293	0.70051
C	-1.58801	-3.59183	-0.5337	-1.55944	-3.48237	-0.54231	-1.5606	-3.49241	-0.55538
C	-0.21878	-3.36577	-0.65612	-0.18086	-3.3243	-0.65682	-0.18909	-3.33655	-0.67288
C	0.58282	-3.46194	-1.89547	0.62663	-3.48397	-1.88302	0.60903	-3.47486	-1.87991
C	0.04941	-3.82362	-3.13306	0.09965	-3.82158	-3.12649	0.1044	-3.7883	-3.15137
C	0.87986	-3.88696	-4.24979	0.95553	-3.9677	-4.21784	0.96723	-3.92126	-4.22661
C	2.23214	-3.58533	-4.10351	2.32428	-3.77889	-4.04299	2.34777	-3.7428	-4.03122
C	2.70702	-3.23012	-2.84387	2.79812	-3.44429	-2.77865	2.8026	-3.43194	-2.76288
C	-3.66643	-3.69108	0.87273	-3.64639	-3.46522	0.8533	-3.6531	-3.51757	0.84174
C	-4.17232	-4.29434	2.04165	-4.19076	-4.03429	2.02161	-4.22121	-3.94152	2.06753
C	-5.53397	-4.51826	2.18816	-5.56393	-4.18155	2.15764	-5.58904	-4.10797	2.20341
C	-6.42452	-4.14071	1.17083	-6.42313	-3.75645	1.13273	-6.45009	-3.85721	1.11911
C	-5.92887	-3.53816	0.0068	-5.88802	-3.18606	-0.02941	-5.8986	-3.43626	-0.10218
C	-4.5634	-3.3165	-0.14271	-4.51112	-3.04401	-0.17136	-4.52748	-3.26914	-0.23964
C	2.43189	-5.63646	0.89246	2.54395	-5.65241	0.8535	2.52651	-5.63081	0.86215
C	2.97183	-6.89323	1.13588	3.10323	-6.90282	1.08219	3.07579	-6.88632	1.09203
C	4.35471	-7.05332	1.06434	4.48787	-7.04067	1.00242	4.45963	-7.0351	1.01395
C	5.14283	-5.95059	0.75195	5.26515	-5.92745	0.69662	5.24584	-5.92794	0.70915
C	4.54238	-4.7102	0.51668	4.6489	-4.69452	0.47569	4.63762	-4.68998	0.4874
C	5.29626	-3.48825	0.18273	5.37928	-3.45836	0.1504	5.37743	-3.45727	0.162
C	6.68792	-3.44193	0.0558	6.76654	-3.38085	0.01743	6.76611	-3.39213	0.02826
C	7.31118	-2.23811	-0.25785	7.35934	-2.15744	-0.28426	7.3697	-2.1748	-0.27594
C	6.52693	-1.09913	-0.43813	6.5543	-1.03117	-0.44751	6.57452	-1.04127	-0.44059
C	5.14791	-1.20907	-0.30044	5.17848	-1.1685	-0.3075	5.19789	-1.16796	-0.29785
C	1.78268	0.44956	-0.43275	1.7715	0.38527	-0.41608	1.75055	0.41045	-0.40805
Ir	1.61353	2.46829	-0.86065	1.54873	2.36302	-0.84523	1.54819	2.40425	-0.84064
C	3.5465	2.69896	-0.13406	3.47091	2.66958	-0.10688	3.48005	2.67806	-0.11896
N	1.22663	2.87117	1.15735	1.13264	2.78169	1.16618	1.15731	2.81784	1.17622
C	4.74651	2.53711	-0.84015	4.67872	2.53486	-0.80272	4.68051	2.53266	-0.82664
C	5.96111	2.66074	-0.17809	5.88395	2.70977	-0.13339	5.89396	2.68934	-0.16843
C	6.05899	2.96145	1.17513	5.96021	3.03599	1.21483	5.98773	3.00607	1.18109
C	4.86728	3.12923	1.86384	4.75839	3.17575	1.89249	4.79425	3.15623	1.87105
C	3.6069	2.99767	1.2591	3.50775	2.99193	1.28067	3.53563	2.99202	1.27045
C	2.31804	3.10649	1.95262	2.2104	3.06916	1.96293	2.24601	3.08233	1.9658
C	2.12844	3.41302	3.31026	1.99993	3.39395	3.31283	2.05318	3.39766	3.32069
C	0.84682	3.47356	3.84268	0.71258	3.41975	3.83446	0.77149	3.43709	3.85518
C	-0.24915	3.22422	3.01634	-0.36841	3.11727	3.00614	-0.32123	3.15794	3.03422
C	-0.01409	2.92683	1.6821	-0.11402	2.80379	1.67939	-0.08357	2.85297	1.70225
C	-0.37499	2.26362	-1.4261	-0.43093	2.10761	-1.43031	-0.43916	2.17519	-1.40524
N	-1.50172	2.15305	-1.73529	-1.55067	1.96686	-1.74927	-1.56426	2.05361	-1.71433
F	7.11032	2.44774	-0.86785	7.0433	2.5223	-0.81133	7.04549	2.49327	-0.85868
F	4.97465	3.41753	3.18628	4.8448	3.48837	3.20944	4.89794	3.46043	3.18939
C	1.58927	4.46206	-1.42131	1.46369	4.35925	-1.40915	1.49164	4.39855	-1.40619
N	2.17285	2.31279	-2.87265	2.13266	2.22756	-2.85484	2.10681	2.25416	-2.85485
C	1.26802	5.56751	-0.62167	1.09482	5.44996	-0.61232	1.15265	5.49846	-0.60764
C	1.32083	6.84894	-1.15493	1.10801	6.73273	-1.14618	1.18476	6.77987	-1.14331

	x	y	z	x	y	z	x	y	z
C	1.68458	7.10384	-2.47262	1.47569	6.99914	-2.46008	1.54404	7.03784	-2.4614
C	1.9995	6.00595	-3.25712	1.83672	5.91339	-3.24129	1.87618	5.94408	-3.24444
C	1.96459	4.68589	-2.77937	1.84392	4.59287	-2.76256	1.86263	4.62434	-2.76423
C	2.27659	3.49015	-3.56745	2.20347	3.40884	-3.54691	2.19178	3.43236	-3.55064
C	2.64914	3.46119	-4.92215	2.59092	3.39448	-4.89753	2.56261	3.40777	-4.90581
C	2.90536	2.25148	-5.55371	2.89532	2.19567	-5.52778	2.83544	2.20168	-5.53705
C	2.78529	1.06464	-4.82999	2.80891	1.0042	-4.80693	2.73354	1.01361	-4.81266
C	2.41592	1.14217	-3.49588	2.42303	1.06669	-3.47718	2.36537	1.08657	-3.4782
F	1.00681	7.90279	-0.36728	0.74909	7.77343	-0.36253	0.85403	7.8291	-0.35747
F	2.35371	6.26784	-4.54184	2.19307	6.18622	-4.52178	2.22544	6.20899	-4.52924
C	-7.87674	-4.37262	1.31527	-7.8895	-3.90535	1.26906	-7.90239	-4.03036	1.24978
O	-8.40162	-4.89205	2.28726	-8.44472	-4.39344	2.23925	-8.47739	-4.39636	2.26758
H	4.12453	-1.73687	2.77356	4.26507	-2.10877	2.78142	4.23923	-2.12563	2.79138
H	3.61645	-1.33226	5.18033	3.79816	-1.7103	5.19601	3.77726	-1.7021	5.19736
H	1.2548	-1.66879	5.98486	1.41722	-1.83399	5.99728	1.38593	-1.7973	6.00037
H	-0.47322	-2.38428	4.35345	-0.37798	-2.35285	4.36463	-0.40899	-2.32437	4.37782
H	-1.88426	-2.93525	2.78753	-1.82955	-2.8375	2.78605	-1.8428	-2.86187	2.78561
H	-2.17124	-3.89062	-1.39576	-2.15001	-3.75973	-1.40589	-2.14251	-3.76588	-1.42695
H	-1.00535	-4.05332	-3.22607	-0.96644	-3.97019	-3.24588	-0.96226	-3.92678	-3.28471
H	0.4737	-4.16699	-5.21599	0.55311	-4.2296	-5.19034	0.57778	-4.16547	-5.20937
H	2.91615	-3.62091	-4.94402	3.02327	-3.88615	-4.86406	3.0553	-3.84563	-4.84575
H	3.75033	-2.98462	-2.6829	3.85313	-3.28367	-2.59508	3.85665	-3.281	-2.5618
H	-3.49017	-4.61207	2.82428	-3.5346	-4.38783	2.81076	-3.57594	-4.17345	2.90906
H	-5.9259	-4.99183	3.08263	-5.98851	-4.62941	3.05023	-6.0146	-4.44476	3.14376
H	-6.61602	-3.23606	-0.7795	-6.55155	-2.84785	-0.82096	-6.55466	-3.22875	-0.94442
H	-4.19569	-2.82541	-1.03817	-4.11128	-2.57743	-1.06593	-4.13234	-2.91038	-1.18459
H	1.36282	-5.46946	0.93793	1.47356	-5.49838	0.90465	1.45809	-5.45893	0.90997
H	2.31425	-7.72121	1.37561	2.45923	-7.74204	1.31713	2.42598	-7.7215	1.32644
H	4.81434	-8.01861	1.24831	4.96016	-8.00153	1.17574	4.9243	-7.99974	1.18787
H	6.21883	-6.05623	0.69329	6.34155	-6.02076	0.63267	6.32175	-6.02972	0.64661
H	7.28236	-4.33562	0.19948	7.38147	-4.26215	0.1473	7.37371	-4.27861	0.15874
H	8.39054	-2.19295	-0.35812	8.4368	-2.08843	-0.38819	8.44778	-2.11568	-0.38123
H	6.96466	-0.13676	-0.68013	6.97252	-0.0578	-0.67783	7.00112	-0.0723	-0.67442
H	4.4962	-0.35387	-0.42875	4.50988	-0.32526	-0.42377	4.53467	-0.31962	-0.41377
H	4.75287	2.29948	-1.89964	4.70118	2.28325	-1.85864	4.68949	2.28575	-1.88396
H	7.01448	3.05585	1.67631	6.90793	3.17062	1.72152	6.94195	3.12598	1.67921
H	2.98774	3.60291	3.93527	2.84695	3.62604	3.94024	2.90956	3.61072	3.94216
H	0.70712	3.71283	4.89236	0.55681	3.67421	4.8782	0.62931	3.68321	4.90289
H	-1.2673	3.25855	3.38746	-1.38966	3.12412	3.36984	-1.33889	3.17505	3.40766
H	-0.82289	2.72623	0.99129	-0.91023	2.5643	0.98649	-0.88959	2.62982	1.01519
H	0.97233	5.45087	0.41623	0.79237	5.32435	0.4222	0.85876	5.37922	0.4303
H	1.72226	8.10898	-2.87431	1.48159	8.0048	-2.86215	1.56532	8.04273	-2.86492
H	2.73179	4.38884	-5.46773	2.64741	4.32526	-5.44085	2.63055	4.33614	-5.45207
H	3.19212	2.23659	-6.60068	3.19348	2.19238	-6.57153	3.12063	2.19036	-6.58443
H	2.96851	0.09549	-5.28035	3.03061	0.04287	-5.25647	2.92948	0.04679	-5.26255
H	2.30376	0.25395	-2.88817	2.33689	0.17117	-2.87604	2.26723	0.195	-2.87306
H	-8.49016	-4.03463	0.45503	-8.47846	-3.53381	0.40614	-8.48142	-3.80071	0.33066

3d	S₀ (-2168.24127801 hartree)			D⁺ (-2168.0506620 hartree)			T₁ (-2168.17876211 hartree)		
	x	y	z	x	y	z	x	y	z
Ru	1.5042	0.06322	0.20662	-1.50578	-0.05868	0.25177	-1.51424	-0.05203	0.26117
N	1.28207	0.6231	2.17882	-1.18167	-0.45181	2.17251	-1.16605	-0.38258	2.20864
N	1.13379	-1.94347	0.74459	-1.13754	2.00358	0.50692	-1.13317	2.01238	0.41748
N	-0.47526	-0.01615	0.03595	0.49085	0.02264	0.01514	0.47292	0.03032	-0.01379
N	1.0726	2.03936	-0.39262	-1.07264	-2.03921	-0.33044	-1.06289	-2.03586	-0.27893
N	1.99911	-0.48851	-1.74513	-2.10157	0.33856	-1.71971	-2.1019	0.28217	-1.72839
N	3.61426	0.11437	0.25086	-3.61058	-0.12541	0.40707	-3.63094	-0.11498	0.39707
C	2.02648	-2.88388	1.09682	-2.05119	2.96454	0.72345	-2.05657	2.98182	0.60181
C	1.65563	-4.18162	1.43981	-1.69112	4.29056	0.94491	-1.7127	4.3071	0.801
C	0.30433	-4.52088	1.41874	-0.33978	4.62817	0.93783	-0.35113	4.65495	0.80661
C	-0.62965	-3.55205	1.05715	0.61172	3.63483	0.70676	0.60402	3.67087	0.60896

C	-0.19816	-2.26734	0.72428	0.19587	2.32326	0.49069	0.21027	2.33856	0.40838
C	-1.11309	-1.17309	0.33301	1.11785	1.20059	0.21446	1.11885	1.22768	0.16341
C	-2.5031	-1.23854	0.26077	2.50737	1.26361	0.13793	2.50143	1.27859	0.08895
C	-3.23939	-0.10028	-0.11011	3.24395	0.0996	-0.1436	3.25693	0.101	-0.14474
C	-2.53931	1.08513	-0.39231	2.54588	-1.10417	-0.34481	2.54418	-1.11546	-0.29855
C	-1.14854	1.10699	-0.30866	1.1557	-1.11959	-0.2567	1.16055	-1.13764	-0.22831
C	-0.26805	2.26714	-0.56632	0.27016	-2.28661	-0.45797	0.29142	-2.29493	-0.38325
C	-0.73795	3.52136	-0.95842	0.72733	-3.564	-0.77297	0.73205	-3.60379	-0.63494
C	0.16598	4.55956	-1.1747	-0.19208	-4.59544	-0.96355	-0.18756	-4.62885	-0.78715
C	1.52639	4.31957	-0.99228	-1.55337	-4.32795	-0.83957	-1.56056	-4.34534	-0.68881
C	1.93603	3.04758	-0.60066	-1.95522	-3.03377	-0.52244	-1.95115	-3.04222	-0.43681
C	-4.71893	-0.14785	-0.19623	4.72293	0.1417	-0.23098	4.72353	0.14033	-0.2249
C	-5.37019	-1.30222	-0.66568	5.37222	1.25951	-0.78319	5.40371	1.31272	-0.62684
C	-6.75889	-1.34387	-0.74844	6.76115	1.29415	-0.86688	6.78943	1.34626	-0.70047
C	-7.52402	-0.23522	-0.36134	7.52412	0.21748	-0.39585	7.55257	0.21146	-0.37707
C	-6.88012	0.91985	0.1105	6.88107	-0.89986	0.15934	6.88686	-0.96195	0.02559
C	-5.49513	0.96359	0.19032	5.49582	-0.93928	0.23806	5.50474	-0.99654	0.09968
C	1.11094	-0.7875	-2.71413	-1.25937	0.56077	-2.74707	-1.24665	0.47425	-2.74905
C	1.493	-1.15199	-3.99949	-1.71025	0.81663	-4.03553	-1.68215	0.69084	-4.05074
C	2.85254	-1.2128	-4.30297	-3.08443	0.8432	-4.26897	-3.05366	0.70863	-4.30202
C	3.77651	-0.90633	-3.30905	-3.95859	0.61429	-3.21006	-3.9407	0.51085	-3.24771
C	3.33269	-0.5448	-2.03331	-3.44909	0.36187	-1.93441	-3.44498	0.29778	-1.95848
C	4.23633	-0.20419	-0.91972	-4.29047	0.10584	-0.75175	-4.29848	0.07789	-0.776
C	5.63124	-0.19816	-1.02034	-5.68694	0.09138	-0.77686	-5.69529	0.06103	-0.8161
C	6.39935	0.13576	0.09094	-6.39091	-0.16398	0.39697	-6.41212	-0.15715	0.35721
C	5.75419	0.4581	1.2851	-5.68454	-0.40047	1.57527	-5.71879	-0.35437	1.5511
C	4.36484	0.43612	1.32324	-4.29502	-0.37236	1.54013	-4.32925	-0.32536	1.52929
C	1.11743	0.94107	3.30219	-0.89922	-0.68021	3.30366	-0.90656	-0.57445	3.34853
S	0.90573	1.3858	4.873	-0.5482	-0.99247	4.8485	-0.57464	-0.83879	4.91709
C	-8.998	-0.29193	-0.45311	9.00056	0.267	-0.48733	9.01693	0.26055	-0.46055
O	-9.74681	0.61953	-0.13895	9.74463	-0.6201	-0.10316	9.76839	-0.67175	-0.19983
H	3.06492	-2.57358	1.10234	-3.08813	2.65191	0.72417	-3.09169	2.66109	0.5938
H	2.4177	-4.90144	1.71654	-2.46196	5.03206	1.11886	-2.48954	5.04843	0.9477
H	-0.02203	-5.52212	1.67949	-0.02414	5.652	1.10688	-0.04677	5.68497	0.96068
H	-1.68514	-3.79553	1.03563	1.66593	3.88277	0.69381	1.6578	3.92429	0.6061
H	-3.02073	-2.15444	0.51752	3.02294	2.19837	0.31703	3.01024	2.2221	0.24391
H	-3.08158	1.97298	-0.69264	3.08733	-2.00874	-0.5904	3.08215	-2.03194	-0.50767
H	-1.79997	3.68813	-1.09317	1.78881	-3.75607	-0.87041	1.79416	-3.80607	-0.71115
H	-0.19036	5.53796	-1.47922	0.15597	-5.59315	-1.20826	0.15293	-5.64018	-0.98348
H	2.2661	5.09712	-1.1463	-2.30043	-5.1	-0.98157	-2.31061	-5.11892	-0.80529
H	2.98278	2.81546	-0.44262	-3.00154	-2.77842	-0.40892	-2.99699	-2.77333	-0.34613
H	-4.78869	-2.15859	-0.99232	4.79207	2.08921	-1.17432	4.83983	2.19396	-0.91523
H	-7.25266	-2.23759	-1.12159	7.25558	2.15732	-1.30482	7.29074	2.25618	-1.02264
H	-7.48109	1.77014	0.41673	7.48198	-1.72433	0.52911	7.47651	-1.83505	0.2881
H	-5.00965	1.85272	0.58048	5.00993	-1.79733	0.6917	5.01908	-1.90348	0.44561
H	0.06549	-0.72941	-2.43768	-0.20148	0.53016	-2.51917	-0.19342	0.45063	-2.49727
H	0.73376	-1.38132	-4.73864	-0.99327	0.98913	-4.82952	-0.95654	0.84083	-4.84175
H	3.19023	-1.49375	-5.29492	-3.47428	1.03927	-5.26198	-3.43127	0.87437	-5.30537
H	4.83636	-0.94919	-3.5263	-5.02747	0.63158	-3.37913	-5.0077	0.52246	-3.43015
H	6.11601	-0.45043	-1.9553	-6.22331	0.27752	-1.69853	-6.22147	0.21633	-1.74947
H	7.48212	0.14336	0.02343	-7.47545	-0.1773	0.38788	-7.49661	-0.17227	0.33646
H	6.31073	0.72394	2.17689	-6.19204	-0.60365	2.51116	-6.23731	-0.52771	2.4871
H	3.81353	0.67893	2.22338	-3.69817	-0.54832	2.42605	-3.74026	-0.47132	2.42656
H	-9.40406	-1.24902	-0.84003	9.40914	1.19197	-0.94257	9.42961	1.23758	-0.78961

1e	S$_0$ (-3461.18964006 hartree)			D$^+$ (-3460.99659448 hartree)			T$_1$ (-3461.12339997 hartree)		
	x	y	z	x	y	z	x	y	z
Ru	6.21228	-0.87948	-3.28152	5.96068	-0.73569	-3.1306	6.2156	-0.86655	-3.34106
N	6.41561	1.11203	-2.80464	6.15057	1.25101	-2.68833	6.34212	1.06348	-2.81631
O	-5.36042	-1.76502	3.32084	-5.65998	-2.10848	3.2414	-5.0778	-1.15437	3.73048
O	-8.68421	2.41439	1.80549	-9.34965	1.57626	1.33909	-8.76488	2.25975	1.3712
N	6.61727	-1.39315	-1.27487	6.31991	-1.21263	-1.10352	6.63831	-1.44392	-1.34816
N	4.3848	-0.81506	-2.49527	4.107	-0.71297	-2.3991	4.39186	-1.07505	-2.64516
N	5.06615	-0.3358	-4.9678	4.84908	-0.24169	-4.85762	5.09339	-0.33156	-5.05615
N	6.24043	-2.88676	-3.86714	6.03003	-2.75325	-3.6814	6.35011	-2.88436	-4.00154
N	8.13213	-1.06777	-4.1359	7.90899	-0.91362	-3.9325	8.18494	-0.99667	-4.19451
C	7.80477	-1.68836	-0.71979	7.49877	-1.45635	-0.50761	7.83645	-1.69516	-0.78961
C	7.94659	-2.00744	0.62791	7.60814	-1.75269	0.84872	7.97981	-2.06759	0.53965
C	6.81218	-2.02158	1.43686	6.4493	-1.79897	1.62029	6.82869	-2.19027	1.32852
C	5.57607	-1.71618	0.87113	5.22162	-1.54568	1.01155	5.58753	-1.93574	0.76303
C	5.496	-1.40303	-0.48628	5.17455	-1.25194	-0.35129	5.49758	-1.55374	-0.58394
C	4.23173	-1.05855	-1.17266	3.92044	-0.96188	-1.08215	4.24541	-1.24722	-1.2726
C	2.97243	-0.95211	-0.58694	2.63745	-0.91788	-0.5428	3.00652	-1.07744	-0.69645
C	1.86541	-0.57594	-1.36748	1.53894	-0.61054	-1.36568	1.88359	-0.66968	-1.47515
C	2.07252	-0.31429	-2.73307	1.78157	-0.34608	-2.72554	2.11061	-0.39	-2.85581
C	3.34823	-0.43673	-3.27895	3.08128	-0.39766	-3.22346	3.35105	-0.5775	-3.42131
C	3.73287	-0.18837	-4.68563	3.50268	-0.14321	-4.61951	3.74209	-0.27638	-4.79826
C	2.82465	0.17412	-5.68093	2.61501	0.17939	-5.64608	2.84314	0.05461	-5.82253
C	3.27611	0.39114	-6.98088	3.10114	0.40665	-6.93207	3.31838	0.33709	-7.09524
C	4.6332	0.24106	-7.25788	4.471	0.30733	-7.16351	4.69599	0.28292	-7.34
C	5.49206	-0.12164	-6.22396	5.30857	-0.0179	-6.09968	5.54297	-0.0557	-6.29382
C	0.5195	-0.44559	-0.76477	0.16658	-0.56238	-0.81321	0.56658	-0.49311	-0.86765
C	0.09271	-1.32921	0.24298	-0.22386	-1.4325	0.22144	0.20774	-1.17848	0.31898
C	-1.17065	-1.21191	0.80774	-1.51014	-1.39226	0.74253	-1.03914	-1.02019	0.89945
C	-2.05222	-0.19537	0.385	-2.45516	-0.46978	0.24713	-2.0013	-0.15881	0.32368
C	-1.62397	0.69518	-0.62137	-2.06592	0.40511	-0.78833	-1.65274	0.53181	-0.85962
C	-0.36151	0.56716	-1.18583	-0.77917	0.3545	-1.30792	-0.40514	0.36605	-1.43698
C	-3.34609	-0.07155	0.96278	-3.77155	-0.42432	0.78327	-3.27742	0.00971	0.91667
C	-4.45293	0.02907	1.45982	-4.89565	-0.39219	1.2498	-4.37453	0.15549	1.42889
C	-5.74848	0.16789	2.02388	-6.21064	-0.33755	1.78226	-5.65583	0.34693	2.00336
C	-6.217	-0.76293	2.98726	-6.60392	-1.22753	2.81542	-6.0202	-0.3307	3.19739
C	-7.49244	-0.5931	3.51334	-7.89926	-1.14103	3.31259	-7.28438	-0.11264	3.73039
C	-8.32501	0.47083	3.11931	-8.82408	-0.20124	2.82128	-8.2108	0.75672	3.12291
C	-7.8559	1.40264	2.15773	-8.4316	0.6874	1.78715	-7.84814	1.43266	1.92866
C	-6.57502	1.2345	1.62569	-7.13038	0.60399	1.28519	-6.57804	1.21661	1.38991
C	-9.65197	0.526	3.75797	-10.16021	-0.22181	3.44331	-9.5108	0.89352	3.79991
C	-5.78947	-2.72578	4.28507	-6.01269	-3.02725	4.2751	-5.39793	-1.8562	4.93081
C	-8.23218	3.36509	0.84022	-8.97566	2.48134	0.29952	-8.42159	2.95167	0.17017
C	5.22704	-3.75811	-3.69529	5.02244	-3.63351	-3.52307	5.36004	-3.78517	-3.86211
C	5.29564	-5.08341	-4.10661	5.11921	-4.96519	-3.90715	5.47955	-5.09772	-4.30307
C	6.46155	-5.53365	-4.72415	6.30837	-5.41164	-4.4808	6.66847	-5.4947	-4.91102
C	7.51314	-4.64133	-4.90515	7.35384	-4.50945	-4.6479	7.69449	-4.56608	-5.05672
C	7.38647	-3.31891	-4.4695	7.19826	-3.18081	-4.24197	7.51675	-3.25971	-4.59469
C	8.44583	-2.30415	-4.61716	8.24895	-2.15572	-4.38021	8.54258	-2.20576	-4.70321
C	9.69103	-2.55618	-5.20106	9.51174	-2.40551	-4.92559	9.80061	-2.39742	-5.28008
C	10.62687	-1.53101	-5.2948	10.43961	-1.37247	-5.01556	10.69989	-1.33663	-5.33266
C	10.29711	-0.26947	-4.79996	10.0831	-0.10558	-4.55597	10.32317	-0.10226	-4.80644
C	9.044	-0.07963	-4.22984	8.81315	0.0822	-4.02344	9.05764	0.02778	-4.2464
C	6.46098	2.24701	-2.51511	6.29622	2.38339	-2.44134	6.36541	2.19274	-2.48678
Ir	6.48433	4.25087	-1.99408	6.72238	4.40773	-2.0604	6.3571	4.14662	-1.90223
C	4.40901	4.21943	-1.83241	4.7978	4.66118	-1.42627	4.28196	4.10544	-1.71003
N	5.9302	4.75568	-3.95199	5.80492	4.90432	-3.88307	5.77179	4.71758	-3.83443
C	3.61422	3.92705	-0.71118	4.28301	4.49835	-0.12389	3.50907	3.77566	-0.58541
C	2.21793	3.9472	-0.77359	2.94942	4.77899	0.16091	2.11189	3.7952	-0.62543
C	1.56711	4.26282	-1.97275	2.08536	5.2039	-0.85929	1.4423	4.14886	-1.80296
C	2.32274	4.55602	-3.10437	2.55583	5.34546	-2.16509	2.17851	4.4819	-2.93618
C	3.72791	4.53569	-3.03958	3.89519	5.06367	-2.45906	3.58447	4.46263	-2.89487

C	4.58492	4.82886	-4.19369	4.46724	5.1729	-3.80527	4.42291	4.79768	-4.05103
C	4.12932	5.16392	-5.47803	3.75707	5.50824	-4.96383	3.94713	5.17915	-5.31476
C	5.03296	5.42127	-6.49981	4.4108	5.5659	-6.18942	4.83503	5.47291	-6.34049
C	6.40147	5.33996	-6.23154	5.77542	5.28128	-6.24662	6.20771	5.38199	-6.09777
C	6.80547	5.0038	-4.94787	6.43748	4.95275	-5.07066	6.63236	5.00069	-4.83372
C	8.53779	4.36299	-2.32171	8.60094	3.92854	-2.89331	8.40764	4.32977	-2.24059
N	9.69315	4.43503	-2.51922	9.62763	3.62974	-3.36998	9.55799	4.44461	-2.44225
C	6.47739	6.20963	-1.30776	7.43054	6.27519	-1.68666	6.32793	6.08512	-1.1489
N	6.83508	3.9494	0.04844	7.53359	4.10482	-0.14811	6.73814	3.78333	0.12704
C	6.29068	7.39741	-2.03451	7.38852	7.404	-2.53263	6.11674	7.29121	-1.83568
C	6.30485	8.64885	-1.41257	7.86179	8.63941	-2.10253	6.12135	8.52141	-1.17251
C	6.50873	8.75179	-0.03128	8.41895	8.77382	-0.82157	6.33949	8.58049	0.20894
C	6.69868	7.59596	0.71959	8.50466	7.6703	0.02835	6.55429	7.40366	0.91961
C	6.68409	6.33645	0.09288	8.03208	6.42403	-0.39665	6.55011	6.16573	0.25174
C	6.88168	5.07909	0.82024	8.09449	5.21134	0.42464	6.77558	4.88797	0.93427
C	7.10895	4.96679	2.20067	8.67518	5.11968	1.69483	7.02052	4.73463	2.30745
C	7.28638	3.72085	2.78553	8.68249	3.90514	2.37112	7.22448	3.47332	2.84912
C	7.23862	2.58096	1.9793	8.10849	2.78698	1.76605	7.18572	2.35962	2.00692
C	7.01319	2.74095	0.62046	7.54512	2.92776	0.50448	6.94228	2.55991	0.65673
O	-10.53465	1.34845	3.56989	-11.11271	0.49648	3.18373	-10.45947	1.58499	3.46134
H	8.659	-1.66235	-1.3864	8.37263	-1.40787	-1.1468	8.69606	-1.58611	-1.44133
H	8.92942	-2.23757	1.02372	8.58517	-1.94217	1.27882	8.96827	-2.25766	0.94188
H	6.8838	-2.26677	2.49123	6.49525	-2.02836	2.6796	6.90181	-2.48611	2.36999
H	4.68147	-1.72272	1.48237	4.30914	-1.57725	1.59488	4.68536	-2.03734	1.35513
H	2.84828	-1.1235	0.47519	2.48525	-1.09211	0.51487	2.8993	-1.1906	0.37524
H	1.23519	-0.03224	-3.35921	0.95355	-0.12314	-3.38657	1.29509	-0.03213	-3.47155
H	1.77311	0.28528	-5.44463	1.55273	0.25191	-5.44576	1.77912	0.08105	-5.61789
H	2.57681	0.67273	-7.76103	2.41786	0.65725	-7.73656	2.62563	0.59289	-7.89034
H	5.0308	0.4008	-8.25387	4.89508	0.47678	-8.14682	5.10898	0.4965	-8.31922
H	6.55553	-0.24665	-6.39162	6.3808	-0.10448	-6.23144	6.61693	-0.10975	-6.43184
H	0.74421	-2.13434	0.56912	0.47567	-2.16895	0.60469	0.90614	-1.87299	0.77448
H	-1.48983	-1.90917	1.57547	-1.79806	-2.07835	1.53229	-1.29009	-1.56887	1.8018
H	-2.28713	1.48944	-0.9484	-2.77873	1.12697	-1.17337	-2.37188	1.2082	-1.31095
H	-0.04335	1.28313	-1.93755	-0.49874	1.05686	-2.0868	-0.16658	0.94353	-2.32379
H	-7.87762	-1.28971	4.24999	-8.22799	-1.8072	4.10284	-7.58809	-0.61621	4.64171
H	-6.18601	1.92624	0.89015	-6.79746	1.26655	0.49709	-6.27001	1.71692	0.48123
H	-9.81182	-0.30073	4.484	-10.25261	-0.99986	4.23211	-9.58011	0.27342	4.72039
H	-4.95884	-3.42358	4.39612	-5.11979	-3.62717	4.45397	-4.51316	-2.44592	5.17313
H	-6.67794	-3.26705	3.93909	-6.83564	-3.6806	3.9622	-6.25421	-2.52525	4.78443
H	-6.00104	-2.25257	5.25117	-6.29074	-2.50185	5.1963	-5.61109	-1.16248	5.75271
H	-9.05339	4.07254	0.72109	-9.86151	3.08766	0.10805	-9.29936	3.54627	-0.08506
H	-7.33996	3.89607	1.19148	-8.14961	3.12957	0.61405	-7.56255	3.61496	0.32384
H	-8.02004	2.88552	-0.12229	-8.69519	1.94461	-0.6141	-8.20436	2.25171	-0.64493
H	4.34002	-3.3674	-3.21174	4.11621	-3.24706	-3.0734	4.45805	-3.42645	-3.38234
H	4.4484	-5.73965	-3.94222	4.27537	-5.62869	-3.75542	4.65221	-5.7847	-4.16693
H	6.55314	-6.56114	-5.05997	6.42275	-6.44398	-4.79387	6.79902	-6.51093	-5.26734
H	8.42594	-4.97379	-5.38337	8.2843	-4.83962	-5.09217	8.62505	-4.85921	-5.52582
H	9.93131	-3.54211	-5.57927	9.77212	-3.3959	-5.27769	10.07908	-3.3618	-5.68563
H	11.59588	-1.71642	-5.7462	11.42204	-1.55704	-5.43732	11.67914	-1.47515	-5.77841
H	10.99372	0.55997	-4.85005	10.76797	0.73365	-4.60214	10.99052	0.75177	-4.82444
H	8.73752	0.87915	-3.82937	8.49784	1.05033	-3.6553	8.71598	0.96461	-3.82393
H	4.09072	3.67759	0.23489	4.93598	4.16552	0.67751	4.00148	3.49563	0.34348
H	1.63252	3.71597	0.11384	2.57482	4.66841	1.17474	1.54123	3.53266	0.26266
H	0.48185	4.28284	-2.02194	1.04448	5.41816	-0.63677	0.35652	4.16439	-1.83509
H	1.81102	4.79989	-4.03167	1.87109	5.67534	-2.94009	1.65163	4.75464	-3.84658
H	3.0644	5.22242	-5.66889	2.6966	5.72019	-4.90247	2.87947	5.24515	-5.48646
H	4.67666	5.68137	-7.49187	3.86145	5.8268	-7.08816	4.46319	5.76866	-7.31667
H	7.14647	5.5318	-6.99569	6.32626	5.31009	-7.17967	6.94021	5.60119	-6.8665
H	7.85174	4.92535	-4.681	7.49466	4.72033	-5.05588	7.68271	4.91471	-4.5861
H	6.1314	7.35069	-3.10981	6.96845	7.31623	-3.52977	5.94599	7.27733	-2.9099
H	6.15705	9.54899	-2.00566	7.80349	9.50274	-2.75928	5.95475	9.43852	-1.73339
H	6.5201	9.72423	0.45314	8.79292	9.7375	-0.48961	6.34299	9.5363	0.72533

	x	y	z	x	y	z	x	y	z
H	6.85749	7.68274	1.79122	8.94116	7.79627	1.01404	6.72429	7.45768	1.99149
H	7.14554	5.8618	2.81021	9.12097	5.99692	2.14755	7.04974	5.60982	2.94529
H	7.46131	3.63823	3.85384	9.13244	3.83247	3.35587	7.41273	3.3589	3.91214
H	7.37317	1.585	2.38644	8.09343	1.81816	2.25185	7.34018	1.35315	2.37944
H	6.96881	1.89225	-0.04984	7.08871	2.09209	-0.00992	6.90417	1.73127	-0.03825

2e	S$_0$ (-3858.12792405 hartree)			D$^+$ (-3857.93175251 hartree)			T$_1$ (-3858.06081564 hartree)		
	x	y	z	x	y	z	x	y	z
Ru	4.8333	-0.41461	-3.90344	4.90969	-0.46489	-4.00026	4.89226	-0.43106	-3.97571
N	4.99259	1.57965	-3.42201	4.9657	1.47543	-3.44505	4.96557	1.51995	-3.41843
O	-3.43234	-2.8185	6.32584	-3.34716	-2.63977	6.29919	-3.31917	-2.59174	6.38913
O	-7.84167	0.53014	5.93504	-7.62544	0.88261	5.9898	-7.81597	0.62468	5.88899
N	5.96371	-0.90777	-2.19098	5.99156	-1.11266	-2.31442	5.95802	-1.09268	-2.29098
N	3.39754	-0.59467	-2.537	3.44577	-0.67938	-2.62153	3.43431	-0.66424	-2.60434
N	3.1194	0.00822	-5.06015	3.17338	-0.17992	-5.15936	3.15	-0.15783	-5.11729
N	4.87495	-2.39357	-4.57896	5.0151	-2.42423	-4.74014	4.96753	-2.4042	-4.69928
N	6.33688	-0.35147	-5.38877	6.42539	-0.30688	-5.45557	6.4066	-0.31845	-5.4561
C	7.29524	-1.05811	-2.09441	7.31408	-1.34825	-2.26545	7.28838	-1.3333	-2.24457
C	7.93022	-1.38621	-0.89964	7.95618	-1.69635	-1.08174	7.94412	-1.64524	-1.06843
C	7.15546	-1.56631	0.24417	7.20043	-1.81157	0.08268	7.19685	-1.72032	0.12099
C	5.77394	-1.4096	0.15534	5.82671	-1.57702	0.03286	5.83263	-1.48711	0.08333
C	5.19401	-1.07756	-1.06939	5.23491	-1.22613	-1.17719	5.2054	-1.17527	-1.13327
C	3.73977	-0.88414	-1.25987	3.79032	-0.97464	-1.35124	3.78261	-0.94242	-1.30663
C	2.75651	-0.95903	-0.27623	2.81316	-1.02058	-0.36163	2.80197	-0.98267	-0.32731
C	1.40999	-0.72832	-0.60968	1.47009	-0.75718	-0.68986	1.44917	-0.71583	-0.64909
C	1.10153	-0.41641	-1.94557	1.16009	-0.45906	-2.03018	1.14343	-0.40419	-1.99547
C	2.11638	-0.3478	-2.89686	2.17249	-0.41998	-2.98374	2.14024	-0.37511	-2.95924
C	1.95869	-0.0242	-4.33171	2.01664	-0.13997	-4.4254	1.98517	-0.08687	-4.37336
C	0.72676	0.23588	-4.93304	0.79815	0.13099	-5.04145	0.77364	0.23184	-5.00764
C	0.67216	0.53384	-6.29281	0.75992	0.35959	-6.4166	0.74374	0.46056	-6.37264
C	1.85706	0.56524	-7.02513	1.9424	0.309	-7.15107	1.93525	0.36904	-7.11558
C	3.05644	0.29774	-6.37073	3.13239	0.03327	-6.48581	3.10708	0.05751	-6.45224
C	0.34732	-0.80395	0.41836	0.41466	-0.7939	0.34347	0.39772	-0.76099	0.38089
C	0.43027	-1.73	1.47436	0.4931	-1.69587	1.42088	0.51535	-1.59975	1.51009
C	-0.56538	-1.80565	2.43956	-0.49588	-1.7309	2.39408	-0.473	-1.64662	2.48218
C	-1.68364	-0.94813	2.38333	-1.59789	-0.85274	2.3267	-1.63362	-0.85066	2.36928
C	-1.76826	-0.01745	1.32698	-1.67696	0.05326	1.24831	-1.75806	-0.00843	1.24289
C	-0.77054	0.04873	0.36356	-0.68916	0.07632	0.27357	-0.76509	0.03224	0.27539
C	-2.70455	-1.01833	3.37109	-2.60684	-0.87799	3.32774	-2.64841	-0.89652	3.36159
C	-3.57845	-1.07555	4.21684	-3.46731	-0.89797	4.18872	-3.51819	-0.9378	4.21427
C	-4.61162	-1.11978	5.1897	-4.48163	-0.89859	5.182	-4.54543	-0.96896	5.1918
C	-4.5339	-2.02251	6.28188	-4.41614	-1.80068	6.27539	-4.44263	-1.8269	6.31875
C	-5.56524	-2.03229	7.21385	-5.42744	-1.76621	7.22902	-5.47067	-1.82992	7.25293
C	-6.67719	-1.17674	7.10336	-6.50588	-0.86732	7.13801	-6.6069	-1.00922	7.1151
C	-6.756	-0.2757	6.01013	-6.5722	0.03361	6.0437	-6.70982	-0.1511	5.98954
C	-5.72077	-0.26227	5.07198	-5.5577	0.00249	5.08367	-5.67817	-0.1457	5.04782
C	-7.69154	-1.29397	8.16621	-7.50272	-0.94151	8.22205	-7.61625	-1.11685	8.18113
C	-3.3114	-3.74321	7.40608	-3.24006	-3.56596	7.3801	-3.17108	-3.46908	7.50415
C	-7.94002	1.44674	4.8442	-7.70977	1.80108	4.89918	-7.93999	1.49759	4.76582
C	4.09547	-3.38759	-4.10983	4.25705	-3.44811	-4.30472	4.19388	-3.40562	-4.24467
C	4.16069	-4.68825	-4.59388	4.3678	-4.72866	-4.83092	4.27666	-4.69592	-4.7539
C	5.0705	-4.98059	-5.60874	5.2969	-4.95729	-5.84438	5.19444	-4.95592	-5.77044
C	5.87936	-3.96087	-6.09928	6.08255	-3.90152	-6.29698	5.99625	-3.92115	-6.24269
C	5.76888	-2.67057	-5.57251	5.92815	-2.63442	-5.7318	5.86832	-2.64339	-5.69245
C	6.58333	-1.52964	-6.02863	6.71078	-1.4545	-6.13607	6.66821	-1.481	-6.11935
C	7.54536	-1.61406	-7.03982	7.68496	-1.46639	-7.13559	7.6344	-1.52598	-7.12692
C	8.26484	-0.47959	-7.40224	8.37437	-0.29424	-7.43557	8.33844	-0.37026	-7.45454
C	8.00821	0.72168	-6.7419	8.07897	0.87082	-6.72943	8.06589	0.81221	-6.7677
C	7.04035	0.74195	-5.74415	7.09723	0.82435	-5.74697	7.09293	0.79598	-5.77547
C	5.12605	2.71922	-3.18629	5.04175	2.61689	-3.17343	5.06946	2.65962	-3.15883
Ir	5.50671	4.73451	-2.9004	5.3198	4.60371	-2.82249	5.39758	4.65687	-2.82987

C	7.40872	4.39812	-3.66645	7.26903	4.37898	-3.51766	7.32144	4.3821	-3.57206
N	6.56194	4.2935	-1.14632	6.32512	4.17017	-1.03463	6.4369	4.20755	-1.06629
C	7.79798	4.40479	-5.01313	7.7073	4.43464	-4.8466	7.72953	4.42392	-4.91184
C	9.10508	4.08555	-5.35722	9.04291	4.19112	-5.14323	9.05076	4.14723	-5.24047
C	10.07992	3.76966	-4.41859	9.99421	3.9071	-4.17148	10.01861	3.84118	-4.29181
C	9.68902	3.77541	-3.08833	9.55162	3.86356	-2.85797	9.60727	3.8115	-2.96787
C	8.37963	4.06891	-2.67499	8.2126	4.07812	-2.49302	8.28375	4.0609	-2.57055
C	7.90018	4.03302	-1.28835	7.68	3.98466	-1.12832	7.78353	3.98557	-1.19251
C	8.67373	3.75822	-0.14848	8.41996	3.72315	0.0362	8.54568	3.70805	-0.04597
C	8.08702	3.74729	1.11064	7.78329	3.65001	1.26886	7.93889	3.6556	1.20267
C	6.7221	4.00921	1.23109	6.40247	3.83601	1.33884	6.56575	3.87851	1.30626
C	5.9984	4.27662	0.07841	5.71226	4.09368	0.16389	5.85337	4.15056	0.14773
C	3.66963	5.03373	-1.97777	3.43522	4.81706	-1.96807	3.54113	4.91154	-1.93
N	2.63786	5.20543	-1.4455	2.3777	4.93719	-1.47551	2.4996	5.06029	-1.41103
F	9.44823	4.04419	-6.6696	9.43777	4.1951	-6.44056	9.41494	4.13965	-6.54742
F	10.64821	3.46038	-2.18045	10.48778	3.58016	-1.91835	10.55986	3.50675	-2.05075
C	5.90339	6.76538	-2.81183	5.63704	6.64815	-2.6545	5.75755	6.6941	-2.69079
N	4.67047	5.37216	-4.71098	4.53591	5.27238	-4.64834	4.57813	5.32098	-4.64
C	6.55286	7.46263	-1.78389	6.21442	7.33073	-1.57688	6.37716	7.37759	-1.6366
C	6.75539	8.83233	-1.89397	6.37233	8.70996	-1.63591	6.5589	8.75273	-1.71399
C	6.33928	9.5708	-2.99627	5.9786	9.46797	-2.73268	6.14972	9.50754	-2.80752
C	5.69675	8.87489	-4.00762	5.40635	8.78406	-3.79303	5.53619	8.82378	-3.84475
C	5.45991	7.49163	-3.95696	5.21798	7.39213	-3.79553	5.32155	7.43593	-3.82773
C	4.77594	6.71006	-4.99121	4.60713	6.62136	-4.88154	4.66728	6.66607	-4.88935
C	4.23763	7.20829	-6.1899	4.10356	7.14017	-6.08645	4.14052	7.18195	-6.0856
C	3.60033	6.35514	-7.08091	3.53388	6.29645	-7.03022	3.53025	6.33912	-7.00473
C	3.49676	4.99851	-6.77172	3.46268	4.92786	-6.76815	3.44173	4.9748	-6.72635
C	4.04316	4.55214	-5.5782	3.9731	4.46101	-5.56711	3.97608	4.51082	-5.53437
F	7.38397	9.48716	-0.89112	6.93175	9.35202	-0.58668	7.15884	9.39514	-0.68673
F	5.29576	9.60688	-5.07907	5.02621	9.53472	-4.85752	5.14157	9.5716	-4.90679
O	-8.72806	-0.65872	8.28027	-8.51162	-0.26678	8.3524	-8.67276	-0.51011	8.27371
H	7.8566	-0.90657	-3.00915	7.85952	-1.24351	-3.19493	7.82032	-1.25887	-3.18576
H	9.0087	-1.49568	-0.87822	9.02547	-1.87183	-1.08603	9.01236	-1.82781	-1.08092
H	7.61522	-1.82401	1.19243	7.66986	-2.08456	1.02156	7.68178	-1.96287	1.06078
H	5.15288	-1.54563	1.03282	5.22395	-1.66989	0.92793	5.2415	-1.54645	0.98995
H	3.02967	-1.16275	0.75167	3.08858	-1.2309	0.66386	3.08018	-1.19023	0.69891
H	0.07202	-0.24796	-2.23552	0.13242	-0.28521	-2.32177	0.11615	-0.21843	-2.28472
H	-0.1831	0.20704	-4.34542	-0.11308	0.16382	-4.45707	-0.13594	0.29631	-4.4216
H	-0.28131	0.73744	-6.7686	-0.1853	0.5713	-6.90453	-0.19277	0.70452	-6.86315
H	1.86369	0.79213	-8.08537	1.95554	0.47835	-8.22128	1.9512	0.53354	-8.18671
H	4.003	0.31302	-6.89848	4.07787	-0.01231	-7.01163	4.05128	-0.02076	-6.97833
H	1.26781	-2.41884	1.52716	1.31754	-2.39922	1.48389	1.37913	-2.24909	1.61411
H	-0.49094	-2.53336	3.24104	-0.42829	-2.44044	3.212	-0.36323	-2.30892	3.3352
H	-2.61754	0.65608	1.27602	-2.51386	0.74112	1.18917	-2.63721	0.6205	1.14319
H	-0.84791	0.79267	-0.42327	-0.76107	0.80231	-0.53021	-0.88043	0.71514	-0.56056
H	-5.5323	-2.71059	8.05959	-5.40376	-2.44269	8.07649	-5.41802	-2.47603	8.12259
H	-5.74835	0.41308	4.22697	-5.57599	0.67586	4.23682	-5.72612	0.49689	4.17848
H	-7.42879	-2.06422	8.92375	-7.25453	-1.71789	8.97804	-7.33047	-1.85062	8.96639
H	-2.36908	-4.267	7.2421	-2.32323	-4.1274	7.19753	-2.21561	-3.97417	7.35809
H	-4.13618	-4.46559	7.40526	-4.09295	-4.25456	7.39928	-3.97635	-4.21265	7.53541
H	-3.27833	-3.22483	8.3716	-3.16528	-3.04654	8.34263	-3.14948	-2.91254	8.4487
H	-8.88038	1.97815	4.99378	-8.62411	2.37071	5.06795	-8.89211	2.01208	4.89982
H	-7.11022	2.16287	4.84967	-6.8514	2.48258	4.88527	-7.12737	2.23279	4.74073
H	-7.96593	0.92075	3.8829	-7.77816	1.27519	3.93993	-7.95699	0.93624	3.82447
H	3.40243	-3.11883	-3.32209	3.54968	-3.22526	-3.51595	3.49872	-3.14861	-3.45466
H	3.50814	-5.44756	-4.17785	3.73553	-5.52083	-4.44758	3.63263	-5.47184	-4.35652
H	5.15092	-5.98405	-6.01308	5.41127	-5.9444	-6.27899	5.28724	-5.95093	-6.19242
H	6.59188	-4.1695	-6.88753	6.8088	-4.06528	-7.08267	6.71344	-4.10913	-7.03151
H	7.73273	-2.55511	-7.54189	7.90694	-2.37763	-7.67621	7.83809	-2.45013	-7.65298
H	9.01253	-0.53578	-8.18646	9.13323	-0.29526	-8.21069	9.09025	-0.39681	-8.23625
H	8.54255	1.63323	-6.98654	8.59372	1.8046	-6.92572	8.59092	1.73512	-6.98708
H	6.80698	1.64859	-5.19997	6.83165	1.70005	-5.16894	6.844	1.68541	-5.20993

	x	y	z	x	y	z	x	y	z
H	7.09388	4.63985	-5.80565	7.02416	4.65312	-5.66172	7.03179	4.65588	-5.71081
H	11.0955	3.52399	-4.70367	11.03208	3.72155	-4.41932	11.04506	3.62906	-4.56461
H	9.72851	3.55781	-0.25971	9.48772	3.58222	-0.03467	9.60706	3.53776	-0.14342
H	8.69082	3.53602	1.9878	8.36168	3.44982	2.16542	8.53402	3.44219	2.08516
H	6.22044	4.01029	2.19229	5.86356	3.787	2.27825	6.04915	3.84604	2.25888
H	4.93752	4.4893	0.1076	4.6414	4.25042	0.15322	4.78687	4.33441	0.16338
H	6.9058	6.95799	-0.89003	6.54553	6.81092	-0.6838	6.72273	6.85987	-0.74756
H	6.50528	10.63864	-3.06865	6.1088	10.54272	-2.76456	6.29911	10.57926	-2.85412
H	4.32222	8.26158	-6.40992	4.16169	8.20217	-6.26964	4.21255	8.24087	-6.28151
H	3.18614	6.74713	-8.00473	3.14622	6.70459	-7.95839	3.1248	6.74491	-7.92639
H	3.00311	4.29433	-7.43207	3.02079	4.23013	-7.47044	2.96856	4.27789	-7.4089
H	3.98832	3.51175	-5.28582	3.93823	3.40972	-5.31369	3.92997	3.46319	-5.26773

3e	S$_0$ (-2704.49010411 hartree)			D$^+$ (-2704.29654599 hartree)			T$_1$ (-2704.42613476 hartree)		
	x	y	z	x	y	z	x	y	z
Ru	4.30121	0.06268	0.1522	4.29082	0.06865	0.19428	4.31576	0.06425	0.2132
N	4.21413	1.17719	1.88507	4.30186	0.98694	1.94098	4.06676	0.87577	2.03157
O	-8.83825	2.4496	0.06703	-8.81067	2.45893	0.06683	-8.85166	2.45386	0.07888
O	-11.60144	-2.35471	-0.23917	-11.59445	-2.33243	-0.23288	-11.62522	-2.34313	-0.26125
N	3.87164	-1.67962	1.26327	3.87901	-1.77377	1.15968	3.8603	-1.87849	0.87764
N	2.31292	0.05285	0.09127	2.30398	0.05581	0.1253	2.31562	0.01841	0.03471
N	3.92341	1.80622	-0.97436	3.92351	1.9153	-0.77661	3.91997	1.87533	-0.78212
N	4.66007	-1.05194	-1.57613	4.56092	-0.91402	-1.66156	4.80022	-0.76858	-1.65611
N	6.41026	-0.00162	0.09486	6.40825	-0.04325	0.01407	6.43725	0.0382	0.26277
C	4.73979	-2.52877	1.83832	4.7522	-2.65361	1.67001	4.75133	-2.82052	1.26116
C	4.33143	-3.64798	2.55929	4.34452	-3.82953	2.29836	4.36468	-4.03526	1.79694
C	2.96727	-3.89945	2.69169	2.98297	-4.0983	2.3982	2.99065	-4.29941	1.94371
C	2.05873	-3.02389	2.10045	2.0692	-3.18455	1.87172	2.06813	-3.34655	1.54532
C	2.52747	-1.91749	1.39073	2.53576	-2.02435	1.25807	2.50415	-2.12669	1.00255
C	1.64148	-0.93176	0.73366	1.64448	-0.98976	0.68124	1.6322	-1.06676	0.5237
C	0.24847	-0.93717	0.7349	0.25569	-0.99739	0.67855	0.24528	-1.06321	0.51195
C	-0.45912	0.08311	0.07421	-0.45405	0.07869	0.10412	-0.47045	0.0557	0.01972
C	0.2785	1.0959	-0.56453	0.28207	1.14875	-0.44707	0.28047	1.16038	-0.45338
C	1.67102	1.06537	-0.53774	1.67034	1.12179	-0.42169	1.66678	1.13218	-0.43584
C	2.58636	2.05293	-1.15022	2.58657	2.16425	-0.94174	2.57299	2.17226	-0.89611
C	2.15073	3.17218	-1.86091	2.14924	3.33709	-1.55328	2.17628	3.40497	-1.43938
C	3.08565	4.05303	-2.40096	3.08621	4.27115	-1.99669	3.12899	4.31386	-1.86903
C	4.44241	3.79451	-2.2163	4.44102	4.01125	-1.81492	4.49312	3.99011	-1.75694
C	4.81723	2.66264	-1.49693	4.81891	2.8193	-1.19844	4.84054	2.76726	-1.21226
C	-1.9396	0.09147	0.05506	-1.92778	0.08687	0.08373	-1.94232	0.06972	0.00153
C	-2.66518	-1.11313	0.00126	-2.65449	-1.11823	0.00236	-2.6853	-1.12717	-0.10004
C	-4.05393	-1.11156	-0.02196	-4.0412	-1.11435	-0.02741	-4.07228	-1.11946	-0.11479
C	-4.76961	0.10361	0.01321	-4.75605	0.1017	0.03527	-4.78858	0.09494	-0.02933
C	-4.0448	1.3126	0.07065	-4.03106	1.31009	0.12453	-4.05293	1.29659	0.07131
C	-2.65595	1.30234	0.08845	-2.64431	1.29946	0.14239	-2.66593	1.27979	0.08639
C	-6.19166	0.10953	-0.0098	-6.17526	0.11033	0.00768	-6.20814	0.10663	-0.0441
C	-7.40904	0.11439	-0.03042	-7.39295	0.11752	-0.01714	-7.42703	0.11688	-0.05642
C	-8.82836	0.09316	-0.05669	-8.81108	0.10238	-0.04867	-8.84486	0.09835	-0.07245
C	-9.56708	1.30429	-0.00544	-9.54343	1.31806	-0.00477	-9.58371	1.30959	-0.00105
C	-10.95581	1.24026	-0.03199	-10.93307	1.25989	-0.03783	-10.97165	1.24858	-0.01718
C	-11.64292	0.01434	-0.10879	-11.62369	0.03706	-0.11329	-11.66367	0.02456	-0.10283
C	-10.90473	-1.19632	-0.16255	-10.89168	-1.17842	-0.15857	-10.92625	-1.18581	-0.1769
C	-9.50892	-1.13619	-0.13455	-9.49617	-1.125	-0.12493	-9.53056	-1.12856	-0.15969
C	-13.11441	0.09537	-0.126	-13.0962	0.12457	-0.13903	-13.13307	0.10839	-0.10668
C	-9.53758	3.69172	0.12428	-9.50329	3.70617	0.11357	-9.54916	3.69517	0.15603
C	-10.87995	-3.58518	-0.29682	-10.87991	-3.56768	-0.28095	-10.9056	-3.57325	-0.33768
C	3.70697	-1.55927	-2.38336	3.55983	-1.33468	-2.45876	3.89339	-1.14539	-2.57556
C	4.00021	-2.29392	-3.52584	3.7881	-1.98487	-3.66559	4.26104	-1.68512	-3.80217
C	5.33669	-2.51829	-3.85421	5.1026	-2.21167	-4.06647	5.61798	-1.83815	-4.08481
C	6.32718	-1.99915	-3.02661	6.14073	-1.77892	-3.24696	6.55844	-1.44956	-3.13502
C	5.97159	-1.26709	-1.88953	5.85148	-1.12907	-2.04518	6.12959	-0.91444	-1.91706

	x	y	z	x	y	z	x	y	z
C	6.95055	-0.68083	-0.95653	6.88247	-0.63738	-1.11519	7.04295	-0.47322	-0.84636
C	8.33636	-0.79289	-1.10779	8.25601	-0.75406	-1.3404	8.43549	-0.5592	-0.92611
C	9.18022	-0.20275	-0.17186	9.15147	-0.25903	-0.39654	9.21207	-0.11295	0.13961
C	8.61851	0.49018	0.90082	8.65449	0.34466	0.75704	8.58177	0.41196	1.26756
C	7.23398	0.56731	0.99755	7.27776	0.4345	0.9261	7.19314	0.46954	1.29062
C	4.12937	1.81285	2.87442	4.28275	1.53762	2.99344	3.86735	1.356	3.09581
O	-13.90978	-0.82941	-0.18334	-13.89333	-0.7978	-0.19819	-13.93329	-0.81316	-0.16806
S	4.02942	2.70095	4.25722	4.26277	2.28636	4.42372	3.61714	2.0159	4.56021
H	5.78965	-2.29146	1.71143	5.8011	-2.40166	1.56942	5.79688	-2.56642	1.13173
H	5.07491	-4.30021	3.0035	5.08922	-4.50958	2.69538	5.117	-4.7576	2.09164
H	2.61186	-4.76153	3.24614	2.62929	-5.00376	2.87929	2.65314	-5.24195	2.36207
H	0.99377	-3.20122	2.1919	1.00579	-3.37698	1.9424	1.00609	-3.53695	1.64792
H	-0.2926	-1.70952	1.26718	-0.28433	-1.81065	1.14529	-0.29503	-1.91282	0.91191
H	-0.23828	1.88672	-1.09374	-0.23645	1.97776	-0.91014	-0.23182	2.02253	-0.863
H	1.09098	3.35666	-1.99089	1.09066	3.52604	-1.68248	1.12112	3.63874	-1.52178
H	2.75608	4.92576	-2.95474	2.75551	5.1874	-2.47368	2.82203	5.26526	-2.29084
H	5.20553	4.45272	-2.61616	5.20305	4.71035	-2.13934	5.26825	4.67262	-2.08551
H	5.86009	2.42366	-1.32372	5.86147	2.57481	-1.03359	5.87732	2.47283	-1.09892
H	-2.13896	-2.06122	-0.05227	-2.13256	-2.06657	-0.07505	-2.16968	-2.0772	-0.20018
H	-4.59718	-2.0494	-0.0755	-4.58519	-2.04954	-0.10673	-4.61796	-2.05365	-0.20442
H	-4.5816	2.25486	0.10853	-4.56794	2.25071	0.1856	-4.58407	2.24009	0.14948
H	-2.12368	2.24592	0.15827	-2.11577	2.24228	0.23885	-2.13599	2.22061	0.19795
H	-11.54678	2.14897	0.00666	-11.52018	2.17128	-0.00568	-11.56042	2.158	0.03691
H	-8.91456	-2.03973	-0.17212	-8.90551	-2.03115	-0.15649	-8.93865	-2.03297	-0.21271
H	-13.48541	1.14244	-0.07838	-13.46327	1.17299	-0.09686	-13.50095	1.15604	-0.04362
H	-8.76766	4.46227	0.17718	-8.72868	4.47187	0.16616	-8.77857	4.465	0.21174
H	-10.174	3.74928	1.01531	-10.14349	3.77181	1.0011	-10.17889	3.74335	1.05254
H	-10.1482	3.84626	-0.77322	-10.10784	3.85857	-0.78816	-10.1672	3.86098	-0.73453
H	-11.63869	-4.36636	-0.35409	-11.64313	-4.34446	-0.33722	-11.66536	-4.35335	-0.39743
H	-10.2403	-3.6309	-1.1859	-10.23703	-3.6216	-1.16718	-10.27261	-3.61032	-1.232
H	-10.27072	-3.73257	0.60246	-10.27551	-3.71345	0.62181	-10.28928	-3.73105	0.55506
H	2.68211	-1.36289	-2.09365	2.55127	-1.144	-2.11658	2.85444	-1.00344	-2.30398
H	3.19143	-2.67707	-4.1378	2.9448	-2.30192	-4.26793	3.49552	-1.97477	-4.51268
H	5.60558	-3.08706	-4.73799	5.32034	-2.71744	-5.0009	5.9433	-2.25437	-5.03232
H	7.37054	-2.16365	-3.26496	7.16808	-1.94839	-3.54218	7.61466	-1.56199	-3.34413
H	8.75527	-1.33414	-1.94703	8.62708	-1.22416	-2.24207	8.91246	-0.97023	-1.80677
H	10.25668	-0.28362	-0.28009	10.21986	-0.34498	-0.56268	10.29377	-0.17572	0.08725
H	9.23574	0.96601	1.65468	9.31297	0.74394	1.5197	9.14825	0.77104	2.11911
H	6.74584	1.0926	1.80932	6.84368	0.89574	1.80348	6.65122	0.86496	2.14107

4	S₀ (-1247.84414634 hartree)			D⁺ (-1247.6586531 hartree)			T₁ (-1247.73775431 hartree)		
	x	y	z	x	y	z	x	y	z
C	-2.39742	1.74826	-3.10194	-2.26501	1.77054	-3.27739	-2.31206	1.67374	-3.20026
C	-2.08535	0.38571	-3.18538	-1.91356	0.41731	-3.39017	-1.88334	0.34149	-3.35929
C	-1.13953	-0.17727	-2.32437	-1.00168	-0.14413	-2.50089	-0.92705	-0.18154	-2.48735
C	-0.472	0.5887	-1.35248	-0.44148	0.61933	-1.4555	-0.39848	0.58336	-1.43198
C	-0.80336	1.97037	-1.28773	-0.78028	2.00647	-1.38166	-0.81385	1.96081	-1.30798
C	-1.75574	2.53871	-2.1535	-1.69995	2.56324	-2.27754	-1.78924	2.4745	-2.19141
C	-0.08469	2.7461	-0.27163	-0.12534	2.77124	-0.31479	-0.18008	2.72889	-0.26094
C	-1.29698	0.19665	2.24391	-1.17075	0.1562	2.43606	-1.09391	0.19267	2.42843
C	-2.31027	-0.34892	3.03668	-2.14888	-0.39128	3.26135	-2.11667	-0.31459	3.23156
C	-2.63497	-1.70736	2.93622	-2.51124	-1.73943	3.12488	-2.55452	-1.63989	3.04231
C	-1.93837	-2.51109	2.03911	-1.89177	-2.54077	2.16496	-1.97568	-2.44949	2.07178
C	-0.91874	-1.96001	1.24145	-0.90612	-1.99779	1.33301	-0.9332	-1.95195	1.25857
C	-0.57248	-0.58303	1.32511	-0.55184	-0.61604	1.43105	-0.50553	-0.58123	1.41192
N	0.80961	2.031	0.4791	0.68806	2.03484	0.4993	0.74954	2.02888	0.49885
C	1.52697	2.65321	1.43731	1.36094	2.63121	1.50113	1.46456	2.67477	1.4412
C	1.39697	4.007	1.70977	1.25307	3.99251	1.75539	1.29611	4.01999	1.72242
C	0.48805	4.75457	0.9571	0.4231	4.76217	0.94029	0.33204	4.74721	0.98835
C	-0.24868	4.11949	-0.03293	-0.26495	4.14693	-0.09949	-0.39095	4.09844	0.00529
C	-0.14465	-2.74924	0.27786	-0.19263	-2.77227	0.3117	-0.24115	-2.73027	0.2569

	x	y	z	x	y	z	x	y	z
C	-0.31126	-4.12113	0.03257	-0.34231	-4.14457	0.08234	-0.45579	-4.09603	-0.02516
C	0.47953	-4.76939	-0.90587	0.40556	-4.77046	-0.90861	0.32091	-4.75589	-0.95862
C	1.44497	-4.03647	-1.60029	1.30494	-4.01477	-1.66078	1.34358	-4.04395	-1.62529
C	1.57534	-2.68363	-1.32333	1.41915	-2.65607	-1.39559	1.51494	-2.70196	-1.33071
N	0.80642	-2.04885	-0.41471	0.68851	-2.04927	-0.44165	0.74935	-2.04522	-0.43677
Ir	0.95447	-0.0099	0.03599	0.80154	-0.00821	0.0331	0.87901	-0.00924	0.03569
C	2.36271	-0.4384	1.50652	2.30793	-0.45121	1.43566	2.39215	-0.45228	1.44714
N	3.14859	-0.66385	2.35008	3.14976	-0.68157	2.21551	3.23205	-0.69018	2.22917
C	2.46221	0.39267	-1.34059	2.40808	0.41267	-1.26127	2.4894	0.41276	-1.27091
N	3.30145	0.60248	-2.13538	3.30515	0.63316	-1.98	3.38238	0.64298	-1.99422
H	-3.13251	2.18765	-3.77074	-2.97287	2.20872	-3.97446	-3.05447	2.08668	-3.87866
H	-2.58214	-0.23775	-3.92621	-2.35302	-0.1914	-4.17551	-2.29984	-0.27327	-4.15266
H	-0.91792	-1.23898	-2.41579	-0.73361	-1.19099	-2.60805	-0.59688	-1.2092	-2.61622
H	-2.00104	3.59599	-2.09443	-1.98449	3.60852	-2.20862	-2.13417	3.50054	-2.0982
H	-1.06757	1.25562	2.34703	-0.89537	1.19915	2.56134	-0.75729	1.21511	2.58026
H	-2.85035	0.28506	3.73719	-2.63163	0.22426	4.01533	-2.57756	0.30717	3.99434
H	-3.42253	-2.13322	3.55196	-3.27049	-2.16701	3.77272	-3.3489	-2.04049	3.66712
H	-2.19437	-3.56496	1.96601	-2.18552	-3.58212	2.07746	-2.3299	-3.46983	1.95405
H	2.21559	2.02389	1.98673	1.99423	1.98652	2.09714	2.18106	2.06728	1.9818
H	1.99732	4.45684	2.49282	1.81326	4.42893	2.57432	1.89541	4.48608	2.49646
H	0.35765	5.81695	1.13944	0.31586	5.82881	1.10887	0.16488	5.8013	1.18732
H	-0.95672	4.68413	-0.62799	-0.90641	4.73095	-0.74821	-1.12532	4.64373	-0.57785
H	-1.06401	-4.67423	0.58178	-1.03905	-4.71766	0.68188	-1.23664	-4.62951	0.50621
H	0.34715	-5.83064	-1.09329	0.2906	-5.83453	-1.08797	0.15027	-5.80695	-1.17026
H	2.08857	-4.49683	-2.34177	1.91327	-4.45993	-2.43966	1.98552	-4.51916	-2.35851
H	2.3066	-2.06548	-1.82856	2.10373	-2.02179	-1.94418	2.2758	-2.10589	-1.82112

5	S_0 (-1644.78272138 hartree)			D^+ (-1644.58549572 hartree)			T_1 (-1644.6782826 hartree)		
	x	y	z	x	y	z	x	y	z
C	-3.21776	-0.62229	-0.98781	-3.26776	-0.66743	-1.19114	-3.22134	-0.6068	-1.00752
C	-2.37487	-1.72845	-0.97087	-2.42961	-1.78156	-1.21437	-2.36739	-1.72948	-0.965
C	-0.99817	-1.62913	-1.12237	-1.05255	-1.67311	-1.3199	-0.98115	-1.62662	-1.10879
C	-0.39877	-0.37379	-1.30153	-0.46292	-0.39788	-1.37916	-0.37956	-0.39074	-1.3032
C	-1.23488	0.78301	-1.32471	-1.29643	0.76851	-1.39512	-1.23131	0.82209	-1.34204
C	-2.61977	0.6152	-1.16592	-2.67961	0.5877	-1.28082	-2.65617	0.62323	-1.19211
C	-0.55287	2.06661	-1.52014	-0.61308	2.05938	-1.51442	-0.58432	2.04799	-1.50942
C	1.62724	1.12827	1.40031	1.82332	1.20375	1.41854	1.63744	1.13135	1.39095
C	1.82366	0.96099	2.76471	2.06236	1.05483	2.77496	1.83315	0.96712	2.75589
C	2.24162	-0.24125	3.3253	2.44179	-0.16314	3.33806	2.24364	-0.23642	3.3192
C	2.46176	-1.29404	2.45132	2.58257	-1.25354	2.48917	2.45839	-1.29385	2.44929
C	2.28191	-1.18969	1.06278	2.36307	-1.17116	1.10935	2.27993	-1.19328	1.06027
C	1.85025	0.05846	0.52102	1.93788	0.08768	0.57069	1.85289	0.05589	0.51832
N	0.80845	1.96873	-1.65094	0.7524	1.967	-1.54977	0.85081	1.95392	-1.64254
C	1.54748	3.08049	-1.84017	1.5045	3.07484	-1.68076	1.5546	3.07072	-1.83448
C	0.98998	4.34877	-1.90524	0.94425	4.34264	-1.77454	0.98624	4.3432	-1.89532
C	-0.39344	4.47194	-1.77246	-0.44334	4.4614	-1.7355	-0.43128	4.48054	-1.74592
C	-1.16228	3.3313	-1.5814	-1.22416	3.31723	-1.60667	-1.18699	3.36013	-1.56005
C	2.50616	-2.26866	0.09505	2.51434	-2.2733	0.15542	2.50389	-2.27643	0.09571
C	2.93763	-3.57321	0.38943	2.97207	-3.56578	0.44543	2.93847	-3.57881	0.39438
C	3.11226	-4.50099	-0.62908	3.08457	-4.50778	-0.5721	3.11944	-4.5073	-0.62269
C	2.8566	-4.12366	-1.94773	2.74186	-4.15258	-1.8749	2.86762	-4.13379	-1.94313
C	2.43427	-2.82526	-2.1911	2.29365	-2.85956	-2.11395	2.44064	-2.83739	-2.18999
N	2.25893	-1.91957	-1.20765	2.17751	-1.94819	-1.13108	2.25852	-1.93275	-1.20785
Ir	1.61918	0.04393	-1.54051	1.53136	0.02435	-1.42609	1.61587	0.03991	-1.54218
F	1.60241	2.0061	3.59642	1.92761	2.11445	3.59142	1.61856	2.01534	3.58435
F	2.86975	-2.46313	3.01229	2.95006	-2.41953	3.06159	2.86008	-2.46257	3.01398
F	-2.9336	-2.94962	-0.7991	-2.99346	-2.99924	-1.13088	-2.93477	-2.94289	-0.78302
F	-3.45489	1.68769	-1.18052	-3.51502	1.64776	-1.25543	-3.4895	1.6967	-1.23531
C	3.59898	0.63309	-1.76394	3.52872	0.57548	-1.76607	3.60907	0.61303	-1.77178
N	4.71479	0.98107	-1.87464	4.6376	0.89409	-1.9605	4.72964	0.9426	-1.88469
C	1.40764	-0.14526	-3.59838	1.41901	-0.1004	-3.51926	1.39743	-0.13532	-3.61075

N	1.27555	-0.26999	-4.75828	1.36343	-0.18054	-4.68519	1.26996	-0.25817	-4.77079
H	-4.29031	-0.71467	-0.86853	-4.34311	-0.76932	-1.10824	-4.29428	-0.71537	-0.89834
H	-0.40751	-2.54011	-1.10097	-0.45481	-2.5773	-1.33787	-0.39211	-2.53838	-1.07244
H	1.30234	2.09943	1.03908	1.53537	2.17796	1.03998	1.31942	2.10166	1.02221
H	2.39044	-0.35753	4.39183	2.62433	-0.26292	4.40128	2.39214	-0.35023	4.38606
H	2.61345	2.91985	-1.9381	2.57538	2.92019	-1.71055	2.62498	2.93623	-1.94146
H	1.63084	5.21007	-2.05754	1.59073	5.20645	-1.87726	1.6274	5.2029	-2.05215
H	-0.87078	5.44606	-1.8181	-0.91816	5.43452	-1.80716	-0.89405	5.4613	-1.78121
H	-2.23405	3.40753	-1.47834	-2.30073	3.39054	-1.5801	-2.25882	3.43333	-1.44466
H	3.13233	-3.8471	1.41521	3.2386	-3.82236	1.45948	3.13133	-3.8508	1.42099
H	3.44561	-5.5073	-0.3944	3.44004	-5.50781	-0.34586	3.45527	-5.51208	-0.38513
H	2.98019	-4.81229	-2.77613	2.81756	-4.85259	-2.6989	2.99668	-4.82384	-2.76944
H	2.22215	-2.4729	-3.19235	2.0187	-2.52506	-3.10601	2.22941	-2.48717	-3.19242

14. References

1. Hue, R.; Mann, K. R.; Gladfelter, W. L., *J. Coord. Chem.* **2014**, *67*, 17-28.
2. Hush, N. S., *Prog. Inorg. Chem.* **1967**, *8*, 391-444.
3. Brunschwig, B. S.; Creutz, C.; Sutin, N., *Chem. Soc. Rev.* **2002,** *31*, 168-184.
4. D'Alessandro, D. M.; Keene, F. R., *Chem. Soc. Rev.* **2006**, *35*, 424-440.
5. Dowling, N.; Henry, P. M.; Lewis, N. A.; Taube, H., *Inorg. Chem.* **1981**, *20*, 2345-2348.
6. Wadman, S. H.; van Leeuwen, Y. M.; Havenith, R. W. A.; van Klink, G. P. M.; van Koten, G., *Organometallics* **2010**, *29*, 5635-5645.

Declaration of Originality

I certify that the work presented here is, to the best of my knowledge and belief, original and the result of my own investigations, except as acknowledged, and has not been submitted, either in part or whole, for a degree at this or any other university.

Ich erkläre, dass ich die vorliegende Arbeit selbstständig und nur unter Verwendung der angegebenen Hilfsmittel, persönlichen Mitteilungen und Quellen angefertigt habe und dass ich nicht die gleiche, eine in wesentlichen Teilen ähnliche oder eine andere Abhandlung bei einer anderen Hochschule als Dissertation eingereicht habe.

ursprüngliche Version:

Jena, 26.06.2017 Joachim Kübel

aktuelle Version:

Jena, 02.01.2018 Joachim Kübel

Curriculum Vitae

Personal information

Name	Joachim Kübel
Date of birth	April 15th 1988 in Gießen, Germany
Nationality	German
Personal status	not married

Professional experience

05/2016-present	Guest Researcher, Group of Prof. S. Westenhoff, Department of Chemistry and Molecular Biology, University of Gothenburg
06/2012–03/2016	Research fellow (doctoral candidate) IPHT Jena e.V., Ultrafast Spectroscopy group, Group of Prof. B. Dietzek (IPC, FSU Jena)

Academic education

05/2012	Graduation ("Diplom-Chemiker"), final grade 1.1
	Diploma thesis (Prof. B. Dietzek, IPC, FSU Jena) "Characterization of the Initial Photoinduced Dynamics in Conjugated Bis-Terpyridine Complexes"
09/2009-05/2010	Study abroad at McMaster University Hamilton (Ontario, Canada) via TASSEP (Trans- Atlantic Science Student Exchange Program)
08/2009	Vordiplom (B.Sc. equivalent)
04/2007-05/2012	Friedrich Schiller University Jena: Chemistry

Prior to University

2006-2007	Civil service, *Klinik und Poliklinik für Mund- Kiefer- und Gesichtschirurgie, Jena*
2006	Abitur, *Carl Zeiss Gymnasium Jena (Spezialklassen)*, grade 1.3

Teaching experience

2014-2015	Physical Chemistry V – research project supervision
2014-2015	Theoretical Chemistry I – seminar

2014	Physical Chemistry III – practicum
2013-2014	Physical Chemistry V – research project supervision
2013-2014	Physical Chemistry III – practicum (teachers)
2013	Chemistry for Biologists (teachers) – practicum/seminar
2013	Physical Chemistry II – practicum (teachers)
2012-2013	Physical Chemistry V – research project supervision

Jena, January 2, 2018 Joachim Kübel

Complete list of publications

Peer-reviewed publications

23. Kübel, J.; Wächtler, M.; Dietzek, B., Excitation Power Modulates Energy-Transfer Dynamics in a Supramolecular Ru^II-Fe^II-Ru^II Triad. *ChemPhysChem* **2017**, *18* (20), 2899-2907.

22. Dura, L.; Wächtler, M.; Kupfer, S.; Kübel, J.; Ahrens, J.; Höfler, S.; Bröring, M.; Dietzek, B.; Beweries, T., Photophysics of BODIPY Dyes as Readily-Designable Photosensitisers in Light-Driven Proton Reduction. *Inorganics* **2017**, *5* (2), 21.

21. Hartlieb, M.; Bus, T.; Kübel, J.; Pretzel, D.; Hoeppener, S.; Leiske, M. N.; Kempe, K.; Dietzek, B.; Schubert, U. S., Tailoring Cellular Uptake and Fluorescence of Poly(2-oxazoline)-Based Nanogels. *Bioconjugate Chem.* **2017**, *28* (4), 1229-1235.

20. Poocza, L.; Gottschaldt, M.; Markweg, E.; Hauptmann, N.; Hildebrand, G.; Pretzel, D.; Hartlieb, M.; Reichardt, C.; Kübel, J.; Schubert, U. S.; Mollenhauer, O.; Dietzek, B.; Liefeith, K., Optimized Photoinitiator for Fast Two-Photon Absorption Polymerization of Polyester-Macromers for Tissue Engineering. *Adv. Eng. Mater.* **2017**, **19** (3), 1600686.

19. Rommel, S. A.; Sorsche, D.; Schönweiz, S.; Kübel, J.; Rockstroh, N.; Dietzek, B.; Streb, C.; Rau, S., Visible-light sensitized photocatalytic hydrogen generation using a dual emissive heterodinuclear cyclometalated iridium(III)/ruthenium(II) complex. *J. Organomet. Chem.* **2016**, *821*, 163-170.

18. Barthelmes, K.; Jäger, M.; Kübel, J.; Friebe, C.; Winter, A.; Wächtler, M.; Dietzek, B.; Schubert, U. S., Efficient Energy Transfer and Metal Coupling in Cyanide-Bridged Heterodinuclear Complexes Based on (Bipyridine)(terpyridine)ruthenium(II) and (Phenylpyridine)iridium(III) Complexes. *Inorg. Chem.* **2016**, *55* (11), 5152-5167.

17. Schönweiz, S.; Rommel, S. A.; Kübel, J.; Micheel, M.; Dietzek, B.; Rau, S.; Streb, C., Covalent Photosensitizer–Polyoxometalate-Catalyst Dyads for Visible-Light-Driven Hydrogen Evolution. *Chem. - Eur. J.* **2016**, *22* (34), 12002-5.

16. Ho, P. C.; Szydlowski, P.; Sinclair, J.; Elder, P. J. W.; Kübel, J.; Gendy, C.; Lee, L. M.; Jenkins, H.; Britten, J. F.; Morim, D. R.; Vargas-Baca, I., Supramolecular macrocycles reversibly assembled by Te··· O chalcogen bonding. *Nat. Commun.* **2016**, *7*, 11299.

15. Happ, B.; Kübel, J.; Pfeffer, M. G.; Winter, A.; Hager, M. D.; Dietzek, B.; Rau, S.; Schubert, U. S., Towards Hydrogen Evolution Initiated by LED Light: 2-(1H-1,2,3-Triazol-4-yl)pyridine-Containing Polymers as Photocatalyst. *Macromol. Rapid Commun.* **2015**, *36* (7), 671-677.

14. Kübel, J.; Schroot, R.; Wächtler, M.; Schubert, U. S.; Dietzek, B.; Jäger, M., Photoredox–Active Dyads Based on a Ru(II) Photosensitizer Equipped with Electron Donor or Acceptor Polymer Chains: A Spectroscopic Study of Light-Induced Processes Towards Efficient Charge Separation. *J. Phys. Chem. C* **2015**, *119* (9), 4742-4751.

13. Bräutigam, M.; Kübel, J.; Schulz, M.; Vos, J. G.; Dietzek, B., Hole injection dynamics from two structurally related Ru-bipyridine complexes into NiOx is determined by the substitution pattern of the ligands. *Phys. Chem. Chem. Phys.* **2015**, *17* (12), 7823-30.

12. Barthelmes, K.; Kübel, J.; Winter, A.; Wächtler, M.; Friebe, C.; Dietzek, B.; Schubert, U. S., New Ruthenium Bis(terpyridine) Methanofullerene and Pyrrolidinofullerene Complexes: Synthesis and Electrochemical and Photophysical Properties. *Inorg. Chem.* **2015**, *54* (7), 3159-3171.

11. Rommel, S. A.; Sorsche, D.; Rockstroh, N.; Heinemann, F. W.; Kübel, J.; Wächtler, M.; Dietzek, B.; Rau, S., Protonation-Dependent Luminescence of an Iridium(III) Bibenzimidazole Chromophore. *Eur. J. Inorg. Chem.* **2015**, *2015* (22), 3730-3739.

10. Wächtler, M.; Kübel, J.; Barthelmes, K.; Winter, A.; Schmiedel, A.; Pascher, T.; Lambert, C.; Schubert, U. S.; Dietzek, B., Energy transfer and formation of long-lived 3MLCT states in multimetallic complexes coordinating extendet highly conjugated bis-terpyridyl ligands. *Phys. Chem. Chem. Phys.* **2015**, *18* (4), 2350-2360.

9. Friebe, N.; Schreiter, K.; Kübel, J.; Dietzek, B.; Moszner, N.; Burtscher, P.; Oehlke, A.; Spange, S., Fluorosolvatochromism of furanyl- and thiophenyl-substituted acetophenones. *New J. Chem.* **2015**, *39* (7), 5171-5179.

8. Habenicht, S. H.; Siegmann, M.; Kupfer, S.; Kübel, J.; Weiß, D.; Cherek, D.; Möller, U.; Dietzek, B.; Gräfe, S.; Beckert, R., And yet they glow: thiazole based push–pull fluorophores containing nitro groups and the influence of regioisomerism. *Methods Appl. Fluoresc.* **2015**, *3* (2), 025005.

7. Sinn, S.; Schulze, B.; Friebe, C.; Brown, D. G.; Jäger, M.; Kübel, J.; Dietzek, B.; Berlinguette, C. P.; Schubert, U. S., A Heteroleptic Bis(tridentate) Ruthenium(II) Platform Featuring an Anionic 1,2,3-Triazolate-Based Ligand for Application in the Dye-Sensitized Solar Cell. *Inorg. Chem.* **2014**, *53* (3), 1637-1645.

6. Kübel, J.; Winter, A.; Schubert, U. S.; Dietzek, B., Structure–Property Relationships in an Iridium(III) Bis(Terpyridine) Complex with Extended Conjugated Side chains. *J. Phys. Chem. A* **2014**, *118* (51), 12137-12148.

5. Sinn, S.; Schulze, B.; Friebe, C.; Brown, D. G.; Jäger, M.; Altuntaş, E.; Kübel, J.; Guntner, O.; Berlinguette, C. P.; Dietzek, B.; Schubert, U. S., Physicochemical Analysis of Ruthenium(II) Sensitizers of 1,2,3-Triazole-Derived Mesoionic Carbene and Cyclometalating Ligands. *Inorg. Chem.* **2014**, *53* (4), 2083-2095.

4. Breul, A. M.; Kübel, J.; Häupler, B.; Friebe, C.; Hager, M. D.; Winter, A.; Dietzek, B.; Schubert, U. S., Synthesis and Characterization of Poly(phenylacetylene)s with Ru(II) Bis-Terpyridine Complexes in the Side-Chain. *Macromol. Rapid Commun.* **2014**, *35* (7), 747-751.

3. Kübel, J.; Elder, P. J. W.; Jenkins, H. A.; Vargas-Baca, I., Structure and formation of the first (-O-Te-N-)4 ring. *Dalton Trans.* **2010**, *39* (46), 11126-11128.

2. Harb, M. K.; Apfel, U.-P.; Kübel, J.; Görls, H.; Felton, G. A. N.; Sakamoto, T.; Evans, D. H.; Glass, R. S.; Lichtenberger, D. L.; El-khateeb, M.; Weigand, W., Preparation and Characterization of Homologous Diiron Dithiolato, Diselenato, and Ditellurato Complexes: [FeFe]-Hydrogenase Models. *Organometallics* **2009**, *28* (23), 6666-6675.

1. Apfel, U.-P.; Kowol, C. R.; Halpin, Y.; Kloss, F.; Kübel, J.; Görls, H.; Vos, J. G.; Keppler, B. K.; Morera, E.; Lucente, G.; Weigand, W., Investigation of amino acid containing

[FeFe] hydrogenase models concerning pendant base effects. *J. Inorg. Biochem.* **2009**, *103* (9), 1236-1244.

Conference contributions

6. 07/2015 ***Poster presentation***. 21st International Symposium on the Photochemistry and Photophysics of Coordination Compounds, Kraków (Poland)

5. 10/2014 ***Poster presentation***. Perspect-H2O Supramolecular Photocatalytic Water Splitting COST Action CM1202, Joint Working Group Meeting of Working Groups 3 and 4, Lund (Sweden)

4. 08/2014 ***Talk***. 24th International Conference on Raman Spectroscopy (ICORS), Jena (Germany)

3. 03/2014 ***Talk & Poster presentation***. COST Young Researcher meeting and European Symposium on Current Challenges in Supramolecular Artificial Photosynthesis, Jena (Germany)

2. 02/2013 ***Poster presentation***. Perspect-H2O Supramolecular Photocatalytic Water Splitting COST CM 1202 Scientific Kickoff Meeting, Prague (Czech Republic)

1. 11/2012 ***Poster presentation***. Manfred-Eigen-Gespräche 2012, Jena (Germany)